Design and development of novel therapeutic interventions: ‘intelligent’ catalytic systems for irreversible cleavage of disease-relevant RNA

A thesis submitted to The University of Manchester for the degree of Doctor of Philosophy in the Faculty of Biology, Medicine and Health

2020

Bahareh Amirloo

School of Health Sciences

Division of Pharmacy and Optometry

Table of Contents

Final word count: 67,366

List of Figures

Chapter 1

Chapter 2

Chapter 3

Figure 3.26. Comparison of explicit and empirical models of POC catalyst activation and inactivation to explain observed velocities within Michaelis-Menten kinetics. Top row compares the model of activation (red dotted trace, explicit & dark grey trace, empirical) and inactivation (blue-dashed trace, explicit & light grey trace, empirical), whose resultants gave the active conjugate concentrations (purple thick trace, explicit & light grey dots, empirical) for three POC catalysts from left to right: (**A)** BC5-α, (**B)** BC5-L-β and (**C)** BC5-L-ββ. Middle row compares the initial reaction velocities expected from the active conjugate (yellow dashed trace, explicit and black dot trace, empirical model) with the observed initial velocities estimated from non-linear fits (dark blue-filled dots) and linear fits (light blue-filled triangles) of the reaction progress curves, from left to right: **(D)** BC5-α, **(E)** BC5-L-β and **(F)** BC5-L-ββ. Error bars are standard deviations from regression analysis of the observed and expected velocities for both the explicit (yellow) and empirical (black) fits. Bottom row compares the residuals of both fits for explicit (yellow dashed trace) and empirical (black dotted trace).

Figure 3.27. Comparison of Michaelis-Menten kinetics alone to the model of conjugate activation and inactivation for **(A)** BC5-α, **(B)** BC5-L-β and **(C)** BC5-L-ββ. Michaelis-Menten kinetics (black trace) combined with the conjugate activation and inactivation model (yellow dashed trace, explicit & grey dotted trace, empirical fits) are compared with fixed total conjugate (no activation & inactivation) as uncompetitive (red dotted trace) and competitive (green dotted trace) substrate inhibition; and with double half-substrate bound conjugate subtracted (light blue dotted trace) and additionally with uncompetitive (orange-red trace) or competitive substrate inhibition (pink dashed trace). Observed initial velocities from non-linear progress curves (blue filled dots) were used for fitting rather than observed velocities from linearized progress curves (light blue filled triangles).

Figure 3.28. Uncompetitive product inhibition for POC catalysts **(A)** BC5-α, **(B)** BC5-L-β and **(C)** BC5-L-ββ. Velocities were estimated from the non-linear fit of reaction progress curves (filled dots) and compared to velocities expected (dotted traces) from the model of active catalyst and available substrate for the estimates of uncompetitive product inhibition.

Figure 3.29. Gel-shift analysis of hybridisation of *"bis"* and *"triple*" bulge-loop inducing conjugates with 3'-FITC-tRNA^{Phe} (1 μM). (**A**) Representative images of PAGE indicating binding of conjugates to target tRNA^{Phe}. The type of conjugate and concentration (1-20 μM) are indicated at the top. (**B**) Secondary plot of data shown in (**A**).

Figure 3.30. Cleavage of 3'-FITC-tRNA^{Phe} with *"bis"* and *"triple"* conjugates at lower excess of conjugate over target. **(A-E)** Representative images of 12% PAAM/8M urea gel after electrophoresis of 3'-FITC-tRNA^{Phe} (1 μM) cleavage products with *"bis"* and *"triple"* conjugates (5 μM) as a function of incubation time. **(G-K)** Representative images of 12% PAAM/8M urea gel after electrophoresis of 3'-FITC-tRNA^{Phe} (1 μM) cleavage products with *"bis"* and *"triple"* conjugates (10 μM) as a function of incubation time. Lanes T1 and Im represent partial 3'-FITC- tRNA^{Phe} digestion with RNase T1 and imidazole, respectively. In lane C, 3'-FITC- tRNA^{Phe} was incubated without conjugates for 72 h. Positions of RNA cleavage by RNase T1 and conjugates are shown on left and right respectively. **(F)** Secondary plot of the data indicating the total cleavage extent (%) plotted against the incubation time presented in **(A-E)** (at 5 μM conjugate concentration).

Chapter 4

Chapter 5

Appendix 1

List of Tables

Chapter 1

Chapter 2

Chapter 3

Chapter 4

Appendix 1

Abbreviations

2´-OMe	2'-O-methylation
2´-MOE	2´-O-Methoxyethyl
A	Adenosine
AcCN	Acetonitrile
AGO	Argonaute
Arg	Arginine
aRNases	Artificial ribonucleases
ASO	Antisense oligonucleotide
ATP	Adenosine triphosphate
BC	Bulge conjugate
Boc	t-butyloxycarbonyl
C	Cytidine
CCND1	Cyclin D1
CO_2	Carbon dioxide
CPPs	Cell penetrating peptides
CRISPR	Clustered regularly interspaced short palindromic repeats
CTAB	Cetyltrimethylammonium bromide
Cu	Copper
CZE	Capillary Zone Electrophoresis
dA	2’-deoxyadenine
dC	2’-deoxycytidine
DCC	N,N′-Dicyclohexylcarbodiimide
DCM	Dichloromethane
DETA	Diethylenetriamine
dG	2’-deoxyguanidine
DGCR8	DiGeorge syndrome critical region 8
DIPEA	N,N-Diisopropylethylamine
DLBCL	Diffuse large B-cell lymphoma
DMAP	4-(Dimethylamine)pyridine
DMEM	Dulbecco’s Modified Eagle Medium
DMF	N,N-Dimethylformamide
DMSO	Dimethyl sulfoxide

DNA	Deoxyribonucleic acid
D_2O	Deuterium oxide
dsRNA	Double-stranded RNA
dT	2’-deoxythymidine
DTT	Dithiothreitol
DUSP2	Dual specificity protein phosphatase 2
Dy	Dysprosium
EC50	Half maximal effective concentration
EDTA	Ethylenediaminetetraacetic acid
EGTA	Ethylene glycol-bis(2-aminoethylether)-N,N,N′ or Egtazic acid
EMSA	Electrophoretic mobility shift assay
ESI	Electrospray ionisation
ESP	Electrostatic potential
Eu	Europium
FBS/ FCS	Fetal bovine serum
FC	Fragment conjugation
FDA	Food and Drug Administration
Fe	Iron
FITC	Fluorescein isothiocyanate
Fmoc	9-fluorenylmethoxycarbonyl
FRET	Förster resonance energy transfer
G	Guanosine
GAFF	General AMBER Force Field
GB	Generalised Born
GDP	guanosine diphosphate
GTFs	General transcription factors
GTP	Guanosine triphosphate
Glu	Glutamic acid
Gly	Glycine
HBTU	N,N,N′,N′-Tetramethyl-O-(1H-benzotriazol-1-yl)uronium hexafluorophosphate
HDV	Hepatitis delta virus
HF	Hydrogen fluoride
His	Histidine

HIV	Human immunodeficiency virus
HMGA2	High-mobility group AT-hook 2
HPLC	High performance liquid chromatography
HPNP	2-hydroxypropyl-p-nitrophenyl phosphate
Ifs	Initiation factors
IFN	Interferons
K_a	Association constant
K_c	Conjugate activation
K_{cat}	Catalytic turnover
K_{cc}	Conjugate complex
K_{cs}	Substrate complex
K_i	Inhibitor
K_{ic}	Competitive inhibition
K_m	Michaelis-Menten constant
K_p	Product complex
K_{ss}	Half substrate complex
Leu	Leucine
Li	Lithium
$LiClO_4$	Lithium perchlorate
LncRNA	Long non-coding ribonucleic acid
LNA	Locked nucleic acid
LoB	Limit of blank
LoD	Limit of detection
LPFC	Liquid phase fragment conjugation
Lu	Lutetium
LVR	Linear viscoelastic region
Lys	Lysine
Mal	Maleimide
MALDI-TOF	Matrix assisted laser desorption ionization time of flight
MB	Molecular beacon
MD	Molecular dynamics
Mg	Magnesium
miRNA	MicroRNA
mRNA	Messenger ribonucleic acid

MRG	Mas-related G
MS	Mass spectrometry
mTORC1	Mammalian target of rapamycin complex 1
MTS	Methane Thiosulfonate
MW	Molecular weight
ncRNA	Non-coding ribonucleic acid
NGS	Next-generation sequencing
Ni	Nickel
nm	Nanometre
NMD	Nonsense-mediated decay
NMP	Nucleotide monophosphates
NMR	Nuclear magnetic resonance
Nt	Nucleotide
ON	Oligonucleotide
ORFs	Open reading frames
OTE	Off target effect
O.U.	Optical unit
PAAM	Polyacrylamide
PAGE	Polyacrylamide gel electrophoresis
Pbf	2,2,4,6,7-Pentamethyldihydrobenzofuran-5-sulfonyl
PBS	Phosphate-buffered saline
PDCD4	Programmed Cell Death 4
Phe	Phenylalanine
piRNA	PIWI-interacting RNA
pKa	Acid dissociation constant
PM	Perfect-match
PMO	Phosphorodiamidate Morpholino oligomer
PNA	Peptide nucleic acid
POC	Peptidyl-oligonucleotide conjugate
ppm	Parts per million
pre-miRNA	Precursor miRNA
pri-miRNA	Primary miRNA
PS	Phosphorothioate
PTGS	Post-transcriptional gene silencing

Pyr	Pyridine
RESP	Restrained electrostatic potential
RC-RNase	Rana catesbeiana ribonuclease
RI	Ribonuclease inhibitor
RIG-1	Retinoic acid-inducible gene 1
RIPA	Radioimmunoprecipitation assay buffer
RISC	RNA induced silencing complex
RNA	Ribonucleic acid
RNAi	Ribonucleic acid interference
RNase	Ribonuclease
RP-HPLC	Reverse phase HPLC
rRNA	Ribosomal RNA
RT	Room temperature
RT-PCR	Reverse transcription polymerase chain reaction
SA	Simulated annealing
SD	Standard deviation
shRNAs	Short-hairpin RNA
siRNA	Small interfering ribonucleic acid
SMA	Spinal muscular atrophy
SMN1	Survival Of Motor Neuron 1,
SN2	Nucleophilic substitution, second order
snoRNA	Small nucleolar ribonucleic acid
snRNA	Small nuclear ribonucleic acid
SPFC	Solid-phase fragment conjugation
SPPS	Solid phase peptide synthesis
SSO	Splice switching oligonucleotide
ssRNA	Single-stranded RNA
TBE	Tris/Borate/EDTA
TBME	Methyl tert-butyl ether
tBu	Tert-butyl
TCEP	Tris(2-carboxyethyl)phosphine
TEM	Transmission electron microscopy
TFA	Trifluoroacetic acid
TFIIB	Transcription factor II B

TFIID	Transcription factor II D
TIPS	Triisopropylsilyl
TLRs	Toll-like receptors
Tm	Melting temperature
Tos	p-toluene sulfonyl
TRBP	Transactivation response element RNA-binding protein
tRNA	Transfer ribonucleic acid
Trp	Tryptophan
TSO	Tosyl
TSP	Trisodium phosphate
T	Thymidine
U	Uracil
UTR	Untranslated region
UV-Vis	Ultraviolet–visible spectroscopy
Vmax	Maximum velocity
VS	Varkud satellite
Zn	Zinc

Abstract

A promising alternative to small molecular drugs is based on the RNA-targeting approaches which offer the potential for absolute selectivity, improved potency and reduced toxicity. Artificial ribonucleases (ARs) have been identified as novel agents capable of recognising and destroying pathogenic RNAs, reverting cellular pathways to their '*normal*' state. However, metal-dependent ARs suffer from time-dependent leakage which can potentially lead to the destruction of non-target biopolymers and toxicity.

Peptidyl-oligonucleotide conjugates (POCs) are metal-independent ARs consisting of an amphiphilic peptide and an antisense oligonucleotide recognition motif. Recent studies have indicated that, in principle, POCs are capable of multiple catalytic turnover. Nonetheless, all designed POCs to this date have exerted cleaving properties at two extremes: (i) base-specific cleavage with high catalytic turnover or (ii) sequence-specific cleavage in the absence of catalytic turnover. Henceforth, to make POCs suitable for therapeutic application, vital changes need to be implemented in their structural design to combine an absolute sequence-specificity with multiple catalytic turnover and produce highly-specific supramolecular catalysts. In this research, "smart" POCs have been designed to achieve precise and potent knockdown of RNAs.

Firstly, a series of structurally diverse *"single"* bulge-loop inducing conjugates was designed. Comprehensive analysis of hybridisation and ribonuclease activity accompanied by dynamic molecular modelling simulations provided structural insights on how duplex-constrained cleavage occurs. Antisense recognition motifs of the conjugates were designed in such a way that a short region of the target was non-complementary upon hybridisation, forcing the target to adapt a bulge loop structure, a phenomenon which was substantiated by enzymatic probing. All type 2 conjugates were catalytically active, with the best structural candidate exhibiting up to 90% cleavage of the target $tRNA^{Phe}$. Subsequently, the next generation bulge-loop inducing *"bis"* and *"triple"* conjugates demonstrated high catalytic efficacy (up to 100% cleavage in 24 hr). The addition of multiple peptide entities augmented ribonuclease activity without diminishing hybridisation capabilities. Furthermore, catalytic turnover studies demonstrated a true supramolecular catalyst. Detailed kinetic studies indicated the presence of complex inter- and intramolecular assembles in the reaction mixture. Avoidance of such non- productive conformations would improve the turnover number of the RNA substrates and may open the translational pathway to successful therapeutics.

Ribonuclease activity in single and multiple turnover mode was preserved when the design was directed towards a biology relevant target (miR-21 and miR-17), which was monitored here using an in-house developed self-assembling peptide hydrogel-based 3D analytical device. We also discovered the ability of conjugates to recruit non-sequence specific RNase H and enhance cleavage efficiency and RNA substrate turnover number. Lastly, chemical modifications (2'OMe) were introduced in the conjugates. Complete modification of antisense recognition motif had a detrimental effect on ribonuclease activity, whereas partial modification improved hybridisation properties and catalytic activity. No statistically significant difference in serum stability was witnessed between all tested conjugates, indicating the inherent stability of the naked conjugate stemmed from the hairpin structure.

The encouraging results presented here will provide a solid ground for the development of potent, highly selective nucleic acid therapeutics.

Declaration

A portion of the data concerning catalytically inactive Type 1 *"single"* bulge-loop inducing conjugates presented in Chapter 2 was previously included in Dr Aled R. Williams's PhD thesis *"Developing a New Generation of Peptidyl-Oligonucleotide Conjugates with Desired Biocatalytic Properties"*, submitted to the University of Manchester for the degree of Doctor of Philosophy in the Faculty of Medical and Human Sciences in September 2015. However, the data presented here is a continuation and further development of that work, which ultimately led to success through the novel design of Type 2 conjugates. Gel electrophoresis data of the peptidyl-oligonucleotide conjugates were also included in Dr Yaroslav Staroseletz's PhD thesis *"Spontaneous and catalysed RNA transesterification induced by peptidyl-oligonucleotides conjugates"*, submitted for the degree of Doctor of Philosophy to the PhD panel of the Research Institute of Chemical Biology and Fundamental Medicine (Novosibirsk, Russia) in December 2019. However, this was a collaborative contribution, where the work has been substantially extended to the level of the joint manuscripts. No other portion of the work referred to in this thesis has been submitted in support of an application for another degree or qualification of this or any other university or other institute of learning.

Copyright Statement

i. The author of this thesis (including any appendices and/or schedules to this thesis) owns certain copyright or related rights in it (the "Copyright") and s/he has given The University of Manchester certain rights to use such Copyright, including for administrative purposes.

ii. Copies of this thesis, either in full or in extracts and whether in hard or electronic copy, may be made **only** in accordance with the Copyright, Designs and Patents Act 1988 (as amended) and regulations issued under it or, where appropriate, in accordance with licensing agreements which the University has from time to time. This page must form part of any such copies made.

iii. The ownership of certain Copyright, patents, designs, trademarks and other intellectual property (the "Intellectual Property") and any reproductions of copyright works in the thesis, for example graphs and tables ("Reproductions"), which may be described in this thesis, may not be owned by the author and may be owned by third parties. Such Intellectual Property and Reproductions cannot and must not be made available for use without the prior written permission of the owner(s) of the relevant Intellectual Property and/or Reproductions.

iv. Further information on the conditions under which disclosure, publication and commercialisation of this thesis, the Copyright and any Intellectual Property and/or Reproductions described in it may take place is available in the University IP Policy (see http://documents.manchester.ac.uk/DocuInfo.aspx?DocID=24420), in any relevant Thesis restriction declarations deposited in the University Library, The University Library's regulations (see http://www.library.manchester.ac.uk/about/regulations/) and in The University's policy on Presentation of Theses.

I dedicate this thesis to my mother, Susan, and my father, Rahmat, for their unconditional love and support. To my father who is not here to see this day but who will always be with me. Let every word written on these pages serve as a testament to my love for them.

"This is not the end. It is not even the beginning of the end. But it is, perhaps, the end of the beginning."

Winston Churchill

Acknowledgements

First, I would like to offer my gratitude to the President's Doctoral Scholar's Award scheme for funding my PhD. I would like to thank my supervisor, Dr Elena V. Bichenkova, without whom this thesis would not have been possible. Thank you, Elena, for accepting me with open arms into your group, for training me and for your constant help and support in every single step of this project. I would like to thank my co-supervisor Dr Harmesh Aojula for his invaluable contribution to peptide design and synthesis section of this project and his support. I am also grateful to Prof. David J. Clarke for his critical input in the project and for all the fruitful scientific discussions. I want to thank all the people who I had the pleasure of collaborating with from the Institute of Chemical Biology and Fundamental Medicine (Novosibirsk), particularly Prof. Marina A. Zenkova, Dr Yaroslav Staroseletz and Dr Olga A. Patutina.

They say it is not the journey nor the destination but the companion that matters and I was so fortunate to meet and befriend the most wonderful group of individuals during my time as a PhD student. A big thank you to Sameen, my lab buddy. We started our PhD journeys together, we laughed, we cried, and we stressed each other out, but I honestly wouldn't have been able to do it without you. Thank you for being there for me and for your friendship. To Budoor who offered nothing but support and encouragement and made everything better with her wise, composed and kind personality. I am going to miss our chats in the office. To our group, Neil, Tom and Andrew for all the laughter and good times. Thank you to all my colleagues and friends at North Manchester General Hospital and Manchester Foundation Trust for being so accommodating and supportive during these three years. It was a privilege to work alongside you as a pharmacist. To all my friends; Bushra and Megan for helping me through my first year and providing me with perspective; Nazanin and Parnian who I am truly blessed to call friends, thank you for giving me hope and believing in me; to Jenny, Ayesha, Samira and so many of my friends.

To my family, my sister, my love, my soul, my biggest cheerleader in this world and my best friend. Thank you for always being there for me, for believing in me even when I didn't believe in myself and for making everything better with your presence. I love you more than words can ever express. You are my inspiration, the one that makes me believe I can be the best version of myself.

Finally, to the two pillars of my life without whom I could not stand, my mom and dad. To my mom, my best friend, my inspiration and my moral compass. Thank you for teaching me English and for proofreading every single piece that I ever wrote. Thank you for filling our house with music, books, love and laughter. Thank you for supporting me financially, intellectually and emotionally throughout my life. Thank you for telling me that I can be whoever I wanted to be and supporting me unconditionally. Your positive energy is infectious. To my dad, the person who inspired me the most to do this degree. It breaks my heart that I do not get to share this moment with the person who would have cherished it the most. Your hard work and dedication to your patients and students inspired us to pursue a career in science. Thank you for your unconditional selfless love and for supporting us financially and emotionally. I love you dad and I will never stop trying to make you proud.

Preface

This thesis submitted to the University of Manchester for the degree of Doctor of Philosophy in the Faculty of Biology, Medicine and Health is presented in the *"Journal Format"*. The research reported here describes the design, synthesis and characterisation of peptidyl-oligonucleotide conjugates (POCs) for potent sequence-selective cleavage of biologically relevant RNA. The first chapter consists of the Introduction providing a thorough review of the relevant literature. Chapters 2, 3,4 and 5 constitute the "RESULTS & DISCUSSION" of this research, which are presented as scientific manuscripts, either published or suitable for future publication. Chapter 2 has already been submitted to Nucleic Acids Research for publishing and was accepted on 7th Sept 2020 as a full research article (Yaroslav Staroseletz, Bahareh Amirloo, Aled Williams, Alexander Lomzov, Kepa Burusco-Goni, David Clarke, Tom Brown, Marina A Zenkova and Elena Bichenkova. "Strict conformational demands of RNA cleavage in bulge-loops created by peptidyl-oligonucleotide conjugates", *Nucl. Acids Res.* (2020)). The nature of this innovative, advanced, cutting edge research required an integrated contribution from various specialist areas (i.e. chemistry, molecular biology, material sciences, kinetics and structural biology) with involvement of several expert researchers in order to provide critical mass and ensure rapid progress of this research. Through established collaborative links, a number of research groups contributed to data compilation in an effort to produce results at the level sufficient for publication in high impact factor journals to disseminate this crucial knowledge to the scientific community. Henceforth, it was our rational decision to present the collective data in the form of scientific papers. My individual contribution to each scientific paper, as well as the level of contribution of the other co-authors and collaborators have been made explicitly clear at the beginning of each Results Chapter.

Chapter 1

Introduction

1 Introduction

1.1 Search for novel pharmaceutical targets

In the past decade, there has been a reduction in the number of newly approved drugs on the market, although more money is being dedicated to research and development in pharmaceutical companies (1). With the growing need to design novel drugs, the application of proteomics and genomics have resulted in a bloom in biology-driven processes (2, 3). If we examine the array of drug targets during the history of the pharmaceutical industry, we will see that the focus has been predominately on proteins as drug targets. Numerous drugs have been designed which exert their agonistic or antagonistic effects on receptors or inhibit enzymatic activity (4).

Proteins are involved in fundamental mechanisms in the cells from communication to division; hence they are instrumental in understanding biological processes in the body (2). However, targeting proteins for drug discovery can be incredibly challenging. Not all proteins are easy to isolate and purify in an appropriate form for drug screening. Acquiring biologically active forms of protein is deemed an expensive and time-consuming step in high-throughput screening (5). Moreover, only 10-15% of the 20,000 expressed human proteins are disease-associated and even within this category, many are deemed undruggable due to the lack of distinctive cleft-like motifs rendering small-molecules ineffective by prohibiting their binding (6).

Furthermore, an overwhelming majority of DNA sequences in the human genome (>95%) are non-protein coding sequences resulting in the generation of several functional non-coding RNA (ncRNA) sequences through transcription. These functional ncRNA molecules undruggable by conventional small molecule drugs hold the promise to introduce a new avenue for drug development (7). Recent advances in the field of molecular biology have improved our understanding of nucleic acid structures and their potential as therapeutic targets. Virulent genes, DNA, DNA replication process, translation apparatus and repair mechanisms have been identified as potential drug targets (2). DNA has been recognised as a receptor for many anticancer, antibiotic and antiviral drugs (8). However, out of the two biological macromolecules, RNA is considered to be a more appealing therapeutic target. The reasons behind that will be explored in the upcoming section. Indeed, the range of druggable targets can be expanded beyond proteins to RNAs as well as the genome by RNA-based therapies. With the increasing demand to produce new drugs, the failure of current drugs to produce satisfactory results

in treating malignant tumours and the side effects associated with them, the time has come to look into other biological macromolecules (9).

1.2 RNA as a potential drug target

The central dogma of molecular biology describes the flow of genetic information during DNA replication, transcription to RNA and translation (see **Figure 1.1**). There are three classes of direct transfer of information: general, special and unknown (10). Information is transferred from DNA to RNA molecules in a process known as transcription which is part of the general transfer. RNA codons are subsequently translated into proteins and transported to their designated place of functioning (10). This is the cell's way of transferring information contained in genes to proteins which are involved in cell functions (11). Reverse transcription which is the synthesis of DNA molecule based on RNA template is mainly associated with retroviruses (12).

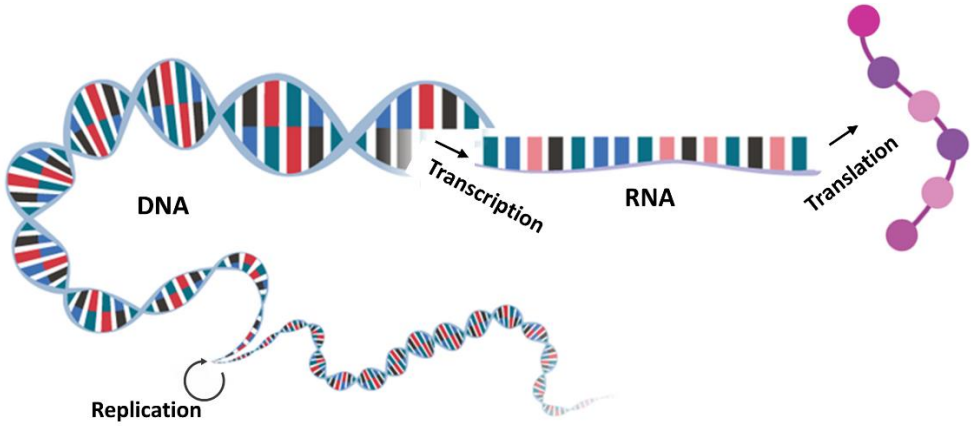

Figure 1.1. The central dogma of molecular biology and the transfer of information. Figure adapted from (13).

RNA is involved in all stages of cell life; functioning as a central conduit for the transfer of information in biological systems (14, 15). RNA is a more attractive pharmaceutical target than DNA due to several features. Structural flexibility is one of the reasons, the presence of secondary and tertiary structures make selective binding a possibility (16). RNA much like protein can have diverse three dimensional forms; it can fold into loops, bulges, turns and pseudoknots (4). RNA is easily accessible since it resides in the cytoplasm and drug molecules only have to pass the cell membrane barrier to reach RNA. Moreover, RNA, unlike DNA, lacks repair mechanisms (16). The presence of OH at the 2′ position results in the formation of a stable dianionic phosphorene which can consequently lead to the cleavage of RNA (17). By targeting RNA at the translation stage, synthesis of protein will be prohibited before it even begins, and protein production can be diminished dramatically.

In recent years, RNA has attracted a lot of attention for drug discovery in the light of advancement in RNA interference (4, 18). RNA holds the potential not to be solely seen as a tool for target validation but also as a means to develop novel therapeutics. Unlike proteins, all RNAs have equivalent solubility and their physical properties are independent of their encoding protein which makes them easy to use in assays for drug screening (5). Several drugs obtained from natural sources such as Thiostrepton have been on the market for years which either work by binding to RNA or RNA-protein complexes.

1.3 Ribonucleic acid

1.3.1 RNA function

RNA is a single-stranded polymer made of ribonucleotide units. The structure of RNA is mostly identical to DNA with two prominent changes: the sugar molecule and the presence of nucleobase uracil. There are 4 types of ribonucleotides in RNA all containing sugar molecule ribose and either one of the 4 bases; adenine (A), guanine (G), cytosine (C) and uracil (U) (19). New studies corroborate the ever-expanding role that RNA plays in cells. The role RNA plays ranging from providing physical scaffolds for protein complexes to catalysing chemical reactions and regulating DNA replication, RNA transcription and protein translation is a testament to the multifaceted functions of RNA. The key to the multifarious role of RNA lies in the diversity of RNA. RNA classes differ in size, chemical modification, structure and sequence (20). Different classes of RNA and their role will be explored in more detail in the upcoming sections.

1.3.2 RNA classes and their function

1.3.2.1 mRNA

Since the discovery of DNA structure over half a century ago by Watson and Crick, mRNAs have been the cornerstone of molecular biology. mRNA is produced from the transcription of genome-encoded information and is subsequently translated into functional proteins. Translation is a highly regulated process with controls in place at initiation, elongation and termination level (20). In the initiation phase, binding of the transcription factors to the promoter (5´) region of DNA molecules results in the recruitment of RNA polymerases and initiation of transcription. TFIIB, TFIID are examples of the general transcription factors (GTFs) necessary to recruit RNA polymerase II (12). A repeated sequence of A and T bases known as TATA exists 25 bases upstream from the start of transcription site which is recognised by TFIID (21).

Upon binding to the TATA box, TFIID recruits other GTFs and RNA polymerase II protein complex. Helicase associated with TFIIH unwinds the DNA molecule. One strand of the helix is enclosed in the polymerase groove and will be the template for the new RNA molecule (12). Throughout the elongation phase, RNA polymerase slides through the DNA molecule adding one nucleotide at the time to the 3´ end of the chain (19, 22). Upon reaching transcription terminators and polyadenylation of the 3´-end of RNA chain, the transcription comes to a halt (22). However, the mRNA molecule needs to undergo post-transcriptional processes. Three main post-transcription changes are 5′ capping, 3′ polyadenylation and splicing (23). One of the first processes occurring following initiation of the synthesis of mRNA is the addition of 5´ cap through 7-methylguanosine. Capping protects the ever-growing mRNA molecule from degradation. Poly(A) polymerase synthesises the addition of a long tail of adenine bases to mRNA molecule. Recognition of AAUAAA sequence residing 10-25 bases upstream of the addition site for polyadenylation is vital for this process (24). This poly A tail is crucial to the export of the molecule from the nucleus to the cytoplasm (12, 25). Post-transcriptional mRNA contains coded regions capable of being translated to proteins also known as exons as well as untranslated regions (UTR). Untranslated regions consist of 5´ UTR and 3´ UTR at both ends of mRNA as well as introns (12). Through splicing, introns are spliced out while exons remain in between 5´ and 3´ UTR. The mature mRNA leaves the nucleus through the pores and is translated in the cytoplasm (19).

Mature mRNA molecules are translated to proteins in the cytoplasm (26). Ribosomes provide the protein factors within the cytoplasm. Ribosomes are made of two small (30S) and large subunits (50S) each made of rRNA (2/3 of their weight) and proteins (26, 27). The small subunit of ribosome provides a framework for tRNA and binds mRNA whilst the large subunit catalyses amino acid binding, contributing to the production of the polypeptide (28). Three binding sites constitute tRNA: A-site (amino acid), P-site (polypeptide) and E-site (exit) (26).

In the initiation state of translation, small ribosomal subunit containing tRNA-M complex on its P-site along with other initiation factors (IFs) are loaded onto the 5´ end of mRNA molecule aligning the A-site to the second mRNA codon (25, 29). Upon recognition of initiation codon (AUG) by tRNA, the large ribosomal subunit is loaded. The next set of codons will occupy the A-site of the ribosome and will form a bond with the matching tRNA containing the corresponding amino acid (19, 25) (see **Figure 1.2**). The large subunit will then form a bond between the two amino acids in the P and A site and will

subsequently release the tRNA molecule. With the movement of the ribosome from 5´ to 3´ direction and positioning of tRNA molecules at E and P sites of the ribosome, the A-site is free to take another complementary tRNA (30). A polypeptide is synthesised by the addition of amino acids from amino to carboxy terminus (31). Conversion of guanosine triphosphate (GTP) to guanosine diphosphate (GDP) provides the energy for the mechanism (26). Translocation will continue in the same manner until any of the three known stop codons UAA, UAG and UGA reside in the A-site. The stop codon results in the dissociation of the protein chain from tRNA, leading to the consequent disassembly of ribosomal subunits, tRNA and release factors (32).

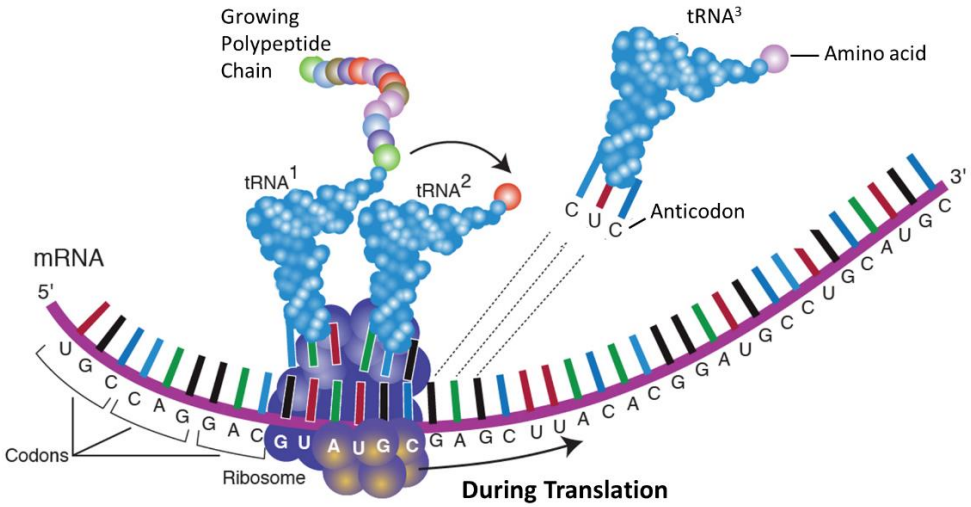

Figure 1.2. Elongation step of mRNA translation. In this step the loaded ribosome slides through mRNA molecule until it reaches the stop codon. The existing polypeptide chain is linked to the amino acid on the tRNA. The mRNA is then shifted by one codon in ribosome, resulting in the positioning of tRNAs at E and P-sites where a free A-site can take up another tRNA-amino acid complex. The incoming tRNA molecule contains an anticodon sequence at one end and carries a particular amino acid specified by the codon at the other end. Figure adapted from (33).

Recent discoveries have highlighted the importance of mRNA as a therapeutic target in cancer. Deregulation of post-transcriptional mechanisms and generation of cancer-specific mRNA through abnormal processing has been linked to cancer. These cancer-specific mRNA molecules alter the expression of normal proteins and generate proteins with new functions, capable of activating oncogenes or deactivating tumour-suppressor genes (34). Several strategies have been devised to target mRNA translation through impeding translocation, impairing peptidyl transferase function and interfering with tRNA binding or accommodation. However, nonspecific toxicity witnessed owing to global blockage of protein synthesis has limited the therapeutic value of elongation inhibitors (35). Contrarily, such compounds hold the potential to be used as antineoplastics where destruction of all cellular RNA would be desirable (36). An

effective, versatile and promising alternative is antisense-mediated RNA targeting which will be explored in detail later on.

1.3.2.2 ncRNA

Long and short ncRNA molecules are involved in regulating gene expression post and pre transcription by modulating chromatin modification and affecting mRNA stability and translation process (37). The most well-known non-coding RNAs are tRNAs, rRNAs as well as snRNAs and snoRNAs (38). The pivotal role of ncRNA, tRNA and rRNA in protein synthesis was established long before the discovery of new classes of ncRNAs (14). Although non-coding RNAs exhibit considerable variation in size, they can be divided into two main groups: long ncRNAs (lncRNAs) and small ncRNAs (<200 nt) (39). LncRNAs are involved in a multitude of processes within the cell such as chromatin remodelling, post-transcriptional processing and transcriptional control (39).

1.3.2.2.1 lncRNA

Long non-coding RNAs comprise over 60 % of non-coding RNAs within the human genome (40). They contain fewer exons and are shorter than mRNA molecules. Even though these molecules are longer than 2kb in length, they have an inconsiderable coding potential (less than 100 amino acids). These big molecules are capable of binding to DNA and RNA and forming triplex/duplex regulatory complexes. Lack of translation capabilities is the direct consequence of ATG start codon displacement and absence of functional open reading frames (ORFs) (41). New genome-wide studies have indicated lncRNAs as nonsense-mediated decay (NMD) substrates (42).

Dysregulation and mutation in lncRNA have been associated with numerous pathogenesis. Dysregulation of lncRNA has particularly been correlated with breast, colorectal and liver cancer as well as glioblastoma and leukaemia (43). lncRNAs influence chromatin remodelling and interactions through recruitment of protein complexes. lncRNAs interact directly with nucleosome-remodelling factors and chromatin-modifying enzymes and control chromatin structure. They influence cancer pathogenesis through the promotion of metastasis, induction of angiogenesis, resistance to apoptosis and tumour suppressors (42, 44–48).

1.3.2.2.2 Small ncRNA

MicroRNAs (miRNAs): MicroRNAs were first discovered in *Nematode elegans*. miRNAs are 22-26 nucleotide long molecules derived from both exonic and intronic regions of transcribed RNA (49, 50). miRNA along with piwi-interacting RNAs are involved in gene regulation. They exert their function in the cytoplasm. The majority of miRNAs studied, inhibit translation by binding to target mRNAs through the pairing of a small number of nucleotides known as "miRNA seed" sequence. They can also impose degradation through RISC complexes or decrease stability halting translation processes (51, 52). It is believed that miRNAs control over half of the protein-coding genes in humans.

PIWI-interacting RNA (Piwi RNA or piRNA): These small RNAs are 26-31 nucleotides long. They are associated with PIWI proteins which are a subfamily of Argonaute proteins capable of forming effector complexes (48, 53). These riboprotein complexes repress transposons and ultimately maintain germline genome integrity. In mammalian cells, piRNAs play a pivotal role in embryonic development and can contribute to cellular processes for generations (53).

Small interfering RNAs (siRNAs): Small interfering RNAs (siRNA) inhibit transcription through incorporation into RNA-induced silencing complex **(**RISC). RISC functions as the driving force and the incorporated strand guides and directs the complex through post-transcriptional gene silencing. Production of siRNAs is comparable to miRNAs; the dissimilarity lies with their mechanisms of repression (54). siRNAs play a significant role in gene regulation, viral defence and transposon activity (55).

Small nucleolar RNAs (snoRNAs): Small nucleolar RNAs are 60 to 300 nucleotides in length. They are involved in the modification of target RNAs through base-pairing (56). They are generated from mRNA intron splicing. Most recent discoveries point to the involvement of snoRNAs in the modification of snRNAs and mRNAs (38).

Small nuclear RNAs (snRNAs): Small nuclear RNAs are a subcategory of small regulatory RNAs involved in gene splicing (11). They are transcribed by RNA polymerase II or III and are involved in the removal of introns from post-transcriptional mRNAs.

1.3.3 MicroRNA

MicroRNAs (miRNAs, miRs) were first discovered over 20 years ago. It was Victor Ambros in 1993 who first discovered miRNAs whilst studying the Lin-14 gene in *Caenorhabditis elegans* (57). He observed that the Lin-4 encodes a regulatory protein which upon binding prevents translation (58). Later, many more small RNA molecules were discovered with similar functions. miRNAs play a principal role in physiological and pathological processes within the cell (59). They are small single-stranded RNA molecules which are approximately 20 to 25 nucleotides long. They exert their effects through sequence-specific hybridisation of 3´ position of the untranslated region (UTR) of messenger RNAs (58). Hybridisation results in either blockage of translation or degradation of target mRNA. A single strand of miRNA is capable of regulating multiple mRNA molecules since complete complementary binding is not required. miRNAs act as regulators in numerous diseases (58). Before exploring the function and rudimentary role miRNAs play in cancer and other diseases, it is important to first focus on biogenesis.

1.3.3.1 Biogenesis of miRNA and function

RNA polymerase II promoters are transcribed into miRNA genes and processed through canonical or non-canonical biogenesis pathway to mature miRNAs. The first intermediate transcript is the primary miRNA which undergoes capping and polyadenylation like mRNA molecules (60). During canonical pathway, RNase III domain-containing protein termed Drosha digests the primary miRNA (pri-miRNA) into precursor miRNA (pre-miRNA). However, in the non-canonical pathway, splicing machineries produce pre-miRNAs (60). Afterwards, nuclear pore complexes export the pre-miRNA out of the nucleus and into the cytoplasm in both pathways (61). In the cytoplasm, pre-miRNA is then processed by RNase III protein Dicer to form a mature double-stranded miRNA (62). Dicer is comprised of an N-terminal ATPase/ Helicase domain, DUF283, PAZ domain, RNase IIIa and RNase IIIb (63). The newly formed miRNA molecule is then loaded into the RNA-induced silencing complex (RISC) (64). One of the pivotal components of RISC is argonaute proteins which exert catalytic activity. These proteins unwind the miRNA duplex and a single strand of miRNA gets incorporated into RISC (60).

miRNA biogenesis process is tightly controlled by transcriptional regulators since the majority of the transcribing genes lies within intrinsic regions. It is these very same transcriptional regulators which control the differentiation of miRNA molecules amongst different tissues and cell types (65). RNA binding proteins like DiGeorge syndrome

critical region 8 (DGCR8) and TAR RNA-binding protein 2 (TRBP) are involved in stabilisation and regulation of Dicer and Drosha regulated DGCR8 expression (66). It is believed that miRNA exerts its effects through different mechanisms including mRNA destabilisation and decay. Whether mRNA targeting results in cleavage or repression depends on the degree of complementarity between miRNA and mRNA. Formation of mismatches and bulges result in repression whereas total complementarity results in cleavage of mRNA strand (67). The main mode of action of miRNA in mammalian cells is destabilisation of mRNA through P-body proteins. A summary of miRNA biogenesis is provided in **Figure 1.3**.

Knowledge about the role miRNA plays in disease management is rapidly accumulating. miRNA molecules are involved in several critical biological processes. Hence, altered expression or function of these molecules can be a direct or indirect causative agent in human diseases. In diseases where miRNA expression has been reduced, the re-introduction of the molecule can restore the balance. In case of increased expression, anti-miRs can inhibit miRNA function and restore normal gene regulation (68). Both inhibitors and mimics of miRNAs are being developed which will be explored in more detail in the upcoming section.

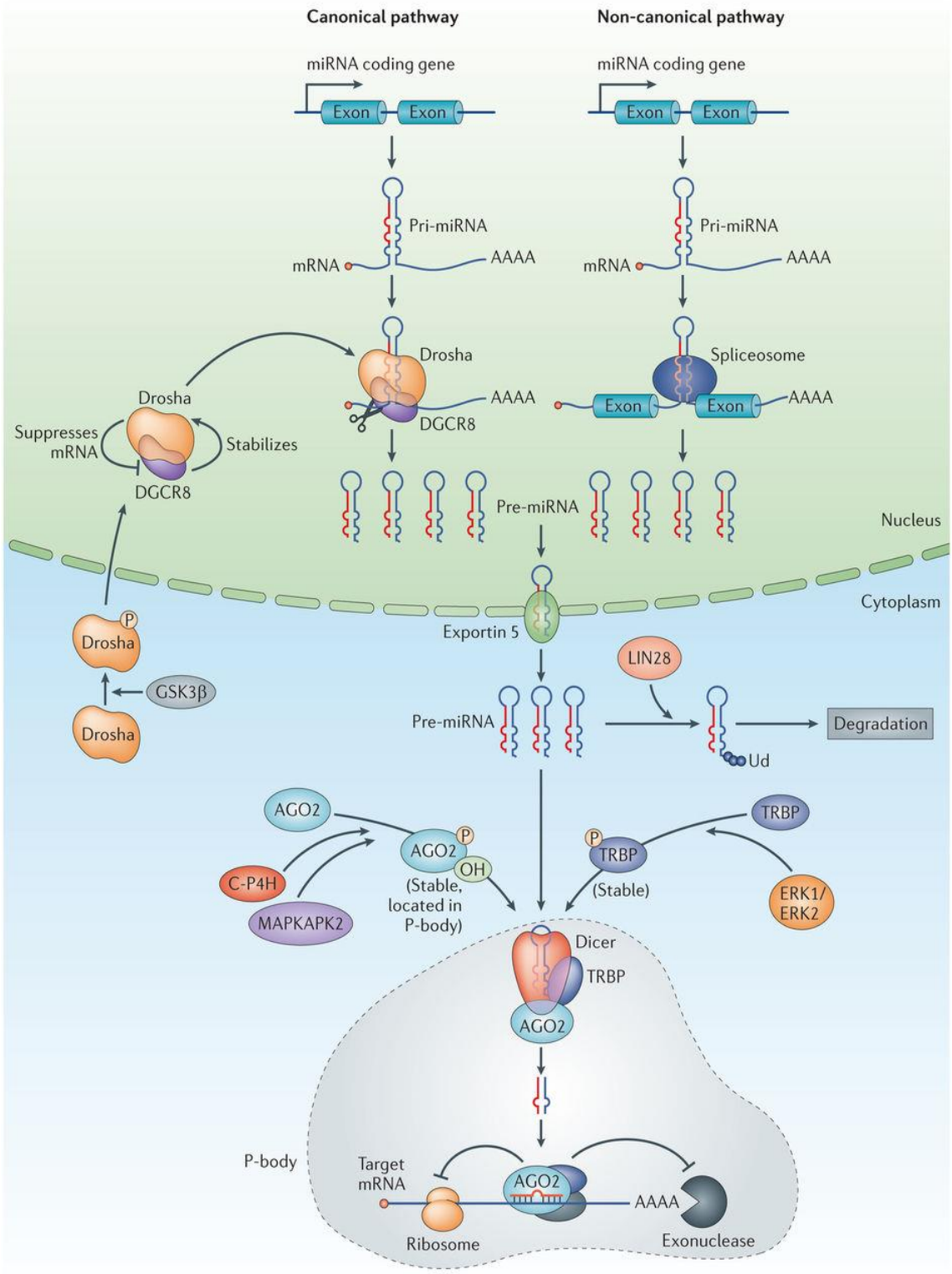

Figure 1.3. Canonical and non-canonical biogenesis pathway of miRNA. In the canonical pathway, primary miRNA is produced by RNA polymerase II which is subsequently processed by Drosha-DGCR8. Thereafter, exportin 5 transfers pre-miRNA molecule into the cytoplasm leading to further processing and loading on to RISC. miRNA can also be produced through spliceosome-dependent mechanisms and other non-canonical methods. Figure taken with permission from (65).

1.3.3.2 Significance in human ailments

miRNA has been deemed as a major negative regulator of gene expression. miRNAs are involved in the regulation of nearly all signalling circuits and one-third of the human genes (69). There have been strong links between miRNA deregulation and every step of tumour biology indicating the key pathophysiological role of miRNA in tumour development and cancer detection. Consequently, miRNAs play a pivotal role in the pathogenesis of cancer, neurodegenerative diseases, autoimmune disorders and cardiovascular illnesses (70–72). One of the most studied miRNAs in human cancers is miR-21, commonly upregulated in solid and haematological malignancies where overexpression has been linked to colorectal (73), breast (74), lung (75), liver (76), oesophageal (77), prostate (77) and endometrial cancers (78). Additionally, recent studies have highlighted the potential role that miRNAs play in regulation of haematopoiesis and T cell differentiation. Hence, high levels of miR-21 have been regarded as a marker for immune cell activation. A significant increase in miR-21 expression has been witnessed upon maturation of various hematopoietic progenitors into “active” state. Numerous positive results have been obtained as a result of the inhibition of miR-21 in cancerous cells. For example, knockdown of miR-21 in cultured glioblastoma cells resulted in an increase in apoptotic cell death as a result of activation of caspases (79). Furthermore, an increase in tumour suppressor phosphatase and tensin homologue was witnessed as a result of miR-21 knockdown in hepatoma cells leading to reduced migration, invasion and cell proliferation (80). A positive correlation has been established between increased level of miR-200a, miR-200b, miR-200c, miR-210, miR-215 and miR-486 and the onset of metastasis and poor prognosis up to two years prior to clinical diagnosis in breast cancer patients (81). A surge of 2 to 2.5 fold has been witnessed in miR-155, miR-21 and miR-210 levels in patients with diffuse large B-cell lymphoma (DLBCL) (82). High levels of miR-155 and miR-21 have been associated with poor prognosis in lung and colonic cancers (83).

A series of studies have investigated the pathogenic role of miRNA in a variety of cancers (84, 85) and have unlocked miRNA potential in diagnosis, prognosis and therapeutics. Up and down-regulation of miRNA has been associated with numerous cancers acting as oncogenes and tumour-suppressors respectively regulating angiogenesis, apoptosis, cell proliferation, differentiation, and various other hallmarks of cancer (see **Figure 1.4**). Moreover, the stability of miRNA allows isolation and measurement from tissues and body fluids boosting their potential as non-invasive diagnostic and prognostic

biomarkers. The exact mechanism underlying the stability of extracellular miRNA is not well understood but several hypotheses have been postulated suggesting lipid or protein conjugation and association of membrane vesicles as protecting factors against RNase activity. Circulating cell-free miRNA molecules have been found in plasma, platelets, leukocytes and erythrocytes as well as various other biological fluids such as serum, urine, cerebrospinal fluids and saliva. These circulating miRNAs can not only be used as prognostic biomarkers but also as indicators of therapeutic efficacy (86). Recently, miRNA expression was used as a diagnostic panel to distinguish healthy subjects from those with pancreatic cancer (87). Significant changes in miRNA molecules result in the presence of specific miRNA signatures in cancerous cells known as miRNome. miRNome defines the characteristics that distinguish malignant from normal cells such as grade, age, sex, aggressiveness, proliferation capacity and vascular invasion (88).

The diversity of neoplastic diseases can be explained through the six hallmarks of cancer. miRNAs affect all six hallmarks of cancer (see **Figure 1.4**) (89). Corresponding miRNAs correlating to each underlying principle are:

1. Self-sufficiency in growth signals (let-7 family)
2. Insensitivity to antigrowth signals (miRNA-17/19 cluster)
3. Evasion of apoptosis (miRNA-34a)
4. Limitless replicative potential (miRNA-372/373 cluster)
5. Angiogenesis (miRNA-210)
6. Invasion and metastasis (miRNA-10b)

Despite intense research in the past 10 years, the pathogenesis of prevalent neurodegenerative diseases like Alzheimer's is still unclear (90). Nevertheless, a link between miRNAs and neurodegenerative diseases has been established. Dysregulation of several miRNA molecules can contribute to the development of neurodegenerative diseases (91). In Parkinson disease, a fundamental transcription factor Pix3 involved in the conservation of dopaminergic neurons is targeted by miR-133b (92). New reports are indicative of the possible contribution of miRNAs to the development of Huntington (93). Downregulation of miR-9/9*, miR-124 and miR-29b and upregulation of miR-132 and miR-29a have been observed in brains of patients diagnosed with Huntington (94–96). Deregulation of eight miRNA families have been witnessed in human samples of Alzheimer's disease patients: miR-15, miR-146, miR-29, miR-107, miR-106, miR-9, miR 212/132, miR-101. Deregulation of miR-22 and miR-132 has been associated with Alzheimer's, Parkinson, Huntington and other neurological conditions (62).

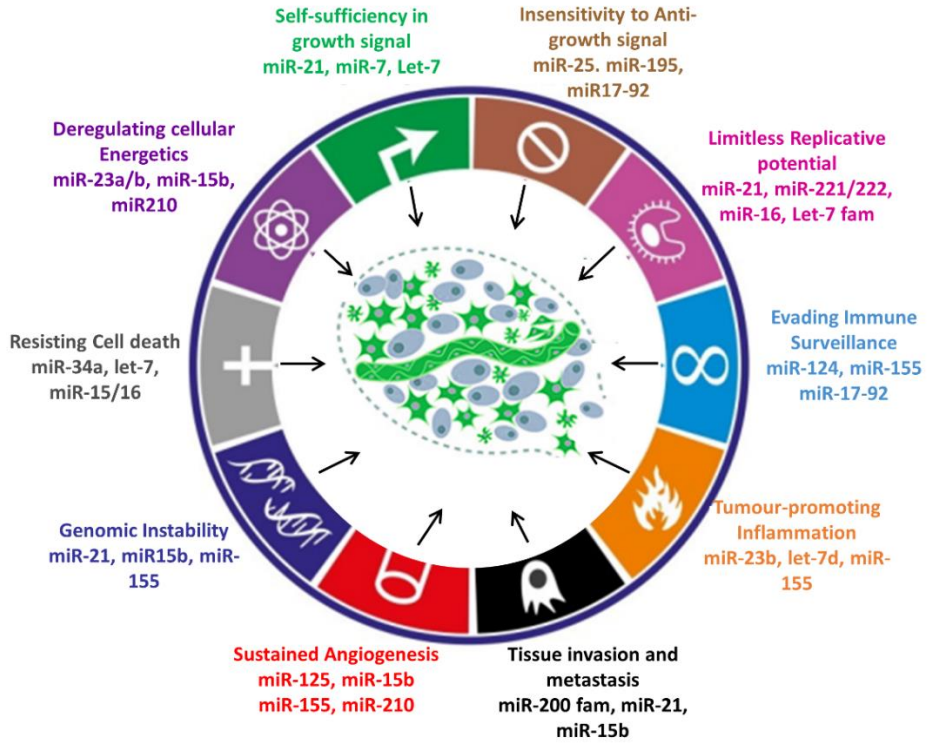

Figure 1.4. Example of different miRNAs influencing cancer hallmarks. Figure adapted from (84).

1.3.3.3 miRNA Therapeutics

The manifold role of miRNA in biological processes and the established link between miRNA deregulation and numerous human ailments have resulted in bloom in miRNA targeting therapeutics research. The potential therapeutic implication of miRNAs can be employed via two main strategies: inhibition of miRNAs using antagonists (such as anti-miRs, locked nucleic acids) and miRNA replacement (97, 98). **Figure 1.5** outlines the strategies based on inhibition and replacement of miRNA.

Suppression of miRNA activity can be achieved via anti-miRs (also known as miRNA inhibitors), which are chemically modified single-stranded oligonucleotides capable of binding to exogenous miRNAs. Binding of anti-miRNA oligonucleotides to the sense strand of miRISC complex impedes the interaction between miRISC and target mRNA thus increasing mRNA expression level. Chemical modifications have been employed in the structure of anti-miRNA oligonucleotides to enhance affinity and promote serum stability. Chemical modifications employed to encourage resistant to nucleases and lower toxicity will be explored in **Section 1.4.1.** Antagomirs contain numerous chemical modifications (2'-methoxy groups in full-length chain, 3'-end cholesterol conjugate, 2-Phosphorothioates and 4-phosphorothioates introduced at 5' and 3' end respectively) boosting their cellular uptake and stability, augmenting their use *in vivo* for

downregulation of miRNA levels (99, 100). Anti-miRNAs are mostly used *in vitro* in conjunction with common transfection reagents such as lipofectamine where they specifically bind to endogenous miRNA and abolish their activity. One effective antisense-based anti-miRNA therapy which has successfully progressed to clinical trials is Miravirsen, an LNA-modified anti-miR-122 designed to combat the hepatitis C virus (101). Encouraging results obtained from Miravirsen phase IIa clinical trials indicated a dose-dependent antiviral activity where stable seroconversion was achieved in several patients. More recently an LNA anti-miR of miRNA-155 MRG-106 progressed to phase I clinical trials in hopes of reducing the proliferation of lymphoma cells (102).

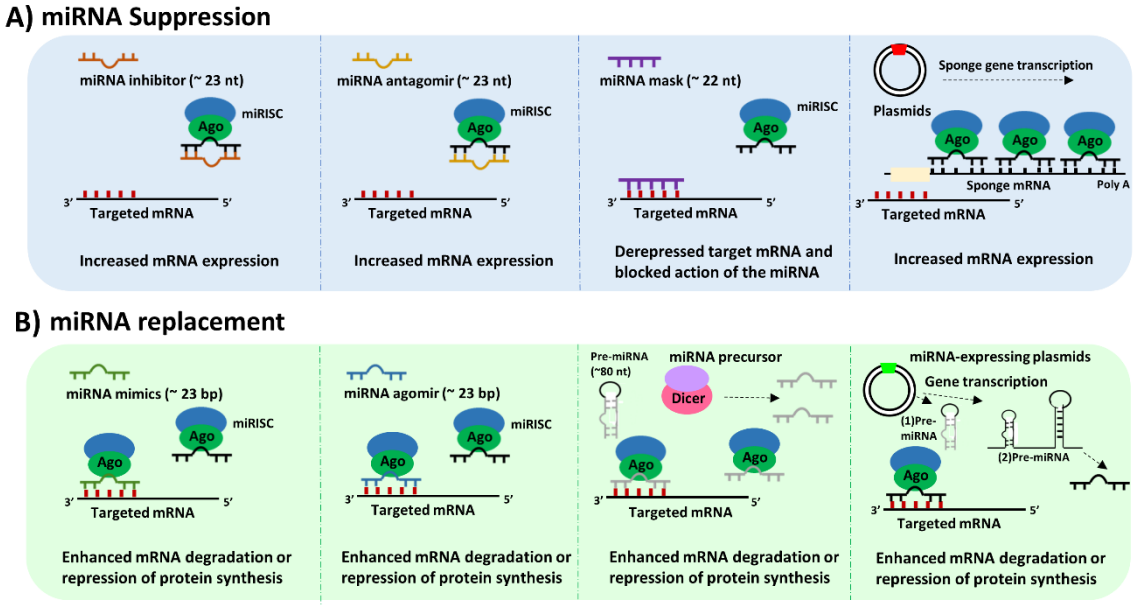

Figure 1.5. miRNA-based therapy. miRNA therapy is categorised to two general types: miRNA suppression therapy (**A**) where the expression of oncomiRs is suppressed as a result of treatment and miRNA replacement therapy (**B**) which restores miRNA levels in tumour cells. (**A)** Range of miRNA suppression therapy using miRNA inhibitors, miRNA antagomirs, miRNA masks and miRNA sponges have been outlined. (**B)** A range of miRNA replacement strategies using miRNA mimics, miRNA agomir, miRNA precursor and miRNA-expressing plasmids have been outlined. Figure adapted from (103).

miRNA sponges which contain multiple seed sites acting as competitive inhibitors, sequester deleterious miRNA, ultimately blocking natural miRNA or disinhibiting signalling pathways allowing the expression of target mRNA (102). In miRNA sponges, transfected plasmids in cells transcribe high level of sponge RNAs containing tandem-binding sites leading to the blockage of miRNA family encompassing the same seed sequence. miRNA masks are 2'-O-methyl modified single-stranded oligonucleotides fully complementary to the predicted binding sites of miRNAs localised in the 3'-UTR region of the target mRNA (104). They reduce the activity of endogenous miRNAs through competitive inhibition (58).

miRNA mimics, agomirs, precursors and expressing plasmids are several miRNA replacement interventions reported to this day. As the name suggests, miRNA mimics are RNA molecules resembling miRNA which can simulate endogenous miRNAs evoking post-transcriptional repression (103). miRNA agomirs similar to antagomirs contain chemical modifications, comparable to miRNA mimics in function but far more superior than them in stability and degree of activity (103). miRNA precursors (pre-miRNAs) can be transfected into cells where they can be cleaved by the Dicer enzyme and transformed to mature miRNAs resulting in down-regulation of the corresponding mRNA. Upregulation of miRNA can also be achieved through miRNA-expressing plasmids carrying a reporter group to accurately verify the expression and localisation of miRNA (103).

Likewise, small molecules such as azobenzene have been identified through a reporter-based assay system by screening a compound library capable of inhibiting miRNA expression (105). The majority of these compounds exert their function through transcriptional regulation of targeted miRNAs. The lack of information on direct targets as well as high EC50 values limits the therapeutic potential of these compounds.

Despite the current advances, miRNA-base therapy is a long way away from becoming a safe and reliable alternative therapy in modern medicine. A number of problems such as designing a delivery vehicle enabling cell-specific uptake, off-target toxic effects and immunological activation remain the major drawbacks prohibiting the transition of miRNA-based therapies to the clinic (106).

1.4 Targeting RNA

Designing functional molecules capable of imposing changes in the three-dimensional nucleic acid structure of RNA is a possible way of targeting RNA (107). Over the past decade, development in biotechnology and improvement in molecular chemistry have resulted in the identification of three main approaches for targeting mRNA for gene silencing:

- Antisense oligonucleotides
- Ribozymes
- RNA interference and small interfering RNAs

RNA interference and antisense oligonucleotides regulate specific mRNA molecules and their corresponding proteins without altering endogenous protein expression (108). In the upcoming sections, we will focus on each approach and explore the advantages and disadvantages associated with each method.

1.4.1 Antisense oligonucleotide

Advances in sequencing human genome, ease of design and cost-saving benefits have led to the utilisation of oligonucleotides as therapeutic agents (109). The concept of antisense oligonucleotides was first reported by Stephenson and Zamecnik back in 1978 (110). In their publication, they reported cell transformation and inhibition of replication in respiratory syncytial virus via synthesis of a 13-nucleotide long DNA molecule complementary to the virus genome. They discussed the potential RNA targeting capabilities of oligonucleotides and the possible mechanisms of action (110, 111). Antisense oligonucleotides (ASO) are a short single strand of 13-25 deoxyribonucleotides capable of hybridising through Watson-Crick base pairing with complementary mRNA sequences. The strength of hydrogen bond is dependent on the proximity of the two molecules (109), the secondary structure of target mRNA and thermodynamic stability (112). The heteroduplex of ASO-mRNA inhibits gene expression through several different mechanisms depending on the location of hybridisation and the compositions of ASO (113). The mechanisms by which ASOs suppress gene expression are manifolds and can be broadly categorised into RNase H dependent degradation of target RNA and steric hindrance of target mRNA. Recruitment of RNase H is dependent on the nature of oligomer chemistry and compatibility of chemical modification where certain chemical modifications such as 2'-modifications hinder RNase H recruitment (114). Protein knockdown is achieved through steric hindrance of ribosomal activity leading to translational arrest (112). Other mechanisms of actions are interference with mRNA maturation either through destabilisation of pre-mRNA or splicing inhibition in the nucleus and RNase H activity, leading to downregulation of the desired protein (115, 116). Activation of endonuclease enzyme RNase H results in cleavage of RNA-DNA substrate and the consecutive degradation of target mRNA (112). RNase H independent ASOs on the other hand, prohibit binding of ribosomal initiation complex, blocking mRNA translation and protein biosynthesis (117). RNase H is a family of non-sequence specific enzymes capable of hydrolysing the RNA strand in the RNA-DNA substrate. They can be employed to modify mutant proteins and reduce the expression of toxic proteins (111). **Figure 1.6** summarises the key approaches behind the ASO concept.

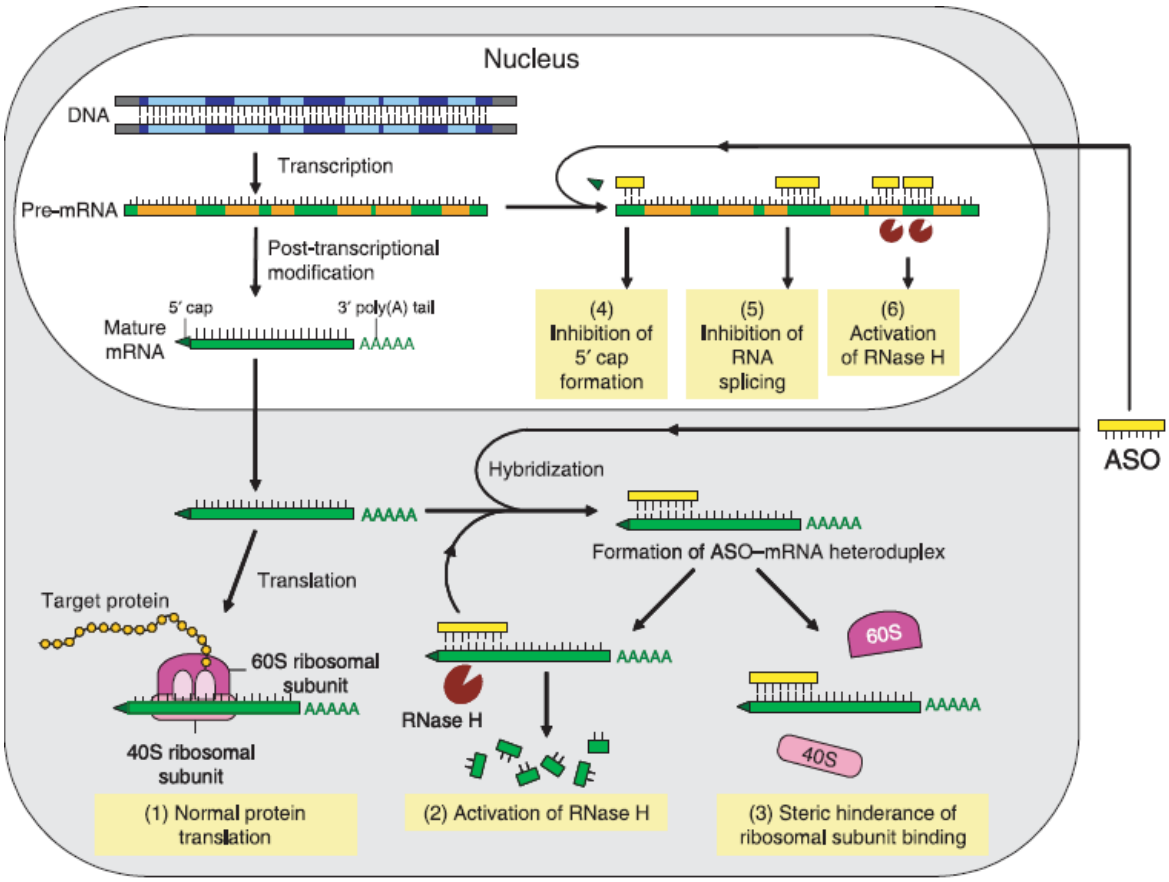

Figure 1.6. Antisense oligonucleotide mode of action. ASO taken by the cellular endocytosis hybridises mRNA molecules in the cytoplasm. ASO-mRNA complex activates RNase H resulting in selective degradation of mRNA (**2**). It can also sterically hinder the assembly of ribosomal subunits (**3**). Both routes result in protein knockdown. If ASO is taken by nucleus then it can regulate post-transcriptional modification through inhibition of 5′ capping (**4**), inhibition of splicing (**5**) and RNase H activation (**6**). The figure is taken with permission from (112).

In disorders derived from splicing defects, modulation of splicing through destabilisation of splicing sites or displacement of splicing factors can result in re-establishment of normal reading frame and restoration of normal gene function (111). One such example is Nusinersen, an FDA approved ASO designed to promote inclusion of exon 7 in the Survival Motor Neuron (SMN1) gene for the treatment of Spinal Muscular Atrophy (SMA) (118).

Despite being discovered over two decades ago, the progression of antisense oligonucleotides into the clinic has been hampered by off-target effects, toxicity, poor cellular uptake and inadequate target engagement. The intact ASOs are vulnerable to degradation via intracellular endonucleases and exonucleases. They possess ionic charges, therefore, face difficulty crossing plasma membrane (109). Hence, numerous modification strategies have been proposed to increase biostability of ASOs, prolong tissue half-life, increase cellular uptake, reduce nuclease cleavage, increase potency and

affinity and reduce off-target effects and toxicity (112). A summary of the reported conformational modifications can be seen in **Figure 1.7**.

First-generation antisense oligonucleotide:

The first generation ASOs contain a phosphorothioate (PS)-modified backbone since one of the non-bridging oxygen atoms in the phosphodiester bond is replaced with a sulphur atom or a methyl group (119). Despite the high intracellular stability, methylphosphonates have low solubility and intracellular uptake (120–122). Phosphorothioate modification not only increases the bioavailability of the oligonucleotide but also enhances the resistance of ASO against nucleases. The modified ASO stimulates RNase H cleavage. However, the reduction of 0.5 ° C per nucleotide in the melting point of ASO-mRNA heteroduplex indicates diminution in the affinity of ASO molecule for the target mRNA (123). Off-target effects have also been reported with phosphorothioate-modified ASOs (115). Nonetheless, PS modification is the most widely used method of ASO modification reported in numerous *in vivo* and *in vitro* studies. The first-ever ASO drug approved by FDA, Fomivirsen, is a 21 bp first-generation PS-modified ASO (124). Regrettably, fast turnover and inability to reach sufficient intracellular concentration instrumental for gene suppression reduced the therapeutic potential of the first-generation antisense oligonucleotides in clinical trials (125).

Second generation ASOs:

To further improve binding affinity for target mRNA molecule and enhance resistance, 2´-alkyl modification of ribose was developed. The two main second-generation antisense oligonucleotide wildly studied to date are the 2´-O-Methyl (2´-OMe) and 2´-O-Methoxyethyl (2´-MOE) (113). Regrettably, 2´-OMe and 2´-MOE do not trigger RNase H activity (126).

To rectify the inactivity problem, a chimeric ASO containing a central "gap" region made of 10-PS-modified 2´-deoxynucleotides was developed. The molecule was flanked by roughly five nucleotides "wings" at both the 5´ and 3´ ends (127). The incorporation of chimeric "gapmer" permits RNase H to execute the degradation of targeted mRNA by sitting in the central gap. The "wings" also protect the design from nuclease cleavage due to the 2´-alkyl modification in both sides (112). The length of the unmodified central region capable of RNase H requirement in gapmers is determined by the nature of the modification in the flanking regions, for example a stretch of seven to eight DNA monomers is sufficient to recruit RNase H for DNA/LNA gapmers (114).

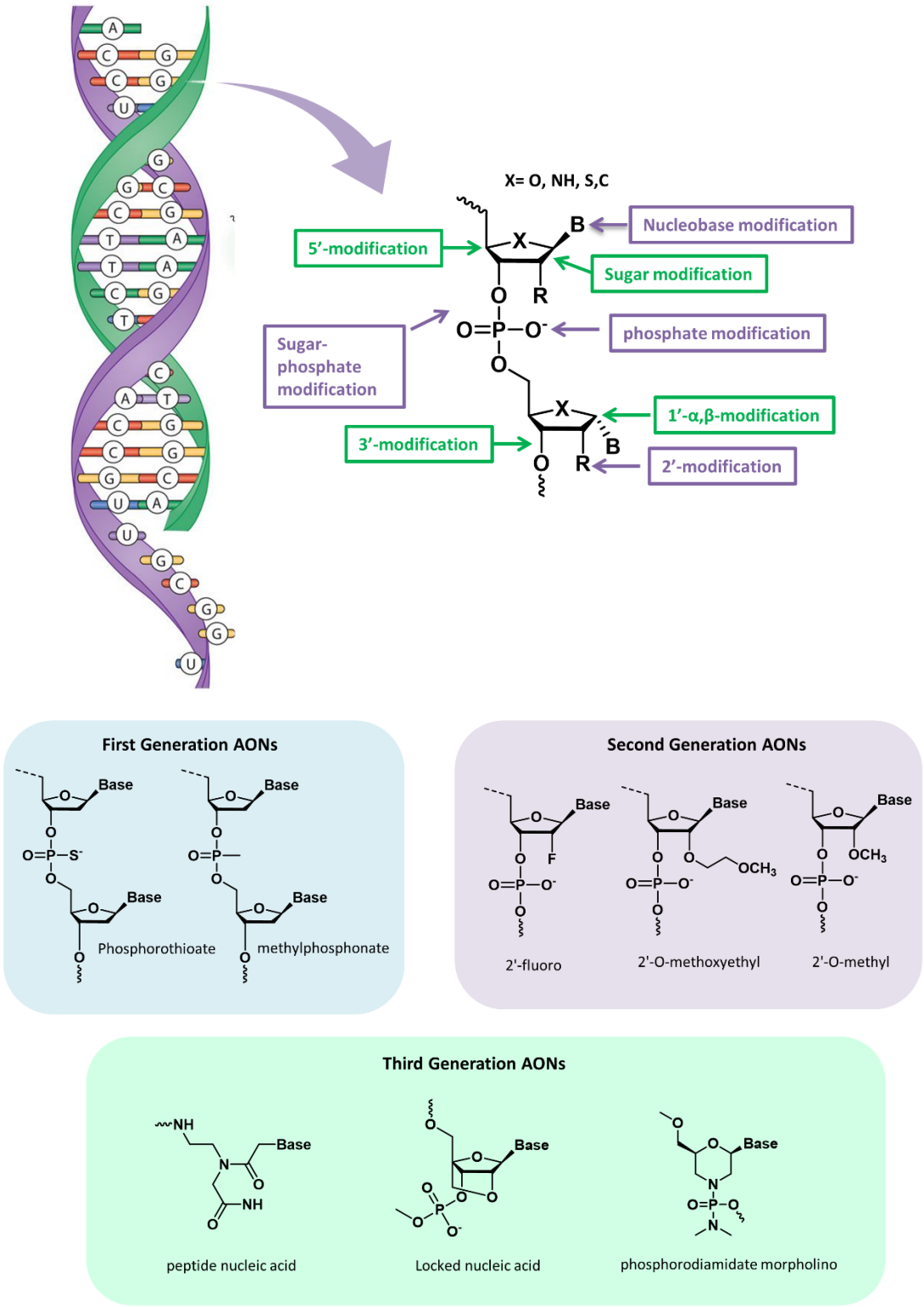

Figure 1.7. Overview of the chemical modifications in antisense oligonucleotide (AONs). B=nucleobase, figure adapted from (128).

Third-generation ASOs:

In the third-generation of ASOs, the focus has been on chemically modifying the furanose ring to further enhance resistance to RNases, pharmacokinetic and affinity (112). The most widely studied third-generation ASOs are locked nucleic acid (LNA), peptide nucleic acid (PNA) and phosphorodiamidate morpholino oligomer (PMO) (115, 129). The introduction of 2´-O, 4´-C-methylene bridge in the β-D-ribofuranosyl configuration produces conformationally restricted locked nucleic acids. The chemical modification can substantially increase the thermal stability of the double-strand, potentiate hybridisation affinity and nuclease resistance (130). Unfortunately, like any other 2´-O-ribose modification, locked nucleic acids do not provoke RNase H activity. This problem can be rectified through the incorporation of LNA monomers in RNA and DNA (112).

In the synthesis of peptide nucleic acids, the phosphodiester backbone is replaced with flexible pseudopeptide polymer (N-(2-aminoethyl) glycine). Furthermore, the carbonyl linkage attaches the nucleobase to the backbone (129, 131). Peptide nucleic acids exert high affinity and specificity towards mRNA molecules. They are non-charged nucleotide analogues demonstrating high biostability in body fluids. Peptide nucleic acids regulate gene expression through the steric hindrance of translational machinery. They form a sequence-specific duplex with mRNA molecules and reduce protein expression. They are incapable of exerting RNase H activity. Moreover, peptide nucleic acids can hybridise with DNA double helix in four different configurations: triplex, triplex invasion, double duplex and duplex invasion, all resulting in a halt in transcription process (112, 129, 132).

Phosphorodiamidate morpholine oligomer is a non-charged antisense oligonucleotide in which ribose sugar and phosphodiester bond are substituted with a six-membered morpholino ring and phosphorodiamidate linkage respectively (133). One of the biggest advantages of this chemical modification is the high resistance to biological nucleases. Similar to LNA and PNA, phosphorodiamidate morpholino oligomer is not a substrate for RNase H activity and it exerts its antisense activity through steric interference of ribosomal assembly (112). A summary of various chemical modifications of antisense oligonucleotide, the advantages and disadvantages of each can be seen in **Table 1.1.**

Table 1.1. Chemical modifications of antisense oligonucleotide. PS backbone and modification are usually seen together in ASO molecules. 2OMe: 2′-O-methyl, LNA: Locked nucleic acid, PMO: phosphorodiamidate morpholino oligomer, MOE: 2′-O-methoxy-ethyl, PNA: peptide nucleic acid, Tc-DNA: tricyclo-DNA (111).

	Modification	Main features	Main disadvantages
Phosphate linkage	phosphoramidate	- High affinity - High nuclease resistance - Does not support RNase H	Quickly cleared by kidney
	phosphodiester	- Naturally occurring - Inexpensive	- Rapidly degraded by nucleases - Quickly cleared by kidney
	Phosphorothioate (PS)	- Improved nuclease resistance - Improved binding to plasma proteins (preventing kidney clearance)	- Cause immune response/cytotoxicity at high concentrations - Reduced binding affinity compared to phosphodiester
Sugar modification	2OMe	- Improved binding affinity - Improved nuclease resistance - Inhibits immune stimulation of PS backbone - Does not support RNase H	- Lower affinity than most other modifications
	2′-Fluoro	- Improved binding affinity - Does not support RNase H cleavage	- Little improvement for nuclease resistance
	LNA	- Strong binding affinity - Increased nuclease resistance - Does not support RNase H	- Higher toxicity than other modifications - Higher risk of a-specific binding - Higher propensity for self-annealing
	MOE	- Improved binding affinity - Improved nuclease resistance - Inhibits immune stimulation of PS backbone	- Lower affinity than most other modifications
	tc-DNA	- Improved nuclease resistance - Improved binding affinity - Does not support RNase H	- Little research data available
Non-ribose modification	PNA	- Uncharged - High binding affinity - Low toxicity - High nuclease resistance	- Rapid clearance - Poor uptake/pharmacokinetic properties
	PMO	-Neutral charge - Improved binding affinity - Excellent nuclease resistance - Does not support RNase H	- Rapid clearance - Poor uptake in cell nucleus - Poor pharmacokinetic properties

1.4.2 Ribozymes

It was Cech and Altman in the early 1980s who first came across RNA molecules able to perform tasks previously attributable to proteins. They discovered that some RNA molecules function as catalysts for other RNA molecules as well as themselves. The majority of naturally occurring ribozymes are intramolecular catalysts. Ever since the discovery, ribozymes' ability to cleave substrates has been put into practice to cleave RNA molecules intermolecularly (134). Ribozymes are ribonucleic acid enzymes with intrinsic strand-cleaving activity. They target unreactive phosphodiester bonds within RNA molecules through forming base pair specific complexes with target RNA molecules. The formed complex subsequently catalyses the cleavage of target RNA; halting protein synthesis by rendering template RNA useless (134, 135). They accelerate the rate of biochemical reactions and exert target specific cleavage (136). The capability of ribozymes to repair mutant RNA molecules or cleave deleterious RNA has made them desirable therapeutic compounds (134). One advantage of ribozymes over RNase H mediated antisense oligonucleotide is the reported increase in transcript turnover via biomolecular kinetics. Contrary to ASOs, ribozymes are RNase H independent and they can be expressed from a vector intracellularly (134, 137). The catalytic activity of ribozymes is enhanced by the presence of divalent metal ions. Despite the common unreactivity associated with phosphodiester bonds, ribozymes can either cleave the 3′ or 5′ carbon-phosphate bonds forming 3′hydroxyl, 5′phosphate or 5′OH and 2′3′cyclic phosphate termini (136). Several different types of ribozymes have been identified so far. The hammerhead, hairpin, *Neurospora* Varkud satellite (VS) and hepatitis delta virus (HDV) are just a few examples of ribozymes capable of self-cleavage (138–141).

Two general ways to deliver ribozymes into cells have been proposed: endogenous expression system and exogenous delivery (136). A summary of three possible sites of action for ribozyme activity can be seen in **Figure 1.8**.

Recent advances in technology have made it possible to generate allosteric ribozymes. Allosteric ribozymes have potentiated the significance of ribozymes as biosensors, genetic control elements and therapeutic agents (142). However, there is a need to optimise stability, delivery and colocalisation of ribozymes before these molecules can have clinical applications. Despite the obstacles facing the clinical application of ribozymes, several hammerhead and hairpin ribozymes are in preliminary clinical trials (136).

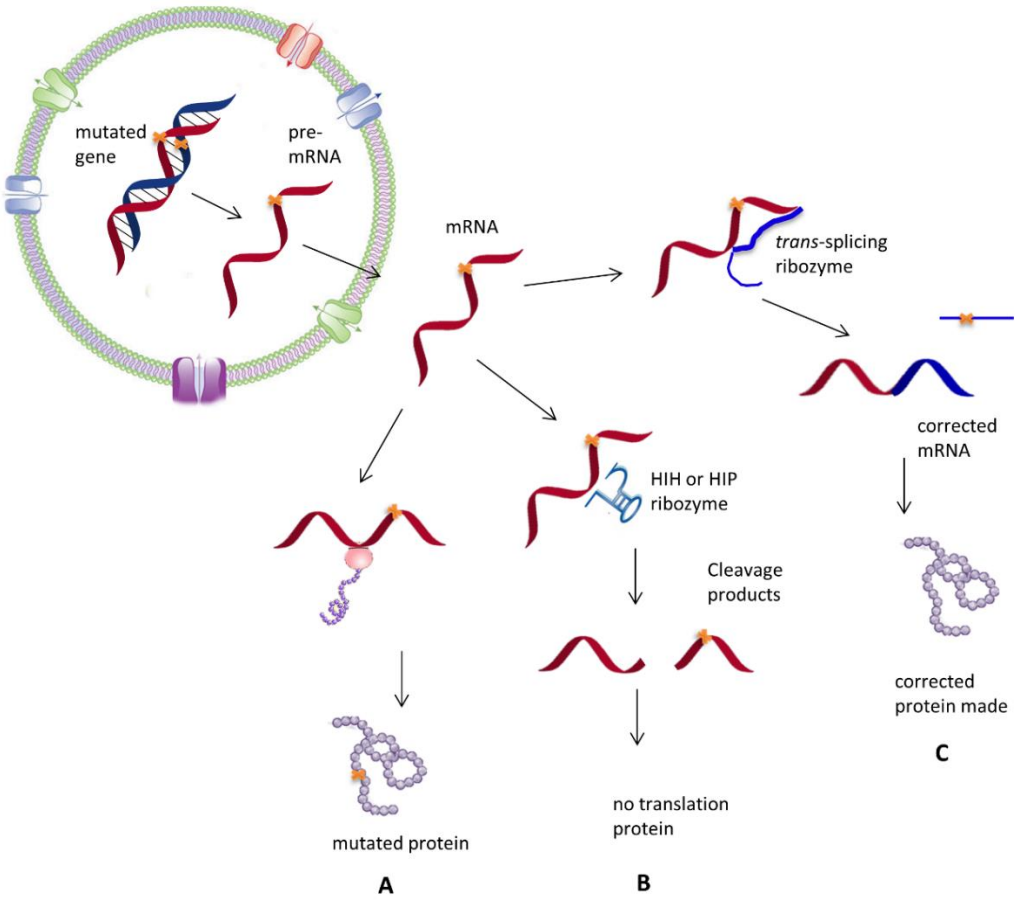

Figure 1.8. Possible sites of actions of ribozymes. These molecules modify gene activity through: prevention of transcription and translation of oncogenes and viral genes (**A**), binding and cleavage of mutated mRNA via hammerhead or hairpin ribozymes (**B**) and trans-splicing and correction of mutant mRNA (**C**). Figure adapted from (136).

1.4.3 RNA interference and small interfering RNA

The experiments conducted on plants in the late 1980s resulted in the discovery of gene silencing mechanism by double-stranded RNA (dsRNA). It was witnessed that the introduction of genes coding for a deep purple colour in petunias yielded white/patchy blossoms. The experiment pointed to unknown gene silencing mechanism incomparable to ASO mediated downregulation which has resulted in silencing both the intrinsic colour gene as well as the introduced gene (143, 144). At the time of the report, gene silencing experiments were confined to antisense oligonucleotide, single-stranded DNA and RNA molecules complementary to target mRNA (145). It was not till 1998 when Fire and co. proposed an explanation for the puzzling discovery in petunias experiment. They witnessed a more potent gene silencing than corresponding antisense molecules after injection of dsRNA in *Caenorhabditis elegans* (146). Their discovery peaked scientific interest and culminated the recognition of RNA as a gene regulator (145, 146).

RNA interference (RNAi) molecules are non-coding RNAs capable of controlling gene expression. RNAi is involved in numerous cellular functions. They are involved in silencing transposable or repetitive genetic elements also known as “jumping genes” (147). Moreover, RNAi molecules constitute an integral part of the nucleic acid-based immune system by protecting human cells from viral infections (148–150). RNAi encompasses several different categories of RNA such as microRNAs, short interfering RNAs (siRNAs) and PiwiRNA (PiRNA) (148). Hamilton and Baulcombe discovered the capability of small RNA molecules to silence genes in plants (151). However, it wasn’t till extensive biochemical analysis was conducted in Drosophila melanogaster that the origin and chemical structure of siRNA molecules were established (152). RNAi mediated gene silencing can be achieved through either an RNA-based approach where siRNA is delivered directly to target cells or a DNA-based approach where siRNA effectors are produced from RNA hairpin transcripts using cellular machinery. In the latter, short-hairpin RNAs (shRNAs) are transported into cytoplasm and subsequently processed to siRNAs by Dicer. Despite the complexity associated with the latter method, it can potentially rectify the need for multiple dosing and prolong effects, leading to long-lasting gene knockdown (153, 154).

siRNA molecules are described as double-stranded molecules consisting of a passenger strand and a guide strand. The guide strand exerts full compatibility with target mRNA (155). The coupling of RNA-inducing silencing complex (RISC) with siRNA triggers the cleavage of double-stranded siRNA molecules to a single strand (see **Figure 1.9**). The cleavage of target RNA molecules serves as a defence mechanism against pathogenic organisms (156).

The mechanisms of action of siRNA molecules can be divided into four distinct steps. First, long double-stranded RNA (dsRNAs) are imported into the cytoplasm and subsequently cleaved by Dicer to form double-stranded siRNAs (157). Dicer cuts dsRNAs into 21-25 nucleotide duplexes with two nucleotide overhangs at both 3’ ends. In the third step, ATP-dependent unwinding of the duplex from the less thermostable 5′ end occurs. The single siRNA strand is loaded into Ago protein. The combination of Ago, Dicer and single-stranded siRNA forms an inactive ribonucleoprotein complex known as the short interfering RNA induced silencing complex (siRISC) (158). The main components of siRNA-mediated post-transcriptional silencing are RNase III enzyme, Dicer, TRBP and Argonaute protein family (155). RISC is a sequence-specific endonuclease capable of cleaving target RNA molecules with high turnover (159–161).

The base pairing between siRNA and target mRNA molecule results in high specific cleavage. siRNA fragments detect target RNA molecules (157). The target RNA is subsequently cleaved by Ago protein into fragments. 5′ to 3′ exoribonuclease Xrn1 and 3′ to 5′ exosome eventually degrade the fragments into nucleotides (162, 163).

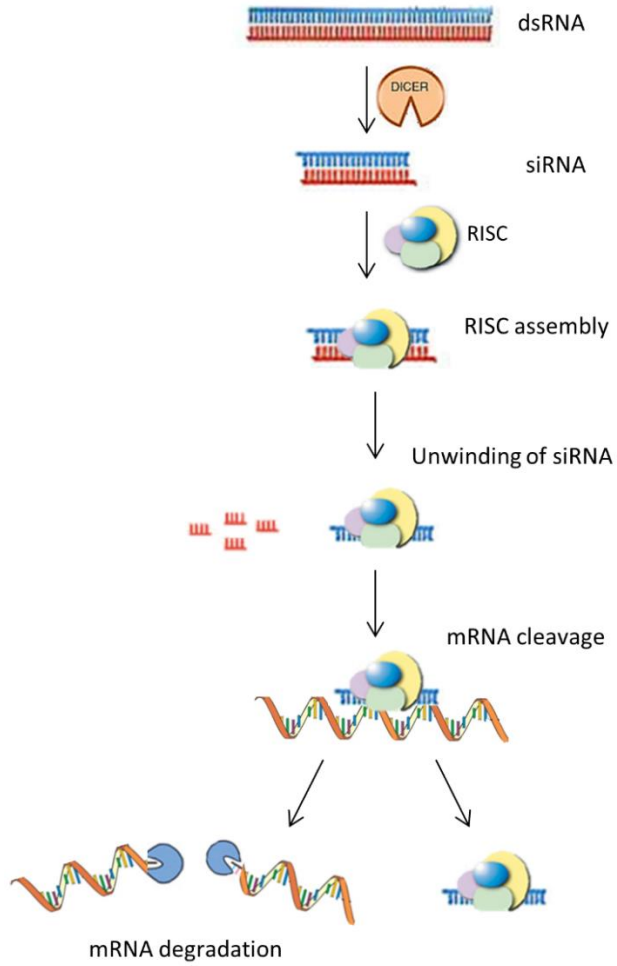

Figure 1.9. RNAi machinery. Dicer cleaves natural or artificial long dsRNA molecules producing siRNA. siRNA can also be transfected into cell. The incorporation of siRNA and RISC results in the unwinding of double-stranded siRNA molecule. The sense strand is then removed from the cleavage site while the antisense strand recruits mRNA molecules. The target mRNA is cleaved by RISC and subsequently degraded. Figure adapted from (145).

siRNAs have the potential to be employed as therapeutic agents capable of combating all gene-dependent diseases (155, 164). They can effectively inhibit replication of malignant cells, viral infections and numerous inflammation-related diseases. Therefore, there is currently great interest to design synthetic siRNA molecules as therapeutic drugs (165). Molecular targeting of cancer mainly focuses on inducing apoptosis, inhibiting proliferation and metastasis (158). Recent studies have solidified the importance of siRNAs in gene regulation in cancer. It was discovered that siRNAs inhibit gene expression and the production of mTORC1, a protein kinase with high expression rate in

numerous types of cancer (166). siRNA molecules are also capable of enhancing apoptosis and inhibiting proliferation in liver cancer cells (167).

There is a fundamental difference between gene silencing via ASOs and RNAi. Protein translation is prevented by antisense oligonucleotide via either RNase H degradation or steric hindrance of the ribosomal machinery (168). The high potency of RNAi in comparison to other conventional antisense based strategies like antisense DNA oligonucleotide and ribozymes means that smaller intracellular concentrations is required (153). **Figure 1.10** indicates the comparison between small interfering RNA and antisense oligonucleotide.

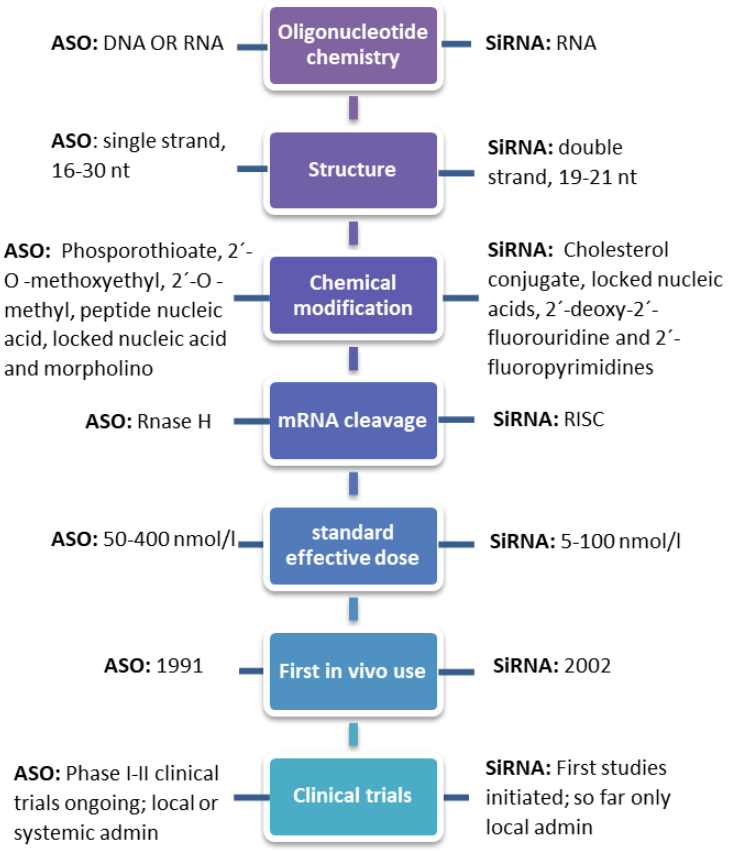

Figure 1.10. Comparison of antisense oligonucleotide and siRNA (145).

Target specificity is a concern with RNAi, although one study reported specific silencing of mutant oncogenic Ras without disturbance to wild-type Ras *in vitro*. Numerous preclinical studies have shown the effective inhibition of tumour growth and survival by RNAi-mediated downregulation of oncogenic genes (158). RNAi has demonstrated potent inhibitory effects on angiogenic factors such as vascular endothelial growth factor, epidermal growth factor as well as human telomerase, translocated oncogenes and viral oncogenes (169). Despite the immense success of siRNA *in vitro*, the efficacy of siRNA *in vivo* is still unknown. Several pharmaceutical companies have experimented with

siRNA-based therapeutics and have conducted clinical trials on human subjects (170–172).

To turn siRNA molecules into viable therapeutic agents, it is vital to increase nuclease resistance, improve cellular uptake and maintain gene silencing properties (145). High molecular weight, presence of a negative charge, hydrophilicity, low potency at target sites and rapid degradation via extracellular and intracellular nucleases are just a number of undesirable properties of siRNA molecules (157). One optimisation approach is through chemical modification (157). Many of the early *in vivo* studies have focused on unmodified siRNAs. However, unmodified siRNA and ASO molecules have limited stability and are rapidly degraded by serum nucleases (115). Problems facing the administration of oligonucleotide in cells are (173):

- Susceptibility to nuclease degradation
- Unwanted participation in miRNA pathways (off-target effect- OTE)
- Activation of the innate immune system (OTE)
- Cell uptake and pharmacokinetics

As reported before, chemically modified ASOs exhibit stability with the conservation of gene-silencing properties in human plasma (115). Nowadays siRNA molecules are chemically synthesised as a single strand oligonucleotide made of phosphoramidite building blocks annealed into a double helix. Hence, it is possible to incorporate a variety of natural or artificial chemical modifications into the siRNA molecules to improve the administration of nucleic acids *in vitro*. The choice of chemical modification is dependent on the design of siRNA, application and method of delivery. Double-stranded nucleic acids have shown more resilience towards degradation in serum, but they still need to be protected from nuclease attack. The protection can be provided either internally through chemical modification or externally through the use of a suitable delivery tool like nanoparticles (173). The 3´ overhangs present in traditional single-stranded siRNA are particularly susceptible to degradation. By placement of a non-nucleotide group or an inverted dT base in the vulnerable position, we would be able to enhance stability (174). Several internucleotide modifications have been tested to enhance stability whilst retaining induction of RNAi such as replacement of non-binding oxygen with boron (boranophosphate), sulfur (PS), methyl (methylphosphonate) and nitrogen (phosphoramidate) (173). In general, backbone modifications increase nuclease

resistance at the expense of binding affinity (175). However, the incompatibility of some chemical modification with cellular RISC machinery limits the type of chemical modifications which can be incorporated in siRNAs (117). **Table 1.2** summarises the differences between the 3 main antisense-based technologies.

Table 1.2. Comparison between RNase H dependent and independent ASOs and siRNA (117).

	Steric blocking oligonucleotides		**RNase H-dependent ASOs**	**siRNA**
Technology	Splice switching oligonucleotide (SSO)	Translation suppressing oligonucleotide (TSO)	Antisense oligonucleotide (ASO)	Short interfering RNA (siRNA)
Target	Pre-mRNA	mRNA	mRNA	mRNA
Mechanism of action	Blocks and redirects splicing machinery in targeted pre-mRNA	Blocks access of translation machinery to initiation codon on targeted mRNA	Degradation of target mRNA by RNase H, reducing protein synthesis	Degradation of target mRNA by RISC, reducing protein synthesis
Outcome	Redirection of splicing, preventing generation of undesirable proteins or generation of desired mRNA splice variants	Inhibition of translation of undesirable protein	Degradation of mRNA, preventing translation of undesirable protein	Degradation of mRNA, preventing translation of undesirable protein
Compatible chemistries	Chemical modification resistant to cellular nucleases which do not support RNase H or RISC; like PMO, LNA, 2'OMe or 2'MOE	Chemical modification resistant to cellular nucleases which do not support RNase H or RISC; like PMO, LNA, 2'OMe or 2'MOE	Oligonucleotides with chemically modified flanks (resistant to degradation) and do not support RNase H activity, and a central core that allows RNase H degradation of target mRNA; 2′OMe, 2′MOE, LNA flanks and a deoxynucleotide phosphorothioate core	Double stranded RNA, with limited chemical modifications which supports RISC; 1-2 2′OMe nucleotides at the ends of the RNA and a single 2′OMe nucleotide close to the centre of the strand
Advantages/ applications	High specificity; restoration of defective proteins in rare disease	High specificity; effective inhibition of translation in viruses and drug-resistant bacteria	High specificity; effective degradation of mRNA in liver diseases	High specificity; highly effective in degrading mRNA in cell culture, effective in local delivery in lung and eye

Disadvantages	Poor intracellular uptake Chemistry-dependent toxicities and plasma stability	Poor intracellular uptake Chemistry dependent toxicities	Poor intracellular uptake Chemistry dependent toxicities	Poor intracellular uptake Chemistry dependent toxicities Relatively poor stability in plasma

Off-target gene silencing of siRNA has been demonstrated in a genome-wide monitoring study using microarray technology (176). Studies of transfected cells *in vitro* have indicated the negative effects of siRNA on cell viability and the potential implication on phenotype. Intelligent siRNA design incorporating chemical modifications such as 2'-OMe at the second base can reduce off-target effects whilst maintaining the degree of target silencing and can improve strand selectivity (177).

Systemic delivery of nucleic-based drugs has been met with difficulties since it can be argued that these large, charged polar molecules do not follow Lipinski's rule of five (178). Intravitreally injected Fomivirsen and Pegaptanib are two locally delivered oligonucleotide therapies which have reached the market (179). An optimum delivery vehicle must take into consideration the unique characteristics of tumour environment such as high interstitial fluid pressure, asymmetrical leakage of tumour vessels to optimise cellular uptake of oligonucleotides (180).

An effective delivery system needs to be designed to provide stability against nucleases, avoid off-target events, cause prolongation of half-life, allow cell entry, evade the immune system and finally be able to incorporate RNAi machinery (181, 182). Countless studies have explored the possible ways to enhance *in vivo* delivery through the application of polymers, peptides, antibodies, aptamers, lipids, viral vectors and small molecules (183–186). Conjugation of siRNA with lipophilic derivatives of cholesterol, lauric acid or lithocholic acid results in an amplified cellular uptake (187). The addition of cholesterol molecule to the 3′ end of sense siRNA strand has shown to dramatically prolong the half-life and reduce the rate of elimination (186). Encapsulation of siRNA with a lipid coat or nanoparticles protects the drug and enables the molecule to travel along the bloodstream until it reaches the target cell (158). Some of the delivery strategies have been successfully investigated in animal models but have yet to pass the test in a patient setting. Several target and non-target delivery strategies can be seen in **Figure 1.11** (155).

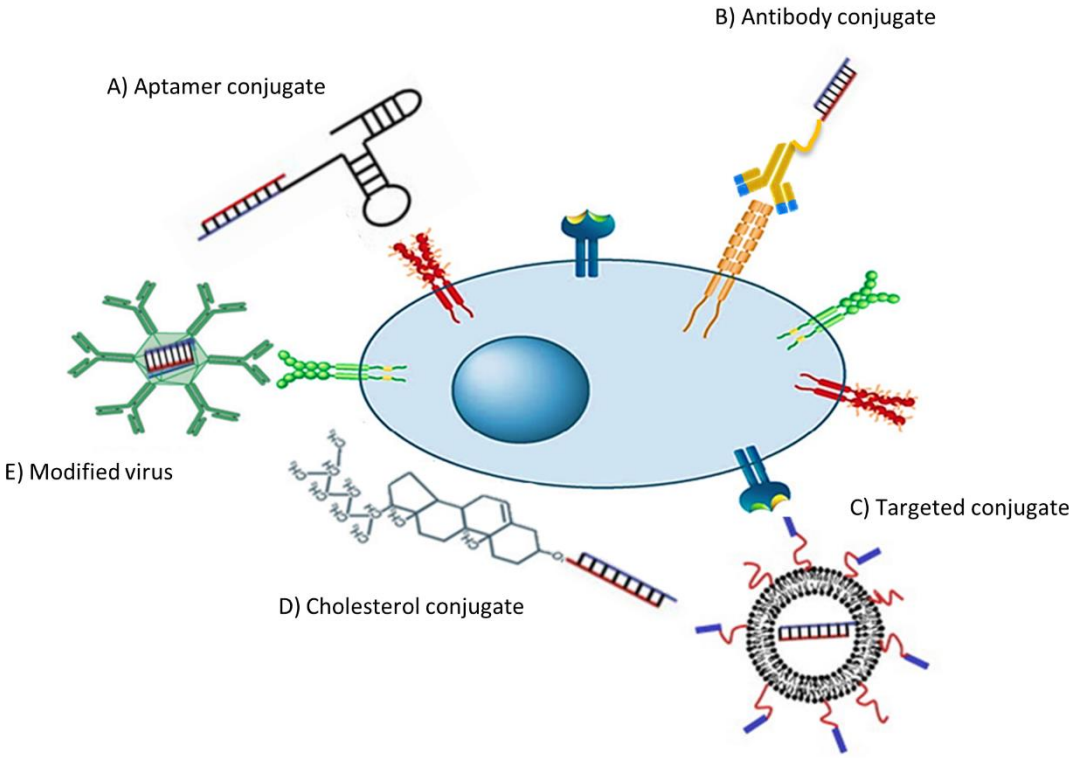

Figure 1.11. Different delivery strategies for RNAi. The cell is shown as a blue ellipse, nucleus and cell membrane are shown as a dark circle and dark ellipse. The receptors can be seen on the cell surface in different colours. siRNAs coloured blue and red are capable of targeting cell surface molecules via numerous delivery vehicles. (**A**) siRNAs conjugated to aptamers can bind to cell surface molecules and be internalised. (**B**) siRNA conjugated with antibodies can recognise target cells through specific antibodies and be internalised via endocytosis. (**C**) RNAi therapeutics can also be transported via nanoparticles. (**D**) Hydrophobic interactions between cholesterol conjugate siRNAs and cell membrane can result in internalisation. (**E**) Another cell-specific delivery method of siRNA is through modified viruses. Figure adapted from (155).

The most efficient way to enhance gene delivery of RNAi *in vivo* is through the application of retroviral, adeno-associated and adenoviral viral vectors (188). Retroviral vectors have been the subject of most studies since they can also transduce terminally differentiated quiescent cells (145). Once siRNA molecules are delivered to the right cell, they also need to overcome endosomal internalisation. Receptor-mediated delivery endocytosis or pinocytosis result in internalisation and elimination of vesicles by Golgi network. Pros and cons of different delivery systems can be seen in **Table 1.3** (155).

One of the most problematic off-target effects associated with siRNAs is the recognition of molecules as foreign bodies by the innate immune system. siRNAs activate the two main components of the innate immune system: IFN response and several signalling mediated receptors such as toll-like receptors (TLRs), RNA helicase protein retinoic acid-inducible gene 1 protein (RIG-1) and protein kinase (189, 190). The activation of immune system by siRNA molecules sets a chain of events in motion leading to a potent inflammatory response (190).

Table 1.3. Pros and cons of different delivery methods for siRNA. Table adapted from (155).

Delivery strategy	Advantages	Disadvantages
Naked siRNA	Stable, non-immunogenic and easy to manufacture	Poor cellular uptake, toll-like receptor activation
Antibodies	Highly target-specific	Costly, multiple-dosing, immunogenic
Aptamer	Highly target-specific, possibility of large-scale manufacture, can modify backbone for *in vivo* application	Multiple-dosing, costly, need modification to enhance circulation and pharmacodynamics
Cholesterol	Non-immunogenic, low-cost, proven *in vivo*	Possible liver toxicity, only for delivery to liver, large doses needed
Viral vectors for shRNA	Possible to combine multiple RNAi triggers in single vector, high affinity	Immune response to vector envelope, costly, potential toxicity from continuous expression of shRNA and gene disruption
Synthetic nanoparticles	Specificity, large scale manufacture possible, can accommodate large amounts of siRNA, can be engineered to escape endosome	Needs to be conjugated to specific ligands for tissue-specific delivery, costly, multiple dosing

siRNA technology allows us to target designated genes with low developmental costs. However, the design of siRNA-based therapeutics is not without challenges. Even the best designs of siRNA drugs can lead to off-target effects. In brief, it seems like the local administration of siRNA is a more feasible objective than systemic application. Like any bioactive drugs which solely relies on cellular machinery, RNAi faces the risk of saturating and disturbing endogenous cellular pathways. Hence, the intercellular concentration of siRNA drugs needs to be maintained within certain limits to exert efficacy without saturating and inhibiting the normal regulatory functions of RISC machinery. Therefore, careful dose optimisation is one of the limiting factors of siRNA drugs (191–193). Whether despite all the pitfalls, more siRNA molecules can make the transition from "bench to bedside" is still a question that needs to be answered through extensive research and design optimisation (145). Recent enhancement in oligonucleotide therapy might pave the way for successful delivery of siRNA-based therapeutics and solve the current challenges.

1.5 Ribonucleases

1.5.1 Natural ribonucleases

The central dogma flow of information is controlled through synthesis and degradation of RNA molecules. As mentioned before, RNA polymerases catalyse the synthesis of RNA molecules. The degradation, on the other hand, is catalysed by RNA depolymerases also known as ribonucleases (194). Ribonucleases (RNases) are a family of hydrolytic enzymes which play a key role in the regulation of cellular processes such as RNA metabolism, transcription, protein synthesis, cell maturation, promotion of blood vessel formation and physiological cell death by catalysing RNA degradation (195–197). RNases also appear to inhibit reproduction of viruses in host cell cultures (197). The degree of catalytic activity, stability and propensity to internalise along with the non-selective nature of inhibitors all influence the cytotoxicity of RNases (198).

Ribonucleases found in mammals and other vertebrates are known for their digestive role. They can digest a large number of RNA molecules produced by the stomach microorganisms (199). They are widely distributed in numerous organs and body fluids and have a range of nondigestive functions (200). Ribonucleases can be divided into two categories based on their RNA processing mechanisms: endoribonucleases and exoribonucleases (201). Exo- and endoribonucleases can be further subdivided into many subgroups; PNPase, RNase D, RNase R and oligoribonucleases are a few examples of exoribonucleases, RNase H, RNase A, RNase P, RNase III and RNase T1 are examples of endoribonucleases (202). Endoribonucleases are capable of cleaving RNA internally whereas exoribonucleases remove terminal nucleotides from either the 3´ or 5´ end of RNA. Exoribonucleases can operate as a processive enzyme, catalysing consecutive reactions without releasing the substrate or as a distributive enzyme, releasing the acceptor substrate after each removal. The majority of known RNases are hydrolytic enzymes, breaking phosphodiesters bonds through consumption of water molecules, although several phosphorolytic exoribonucleases have been identified (201, 203). The discovery of the three-dimensional structure of a range of RNase enzymes has permitted the dissection of their function.

RNase H is an endonuclease which requires divalent metal ions (Mg^{2+}) to hydrolyse the RNA strand of DNA-RNA hybrid yielding 5'-phosphate and 3'-hydroxyl residues (204). RNase H mostly recognises structure rather than sequence, distinguishing the RNA strand

from DNA through extensive contact with 2'-OH groups in RNA and the ability of DNA to adopt a flexible B-form conformation (205).

RNases can also be classed based on amino acid sequence, size and base specificity into three major groups: RNase A, RNase T1 and RNases T2 families (also known as non-specific RNase). Ribonuclease T1 is a family of endoribonucleases which specifically cleave RNA molecules between the 3´-phosphate group of guanine and 5´-hydroxyl group of adjacent ribonucleotide (206). RNase A family comprises human angiogenin, pancreatic RNase A, RC-RNase and Onconase from Rana pipiens eggs. RNase A and RNase T1 exert pyrimidine and guanine specificity respectively (207). The letter "A" in RNase A refers to the predominant enzymatic form of the molecule in the pancreas of Bos taurus (194). Extensive research on the three-dimensional structure and amino acid sequence of RNase A (see **Figure 1.12** (**A**)) has resulted in extensive application of the molecule as a model for artificial ribonuclease design.

Bovine pancreatic ribonuclease A (RNase A) is a small endoribonuclease which specifically hydrolyses RNA after C and U residues (208). The rate of cleavage of RNA by RNase A is dependent on pH (194). Major components of RNase A active site involved in transesterification can be seen in **Figure 1.12** (**B**).

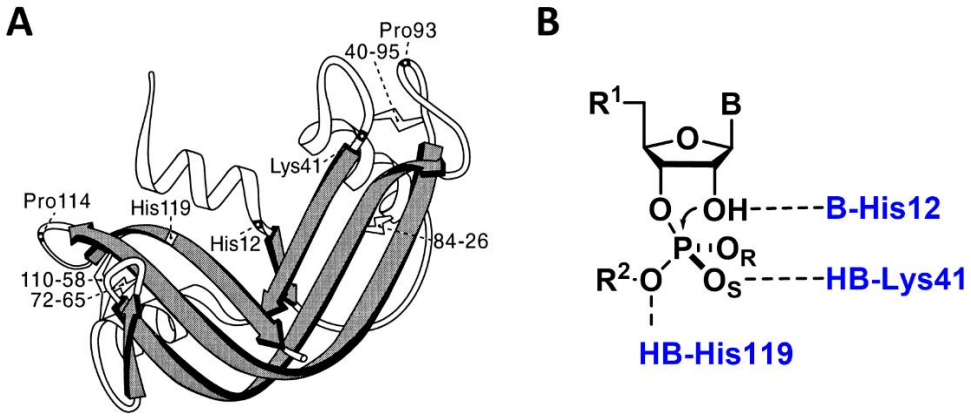

Figure 1.12. RNase A 3D structure highlighting the major components of the active site. (**A)** Ribbon diagram of the 3D structure of ribonuclease A. RNase A contains eight cysteine residues, two proline residues as well as three fundamental residues for catalysis: His 12, His 119 and Lys41. (**B)** Major components of RNase A active site involved in the transesterification reaction. Figure adapted from (194, 209).

The cleavage mechanism is initiated by transphosphorylation, His12 acts as a base and abstracts a proton from 2´ oxygen atom in the substrate molecule. Subsequently, a strained dianionic phosphorane intermediate is formed as a result of 2'-oxyanion attack on the adjacent phosphorus atom. Interaction between Lys41 and non-bridging oxygen in the intermediate molecule leads to a reduction in electron density of phosphorus atom. The

pentacoordinate intermediate is stabilised by the positively charged Lys41 and Phe120. Afterwards, 5'-linked released oxyanion is protonated by His119 leading to an attack of 2',3'-cyclic phosphodiester and consequent release of 2'- and 3' nucleotide monophosphates (NMP) (210). The acid-base mechanism comes to an end with deprotonation of His12 by the 2'-oxyanion (194).

Most ribonucleases are potential cytotoxic or cytostatic agents capable of degrading RNA molecules and halting protein biogenesis (211, 212). Cytotoxic capabilities of ribonucleases were discovered in the 1950s when the toxicity of RNase A to malignant cells *in vivo* and *in vitro* was reported (213). Numerous studies reported the ability of RNase A to impede tumour growth (214). Apart from RNase A, RNase T1 superfamily has also demonstrated anti-tumour properties. RNases exert their cytotoxic activities through binding to cell-surface glycolipids which is followed by transportation to Golgi body, endoplasmic reticulum and the subsequent translocation into cytosol and degradation of ribonucleic acid (215). Ribonuclease inhibitor (RI) is the most potent inhibitor of RNase A. RI is a small protein in mammalian cytosol responsible for protecting cytosolic RNA against the inversion of pancreatic ribonucleases (216). Cellular RI are compounds intended to counteract the ribonucleolytic actions of RNases through forming a tight and irreversible complex with monomeric RNases, rendering them inactive (217).

One of the biggest problems facing the application of RNases as therapeutic agents is immunogenicity. RNase molecules extracted from other species can also trigger an immune response leading to clearance from the body. For RNase molecules to exert their cytotoxic activity, they need to reach the target cells intact. Hence, conjugated RNase molecules can be administrated in an attempt to direct the protein to specific tumour cells (197). Apart from RNases in Rana japonica (RJ-RNase) and Rana catesbeiana (RC-RNase) which induce cell death through binding to surface proteins, RNases need to be internalised (218). As mentioned before, one of the drawbacks of the application of natural ribonucleases in therapeutics is binding with ribonuclease inhibitors (RI). Bound RNases no longer exert cytotoxicity and are incapable of cleaving RNA molecules (219). RNase can potentially evade inactivation by RI through dimerisation or multimerisation (217). Several RNases have been chemically modified with polyethyleneimine or ethylenediamine or conjugated to other molecules to reduce RI affinity and enhance cellular uptake (220). As witnessed with Onconase, genetically modified RNases have low residual activity.

Onconase, an amphibian RNase originally extracted from Northern Leopard Frogs, is a well-known example of ribonuclease which has been evaluated in phase I and II clinical trials. It targets rRNA, tRNA, mRNA as well as the non-coding RNA. The results of the trials indicated that Onconase is active in patients with unresectable malignant mesothelioma and prolonged exposure can result in apoptosis (197). A recent Onconase study reported the inhibition of human immunodeficiency virus (HIV) infection and degradation of HIV-1mRNA (221). Another ribonuclease under investigation for anticancer activities is Bacillus intermedius Binase (222). One difference between RNases in comparison to ASOs or siRNAs is the fact that they are directed towards specific ribonucleotides rather than RNA sequences. Contrary to antisense oligonucleotides and siRNA-based therapeutics, RNases are not reliant on recruitment of cellular multi-component machinery and can trigger a cascade of events free of exogenous enzymes (e.g. RISC, Dicer, RNase H). Moreover, they are capable of irreversible cleavage of pathogenic RNA sequences in a catalytic manner.

Artificial ribonucleases are designed based on RNA-binding domains. They are made up of low molecular weight constructs bearing resemblance to the functional groups involved in catalytic centres of natural ribonucleases RNA-binding domains. These molecules must exhibit high efficiency and specificity towards target RNA molecules. The efficacy is dependent on the catalytic properties of active groups whereas specificity is dependent on the affinity of compounds to target RNA sites. Artificial ribonucleases will be explored in detail in **Section 1.5.3**.

1.5.2 Ribonuclease transesterification mechanism

The inherent adjacency of 2'-hydroxyl group to the phosphodiester linkage is the primary causative factor behind RNA phosphodiester bonds chemical and enzymatic instability in comparison to DNA (223). RNA hydrolysis happens in 3 main stages: nucleophilic attack of 2'-hydroxy group on the phosphorus atom, formation of a pentavalent phosphate transition state and production of 2',3'- cyclic phosphate and 5'-hydroxyl termini (see **Figure 1.13**) (224, 225). In the absence of enzymes, spontaneous intramolecular phosphoester transfer (transesterification) of RNA exhibits first-order kinetics with a pH-dependent rate constant (226). Additionally, RNA phosphodiester bonds can undergo a pH-independent cleavage at a narrow pH range (pH~ 5) (227).

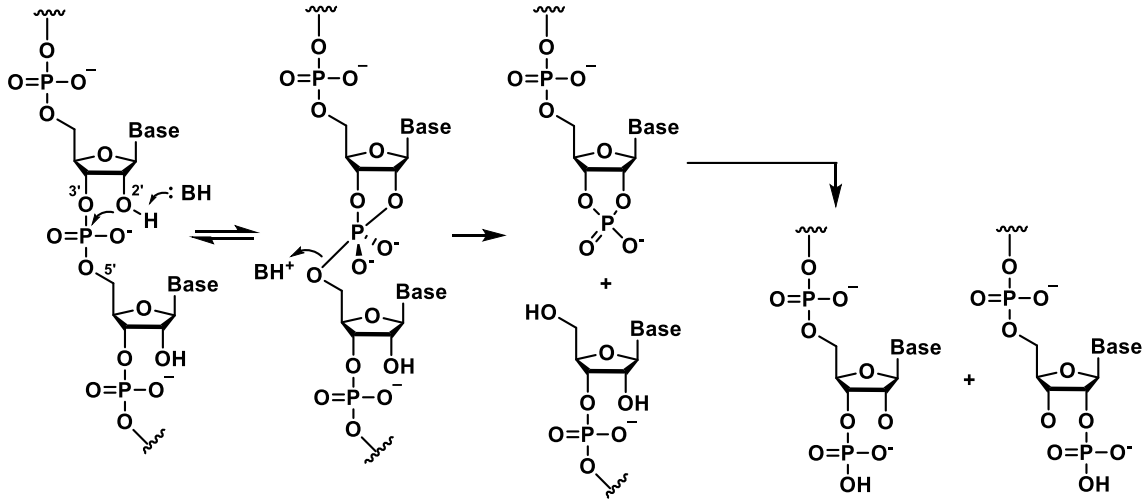

Figure 1.13. The acid-base mechanism of RNA cleavage. This SN2 reaction involves the production of 2'- and 3'-nucleotide monophosphates and 5'-hydroxyl termini through nucleophilic attack of phosphorus centre adjacent to 2'-oxygen. Figure adapted from (228).

Acid-based RNA hydrolysis is based on the premise that a general base and acid are required to deprotonate the attacking water molecule and protonate the leaving group respectively (229). The rate of transesterification can be accelerated under acidic and basic conditions where protonation of non-bridging phosphate oxygen and 5'-oxyanion leaving group under acidic conditions and deprotonation of the 2'hydroxyl group under basic conditions can expedite the reaction (223, 225). Moreover, the rate of the reaction is also affected by the conformation of the attacking nucleophile; a near-attack conformation is required for the reaction to proceed where relative to the nucleophile the 5'oxyanion leaving group is on the opposite side of the target phosphorus centre (223). Westheimer's rule states that the initiation of nucleophilic attack on the phosphorus and the departure of nucleophile from the penta-coordinate phosphorane intermediate is only permitted through an apical position (210). Engagement of RNA cleavage sites in double helixes forces the 5'-O into equatorial position hindering the rearrangement of phosphorane intermediate into the required apical position instrumental for cleavage (17, 210). Moreover, high abundancy of purines in the target RNA sequence impedes RNA cleavage due to tight binding and high level of interaction with neighbouring bases.

Ribonucleases employ one or more of these methods to facilitate transesterification. It has been proposed that RNase A combines both basic and acidic catalysis to promote transesterification (223). The majority of polymerases and nucleases employ bound metal ions for catalysis of transesterification. The synergetic action of two divalent metal ions results in activation of nucleophile and labilisation of oxyanion leaving group in these enzymes (230).

1.5.3 Artificial ribonuclease

Artificial ribonucleases (aRNases) can be visualised as molecular scissors. They not only catalyse RNA cleavage, but they also display chaotropic and membranolytic like activities (231). A number of artificial ribonucleases exert their effects through bifunctional general acid/base mechanisms similar to RNase A. Phosphate diester displacement is the result of charge neutralisation and electrophilic activation of phosphate ester. Artificial ribonucleases are chemically engineered compounds that catalyse sequence-selective hydrolysis of phosphodiester bonds in target RNA molecules (232). They are composed of two structural entities; a phosphodiester cleaver group and a recognition motif made of oligonucleotides capable of recognising target RNA molecules. The hybridisation of recognition motif with target RNA enhances the concentration of cleaver group in the vicinity of the phosphodiester bond. The two subsections are connected through a linker group which provides the optimum spatial orientation (17). A schematic representation of sequence-specific artificial ribonuclease can be seen in **Figure 1.14**.

Figure 1.14. Schematic representation of sequence-specific artificial ribonuclease. Artificial ribonucleases are composed of a recognition motif and a phosphodiester cleaver group linked together.

This design incorporates the sequence-specific targeting of antisense oligonucleotides with RNA cleavage capabilities of ribonucleases. An ideal aRNase is designed in such a way to enhance deprotonation of the 2'-OH group, encourage nucleophilic attack of 2'-oxyanion through the reduction of electron density at the bridging phosphorus, stabilise phosphorane intermediate and facilitate the cleavage of the P-O5' bond. The presence of guanidinium in several natural ribonucleases such as RNase A and T1 is instrumental in coordinating phosphate groups (17, 228).

1.5.3.1 Metal-dependent artificial ribonucleases

RNA transesterification and hydrolysis can be catalysed by several catalytic moieties such as hydroxides, amines, peptides, protons and metal ions like Cu^{2+}, Fe^{3+}, Mg^{2+}, Ni^{2+} and trivalent lanthanides (233). Artificial ribonucleases currently developed can be categorised based on their conjugate groups into three distinctive categories: lanthanide ion chelates, Cu^{2+} and Zn^{2+} chelates, and metal ion-independent (17). Metal-independent artificial ribonuclease will be explored in **Section 1.5.3.2**.

1. Lanthanide-based artificial ribonucleases: It has been proven that metal chelates catalyse the cleavage of phosphodiester bonds in deoxyribonucleotides under physiological conditions. One of the most effective metal ions ever studied is lanthanide (234). In 1994 Komiyama *et al*. witnessed sequence selective cleavage of a 39-mer oligoribonucleotide with a Lu^{3+} ion-based iminodiacetic acid tethered to 15-mer oligodeoxyribonucleotide (235). The Lu^{3+} chelate conjugate showed modest cleaving activity. Arrangement of the 2-hydroxyl group into a more favourable position can enhance the cleaving activity (236). Enhanced cleavage activity of lanthanide-based chelates was reported at bulged-out sites of RNA molecules (**Figure 1.15**) (237).

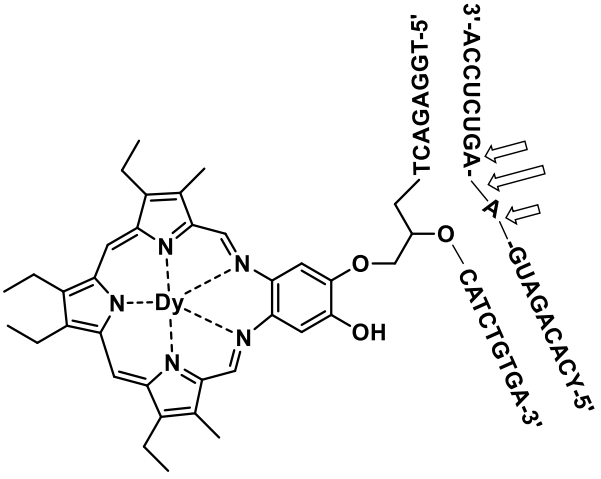

Figure 1.15. Example of lanthanide metal base artificial ribonucleases. Figure adapted from (238).

2. Cu^{2+} and Zn^{2+}-based artificial ribonucleases: Even though Cu^{2+}-based artificial ribonucleases are less effective than lanthanide ions, the fact that Cu^{2+} is present in intracellular fluids has peaked scientific interest. The first-ever Cu^{2+}-based artificial ribonuclease was reported in 1994. The reported molecule successfully cleaved a 159-mer segment of the gag-mRNA (239). The cleaving activity was further enhanced later by inserting propane 1,3-diol spacers to both sides of serinol unit and tethering

the cleaving agent to a serinol backbone. Another transition ion that has been employed in the design of artificial ribonucleases is Zn^{2+}. It has been reported that the cleaving activity of 5-amino-2,9-dimethylphenanthroline Zn^{2+}chelate is considerably less than Cu^{2+} containing counterpart (240). A number of studies have explored the relationship between linker structure and site of tethering and the cleaving activity of Zn^{2+}-based artificial ribonucleases (241, 242). These multivalent metal ions can readily detect negatively charged phosphodiester bonds. Examples of copper and zinc ion chelates of terpyridine, 1,5,9-triazacyclodo-decane and 5-amino-2,9-dimethyl-1,10-phenanthroline used as the cleaving moiety in oligonucleotide-based artificial nucleases can be seen in **Figure 1.16.**

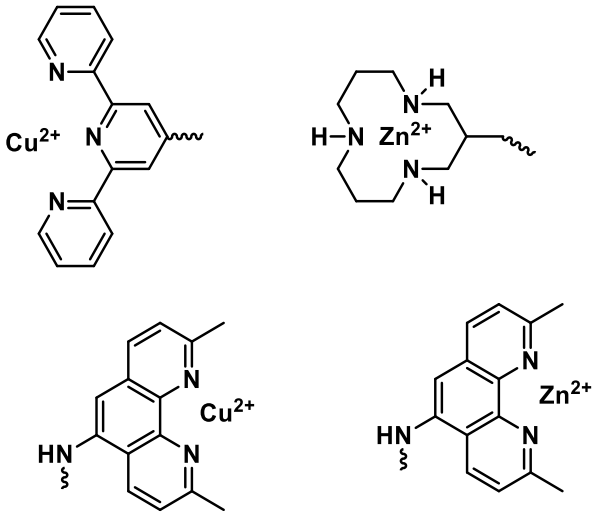

Figure 1.16. Examples of Cu^{2+} and Zn^{2+} ion chelates used as cleaving moiety in artificial ribonucleases. Figure adapted from (238).

For artificial ribonucleases to catalyse reactions effectively *in vivo*, they must be stable under physiological conditions and operate without the need for additional exogenous factors such as oxygen and redox reagents like endogenous metal ions (i.e., iron, copper and cobalt) (243). Attempts have been made to replicate the catalytic site of natural ribonucleases in synthetic cleaving constructs. Several artificial ribonucleases reported in the literature have been generated by conjugation of a recognition motif and a cleaving construct made of peptides (244, 245), oligoamines (246), imidazole-based compounds (247, 248) resembling catalytic domain of natural ribonucleases possessing imidazole, carboxyl or amine functional groups which will be explored in the upcoming section (243).

1.5.3.2 Metal-independent artificial ribonucleases

Metal-independent artificial ribonucleases mimic the active site of natural ribonucleases by encompassing an organic catalytic moiety. Incorporation of a catalytic moiety in an antisense deoxyribonucleotide sequence ensures sequence-selective hybridisation and cleavage (228). The metal-independent systems do not rely on the detection of metal ion compartment in living cells and are less toxic. Several catalytic structures normally constituting natural ribonucleases such as peptides, imidazole-based compounds and oligoamines have been conjugated and studied for their cleaving capabilities (245, 249). One well-known example of organic sequence-selective nucleases is diethylenetriamine conjugates of oligodeoxyribonucleotide. A hybrid of ethylenediamine and a 19-mer DNA sequence acting as a recognition motif, complementary to A44-A62 sequence of $tRNA^{Phe}$ selectively hydrolysed target RNA (250). The presence of ethylenediamine residues in monocationic states resulted in acid-base catalysis of phosphodiester bond where the ammonium cation and neutral amine act as acid and base, respectively. Neither of the components (free ethylenediamine or DNA) of this artificial ribonuclease was capable of hydrolysis on their own indicating the boost in catalytic efficacy of ethylenediamine as a result of hybridisation with tRNA (250). Reynolds *et al.* reported the design of a novel series of antisense methyphosphonate oligonucleotide ribonucleases containing a non-nucleotide-based linking moiety in the middle of the sequence which displayed site-specific cleavage. Upon hybridisation the surrounding neighbouring bases directly opposite the non-nucleotide-linker will be less constrained, made assailable to nuclease attack due to the presence of an unpaired base on the target RNA strand (251).

Artificial ribonucleases have been synthesised by incorporating polyamine derivatives which function as catalytic moieties bearing imidazole and/or primary amine groups and deoxyribonucleotide recognition motifs which place the enzyme directly adjacent to the target complementary sequence. Imidazole and/or primary amine tethered to the 5'-end of DNA oligonucleotide have been directed to a specific sequence on $tRNA^{ASP}$ (252). Two notable developments in non-metal ion cleavers are the incorporation of bis-imidazole and tris-benzimidazole moieties in the design of ribonuclease (253, 254). In one study, the influence of incorporating multiple imidazole groups in the catalytic domain on ribonuclease activity was investigated. It was demonstrated that ribonuclease activity is influenced by the number of imidazole residues, the type of anchor group, connecting linker structure as well as the length of the linker between the oligonucleotide and catalytic imidazole groups (255). Although the molecule was capable of cleaving the

target RNA at 3´-side of the first unpaired nucleoside, the cleavage was rather ineffective. In a later study, the design of oligonucleotide-based artificial ribonucleases carrying two imidazole containing constructs was reported. The recognition motif was directed towards the T-arm of yeast $tRNA^{Phe}$ (44-60 nt) placing the catalytic construct adjacent to the fragile sequence of C_{61}-ACA-G_{65} of the tRNA. The designed conjugates exhibited ribonuclease activity far superior than previous studies (251, 252, 254, 256) at neutral pH mainly hydrolysing C_{63}-A_{64} phosphodiester bond. The significant difference seen in efficacy between metal complexes and organic catalysts is attributable to the fact that imidazole, carboxy and amino groups are weak catalysts in nature for corresponding reactions. The high catalytic efficacy of these groups witnessed in natural ribonuclease is attributed to the three-dimensional orientation of the catalytic site (257). A relatively new class of metal-independent artificial ribonucleases is peptidyl-oligonucleotide conjugates (POCs) which will be discussed in length in the upcoming section.

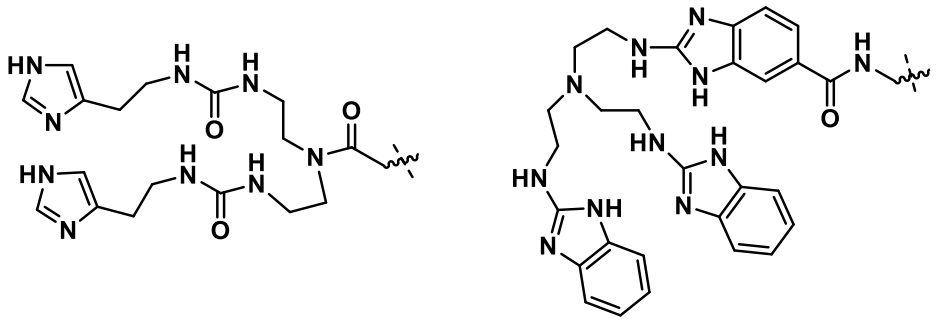

Figure 1.17. Two examples of non-metal ion cleavers for artificial ribonucleases. Figure adapted from (238).

Natural ribonucleases only recognise a small stretch of deoxyribonucleotides; therefore, they can produce multiple cuts in a single molecule. Consequently, it is more appropriate to consider them as base-specific RNA cleaving enzymes. Artificial ribonucleases, on the other hand, have the potential to be sequence-specific (17). In the past few years, the research on artificial ribonucleases has taken central stage since they can potentially be employed as catalytic antisense oligonucleotides in chemotherapy (113). Artificial ribonucleases have been recognised as potential virus-inactivating agents since they possess desirable properties and are capable of catalysing reactions under physiological conditions (258). Unfortunately, a number of barriers have prevented the transition of artificial ribonucleases from “bench to bedside” (113). Artificial ribonucleases need to exhibit high enzymatic turnover to be able to cleave target RNA present in higher concentration than nuclease. The stability of RNase:RNA heteroduplex formed between a ribonuclease and their target RNA molecule can prevent dissociation upon cleavage

(17). So far, the cleavage activity of chemically engineered artificial ribonucleases has been inferior to their natural counterparts. One possible way to improve on this is by the iterative design of different cleavage domains to synthesise molecules capable of forming the correct spatial orientation with respect to target RNA.

The two dominant factors contributing to the cleavage activity are the dynamic behaviour of cleaving motif and the structural orientation of artificial ribonucleases (255). The efficiency of ribonuclease activity is also dependent on the sensitivity of phosphodiester bonds of the target RNA molecules towards cleavage (259). It is vital to develop catalytic groups with the right amount of catalytic activity so that they can efficiently cleave target RNA molecules without cleaving non-hybridised non-complementary RNA. The presence of an extensive number of chelating sites in biological components can lead to dissociation of metal catalysts and non-specific destruction of biopolymers (257). Hence, the design of site-specific metal–independent artificial ribonucleases is one of the most challenging tasks facing development in RNA targeting (245, 260).

An optimal site-specific artificial ribonuclease is a chemically stable, self-reliant compound which is easily synthesised and exerts high efficiency in cleaving phosphodiester bonds. Oligonucleotide-based artificial ribonucleases seem to match the above criteria since theoretically they are capable of binding to any desired region of RNA molecules complementary to the recognition motif (255).

1.5.3.3 Catalytic turnover and design optimisation

For the peptide nucleic acid and oligonucleotide-based artificial ribonucleases to reach therapeutic application, catalytic activity and reaction turnover needs to be enhanced so that the cleavage reaction is catalytic rather than stoichiometric. The ability to reuse chemical ribonucleases due to substrate turnover where one ribonuclease molecule is capable of cleaving more than one target molecule can improve potency and efficacy of ribonucleases as therapeutic drugs. Many research groups have reported the design of artificial ribonucleases containing catalytic groups functioning as molecular scissors at the termini (253, 261, 262). These molecules were capable of cleaving RNA molecules outside the complementary sequence. Hence, they do not exert catalytic turnover of the substrate and can be construed as cleavers rather than catalysts (242). Antisense recognition motif of artificial ribonuclease places the cleaving moiety at the vicinity of the target phosphodiester bond and can encourage duplex chain folding optimal for cleavage (17). The efficiency of turnover is influenced by the length of the

complementary region as well as the site of tethering of the conjugate group. The ribonuclease molecule must have a higher binding affinity to the intact chain rather than the cleavage products (17).

It is desirable to cleave a single-stranded RNA molecule rather than a duplex (238). Site-selective cleavage of RNA in single-stranded forms (loops or bulges) is an effective way to counteract the difficulties faced in imposing double-helical RNA cleavage. Designing artificial ribonucleases capable of distorting RNA target strands and forcing the target to form a favourable geometry for cleavage can solve the apparent shortcoming of artificial ribonucleases and improve the catalytic efficacy of such compounds (251). A significant difference in the rate of acid/base catalysis for single and double-stranded RNA has been reported. Imidazole-based catalysts are one such example where the majority of cleavage was recorded at junctions between stem and loop regions (249). The formation of a double helix RNA places the 2'-hydroxyl and 5'-bonded oxygen of the first and second base in constrained stacked geometry (263). Metal ion chelates are unable to cleave phosphodiester bonds in double-helical RNA molecules due to strong base-stacking interactions between base pairs. One method to enhance catalytic turnover is cleavage within RNA bulge loops (264). The presence of non-complementary regions results in the inability of the molecule to form hydrogen bonds and ultimately adopt a bulge-loop structure. Recently, zinc ion dependent oligonucleotide-based artificial nucleases consisting of 2′-O-methyloligoribonucleosides and 5-amino-2,9-dimethylphenanthroline residue was directed towards varied RNA target sequences specifically designed to form different bulge loop sizes (0-5 nucleotides) (see **Figure 1.18**). Amongst these oligonucleotide-based artificial nucleases, the ones with centrally positioned C-5 linked zinc chelate exhibited multiple turnover mode, obeying Michaelis-Menten kinetics (242).

The correlation between the size of the formed bulges and cleavage activity of ribonucleases was demonstrated through the modification of 2´-O-methyloligoribonucleotide constructs with Zn^{2+}-neocuproine groups attached to different positions (242). It was witnessed that only phosphodiester bonds located within the formed bulge were cleaved and the cleavage was dependent on the position of the metal ion in the oligonucleotide (241). The highest cleavage rate was seen when a metal chelate was protruding from 5´ position of centrally placed uridine. The optimum cleavage corresponded with bulge size 3-4 nucleotide (238). In addition, positioning of the cleaving construct in such a way to be able to cleave the target sequence in a central position will encourage dissociation of cleaved fragments (265).

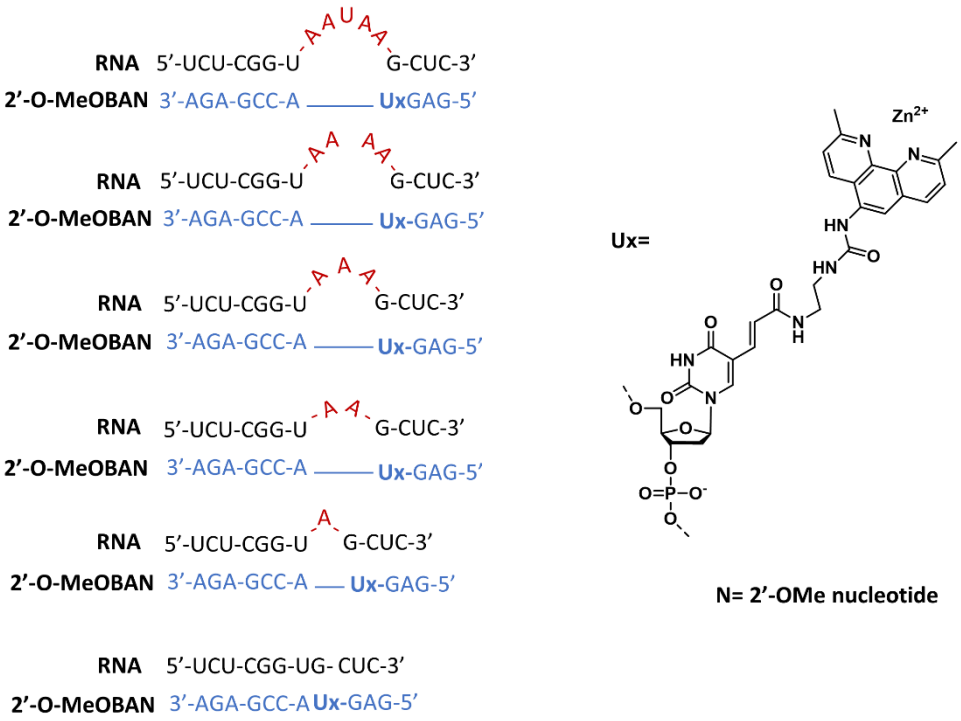

Figure 1.18. Different bulge sizes for 2´-O-MeOBAN. Figure adapted from (238).

One of the most effective artificial ribonucleases ever created contains a peptide nucleic acid (PNA) and a catalytic Cu^{2+}-neocuproine. This PNAzyme is capable of cleaving RNA molecules through the formation of a bulge structure (266).

1.6 Peptidyl-oligonucleotide conjugates

Peptidyl-oligonucleotides are made of short synthetic peptides containing alternates of basic (such as arginine and lysine) and hydrophobic (such as leucine and alanine) amino acids fused with a short oligonucleotide sequence (see **Figure 1.19**) (267). The oligonucleotide compartment actively interacts with the target molecule via formation of Watson-Crick hydrogen bonding providing specificity, while the peptide compartment is responsible for substrate affinity and catalysis. The peptide compartment does not exert catalytic activity in the absence of oligonucleotide fragment (268). Indeed, conjugation of the peptide with even a single nucleotide led to the appearance of some ribonuclease activity (269). Recent studies have demonstrated the potential for POCs to be further developed as therapeutic drugs capable of targeting disease-specific RNA molecules. The cleaving moiety is attached to an antisense oligonucleotide which delivers it to the desired RNA region. Together they cleave RNA molecules without the need for any cofactors or enzymes (268, 270, 271).

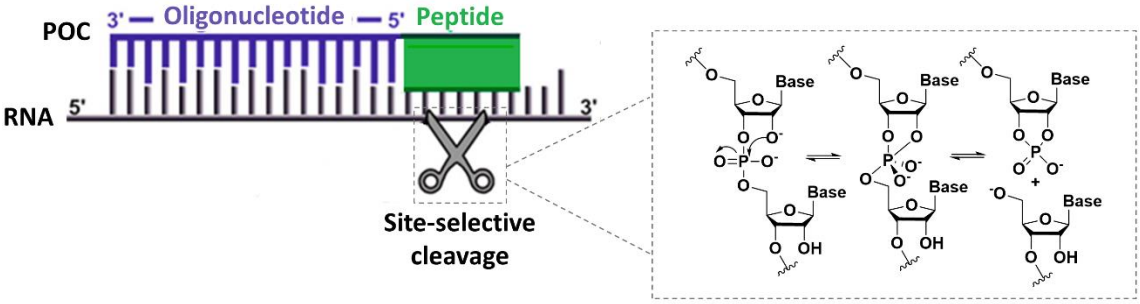

Figure 1.19. Schematic representation of POC bound to RNA molecule. Figure adapted from (267).

1.6.1 Peptidyl-oligonucleotide conjugates Synthesis

Two different approaches have been described for the synthesis of peptide oligonucleotide conjugates (POCs) which are as follows:

1. **Solid-phase synthesis (divergent method)**
2. **Fragment conjugation (convergent method)** (272, 273)

Solid-phase synthesis of POCs involves the sequential assembly of the peptide and oligonucleotide components on a single solid support during standard synthesis until a complete conjugate is generated. In contrast, the fragment conjugation method involves the separate synthesis of the oligonucleotide and peptide fragments to be linked post-synthetically (274).

Solid-Phase Stepwise Synthesis (Divergent Method)

In the solid phase synthesis method, a POC is generated through the sequential assembly of oligomer A (peptide) and oligomer B (oligonucleotide) on a solid matrix. A reactive but masked functional group is present at the conjugation site of the Oligomer A. The points of conjugation are usually the termini or the side chain of the oligonucleotides and peptides respectively. The peptide oligonucleotide assembly can follow one of the two patterns, either “oligo-first-peptide-next” or “peptide-first-oligo-next”. Predominantly, peptides are synthesised first using Boc or Fmoc method (peptide is shown as oligomer A in **Figure 1.20**), followed by oligonucleotides conjugation via the phosphoramidite method (oligonucleotide is shown as oligomer B in **Figure 1.20**) (274).

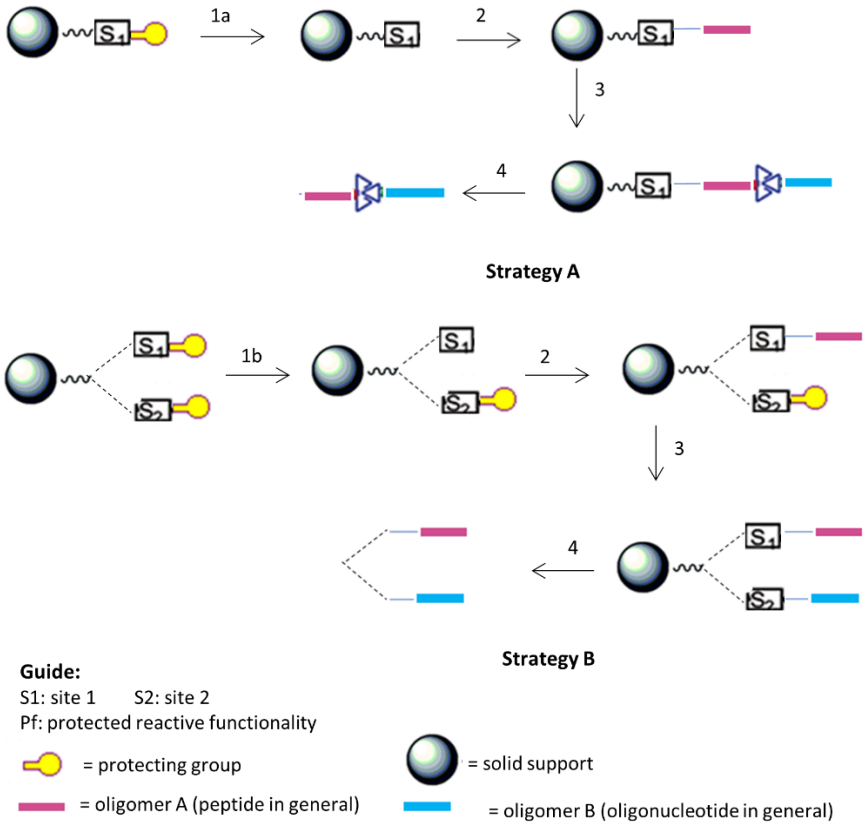

Figure 1.20. Solid-phase stepwise synthesis. 1a and 1b deprotection and selective deprotection of S_1P. 2) Construction of oligomer A in a stepwise manner. 3) Deprotection and construction of oligomer B from S_2P. 4) Cleavage from the solid support. Figure adapted from (274).

The lack of mutual compatibilities in the reaction conditions necessary for the synthesis of oligomers witnessed in the solid-phase method is one of the major bottlenecks of this method. This is particularly in the case of "oligo-first-peptide-next" approach where the acid-labile oligonucleotides are subjected to the relatively harsh reaction conditions essentially used for the synthesis of peptide fragment. Thus, oligonucleotide chains are likely to undergo depurination and cleavage. On the contrary, in the "peptide-first-oligo-next" scheme, the former assembled peptide component remains stable during the synthesis of the oligonucleotide fragment. However, it is to be noted that peptide chains are not always stable during ammonia deprotection steps. Moreover, the activating/deblocking agents and protecting groups used for oligomer A synthesis may not be useful for oligomer B assembly. Therefore, a careful selection of reaction conditions and protecting groups play a fundamental role in the ease of isolation and the percentage of yield acquired (274). One limitation for solid-phase synthesis is finding the right protecting group compatible with both oligonucleotide and peptide moieties. Despite the avoidance of multiple purification steps, the innate incompatibility present between the standard protecting groups limits the degree of functionality incorporated (274, 275). Only amino acids with no reactive side chains like alanine and leucine or those

with easily removable side chains can be conjugated with oligonucleotide deprotection via the divergent method.

Fragment Conjugation (Convergent Method)

The key steps of the fragment conjugation (FC) method for POCs synthesis are described in **Figure 1.21**. In the fragment conjugation approach, both oligomer A and oligomer B are synthesised separately on their solid matrices and are subsequently conjugated together. At the desired point of conjugation, a reaction functionality group is added. In peptides, the conjugation site can be amino acids side chains or C-or N-termini of the peptide chain. In oligonucleotides, conjugation point can be a base, nucleoside or inter-nucleosidic linkages. If the post-synthetic oligomers coupling is performed with an oligomer linked to the solid support, it is termed as solid-phase fragment conjugation (SPFC) method. The resultant POC undergoes cleavage, purification and characterisation afterwards. Alternatively, if the purified peptide and oligonucleotide is conjugated post-synthetically then the method is referred to as fragment conjugation in liquid phase (LPFC) (274). TFA and HF can be used for resin cleavage in the convergent method (276). Many linkages can also be employed through this method, permitting optimisation of rudimentary characteristics such as LogP and solubility in the conjugate. Despite widespread application, the convergent method suffers from some disadvantages like multiple purification stages and poor coupling efficiencies.

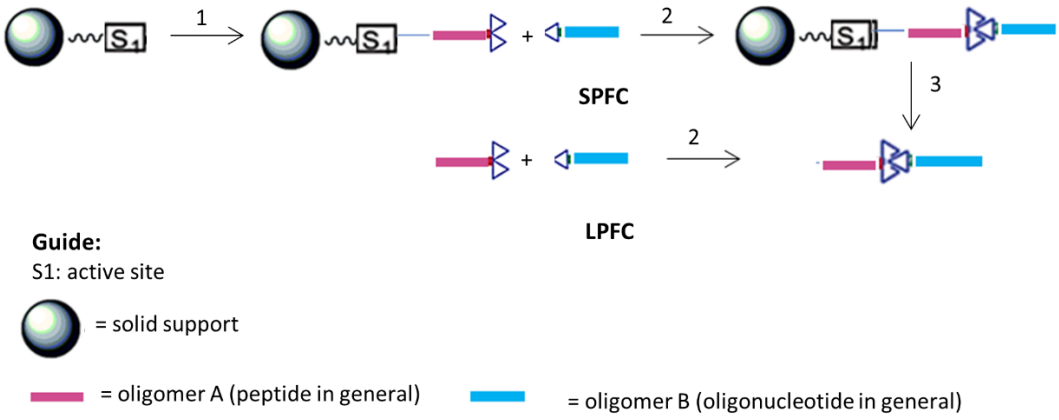

Figure 1.21. Fragment conjugation. 1) Construction of oligomer A 2) conjugation of A to B 3) cleavage from the solid support. Figure adapted from (274).

For wide-scale preparation of POCs, the solid-phase method is considered an ideal method. The less laborious purification step is the major benefit of the solid-phase synthesis in comparison to the liquid-phase method as the majority of the soluble impurities and products of side-chain reactions are washed away in each step. Therefore,

after the detachment of bioconjugates from solid matrices, the rest of the impurities are removed usually in a single step. In addition, the solid phase comprises the fully automated machine-assisted systems from start to end of the POCs synthesis process. Moreover, the use of solid-phase method has considerably increased through the introduction of various microarray techniques. Alternatively, liquid-phase methods (e.g. in LPFC), requires laborious purification steps before and after biopolymers conjugation. The conjugate purification is much more difficult in the case of liquid-phase synthesis in comparison to the purification of peptides and oligonucleotides, particularly if highly polar amino acids are present in conjugates. The solid-phase synthesis method is not the most convenient way to prepare relatively longer conjugates. The POCs obtained from the solid-phase method usually contains 10-15 monomers of peptide and oligonucleotides sequences. Fragment conjugation is the method of choice for the synthesis of peptide oligonucleotide conjugates used in biological studies. Any length of oligonucleotides and peptides can be coupled using the LPFC method, considering other appropriate conditions such as solubility is provided. In the case of conjugates rich in arginine, the solution phase coupling cannot be performed due to peptide precipitation caused by electrostatic interactions. This issue was resolved by employing the on-resin fragment conjugation approach where oligonucleotide was adsorbed onto the anion exchange resin and conjugation was performed passing coupling agents and peptide solutions over the resin. Alternatively, under denaturing conditions cationic peptides can be successfully conjugated to the oligonucleotides moiety (274, 277, 278).

The C/N terminal or the side chain of the peptide fragment can be conjugated to either the phosphate backbone or the 3´ or 5´ position of the sugar unit of the oligonucleotide. Various chemical linkages exist (see **Figure 1.22**) which can be used to link the two fragments of peptidyl-oligonucleotide such as amide, disulfide, thioether, oxime, thioester, thiazolidine and N-acylphosphoramidate. It is believed that the choice of chemical linkage is based on the ease of synthetic accessibility (274). Disulfide linkage of the CPP—S-S-cargo is reducible which can lead to enhanced cellular uptake of peptide conjugates (279).

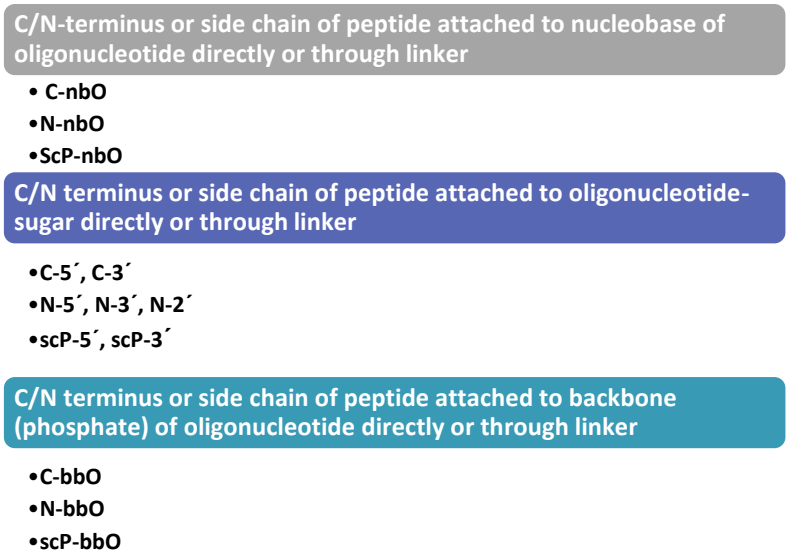

Figure 1.22. Types of peptide oligonucleotide conjugates classified based on point of linkage. Figure adapted from (274).

1.6.2 Mechanism of RNA cleavage by peptidyl-oligonucleotide conjugates

Arginine owes its basicity to the presence of proton-loving guanidine moiety. Arginine has the highest proton affinity of all natural amino acids, followed closely by lysine and histidine (280). The guanidinium functionality is capable of interacting with polar and anionic molecules through hydrogen bonds (280). The guanidinium group is naturally present in several proteins and plays an important role as an anchoring activating group in hydrolysis. Several studies have focused on the catalytic activity of artificial systems containing guanidinium units on their own or in conjugation with hydroxyl or metal centre (281–284). Moreover, the guanidium group has been used as a transfecting agent, transporting DNA across the cellular membrane as a result of its high affinity to nucleic acid strands (285, 286). Incorporation of guanidinium groups in a non-metallic catalyst such as tris[2-(benzimidazol-2-yl)ethyl]amine has been shown to encourage RNA transesterification independent from secondary structure or base composition of RNA (253). The guanidinium group potentially accelerated the rate of the reaction by protonating the non-bridging oxygen in the phosphorane intermediate state (228).

In a recent study, Baldini *et al.* demonstrated catalytic capabilities of calix[4]arene scaffold derivatives functionalised with two to four guanidinium units in cleaving an RNA mimic (2-hydroxypropyl-p-nitrophenyl phosphate (HPNP)). Bi- and trimetallic derivatives of calix[4]arene was proven to be effective phosphodiester cleavers due to the presence of metal centre acting as binding and activating units (287). The superiority of

di-guanidium constructs in comparison to monofunctional model unequivocally showed the cooperative action of catalytic moieties. The simultaneous presence of a neutral guanidine group (general base) and protonated guanidine residue (general acid) on the same molecular framework encourages cleavage (288). The mechanism of catalysis induced by synchronised action of two guanidinium groups can be seen in **Figure 1.23.** Electrostatic repulsion between di or multi- guanidinium groups facilitates electron deprotection from one of the groups. No evidence of transition state stabilisation from other functional groups than the guanidine–guanidinium pair was witnessed in the study (288). The structural properties of the molecular scaffold between the guanidine residues are crucial to balance preorganisation and flexibility, keeping the active functions in close proximity and enhancing cleavage (289). Furthermore, a study on the catalytic activity of three bifunctional catalysts incorporating two di-guanidine functional groups further reaffirmed the synchronised action of two guanidine groups. Only the monoprotonated form of the compounds was catalytically active (289).

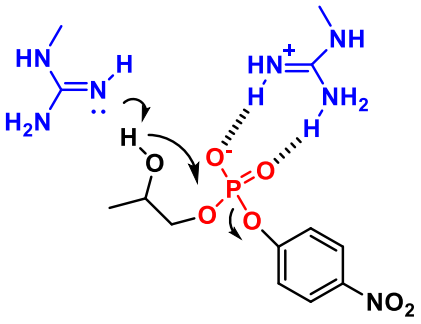

Figure 1.23. Proposed mechanism of guanidine-guanidinium mediated HPNP cleavage, adapted from (289).

Although the mechanism of action of guanidinium-medicate RNA cleavage is not fully understood, the interaction between phosphate and guanidinium is well established (280, 290, 291). The positively charged guanidinium moiety catalyses the cleavage through electrostatic interaction with negatively charged phosphate groups together with the enhancement of transesterification reaction (18, 280, 292). The interaction between guanidium and phosphate anion was investigated using methyl guanidinium and dimethyl phosphate prototypes and molecular dynamics simulation. A study reported the formation of noncovalent complexes between the two functionalities correlating the results obtained before (293). Additionally, the formation of hydrogen bonds between guanidium and DNA was reported in a study by Vallet *et al.* (294). As a negatively charged anion, the phosph[on]ate moiety has a high affinity for neighbouring electropositive groups.

Therefore, the catalytic activity of peptidyl-oligonucleotide conjugates is attributed to the presence of amphipathic arginine-rich peptide constructs. The theory postulated for guanidinium-mediated cleavage of RNA via POCs is in agreement with previous studies proposing the catalysis of phosphodiester bond through stabilisation of phosphorane transition state, promotion of 'in-line' geometry and acting as a general acid-base catalyst (17, 17, 267, 290, 291, 295). Hence, several functional moieties can be introduced in the conjugate structure to facilitate transesterification. These constructs can accelerate the rate of hydrolysis by (i) enhancing the rate of deprotonation at 2' hydroxyl group (ii) stabilising pentacoordinate phosphorane intermediate and/or leaving group (iii) promoting the active 'in-line' conformation when 2'-oxyanion enters or 5' linked nucleotide leaves the phosphorane intermediate state (267, 295).

Despite the valuable insight provided by these mechanistic studies, the difference between the experiment medium from the mixture of organic solvents in these simulations to purely aqueous solutions and physiological conditions in cleavage experiments only allows a tentative comparison. Further studies are needed to answer the unsolved questions concerning the base-specific mechanism of RNA cleavage by POCs.

1.6.3 Peptidyl-oligonucleotide conjugates design development

Barbier and Brack were first to report acceleration of oligonucleotide hydrolysis via basic polypeptides (296). They examined the effects of three polypeptide families on polymerisation of adenosine 5'-phospho-2-methylimidazole (2-MeImpA) and oligonucleotide degradation. The first family of polypeptides consisted of insoluble glycine and alanine polymers while the second family included water-soluble alternates of hydrophilic (Arg) and hydrophobic (Leu) residues (245). The third family contained mono or di Glu amino acids with either Lue, Arg or Ser possibly capable of forming ternary complexes with divalent cations and oligonucleotides (245). Acceleration in the hydrolysis of oligoadenylates was only witnessed when arginine residues were incorporated into polypeptide chains (245). Additionally, polypeptide chains made of alternating sequences of L-Leu and L-Lys exhibited catalytic activity. The hydrolytic activity was sensitive to hydrophobic residues, increasing proportionally with the number of hydrophobic residues incorporated in the polypeptide chain (296).

Pyshnyi *et al.* studied the possibility of oligodeoxyribonucleotide-peptide conjugate site-directed cleavage of a fragment of the anticodon loop of *E.coli* $tRNA^{Phe}$ back in 1997. Site-specific hydrolysis of RNA phosphodiester bonds was witnessed where cleavage

localisation and efficiency was determined by the number of Arg residues in the conjugate (297). Conjugation of short peptide moieties made of alternating basic and hydrophobic amino acids to 5'- terminal phosphate of antisense oligonucleotides resulted in high ribonuclease activity where Pyr-A and G-X motifs were cleaved in both nearby complementary sites and at phosphodiester bonds in a random manner (268).

One study reported sequence-specific cleavage of *in vitro* transcript of $tRNA^{Lys}_3$ by a peptidyl-oligonucleotide conjugate $^{C}NH_2Gly(ArgLeu)_3ArgLeu^{N}$—p-DEG-5´CCCTGGACCCTCAGAT-3´ using peptide $[LeuArg]_4$-Gly-NH_2 (271). In this experiment, conjugation of a short peptide $[LeuArg]_{2—4}$ to 5´ terminal phosphate group resulted in a catalytically active conjugate. The molecule was able to bind to several different regions within the RNA molecule and cleave C56_A57 phosphodiester bond of target RNA under physiological conditions (271). Subsequently, non-sequence specific cleavage of enzyme mimics through the fusion of divergent short oligodeoxyribonucleotides and peptides built of alternating leucine and arginine residues was reported (268). The chosen oligonucleotide sequences lacked complementarity with the target RNA domain longer than dinucleotides. A short peptide sequence, $[LR]_4$-G-NH_2 was chosen for conjugation. The catalytic activity of conjugates was tested against *in vitro* transcripts of human $tRNA_3^{Lys}$ and HIV-1 RNA (123-218 nt). The designed single-stranded artificial ribonucleases exhibited catalytic activity, cleaving RNA within loops and junctions. Cleavage selectivity of conjugates varied from one conjugate to another depending on the sequence and length of oligonucleotide recognition motif, with conjugates exhibiting either G-X or Pyr-A specificity (268). Pyr-A motifs are known to be particularly susceptible to phosphodiester transesterification (232, 298). The activity of unconjugated components of these conjugates and equimolar mixtures of the two components (i.e. peptide and oligonucleotide) was also tested. Remarkably, the inactivity of unconjugated components was witnessed in all cases indicating the indispensability of oligonucleotide component which provides an "active" conformation for peptide (268).

Mironova *et al.* was first to report the synthesis and assessment of ribonuclease activity of conjugates which displayed G-X specificity similar to RNase T1 (269). In the study, a series of conjugates were made through incorporation of various oligonucleotide sequences with $(LR)_4$-G-NH_2 peptide to investigate the effect of the recognition motif on efficiency and specificity of RNA cleavage. The conjugates were tested against a non-complementary *in vitro* transcript of 96 nt fragment of HIV-1 RNA. Circular dichroism analysis of unconjugated and conjugated peptide and oligonucleotide structures hinted at

a change in peptide repositioning and folding upon conjugation irrespective of the oligonucleotide sequence which triggers ribonuclease activity of the construct (269). Only conjugates containing peptides made of leucine and arginine building blocks exerted considerable ribonuclease activity. Peptides made solely of arginine or arginine and serine residues displayed negligible catalytic capability. Moreover, the influence of peptide length on ribonuclease activity was investigated where conjugates of H_2N-G$(RL)_n$ peptide were made, n ranging from 2 to 4. The study reported a correlation between peptide length and ribonuclease activity. All designed conjugates displayed G-X+PyrA cleavage specificity, cleaving RNA within single-stranded regions (269).

Furthermore, in a later study Mironova *et al.* reported the synthesis of RNase T1 mimicking artificial ribonucleases, where the most catalytically active candidate was built of a nonadeoxyribonucleotide connected to $(LR)_4$-G-NH_2 peptide via a linker made of three abasic deoxyribonucleotides (270). Despite the catalytic efficacy and distinctive cleavage patterns (G-X, Pyr-A) shown in the earlier studies, the reported artificial ribonucleases were base-specific rather than sequence-specific, capable of recognising mono or dinucleotide blocks in the target sequence (267).

In a study by the group in 2015, Williams *et al.* examined the effect of different structural variants of POCs on selective cleavage of TΨC loop of $tRNA^{Phe}$ extracted from brewer's yeast and reported a new class of sequence-specific catalytic POCs. The study indicated the importance of peptide structural properties i.e. sequence, length, charge separation, secondary structure and conformational flexibility on catalytic efficiency. The reported conjugates contained a 17-mer antisense oligonucleotide stretch (pGATCGAACACAGGACCT) covalently attached to different variations of the core polycationic peptide $[LR]_nG$ (LRLRG (P2), LRLRLRLRG (P4), LRLRGLRLRG (P4G)) (see **Figure 1.24** (**A**) and (**B**) for general schematic) (267). Two different variations of peptide C terminal, carboxylic acid and carboxamide, were synthesised to investigate C-terminal effects on hybridisation and cleavage. Shorter peptides showed minimal catalytic activity, whereas conjugation with the carboxamide containing decapeptide showed a significant increase in the catalytic activity of POC (267). It was also observed that peptides containing C-terminal carboxamide had superior cleavage capabilities than their corresponding analogues. Molecular flexibility plays an instrumental role in catalysis and has a direct correlation with conformational freedom. Hence, enhancement in flexibility allows the catalyst to adapt to the substrate in the transition state (18). However, the accompanying entropic cost might be detrimental for catalytic efficiency. The presence

of an additional glycine residue in acetyl-pep4G sequence enhanced the flexibility of molecule allowing it to explore more energetically favourable conformations (299–302). Therefore, the addition of extra glycine residue had a positive impact on both the pattern and extent of cleavage (18). In fact, a 4-fold increase in the catalytic activity of conjugate encompassing an additional glycine residue (P4G-A-COOH) was seen in comparison to P4-A-COOH. Upon binding, the tRNA was unfolded and became single-stranded and the conjugated oligonucleotides delivered the peptide to the susceptible ^{61}CACAG^{65} sequence. High level of cleavage (up to 100% in 24 hr) under RNase A inactivation conditions was seen with some conjugates with major cuts at C63-A64 and minor cuts at C61-A62 and A62-C63 sites. All cleavage sites directed by the recognition motif were located at accessible proximity within the reach of the catalytic peptide (267).

Subsequently, Staroseletz *et al.* reported a new generation of dual conjugates consisting of two short spatially-separated RNA recognition motifs complementary to TΨC loop and 3' accepter stem of $tRNA^{Phe}$ bound together via an amphipathic peptide (see **Figure 1.24** (**C**) and (**D**) for general schematic) (18). The strategic design of the conjugate allowed the catalytic peptide to be placed adjacent to the single-stranded region of $tRNA^{Phe}$ resulting in high catalytic efficiency (up to 100% cleavage within 4 hours in the best structural candidate) with a potential for catalytic turnover (18). A library of 11 novel dual peptidyl-oligonucleotide conjugates varying in structure and length of linker and recognition motifs were synthesised to test the influence of conformational flexibility on hybridisation and cleavage (18). Additional flexibility was introduced through the incorporation of two linkers where the peptide sequences chosen for conjugation were $[LR]_4G$, Mal-$[LR]_4G$ and Mal-$[LRLRG]_2$. Variations in antisense recognition motif were also made to differ the size of the single-stranded region in target tRNA from 3 to 5 nt long. Covalent attachment of peptide to the oligonucleotide via a zero-length phosphoramidate linker resulted in a conformational constrained and a catalytically inactive conjugate (18). Conformational freedom was the key determinant of catalytic activity where incorporation of an extra glycine residue in catalytic peptide, presence of a flexible linker and inclusion of a truncated recognition motif all led to high catalytic activity. Therefore, a fine balance needs to be maintained between conformational freedom and base-pair matching to result in catalytically active artificial enzymes (18).

Building on previous 'single'(267) and 'dual'(18) conjugates design strategy, chemically engineered peptidyl oligonucleotides were directed towards a biologically relevant oncogenic miR-21 target (from this point forward POCs are known as miRNases). Linear

or hairpin oligonucleotide recognition motifs were attached to catalytic active peptide acetyl-$(LRLRG)_2$ via an aminohexyl linker at either 3' or 5' end. To encourage specific effective binding to target miR-21, the hairpin oligonucleotide design encompassed a stretch of 10-16 nucleotides, a 5-nucleotide long loop and a stem consisting of 6-9 base pairs (see **Figure 1.24** (**E**) and (**F**) for general schematic) (303). Stronger binding affinity was witnessed in conjugates with elongated recognition motifs where a stretch of 14-16 nt even in hairpin oligonucleotides was instrumental to binding affinity (303). High cleavage extent was reported in 5'-conjugates where several miRNases demonstrated site-selective catalytic efficiency at G-X linkages with the best structural candidate leading to downregulation of miR-21 lymphosarcoma cells, reactivation of tumour-suppressor protein $PDCD_4$ and diminished proliferative activity (303).

Subsequently, a novel series of miRNases were developed through the conjugation of oligodeoxyribonucleotide recognition motif containing a hairpin at 3'-end and catalytic construction NH_2-$G(RL)_4$-$^{5'}TCAA^{3'}$ at 5' end (304). The hairpin structure was incorporated into the oligonucleotide sequence to optimise hybridisation and provide protection against exonuclease attacks (305, 306). Efficient cleavage of phosphodiester bonds at miR-21 and miR-17 target sequences in Pyr-X motifs was observed. In addition, a significant enhancement (>11- fold) in ribonuclease activity of conjugate was seen in the presence of RNase H indicating the capability of the conjugate to recruit intracellular RNase H (304). The presence of RNase H can potentially force the cleaving domain to interact more often with the single-stranded region of the target and can facilitate dissociation of cleaved fragments promoting multiple turnover mode. An optimal miRNase design can be achieved through balancing binding affinity, stability and catalytic turnover while minimising toxicity and off-target effects (304).

Lastly, a comprehensive study of serum stability and biological performance was undertaken using the best miR-21-miRNase candidate (5'-h-9/14) exhibiting the highest degree of catalytic activity previously reported in (303), comprised of a peptide moiety $(LRLRG)_2$ and a miR-21-targeted oligodeoxyribonucleotide. The strategic placement of hairpin and peptide at 3' and 5'end respectively provided stability against nucleases without the need for incorporation of chemically modified nucleotides (307). This was the first time that an anti-miR artificial ribonuclease with a true catalytic character was reported. Transfection of the miR-21-miRNase resulted in miR-21 knockdown, inhibition of cell growth, induction of apoptosis and retardation of tumour growth (307). The oncosupressive effects of miRNase persisted upon transplantation of tumour cells into

mice where retardation of tumour cell growth *in vivo* was witnessed with a single treatment of tumour cells with miR-21-miRNase (307). The synergetic action of non-sequence specific RNase H with miRNase witnessed elevated the catalytic turnover, augmenting multiple turnover catalysis (307).

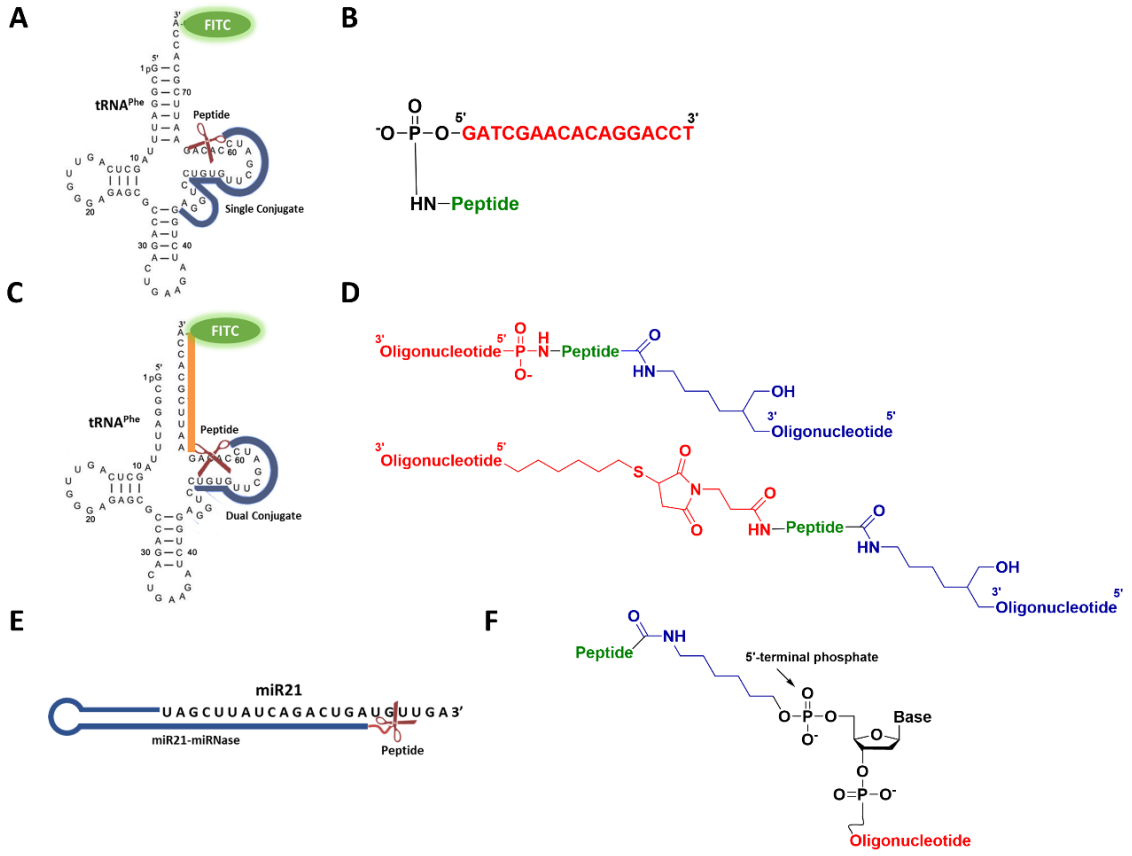

Figure 1.24. Schematic summary of POC design development over time. (**A)** Schematic representation of the general complex of sequence-specific POC and $tRNA^{Phe}$. The conjugates were designed to target TΨC- loop and acceptor stem of $tRNA^{Phe}$ (267). (**B)** General structure of sequence-specific POC containing the same 17-mer oligonucleotide recognition motif (red) but different catalytic peptide construct (green) (267). (**C)** Secondary structure of $tRNA^{Phe}$ along with the TΨC loop and accepter stem binding sites targeted by the recognition motifs in dual conjugates (18). (**D)** General structure of dual conjugates showing the catalytic peptide construct (green) placed between two oligonucleotide recognition motifs (presented in red and blue) (18). (**E)** Schematic representation of a general structure of anti-miR21 POCs with catalytic peptide placed at the 5'-end of the antisense recognition motif (303). (**F)** General structure of anti-miR21 conjugate where the catalytic peptide was conjugated via the carboxylic group at C-terminus to the aminohexyl linker attached to 5'-terminal phosphate of the antisense oligonucleotide recognition motif (303).

Even though oligonucleotide research has taken centre stage in the past two decades, an effective oligonucleotide therapeutic agent has not yet reached the market. The failure is attributed to the number of factors: lack of stability in intracellular fluid, poor cellular intake of the naked molecule, low binding affinity and lack of target specificity (274). Enhancing the potency of POCs is an important step for transition into clinical practice. The concentration of POCs in the cellular environment must be substoichiometric (267).

The size of the oligonucleotide fragment needs to be long enough to interact effectively with the target molecule but short enough to provide dynamic equilibrium between bound and free conjugates. The cellular uptake of oligonucleotides has been reported in several reviews. Additionally, the presence of peptides and oligonucleotides in the same medium whether as non-covalent complexes or covalent conjugates can enhance cellular membrane permeability and uptake of oligonucleotides. Furthermore, peptide conjugation can enhance binding affinity and potentially stabilise oligonucleotides protecting them from enzymatic digestion (274). Peptides such as CPPs, Tat, arginine rich MTS and histidine-rich peptides have been used to enhance cellular uptake of oligonucleotides (308–310).

The studies highlight the remarkable scientific progress in the field of peptidyl-oligonucleotide therapeutics. Recent advances illuminate the key structural requisite for a sequence-specific catalytically active POC. Despite the recent encouraging results, the need for a specific, self-reliant and efficient artificial catalyst is still at large. It is imperative to optimise substrate turnover, reduce effective dosage and improve potency. Indeed, the majority of POCs designed to date have either cleaved RNA sequences next to the recognition motif in a non-catalytic manner or have cleaved non-complementary regions of target RNA with high catalytic turnover. Neither of the two extremes will make POCs desirable for therapeutics (267). Hence, it is vital to implement changes in POC structure to enhance specificity, boost multiple turnover allowing the conjugate to turnover multiple substrate molecules and emancipate the conjugate from reliance on cellular enzymes.

1.7 Aims and objectives

RNA-based therapeutics is a promising alternative to small molecule drugs and biologics. They hold the potential to greatly extend the domain of 'druggable' targets and revolutionise drug development. One of the promising approaches to develop RNA-based therapeutics is peptidyl-oligonucleotide conjugates (POCs), which to this date have exerted cleaving properties at two extremes: (1) base-specific cleavage with high catalytic turnover or (2) sequence-specific cleavage in the absence of catalytic turnover (see **Section 1.6.3**). A desirable POC should combine both extremes and should be able to cleave RNA with high efficiency and catalytic turnover without the need for endogenous enzymes (RNase H, RISC or Cas9 protein) or exogenous cofactors. One of the recognised methods to encourage catalytic turnover is cleavage within RNA bulge-loops. Antisense oligonucleotide recognition motif is designed in such a way to create bulge-loops in the target RNA upon hybridisation. Hence, the overall aim of this project is to design, synthesise and characterise POCs capable of sequence-specific cleavage of RNA in the bulge-loop regions to ultimately achieve multiple catalytic turnover. Building on the previous work done by this group in collaboration with the Institute of Chemical Biology and Fundamental Medicine, Novosibirsk, Russia, we aim to design, synthesise, characterise, and biologically test novel bulge-loop inducing POC molecules against both model RNA sequences and biologically-relevant RNAs ($tRNA^{Phe}$, miRNA-21 and miRNA-17). The peptide molecule will be tethered to the antisense recognition motif at various positions and/or configurations to optimise the spatial orientation of the peptide and encourage RNA cleavage. The expectation here is that by forcing the target to form a bulge-loop structure upon hybridisation with POCs, we can promote potent RNA cleavage, if/when the key players involved in catalysis are favourably positioned against the target site of the RNA target.

In the first phase of the project, *"single"* bulge-loop inducing peptidyl oligonucleotide conjugates will be designed, synthesised and fully characterised where the catalytic peptide is conjugated to an antisense recognition motif through central incorporation of either a modified adenosine residue or an abasic nucleotide. By changing the number of non-complementary nucleotides in the target sequence, the size of the bulge is tailored to find the optimum cleavage conditions. The design will be directed towards the TΨC loop and the 3' acceptor stem of $tRNA^{Phe}$. Even though tRNA is not deemed a clinical target, the presence of numerus common secondary structural elements makes it an optimal model target for *proof-of-principle* section of this research. Hybridisation properties,

cleavage activity and the dynamic molecular interactions will be assessed (in collaboration with colleagues from the University of Manchester and Institute of Chemical Biology and Fundamental Medicine (Novosibirsk, Russia)) to obtain structural insights vital for the next stage of our work.

Subsequently, in the second phase, to boost potency and achieve reaction catalytic turnover, the design will be further optimised through incorporation of multiple peptide entities. *"Bis"* and *"triple"* conjugates will be synthesised and fully characterised. A variation in the peptide sequence will be made, where a shorter heptapeptide (Ac-$[LR]_3G$) will be utilised in the *"triple"* conjugate synthesis. Hybridisation and ribonuclease activity will be tested using both the conventional gel electrophoresis (in collaboration with the Institute of Chemical Biology and Fundamental Medicine, Novosibirsk, Russia) and a versatile in-house fluorescent assay developed in Manchester against a model, fluorescently labelled hybrid RNA sequence. The assay will provide us with the opportunity to test the catalytic turnover capabilities of multiple samples and to assess reaction kinetics (in collaboration with colleagues from the University of Manchester). A detailed ribonuclease kinetic modelling will be reported for the first time for POCs where conventional kinetic parameters (K_m, V_{max} and K_{cat}) will be calculated.

In the third phase of this research, building on the structural insights gained in the previous phases, the bulge-loop inducing conjugate design will be directed towards biologically relevant targets (i.e. oncogenic miR-21 and miR-17). In this instance, we will employ either conventional gel electrophoresis or an in-house developed self-assembling peptide hydrogel-based analytical device to follow the disappearance of miRNA upon sequence-specific cleavage by miRNA-targeting conjugates. Conjugates' ability to recruit natural ribonucleases (i.e. RNase H) in multiple turnover mode will also be tested.

Finally, in the fourth phase of this research, the effects of 2'-O-methyl chemical modification on hybridisation, ribonuclease activity and serum stability will be tested using a previously reported miRNA-specific POC (hereafter known as miRNase) which demonstrated efficient catalytic activity. Pre-existing knowledge of the catalytic efficacy of the naked miRNase is fundamental in establishing the role of chemical modification in prolongation of half-life and evasion of natural ribonuclease in the cellular environment as well as catalytic efficacy.

To achieve the above aims, the following objectives will be addressed:

1. Design and synthesis of an array of novel peptidyl-oligonucleotide conjugates as listed below:

   i. "*Single*" bulge-loop inducing conjugates consisting of an antisense recognition motif and a cleaving construct. The length of the recognition motif and the size of the bulge-loop induced will be varied, and the influence of peptide sequence and the point of attachment on catalytic activity will be assessed against $tRNA^{Phe}$.

   ii. *"Bis"* and *"triple"* bulge-loop inducing conjugates consisting of an antisense recognition motif and two and three cleaving contructs, respectively, to target both $tRNA^{Phe}$ and a model, fluorescently labelled linear RNA hybrid.

   iii. *"Single"* bulge-loop inducing conjugates directed towards biologically-relevant oncogenic miR-21 and miR-17.

   iv. *"Single"* conjugates consisting of a hairpin antisense oligonucleotide and a catalytic peptide, where the recognition motif has been partially or fully modified by incorporation of 2'-O-methyl groups into deoxyribose residues, directed towards oncogenic miR-21.

2. Isolation and purification of the synthesised compounds using RP-HPLC and size-exclusion chromatography.

3. Full characterisation of the synthesised conjugates using ^{1}H NMR spectroscopy and MALDI-TOF mass-spectrometry methods.

4. Analysis of hybridisation properties of synthesised POCs with target molecule using gel-shift electrophoresis (in collaboration with the Institute of Chemical Biology & Fundamental Medicine (ICBFM), Russia).

5. Assessment of the ribonuclease activity of *"single"*, *"bis"* and *"triple"* conjugates against intact $tRNA^{Phe}$ using gel electrophoresis (in collaboration with the Institute of Chemical Biology & Fundamental Medicine (ICBFM), Russia).

6. Assessment of the ribonuclease activity of modified and unmodified miRNases against miR-21 and miR-17 via gel electrophoresis (in collaboration with the Institute of Chemical Biology & Fundamental Medicine (ICBFM), Russia).

7. Design and optimisation of FRET-based cleavage assay capable of monitoring RNA cleavage in real time (in collaboration with Sameen Yousaf, the University of Manchester).

8. Assessment of the catalytic turnover of the designed anti-tRNA conjugates via FRET-based cleavage assay (in collaboration with Sameen Yousaf, the University of Manchester).

9. Establishing kinetic modelling for the best structural candidates of *"single"* and *"bis"* conjugates.

10. Evaluation of cleavage activity of designed bulge-loop inducing miRNases (miR-21-miRNase) using in-house developed multi-functional peptide hydrogel system (in collaboration with Sameen Yousaf, the University of Manchester).

11. Test the ability of miR-21-miRNases to recruit RNase H for RNA cleavage using multi-functional peptide hydrogel system (in collaboration with Sameen Yousaf, the University of Manchester).

12. Evaluate the cleavage activity, serum stability and tumour proliferation of partially or fully modified miR-21-miRNase conjugates (in collaboration with the Institute of Chemical Biology & Fundamental Medicine (ICBFM), Russia), incorporating 2'-O-methyl protecting groups.

1.8 References

1. Lindsay,M.A. (2003) Target discovery. *Nat. Rev. Drug Discov.*, **2**, 831–8.

2. Singh,S., Malik,B.K. and Sharma,D.K. (2007) Molecular drug targets and structure based drug design: A holistic approach. *Bioinformation*, **2**, 68–72.

3. Rollinger,J.M., Stuppner,H. and Langer,T. (2008) Virtual screening for the discovery of bioactive natural products. *Prog. Drug Res.*, **65**, 211, 213–49.

4. Zaman,G.J.R., Michiels,P.J.A. and Van Boeckel,C.A.A. (2003) Targeting RNA: New opportunities to address drugless targets. *Drug Discov. Today*, **8**, 297–306.

5. Ecker,D.J. and Griffey,R.H. (1999) RNA as a small-molecule drug target: doubling the value of genomics. *Drug Discov. Today*, **4**, 420–429.

6. Warner,K.D., Hajdin,C.E. and Weeks,K.M. (2018) Principles for targeting RNA with drug-like small molecules. *Nat. Rev. Drug Discov.*, **17**, 547–558.

7. Yu,A.-M., Jian,C., Yu,A.H. and Tu,M.-J. (2019) RNA therapy: Are we using the right molecules? *Pharmacol. Ther.*, **196**, 91–104.

8. Hurley,L. and Boyd,F.L. (1988) DNA as a target for drug action. *TIPS*, **9**, 402–407.

9. Haq,I. (2002) Thermodynamics of drug-DNA interactions. *Arch. Biochem. Biophys.*, **403**, 1–15.

10. Kassem,H.S., Girolami,F. and Sanoudou,D. (2012) Molecular genetics made simple. *Glob Cardiol Sci Pr.*, **1**, 1–16.

11. Clancy,S. (2008) RNA Functions. *Nat. Educ.*, **1**, 102.

12. Abu-Jamous,B., Fa,R. and Nandi,A.K. (2015) Integrative Cluster Analysis in Bioinformatics Wiley.

13. Garvan Institute of Medical Research. Copying, transferring and translating DNA. https://www.garvan.org.au/research/kinghorn-centre-for-clinical-genomics/learn-about-genomics/dna-base/collection1/copying-transferring-and-translating-dna (accessed May 20, 2020).

14. Cech,T.R. and Steitz,J.A. (2014) The noncoding RNA revolution-trashing old rules to forge new ones. *Cell*, **157**, 77–94.

15. Sharp,P.A. (2009) The centrality of RNA. *Cell*, **136**, 577–580.

16. Pearson ND,P.C. (1997) RNA as a Drug Target. *Chem. Biol.*, **4**, 409–414.

17. Niittymäki,T. and Lönnberg,H. (2006) Artificial ribonucleases. *Org. Biomol. Chem.*, **4**, 15–25.

18. Staroseletz,Y., Williams,A., Burusco,K.K., Alibay,I., Vlassov,V. V., Zenkova,M.A. and Bichenkova,E. V. (2017) 'Dual' peptidyl-oligonucleotide conjugates: Role of conformational flexibility in catalytic cleavage of RNA. *Biomaterials*, **112**, 44–61.

19. Alberts B, Johnson A, Lewis J, et al. (2002) From DNA to RNA. In *Molecular Biology of the Cell*. New York: Garland Science, pp. 1–19.

20. Wu,J., Xiao,J., Zhang,Z., Wang,X., Hu,S. and Yu,J. (2014) Ribogenomics: the science and knowledge of RNA. *Genomics. Proteomics Bioinformatics*, **12**, 57–63.

21. Clancy,S. (2008) DNA transcription. *Nat. Educ.*, **1**, 41.

22. Huang,Y. and Carmichael,G.G. (1996) Role of polyadenylation in nucleocytoplasmic transport of mRNA. *Mol. Cell. Biol.*, **16**, 1534–1542.

23. Zhao,B.S., Roundtree,I.A. and He,C. (2017) Post-transcriptional gene regulation by mRNA modifications. *Nat. Rev. Mol. Cell Biol.*, **18**, 31–42.

24. Bhagavan,N.V. and Ha,C.E. (2015) RNA and Protein Synthesis. In Bhagavan,N. V, Ha,C.-E. (eds), *Essentials of Medical Biochemistry*. Elsevier, San Diego, pp. 419–446.

25. Cooper GM (2000) Eukaryotic RNA Polymerases and General Transcription Factors. In *The Cell: A Molecular Approach*. Sunderland (MA): Sinauer Associates.

26. Clancy, S. & Brown,W. (2008) Translation: DNA to mRNA to Protein. *Nat. Educ.*, **1**, 101.

27. Gebauer,F. and Hentze,M.W. (2004) Molecular mechanisms of translational control. *Nat. Rev. Mol. Cell Biol.*, **5**, 827–835.

28. Noller,H.F., Green,R., Heilek,G., Hoffarth,V., Huttenhofer,A., Joseph,S., Lee,I., Lieberman,K., Mankin,A., Merryman,C., *et al.* (1995) Structure and function of ribosomal RNA. *Biochem. Biol.*, **73**, 997–1009.

29. Browning KS,B.-S.J. (2015) Mechanism of Cytoplasmic mRNA Translation. *Arabidopsis Book*, **13**.

30. Alberts B, Johnson A, Lewis J, et al. (2002) From RNA to Protein. In *Molecular Biology of the Cell*. New York: Garland Science.

31. Griffiths AJF, Miller JH, Suzuki DT, et al. (2000) Transcription and RNA polymerase. In *An Introduction to Genetic Analysis*. New York: W. H. Freeman.

32. Crommelin,D.J.A., Sindelar,R.D. and Meibohm,B. (2013) Pharmaceutical Biotechnology: Fundamentals and Applications Springer New York.

33. Margulies,E. Transfer RNA (tRNA) https://www.genome.gov/genetics-glossary/Transfer-RNA#:~:text=The%20transfer%20RNA%20matches%20up,Elliott%20Margulies%2C%20Ph (accessed May 22, 2020).

34. Desterro,J., Bak-Gordon,P. and Carmo-Fonseca,M. (2020) Targeting mRNA processing as an anticancer strategy. *Nat. Rev. Drug Discov.*, **19**, 112–129.

35. Malina,A., Mills,J.R. and Pelletier,J. (2012) Emerging Therapeutics Targeting mRNA Translation. *Cold Spring Harb. Perspect. Biol.*, **4**, a012377.

36. Rosshandler,Y., Shen,A.Q., Cortes,J. and Khoury,H.J. (2016) Omacetaxine Mepesuccinate for Chronic Myeloid Leukemia. *Expert Rev. Hematol.*, **9**, 419–424.

37. Lieberman,J. (2018) Tapping the RNA world for therapeutics. *Nat. Struct. Mol. Biol.*, **25**, 357–364.

38. Mattick,J.S. and Makunin,I. V (2006) Non-coding RNA. *Hum. Mol. Genet.*, **15**, 17–29.

39. He,Y., Meng,X.M., Huang,C., Wu,B.M., Zhang,L., Lv,X.W. and Li,J. (2014) Long noncoding RNAs: Novel insights into hepatocelluar carcinoma. *Cancer Lett.*, **344**,

20–27.

40. Malek,E., Jagannathan,S. and Driscoll,J.J. (2014) Correlation of long non-coding RNA expression with metastasis, drug resistance and clinical outcome in cancer. *Oncotarget*, **5**, 8027–8038.

41. Derrien,T., Johnson,R., Bussotti,G., Tanzer,A., Djebali,S., Tilgner,H., Guernec,G., Martin,D., Merkel,A., Knowles,D.G., *et al.* (2012) The GENCODE v7 catalog of human long noncoding RNAs: analysis of their gene structure, evolution, and expression. *Genome Res.*, **22**, 1775–1789.

42. Smith,J.E. and Baker,K.E. (2015) Nonsense-mediated RNA decay – a switch and dial for regulating gene expression. *Bioessays*, **37**, 612–623.

43. Liu,S., Mitra,R., Zhao,M.-M., Fan,W., Eischen,C.M., Yin,F. and Zhao,Z. (2016) The Potential Roles of Long Noncoding RNAs (lncRNA) in Glioblastoma Development. *Mol. Cancer Ther.*, **15**, 2977–2986.

44. Tang,Y., Zhou,T., Yu,X., Xue,Z. and Shen,N. (2017) The role of long non-coding RNAs in rheumatic diseases. *Nat. Rev. Rheumatol.*, **13**, 657.

45. Cao,J. (2014) The functional role of long non-coding RNAs and epigenetics. *Biol. Proced. Online*, **16**, 11.

46. Fang,Y. and Fullwood,M.J. (2016) Roles, Functions, and Mechanisms of Long Non-coding RNAs in Cancer. *Genomics. Proteomics Bioinformatics*, **14**, 42–54.

47. Hu,X., Sood,A.K., Dang,C. V and Zhang,L. (2018) The role of long noncoding RNAs in cancer: the dark matter matters. *Curr. Opin. Genet. Dev.*, **48**, 8–15.

48. Delpu,Y., Larrieu,D., Gayral,M., Arvanitis,D., Dufresne,M., Cordelier,P. and Torrisani,J. (2016) Noncoding RNAs. In *Drug Discovery in Cancer Epigenetics*. Elsevier, Boston, pp. 305–326.

49. Mattick,J.S. and Makunin,I. V (2005) Small regulatory RNAs in mammals. *Hum. Mol. Genet.*, **14 Spec No**, 121–32.

50. Lee,Y., Kim,M., Han,J., Yeom,K.-H., Lee,S., Baek,S.H. and Kim,V.N. (2004) MicroRNA genes are transcribed by RNA polymerase II. *EMBO J.*, **23**, 4051–4060.

51. Du,T. and Zamore,P.D. (2005) microPrimer: the biogenesis and function of microRNA. *Development*, **132**, 4645–4652.

52. Eulalio,A., Huntzinger,E. and Izaurralde,E. (2008) Getting to the root of miRNA-mediated gene silencing. *Cell*, **132**, 9–14.

53. Iwasaki,Y.W., Siomi,M.C. and Siomi,H. (2015) PIWI-Interacting RNA: Its Biogenesis and Functions. *Annu. Rev. Biochem.*, **84**, 405–433.

54. He,L. and Hannon,G.J. (2004) Correction: MicroRNAs: small RNAs with a big role in gene regulation. *Nat. Rev. Genet.*, **5**, 631–631.

55. Großhans,H. (2010) Regulation of microRNAs Springer New York.

56. Falaleeva,M., Pages,A., Matuszek,Z., Hidmi,S., Agranat-Tamir,L., Korotkov,K., Nevo,Y., Eyras,E., Sperling,R. and Stamm,S. (2016) Dual function of C/D box small nucleolar RNAs in rRNA modification and alternative pre-mRNA splicing. *Proc. Natl. Acad. Sci.*, **113**, E1625–E1634.

57. Bartel,D.P. (2004) MicroRNAs: genomics, biogenesis, mechanism, and function. *Cell*, **116**, 281–297.

58. Christopher,A.F., Kaur,R.P., Kaur,G., Kaur,A., Gupta,V. and Bansal,P. (2016) MicroRNA therapeutics: Discovering novel targets and developing specific therapy. *Perspect. Clin. Res.*, **7**, 68–74.

59. Tufekci,K.U., Oner,M.G., Meuwissen,R.L.J. and Genc,S. (2014) The role of microRNAs in human diseases. *Methods Mol. Biol.*, **1107**, 33–50.

60. Ha,M. and Kim,V.N. (2014) Regulation of microRNA biogenesis. *Nat. Rev. Mol. Cell Biol.*, **15**, 509–24.

61. Macara,I. a N.G., Macara,I. a N.G., To,G., To,G., Nucleus,T.H.E., Nucleus,T.H.E., Nuclear,T.H.E., Nuclear,T.H.E., Complex,P., Complex,P., *et al.* (2001) Transport into and out of the Nucleus. *Society*, **65**, 570–594.

62. Quinlan,S., Kenny,A., Medina,M., Engel,T. and Jimenez-Mateos,E.M. (2017) MicroRNAs in Neurodegenerative Diseases 1st ed. Elsevier Inc.

63. Ma,E., Zhou,K., Kidwell,M.A. and Doudna,J.A. (2012) Coordinated Activities of Human Dicer Domains in Regulatory RNA Processing. *J. Mol. Biol.*, **422**, 466–476.

64. Li,Z. and Rana,T.M. (2012) Molecular Mechanisms of RNA-Triggered Gene Silencing Machineries. *Acc. Chem. Res.*, **45**, 1122–1131.

65. Li,Z. and Rana,T.M. (2014) Therapeutic targeting of microRNAs: current status and future challenges. *Nat. Rev. Drug Discov.*, **13**, 622–638.

66. Krol,J., Loedige,I. and Filipowicz,W. (2010) The widespread regulation of microRNA biogenesis, function and decay. *Nat. Rev. Genet.*, **11**, 597–610.

67. MacFarlane,L.-A. and Murphy,P.R. (2010) MicroRNA: Biogenesis, Function and Role in Cancer. *Curr. Genomics*, **11**, 537–561.

68. Jackson,A. and Linsley,P.S. (2010) The therapeutic potential of microRNA modulation. *Discov. Med.*, **9**, 311—318.

69. Tomankova,T., Petrek,M. and Kriegova,E. (2010) Involvement of microRNAs in physiological and pathological processes in the lung. *Respir. Res.*, **11**, 159.

70. Sonntag,K.-C. (2010) MicroRNAs and deregulated gene expression networks in neurodegeneration. *Brain Res.*, **1338**, 48–57.

71. De Smaele,E., Ferretti,E. and Gulino,A. (2010) MicroRNAs as biomarkers for CNS cancer and other disorders. *Brain Res.*, **1338**, 100–111.

72. Lau,P. and de Strooper,B. (2010) Dysregulated microRNAs in neurodegenerative disorders. *Semin. Cell Dev. Biol.*, **21**, 768—773.

73. Toiyama,Y., Takahashi,M., Hur,K., Nagasaka,T., Tanaka,K., Inoue,Y., Kusunoki,M., Boland,C.R. and Goel,A. (2013) Serum miR-21 as a diagnostic and prognostic biomarker in colorectal cancer. *J. Natl. Cancer Inst.*, **105**, 849–859.

74. Li,S., Yang,X., Yang,J., Zhen,J. and Zhang,D. (2016) Serum microRNA-21 as a potential diagnostic biomarker for breast cancer: a systematic review and meta-analysis. *Clin. Exp. Med.*, **16**, 29–35.

75. Yang,X., Guo,Y., Du,Y., Yang,J., Li,S., Liu,S., Li,K. and Zhang,D. (2014) Serum

microRNA-21 as a diagnostic marker for lung carcinoma: a systematic review and meta-analysis. *PLoS One*, **9**, e97460.

76. Wang,H., Hou,L., Li,A., Duan,Y., Gao,H. and Song,X. (2014) Expression of serum exosomal microRNA-21 in human hepatocellular carcinoma. *Biomed Res. Int.*, **2014**, 864894.

77. Tanaka,Y., Kamohara,H., Kinoshita,K., Kurashige,J., Ishimoto,T., Iwatsuki,M., Watanabe,M. and Baba,H. (2013) Clinical impact of serum exosomal microRNA-21 as a clinical biomarker in human esophageal squamous cell carcinoma. *Cancer*, **119**, 1159–1167.

78. Gao,Y., Dai,M., Liu,H., He,W., Lin,S., Yuan,T., Chen,H. and Dai,S. (2016) Diagnostic value of circulating miR-21: An update meta-analysis in various cancers and validation in endometrial cancer. *Oncotarget*, **7**, 68894–68908.

79. Chan,J.A., Krichevsky,A.M. and Kosik,K.S. (2005) MicroRNA-21 is an antiapoptotic factor in human glioblastoma cells. *Cancer Res.*, **65**, 6029–6033.

80. Meng,F., Henson,R., Wehbe-Janek,H., Ghoshal,K., Jacob,S.T. and Patel,T. (2007) MicroRNA-21 regulates expression of the PTEN tumor suppressor gene in human hepatocellular cancer. *Gastroenterology*, **133**, 647–658.

81. Madhavan,D., Peng,C., Wallwiener,M., Zucknick,M., Nees,J., Schott,S., Rudolph,A., Riethdorf,S., Trumpp,A., Pantel,K., *et al.* (2016) Circulating miRNAs with prognostic value in metastatic breast cancer and for early detection of metastasis. *Carcinogenesis*, **37**, 461–470.

82. Lawrie,C.H., Gal,S., Dunlop,H.M., Pushkaran,B., Liggins,A.P., Pulford,K., Banham,A.H., Pezzella,F., Boultwood,J., Wainscoat,J.S., *et al.* (2008) Detection of elevated levels of tumour-associated microRNAs in serum of patients with diffuse large B-cell lymphoma. *Br. J. Haematol.*, **141**, 672–675.

83. Schetter,A.J., Leung,S.Y., Sohn,J.J., Zanetti,K.A., Bowman,E.D., Yanaihara,N., Yuen,S.T., Chan,T.L., Kwong,D.L.W., Au,G.K.H., *et al.* (2008) MicroRNA expression profiles associated with prognosis and therapeutic outcome in colon adenocarcinoma. *JAMA*, **299**, 425–436.

84. Shah,M.Y., Ferrajoli,A., Sood,A.K., Lopez-Berestein,G. and Calin,G.A. (2016) microRNA Therapeutics in Cancer — An Emerging Concept. *EBioMedicine*, **12**, 34–42.

85. Price,C. and Chen,J. (2014) MicroRNAs in cancer biology and therapy: Current status and perspectives. *Genes Dis.*, **1**, 53–63.

86. Pogribny,I.P. (2018) MicroRNAs as biomarkers for clinical studies. *Exp. Biol. Med. (Maywood).*, **243**, 283–290.

87. Schultz,N.A., Dehlendorff,C., Jensen,B. V, Bjerregaard,J.K., Nielsen,K.R., Bojesen,S.E., Calatayud,D., Nielsen,S.E., Yilmaz,M., Holländer,N.H., *et al.* (2014) MicroRNA biomarkers in whole blood for detection of pancreatic cancer. *JAMA*, **311**, 392–404.

88. Calin,G.A. and Croce,C.M. (2006) MicroRNA signatures in human cancers. *Nat. Rev. Cancer*, **6**, 857–866.

89. Di Leva,G., Garofalo,M. and Croce,C.M. (2014) MicroRNAs in Cancer. *Annu. Rev. Pathol. Mech. Dis.*, **9**, 287–314.

90. Pistollato,F., Ohayon,E.L., Lam,A., Langley,G.R., Novak,T.J., Pamies,D., Perry,G., Trushina,E., Williams,R.S.B., Roher,A.E., *et al.* (2016) Alzheimer disease research in the 21(st) century: past and current failures, new perspectives and funding priorities. *Oncotarget*, **7**, 38999–39016.

91. Karnati,H.K., Panigrahi,M.K., Gutti,R.K., Greig,N.H. and Tamargo,I.A. (2015) miRNAs: Key Players in Neurodegenerative Disorders and Epilepsy. *J. Alzheimers. Dis.*, **48**, 563–580.

92. De Mena,L., Coto,E., Cardo,L.F., Díaz,M., Blázquez,M., Ribacoba,R., Salvado,C., Pastor,P., Samaranch,Ll., Moris,G., *et al.* (2010) Analysis of the micro-RNA-133 and PITX3 genes in Parkinson's disease. *Am. J. Med. Genet. Part B Neuropsychiatr. Genet.*, **153**, 1234–1239.

93. Ardekani,A.M. and Naeini,M.M. (2010) The Role of MicroRNAs in Human Diseases. *Avicenna J. Med. Biotechnol.*, **2**, 161–179.

94. Packer,A.N., Xing,Y., Harper,S.Q., Jones,L. and Davidson,B.L. (2008) The bifunctional microRNA miR-9/miR-9* regulates REST and CoREST and is downregulated in Huntington's disease. *J. Neurosci.*, **28**, 14341–14346.

95. Johnson,R., Zuccato,C., Belyaev,N.D., Guest,D.J., Cattaneo,E. and Buckley,N.J. (2008) A microRNA-based gene dysregulation pathway in Huntington's disease. *Neurobiol. Dis.*, **29**, 438–445.

96. Shi,J. (2014) Regulatory networks between neurotrophins and miRNAs in brain diseases and cancers. *Acta Pharmacol. Sin.*, **36**, 149.

97. Ling,H., Fabbri,M. and Calin,G.A. (2013) MicroRNAs and other non-coding RNAs as targets for anticancer drug development. *Nat. Publ. Gr.*, **12**, 847–865.

98. van Rooij,E. and Kauppinen,S. (2014) Development of microRNA therapeutics is coming of age. *EMBO Mol. Med.*, **6**, 851–864.

99. Krützfeldt,J., Kuwajima,S., Braich,R., Rajeev,K.G., Pena,J., Tuschl,T., Manoharan,M. and Stoffel,M. (2007) Specificity, duplex degradation and subcellular localization of antagomirs. *Nucleic Acids Res.*, **35**, 2885–2892.

100. Krützfeldt,J., Rajewsky,N., Braich,R., Rajeev,K.G., Tuschl,T., Manoharan,M. and Stoffel,M. (2005) Silencing of microRNAs in vivo with 'antagomirs'. *Nature*, **438**, 685–689.

101. Janssen,H.L.A., Reesink,H.W., Lawitz,E.J., Zeuzem,S., Rodriguez-Torres,M., Patel,K., van der Meer,A.J., Patick,A.K., Chen,A., Zhou,Y., *et al.* (2013) Treatment of HCV infection by targeting microRNA. *N. Engl. J. Med.*, **368**, 1685–1694.

102. Kreth,S., Hübner,M. and Hinske,L.C. (2018) MicroRNAs as Clinical Biomarkers and Therapeutic Tools in Perioperative Medicine. *Anesth. Analg.*, **126**.

103. Fu,Y., Chen,J. and Huang,Z. (2019) Recent progress in microRNA-based delivery systems for the treatment of human disease. *ExRNA*, **1**, 24.

104. Wang,Z. (2011) The principles of MiRNA-masking antisense oligonucleotides technology. *Methods Mol. Biol.*, **676**, 43–49.

105. Gumireddy,K., Young,D.D., Xiong,X., Hogenesch,J.B., Huang,Q. and Deiters,A. (2008) Small-molecule inhibitors of microrna miR-21 function. *Angew. Chem. Int. Ed. Engl.*, **47**, 7482–7484.

106. Xue,J., Yang,J., Luo,M., Cho,W.C. and Liu,X. (2017) MicroRNA-targeted therapeutics for lung cancer treatment. *Expert Opin. Drug Discov.*, **12**, 141–157.

107. Hermann,T. (2000) Strategies for the Design of Drugs Targeting RNA and RNA-Protein Complexes. *Angew Chem Int Ed Engl*, **39**, 1890–1904.

108. Li,J., Jiang,D., Zhou,H., Li,F., Yang,J., Hong,L., Fu,X., Li,Z., Liu,Z., Li,J., *et al.* (2011) Expression of RNA-Interference/Antisense Transgenes by the Cognate Promoters of Target Genes Is a Better Gene-Silencing Strategy to Study Gene Functions in Rice. *PLoS One*, **6**, 1–9.

109. Dias,N. and Stein,C.A. (2002) Antisense Oligonucleotides: Basic Concepts and Mechanisms. *Mol. Cancer Ther.*, **1**, 347– 355.

110. Stephenson,M.L. and Zamecnik,P.C. (1978) Inhibition of Rous sarcoma viral RNA translation by a specific oligodeoxyribonucleotide. *Proc. Natl. Acad. Sci. U. S. A.*, **75**, 285–288.

111. Evers,M.M., Toonen,L.J.A. and van Roon-Mom,W.M.C. (2015) Antisense oligonucleotides in therapy for neurodegenerative disorders. *Adv. Drug Deliv. Rev.*, **87**, 90–103.

112. Chan,J.H.P., Lim,S. and Wong,W.S.F. (2006) Antisense oligonucleotides: from design to therapeutic application. *Clin. Exp. Pharmacol. Physiol.*, **33**, 533–540.

113. Crooke,S.T. (2004) Progress in antisense technology. *Annu. Rev. Med.*, **55**, 61–95.

114. Kurreck,J., Wyszko,E., Gillen,C. and Erdmann,V.A. (2002) Design of antisense oligonucleotides stabilized by locked nucleic acids. *Nucleic Acids Res.*, **30**, 1911–1918.

115. Kurreck,J. (2003) Antisense technologies. Improvement through novel chemical modifications. *Eur. J. Biochem.*, **270**, 1628–1644.

116. Wu,H., Lima,W.F., Zhang,H., Fan,A., Sun,H. and Crooke,S.T. (2004) Determination of the role of the human RNase H1 in the pharmacology of DNA-like antisense drugs. *J. Biol. Chem.*, **279**, 17181–17189.

117. Kole,R., Krainer,A.R. and Altman,S. (2012) RNA therapeutics: beyond RNA interference and antisense oligonucleotides. *Nat. Rev. Drug Discov.*, **11**, 125–140.

118. Havens,M.A. and Hastings,M.L. (2016) Splice-switching antisense oligonucleotides as therapeutic drugs. *Nucleic Acids Res.*, **44**, 6549–6563.

119. Eckstein,F. (2000) Phosphorothioate oligodeoxynucleotides: what is their origin and what is unique about them? *Antisense Nucleic Acid Drug Dev.*, **10**, 117–121.

120. Blake,K.R., Murakami,A., Spitz,S.A., Glave,S.A., Reddy,M.P., Ts'o,P.O. and Miller,P.S. (1985) Hybridization arrest of globin synthesis in rabbit reticulocyte lysates and cells by oligodeoxyribonucleoside methylphosphonates. *Biochemistry*, **24**, 6139–6145.

121. Miller,P.S., McParland,K.B., Jayaraman,K. and Ts'o,P.O. (1981) Biochemical and biological effects of nonionic nucleic acid methylphosphonates. *Biochemistry*, **20**, 1874–1880.

122. Miller,P.S., Yano,J., Yano,E., Carroll,C., Jayaraman,K. and Ts'o,P.O. (1979) Nonionic nucleic acid analogues. Synthesis and characterization of dideoxyribonucleoside methylphosphonates. *Biochemistry*, **18**, 5134–5143.

123. Crooke,S.T. (2000) Progress in antisense technology: the end of the beginning. *Methods Enzymol.*, **313**, 3–45.

124. Group,V.S. (2002) A randomized controlled clinical trial of intravitreous fomivirsen for treatment of newly diagnosed peripheral cytomegalovirus retinitis in patients with AIDS. *Am. J. Ophthalmol.*, **133**, 467–474.

125. Muntoni,F. and Wood,M.J.A. (2011) Targeting RNA to treat neuromuscular disease. *Nat. Rev. Drug Discov.*, **10**, 621–637.

126. Altmann,K.H., Fabbro,D., Dean,N.M., Geiger,T., Monia,B.P., Muller,M. and Nicklin,P. (1996) Second-generation antisense oligonucleotides: structure-activity relationships and the design of improved signal-transduction inhibitors. *Biochem. Soc. Trans.*, **24**, 630–637.

127. McKay,R.A., Miraglia,L.J., Cummins,L.L., Owens,S.R., Sasmor,H. and Dean,N.M. (1999) Characterization of a potent and specific class of antisense oligonucleotide inhibitor of human protein kinase C-alpha expression. *J. Biol. Chem.*, **274**, 1715–1722.

128. Sharma,V.K., Sharma,R.K. and Singh,S.K. (2014) Antisense oligonucleotides: modifications and clinical trials. *Med. Chem. Commun.*, **5**, 1454–1471.

129. Nielsen,P.E. (2004) PNA Technology. *Mol. Biotechnol.*, **26**, 233–248.

130. Vester,B. and Wengel,J. (2004) LNA (Locked Nucleic Acid): High-Affinity Targeting of Complementary RNA and DNA. *Biochemistry*, **43**, 13233–13241.

131. Nielsen,P.E., Egholm,M., Berg,R.H. and Buchardt,O. (1991) Sequence-selective recognition of DNA by strand displacement with a thymine-substituted polyamide. *Science*, **254**, 1497–1500.

132. Koppelhus,U. and Nielsen,P.E. (2003) Cellular delivery of peptide nucleic acid (PNA). *Adv. Drug Deliv. Rev.*, **55**, 267–280.

133. Amantana,A. and Iversen,P.L. (2005) Pharmacokinetics and biodistribution of phosphorodiamidate morpholino antisense oligomers. *Curr. Opin. Pharmacol.*, **5**, 550–555.

134. Aue,G. and Gewirtz,A.M. (2002) Antisense Nucleic Acids: Clinical Applications. In Joseph R. Bertino (ed), *Encyclopedia of Cancer*. Elsevier, New York, pp. 119–125.

135. James,H.A. (1999) The potential application of ribozymes for the treatment of hematological disorders. *J. Leukoc. Biol.*, **66**, 361–368.

136. James,H. a (2002) Ribozymes and Their Applications. In *Encyclopedia of cancer*. Elsevier Science, Vol. 4, pp. 179–187.

137. Vickers,T.A. and Crooke,S.T. (2014) Antisense Oligonucleotides Capable of Promoting Specific Target mRNA Reduction via Competing RNase H1-Dependent and Independent Mechanisms. *PLoS One*, **9**, e108625.

138. Doherty,E.A. and Doudna,J.A. (2001) Ribosomes structures and mechanisms. *Annu. Rev. Biophys. Biomol. Struct.*, **30**, 457–475.

139. Esteban,J.A., Walter,N.G., Kotzorek,G., Heckman,J.E. and Burke,J.M. (1998) Structural basis for heterogeneous kinetics: Reengineering the hairpin ribozyme. *Proc. Natl. Acad. Sci. U. S. A.*, **95**, 6091–6096.

140. Shippy,R., Lockner,R., Farnsworth,M. and Hampel,A. (1999) The hairpin ribozyme. Discovery, mechanism, and development for gene therapy. *Mol. Biotechnol.*, **12**, 117–129.

141. Lilley,D.M.J. (2004) The Varkud satellite ribozyme. *RNA*, **10**, 151–158.

142. Koizumi,M., Soukup,G.A., Kerr,J.N. and Breaker,R.R. (1999) Allosteric selection of ribozymes that respond to the second messengers cGMP and cAMP. *Nat. Struct. Biol.*, **6**, 1062–1071.

143. Napoli,C., Lemieux,C. and Jorgensen,R. (1990) Introduction of a Chimeric Chalcone Synthase Gene into Petunia Results in Reversible Co-Suppression of Homologous Genes in trans. *Plant Cell*, **2**, 279–289.

144. van der Krol,A.R., Mur,L.A., Beld,M., Mol,J.N. and Stuitje,A.R. (1990) Flavonoid genes in petunia: addition of a limited number of gene copies may lead to a suppression of gene expression. *Plant Cell*, **2**, 291–299.

145. Cejka,D., Losert,D. and Wacheck,V. (2006) Short interfering RNA (siRNA): tool or therapeutic? *Clin. Sci. (Lond).*, **110**, 47–58.

146. Fire,A., Xu,S., Montgomery,M.K., Kostas,S.A., Driver,S.E. and Mello,C.C. (1998) Potent and specific genetic interference by double-stranded RNA in Caenorhabditis elegans. *Nature*, **391**, 806–811.

147. Sijen,T. and Plasterk,R.H.A. (2003) Transposon silencing in the Caenorhabditis elegans germ line by natural RNAi. *Nature*, **426**, 310–314.

148. Gitlin,L. and Andino,R. (2003) Nucleic acid-based immune system: the antiviral potential of mammalian RNA silencing. *J. Virol.*, **77**, 7159–7165.

149. Gitlin,L., Karelsky,S. and Andino,R. (2002) Short interfering RNA confers intracellular antiviral immunity in human cells. *Nature*, **418**, 430–434.

150. Lecellier,C.-H., Dunoyer,P., Arar,K., Lehmann-Che,J., Eyquem,S., Himber,C., Saib,A. and Voinnet,O. (2005) A cellular microRNA mediates antiviral defense in human cells. *Science*, **308**, 557–560.

151. Hamilton,A.J. and Baulcombe,D.C. (1999) A species of small antisense RNA in posttranscriptional gene silencing in plants. *Science*, **286**, 950–952.

152. Zamore,P.D., Tuschl,T., Sharp,P.A. and Bartel,D.P. (2000) RNAi. *Cell*, **101**, 25–33.

153. Aagaard,L. and Rossi,J.J. (2007) RNAi therapeutics: principles, prospects and challenges. *Adv. Drug Deliv. Rev.*, **59**, 75–86.

154. Lam,J.K.W., Chow,M.Y.T., Zhang,Y. and Leung,S.W.S. (2015) siRNA Versus miRNA as Therapeutics for Gene Silencing. *Mol. Ther. - Nucleic Acids*, **4**.

155. Tiemann,K. and Rossi,J.J. (2009) RNAi-based therapeutics-current status, challenges and prospects. *EMBO Mol. Med.*, **1**, 142–151.

156. Khvorova,A., Reynolds,A. and Jayasena,S.D. (2003) Functional siRNAs and miRNAs exhibit strand bias. *Cell*, **115**, 209–216.

157. Manoharan,M. (2004) RNA interference and chemically modified small interfering RNAs. *Curr. Opin. Chem. Biol.*, **8**, 570–579.

158. Tam,C., Wong,J.H., Cheung,R.C.F., Zuo,T. and Ng,T.B. (2017) Therapeutic

potentials of short interfering RNAs. *Appl. Microbiol. Biotechnol.*, **101**, 7091–7111.

159. Nykänen,A., Haley,B. and Zamore,P.D. (2001) ATP Requirements and Small Interfering RNA Structure in the RNA Interference Pathway. *Cell*, **107**, 309–321.

160. Martinez,J., Patkaniowska,A., Urlaub,H., Lührmann,R. and Tuschl,T. (2002) Single-Stranded Antisense siRNAs Guide Target RNA Cleavage in RNAi. *Cell*, **110**, 563–574.

161. Schwarz,D.S., Hutvágner,G., Haley,B. and Zamore,P.D. (2002) Evidence that siRNAs Function as Guides, Not Primers, in the Drosophila and Human RNAi Pathways. *Mol. Cell*, **10**, 537–548.

162. Carthew,R.W. and Sontheimer,E.J. (2009) Origins and Mechanisms of miRNAs and siRNAs. *Cell*, **136**, 642–655.

163. He,L. and Hannon,G.J. (2004) MicroRNAs: small RNAs with a big role in gene regulation. *Nat. Rev. Genet.*, **5**, 522–531.

164. Aigner,A. (2006) Gene silencing through RNA interference (RNAi) in vivo: strategies based on the direct application of siRNAs. *J. Biotechnol.*, **124**, 12–25.

165. Dorsett,Y. and Tuschl,T. (2004) siRNAs: applications in functional genomics and potential as therapeutics. *Nat. Rev. Drug Discov.*, **3**, 318–329.

166. Papageorgiou,A., Rapley,J., Mesirov,J.P., Tamayo,P. and Avruch,J. (2015) A genome-wide siRNA screen in mammalian cells for regulators of S6 phosphorylation. *PLoS One*, **10**, e0116096.

167. Chen,P., Hu,T., Liang,Y., Jiang,Y., Pan,Y., Li,C., Zhang,P., Wei,D., Li,P., Jeong,L.S., *et al.* (2015) Synergistic inhibition of autophagy and neddylation pathways as a novel therapeutic approach for targeting liver cancer. *Oncotarget*, **6**, 9002–9017.

168. Opalinska,J.B. and Gewirtz,A.M. (2002) Nucleic-acid therapeutics: basic principles and recent applications. *Nat. Rev. Drug Discov.*, **1**, 503–514.

169. Devi,G.R. (2006) siRNA-based approaches in cancer therapy. *Cancer Gene Ther.*, **13**, 819–829.

170. Behlke,M.A. (2006) Progress towards in vivo use of siRNAs. *Mol. Ther.*, **13**, 644–670.

171. de Fougerolles,A., Vornlocher,H.-P., Maraganore,J. and Lieberman,J. (2007) Interfering with disease: a progress report on siRNA-based therapeutics. *Nat. Rev. Drug Discov.*, **6**, 443–453.

172. Kim,D.H. and Rossi,J.J. (2007) Strategies for silencing human disease using RNA interference. *Nat. Rev. Genet.*, **8**, 173–184.

173. Behlke,M.A. (2008) Chemical Modification of siRNAs for *In Vivo* Use. *Oligonucleotides*, **18**, 305–320.

174. Zou,Y., Tiller,P., Chen,I.-W., Beverly,M. and Hochman,J. (2008) Metabolite identification of small interfering RNA duplex by high-resolution accurate mass spectrometry. *Rapid Commun. Mass Spectrom.*, **22**, 1871–1881.

175. Harborth,J., Elbashir,S.M., Vandenburgh,K., Manninga,H., Scaringe,S.A., Weber,K. and Tuschl,T. (2003) Sequence, chemical, and structural variation of small

interfering RNAs and short hairpin RNAs and the effect on mammalian gene silencing. *Antisense Nucleic Acid Drug Dev.*, **13**, 83–105.

176. Jackson,A.L., Bartz,S.R., Schelter,J., Kobayashi,S. V, Burchard,J., Mao,M., Li,B., Cavet,G. and Linsley,P.S. (2003) Expression profiling reveals off-target gene regulation by RNAi. *Nat. Biotechnol.*, **21**, 635–637.

177. Jackson,A.L., Burchard,J., Leake,D., Reynolds,A., Schelter,J., Guo,J., Johnson,J.M., Lim,L., Karpilow,J., Nichols,K., *et al.* (2006) Position-specific chemical modification of siRNAs reduces 'off-target' transcript silencing. *RNA*, **12**, 1197–1205.

178. Lipinski,C.A. (2000) Drug-like properties and the causes of poor solubility and poor permeability. *J. Pharmacol. Toxicol. Methods*, **44**, 235–249.

179. Moshfeghi,A.A. and Puliafito,C.A. (2005) Pegaptanib sodium for the treatment of neovascular age-related macular degeneration. *Expert Opin. Investig. Drugs*, **14**, 671–682.

180. Barata,P., Sood,A.K. and Hong,D.S. (2016) RNA-targeted therapeutics in cancer clinical trials: Current status and future directions. *Cancer Treat. Rev.*, **50**, 35–47.

181. Whitehead,K.A., Langer,R. and Anderson,D.G. (2009) Knocking down barriers: advances in siRNA delivery. *Nat. Rev. Drug Discov.*, **8**, 129–138.

182. Kanasty,R.L., Whitehead,K.A., Vegas,A.J. and Anderson,D.G. (2012) Action and reaction: the biological response to siRNA and its delivery vehicles. *Mol. Ther.*, **20**, 513–524.

183. Singha,K., Namgung,R. and Kim,W.J. (2011) Polymers in Small-Interfering RNA Delivery. *Nucleic Acid Ther. (Formerly Oligonucleotides)*, **21**, 133–147.

184. Akinc,A., Zumbuehl,A., Goldberg,M., Leshchiner,E.S., Busini,V., Hossain,N., Bacallado,S.A., Nguyen,D.N., Fuller,J., Alvarez,R., *et al.* (2008) A combinatorial library of lipid-like materials for delivery of RNAi therapeutics. *Nat. Biotechnol.*, **26**, 561–569.

185. Mo,R.H., Zaro,J.L. and Shen,W.-C. (2012) Comparison of cationic and amphipathic cell penetrating peptides for siRNA delivery and efficacy. *Mol. Pharm.*, **9**, 299–309.

186. Soutschek,J., Akinc,A., Bramlage,B., Charisse,K., Constien,R., Donoghue,M., Elbashir,S., Geick,A., Hadwiger,P., Harborth,J., *et al.* (2004) Therapeutic silencing of an endogenous gene by systemic administration of modified siRNAs. *Nature*, **432**, 173–178.

187. Lorenz,C., Hadwiger,P., John,M., Vornlocher,H.-P. and Unverzagt,C. (2004) Steroid and lipid conjugates of siRNAs to enhance cellular uptake and gene silencing in liver cells. *Bioorg. Med. Chem. Lett.*, **14**, 4975–4977.

188. Shen,C., Buck,A.K., Liu,X., Winkler,M. and Reske,S.N. (2003) Gene silencing by adenovirus-delivered siRNA. *FEBS Lett.*, **539**, 111–114.

189. Samuel,C.E. (2004) Knockdown by RNAi—proceed with caution. *Nat. Biotechnol.*, **22**, 280–282.

190. Sioud,M. (2005) Induction of inflammatory cytokines and interferon responses by double-stranded and single-stranded siRNAs is sequence-dependent and requires endosomal localization. *J. Mol. Biol.*, **348**, 1079–1090.

191. Grimm,D., Streetz,K.L., Jopling,C.L., Storm,T.A., Pandey,K., Davis,C.R., Marion,P., Salazar,F. and Kay,M.A. (2006) Fatality in mice due to oversaturation of cellular microRNA/short hairpin RNA pathways. *Nature*, **441**, 537–541.

192. Grimm,D. (2011) The dose can make the poison: lessons learned from adverse in vivotoxicities caused by RNAi overexpression. *Silence*, **2**, 8.

193. Jackson,A.L. and Linsley,P.S. (2010) Recognizing and avoiding siRNA off-target effects for target identification and therapeutic application. *Nat. Rev. Drug Discov.*, **9**, 57–67.

194. Raines,R.T. (1998) Ribonuclease A. *Chem. Rev.*, **98**, 1045–1066.

195. Shlyakhovenko,V.O. (2016) Ribonucleases. Possible new approach in cancer therapy. *Exp. Oncol.*, **38**, 2–8.

196. Benito,A., Ribo,M. and Vilanova,M. (2005) On the track of antitumour ribonucleases. *Mol. Biosyst.*, **1**, 294–302.

197. Rybak,S.M. and Newton,D.L. (1999) Natural and engineered cytotoxic ribonucleases: therapeutic potential. *Exp. Cell Res.*, **253**, 325–335.

198. Kumar,R. and Kanwar,S. (2017) Ribonuclease as Anticancer Therapeutics. *J. Mol. Catal. B Enzym.*, **06**.

199. Barnard,E. (1969) Biological Function of Pancreatic Ribonuclease. *Nature*, **221**, 340–344.

200. Beintema,J.J., Schüller,C., Irie,M. and Carsana,A. (1988) Molecular evolution of the ribonuclease superfamily. *Prog. Biophys. Mol. Biol.*, **51**, 165–192.

201. Condon,C. (2009) RNA Processing. In *Encyclopedia of Microbiology*. Elsevier, Oxford, pp. 395–408.

202. Suruchi,S., Bibhu Prasad,P., Saleem,J. and Ali,M. (2007) RNase: A Novel Enzyme For Treatment Of Cancers. *Internet J. Oncol.*, **5**, 6.

203. Stone,C.M., Butt,L.E., Bufton,J.C., Lourenco,D.C., Gowers,D.M., Pickford,A.R., Cox,P.A., Vincent,H.A. and Callaghan,A.J. (2017) Inhibition of homologous phosphorolytic ribonucleases by citrate may represent an evolutionarily conserved communicative link between RNA degradation and central metabolism. *Nucleic Acids Res.*, **45**, 4655–4666.

204. Nakamura,H., Oda,Y., Iwai,S., Inoue,H., Ohtsuka,E., Kanaya,S., Kimura,S., Katsuda,C., Katayanagi,K., Morikawa,K., *et al.* (1991) How does RNase H recognize a DNA.RNA hybrid? *Proc. Natl. Acad. Sci. U. S. A.*, **88**, 11535–11539.

205. Nowotny,M., Gaidamakov,S.A., Ghirlando,R., Cerritelli,S.M., Crouch,R.J. and Yang,W. (2007) Structure of Human RNase H1 Complexed with an RNA/DNA Hybrid: Insight into HIV Reverse Transcription. *Mol. Cell*, **28**, 264–276.

206. Uchida, T. and Egami,F. (1971) Microbial ribonucleases with special reference to RNases T1, T2, N1, and U2. In *The Enzymes, Vol. IV*. Academic Press, pp. 205–250.

207. Mironova,N.L., Pyshnyi,D. V and Ivanova,E.M. (2004) RNA-Cleaving Oligonucleotide-Peptide Conjugates. In Zenkova,M.A. (ed), *Artificial Nucleases*. Springer Berlin Heidelberg, Berlin, Heidelberg, pp. 151–172.

208. Nichols,N.M. and Yue,D. (2008) Ribonucleases. *Curr. Protoc. Mol. Biol.*, **84**, 1–8.

209. Kubiak,R.J., Yue,X., Hondal,R.J., Mihai,C., Tsai,M.-D. and Bruzik,K.S. (2001) Involvement of the Arg−Asp−His Catalytic Triad in Enzymatic Cleavage of the Phosphodiester Bond. *Biochemistry*, **40**, 5422–5432.

210. Westheimer,F.H. (1968) Pseudo-rotation in the hydrolysis of phosphate esters. *Acc. Chem. Res.*, **1**, 70–78.

211. Arnold,U. (2008) Aspects of the cytotoxic action of ribonucleases. *Curr. Pharm. Biotechnol.*, **9**, 161–168.

212. Matousek,J., Soucek,J., Slavik,T., Tomanek,M., Lee,J.E. and Raines,R.T. (2003) Comprehensive comparison of the cytotoxic activities of onconase and bovine seminal ribonuclease. *Comp. Biochem. Physiol. C. Toxicol. Pharmacol.*, **136**, 343–356.

213. Ledoux,L. (1955) Action of Ribonuclease on Certain Ascites Tumours. *Nature*, **175**, 258–259.

214. Ledoux,L. (1955) Action of Ribonuclease on Two Solid Tumours in vivo. *Nature*, **176**, 36–37.

215. Wu,Y., Saxena,S.K., Ardelt,W., Gadina,M., Mikulski,S.M., De Lorenzo,C., D'Alessio,G. and Youle,R.J. (1995) A study of the intracellular routing of cytotoxic ribonucleases. *J. Biol. Chem.*, **270**, 17476–17481.

216. Blackburn P,M.S. (1982) Pancreatic ribonucleases. *Enzym. XV*.

217. Gotte,G. and Menegazzi,M. (2019) Biological Activities of Secretory RNases: Focus on Their Oligomerization to Design Antitumor Drugs. *Front. Immunol.*, **10**, 2626.

218. Arnold,U. and Ulbrich-Hofmann,R. (2006) Natural and engineered ribonucleases as potential cancer therapeutics. *Biotechnol. Lett.*, **28**, 1615–1622.

219. Dickson,K.A., Haigis,M.C. and Raines,R.T. (2005) Ribonuclease Inhibitor: Structure and Function. *Prog. Nucleic Acid Res. Mol. Biol.*, **80**, 349–374.

220. Futami,J., Maeda,T., Kitazoe,M., Nukui,E., Tada,H., Seno,M., Kosaka,M. and Yamada,H. (2001) Preparation of potent cytotoxic ribonucleases by cationization: enhanced cellular uptake and decreased interaction with ribonuclease inhibitor by chemical modification of carboxyl groups. *Biochemistry*, **40**, 7518–7524.

221. Saxena,S.K., Gravell,M., Wu,Y.N., Mikulski,S.M., Shogen,K., Ardelt,W. and Youle,R.J. (1996) Inhibition of HIV-1 production and selective degradation of viral RNA by an amphibian ribonuclease. *J. Biol. Chem.*, **271**, 20783–20788.

222. Ulyanova,V., Vershinina,V. and Ilinskaya,O. (2011) Barnase and binase: twins with distinct fates. *FEBS J.*, **278**, 3633–3643.

223. Soukup,G.A. and Breaker,R.R. (1999) Relationship between internucleotide linkage geometry and the stability of RNA. *RNA*, **5**, 1308–1325.

224. Kuimelis,R.G. and McLaughlin,L.W. (1998) Mechanisms of Ribozyme-Mediated RNA Cleavage. *Chem. Rev.*, **98**, 1027–1044.

225. Oivanen,M., Kuusela,S. and Lönnberg,H. (1998) Kinetics and Mechanisms for the Cleavage and Isomerization of the Phosphodiester Bonds of RNA by Brønsted Acids and Bases. *Chem. Rev.*, **98**, 961–990.

226. Li,Y. and Breaker,R.R. (1999) Kinetics of RNA Degradation by Specific Base

Catalysis of Transesterification Involving the 2‘-Hydroxyl Group. *J. Am. Chem. Soc.*, **121**, 5364–5372.

227. Jarvinen,P., Oivanen,M. and Lonnberg,H. (1991) Interconversion and phosphoester hydrolysis of 2’,5’- and 3’,5’-dinucleoside monophosphates: kinetics and mechanisms. *J. Org. Chem.*, **56**, 5396–5401.

228. Lonnberg,H. (2011) Cleavage of RNA phosphodiester bonds by small molecular entities: a mechanistic insight. *Org. Biomol. Chem.*, **9**, 1687–1703.

229. Rosta,E., Nowotny,M., Yang,W. and Hummer,G. (2011) Catalytic Mechanism of RNA Backbone Cleavage by Ribonuclease H from Quantum Mechanics/Molecular Mechanics Simulations. *J. Am. Chem. Soc.*, **133**, 8934–8941.

230. Yang,W., Lee,J.Y. and Nowotny,M. (2006) Making and Breaking Nucleic Acids: Two-Mg^{2+}-Ion Catalysis and Substrate Specificity. *Mol. Cell*, **22**, 5–13.

231. Fedorova,A.A., Goncharova,E.P., Koroleva,L.S., Burakova,E.A., Ryabchikova,E.I., Bichenkova,E. V, Silnikov,V.N., Vlassov,V. V and Zenkova,M.A. (2016) Artificial ribonucleases inactivate a wide range of viruses using their ribonuclease, membranolytic, and chaotropic-like activities. *Antiviral Res.*, **133**, 73–84.

232. Morrow,J.R. (1994) Artificial ribonucleases. *Adv. Inorg. Biochem.*, **9**, 41–74.

233. Trawick,B.N., Daniher,A.T. and Bashkin,J.K. (1998) Inorganic Mimics of Ribonucleases and Ribozymes: From Random Cleavage to Sequence-Specific Chemistry to Catalytic Antisense Drugs. *Chem. Rev.*, **98**, 939–960.

234. Eichhorn,G.L. and Butzow,J.J. (1965) Interactions of metal ions with polynucleotides and related compounds. III. Degradation of polyribonucleotides by lanthanum ions,. *Biopolymers*, **3**, 79–94.

235. Matsumura,K., Endo,M. and Komiyama,M. (1994) Lanthanide complex–oligo-DNA hybrid for sequence-selective hydrolysis of RNA. *J. Chem. Soc., Chem. Commun.*, 2019–2020.

236. Hüsken,D., Goodall,G., Blommers,M.J.J., Jahnke,W., Hall,J., Häner,R. and Moser,H.E. (1996) Creating RNA Bulges: Cleavage of RNA in RNA/DNA Duplexes by Metal Ion Catalysis. *Biochemistry*, **35**, 16591–16600.

237. Hall,J., Hüsken,D. and Häner,R. (1996) Towards artificial ribonucleases: the sequence-specific cleavage of RNA in a duplex. *Nucleic Acids Res.*, **24**, 3522–6.

238. Ghidini,A., Murtola,M. and Strömberg,R. (2017) Oligonucleotide Based Artificial Ribonucleases (OBANs). In *DNA in Supramolecular Chemistry and Nanotechnology*. John Wiley & Sons, Ltd, Chichester, UK, pp. 158–171.

239. Bashkin,J.K., Frolova,E.I. and Sampath,U. (1994) Sequence-Specific Cleavage of HIV mRNA by a Ribozyme Mimic. *J. Am. Chem. Soc.*, **116**, 5981–5982.

240. Putnam,W.C. and Bashkin,J.K. (2000) synthesis of artificial ribonucleases with benign metal catalysts. *Chem. Commun.*, 767.

241. Astrom,H. and Stromberg,R. (2004) Synthesis of new OBAN’s and further studies on positioning of the catalytic group. *Org. Biomol. Chem.*, **2**, 1901–1907.

242. Astrom,H., Williams,N.H. and Stromberg,R. (2003) Oligonucleotide based artificial nuclease (OBAN) systems. Bulge size dependence and positioning of catalytic group in cleavage of RNA-bulges. *Org. Biomol. Chem.*, **1**, 1461–1465.

243. Beloglazova,N.G., Fabani,M.M., Zenkova,M.A., Bichenkova,E. V, Polushin,N.N., Sil'nikov,V. V, Douglas,K.T. and Vlassov,V. V (2004) Sequence-specific artificial ribonucleases. I. Bis-imidazole-containing oligonucleotide conjugates prepared using precursor-based strategy. *Nucleic Acids Res.*, **32**, 3887–3897.

244. Li,Y., Zhao,Y., Hatfield,S., Wan,R., Zhu,Q., Li,X., McMills,M., Ma,Y., Li,J., Brown,K.L., *et al.* (2000) Dipeptide seryl-histidine and related oligopeptides cleave DNA, protein, and a carboxyl ester. *Bioorg. Med. Chem.*, **8**, 2675–2680.

245. Barbier,B. and Brack,A. (1987) Search for catalytic properties of simple polypeptides. *Orig. Life Evol. Biosph.*, **17**, 381–390.

246. Yoshinari,K., Yamazaki,K. and Komiyama,M. (1991) Oligoamines as simple and efficient catalysts for RNA hydrolysis. *J. Am. Chem. Soc.*, **113**, 5899–5901.

247. Vlassov,V. V, Zuber,G., Felden,B., Behr,J.P. and Giege,R. (1995) Cleavage of tRNA with imidazole and spermine imidazole constructs: a new approach for probing RNA structure. *Nucleic Acids Res.*, **23**, 3161–3167.

248. Konevetz,D.A., Beck,I.E., Beloglazova,N.G., Sulimenkov,I. V., Sil'nikov,V.N., Zenkova,M.A., Shishkin,G. V. and Vlassov,V. V. (1999) Artificial ribonucleases: Synthesis and RNA cleaving properties of cationic conjugates bearing imidazole residues. *Tetrahedron*, **55**, 503–512.

249. Podyminogin,M.A., Vlassov,V. V and Giege,R. (1993) Synthetic RNA-cleaving molecules mimicking ribonuclease A active center. Design and cleavage of tRNA transcripts. *Nucleic Acids Res.*, **21**, 5950–5956.

250. Komiyama,M. and Inokawa,T. (1994) Selective Hydrolysis of tRNA by Ethylenediamine Bound to a DNA Oligomer. *J. Biochem.*, **116**, 719–720.

251. Reynolds,M.A., Beck,T.A., Say,P.B., Schwartz,D.A., Dwyer,B.P., Daily,W.J., Vaghefi,M.M., Metzler,M.D., Klem,R.E. and Arnold,L.J. (1996) Antisense oligonucleotide containing an internal, non-nucleotide-based linker promote site-specific cleavage of RNA. *Nucleic Acids Res.*, **24**, 760–765.

252. Ushijima,K., Gouzu,H., Hosono,K., Shirakawa,M., Kagosima,K., Takai,K. and Takaku,H. (1998) Site-specific cleavage of tRNA by imidazole and/or primary amine groups bound at the 5′-end of oligodeoxyribonucleotides. *Biochim. Biophys. Acta - Gen. Subj.*, **1379**, 217–223.

253. Scheffer,U., Strick,A., Ludwig,V., Peter,S., Kalden,E. and Gobel,M.W. (2005) Metal-free catalysts for the hydrolysis of RNA derived from guanidines, 2-aminopyridines, and 2-aminobenzimidazoles. *J. Am. Chem. Soc.*, **127**, 2211–2217.

254. Vlassov,V., Abramova,T., Godovikova,T., Giege,R. and Silnikov,V. (1997) Sequence-Specific Cleavage of Yeast tRNA(Phe) with Oligonucleotides Conjugated to a Diimidazole Construct. *Antisense Nucleic Acid Drug Dev.*, **7**, 39–42.

255. Beloglazova,N.G., Fabani,M.M., Polushin,N.N., Sil'nikov,V. V, Vlassov,V. V, Bichenkova,E. V and Zenkova,M.A. (2011) Site-selective artificial ribonucleases: oligonucleotide conjugates containing multiple imidazole residues in the catalytic domain. *J. Nucleic Acids*, **2011**, 748632.

256. Beloglazova,N.G., Sil'nikov,V.N., Zenkova,M.A. and Vlassov,V.V. (2000) Cleavage of yeast tRNA Phe with complementary oligonucleotide conjugated to a small ribonuclease mimic. *FEBS Lett.*, **481**, 277–280.

257. Garipova,I.Y. and Silnikov,V.N. (2002) Site-specific synthetic ribonucleases based on oligonucleotide conjugates with metal-independent organic catalysts of hydrolysis of phosphodiester bonds. *Russ. Chem. Bull.*, **51**, 1112–1117.

258. Goncharova,E.P., Kovpak,M.P., Ryabchikova,E.I., Konevets,D.A., Sil'nikov,V.N., Zenkova,M.A. and Vlasov,V. V (2009) Viral genome cleavage with artificial ribonucleases: a new method to inactivate RNA-containing viruses. *Dokl. Biochem. Biophys.*, **427**, 221–224.

259. Zenkova,M.A. and Beloglazova,N.G. (2004) Site-Specific Artificial Ribonucleases: Conjugates of Oligonucleotides with Catalytic Groups BT - Artificial Nucleases. In Zenkova,M.A. (ed). Springer Berlin Heidelberg, Berlin, Heidelberg, pp. 189–221.

260. Keck,M. V and Hecht,S.M. (1995) Sequence-Specific Hydrolysis of Yeast tRNAPhe Mediated by Metal-Free Bleomycin. *Biochemistry*, **34**, 12029–12037.

261. Modak,A., Gard,J., Merriman,M., Winkeler,K., Bashkin,J. and Stern,M. (1991) Toward Chemical Ribonucleases. 2. Synthesis and Characterization of Nucleoside-Bipyridine Conjugates. Hydrolytic Cleavage of RNA by Their Copper(II) Complexes. *J. Am. Chem. Soc.*, **113**, 283–291.

262. Hall,J., Husken,D., Pieles,U., Moser,H.E. and Haner,R. (1994) Efficient sequence-specific cleavage of RNA using novel europium complexes conjugated to oligonucleotides. *Chem. Biol.*, **1**, 185–190.

263. Usher,D.A. and McHale,A.H. (1976) Hydrolytic stability of helical RNA: a selective advantage for the natural 3',5'-bond. *Proc. Natl. Acad. Sci. U. S. A.*, **73**, 1149–1153.

264. Kuznetsova,I.L., Zenkova,M.A., Gross,H.J. and Vlassov,V. V (2005) Enhanced RNA cleavage within bulge-loops by an artificial ribonuclease. *Nucleic Acids Res.*, **33**, 1201–1212.

265. Trawick,B.N., Osiek,T.A. and Bashkin,J.K. (2001) Enhancing sequence-specific cleavage of RNA within a duplex region: incorporation of 1,3-propanediol linkers into oligonucleotide conjugates of serinol-terpyridine. *Bioconjug. Chem.*, **12**, 900–905.

266. Murtola,M., Wenska,M. and Strömberg,R. (2010) PNAzymes That Are Artificial RNA Restriction Enzymes. *J. Am. Chem. Soc.*, **132**, 8984–8990.

267. Williams,A., Staroseletz,Y., Zenkova,M.A., Jeannin,L., Aojula,H. and Bichenkova,E. V. (2015) Peptidyl-Oligonucleotide Conjugates Demonstrate Efficient Cleavage of RNA in a Sequence-Specific Manner. *Bioconjug. Chem.*, **26**, 1129–1143.

268. Mironova,N.L., Pyshnyi,D. V, Ivanova,E.M., Zenkova,M.A., Gross,H.J. and Vlassov,V. V (2004) Covalently attached oligodeoxyribonucleotides induce RNase activity of a short peptide and modulate its base specificity. *Nucleic Acids Res.*, **32**, 1928–1936.

269. Mironova,N.L., Pyshnyi,D. V, Stadler,D. V, Prokudin,I. V, Boutorine,Y.I., Ivanova,E.M., Zenkova,M.A., Gross,H.J. and Vlassov,V. V (2006) G-specific RNA-cleaving conjugates of short peptides and oligodeoxyribonucleotides. *J. Biomol. Struct. Dyn.*, **23**, 591–602.

270. Mironova,N.L., Pyshnyi,D. V, Shtadler,D. V, Fedorova,A.A., Vlassov,V. V and Zenkova,M.A. (2007) RNase T1 mimicking artificial ribonuclease. *Nucleic Acids*

Res., **35**, 2356–2367.

271. Mironova,N.L., Pyshnyi,D. V, Ivanova,E.M., Zarytova,V.F., Zenkova,M.A., Gross,H.J. and Vlassov,V. V (2002) Sequence-specific RNA cleavage by oligonucleotide-peptide conjugates. *Russ. Chem. Bull.*, **51**, 1177–1186.

272. Virta,P., Katajisto,J., Niittymäki,T. and Lönnberg,H. (2003) Solid-supported synthesis of oligomeric bioconjugates. *Tetrahedron*, **59**, 5137–5174.

273. Stetsenko,D.A. and Gait,M.J. (2005) Chemical methods for peptide-oligonucleotide conjugate synthesis. *Methods Mol. Biol.*, **288**, 205–224.

274. Venkatesan,N. and Kim,B.H. (2006) Peptide Conjugates of Oligonucleotides: Synthesis and Applications. *Chem. Rev.*, **106**, 3712–3761.

275. Grandas,A., Marchán,V., Debéthune,L. and Pedroso,E. (2001) Stepwise Solid-Phase Synthesis of Nucleopeptides. In *Current Protocols in Nucleic Acid Chemistry*. John Wiley & Sons, Inc.

276. Antopolsky,M. and Azhayev,A. (2000) Stepwise solid-phase synthesis of peptide–oligonucleotide phosphorothioate conjugates employing Fmoc peptide chemistry. *Tetrahedron Lett.*, **41**, 9113–9117.

277. Ollivier,N., Desmet,R., Drobecq,H., Blanpain,A., Boll,E., Leclercq,B., Mougel,A., Vicogne,J. and Melnyk,O. (2017) A simple and traceless solid phase method simplifies the assembly of large peptides and the access to challenging proteins. *Chem. Sci.*, **8**, 5362–5370.

278. Zubin,E.M., Romanova,E.A., Volkov,E.M., Tashlitsky,V.N., Korshunova,G.A., Shabarova,Z.A. and Oretskaya,T.S. (1999) Oligonucleotide-peptide conjugates as potential antisense agents. *FEBS Lett.*, **456**, 59–62.

279. Tripathi,S., Chaubey,B., Ganguly,S., Harris,D., Casale,R.A. and Pandey,V.N. (2005) Anti-HIV-1 activity of anti-TAR polyamide nucleic acid conjugated with various membrane transducing peptides. *Nucleic Acids Res.*, **33**, 4345–4356.

280. Schug,K.A. and Lindner,W. (2005) Noncovalent Binding between Guanidinium and Anionic Groups: Focus on Biological- and Synthetic-Based Arginine/Guanidinium Interactions with Phosph[on]ate and Sulf[on]ate Residues. *Chem. Rev.*, **105**, 67–114.

281. Sayin,S., Azak,H., Yildiz,H.B., Camurlu,P., Akkus,G.U., Toppare,L. and Ersoz,M. (2015) Calixarene assembly with enhanced photocurrents using P(SNS-NH 2)/CdS nanoparticle structure modified Au electrode systems. *Phys. Chem. Chem. Phys.*, **17**, 19911–19918.

282. Salvio,R. (2015) The Guanidinium Unit in the Catalysis of Phosphoryl Transfer Reactions: From Molecular Spacers to Nanostructured Supports. *Chem. - A Eur. J.*, **21**, 10960–10971.

283. Cho,B. and Wong,M.W. (2015) Unconventional Bifunctional Lewis-Brønsted Acid Activation Mode in Bicyclic Guanidine-Catalyzed Conjugate Addition Reactions. *Molecules*, **20**, 15108–15121.

284. Sahariah,P., Óskarsson,B.M., Hjálmarsdóttir,M.Á. and Másson,M. (2015) Synthesis of guanidinylated chitosan with the aid of multiple protecting groups and investigation of antibacterial activity. *Carbohydr. Polym.*, **127**, 407–417.

285. Bagnacani,V., Sansone,F., Donofrio,G., Baldini,L., Casnati,A. and Ungaro,R.

(2008) Macrocyclic Nonviral Vectors: High Cell Transfection Efficiency and Low Toxicity in a Lower Rim Guanidinium Calix[4]arene. *Org. Lett.*, **10**, 3953–3956.

286. Sansone,F., Dudič,M., Donofrio,G., Rivetti,C., Baldini,L., Casnati,A., Cellai,S. and Ungaro,R. (2006) DNA Condensation and Cell Transfection Properties of Guanidinium Calixarenes: Dependence on Macrocycle Lipophilicity, Size, and Conformation. *J. Am. Chem. Soc.*, **128**, 14528–14536.

287. Cacciapaglia,R., Casnati,A., Mandolini,L., Peracchi,A., Reinhoudt,D.N., Salvio,R., Sartori,A. and Ungaro,R. (2007) Efficient and Selective Cleavage of RNA Oligonucleotides by Calix[4]arene-Based Synthetic Metallonucleases. *J. Am. Chem. Soc.*, **129**, 12512–12520.

288. Baldini,L., Cacciapaglia,R., Casnati,A., Mandolini,L., Salvio,R., Sansone,F. and Ungaro,R. (2012) Upper rim guanidinocalix[4]arenes as artificial phosphodiesterases. *J. Org. Chem.*, **77**, 3381–3389.

289. Salvio,R., Mandolini,L. and Savelli,C. (2013) Guanidine–Guanidinium Cooperation in Bifunctional Artificial Phosphodiesterases Based on Diphenylmethane Spacers; gem-Dialkyl Effect on Catalytic Efficiency. *J. Org. Chem.*, **78**, 7259–7263.

290. Ariga,K. and Anslyn,E. V (1992) Manipulating the stoichiometry and strength of phosphodiester binding to a bisguanidine cleft in DMSO/water solutions. *J. Org. Chem.*, **57**, 417–419.

291. Corona-Martinez,D.O., Taran,O. and Yatsimirsky,A.K. (2010) Mechanism of general acid-base catalysis in transesterification of an RNA model phosphodiester studied with strongly basic catalysts. *Org. Biomol. Chem.*, **8**, 873–880.

292. Frankel,A.D. (1992) Peptide models of the Tat-TAR protein-RNA interaction. *Protein Sci.*, **1**, 1539–1542.

293. Frigyes,D., Alber,F., Pongor,S. and Carloni,P. (2001) Arginine–phosphate salt bridges in protein–DNA complexes: a Car–Parrinello study. *J. Mol. Struct. THEOCHEM*, **574**, 39–45.

294. Vallet,C., Aschmann,D., Beuck,C., Killa,M., Meiners,A., Mertel,M., Ehlers,M., Bayer,P., Schmuck,C., Giese,M., *et al.* (2020) Functional Disruption of the Cancer-Relevant Interaction between Survivin and Histone H3 with a Guanidiniocarbonyl Pyrrole Ligand. *Angew. Chem. Int. Ed. Engl.*, **59**, 5567–5571.

295. Morrow,J.R. (2008) Speed limits for artificial ribonucleases. *Comments Inorg. Chem.*, **29**, 169–188.

296. Barbier,B. and Brack,A. (1988) Basic polypeptides accelerate the hydrolysis of ribonucleic acids. *J. Am. Chem. Soc.*, **110**, 6880–6882.

297. Pyshnyi,D., Repkova,M., Lokhov,S., Ivanova,E., Venyaminova,A. and Zarytova,V. (1997) Oligonucleotide-Peptide Conjjugates for RNA Cleavage. *Nucleosides and Nucleotides*, **16**, 1571–1574.

298. Dock-Bregeon,A.C. and Moras,D. (1987) Conformational changes and dynamics of tRNAs: evidence from hydrolysis patterns. *Cold Spring Harb. Symp. Quant. Biol.*, **52**, 113–121.

299. Yan,B.X. and Sun,Y.Q. (1997) Glycine residues provide flexibility for enzyme active sites. *J. Biol. Chem.*, **272**, 3190–3194.

300. Bartlett,G.J., Porter,C.T., Borkakoti,N. and Thornton,J.M. (2002) Analysis of catalytic residues in enzyme active sites. *J. Mol. Biol.*, **324**, 105–121.

301. Okoniewska,M., Tanaka,T. and Yada,R.Y. (2000) The pepsin residue glycine-76 contributes to active-site loop flexibility and participates in catalysis. *Biochem. J.*, **349**, 169–177.

302. Tiwari,M.K., Singh,R.K., Singh,R., Jeya,M., Zhao,H. and Lee,J.-K. (2012) Role of conserved glycine in zinc-dependent medium chain dehydrogenase/reductase superfamily. *J. Biol. Chem.*, **287**, 19429–19439.

303. Patutina,O.A., Bichenkova,E. V, Miroshnichenko,S.K., Mironova,N.L., Trivoluzzi,L.T., Burusco,K.K., Bryce,R.A., Vlassov,V. V and Zenkova,M.A. (2017) miRNases: Novel peptide-oligonucleotide bioconjugates that silence miR-21 in lymphosarcoma cells. *Biomaterials*, **122**, 163–178.

304. Patutina,O.A., Bazhenov,M.A., Miroshnichenko,S.K., Mironova,N.L., Pyshnyi,D. V, Vlassov,V. V and Zenkova,M.A. (2018) Peptide-oligonucleotide conjugates exhibiting pyrimidine-X cleavage specificity efficiently silence miRNA target acting synergistically with RNase H. *Sci. Rep.*, **8**, 14990.

305. Hirao,I., Nishimura,Y., Tagawa,Y., Watanabe,K. and Miura,K. (1992) Extraordinarily stable mini-hairpins: electrophoretical and thermal properties of the various sequence variants of d(GCFAAAGC)and their effect on DNA sequencing. *Nucleic Acids Res.*, **20**, 3891–3896.

306. Hirao,I., Nishimura,Y., Naraoka,T., Watanabe,K., Arata,Y. and Miura,K. (1989) Extraordinary stable structure of short single-stranded DNA fragments containing a specific base sequence: d(GCGAAAGC). *Nucleic Acids Res.*, **17**, 2223–2231.

307. Patutina,O.A., Miroshnichenko,S.K., Mironova,N.L., Sen'kova,A. V, Bichenkova,E. V, Clarke,D.J., Vlassov,V. V and Zenkova,M.A. (2019) Catalytic Knockdown of miR-21 by Artificial Ribonuclease: Biological Performance in Tumor Model. *Front. Pharmacol.*, **10**, 879.

308. Trehin,R. and Merkle,H.P. (2004) Chances and pitfalls of cell penetrating peptides for cellular drug delivery. *Eur. J. Pharm. Biopharm.*, **58**, 209–223.

309. Tung,C.-H. and Weissleder,R. (2003) Arginine containing peptides as delivery vectors. *Adv. Drug Deliv. Rev.*, **55**, 281–294.

310. Lindsay,M.A. (2002) Peptide-mediated cell delivery: application in protein target validation. *Curr. Opin. Pharmacol.*, **2**, 587–594.

Chapter 2

Strict conformational demands of RNA cleavage in bulge-loops created by peptidyl-oligonucleotide conjugates

Strict conformational demands of RNA cleavage in bulge-loops created by peptidyl-oligonucleotide conjugates

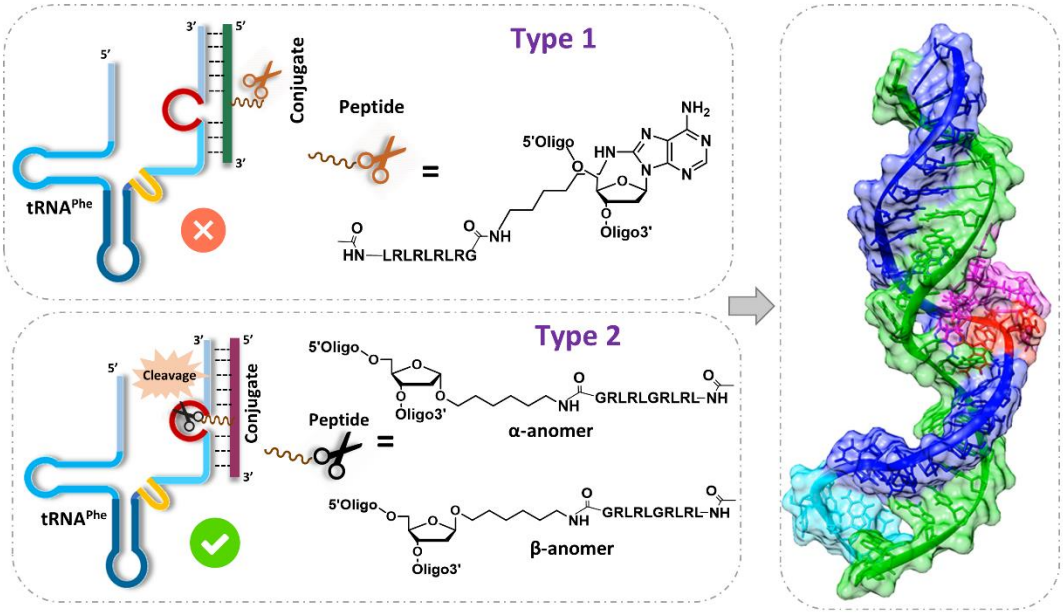

2.1 Declaration

This chapter consists of one scientific article recently accepted in Nucleic Acids Research (NAR):

Yaroslav Staroseletz,[*] Bahareh Amirloo,[*] Aled Williams, Alexander Lomzov, Kepa K. Burusco, David J. Clarke, Tom Brown, Marina A. Zenkova, and Elena V. Bichenkova. (2020) Strick conformational demands of RNA cleavage in bulge-loops created by peptidyl-oligonucleotide conjugates. *Nucleic Acids Res.* Accepted 7 Sep 2020.

This paper is directly relevant to my main research reported in this thesis. It provides the full experimental and analytical details on how we progressed from initially unsuccessful design of *"single"* bulge-loop inducing conjugates (Type 1) to catalytically active structural variants (Type 2), capable of cleaving RNA sequences with high level of efficiency. The data reported in this paper (**Chapter 2**) provided us with the crucial structural information to develop this design further and ultimately achieve the reaction catalytic turnover in RNA cleavage, which is presented in the next paper (**Chapter 3**). This article and supporting information have been reproduced in an unchanged format except for minor formatting adjustments to incorporate it into this thesis.

As joint first author for this publication, I carried out the design, synthesis and characterisation of the Type 2 peptidyl-oligonucleotide conjugates. Type 1 conjugates were designed and synthesised by Dr Aled Williams. RNA binding experiments using gel-shift assays and all cleavage experiments, with full electrophoretic analysis were performed by Dr Yaroslav Staroseletz. Dr Alexander Lomzov, and Dr. Kepa K. Burusco carried out Molecular Dynamics simulations and cluster analysis. I analysed the data (with the contribution from the other authors), prepared figures and drafted the manuscript. Dr. Elena Bichenkova, Prof. Marina Zenkova, Prof. David Clarke and Prof. Tom Brown conceived the scientific ideas, supervised the relevant experimental work and were involved in project management, data analysis and manuscript editing at various stages.

Strict conformational demands of RNA cleavage in bulge-loops created by peptidyl-oligonucleotide conjugates

Yaroslav Staroseletz[1,†], Bahareh Amirloo[2,†], Aled Williams[2], Alexander Lomzov[1], Kepa K. Burusco[2], David J. Clarke[2], Tom Brown[3], Marina A. Zenkova[1] and Elena V. Bichenkova[2,*]

[1] Institute of Chemical Biology and Fundamental Medicine SB RAS, 8 Laurentiev Avenue, 630090, Novosibirsk, RF

[2] School of Health Sciences, Faculty of Biology, Medicine and Health, University of Manchester, Oxford Road, Manchester, M13 9PT, UK

[3] Department of Chemistry, Chemistry Research Laboratory, University of Oxford, 12 Mansfield Road, Oxford, OX1 3TA, UK

[†] These authors contributed equally to this work

2.2 Abstract

Potent knockdown of pathogenic RNA *in vivo* is an urgent health need unmet by both small-molecule and biologic drugs. 'Smart' supramolecular assembly of catalysts offers precise recognition and potent destruction of targeted RNA, hitherto not found in nature. Peptidyl-oligonucleotide ribonucleases are here chemically-engineered to create and attack bulge-loop regions upon hybridisation to target RNA. Catalytic peptide was incorporated either via a centrally-modified nucleotide (Type 1) or through an abasic sugar residue (Type 2) within the RNA-recognition motif to reveal striking differences in biological performance and strict structural demands of ribonuclease activity. None of the Type 1 conjugates were catalytically active, whereas all Type 2 conjugates cleaved RNA target in a sequence-specific manner, with up to 90% cleavage from 5 nucleotide bulge-loops (BC5-α and BC5L-β anomers) through multiple cuts, including in folds nearby. Molecular dynamics simulations provided structural explanation of accessibility of the RNA cleavage sites to the peptide with adoption of an *"in-line"* attack conformation for catalysis. Hybridisation assays and enzymatic probing with RNases illuminated how RNA binding specificity and dissociation after cleavage can be balanced to permit turnover of the catalytic reaction. This is an essential requirement for inactivation of multiple copies of disease-associated RNA and therapeutic efficacy.

2.3 Introduction

Irreversible sequence-selective cleavage of disease-associated RNA is recognised as a promising therapeutic strategy against abnormal gene expression in disease states (1–3). In contrast to low molecular weight drugs, which are designed to confront disease *downstream*, when it is already established in cell components at the level of expressed pathogenic proteins, *upstream* RNA targeting allows a desirable therapeutic response through controlled translational arrest of such proteins, well before they are translated into disease states. Contrary to small-molecule drug chemotherapeutic treatments, which suffer from cytotoxicity, with inevitable side effects which limit their success, (4, 5) RNA therapeutics offer the opportunity of high selectivity, improved potency and reduced toxicity (6). The lack of repair mechanisms and accessibility of many RNAs in the cytoplasm make RNA an attractive and less risky biotarget than DNA, because RNA targeting avoids gene manipulation or editing (*cf.* with CRISPR). RNA-targeting interventions can be directed toward a diverse variety of RNA sequences ranging from messenger RNAs encoding pathogenic proteins, or viral genomic RNAs, to non-coding RNAs involved in cellular signaling pathways. It is now well recognised that non-coding RNA molecules (e.g. miRNA, lncRNA, piRNA) play a major role in numerous human diseases including ovarian, breast and lung cancer, as well as in inflammatory and degenerative diseases (7–9). Currently, RNA degradation and protein expression knockdown by siRNA and antisense oligonucleotide (ASO) therapeutics must recruit enzyme complexes: RNA-induced silencing complex (RISC) and ribonuclease H, respectively. However, recruiting enzymes, which are required to regulate normal cellular RNA, inevitably led to toxic effects such as upregulation of oncogenes (e.g. HMGA2, CCND1 and DUSP2) (10). Also, the use of siRNA technology often triggers the activation of the innate immune response, (11, 12) which presents another clinical barrier. ASOs struggle with their 1:1 binding stoichiometry, both to reach their therapeutic threshold and to maintain a therapeutic effect against fresh transcription and turnover (3). This requires high concentrations of ASOs to be maintained within the cellular environment for lengthy periods, which is often difficult to achieve due to their rapid clearance and poor cellular delivery, even if insufficient chemical stability of oligonucleotide therapeutics is overcome (13). Therefore, the development of novel chemical agents capable of achieving potent, irreversible destruction of disease-relevant RNA sequences without reliance on intracellular molecular components is of particular importance.

Chemically-engineered artificial (or chemical) ribonucleases (14–20) offer unique opportunities for catalytic destruction of disease-relevant RNA without engaging complex multi-component machinery (e.g. RISC, RNase H) that normally act *via* recruitment of a guide RNA or DNA sequence for target recognition and a protein–RNA assembly for RNA cleavage. We have recently developed peptidyl-oligonucleotide conjugates (15–20) (POCs) as a new class of metal-free chemical ribonucleases, which consist of an antisense oligonucleotide targeted towards a specific RNA sequence, and an RNA-cleaving catalyst (e.g. amphiphilic peptide). Such bioconjugates (15–19) are capable of inducing complete phosphodiester transesterification of target RNA sequence without requirement of enzymes, additional endogenous cofactors or exogenous agents (e.g. metal ions) that can fluctuate within and between cell types. Recently, we have demonstrated (17,20) that this type of biologically-active conjugates can selectively knockdown highly-oncogenic microRNA (miR-21) by irreversible cleavage and thereby induce apoptosis in tumor cells, suppress their invasive properties and knockdown tumor proliferation *in vitro*. A single treatment of tumor cells with such catalytic conjugates eliminated their malignant behavior and persisted to retard subsequent tumor growth *in vivo* after their transplantation into mice (20).

In order to improve their potency against disease-relevant RNAs, so that dosage and systemic delivery issues are overcome, it is imperative to ensure that each POC molecule inactivates many copies of pathogenic RNA for a lengthy period of time. This can only be achieved through catalytic turnover which persists in cells. Reaction turnover of multiple RNA substrates requires rapid release of cleaved RNA fragments after each cleavage event, to liberate the POC from the hybridised complex and allow it to attack the next RNA molecule. However, the high stability of hybridised *RNA:DNA* heteroduplexes, hitherto essential to ensure the high level of precision in RNA recognition to avoid off-target effects and associated toxicity, opposes the ability of conjugates to leave RNA after cleavage (14,15). Although our “hairpin” peptidyl-oligonucleotide conjugates have recently demonstrated the ability to cleave RNA in a multiple turnover mode by working synergistically with cellular enzymes (20), they continue to rely on the variable cytosolic abundance of RNase H1 (21) to achieve turnover of RNA substrates. The main challenge is therefore to develop fully-independent, self-reliant RNA-specific conjugates that combine absolute sequence-specificity with a high level of catalytic turnover, which can operate autonomously under physiological conditions. This can be achieved by optimising the length of the conjugate recognition motifs and the point for

attachment of the catalytic functionality to ensure that the binding affinity of the RNA cleavage products towards the conjugate is considerably lower than that of the intact RNA chain (14). Artificial ribonucleases with metal-coordinated (e.g. Dy(III), Cu(II), Eu(III)) RNA-cleaving constructs, although toxic and unstable, provide evidence that, in principle, catalytic turnover of RNA substrates can be achieved (22–26). However, they are susceptible to metal loss from their coordinating ligands and may cause degradation of non-target biopolymers, (14,15, 27) thus leading to undesirable side effects and cytotoxicity. Our focus is therefore to develop *metal-independent* ribonucleases, suitable for *in vivo* studies and therapeutic applications.

The nature of the RNA target is particularly important when designing artificial ribonucleases. Single-stranded RNA regions that can be found in bulge-loops are more susceptible to cleavage than duplex RNA fragments (27, 28). This is due to the orientation of the 2'- hydroxyl in an RNA duplex being unsuitable for intramolecular transesterification, and a conformational change would require unfavorable duplex disruption (29). Cleavage within RNA bulge-loops is widely regarded as a method to encourage catalytic turnover of chemical nucleases (30, 31). In order to induce bulge-loops in a target RNA, the sequence of the conjugate recognition motif must be designed so that a short region (2nt – 5nt) in the middle of the target RNA sequence remains non-complementary, thus forcing the RNA to adopt a bulge-loop structure upon hybridisation. The size of the bulge-loop can be fine-tuned by altering the size of the non-complementary regions. Previously, 3- and 4-member bulge-loops have shown the greatest potential for cleavage (30, 31) by different catalysts, presumably due to their ability to provide the optimum flexibility for the *'in-line'* attack of the 2'-oxyanion onto the bridging phosphodiester group, the rate-limiting step of the phosphodiester cleavage mechanism (30, 31). Recently developed bulge-loop inducing peptide nucleic acid-based conjugates, PNAzymes, carrying toxic Cu^{2+}-2,9-dimethylphenanthroline or tris(2-aminobenzimidazole) cleaving units demonstrated multiple substrate turnover against a model 15-nt RNA (23, 32, 33).

Herein we designed and synthesised a series of metal-free bulge-loop inducing peptidyl-oligonucleotide conjugates (BCs) against the 3' acceptor stem and TΨC arm of $tRNA^{Phe}$ (see **Figure 2.1** and **Supplementary Figures 2.9** and **2.10**). The presence of common secondary structural elements and its characteristic folding makes $tRNA^{Phe}$ a desirable target for scientific discovery. Through central incorporation of a modified adenosine or abasic nucleotide, changes in loop size, peptide structure and its orientation, a library of

14 novel conjugates were designed, synthesised and fully characterised here. We report their hybridisation properties and catalytic activity, alongside comprehensive analysis of their interactions with target RNA using molecular modelling stimulations. This work illuminates the importance of strict structural and dynamic considerations for molecular design of peptidyl-oligonucleotide conjugates attacking bulge-loop regions of RNA sequences. The structural insights gained here inform how duplex-constrained cleavage occurs, so that a single molecule catalyst can be designed to destroy manifold copies of target RNA in a specific sequence-controlled manner.

2.4 Materials and Methods

2.4.1 Chemical, reagents, equipment and facilities

Oligonucleotides containing an aminohexyl-modified adenosine residue were acquired from ATDBio Ltd (Southampton, UK), and those incorporating an internal abasic nucleotide with aminohexyl linker attached at the C1' position in α- or β- configuration were purchased from the Institute of Chemical Biology and Fundamental Medicine (Novosibirsk, Russian Federation). α- and β- aminohexyl abasic sugar phosphoramidite monomers were purchased from Link Technologies Ltd (Scotland, UK). Acetyl-$[LRLRG]_2$-CO_2H was purchased from Biomatik (Cambridge, Ontario, Canada). Reagents and materials were purchased from Sigma-Aldrich (UK), unless otherwise indicated. Water was purified in house *via* a Milli-Q purification system (Millipore, USA).

HPLC purifications were carried out using an Agilent 1100 HPLC system (Agilent Technologies, Santa Clara, CA) equipped with a diode array detector and Rheodyne (3725i) manual injector. Peptides and peptidyl-oligonucleotide conjugates were purified by reverse phase chromatography using a semipreparative Phenomenex Luna C-18 column (5 μm, 4.6 × 10 x 250 mm, 100 A, Phenomenex; CA, USA), with a flow rate of 2 mL min^{-1}. All peptidyl-oligonucleotide conjugates were additionally purified by gel filtration chromatography using Illustra^{TM} NAP disposable columns, prepacked with Sephadex G-25 (DNA grade) and purchased from GE Healthcare Life Sciences, to remove possible traces of counter cations. UV-visible spectroscopy measurements were carried out using a Cary-4000 UV-Visible spectrophotometer from Varian (Australia) connected to a Cary Peltier temperature controller, operating under Varian Cary WinUV software. Oligonucleotide concentrations were calculated by measuring UV absorbance at 260 nm and using the millimolar extinction coefficient ε_{260} of the corresponding oligonucleotide at 260 nm ($mM^{-1} \cdot cm^{-1}$) (see **Supplementary Table 2.2**). ESI mass

spectral data was collected on a Thermo Scientific LTQ Orbitrap XL (MA, USA) at the EPSRC UK National Mass Spectrometry Facility at Swansea University (Swansea, UK). MALDI (Matrix-Assisted Laser Desorption Ionisation) mass spectra was collected on a Bruker Dal-tonics Ultraflex TOF/TOF mass spectrometer (MA, USA) at the Manchester Interdisciplinary Biocentre, University of Manchester as described earlier (34). ^{1}H NMR spectra were recorded using Bruker Avance II+ spectrometers operating at proton frequencies of 400 MHz using BBI ^{1}H/D-BB Z-GRD Z8202/0347 probe using previously described methods (34, 35). The acquired data was processed using Bruker software Topspin 4.0.3.

The analytical data presenting the full characterisation of the generated peptides and peptidyl-oligonucleotide conjugates are given in the **Supplementary Information** (see **Supplementary Figures 2.11 -2.20**).

2.4.2 Peptide synthesis, purification and characterisation

Acetyl-$[LR]_4G$-CO_2H was synthesised by manual solid-phase methodology on Fmoc-Gly-Wang resin (250 mg, 0.2 mmol) using the Fmoc/tBu strategy. Fmoc deprotections were achieved with 20% piperidine in N,N-dimethylformamide (DMF) solution for 30 minutes at room temperature (RT). Before each coupling step, resin was washed with DMF (2 × 10 mL), dichloromethane (DCM) (2 × 10 mL) and DMF (2 × 10 mL). Amino acid couplings were achieved by pre-activating either Fmoc-Leu-OH (212 mg, 0.6 mmol); Fmoc-Gly-OH (178 mg, 0.54 mmol) or Fmoc-Arg(Pbf)-OH (389 mg, 0.6 mmol) in DMF (10 mL) with N,N,N′,N′-tetramethyl-O-(1H-benzotriazol-1-yl)uronium hexafluorophosphate (HBTU) (220 mg, 0.58 mmol) and N,N-di-isopropylethylamine (DIPEA) (122 µl, 0.7 mmol). Following addition to the resins, the reactions proceeded at RT for 30 minutes under mechanical shaking. Following completion of the peptide sequence, the N-terminus was acetylated by shaking with acetic anhydride (10 mmol) and DIPEA (10 mmol) in DMF (10 mL) for 30 minutes, followed by washing of the resin with DMF (2 × 10 mL), DCM (2 × 10 mL) and DMF (2 × 10 mL). Successful Fmoc deprotection and amino acid coupling was visualised by carrying out a Kaiser test. After completing the acetylation procedure, the peptide was cleaved from the resin by shaking with the mixture trifluoroacetic acid (TFA): triisopropyl silane (TIPS):H_2O (95:2.5:2.5) (15 mL) at RT for 3 hours. The volume of the resulting solution was reduced by 66%, pipetted into cold (-20 °C) methyl tert-butyl ether (TBME) and stored at -20 °C overnight. The precipitate was collected by centrifugation (4000 rpm, 5 minutes, 4°C) and the

resulting pellets were washed with cold TBME (2 × 10 mL) and isolated by centrifugation. Once air dried, the pellets were solubilised in acetonitrile/water/TFA (40/60/0.1) and freeze dried.

Crude lyophilised peptide was solubilised in 30% acetic acid and purified using reverse-phase HPLC (RP-HPLC). The flow rate was maintained at 1.5 mL/min using 0.1% TFA/water as eluent A and 0.1% TFA/ acetonitrile (AcCN) as eluent B. The absorbance was monitored at 220 nm, while the following gradient was applied: 5% B for 1 minute, 5% B to 40% B in 40 minutes.

Acetyl-[LR]$_4$G-CO$_2$H. Fractions at 33 minutes were collected, combined and lyophilised to yield the TFA salt of peptide as a fluffy white material (240 mg, 73%). ESI-MS: m/z = 597.9 for $[M+H+H]^{2+}$ (MW = 1193.78 calc. for $[C_{52}H_{99}N_{21}O_{11}]$) (**Supplementary Figure 2.13**). ^{1}H NMR (**Supplementary Figure 2.14**) (D_2O with TSP (0.1 μM), 400 MHz): δ 0.85- 0.96 (m, 24H, Leu-H$^{\delta}$), 1.50-1.93 (m, 28H, 8 × Arg-H$^{\beta}$, 8 × Arg-H$^{\gamma}$, 8 × Leu-H$^{\beta}$, 4 × Leu-H$^{\gamma}$), 2.03 (s, 3H, Ac-CH$_3$), 3.20 (m, 8H, Arg-H$^{\delta}$), 3.85 (d, 2H, 2 × Gly-H), 4.15-4.38 (m, 8H, 8 × Leu/Arg-H$^{\alpha}$).

Acetyl-[LRLRG]$_2$-CO$_2$H. Fractions at 33 minutes were collected, combined and lyophilised to yield the TFA salt of the peptide as a fluffy white material. MALDI-TOF-MS: m/z = 1252 for $[M+H]^+$, (MW = 1251 calc. for $[C_{54}H_{102}N_{22}O_{12}]$) (**Supplementary Figure 2.15**). ^{1}H NMR (**Supplementary Figure 2.16**) (D_2O with TSP (0.1 μM), 400 MHz): δ 0.91-0.97 (m, 24H, Leu-H$^{\delta}$), 1.55- 1.99 (m, 28H, 8 × Arg-H$^{\beta}$, 8 × Arg-H$^{\gamma}$, 8 × Leu-H$^{\beta}$, 4 × Leu-H$^{\gamma}$), 2.06 (s, 3H, Ac-CH$_3$), 3.24 (m, 8H, Arg-H$^{\delta}$), 3.88-4.41 (m, 12H, 4 × Gly-H, 8 × Leu/Arg-H$^{\alpha}$).

2.4.3 Conjugate synthesis

Type 1 peptidyl-oligonucleotide conjugates (BC2-BC5). Oligonucleotides containing an aminohexyl-modified adenosine residue (50 nmol) in H_2O (100 μL) were converted into dimethyl sulfoxide (DMSO) soluble salts through multiple (10 μL) additions of a 4% (w/v) cetyltrimethylammonium bromide (CTAB) solution. After each subsequent addition, the solution was centrifuged (13400 rpm, 4 minutes). When oligonucleotide precipitation had completed, the pellet was harvested by centrifugation and washed with H_2O (2 × 500 μL) and freeze dried overnight. The pellet was solubilised in anhydrous DMSO (50 μL). Peptide acetyl-[LR]$_4$G-CO$_2$H (2.3 μmol,) and 4-dimethylaminopyridine (DMAP, 3.5 μmol) were dissolved in a minimum volume of anhydrous DMSO (≈20 μL)

before N, N'-dicyclohexylcarbodiimide (DCC, 3.5 μmol) was added and vortexed. The resulting peptide solution was added directly to oligonucleotide solutions and left at 40°C for 4 hours. Lithium perchlorate ($LiClO_4$, 4% w/v) in acetone (1.8 mL) was added and the reaction mixture left at -80°C overnight. After centrifugation (13,400 rpm, 4 minutes), the supernatant was discarded and the pellet left to air dry. The dry pellet was vortexed vigorously with 3M $LiClO_4$ (120 μL) and centrifuged (13,400 rpm, 4 minutes). The supernatant was carefully transferred into 4% $LiClO_4$ in acetone (w/v) (1.8 mL) and kept at - 80°C for 3 hours. Following centrifugation (13,400 rpm, 4 minutes), the supernatant was discarded, and the pellet left to air dry before RP-HPLC purification.

Type 2 conjugates (BC-α and BC-βs). The water-soluble lithium salt of the oligonucleotide was converted to its CTAB (50 nmol) salt (to solubilise in DMSO) using the same protocol as described for Type 1 conjugates. Following lyophilisation, the dry pellet was solubilised in 30 μl of anhydrous DMSO. In an attempt to achieve complete dissolution in the minimum of DMSO, the oligonucleotide was vigorously vortexed and heated up to 60°C. Subsequently, dried acetyl-$[LRLRG]_2$-CO_2H (50-fold excess over oligonucleotide, 2.5 μmol), DMAP and DCC (1.5-fold excess over peptide each, 3.75 μmol) were dissolved in the minimum volume of anhydrous DMSO (≈40 μL) and vortexed. The resulting solution was then added directly to oligonucleotide solution and incubated at 60°C for 12 hours. Subsequently, $LiClO_4$ (1.8 ml of 4% w/v) in acetone was added directly to the reaction vessel and left at -80°C for 36 hours. Following centrifugation (13,400 rpm, 5 min), the supernatant was decanted when the precipitate was left to air dry. The dry pellet was dissolved in water (2×1 ml) and prepared for size-exclusion chromatography before purification through RP-HPLC. Where different amounts of the oligonucleotide were used, the amounts of peptide, DMAP and DCC were scaled accordingly to maintain the same molar ratios.

2.4.4 Conjugate purification

Purification of Type 1 conjugates. Crude conjugates were dissolved in 0.05M $LiClO_4$ and purified by RP-HPLC. The flow rate was maintained at 2.0 mL/min using 0.05M $LiClO_4$ as eluent A and 0.05M $LiClO_4$ in AcCN as eluent B. The absorbance was monitored at 260 nm and the following gradient was applied: 100% A for 5 minutes, 0% B to 40% B in 27 minutes (see **Supplementary Figure 2.11**).

Purification of Type 2 conjugates. Crude conjugates were dissolved in water and purified using RP-HPLC. The flow rate was maintained at 2.0 ml/min using 0.05M

$LiClO_4$ as eluent A and 0.05M $LiClO_4$ in AcCN as eluent B. The absorbance was monitored at 260 nm and the following gradient was applied: 0% B for 3 minutes, 0-100% B in 30 minutes (see **Supplementary Figure 2.12**).

2.4.5 Conjugate characterisation

BC2. Fractions at 27 minutes were collected, combined and lyophilised. The excess salt was removed by dissolving the material in H_2O (100 μL) and precipitating overnight in $LiClO_4$ in acetone (1.8 mL of 4% w/v). The product was collected by centrifugation (13,400 rpm, 4 minutes), air dried and then freeze dried to give a white powder (24 nmol, 48%). MALDI-MS: *m/z* = 4088 $[M+H+Na]^{2+}$,8184 for $[M+K]^+$ (MW = 8144 calc. for $[C_{276}H_{382}N_{111}O_{140}P_{21}]$) (**Supplementary Figure 2.17**). ^1H NMR (**Supplementary Figure 2.18**) (D_2O with TSP (0.01 mM), 400 MHz): δ 0.70-0.99 (m, 24H, Leu- H^{δ}), 0.85-3.25 (m, 105H, 22×H2' and 22×H2'' sugar ring protons, 6×CH_3 of 6×dT, 8× Arg-H^{β}, 8×Arg-H^{γ}, 8×Leu-H^{β}, 4×Leu-H^{γ}, 6×CH_2 (aminohexyl linker), acetyl-CH_3), 3.21 (m, 8H, 8×Arg-H^{δ}), 3.51-4.23 (m, 76H, 22×H4'/H5'H5" sugar ring protons, 2×Gly-H, 8× Leu/Arg-H^{α}), 4.52-4.94 (m, 22H, 22×H3' sugar ring protons), 5.40-6.33 (m, 24H, 22×H1' sugar ring protons, 2×H5 of dC), 7.25-8.31 (m, 27H, 27×Ar-H from dG(H8×8), dA(H8×5), dA(H2×6), dC(H6×2) and dT(H6×6). H3' sugar ring protons (4.3-5.2 ppm) were not analysed due to suppression of residual water signal at 4.78 ppm.

BC3. Fractions at 26 minutes were collected, combined and lyophilised. The excess salt was removed by dissolving the material in H_2O (100 μL) and precipitating in 4% $LiClO_4$ in acetone (w/v) (1.8 mL) overnight. The product was collected by centrifugation (13,400 rpm, 4 minutes), air-dried and then freeze-dried to give a white powder (19 nmol, 38%). MALDI-MS: *m/z* = 3919 $[M+H+Na]^{2+}$,7816 for $[M+K]^+$ (MW = 7815 calc. for $[C_{266}H_{370}N_{106}O_{134}P_{20}]$) (**Supplementary Figure 2.17**). ^1H NMR (**Supplementary Figure 2.18**) (D_2O with TSP (0.01 mM), 400 MHz): δ 0.70-0.99 (m, 24H, Leu- H^{δ}), 0.85-3.25 (m, 103H, 21×H2' and 21×H2'' sugar ring protons, 6×CH_3 of 6×dT, 8× Arg-H^{β}, 8×Arg-H^{γ}, 8×Leu-H^{β}, 4×Leu-H^{γ}, 6×CH_2 (aminohexyl linker), acetyl-CH_3), 3.21 (m, 8H, 8×Arg-H^{δ}), 3.51-4.23 (m, 73H, 21×H4'/H5'H5" sugar ring protons, 2×Gly-H, 8× Leu/Arg-H^{α}), 5.40-6.33 (m, 23H, 21×H1' sugar ring protons, 2×H5 of dC), 7.25-8.31 (m, 26H, 26×Ar-H from dG(H8×7), dA(H8×5), dA(H2×6), dC(H6×2) and dT(H6×6)). H3' sugar ring protons (4.3-5.2 ppm) were not analysed due to suppression of residual water signal at 4.78 ppm.

BC4. Fractions at 26.5 minutes were collected, combined and lyophilised. The excess salt was removed by dissolving the material in H_2O (100 μL) and precipitating overnight in $LiClO_4$ (1.8 mL of 4% w/v in acetone). The product was collected by centrifugation (13,400 rpm, 4 minutes), air dried and then freeze dried to give a white powder (22 nmol, 44%). MALDI-MS: *m/z* = 3790 $[M+2H+2ACN]^{2+}$, 7541 for $[M+Na+Na\text{-}H]^{+}$ (MW = 7497 calc. for $[C_{256}H_{357}N_{104}O_{127}P_{19}]$) (**Supplementary Figure 2.17**). ^{1}H NMR (**Supplementary Figure 2.18**) (D_2O with TSP (0.01 mM), 400 MHz): δ 0.70-0.99 (m, 24H, Leu-H^{δ}), 0.85-3.25 (m, 98H, 20×H2' and 20×H2'' sugar ring protons, 5×CH_3 of 5×dT, 8× Arg-H^{β}, 8×Arg-H^{γ}, 8×Leu-H^{β}, 4×Leu-H^{γ}, 6×CH_2 (aminohexyl linker), acetyl-CH_3), 3.21 (m, 8H, 8×Arg-H^{δ}), 3.51-4.23 (m, 70H, 20×H4'/H5'H5" sugar ring protons, 2×Gly-H, 8× Leu/Arg-H^{α}), 5.40-6.33 (m, 22H, 20×H1' sugar ring protons, 2×H5 of dC), 7.25-8.31 (m, 25H, 25×Ar-H from dG(H8×7), dA(H8×5), dA(H2×6), dC(H6×2) and dT(H6×5)). H3' sugar ring protons (4.3-5.2 ppm) were not analysed due to suppression of residual water signal at 4.78 ppm.

BC5. Fractions at 27 minutes were collected, combined and lyophilised. The excess salt was removed by dissolving the material in H_2O (100 μL) and precipitating overnight in $LiClO_4$ (1.8 mL of 4% w/v in acetone). The product was collected by centrifugation (13,400 rpm, 4 minutes), air dried and then freeze dried to give a white powder (19 nmol, 38%). MALDI-MS: *m/z* = 3603 $[M+H+K]^{2+}$,7201 for $[M+CH3OH+H]^{+}$ (MW = 7168 calc. for $[C_{247}H_{347}N_{99}O_{121}P_{18}]$) (**Supplementary Figure 2.17**). ^{1}H NMR (**Supplementary Figure 2.18**) (D_2O with TSP (0.01 mM), 400 MHz): δ 0.70-0.99 (m, 24H, Leu-H^{δ}), 0.85-3.25 (m, 96H, 19×H2' and 19×H2'' sugar ring protons, 5×CH_3 of 5×dT, 8× Arg-H^{β}, 8×Arg-H^{γ}, 8×Leu-H^{β}, 4×Leu-H^{γ}, 6×CH_2 (aminohexyl linker), acetyl-CH_3), 3.21 (m, 8H, 8×Arg-H^{δ}), 3.51-4.23 (m, 67H, 20×H4'/H5'H5" sugar ring protons, 2×Gly-H, 8 × Leu/Arg-H^{α}), 5.40-6.33 (m, 21H, 19×H1' sugar ring protons, 2×H5 of dC), 7.25-8.31 (m, 24H, 24×Ar-H from dG(H8×6), dA(H8×5), dA(H2×6), dC(H6×2) and dT(H6×5)). H3' sugar ring protons (4.3-5.2 ppm) were not analysed due to suppression of residual water signal at 4.78 ppm.

BC2-α. MALDI-ToF: *m/z* = 9636 $[M+2Na]^{+}$ (MW = 9590 calc. For $[C_{320}H_{439}N_{127}O_{170}P_{26}$) (**Supplementary Figure 2.19**). ^{1}H NMR (**Supplementary Figure 2.20**) (D_2O with TSP (0.01 mM), 400 MHz): δ 0.77-0.87 (m, 24H, Leu- H^{δ}), 1.05-2.72 (m, 115H, 27×H2' and 27×H2'' sugar ring protons, 6×CH_3 of 6×dT, 8× Arg-H^{β}, 8×Arg-H^{γ}, 8×Leu-H^{β}, 4×Leu-H^{γ}, 6×CH_2 (aminohexyl linker), acetyl-CH_3), 3.16 (m, 8H, 8×Arg-H^{δ}), 3.22-4.66 (m, 93H, 81×H4'/H5'H5" sugar ring protons, 2×Gly-CH_2, 8 × Leu/Arg-H^{α}), 4.85-6.27 (m, 31H,

27×H1’ sugar ring protons, 4×H5 of dC), 7.25-8.42 (m, 33H, 33×Ar-H from dG(H8×9), dA(H8×7), dA(H2×7), dC(H6×4) and dT(H6×6)). H3’ sugar ring protons (4.3-5.2 ppm) were not analysed due to suppression of residual water signal at 4.76 ppm. Not all H4’/H5’H5” sugar ring protons were fully resolved, and suppression of residual water prevented signal detection.

BC3-α. MALDI-ToF: *m/z* = 9305 $[M+Na+Li]^+$ (MW = 9275 calc. For $[C_{311}H_{429}N_{122}O_{164}P_{25}]$) (**Supplementary Figure 2.19**). ^{1}H NMR (**Supplementary Figure 2.20**) (D_2O with TSP (0.01 mM), 400 MHz): δ 0.81-0.90 (m, 24H, Leu- H^{δ}), 1.12-3.09 (m, 113H, 26×H2’ and 26×H2’’ sugar ring protons, 6×CH_3 of 6×dT, 8× Arg-H^{β}, 8×Arg-H^{γ}, 8×Leu-H^{β}, 4×Leu-H^{γ}, 6×CH_2 (aminohexyl linker), Acetyl-CH_3), 3.21 (m, 8H, 8×Arg-H^{δ}), 3.29-4.74 (m, 90H, 78×H4’/H5’H5” sugar ring protons, 2×Gly-CH_2, 8 × Leu/Arg-H^{α}), 4.92-6.24 (m, 30H, 26×H1’ sugar ring protons, 4×H5 of dC), 7.26-8.44 (m, 32H, 32×Ar-H from dG(H8×8), dA(H8×7), dA(H2×7), dC(H6×4) and dT(H6×6)). H3’ sugar ring protons (4.3-5.2 ppm) were not analysed due to suppression of residual water signal at 4.76 ppm.

BC4-α. MALDI-ToF: *m/z* = 9003 $[M+2Na]^+$ (MW = 8957 calc. For $[C_{300}H_{414}N_{120}O_{157}P_{24}]$) (**Supplementary Figure 2.19**). ^{1}H NMR (**Supplementary Figure 2.20**) (D_2O with TSP (0.01 mM), 400 MHz): δ 0.82-0.89 (m, 24H, Leu- H^{δ}), 1.05-2.83 (m, 108H, 25×H2’ and 25×H2’’ sugar ring protons, 5×CH_3 of 5×dT, 8× Arg-H^{β}, 8×Arg-H^{γ}, 8×Leu-H^{β}, 4×Leu-H^{γ}, 6×CH_2 (aminohexyl linker), acetyl-CH_3), 3.17 (m, 8H, 8×Arg-H^{δ}), 3.24-4.69 (m, 87H, 75×H4’/H5’H5” sugar ring protons, 2×Gly-CH_2, 8 × Leu/Arg-H^{α}), 4.91-6.29 (m, 29H, 25×H1’ sugar ring protons, 4×H5 of dC), 7.26-8.45 (m, 31H, 31×Ar-H from dG(H8×8), dA(H8×7), dA(H2×7), dC(H6×4) and dT(H6×5)). H3’ sugar ring protons (4.3-5.2 ppm) were not analysed due to suppression of residual water signal at 4.32 ppm.

BC5-α. MALDI-ToF: *m/z* = 8666 $[M+K]^+$ (MW = 8627 calc. For $[C_{290}H_{402}N_{115}O_{151}P_{23}]$) (**Supplementary Figure 2.19**). ^{1}H NMR (**Supplementary Figure 2.20**) (D_2O with TSP (0.01 mM), 400 MHz): δ 0.81-0.90 (m, 24H, Leu- H^{δ}), 1.20-2.40 (m, 106H, 24×H2’ and 24×H2’’ sugar ring protons, 5×CH_3 of 5×dT, 8× Arg-H^{β}, 8×Arg-H^{γ}, 8×Leu-H^{β}, 4×Leu-H^{γ}, 6×CH_2 (aminohexyl linker), acetyl-CH_3), 3.18 (m, 8H, 8×Arg-H^{δ}), 3.52-4.41 (m,84H, 72×H4’/H5’H5” sugar ring protons, 2×Gly- CH_2, 8×Leu/Arg-H^{α}), 5.50-6.26 (m, 28H, 24×H1’ sugar ring protons, 4×H5 of dC), 7.25-8.45 (m, 30H, 30×Ar-H from dG(H8×7), dA(H8×7), dA(H2×7), dC(H6×4) and dT(H6×5)). Unfortunately, low signal-to-noise and distortion in NMR signals prevented full assignment of all peaks and resulted in the

presence of extra signals. H3' sugar ring protons (4.3-5.2 ppm) were not analysed due to suppression of residual water signal at 4.30 ppm.

BC5L-α. MALDI-MS: *m/z* = 9605 $[M+2Na]^+$ (MW = 9559 calc. For $[C_{319}H_{438}N_{128}O_{168}P_{26}]$) (**Supplementary Figure 2.19**). ^{1}H NMR (**Supplementary Figure 2.20**) (D_2O with TSP (0.01 mM), 400 MHz): δ 0.80-0.85 (m, 24H, Leu- H^{δ}), 1.20-2.56 (m, 112H, 27×H2' and 27×H2'' sugar ring protons, 5×CH_3 of 5×dT, 8× Arg-H^{β}, 8×Arg-H^{γ}, 8×Leu-H^{β}, 4×Leu-H^{γ}, 6×CH_2 (aminohexyl linker), acetyl-CH3), 3.17 (m, 8H, 8×Arg-H^{δ}), 3.51-4.40 (m,93H, 81×H4'/H5'H5" sugar ring protons, 2×Gly- CH_2, 8× Leu/Arg-H^{α}), 4.84-6.36 (m, 32H, 27×H1' sugar ring protons, 5×H5 of dC), 7.24-8.45 (m, 34H, 34×Ar-H from dG(H8×8), dA(H8×8), dA(H2×8), dC(H6×5) and dT(H6×5)). Unfortunately, low signal-to-noise and distortion in NMR signals prevented full assignment of all peaks and resulted in the presence of extra signals. A slight shift in the position of sugar ring protons was witnessed. H3' sugar ring protons (4.3-5.2 ppm) were not analysed due to suppression of residual water signal at 4.30 ppm.

BC3-β. MALDI-MS: *m/z* = 9304 $[M+Na+Li]^+$ (MW = 9275 calc. For $[C_{311}H_{429}N_{122}O_{164}P_{25}]$) (**Supplementary Figure 2.19**). ^{1}H NMR (**Supplementary Figure 2.20**) (D_2O with TSP (0.01 mM), 400 MHz): δ 0.81-0.90 (m, 24H, Leu- H^{δ}), 1.12-2.55 (m, 113H, 26×H2' and 26×H2'' sugar ring protons, 6×CH_3 of 6×dT, 8×Arg-H^{β}, 8×Arg-H^{γ}, 8×Leu-H^{β}, 4×Leu-H^{γ}, 6×CH_2 (aminohexyl linker), acetyl-CH_3), 3.17 (m, 8H, 8×Arg-H^{δ}), 3.54-4.39 (m, 90H, 78×H4'/H5'H5" sugar ring protons, 2×Gly- CH_2, 8×Leu/Arg-H^{α}), 4.92-6.24 (m, 30H, 26×H1' sugar ring protons, 4×H5 of dC), 7.25-8.44 (m, 32H, 32×Ar-H from dG(H8×8), dA(H8×7), dA(H2×7), dC(H6×4) and dT(H6×6)). H3' sugar ring protons (4.3-5.2 ppm) were not analysed due to suppression of residual water signal at 4.76 ppm.

BC5L-β. MALDI-MS: *m/z* = 9606 $[M+2Na]^+$ (MW = 9559 calc. For $[C_{319}H_{438}N_{128}O_{168}P_{26}]$) (**Supplementary Figure 2.19**). ^{1}H NMR (**Supplementary Figure 2.20**) (D_2O with TSP (0.01 mM), 400 MHz): δ 0.81-0.88 (m, 24H, Leu- H^{δ}), 1.20-2.54 (m, 112H, 27×H2' and 27×H2'' sugar ring protons, 5×CH_3 of 5×dT, 8×Arg-H^{β}, 8×Arg-H^{γ}, 8×Leu-H^{β}, 4×Leu-H^{γ}, 6×CH_2 (aminohexyl linker), acetyl-CH_3), 3.17 (m, 8H, 8×Arg-H^{δ}), 3.38-4.20 (m,93H, 81×H4'/H5'H5" sugar ring protons, 2×Gly- CH_2, 8× Leu/Arg-H^{α}), 4.37-6.26 (m, 32H, 27×H1' sugar ring protons, 5×H5 of dC), 7.25-8.44 (m, 34H, 34×Ar-H from dG(H8×8), dA(H8×8), dA(H2×8), dC(H6×5) and dT(H6×5)). H3' sugar ring protons (4.3-5.2 ppm) were not analysed due to suppression of residual water signal at 4.10 ppm.

2.4.6 Preparation of linearised plasmids and *in vitro* RNA transcripts

Preparation of linearised plasmid p67YF0 as well as *in vitro* transcript of yeast $tRNA^{Phe}$ were as reported earlier (15). 3'-end labelling of RNA transcript with fluorescein isothiocyanate (FITC) and 5'-labeling of RNA fragments with [γ-^{32}P]ATP were carried out as reported (15, 36).

2.4.7 Hybridisation of 3'-FITC $tRNA^{Phe}$ with BCs

The hybridisation assays between 3'-FITC-$tRNA^{Phe}$ at concentration 1 µM and one of the BCs at concentrations varying from 0.25 µM to 10 µM, as well as subsequent quantitative data analysis were carried out as described earlier (15).

2.4.8 Cleavage of 3'-FITC $tRNA^{Phe}$ with BCs

Cleavage experiments were carried out for 3'-FITC labelled $tRNA^{Phe}$ at 1 µM (single turnover conditions) and one of the BCs at concentration 20 µM in 50 mM Tris-HCl pH 7.0, 0.2 M KCl, 1 mM EDTA according to the previously reported protocols (15).

2.4.9 Ribonuclease H cleavage assay

The reaction mixture (5 µl) contained 3'-FITC-$tRNA^{Phe}$ (1 µM), one of the bulge-inducing conjugates (at 40 µM concentration), 50 mM Tris–HCl pH 7.0, 0.2 M KCl and 1 mM EDTA. In parallel, the control experiment was carried out under identical conditions, but with 3'-FITC-$tRNA^{Phe}$ alone. Considerable excess of the conjugate (BC2, BC3, BC4 or BC5) was used over 3'-FITC-$tRNA^{Phe}$ (40:1) to ensure efficient hybridisation prior to treatment with ribonuclease H. The mixtures were incubated at 37°C for 30 minutes. RNase H (1U) was added to BC:RNA complexes and incubated at 37°C for 15 minutes. The reactions were quenched by RNA precipitation with 2% (w/v) lithium perchlorate in acetone (75 µl). RNA pellet was collected by centrifugation and dissolved in loading buffer (8 M urea, 0.025% bromophenol blue, 0.025% xylene cyanol). RNA cleavage products were resolved in 12% polyacrylamide/8 M urea gel electrophoresis using Tris/Borate/EDTA (TBE) as running buffer. To identify cleavage sites, an imidazole ladder and an RNase T1-ladder produced by partial $tRNA^{Phe}$ cleavage with 2 M imidazole buffer (pH 7.0) and RNase T1, respectively, were run in parallel. The gel was analysed using ChemiDoc-MP (Bio-Rad).

2.4.10 RNase A probing of $tRNA^{Phe}$ / bulge-inducing conjugates complex

Prior to cleavage with RNase A under physiological conditions, the complex of 3'-FITC-$tRNA^{Phe}$ (1 µM) with one of the bulge-inducing conjugates (20 µM) was pre-formed in 10 µL of 50 mM Tris-HCl, pH 7.0, 0.2 M KCl, 1 mM EDTA and 100 µg/mL total tRNA from *E.coli* as carrier and maintained at 37°C for 20 min. Subsequently, RNase A was added to the reaction mixture to achieve 1 nM final concentration, and the cleavage reaction was carried out for 10 min at 37˚C. The reactions were quenched by RNA precipitation with 100 µL of 2% lithium perchlorate in acetone. RNA was collected by centrifugation and dissolved in loading buffer (8 M urea, 0.025% bromophenol blue, 0.025% xylene cyanol). RNA cleavage products were resolved in 12% polyacrylamide/8 M urea gel using TBE (15) as running buffer. To identify cleavage sites, an imidazole ladder and an RNase T1-ladder produced by partial $tRNA^{Phe}$ cleavage with 2 M imidazole buffer (pH 7.0) and RNase T1, respectively, were run in parallel. The gel was analysed using PharosFX Plus System (Bio-Rad).

2.4.11 Molecular Modelling

Computational studies were performed with AMBER (37) (AMBER 16 and AMBERTOOLS 16) gaussian 09 (38), GaussView6 (39) and Chimera (40) molecular modelling packages.

Generation of the initial structures

The initial 3D structures of the complexes between the tRNA fragment and peptidyl-oligonucleotide conjugates were generated via assembly of distinct components. The *RNA-DNA* hybrid double helices were modelled in the Type-A form using the *Make-NA* online server (http://structure.usc.edu/make-na/server.htm). The peptide was created initially in an extended conformation, and the connection to the DNA structure was achieved using special nucleotides: ADX (Type 1), the abasic residues AXA "alpha" or AXB "beta" (Type 2) and the linkers N6N (Type 1) and N6O (Type 2). By combining these components with the appropriate RNA and DNA chains, all the systems were built with the required specifications of stereochemistry and geometry.

The linkers and special residues were created following the RESP methodology in AMBER (41). The geometries were first optimised, and the electrostatic potential was calculated using Gaussian09 Hartree-Fock method and the 6-31G* basis set. The geometries and ESP charges were processed with antechamber and RESP Amber

modules to obtain the restrained ESP charges, in order to safely remove the capping groups from the units. Finally, the oligonucleotide was built, and the components of the complex assembled via xLEaP. Parameters were assigned to the DNA, RNA, special residues ADX, AXA, AXB and peptide from the ff14SB (42) (explicit water model) and ff14SBonlysc (implicit solvent model) while the GAFF force field (43) was used for the linkers N6N and N6O.

Molecular dynamics simulations

The molecular modelling simulations included series of Simulated Annealing steps using a Molecular Dynamics engine to optimally explore the conformational space and generate an ensemble of conformations.

Structure Preparation. The lack of available X-ray or NMR experimental data on such structures makes the election of input coordinates a challenging task. The initial configurations were designed in-house after discussions with the experimental team. A hybrid double helix RNA-DNA (44) was used in order to describe the complex state during the cleavage.

Simulated Annealing protocol. The next stage consisted of a conformational search by rounds of 100 restrained simulated annealing steps in implicit solvent. The mechanism of action of the conjugates involves the peptide approaching the RNA to catalyse the bond break. In order to model this process, an ensemble of conformations of the peptide was generated by maintaining the *DNA-RNA* complex fixed with soft harmonic positional restrains and by running a sequence of simulated annealing steps to allow the peptide exploring the surface available at reach distance.

Each Simulated Annealing (SA) step consisted of a chain of four Molecular Dynamics (MD) simulations with a total time of 11 ns: (i) a heating ramp over 0.5 ns, when the temperature was brought from 300 K to 800 K, (ii) an equilibration over 5.0 ns at 800K, (iii) a cooling ramp over 0.5 ns, when the temperature was lowered from 800 K to 300 K, and (iv) an equilibration over 5 ns at 300 K. In each SA step the Generalised Born (GB) implicit solvent model (45–47) was used (igb=1). Salt concentration was set to 0.1 M with the Debye-Hückel salt concentration model. The temperature coupling with the external bath was modelled using the Andersen thermostat (48, 49). The SHAKE algorithm was applied to constrain all bonds containing hydrogen atoms. The equations of motion were propagated with a timestep of 1 fs. The non-bonded interactions were truncated using a cutoff value of 9999.0 Å.

Soft harmonic positional restrains with a force constant of 0.01 kcal·mol^{-1}·Å^{-1} were applied to a group of nucleotides to keep the complex in place. The low value of the force constant helps the system to smoothly adapt to the heating-cooling SA process. The nucleotides in the vicinity of the special residue bridging the DNA with the peptide and the ones in the tail of the DNA were not retrained to ensure a proper conformational exploration. Every complex was annealed 100 times and the structures obtained were used in the next stage for analysis.

Cluster analysis. The geometrical analysis of the ensembles of structures was achieved using ptraj/cpptraj modules in AMBER 16, and the visualisation and clustering was carried out with the Chimera set of tools. In order to cluster the obtained *Conjugate-RNA* structures into conformationally related subfamilies, which are most different from each other in terms of RMSD values of heavy atoms, we used Chimera software. This approach allows (i) automatically, systematically and rapidly clustering structures into a set of conformationally related subfamilies generated during the SA/MD simulations, and (ii) selects a representative structure from each cluster, as previously described in detail (40, 50). The probability of *"in-line"* conformation implementation for every phosphate in the bulge-loop region of the *RNA-Conjugate* hybrid was calculated as the ratio between the number of structures with $\theta > 155°$ in MD trajectory to the overall number of all frames. The distance distribution between the phosphorus atom or O2' atom in the bulge region and the nitrogen atoms in guanidinium group of all four arginine residues was calculated for the frames of the productive trajectories.

2.5 Results and discussion

2.5.1 Design and synthesis of BCs, BC-α and BC-β

Figure 2.1 (**A-B**) illustrates the general concept of structural design, common for all bulge-loop inducing conjugates studied here against the 3'-acceptor stem and TΨC arm of tRNA^{Phe}. Conjugates were synthesised with 2 different strategies for the attachment of the catalytic peptide: either via a centrally-modified nucleotide (Type 1) or through an abasic sugar residue (Type 2) located in the middle of the RNA recognition motif (**Figure 2.1** (**C**) and (**D**), respectively). Upon hybridisation of such conjugates to the tRNA^{Phe}, a bulge-loop of 2-nt, 3-nt, 4-nt or 5-nt size was expected to be formed around the ^{61}C-A-C-A-G^{65} region of the tRNA^{Phe}, whilst maintaining Watson-Crick hydrogen-bonding with the 3'-acceptor stem and TΨC loop/arm (see **Figure 2.1** (**A-B**)). The induced bulge-loops regions were expected to be susceptible to cleavage by an RNA-cleaving peptide.

Positioning the cleaving peptide in the middle of the oligonucleotide sequence paves the way to achieve catalytic turnover of RNA substrate. The number of base pairs stabilising the *POC:RNA* heteroduplex is cut in half upon RNA cleavage, which favors dissociation of the POC from RNA after a cleavage event, and may promote competitive displacement of cleaved products by fresh target substrate.

Type 1 bulge-loop inducing conjugates (BC2 - BC5) contained relatively short recognition motifs designed to hybridise mainly to the loop region of the TΨC arm, in addition to the 3' acceptor stem of the $tRNA^{Phe}$ (indicated by purple line in **Figure 2.1 (A)**). By truncating the length of the oligonucleotide recognition motifs (from 23 to 22, 21, 20 or 19-mer) and by replacing cytidine residue at position 12 with aminohexyl modified adenosine A* (see **Figure 2.1** (**C**) and **Supplementary Figure 2.9**), non-complementary nucleobases of the tRNA strand (ranging from 0 to 2, 3, 4 or 5 residues, respectively) were induced at the position opposite to the peptide-modified adenosine A* within the hybridised complex. Amphiphilic peptide acetyl-$[LR]_4G$-CO_2H, which has previously demonstrated efficient cleavage of $tRNA^{Phe}$ *in vitro*, (15) was conjugated via its C-terminus to the aminohexyl linker of the A* nucleotide residue, as described in **Materials and Methods**.

Type 2 bulge-loop inducing conjugates were structurally different from Type 1 (**Figure 2.1** (**D**)). First, the peptide was incorporated via an abasic sugar residue, through an aminohexyl linker attached to the anomeric C1' carbon, either in α- or in β-configuration (see also **Supplementary Figure 2.10**). This approach provided us with the opportunity to generate two stereospecific series of Type 2 conjugates: BC-α (BC2-α, BC3-α, BC4-α, BC5-α and BC5L-α) and BC-β (BC2-β, BC3-β, BC4-β, BC5-β and BC5L-β). In order to explore the impact of enhanced hybridisation on potency, Type 2 conjugates incorporated longer oligonucleotide recognition motifs than Type 1 conjugates, ranging from 23- to 26-mer (indicated by brown line in **Figure 2.1 (A)**). Furthermore, BC5L-α and BC5L-β were elongated by 3 extra nucleotides to bind additionally the variable loop (indicated by arrows in **Figure 2.1 (A)**) in order to compensate for the largest (5 nt) bulge-loop size. Finally, Type 2 conjugates carried an elongated catalytic peptide acetyl-$[LRLRG]_2$-CO_2H bearing an extra glycine residue in the middle of the chain. It has been shown earlier (16) that the elongated peptide can provide more efficient RNA cleavage, presumably due to higher degree of conformational flexibility. The conjugates within the same category differed from each other by the size of the bulge-loop they could induce, which is indicated in their nomenclature by the number of nucleotides involved.

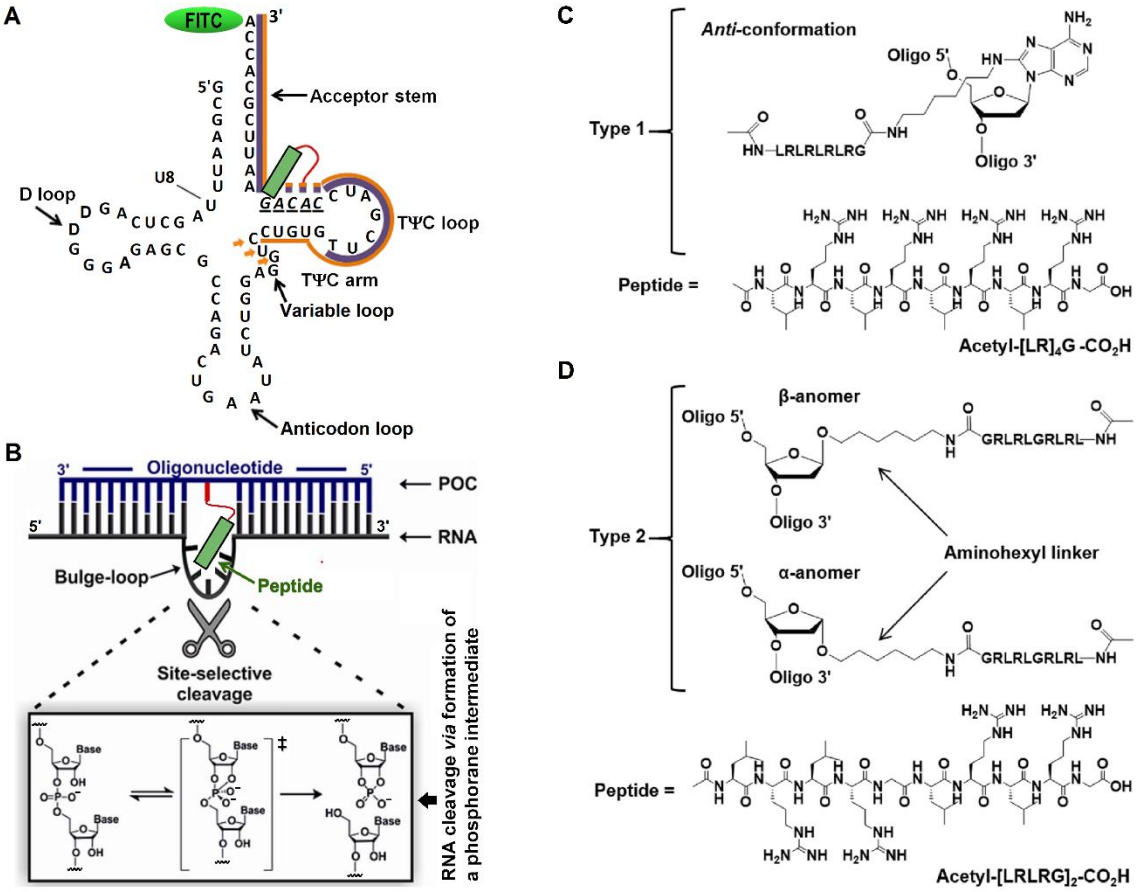

Figure 2.1. (**A**) Secondary structure of *in vitro* transcript of $tRNA^{Phe}$ showing the TΨC arm and acceptor stem binding sites targeted by the recognition motifs of the Type 1 and Type 2 conjugates (shown by purple and orange lines, respectively). Solid lines represent regions common for all conjugates from each series. Orange arrows indicate the extended binding region for the elongated conjugates BC5L-α and BC5L-β. Dotted lines show variable regions between oligonucleotide sequences bearing the catalytic peptide (green). The bulge-loop forming target site is underlined in italics. (**B**) Illustration of the bulge-loop inducing peptidyl-oligonucleotide conjugate (**POC,** shown here by blue line) bound to the target RNA sequence incorporating the 3' acceptor stem and TΨC arm of $tRNA^{Phe}$ (**RNA**, shown here by black line). Non-complementary regions around the peptide create a bulge-loop in the target RNA, which is susceptible to cleavage by the catalytic peptide. (**C, D**) Structural features of the peptide conjugation points for Type 1 and Type 2 bulge-loop inducing conjugates. (**C**) Type 1 conjugates (BC2–BC5) incorporate acetyl-$[LR]_4G$-CO_2H peptide *via* an internal aminohexyl-modified adenosine, here shown in more favored *anti* conformation. (**D**) Type 2 conjugates (BC2-α - BC5L-α and BC2-β - BC5L-β) contain acetyl-$[LRLRG]_2$-CO_2H peptide attached to an internal abasic sugar residue *via* anomeric C1' carbon either in α- or in β-configuration.

These variations in structural design between and within Type 1 and Type 2 conjugates allowed us to investigate the impact on RNA cleavage of key factors, including: (i) the mode of peptide attachment and/or its configuration, (ii) the size of the induced single-stranded RNA bulge-loop region, (iii) the length and the structure of the catalytic peptide, (iv) the hybridisation power of the oligonucleotide recognition motif and (v) the level of conformational flexibility. Molecular flexibility plays a vital role in catalysis, since a sufficient level of conformational freedom allows the substrate to adopt the reaction transition state (16). The use of a flexible aminohexyl linker between the oligonucleotide

and peptide, and incorporation of the additional glycine in the peptide for Type 2 conjugates, allowed us to explore conformational possibilities that might favor catalysis (17).

Synthesis and full characterisation of the peptides and conjugates are described in the **Materials and Methods**. HPLC analysis of Type 1 and Type 2 conjugates (**Supplementary Figures 2.11** and **2.12**) showed a consistent 4-5 minutes increase in retention time relative to unmodified oligonucleotides, thus confirming conjugation. The identity and purity of the peptides and synthesised conjugates were confirmed by ^{1}H NMR spectroscopy, and mass spectrometry (see **Supplementary Figures 2.13-2.20**). ^{1}H-NMR analysis (**Supplementary Figure 2.18 and 2.20**) of such large biomolecules containing 19-26 nucleotides, 9 or 10 amino acids and aminohexyl linker is complicated by the large number of overlapping proton resonances, especially in the peptide and deoxyribose H2'/H2"/H4'/H5'/H5" regions. Thus, unambiguous assignment of individual ^{1}H NMR signals was not possible. However, comparison of the ^{1}H NMR spectra of the conjugates and original oligonucleotides allowed us to confirm successful conjugation.

Characteristic peptide signals, corresponding to the Leu H^{δ} (0.8-1.0 ppm) and Arg-H^{δ} (3.1-3.3 ppm) protons were easily identifiable in the NMR spectra of the conjugates. Careful integration of these peptide protons, against the oligonucleotide aromatic region (7.26-8.44) and H1' sugar ring protons, allowed us to confirm the 1:1 stoichiometric ratio of peptide attachment to the oligonucleotide (see **Supplementary Figures 2.18** and **2.20**). This was further verified by MALDI-ToF mass spectrometry of conjugates, which showed experimental masses in close agreement with the calculated values (see **Supplementary Figure 2.17** and **2.19**).

2.5.2 Hybridisation of bulge-inducing conjugates to tRNA^{Phe}

The ability of bulge-inducing conjugates to hybridise with tRNA^{Phe} target was assessed by the electrophoretic mobility shift assay (EMSA) (see **Figure 2.2**). Binding of the conjugates to the 3'-FITC-tRNA^{Phe} led to the formation of a heteroduplex with lower electrophoretic mobility relative to free 3'-FITC-tRNA^{Phe}. By measuring the proportion of the 3'-FITC-tRNA^{Phe} hybridised to the conjugate as a function of the increasing conjugate concentration, the association constants (K_a) were estimated (see **Table 2.1**):

$$Ka = \frac{\alpha}{[BC]_0(1-\alpha)\left(1-\alpha\left(\frac{[tRNA]_0}{[BC]_0}\right)\right)} \quad (\mathbf{1})$$

where α is the fraction of RNA bound; $[tRNA]_0$ and $[BC]_0$ are the total $tRNA^{Phe}$ and conjugate concentrations, respectively.

All studied conjugates were capable of binding the $tRNA^{Phe}$ in a concentration-dependent manner (**Figure 2.2**). The association constants of Type 1 conjugates progressively decreased with a stepwise increase in the size of the induced RNA bulge-loop structures. The conjugate with the longest recognition motif (BC2), which was designed to induce the smallest (2-nt) RNA bulge-loop upon hybridisation, showed greater binding affinity towards $tRNA^{Phe}$ than those inducing 3-nt (BC3), 4-nt (BC4) and especially 5-nt (BC5) bulge-loop regions. In fact, K_a measured for BC5 under identical conditions (K_a=0.0042±0.002×10^6 M^{-1}) was found to be lower by (at least) two orders of magnitude than K_a values estimated for BC2, BC3 and BC4 from the same type of conjugates. Such a big drop in binding affinity for BC5 could be attributed to the relatively high stability of the TΨC stem region with three G-C base pairs, none of which was targeted in an antisense fashion by BC5.

Table 2.1. Bulge-inducing conjugates: nomenclature, sequence, peptide and association constants (K_a).

Conjugate	**Oligonucleotide (5'→3')**	**Peptide**	**K_a×10^6 M^{-1}**
BC2	TGGTGCGAATT-A*-GTGGATCGAA	$[LR]_4G$	0.9±0.3
BC3	TGGTGCGAATT-A*-TGGATCGAA	$[LR]_4G$	0.5±0.1
BC4	TGGTGCGAATT-A*-GGATCGAA	$[LR]_4G$	0.4±0.2
BC5	TGGTGCGAATT-A*-GATCGAA	$[LR]_4G$	0.0042± 0.002
BC2-α/ BC2-β	TGGTGCGAATT-dR-GTGGATCGAACACAG	$[LRLRG]_2$	0.9±0.6 0.8±0.3
BC3-α/ BC3-β	TGGTGCGAATT-dR-TGGATCGAACACAG	$[LRLRG]_2$	0.7±0.6 1.0±0.5
BC4-α/ BC4-β	TGGTGCGAATT-dR-GGATCGAACACAG	$[LRLRG]_2$	1.0±0.8 0.9±0.6
BC5-α/ BC5-β	TGGTGCGAATT-dR-GATCGAACACAG	$[LRLRG]_2$	0.4±0.2 0.5±0.2
BC5L-α/ BC5L-β	TGGTGCGAATT-dR-GATCGAACACAGGAC	$[LRLRG]_2$	0.9±0.6 0.5±0.2

Previously, using the 216-312 fragment of influenza virus M2 RNA (M2-96 RNA) (30), we showed that up to seven bulged bases could be tolerated in terms of detectable hybridisation. Here, we demonstrate that the significant loss of the binding affinity seen for the 5-nt bulge-loop inducing conjugate (i.e. BC5) can be sufficiently compensated by

the elongated recognition motifs. Indeed, the hybridisation power of the BC5-α/BC5-β, and especially that of the elongated BC5L-α/BC5L-β conjugates, was re-gained by implementing the longer oligonucleotide recognition motifs, which were designed to cover the entire TΨC arm, and even invade the variable loop of the $tRNA^{Phe}$. The association constants of the Type 2 conjugates (BC-α and BC-β series) remained similar (differences in K_a did not exceed the statistical errors). The longer recognition motifs used for Type 2 conjugates seem to mask any significant destabilisation effects from the induced bulge-loops, which can be easily tolerated if their size is equal or less than 5-nt.

2.5.3 Cleavage activity against $tRNA^{Phe}$

Cleavage activities of the bulge-loop inducing conjugates were examined against 3'-FITC-$tRNA^{Phe}$ (1 μM) under physiological conditions (37 °C, pH 7.0) over 6, 24, 48 and 72 hours (see **Materials and Methods**). 20-fold excess of the conjugate (20 μM) over tRNA was used in the cleavage assays to ensure that even shorter conjugates from Type 1 could achieve the maximum level of binding with the $tRNA^{Phe}$ (**Figure 2.2**), although this was impossible to attain for BC5 due to its poor hybridisation. Tris buffer (50 mM Tris-HCl pH 7.0, 0.2 M KCl, 1 mM EDTA) was used, because it does not interfere with the RNA transesterification process. The presence of EDTA avoided spontaneous RNA cleavage, which is potentially catalysed by any traces of (non-univalent) metal ions. Cleavage products were analysed by electrophoresis in 12% PAGE under denaturing conditions and identified by comparison with RNase T1 and 2 M imidazole $tRNA^{Phe}$ hydrolysis ladders.

Strikingly, Type 1 bulge-loop inducing conjugates (BC2-BC5) were inactive against $tRNA^{Phe}$ (**Supplementary Figure 2.21**), even though all conjugates (except for BC5) were able to fully bind to the RNA under these conditions (**Figure 2.2**). BC2 showed a very weak cleavage (< 5% after 24 h) at U8-A9 site, but outside the target bulge-loop region. In contrast, all Type 2 conjugates (both from BC-α and BC-β series) showed high levels of cleavage activity against the same RNA target (**Figure 2.3**), overall reaching 90% and 82%, respectively, for the best structural variants from each series. No spontaneous cleavage of tRNA in the absence of conjugates was seen under these conditions over 72 hours (see lanes labelled as C ("control") in **Figure 2.3**).

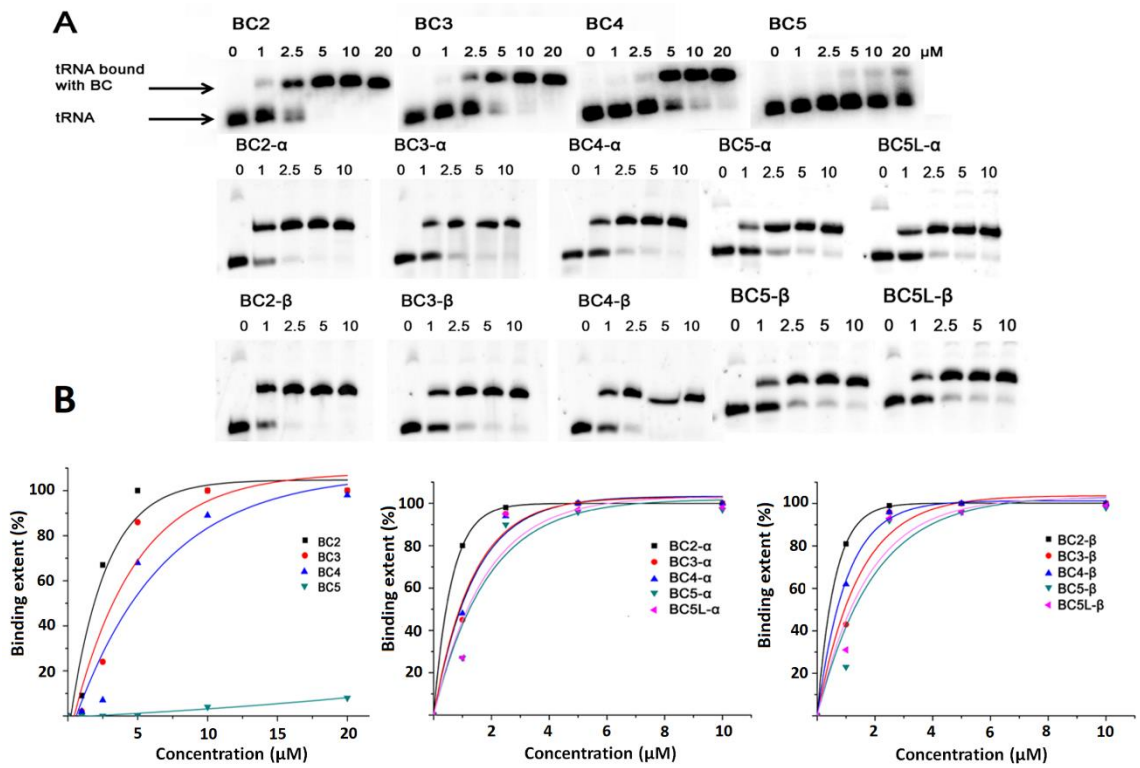

Figure 2.2. Gel-shift analysis of hybridisation of bulge-loop inducing conjugates BCn, BCn-α and BCn-β with 3'-FITC-tRNA^{Phe}. (**A**) Representative images of the PAGE showing binding of BCn, BCn-α and BCn-β at various concentrations (0 - 20 μM) with 3'-FITC-tRNA^{Phe} (1μM). (**B**) Secondary plot of the data shown in (**A**).

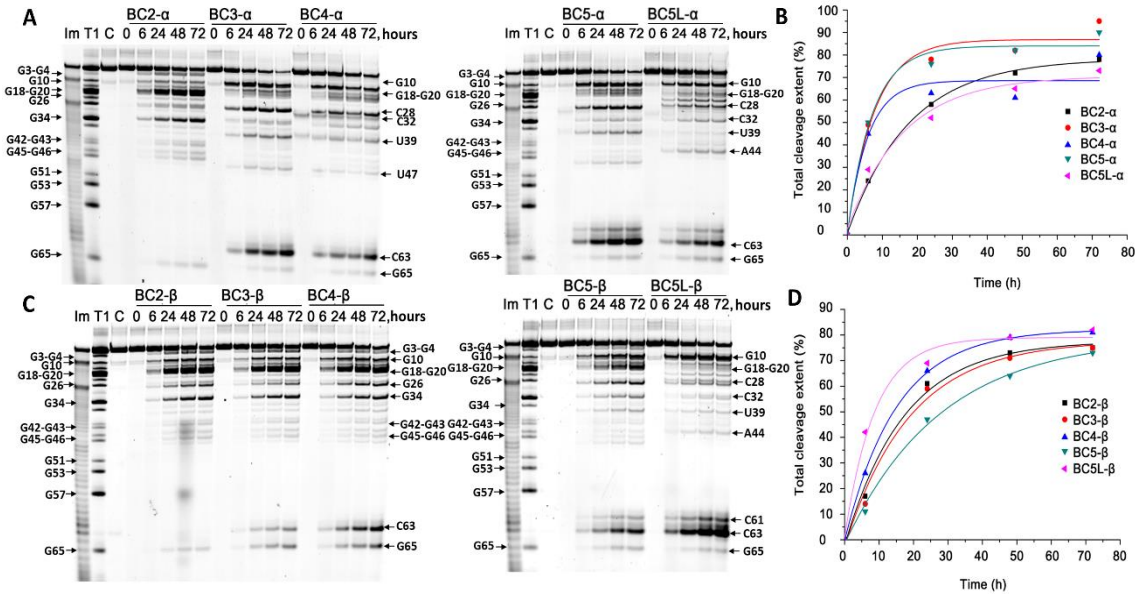

Figure 2.3. Cleavage of 3'-FITC-tRNA^{Phe} with bulge-forming conjugates BCn-α and BCn-β. Representative images of 12% PAAM/8 M urea gels after electrophoresis of 3'-FITC-tRNA^{Phe} cleavage products with BCn-α (**A**) and BCn-β (**C**) as a function of the incubation time. 3'-FITC-tRNA^{Phe} (1 μM) was incubated with the conjugates (20 μM) in Tris buffer (50 mM Tris-HCl pH 7.0, 0.2 M KCl, 1 mM EDTA) at 37° C. Lanes T1 and Im represent partial 3'-FITC- tRNA^{Phe} digestion with RNase T1 and imidazole, respectively. In lane C, 3'-FITC- tRNA^{Phe} was incubated without conjugates for 72 h. Positions of RNA cleavage by RNase T1 and conjugates are shown on left and right respectively. Secondary plot of the data indicating the total cleavage extent (%) plotted against the incubation time for BCn-α (**B**) and BCn-β (**D**).

Although Type 2 conjugates showed some variations both in cleavage patterns and in cleavage efficiency, which are detailed in **Figure 2.4**, there was a clear similarity in their activity against the $tRNA^{Phe}$ with some common trends seen within and between BC-α and BC-β conjugates. First, all Type 2 conjugates catalysed cleavage within the targeted region ^{61}C-^{62}A-^{63}C-^{64}A-^{65}G, with efficiency generally related to the size of the induced RNA bulge-loop structure. For example, BC-β conjugates (**Figure 2.3**) showed progressive increase in the extent of RNA cleavage at this region from very low (0.5 %) for BC2-β, which was expected for the smallest (2-nt) bulge; to 6 % (for BC3-β), 16 % (for BC4-β), and reaching 19 % and 54% respectively for BC5-β and BCL5-β, which induced the largest (5-nt) bulge-loop in the $tRNA^{Phe}$. Although, in general, the BC-α series demonstrated a similar cleavage trend at the bulge-loop regions, BC4-α and BC5L-α deviated slightly from this trend (**Figure 2.3**). This can be related to the α-configuration of the peptide attachment to the oligonucleotide recognition motif, thus presumably reflecting a higher degree of steric hindrance at the conjugation point for BC-α series. This would lead to more frustrated modes of interaction with $tRNA^{Phe}$, which can potentially mask the direct effect from the loop size on cleavage efficiency.

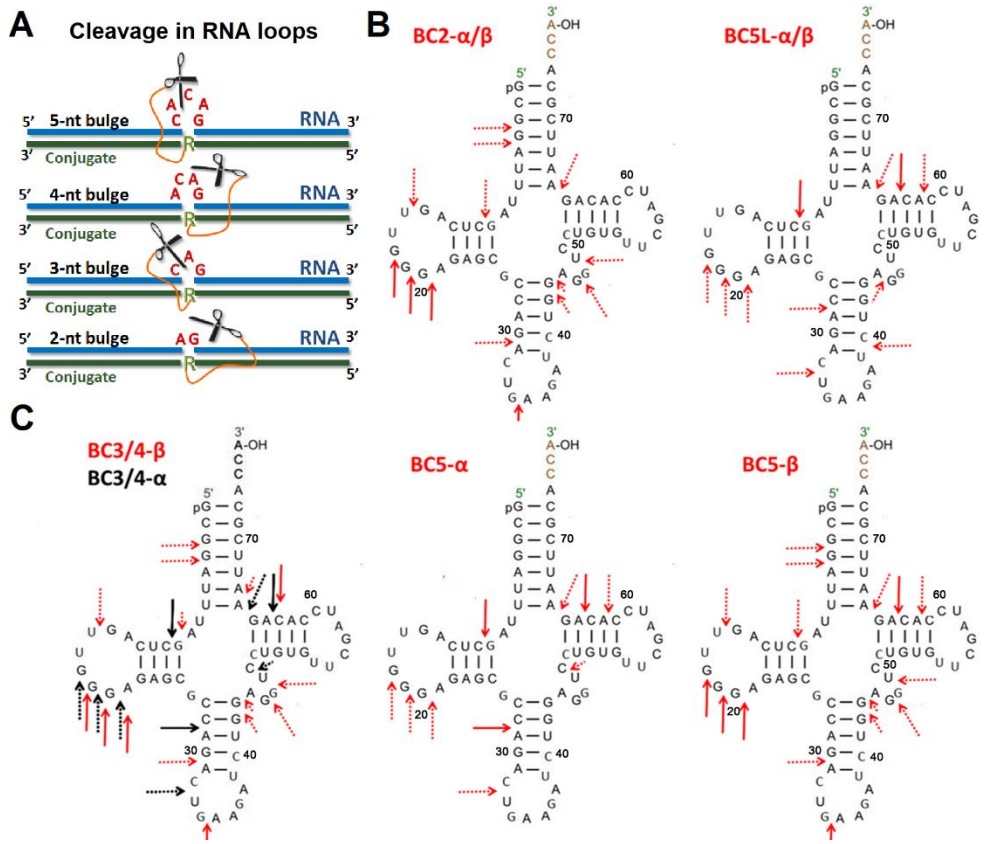

Figure 2.4. (**A**) Induction of 2-nt, 3-nt, 4-nt or 5-nt bulge-loops in the RNA (blue) upon hybridisation with the peptidyl-oligonucleotide conjugates (green), which become susceptible to cleavage by closely juxtaposed peptide (scissors). (**B**-**C**) Cleavage patterns of 3'-FITC-$tRNA^{Phe}$ observed upon treatment with α- and β- series of Type 2 conjugates, summarising data

shown in **Figure 2.3**. Arrows indicate the point of cleavage. Major cleavage sites are presented with solid line arrows, whereas minor cleavage sites are indicated with dotted arrows. (**B**) Identical cleavage patterns of 3'-FITC-tRNA^{Phe} were witnessed for BC-2α and BC-2β, as well as for BC5L-α and BC5L-β conjugates. (**C**) Differences in cleavage patterns were witnessed for BC3/4-α conjugates (black arrows) versus BC3/4-β conjugates (red arrows), as well as for BC5-α conjugates against BC5-β conjugates.

The expansion of the induced bulge-loop afforded the increase in the number of cleaved bonds within the targeted region ^{61}C-^{62}A-^{63}C-^{64}A-^{65}G. Indeed, the single-stranded 2-nt bulge of BC2-α/β constrained its cleavage to only a single cut at G65-A66. Two cuts were possible from the 3-nt and 4-nt bulge-loop of BC3-α/β and BC4-α/β, respectively. However, the 5-nt bulge-loop of BC5-α/β and BC5L-α/β allowed three cuts in the ^{61}C-^{62}A-^{63}C-^{64}A-^{65}G region targeted by the recognition motif, with cleavage mainly at the C63-A64 position, and fewer cuts at the G65-A66 and C61-A62 sites.

Another important feature common for all Type 2 conjugates was that, upon sequence-specific hybridisation, they were able to attack structural elements of the tRNA^{Phe} located outside the induced bulge-loop region (**Figure 2.3**). Indeed, several G-X and Pyr-X sites within the D-arm (e.g. G10), D-loop (e.g. G18-G19-G20-A21), anti-codon stem (e.g. C28-A29) and/or loop (e.g. C32-U33) and variable loop (e.g. U47-C48) were found to be vulnerable for cleavage by this type of conjugates. We have previously reported the ability of the peptidyl-oligonucleotide conjugates to attack distantly-located sites within the tertiary tRNA structure upon sequence-specific hybridisation. (15, 16) Even zero-linker conjugates (15) (P2-A-COOH, P4-A-COOH and P4-A-CONH$_2$), with relatively limited conformational freedom, were able to catalyse efficient cleavage at the distant U8-A9 and C72-A73 positions (in addition to their target C63-A64 site), after being hybridised to the TΨC arm and variable loop of the tRNA^{Phe}. Furthermore, the "dual" conjugate DC6 with the catalytic peptides located between two recognition motifs (16), targeted to the acceptor stem and the TΨC loop, showed even wider cleavage spectrum by attacking a D-loop (e.g. G18-G19-G20), anti-codon loop (e.g. C34-U35) and a variable loop (e.g. G45-U47) of tRNA^{Phe}, in addition to A64-G65 within the closely-positioned target region ^{61}C-^{62}A-^{63}C-^{64}A-^{65}G. In all cases, non-specific cleavage at the distantly-located regions was confidently eliminated (15,16) by independent experiments with the 3'-FITC-labelled 96-mer HIV-RNA, which has essentially no homology with yeast tRNA^{Phe}. As 3'-FITC-HIV-RNA was unaffected by conjugates under identical conditions (15,16), such cleavage can only occur within the complementary complex with tRNA formed upon sequence-specific hybridisation.

The bulge-loop inducing conjugates invented here showed even more diverse and complex cleavage profiles than those reported previously (15,16). This appears to reflect the higher degree of conformational freedom of the catalytic peptide within their hybridised complex with $tRNA^{Phe}$, presumably due to its flexible attachment to the mobile abasic sugar ring (**Figure 2.1**). The overall length of the catalytic peptide (45.1 Å), estimated from the maximum size of the unfolded peptide (36.5 Å) measured previously (15) and the length of the aminohexyl linker (8.6 Å), seems to be sufficient to reach most of the sites identified in the $tRNA^{Phe}$ cleavage profiles. Indeed, the distances between the observed cleavage sites and the bridging phosphorus atoms of the ^{61}C-^{62}A-^{63}C-^{64}A-^{65}G region, opposite to the peptide attachment point, which were evaluated from the available X-ray structure (51) of yeast $tRNA^{Phe}$ as described earlier (16), did not exceed 45 Å. The only exception was the C34-U35 site, which was separated by 54 Å from the peptide conjugation point (16). However, this relatively distant region can potentially be reached by the peptide. When the tertiary structure of tRNA is compromised by partial unfolding of the TΨC loop and acceptor stem upon hybridisation with the conjugate, (15, 16) the possibility for structural fluctuations make even such distant regions accessible for cleavage. The high degree of conformational freedom of the catalytic peptide, flexibly anchored to the recognition motif of the conjugate, could provide an advantage for potent catalytic destruction of long RNA sequences, especially those with the complex secondary and tertiary structural organisation (e.g. long non-coding RNA or viral genomic RNA). Multiple cuts at different locations of the long RNA sequence, induced by a single conjugate molecule upon sequence-specific hybridisation, will enhance the potency of the catalytic reaction, and may also increase the turnover effect on potency as well.

The catalytic performance of BC-α conjugates seemed to be slightly superior than that of the BC-β series, extending to 90% and 82% cleavage for the best structural candidates from each category (BC5-α and BC5L-β, respectively). However, the extent of RNA cleavage in loops was higher for the BC-β series as compared to that for the BC-α series (*cf.* 54 % *vs.* 45% for BC5L-β and BC5-α, respectively), which might be linked to a higher degree of steric hindrance at the peptide attachment point for α-configuration anomers.

2.5.4 Enzymatic probing

Since none of the Type 1 conjugates (BC2-BC5) were active against $tRNA^{Phe}$, we investigated the possible reasons behind such catalytic failure. First, we examined the structural rearrangements of the $tRNA^{Phe}$ upon hybridisation with BC2 – BC5 conjugates, using enzymatic probing with RNase A (**Figure 2.5**), in order to assess the accessibility of the target RNA regions for cleavage. The molar excess of conjugates over 3'-FITC-$tRNA^{Phe}$ (20:1) was used to achieve the highest possible level of hybridisation.

In the absence of conjugates (**Figure 2.5**; lane C within the 'RNase A' band), RNase A produced one major cut in the $tRNA^{Phe}$ structure at the U8-A9 position and two faint cuts at the C28-A29 and C63-A64 positions. Hybridisation of $tRNA^{Phe}$ with BC3, BC4 and BC5 (but not with BC2) led to a significant (> 100 times) increase in cleavage at C63-A64 site within the ^{61}C-^{62}A-^{63}C-^{64}A-^{65}G target region. Presumably, the formation of 3-, 4- and 5-nt containing bulge-loop structures made C63-A64 linkage accessible for cleavage by RNase A. Surprisingly, although BC5 showed poor binding affinity towards 3'-FITC-$tRNA^{Phe}$ (with only 5% of 3'-FITC-$tRNA^{Phe}$ being hybridised with this conjugate under such conditions), it showed increased cleavage at the C63-A64 site. In the presence of BC5, cleavage extended almost to that seen for BC3 and BC4, which showed 100% binding with 3'-FITC-$tRNA^{Phe}$ under these conditions (see **Figure 2.2**). This illuminates an important implication that even relatively weak binding affinities of conjugates might be sufficient to promote cleavage of the exposed phosphodiester bonds. An advantage of inducing relatively large bulge-loop structures upon hybridisation could be that they provide RNA with sufficient conformational freedom to adopt the *'in-line'* conformation essential for cleavage.

In contrast, hybridisation of BC2 with $tRNA^{Phe}$, which showed the highest binding affinity, did not promote cleavage at the C63-A64 site, because the 2-nt ^{64}A-G^{65} bulge-loop formed did not contain any sites sensitive to RNase A cleavage. Interestingly, hybridisation of the conjugates with 3'-FITC-$tRNA^{Phe}$ seems to disturb the intact tertiary structure of tRNA, thus leading to the exposure of additional RNA regions and making them accessible for RNase A cleavage. Indeed, all Type 1 conjugates considerably enhanced cleavage by RNase at the U8-A9 and C28-A29 linkages, as compared to that seen for unbound $tRNA^{Phe}$. Furthermore, two additional sites (i.e. C13-A14 and U52-G53) were efficiently cleaved by RNase A when $tRNA^{Phe}$ was hybridised with BC2 > BC3 ≥ BC4, but not with BC5. The extent of tRNA cleavage at these additional sites seems to correlate well with the stability of the hybridised complexes and their K_a values

(**Table 2.1**). The data confirmed our hypothesis that sequence-specific hybridisation of such conjugates with large, complex RNA molecules may promote partial distortion of the key elements of their secondary and tertiary structures and expose distant regions for opportunistic cleavage by the catalytic peptide, flexibly anchored to the conjugate recognition motifs.

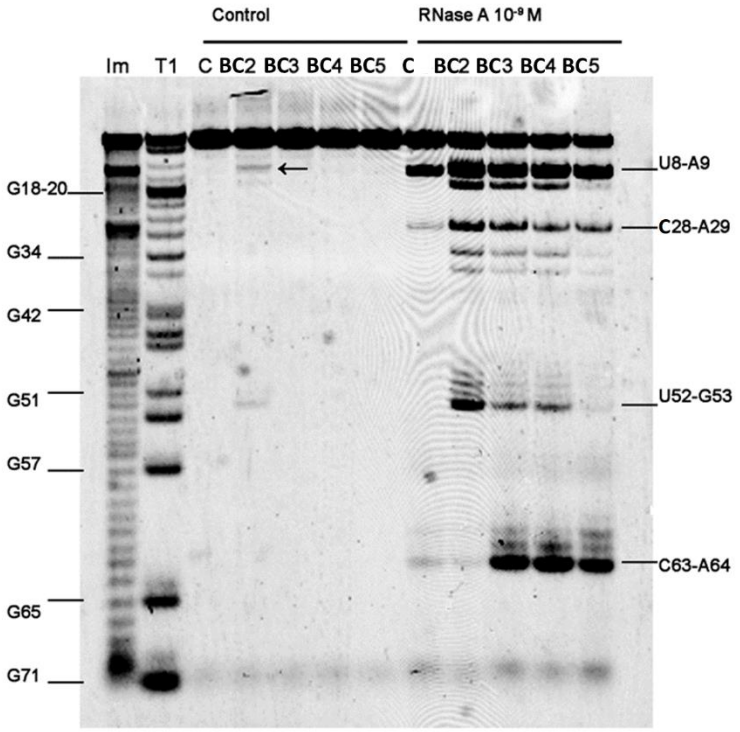

Figure 2.5. RNase A probing 3'-FITC-tRNA^{Phe} structure within hybridised complexes with the bulge-forming conjugates. Image of 12% PAAM/8 M urea gel electrophoresis: 'Control' and 'RNase A' at the top indicate samples incubated in the absence and in the presence of RNase A, respectively. In the test experiments, 3'-FITC-tRNA^{Phe} (1 μM) was incubated with one of the Type 1 conjugate (20 μM), for 20 min at 37˚C followed by cleavage with RNase A (1 nM) for 10 min at 37˚C. Lanes BC2, BC3, BC4, BC5 correspond to complexes of 3'-FITC-tRNA^{Phe} with the respective conjugate. Lane C, 3'-FITC-tRNA^{Phe} incubated without conjugates. Lanes **Im** and **T1**, indicate partial tRNA^{Phe} digestion with 2 M imidazole buffer or RNase T1, respectively. Positions of tRNA^{Phe} digestion with RNases A and T1 are shown on the right and on the left, respectively.

RNase H cleaves RNA only when it forms a hybrid complex with DNA. As anticipated, the conjugates BC2-BC5 enhanced tRNA^{Phe} cleavage by RNase H in the 3'-acceptor and TΨC regions (**Supplementary Figure 2.22**), whereas the size of the "silent" (single stranded) region for cleavage (symptomatic for the bulge-loop formation) correlates well with the expected number of bulged nucleotides (BC5 > BC4 > BC3 > BC2). Catalytic failure of Type 1 conjugates does not appear to be linked to inability to induce single-stranded bulge-loop regions and/or to expose the other secondary and tertiary elements for successful cleavage.

2.5.5 Molecular dynamics simulations

The structural dissimilarity of Type 1 and Type 2 conjugates could be another reason behind the striking difference in their catalytic performance. Although the peptide length and sequence may also contribute, most important mechanistically is the two different modes of incorporation of the catalytic peptide into the conjugate structure (**Figure 2.1**). Indeed, the well-established mechanism of RNA catalytic cleavage (16, 52–56) involves well-coordinated and synchronised action of all key players involved. This is initiated by deprotonation of the 2'-OH group, followed by the formation of a di-anionic pentaoxyphosphorane intermediate and subsequent departure of the 5'-linked nucleotide.(14, 52, 53) Such a phosphodiester transesterification reaction can be facilitated by various functional groups introduced into the conjugate structure, which can: (i) enhance the rate of deprotonation at the 2'-hydroxyl group, (ii) stabilise the phosphorane intermediate and (iii) the leaving group and/or (iv) promote the *"in-line"* geometry, when the 2'-oxyanion enters (or the 5'-linked nucleotide leaves) the phosphorane intermediate.(53, 54) In such an *"in-line"* configuration, which is crucial for catalysis, the penta-coordinate intermediates assume trigonal bipyramidal geometry, with the 2' and 5' oxygens occupying apical positions around 180° from one to another (52). Arginine guanidinium groups of the catalytic peptide (acetyl-$[LR]_4G$-CO_2H or acetyl-$[LRLRG]_2$-CO_2H) are key in promoting catalysis (15, 16). They appear to act as proton shuttles (53) through various tautomeric forms, by facilitating the proton transfer between the attacking 2´-OH, non-bridging phosphate oxygen and departing 5´-O group. A few reports (55–57) provide evidence of synchronised action of two guanidinium groups in catalysis, when they are present in the same molecular structure. It is postulated that catalysis by such a guanidine-guanidinium dyad is achieved through cooperative proton transfer between the neutral and protonated guanidinium residues. A neutral guanidine acts as a general base to deprotonate the hydroxyl group, while the protonated guanidinium moiety plays a dual role in catalysis by: (i) coordinating the phosphate group, by electrostatic interaction; and (ii) acting as an electrophilic activator, facilitating the transesterification reaction.

Given a strict structural demand for all functional groups involved in catalysis, and the necessity for the RNA cleavage sites to attain an *"in-line"* geometry to promote transesterification, we used molecular dynamic (MD) simulations. 12 *RNA-Conjugate* hybrids model systems were generated, 4 from each category (4×Type 1 conjugates including BC2-BC5, and 8×Type 2 conjugates including 4×BC-α and 4×BC-β

conjugates), each interacting with the RNA fragment replicating the relevant part of the yeast $tRNA^{Phe}$ sequence with an elongated 5'-dangling end (**Figure 2.6** (**A**)). We maintained the same sequence and length of the oligonucleotide for each type of bulge-loop category (i.e. 2-nt, 3-nt, 4-nt or 5-nt), which was identical to the recognition motif of BC2, BC3, BC4 or BC5 conjugates (**Figure 2.6** (**A**)). Before the 10 ns productive simulation, each model system was subjected to a series of 100 simulated annealing runs in implicit solvent, involving heating to 800 K for 0.5 ns, followed by an equilibration at 800 K for 5 ns and cooling down to 300 K over 0.5 ns, with subsequent equilibration at 300 K over another 5 ns (see **Materials and Methods** for details). Cluster analysis of 10 ns productive simulation (**Figure 2.6** (**B**)) showed that all calculated *DNA:RNA* hybrids adopted the intermediate conformation between A and B forms of a double-stranded nucleic acid. The introduction of the bulge-loops caused bending of the overall structure, as earlier reported for *DNA:DNA* duplexes, but without significant change of the global conformation (58). Such a *RNA-Conjugate* complex can potentially be recognised by cellular RNase H, thus boosted by a synergetic effect from the joint action of conjugates and RNase H, as we recently demonstrated experimentally (20).

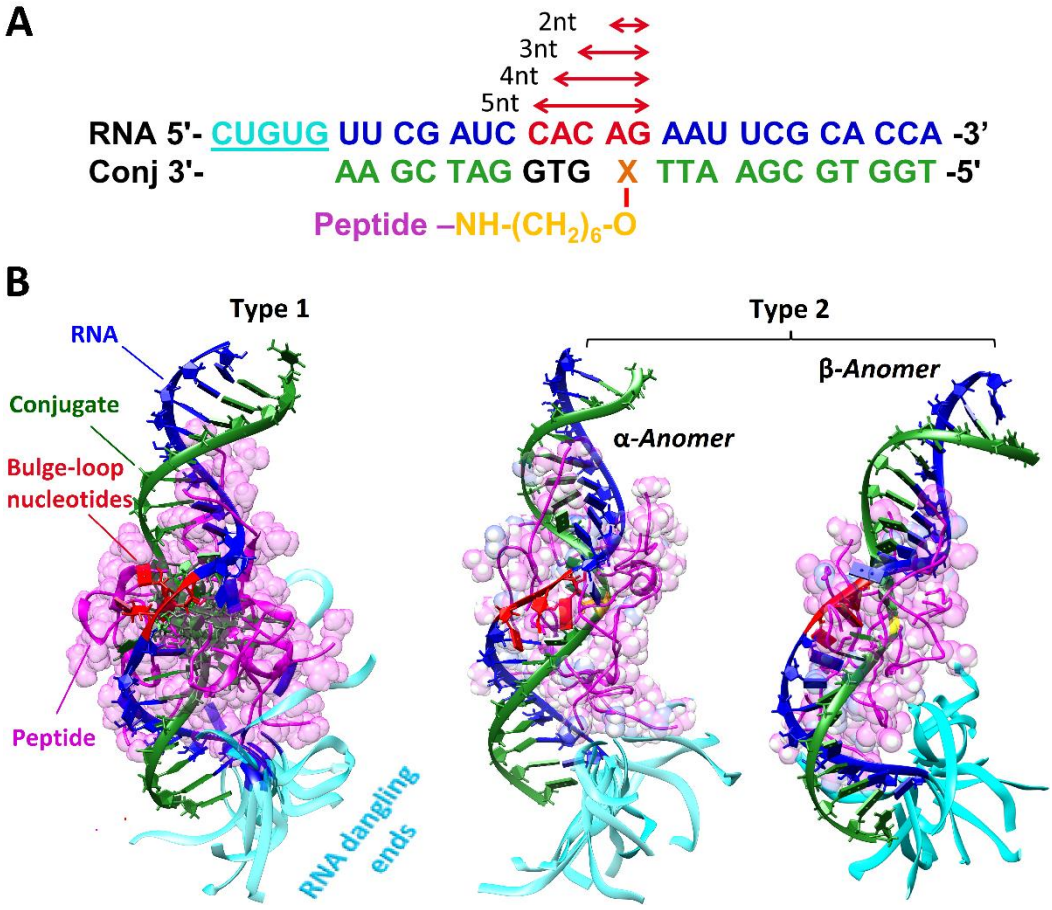

Figure 2.6. (**A**) Model systems used for the molecular dynamic simulations. The RNA sequences (blue) replicate the 3'-acceptor stem and the TΨC-loop of the yeast $tRNA^{Phe}$ with an additional

dangling end (underlined single-stranded sequence; cyan). The bulge-loop regions of different sizes ranging from 2-nt to 5-nt are highlighted in red. The representative conjugate sequences are shown in green, with the variable region (i.e. truncated for the 3-nt, 4-nt and 5-nt bulge-loop inducing conjugates) shown in black. **X** represents the point of attachment of the peptide (either Acetyl-$[LR]_4G$-CO_2H or Acetyl-$[LRLRG]_2$-CO_2H) to either modified adenosine residue (Type 1 conjugates) or abasic nucleotide (Type 2 conjugates from BC-α and BC-β series). The linker and peptide are indicated in yellow and pink, respectively. (**B**) Cluster analysis of a series of 100 MD simulations of the RNA-Conjugate heteroduplexes, using simulated annealing. The RNA fragment (blue) was hybridised with the bulge-loop conjugate (green) either from Type 1 BC3 (**left**), or Type 2 series (BC3-α (**center**) or BC3-β (**right**)). The peptide backbone and sidechains are shown in pink, bulge loop regions in red, and the single-stranded 5'-dangling ends in cyan. The corresponding rotating images of the structures are given in the **Supplementary Information**.

For each hybrid complex, we have estimated a propensity for RNA cleavage *via "in-line attack"* based on the measured angle **Θ** (O2'–P–O5') of the RNA nucleotides from the bulge-loop-region (59). The realisation of the *"in-line attack"* conformation to promote catalysis can be achieved by satisfying a specific range of values for the dihedral angle **Φ** ($-25 \leq \mathbf{\Phi} \leq 10°$), which strongly correlates to the region of the optimal "*in-line*" geometry (59) defined by angle **Θ**, when $\mathbf{\Theta} \geq 155°$ (**Figure 2.7**). We found that relatively favorable values of **Θ** could potentially be achieved by most of the nucleotides from the bulge-loop region ^{61}C-^{62}A-^{63}C-^{64}A-^{65}G, when RNA is hybridised with either Type 1 or Type 2 conjugates, regardless of their category. Instead, the probability of adopting *"in-line"* geometry seemed to correlate strongly with the length of the induced RNA bulge-loop region, with the clear preference of the larger loop size in the order 5-nt >4-nt >3-nt >2-nt ((**B**), (**C**) and (**D**) in **Figure 2.7**).

Although in some cases 2-nt bulge-loop inducing conjugates may allow adoption of *"in-line"* geometry for A62, C63 and/or G65 nucleotides, most of these residues (except for G65) are involved in duplex formation, which seems to protect these sites from cleavage. Interestingly, most of the nucleotides from the RNA single-stranded dangling ends (**Figure 2.7** (**E**), (**F**) and (**G**)) showed the probabilities for achieving an *"in-line"* geometry similar to those in loops, thus suggesting that such flexible single-stranded RNA regions are inherently vulnerable for cleavage and ready for an opportunistic attack from closely located catalytic groups. This agrees with our experimental data (**Figures 2.3** and **2.4**), showing that the single-stranded regions from D-loop (e.g. G18-G19-G20-A21), anti-codon loop (e.g. C32-U33) and variable loop (e.g. U47-C48) could be cleaved by all Type 2 conjugates, irrespective to their length. The expanded regions of the selected hybrid structures RNA-BC3-α and RNA-BC3-β showing a realisation of an "in-line attack" conformation are given in **Figure 2.8** (see also the corresponding rotating images in the **Supplementary Information**).

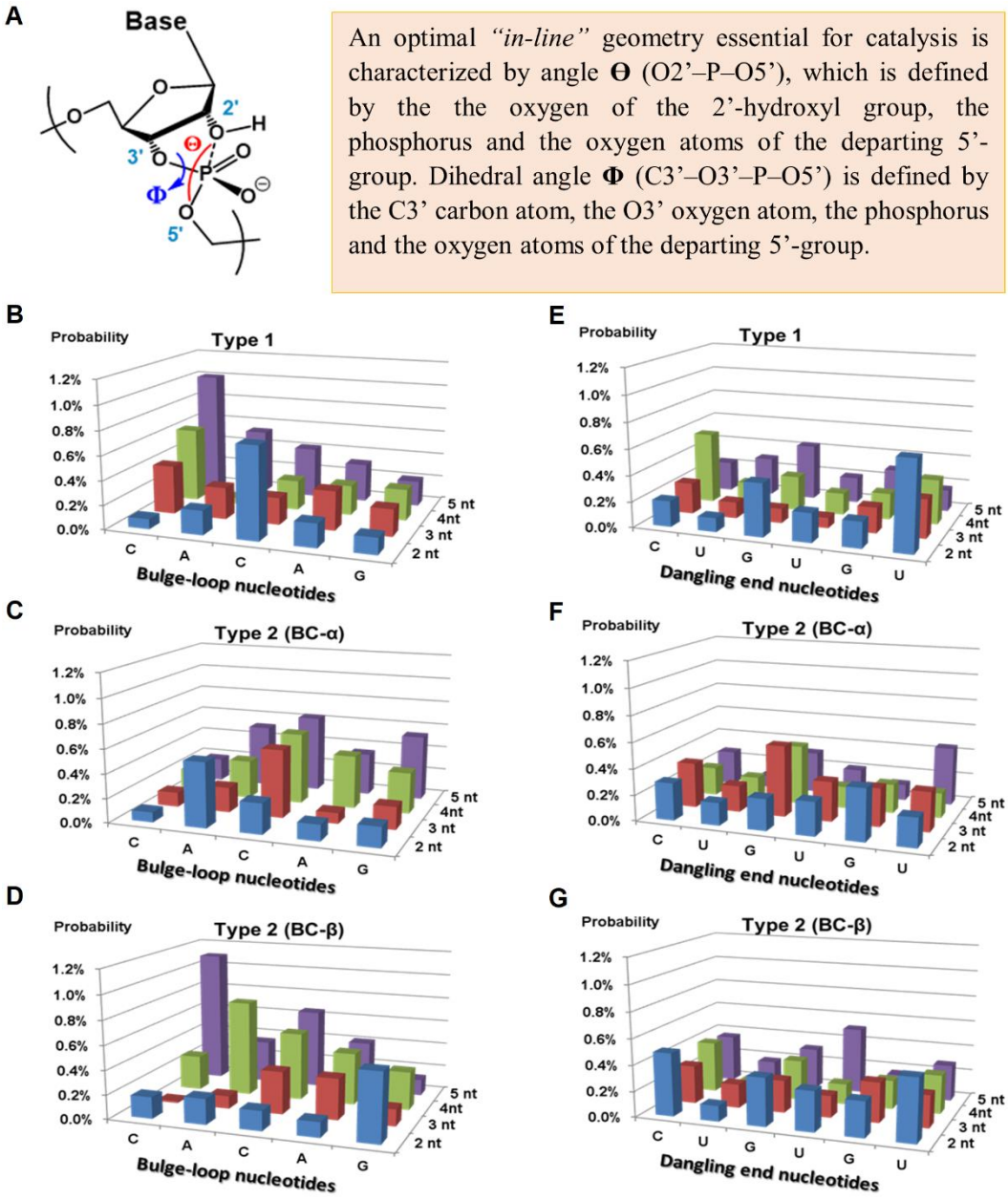

Figure 2.7. (**A**) An optimal *"in-line"* geometry (59) essential to promote catalysed transesterification in RNA sequences. (**B – D**) The probability of *"in-line"* conformation evaluated for the RNA nucleotides within the bulge-loop regions of the complexes formed between RNA and Type 1 conjugates (**B**) and Type 2 conjugates from BC-α (**C**) and BC-β (**D**) series. (**E – F**) The probability of *"in-line"* geometry evaluated for the RNA nucleotides from the dangling ends of the complexes formed between RNA and Type 1 conjugates (**E**) and Type 2 conjugates from BC-α (**F**) and BC-β (**G**) series. The probabilities of achieving an *"in-line"* geometry optimal for catalysis, estimated from the favorable values of **Θ** (when **Θ** >155°), which can be achieved during the MD simulation, were calculated as the ratio between the number of structures with **Θ** > 155° in MD trajectory to the overall number of all structures.

The cluster analysis showed that in all hybrid structures the positively-charged peptide was engaged in strong interactions with the negatively-charged sugar-phosphate backbone of the nucleic acids through electrostatic molecular forces (see **Figure 2.6** and the corresponding rotating images in the **Supplementary Information**). These contacts

included the interactions with the single-stranded bulge-loop sites (red) opposite to the peptide conjugation point, the double-stranded *RNA-DNA* regions, and even with the RNA dangling ends, all of which could potentially be destructive for catalysis. This is consistent with our experimental data (see **Figures 2.3** and **2.4**) showing that Type 2 conjugates (BC-α and BC-β) cleaved RNA at distantly-located sites, in addition to the target bulge-loop region.

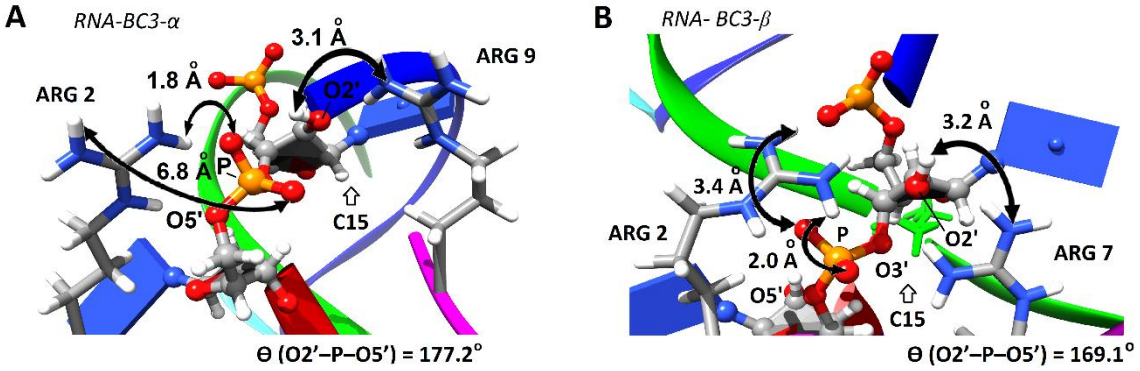

Figure 2.8. The expanded regions of the selected hybrid structures *RNA-BC3-α* (**A**) and *RNA-BC3-β* (**B**) showing a realisation of an *"in-line attack"* conformation with **Θ** (O2'-P-O5') ≥155°. The guanidinium groups of the two arginine residues are located close to the sugar-phosphate backbone of the bulged nucleotide C15 to form a *guanidine-guanidinium* dyad, essential for catalysis.

Finally, we have analysed the ability of the catalytic guanidinium groups of the four arginine residues in BC3, BC3-α and BC3-β to reach the RNA bulge-loop region, by evaluating the distribution of distances between the nitrogen atoms of each guanidinium group and O2' and/or phosphorus atoms of every "bulged" nucleotide (**Supplementary Figure 2.23**). Based on the suggested mechanism of the guanidinium-catalysed transesterification, (55–57) we assumed that, within the same molecular framework, a prerequisite for successful cleavage is the simultaneous presence of all these atoms at short distances, not exceeding 6 Å.

We discovered (**Supplementary Figure 2.23**) that, although there is a high probability of finding the catalytic guanidinium groups at locations distant from the sugar-phosphate backbone of the bulge-loops (i.e. between 6 Å and 43 Å), there was a certain proportion of structures, where the key atomic players were closely located at distances ≤6 Å (see **Figures 2.8** and **Supplementary Figure 2.23** (**B**), as well as the corresponding rotating images in the **Supplementary Information**). Crucially, the peptide attachment through a flexible abasic sugar residue (BC3-α and BC3-β from Type 2 series) led to approximately 3-fold higher contribution from the short-range distance distribution (**Supplementary Figure 2.23** (**B**)) for these atoms as compared to Type 1 series. As

anticipated, the presence of an additional glycine residue in the longer peptide acetyl-$[LRLRG]_2$-CO_2H in Type 2 conjugates enhanced the overall flexibility of its catalytic function, allowing exploration of more energetically favorable conformations, which is in agreement with the high activity of the Type 2 conjugates. Importantly, the nuclease-resistant α-anomer, which offers an advantage of potentially superior cellular stability of the conjugates *in vivo,* also showed a slightly more favorable setting for cleavage as compared with β-anomer (**Supplementary Figure 2.23** (**B**)). Overall, in the hybrid complexes formed by Type 1 conjugates, the catalytic peptide was located more distantly from the RNA bulge-loop region (**Supplementary Figure 2.23** (**A**)), with the weighted average distance of 20 Å between the catalytic guanidinium groups and O2' and/or phosphorus atoms of the "bulged" nucleotides (*cf.* with 17 Å and 18 Å for BC3-α and BC3-β, respectively). The adenosine residue was the peptide attachment point for Type 1 and tends to adopt more energetically favoured *anti* conformation, thus restricting the ability of the peptide to approach the RNA bulge-loop region and exert its function.

2.6 Conclusions

Of the library of 14 bulge-loop inducing peptidyl-oligonucleotide conjugates, developed here for catalytic sequence-specific destruction of RNA sequences, two very distinct types of behavior arose. Type 1, exemplified by conjugation of catalytic peptide via an aminohexyl-modified adenosine, showed zero activity against RNA. In contrast, Type 2, achieved by conjugation of the longer catalytic peptide via an internal abasic nucleotide, whether in α- or β-configuration, showed up to 90% total RNA cleavage. This striking difference can be related to structural requirements of catalysis, also illuminated by MD simulations of these bulge-loop inducing conjugates: (i) flexible attachment of the catalytic peptide via an internal abasic nucleotide either in α- or β-configuration; (ii) avoidance of peptide incorporation via the aromatic nucleotide base, to minimise any conformational restraints; (iii) induction of ≥ 3-nt RNA bulge-loop regions to provide an opportunity for RNA to adopt *"in-line"* conformation; and (iv) incorporation of a longer peptide with an additional glycine in the middle to enhance structural flexibility. Our insights into the structural organisation of the hybrid complexes between the conjugates and RNA, and their MD simulation can now guide the design to optimise interactions vital for catalysis, particularly (a) to minimise the probability of "non-productive" conformations and (b) to achieve multiple catalytic turnover by each conjugate molecule, which is essential for therapeutic destruction of pathogenic cellular RNA.

In order to allow these discoveries to progress into translational success, it will be crucial in the future to achieve sufficient serum stability of such bioconjugates *in vivo*. Although the peptide provides the oligonucleotide with some level of protection from cellular nucleases, (17, 20) yet more biologically stable variants can be produced by harnessing recent advances in nuclease-resistant chemical modification, (60, 61) which may also enhance binding to the target RNA. Indeed, the newly discovered triazole-LNA and carbamate-LNA modified oligonucleotides (62, 63) show a much reduced level of degradation *in vivo* and significantly higher affinity towards RNA/DNA, which is re-enforced by locked nucleic acid sugars, thus providing us with new opportunities. This might allow the use of shorter oligonucleotides with improved cellular uptake properties, especially when conjugated to the arginine-rich catalytic peptides, which have been previously shown to facilitate transport of large hydrophilic molecules across biological barriers (64–68).

2.7 Funding

This work was supported by the Biotechnology and Biological Sciences Research Council [BB/K012622/1]; Engineering and Physical Sciences Research Council [EP/E003400/1, EP/G03737X/1]; and by the Russian Science Foundation [14-44-00068, 9-14-00250]. Funding for open access charge: Engineering and Physical Sciences Research Council.

2.8 Acknowledgments

We are grateful to the Biological Mass Spectrometry Facility at the University of Manchester, and especially to Dr. David Knight, for providing access to mass spectrometry facility and support. The authors would like to thank Dr. Harmesh Aojula for his advice on peptide synthesis and Neil O'Hara for his technical support.

2.9 References

1. Milhavet,O., Gary,D.S. and Mattson,M.P. (2003) RNA interference in biology and medicine. *Pharmacol. Rev.*, **55**, 629–648.

2. Jones,D. (2011) The long march of antisense. *Nat. Rev. Drug Discov.*, **10**, 401–402.

3. Kole,R., Krainer,A.R. and Altman,S. (2012) RNA therapeutics: beyond RNA interference and antisense oligonucleotides. *Nat. Rev. Drug Discov.*, **11**, 125–140.

4. Scannell,J.W., Blanckley,A., Boldon,H. and Warrington,B. (2012) Diagnosing the decline in pharmaceutical R&D efficiency. *Nat. Rev. Drug Discov.*, **11**, 191–200.

5. Casi,G. and Neri,D. (2015) Antibody-Drug Conjugates and Small Molecule-Drug Conjugates: Opportunities and Challenges for the Development of Selective Anticancer Cytotoxic Agents. *J. Med. Chem.*, **58**, 8751–8761.

6. Bennett,C.F., Baker,B.F., Pham,N., Swayze,E. and Geary,R.S. (2017) Pharmacology of Antisense Drugs. *Annu. Rev. Pharmacol. Toxicol.*, **57**, 81–105.

7. Connelly,C.M., Moon,M.H. and Schneekloth Jr,J.S. (2016) The Emerging Role of RNA as a Therapeutic Target for Small Molecules. *Cell Chem. Biol.*, **23**, 1077–1090.

8. Esteller,M. (2011) Non-coding RNAs in human disease. *Nat. Rev. Genet.*, **12**, 861–874.

9. Cheetham,S.W., Gruhl,F., Mattick,J.S. and Dinger,M.E. (2013) Long noncoding RNAs and the genetics of cancer. *Br. J. Cancer*, **108**, 2419–2425.

10. Khan,A.A., Betel,D., Miller,M.L., Sander,C., Leslie,C.S. and Marks,D.S. (2009) Transfection of small RNAs globally perturbs gene regulation by endogenous microRNAs. *Nat. Biotechnol.*, **27**, 549–555.

11. Marques,J.T. and Williams,B.R.G. (2005) Activation of the mammalian immune system by siRNAs. *Nat. Biotechnol.*, **23**, 1399–1405.

12. Sioud,M. (2005) Induction of inflammatory cytokines and interferon responses by double-stranded and single-stranded siRNAs is sequence-dependent and requires endosomal localization. *J. Mol. Biol.*, **348**, 1079–1090.

13. Rojanasakul,Y. (1996) Antisense oligonucleotide therapeutics: drug delivery and targeting. *Adv. Drug Deliv. Rev.*, **18**, 115–131.

14. Niittymäki,T. and Lönnberg,H. (2006) Artificial ribonucleases. *Org. Biomol. Chem.*, **4**, 15–25.

15. Williams,A., Staroseletz,Y., Zenkova,M.A., Jeannin,L., Aojula,H. and Bichenkova,E. V. (2015) Peptidyl-Oligonucleotide Conjugates Demonstrate Efficient Cleavage of RNA in a Sequence-Specific Manner. *Bioconjug. Chem.*, **26**, 1129–1143.

16. Staroseletz,Y., Williams,A., Burusco,K.K., Alibay,I., Vlassov,V. V., Zenkova,M.A. and Bichenkova,E. V. (2017) 'Dual' peptidyl-oligonucleotide conjugates: Role of conformational flexibility in catalytic cleavage of RNA. *Biomaterials*, **112**, 44–61.

17. Patutina,O.A., Bichenkova,E. V, Miroshnichenko,S.K., Mironova,N.L., Trivoluzzi,L.T., Burusco,K.K., Bryce,R.A., Vlassov,V. V and Zenkova,M.A. (2017) miRNases: Novel peptide-oligonucleotide bioconjugates that silence miR-21 in lymphosarcoma cells. *Biomaterials*, **122**, 163–178.

18. Mironova,N.L., Pyshnyi,D. V, Shtadler,D. V, Fedorova,A.A., Vlassov,V. V and Zenkova,M.A. (2007) RNase T1 mimicking artificial ribonuclease. *Nucleic Acids Res.*, **35**, 2356–2367.

19. Serikov,R., Petyuk,V., Vorobijev,Y., Koval,V., Fedorova,O., Vlassov,V. and Zenkova,M. (2011) Mechanism of Antisense Oligonucleotide Interaction with Natural RNAs. *J. Biomol. Struct. Dyn.*, **29**, 27–50.

20. Patutina,O.A., Miroshnichenko,S.K., Mironova,N.L., Sen'kova,A. V., Bichenkova,E. V., Clarke,D.J., Vlassov,V. V. and Zenkova,M.A. (2019) Catalytic Knockdown of miR-21 by Artificial Ribonuclease: Biological Performance in Tumor Model. *Front. Pharmacol.*, **10**, 1–13.

21. Vickers,T.A. and Crooke,S.T. (2015) The rates of the major steps in the molecular mechanism of RNase H1-dependent antisense oligonucleotide induced degradation of RNA. *Nucleic Acids Res.*, **43**, 8955–8963.

22. Magda,D., Wright,M., Crofts,S., Lin,A. and Sessler,J.L. (1997) Metal Complex Conjugates of Antisense DNA Which Display Ribozyme-Like Activity. *J. Am. Chem. Soc.*, **119**, 6947–6948.

23. Murtola,M., Wenska,M. and Strömberg,R. (2010) PNAzymes That Are Artificial RNA Restriction Enzymes. *J. Am. Chem. Soc.*, **132**, 8984–8990.

24. Sakamoto,S., Tamura,T., Furukawa,T., Komatsu,Y., Ohtsuka,E., Kitamura,M. and Inoue,H. (2003) Highly efficient catalytic RNA cleavage by the cooperative action of two Cu(II) complexes embodied within an antisense oligonucleotide. *Nucleic Acids Res.*, **31**, 1416–1425.

25. Trawick,B.N., Osiek,T.A. and Bashkin,J.K. (2001) Enhancing sequence-specific cleavage of RNA within a duplex region: incorporation of 1,3-propanediol linkers into oligonucleotide conjugates of serinol-terpyridine. *Bioconjug. Chem.*, **12**, 900–905.

26. Häner,R., Hall,J., Pfützer,A. and Hüsken,D. (1998) Development of artificial ribonucleases. *Pure Appl. Chem.*, **70**, 111–116.

27. Astrom,H. and Stromberg,R. (2004) Synthesis of new OBAN's and further studies on positioning of the catalytic group. *Org. Biomol. Chem.*, **2**, 1901–1907.

28. Kaukinen,U., Bielecki,L., Mikkola,S., Adamiak,R.W. and Lönnberg,H. (2001) The cleavage of phosphodiester bonds within small RNA bulges in the presence and absence of metal ion catalysts. *J. Chem. Soc. Perkin Trans.* **2**, 1024–1031.

29. Hüsken,D., Goodall,G., Blommers,M.J.J., Jahnke,W., Hall,J., Häner,R. and Moser,H.E. (1996) Creating RNA Bulges: Cleavage of RNA in RNA/DNA Duplexes by Metal Ion Catalysis. *Biochemistry*, **35**, 16591–16600.

30. Kuznetsova,I.L., Zenkova,M.A., Gross,H.J. and Vlassov,V. V (2005) Enhanced RNA cleavage within bulge-loops by an artificial ribonuclease. *Nucleic Acids Res.*, **33**, 1201–1212.

31. Kuznetsova,I.L., Zenkova,M.A. and Vlassov,V. V (2006) Cleavage of RNA bulge loops by artificial RNases. *Russ. Chem. Bull.*, **55**, 1284–1294.

32. Dogandzhiyski,P., Ghidini,A., Danneberg,F., Strömberg,R. and Göbel,M.W. (2015) Studies on Tris(2-aminobenzimidazole)-PNA Based Artificial Nucleases: A Comparison of Two Analytical Techniques. *Bioconjug. Chem.*, **26**, 2514–2519.

33. Ghidini,A., Murtola,M. and Strömberg,R. (2016) Influence of conjugation and other structural changes on the activity of Cu^{2+} based PNAzymes. *Org. Biomol. Chem.*, **14**, 2768–2773.

34. Gebrezgiabher,M., Zalloum,W.A., Clarke,D.J., Miles,S.M., Fedorova,A.A., Zenkova,M.A. and Bichenkova,E. V (2020) RNA knockdown by synthetic peptidyl-oligonucleotide ribonucleases: behavior of recognition and cleavage elements under physiological conditions. *J. Biomol. Struct. Dyn.*, 1–20.

35. Bichenkova,E. V, Raju,A.P.A., Burusco,K.K., Kinloch,I.A., Novoselov,K.S. and Clarke,D.J. (2017) NMR detects molecular interactions of graphene with aromatic and aliphatic hydrocarbons in water. *2D Mater.*, **5**, 15003.

36. Silberklang,M., Gillum,A.M. and RajBhandary,U.L. (1979) Use of in Vitro 32P Labeling in the Sequence Analysis of Nonradioactive tRNAs. *Methods Enzym.*, **59**, 58–109.

37. Case,D.A., Babin,V., Berryman,J.T., Betz,R.M., Cai,Q., Cerutti,D.S., Cheatham,T.E., Darden,T.A., Duke,R.E., Gohlke,H., Goetz,A.W., Gusarov,S., Homeyer,N., Janowski,P., Kaus,J., Kolossváry,I., Kovalenko,A., Lee,T.S., LeGrand,S., Luchko,T., Luo,R., Madej,B., Merz,K.M., Paesani,F., Roe,D.R., Roitberg,A., Sagui,C., Salomon-Ferrer,R., Seabra,G., Simmerling,C.L., Smith,W., Swails,J., Walker,R.C., Wang,J., Wolf,R.M., Wu,X. and Kollman,P.A (2014) AMBER 14, University of California, San Francisc.

38. Frisch,M.J., Trucks,G.W., Schlegel,H.B., Scuseria,G.E., Robb,M.A., Cheeseman,J.R, Scalmani,G., Barone,V., Mennucci,B., Petersson,G.A., Nakatsuji,H., Caricato,M., Li,X., Hratchian,H.P., Izmaylov,A.F., Bloino,J.,. Zheng,G, Sonnenberg,J.L., Hada,M., Ehara,M., Toyota,K., Fukuda,R., Hasegawa,J., Ishida,M., Nakajima,T., Honda,Y., Kitao,O., Nakai,H., Vreven,T., Montgomery,J.A., Peralta,Jr.J.E., Ogliaro,F., Bearpark,M., Heyd,J.J., Brothers,E., Kudin,K.N., Staroverov,V.N., Kobayashi,R., Normand,J., Raghavachari,K., Rendell,A., Burant,J.C.,. Iyengar,S.S, Tomasi,J., Cossi,M., Rega,N., Millam,J.M., Klene,M., Knox,J.E., Cross,J.B., Bakken,V., Adamo,C., Jaramillo,J., Gomperts,R., Stratmann,R.E., Yazyev,O., Austin,A.J., Cammi,R., Pomelli,C., Ochterski,J.W., Martin,R.L., Morokuma,K., Zakrzewski,V.G., Voth,G.A., Salvador,P., Dannenberg,J.J., Dapprich,S., Daniels,A.D., Farkas,O., Foresman,J.B., Ortiz,J.V., Cioslowski,J. and Fox,D.J. (2009) Gaussian 09, Revision A.01. Gaussian, Inc., Wallingford CT.

39. Dennington,R., Keith,T.A. and Millam, J.M. (2016) GaussView, Version 6, Semichem Inc., Shawnee Mission, KS .

40. Pettersen,E.F., Goddard,T.D., Huang,C.C., Couch,G.S., Greenblatt,D.M., Meng,E.C. and Ferrin,T.E. (2004) UCSF Chimera--a visualization system for exploratory research and analysis. *J. Comput. Chem.*, **25**, 1605–1612.

41. Bayly,C.I., Cieplak,P., Cornell,W. and Kollman,P.A. (1993) A well-behaved electrostatic potential based method using charge restraints for deriving atomic charges: the RESP model. *J. Phys. Chem.*, **97**, 10269–10280.

42. Maier,J.A., Martinez,C., Kasavajhala,K., Wickstrom,L., Hauser,K.E. and Simmerling,C. (2015) ff14SB: Improving the Accuracy of Protein Side Chain and Backbone Parameters from ff99SB. *J. Chem. Theory Comput.*, **11**, 3696–3713.

43. Wang,J., Wolf,R.M., Caldwell,J.W., Kollman,P.A. and Case,D.A. (2004) Development and testing of a general amber force field. *J. Comput. Chem.*, **25**, 1157–1174.

44. Rich,A. (2006) Discovery of the hybrid helix and the first DNA-RNA hybridization. *J. Biol. Chem.*, **281**, 7693–7696.

45. Hawkins,G.D., Cramer,C.J. and Truhlar,D.G. (1996) Parametrized models of aqueous free energies of solvation based on pairwise descreening of solute atomic charges from a dielectric medium. *J. Phys. Chem.*, **100**, 19824–19839.

46. Hawkins,G.D., Cramer,C.J. and Truhlar,D.G. (1995) Pairwise solute descreening of solute charges from a dielectric medium. *Chem. Phys. Lett.*, **246**, 122–129.

47. Tsui,V. and Case,D.A. (2000) Theory and applications of the generalized Born solvation model in macromolecular simulations. *Biopolymers*, **56**, 275–291.

48. Andrea,T., Swope,W. and Andersen,H. (1983) The role of long ranged forces in determining the structure and properties of liquid water. *J. Chem. Phys.*, **79**, 4576–4584.

49. Andersen,H.C. (1980) Molecular dynamics simulations at constant pressure and/or temperature. *J. Chem. Phys.*, **72**, 2384–2393.

50. Kelley,L.A., Gardner,S.P. and Sutcliffe,M.J. (1996) An automated approach for clustering an ensemble of NMR-derived protein structures into conformationally related subfamilies. *Protein Eng. Des. Sel.*, **9**, 1063–1065.

51. Shi,H. and Moore,P.B. (2000) The crystal structure of yeast phenylalanine tRNA at 1.93 A resolution: a classic structure revisited. *RNA*, **6**, 1091–1105.

52. Lönnberg,H. (2011) Cleavage of RNA phosphodiester bonds by small molecular entities: a mechanistic insight. *Org. Biomol. Chem.*, **9**, 1687–1703.

53. Mikkola,S., Lönnberg,T. and Lönnberg,H. (2018) Phosphodiester models for cleavage of nucleic acids. *Beilstein J. Org. Chem.*, **14**, 803–837.

54. Morrow,J.R. (2008) Speed limits for artificial ribonucleases. *Comments Inorg. Chem.*, **29**, 169–188.

55. Baldini,L., Cacciapaglia,R., Casnati,A., Mandolini,L., Salvio,R., Sansone,F. and Ungaro,R. (2012) Upper rim guanidinocalix[4]arenes as artificial phosphodiesterases. *J. Org. Chem.*, **77**, 3381–3389.

56. Salvio,R., Mandolini,L. and Savelli,C. (2013) Guanidine–Guanidinium Cooperation in Bifunctional Artificial Phosphodiesterases Based on Diphenylmethane Spacers; gem-Dialkyl Effect on Catalytic Efficiency. *J. Org. Chem.*, **78**, 7259–7263.

57. Salvio,R. and Casnati,A. (2017) Guanidinium Promoted Cleavage of Phosphoric Diesters: Kinetic Investigations and Calculations Provide Indications on the Operating Mechanism. *J. Org. Chem.*, **82**, 10461–10469.

58. Vinogradova,O.A., Eremeeva,E. V, Lomzov,A.A., Pyshnaia,I.A. and Pyshnyi,D. V (2009) Bent dsDNA with defined geometric characteristics in terms of complexes of bridged oligonucleotides. *Bioorg. Khim.*, **35**, 384–396.

59. Min,D., Xue,S., Li,H. and Yang,W. (2007) 'In-line attack' conformational effect plays a modest role in an enzyme-catalyzed RNA cleavage: a free energy simulation study. *Nucleic Acids Res.*, **35**, 4001–4006.

60. Taemaitree,L., Shivalingam,A., El-Sagheer,A.H. and Brown,T. (2019) An artificial triazole backbone linkage provides a split-and-click strategy to bioactive chemically modified CRISPR sgRNA. *Nat. Commun.*, **10**, 1610.

61. Shivalingam,A. and Brown,T. (2016) Synthesis of chemically modified DNA. *Biochem. Soc. Trans*., **44**, 709–715.

62. Thorpe,C., Epple,S., Woods,B., El-Sagheer,A.H. and Brown,T. (2019) Synthesis and biophysical properties of carbamate-locked nucleic acid (LNA) oligonucleotides with potential antisense applications. *Org. Biomol. Chem*., **17**, 5341–5348.

63. Kumar,P., Truong,L., Baker,Y.R., El-Sagheer,A.H. and Brown,T. (2018) Synthesis, Affinity for Complementary RNA and DNA, and Enzymatic Stability of Triazole-Linked Locked Nucleic Acids (t-LNAs). *ACS Omega*, **3**, 6976–6987.

64. Caesar,C.E.B., Esbjörner,E.K., Lincoln,P. and Nordén,B. (2006) Membrane interactions of cell-penetrating peptides probed by tryptophan fluorescence and dichroism techniques: correlations of structure to cellular uptake. *Biochemistry*, **45**, 7682–7692.

65. Thorén,P.E.G., Persson,D., Esbjörner,E.K., Goksör,M., Lincoln,P. and Nordén,B. (2004) Membrane Binding and Translocation of Cell-Penetrating Peptides. *Biochemistry*, **43**, 3471–3489.

66. Persson,D., Thorén,P.E.G., Esbjörner,E.K., Goksör,M., Lincoln,P. and Nordén,B. (2004) Vesicle size-dependent translocation of penetratin analogs across lipid membranes. *Biochim. Biophys. Acta*, **1665**, 142–155.

67. Thorén,P.E.G., Persson,D., Isakson,P., Goksör,M., Onfelt,A. and Nordén,B. (2003) Uptake of analogs of penetratin, Tat(48-60) and oligoarginine in live cells. *Biochem. Biophys. Res. Commun*., **307**, 100–107.

68. Persson,D., Thorén,P.E.G., Herner,M., Lincoln,P. and Nordén,B. (2003) Application of a novel analysis to measure the binding of the membrane-translocating peptide penetratin to negatively charged liposomes. *Biochemistry*, **42**, 421–429.

2.10 Supporting information

2.10.1 Sequences of the unconjugated oligonucleotides and peptides

Table 2.2. Sequences of the unconjugated oligonucleotides and peptides used for conjugate reactions along with their millimolar extinction coefficients.

Name	Sequence (5' to 3')	E_{260} ($mM^{-1} \cdot cm^{-1}$)[a]
Acetyl-$[LR]_4G$-CO_2H	Ac-Leu-Arg-Leu-Arg-Leu-Arg-Leu-Arg-Gly	n/a
Acetyl-$[LRLRG]_2$-CO_2H	Ac-Leu-Arg-Leu-Arg-Gly-Leu-Arg-Leu-Arg-Gly	n/a
BC2	TGGTGCGAATT**A***GTGGATCGAA [b]	226.3
BC3	TGGTGCGAATT**A***TGGATCGAA [b]	215.9
BC4	TGGTGCGAATT**A***GGATCGAA [b]	208.1
BC5	TGGTGCGAATT**A***GATCGAA [b]	197.7
BC2-α	TGGTGCGAATT-**dR^{alpha}**-GTGGATCGAACACAG [c]	266.7
BC3-α	TGGTGCGAATT-**dR^{alpha}**-TGGATCGAACACAG [c]	256.3
BC4-α	TGGTGCGAATT-**dR^{alpha}**-GGATCGAACACAG [c]	248.3
BC5-α	TGGTGCGAATT-**dR^{alpha}**-GATCGAACACAG [c]	237.9
BC5L-α	TGGTGCGAATT-**dR^{alpha}**-GATCGAACACAGGAC [c]	269.1
BC2-β	TGGTGCGAATT-**dR^{beta}**-GTGGATCGAACACAG [c]	266.7
BC3-β	TGGTGCGAATT-**dR^{beta}**-TGGATCGAACACAG[c]	256.3
BC4-β	TGGTGCGAATT-**dR^{beta}**-GGATCGAACACAG [c]	248.3
BC5-β	TGGTGCGAATT-**dR^{beta}**-GATCGAACACAG [c]	237.9
BC5L-β	TGGTGCGAATT-**dR^{beta}**-GATCGAACACAGGAC [c]	269.1

a) E_{260} denotes the millimolar extinction coefficient

b) A* denotes aminohexyl-modified adenosine residue

c) dR denotes abasic nucleotide incorporated in oligonucleotide sequence

2.10.2 Design concept for Type 1 bulge-loop inducing conjugates (BC2 - BC5)

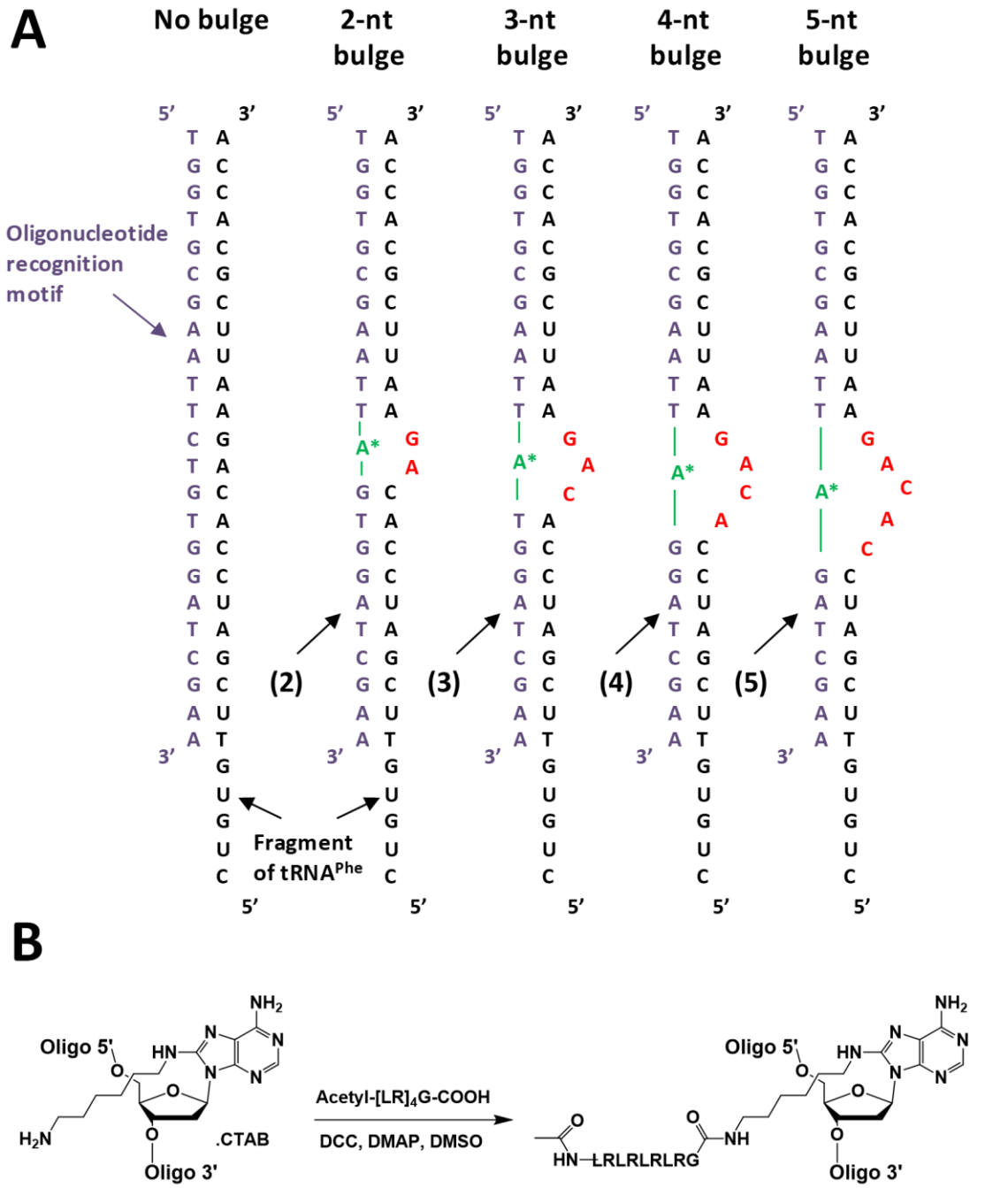

Figure 2.9. A. Schematic representation of the design concept for the Type 1 bulge-loop inducing conjugates. Oligonucleotides **2**, **3**, **4** and **5** (indicated here by arrows) were used as the recognition motifs for the peptidyl-oligonucleotide conjugates BC2, BC3, BC4 and BC5, respectively. **B.** Synthetic route for the conjugation. Chemical structure of the aminohexyl modified adenosine residue **A*** is indicated along with the oligonucleotide and peptide sequences. To avoid peptide self-conjugation and cyclisation during amide coupling reaction, acetylated N-termini peptides were used.

2.10.3 Design concept for Type 2 bulge-loop inducing conjugates BC-α and BC-β

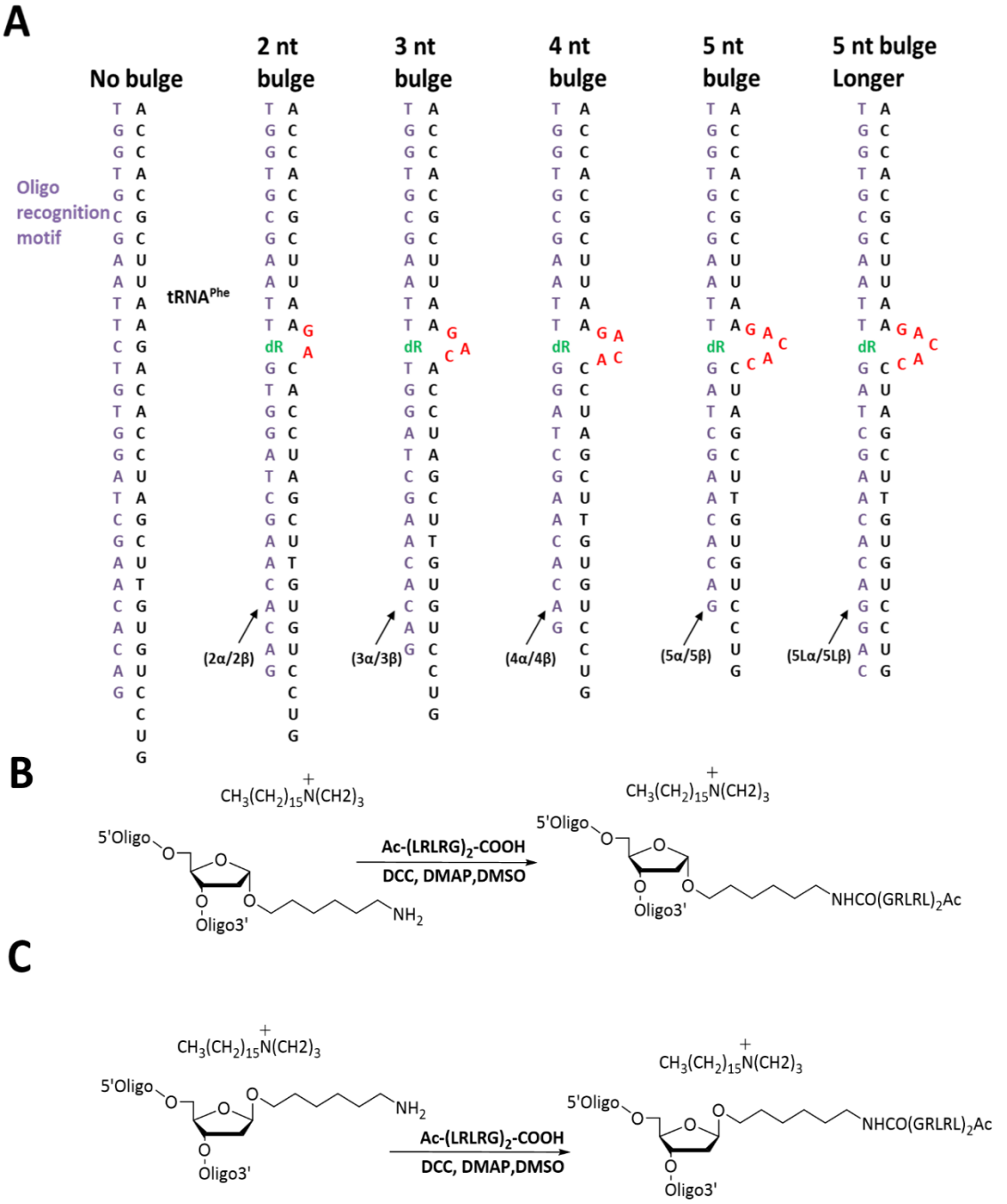

Figure 2.10. A. Schematic representation of the design concept for the α- and β- anomers of Type 2 bulge-loop inducing conjugates. Oligonucleotides **2α/2β**, **3α/3β**, **4α/4β, 5α/5β** and **5Lα/5Lβ** (indicated by arrows) were used as the recognition motifs for conjugates BC2-α/ BC2-β, BC3-α/ BC3-β, BC4-α/ BC4-β, BC5-α/ BC5-β and BC5L-α/BC5L-β, respectively. **B.** Synthetic route for the preparation of α-series of the conjugates. **C.** Synthetic route for the conjugation of β-series of the conjugates. Chemical structure of the abasic nucleotide with aminohexyl linker attached at C1' position **dR** is indicated along with the oligonucleotide and peptide sequences. To avoid peptide self-conjugation and cyclisation during amide coupling reaction, acetylated N-termini peptides were used.

2.10.4 Shift in RP-HPLC purification chromatogram for Type 1 conjugates (BC2-BC5)

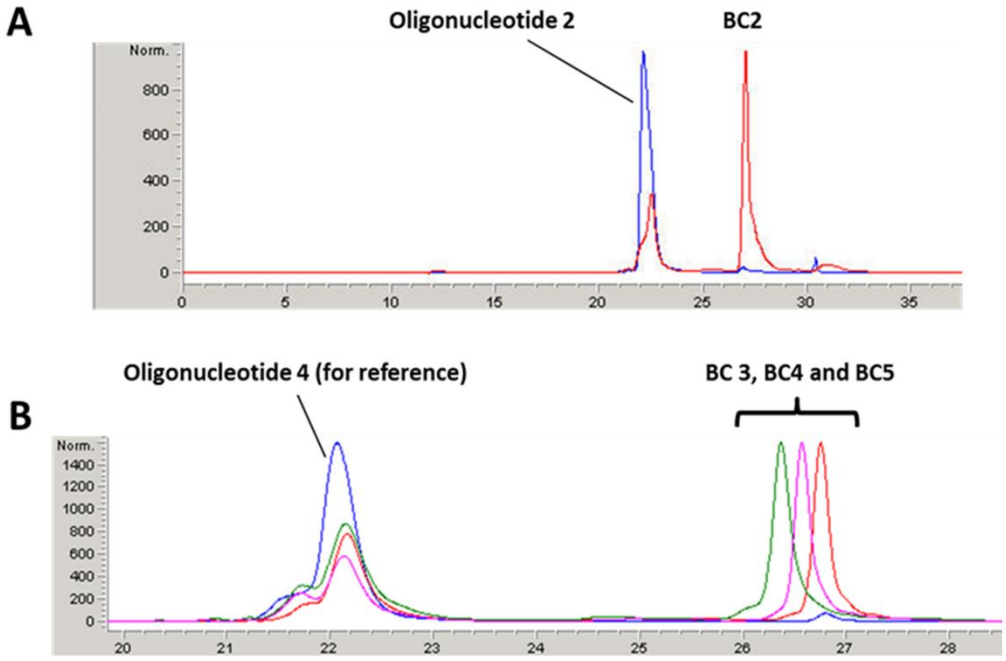

Figure 2.11. A. An overlay of the RP-HPLC purification chromatograms showing the shift in retention of BC2 (red) compared to unmodified oligonucleotide 2 (blue). **B.** An overlay of the RP-HPLC purification chromatograms of BC3 (green), BC4 (pink) and BC5 (red) showing retention time shifts compared to unmodified oligonucleotide 4 (blue), as a reference.

2.10.5 Shift in RP-HPLC purification chromatogram for Type 2 conjugates

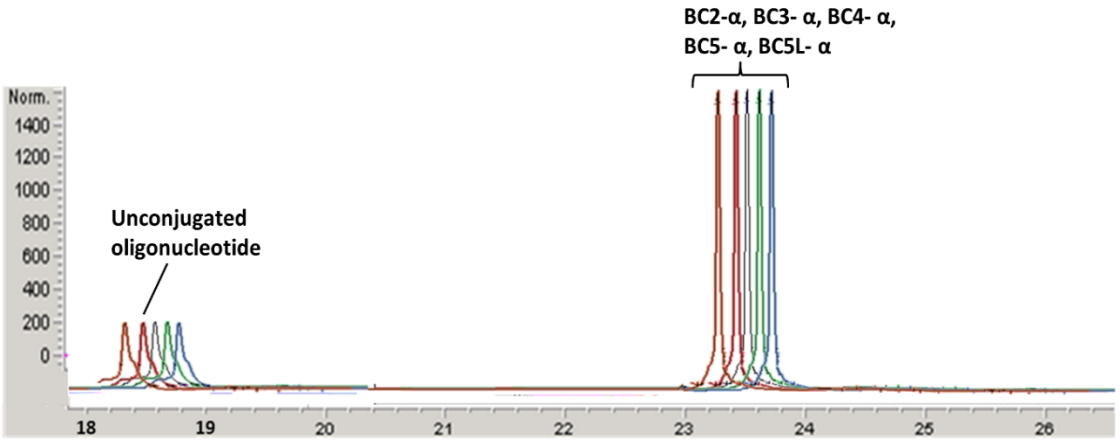

Figure 2.12. An overlay of the RP-HPLC purification chromatogram of BC2-α (orange), BC3-α (red), BC4-α (black), BC5-α (green), BC5L-α (blue) showing the shift in retention from unconjugated oligonucleotide to conjugate. The same shift in retention time was witnessed during RP-HPLC purification of β-series of the conjugates.

2.10.6 ESI-MS spectra of acetyl-[LR]$_4$G-CO$_2$H peptide

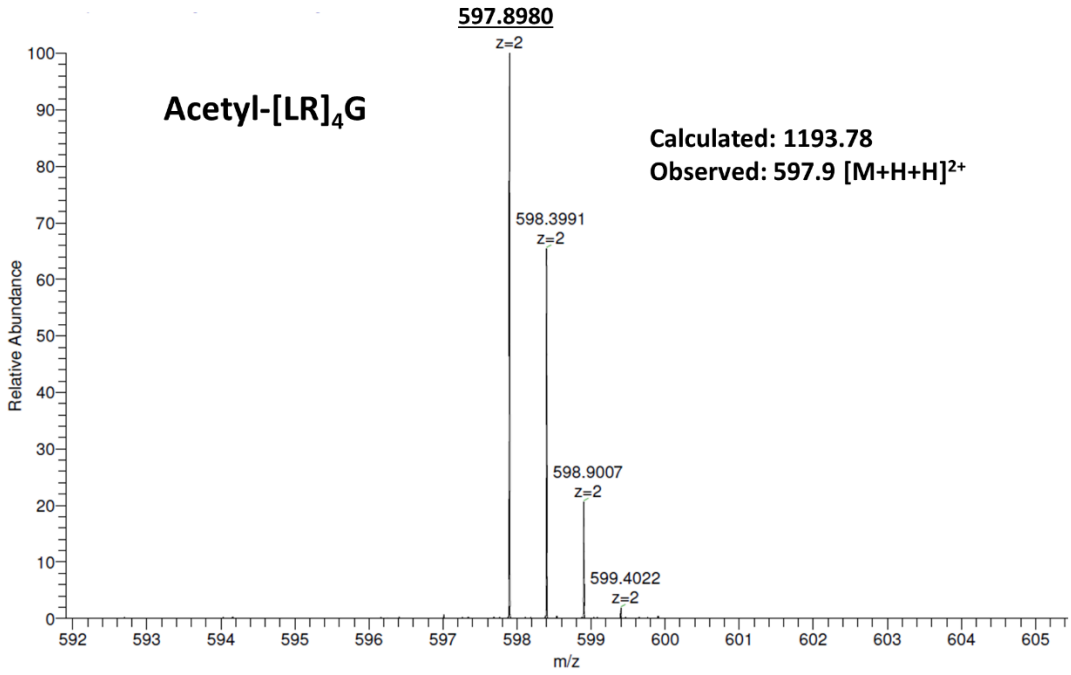

Figure 2.13. ESI-MS mass spectra of acetyl-[LR]$_4$G peptide. The spectrum was recorded by a Thermo Scientific LTQ Orbitrap XL mass spectrometer.

2.10.7 ^{1}H-NMR spectra of the acetyl-[LR]$_4$G-CO$_2$H peptide

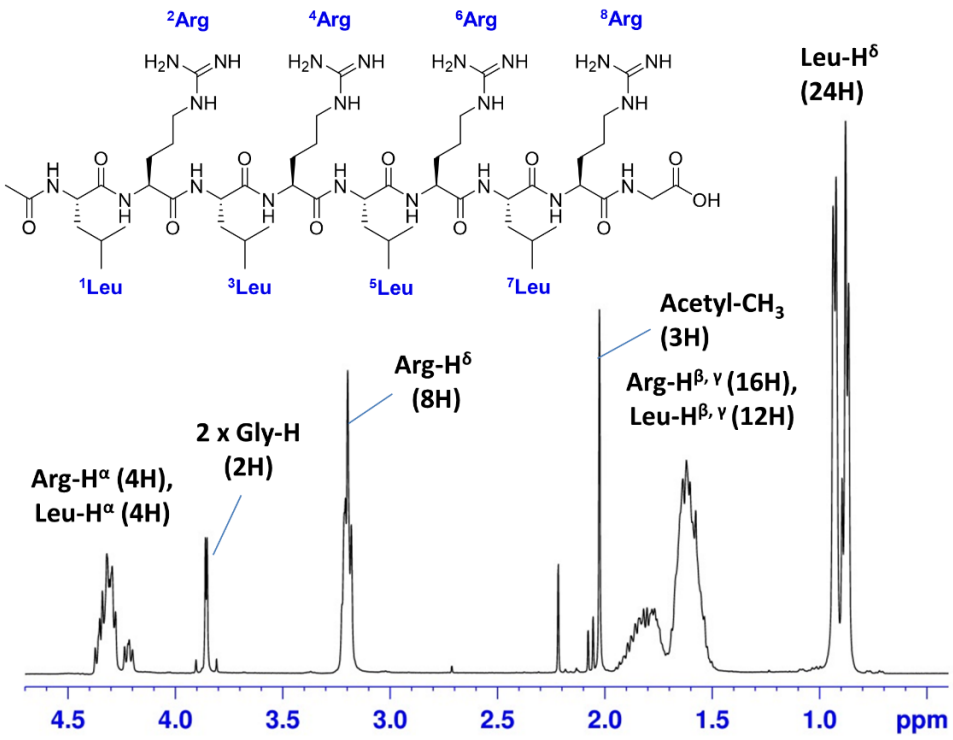

Figure 2.14. ^{1}H-NMR spectra of the peptide acetyl-[LR]$_4$G-CO$_2$H. The spectrum was recorded in D$_2$O at 25 °C using a 400 MHz NMR spectrometer (Bruker Avance II+ 400).

2.10.8 MALDI-ToF mass spectrum of acetyl-[LRLRG]$_2$-CO$_2$H

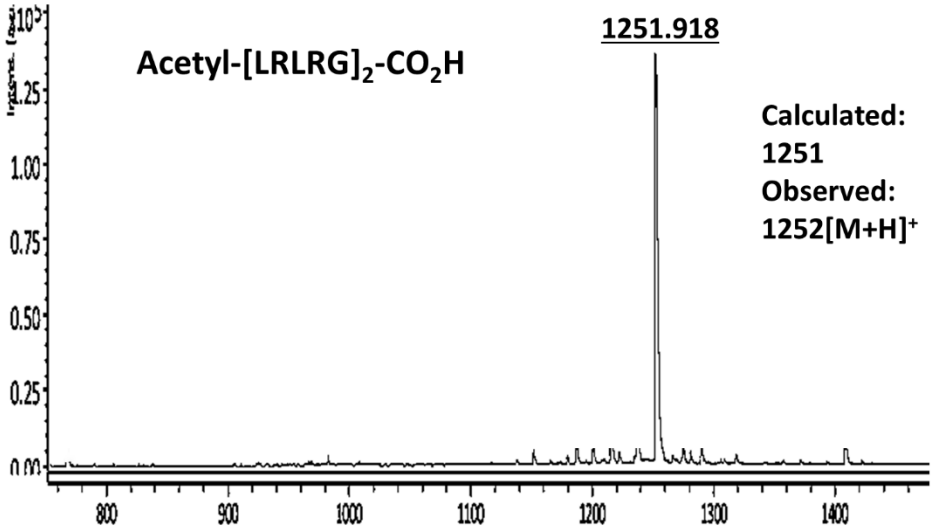

Figure 2.15. MALDI-TOF spectrum of peptide acetyl-[LRLRG]$_2$-CO$_2$H. Spectra were recorded using a Bruker Daltonics Ultraflex TOF/TOF mass spectrometer.

2.10.9 ^{1}H-NMR spectrum of acetyl-[LRLRG]$_2$-CO$_2$H peptide

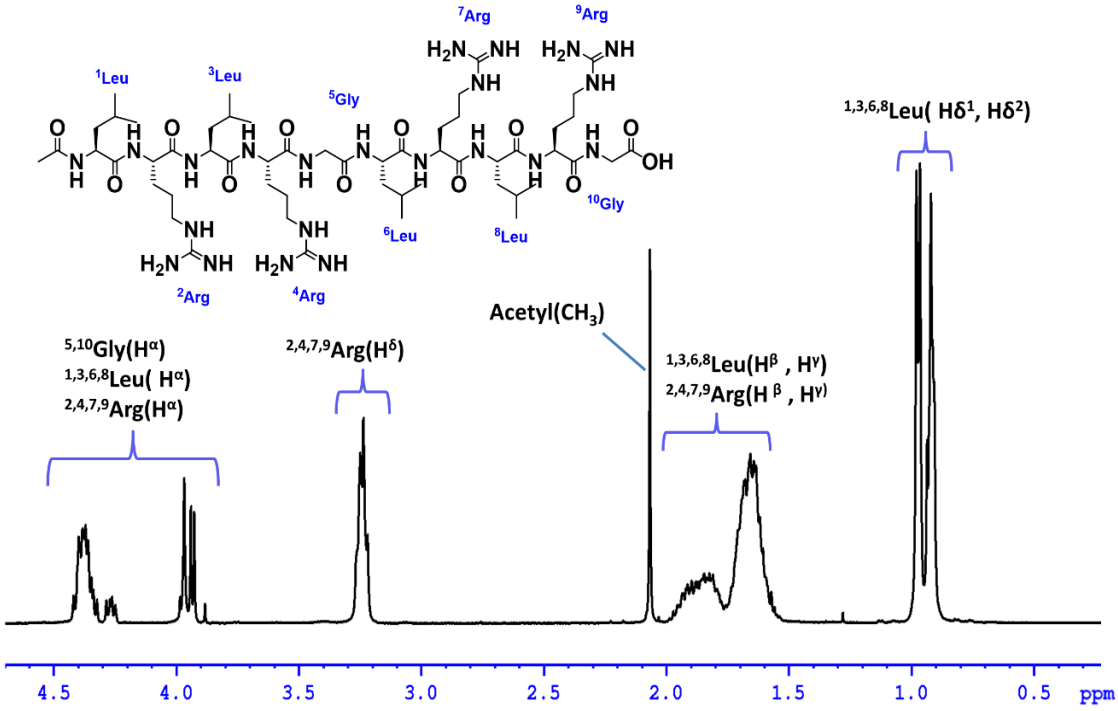

Figure 2.16. ^{1}H NMR spectrum for acetyl-[LRLRG]$_2$-CO$_2$H peptide. The spectrum was recorded in D$_2$O at 25 °C using a 400 MHz NMR spectrometer (Bruker Avance II+ 400).

2.10.10 MALDI-ToF mass spectra of the peptidyl-oligonucleotide conjugates BC2-BC5

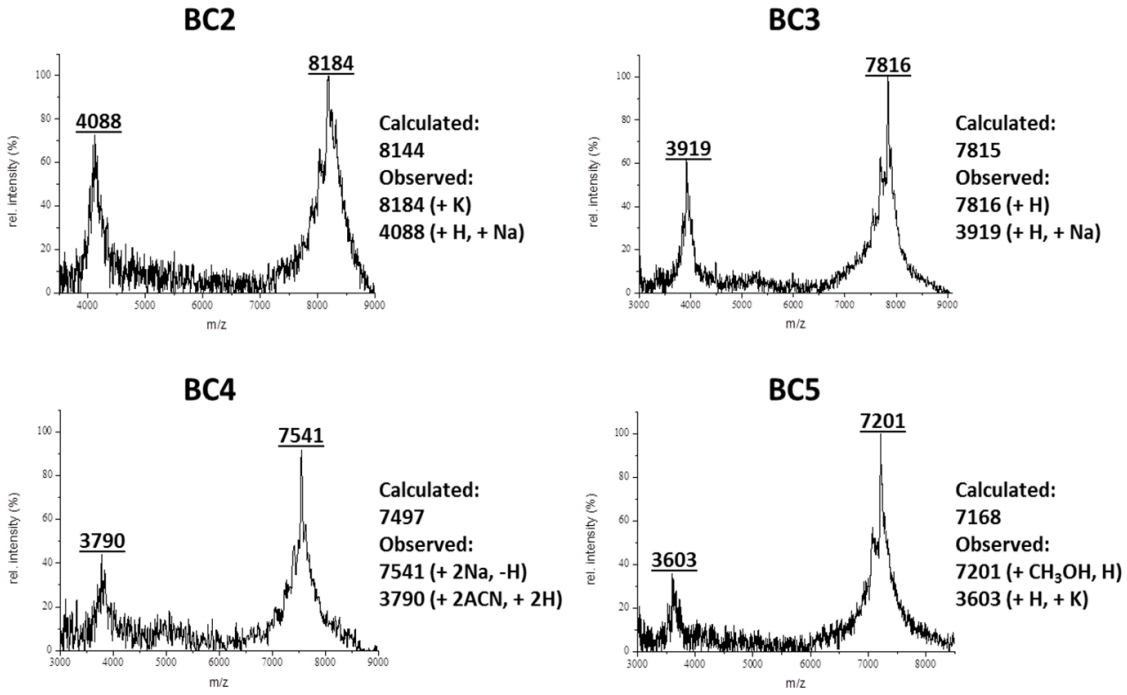

Figure 2.17. MALDI-TOF spectra of peptidyl-oligonucleotide conjugates BC2 - BC5. Spectra were recorded using a Bruker Daltonics Ultraflex TOF/TOF mass spectrometer.

2.10.11 ^{1}H NMR spectra of the bulge-loop inducing conjugates BC2-BC5

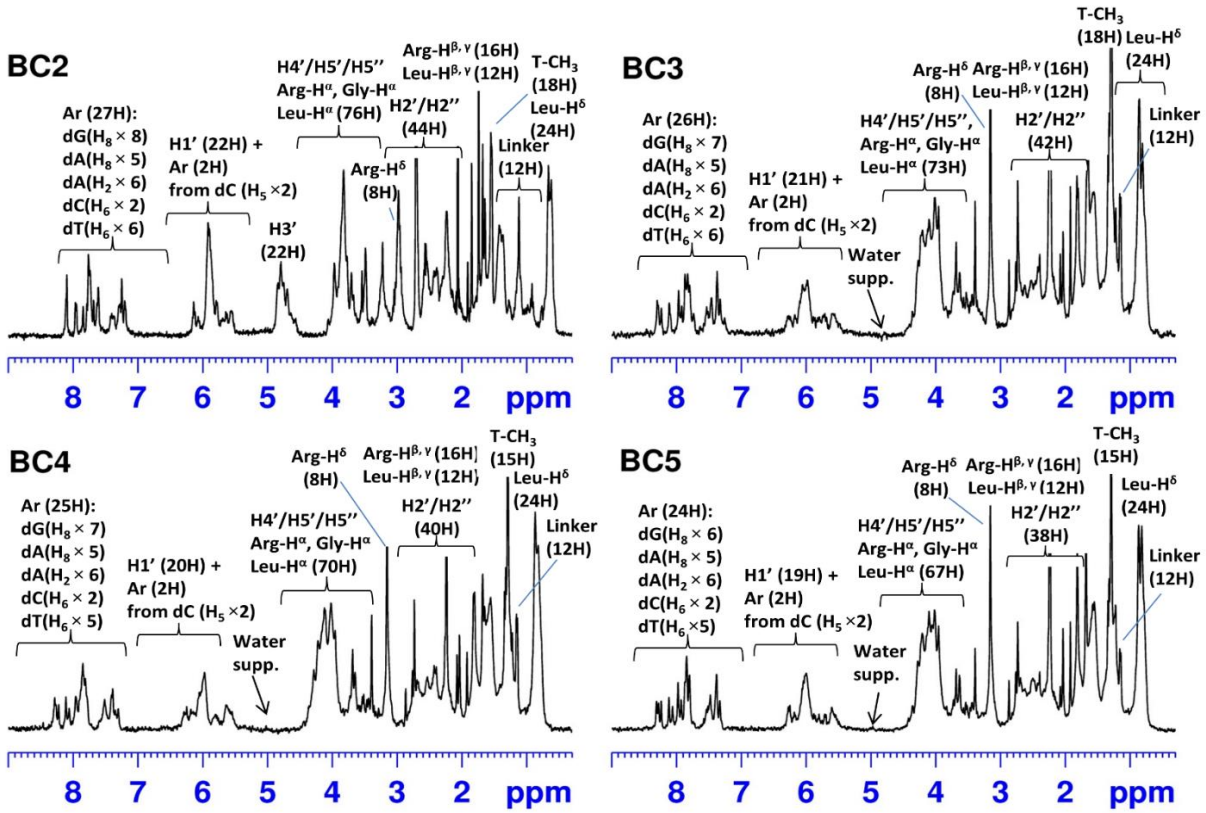

Figure 2.18. ^{1}H-NMR spectra of bulge conjugates BC2 – BC5 showing the characteristic resonance areas of the oligonucleotide protons, peptide protons, aminohexyl linker and acetyl protecting group. Assignments of the key ^{1}H resonance regions along with the integral intensities for certain protons are indicated above each spectrum. Analysis of the H3' region was not carried out due to influence of water suppression (indicated as **'Water sup.'**) at 4.78 ppm. The spectra were recorded in D_2O at 25 °C using a 400 MHz NMR spectrometer (Bruker Avance II+ 400).

2.10.12 MALDI-ToF mass spectra of the peptidyl-oligonucleotide conjugates BC-α and BC-β

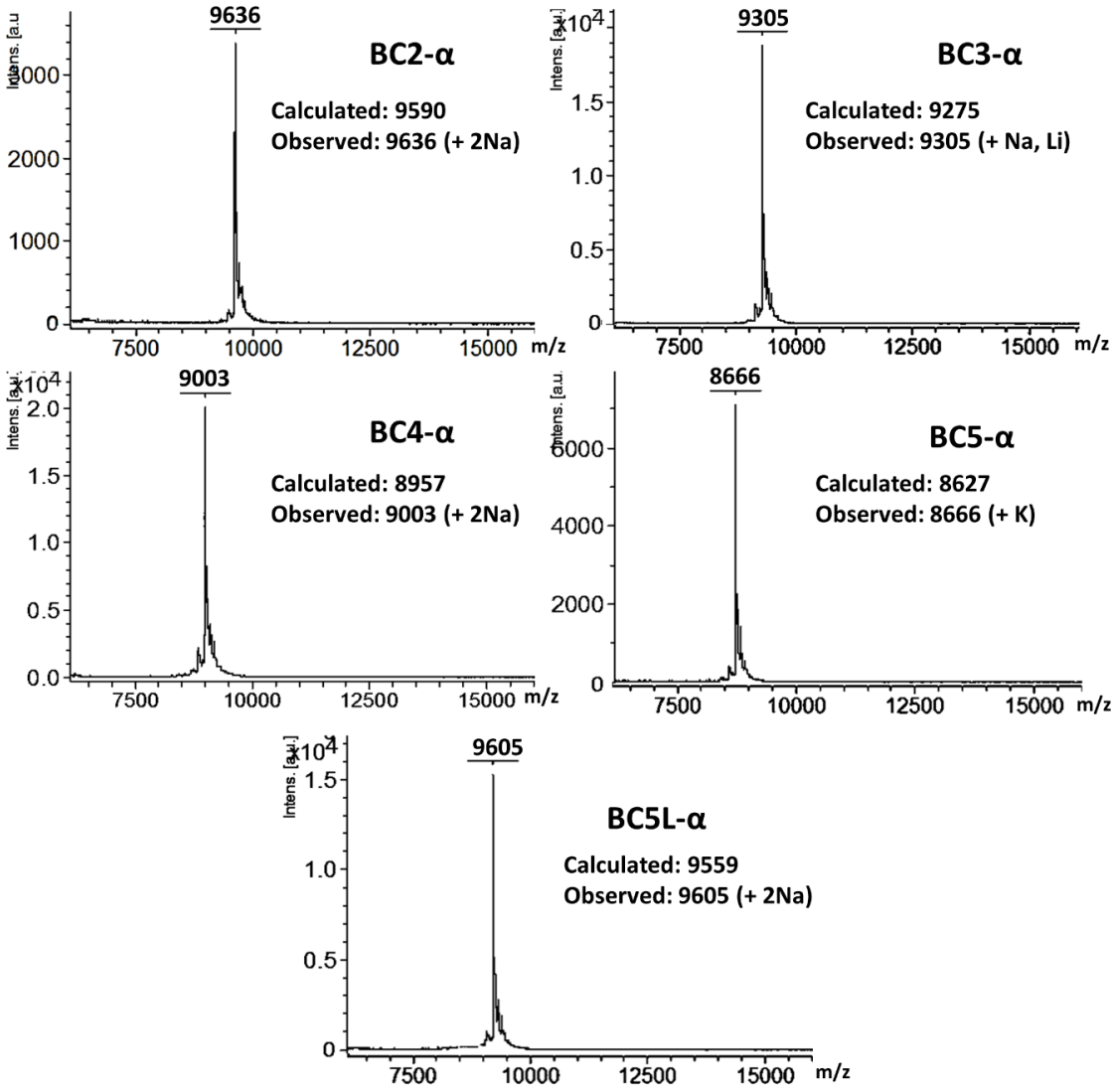

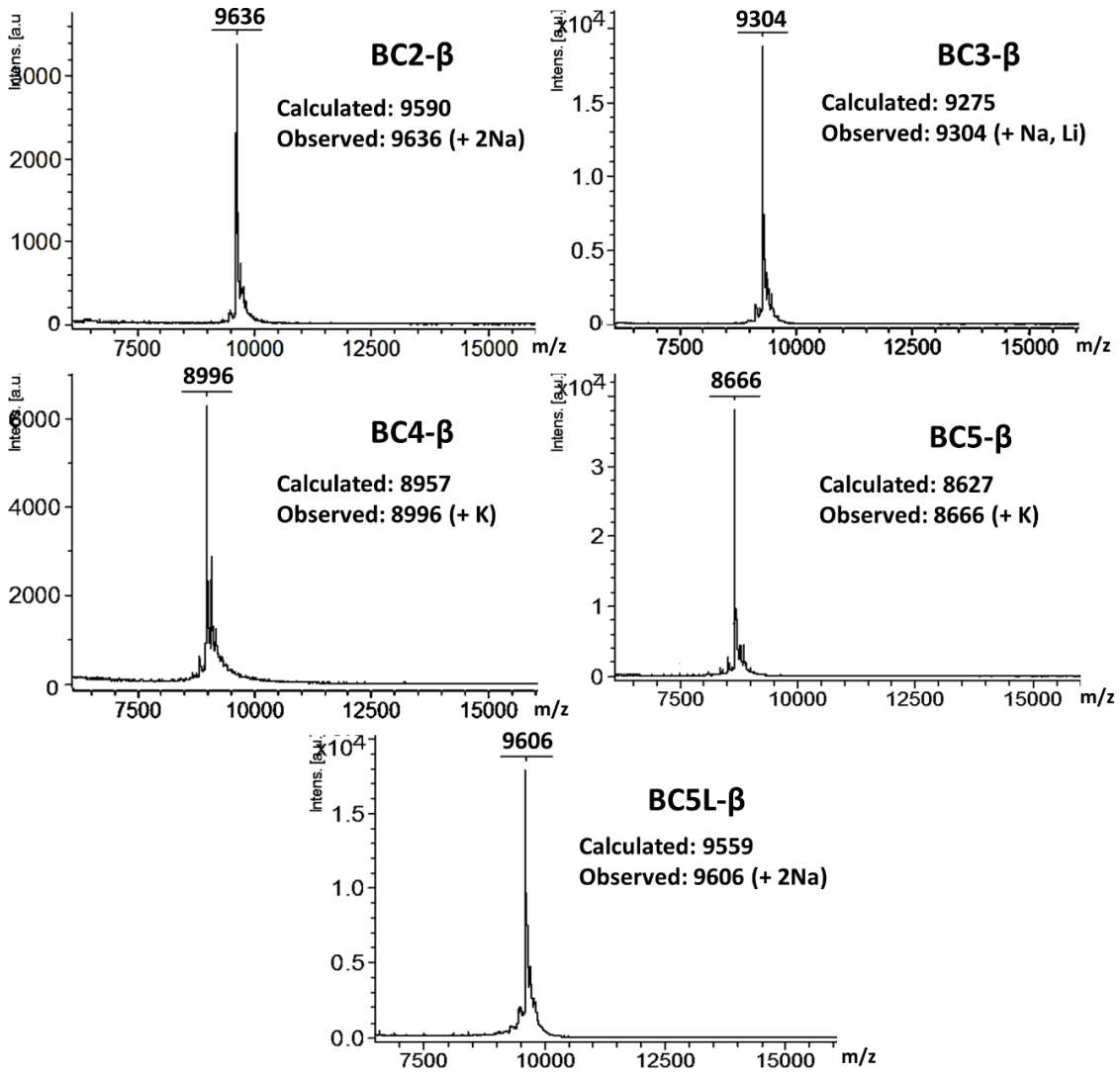

Figure 2.19. MALDI-ToF spectra of peptidyl-oligonucleotide conjugates BC-α and BC-β. Spectra were recorded using 0.7 M 3-Hydroxy picolinic acid matrix (97 mg/mL, with 0.07 M ammonium citrate, 16 mg/mL in 50:50 ACN:H_2O) on a Bruker Daltonics Ultraflex ToF/ToF mass spectrometer..

2.10.13 ^{1}H NMR spectra of the bulge-loop inducing conjugates BC-α and BC-β

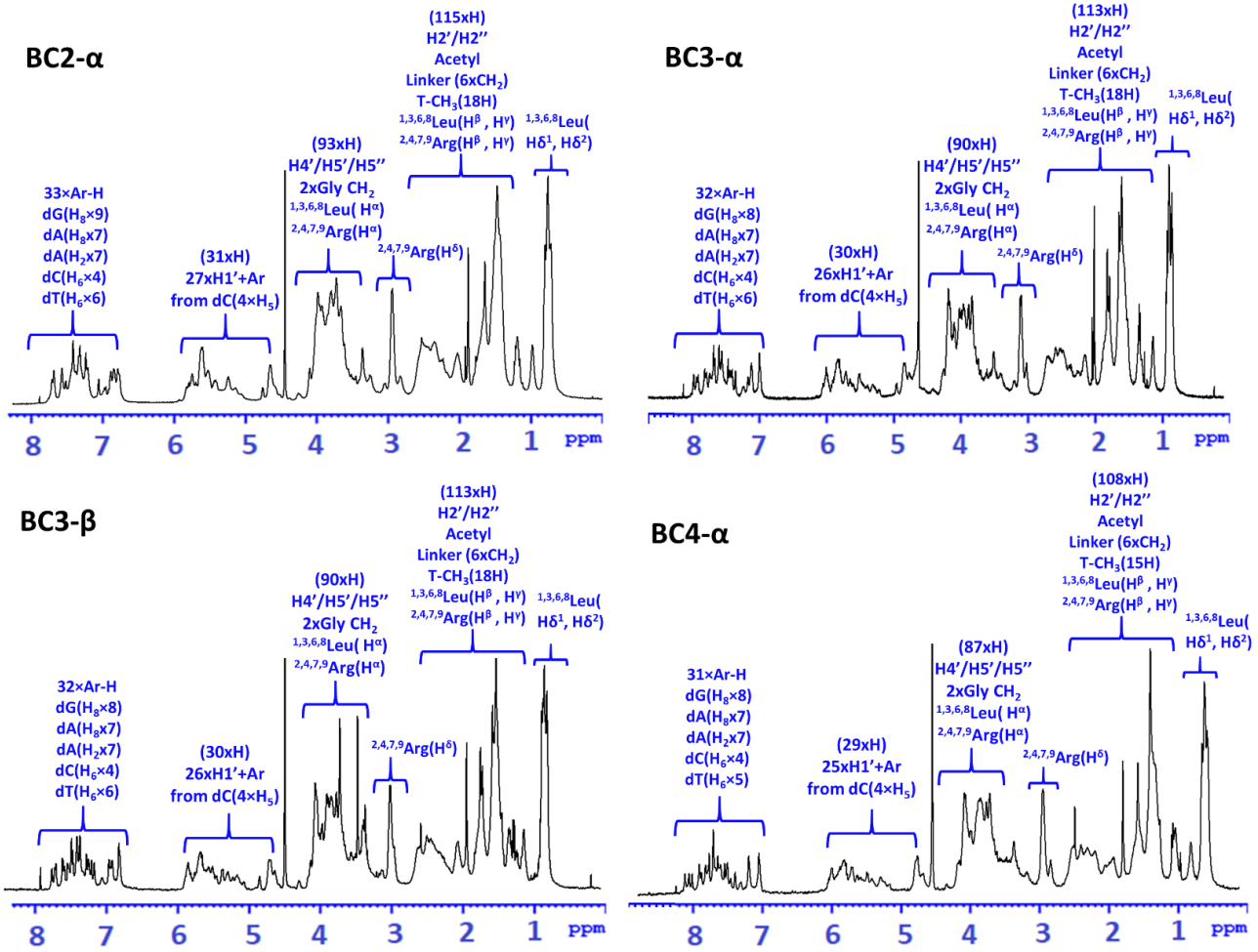

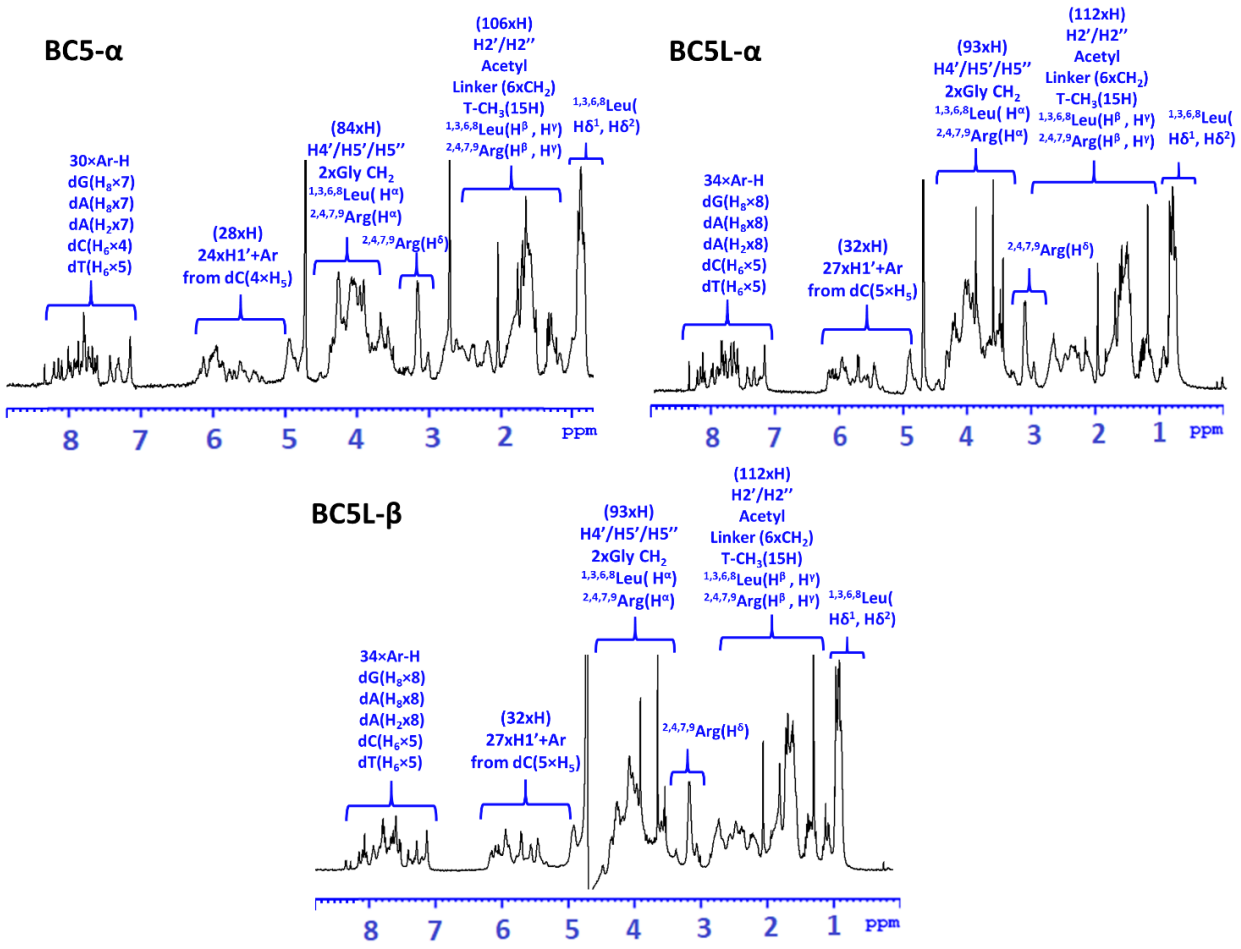

Figure 2.20. ^{1}H NMR spectra (400 MHz, Bruker Avance IIþ 400) of conjugates, BC2-α to BC5L-α along with BC3-β and BC5L-β conjugates indicating prominent chemical shift of protons from oligonucleotides, peptide, aminohexyl linker and acetyl protecting group and the similarities between α and β conjugates. In each spectrum, the breakdown of proton assignment for each region as well as integral intensity has been indicated. H3' region has not been assigned since water suppression prohibits full assignment.

2.10.14 Cleavage of 3'-FITC-tRNA^{Phe} with Type 1 conjugates (BC2-BC5)

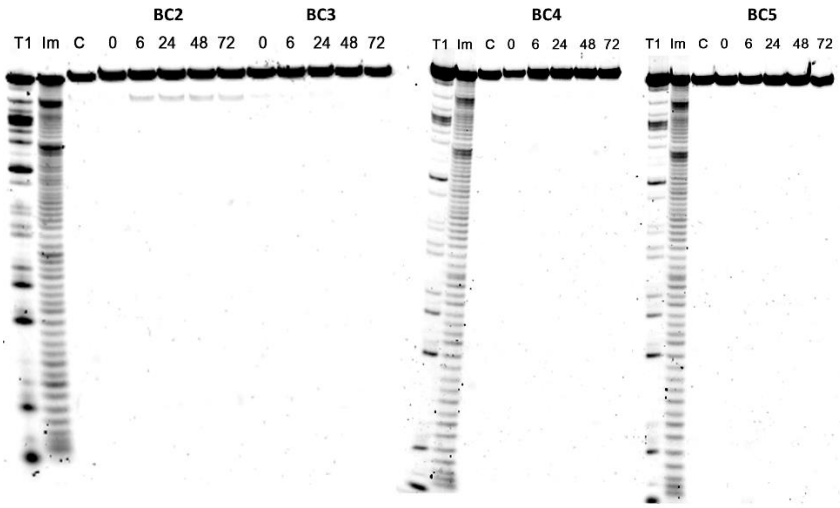

Figure 2.21. Cleavage of 3'-FITC-tRNA^{Phe} with Type 1 conjugates BC2-BC5. Representative images of 12% PAAM/8 M urea gel after electrophoresis of 3'-FITC-tRNA^{Phe} after incubation with Type 1 conjugates. 3'-FITC- tRNA^{Phe} (1 µM) was incubated with the conjugates (20 µM) in Tris buffer (50 mM Tris-HCl pH 7.0, 0.2 M KCl, 1 mM EDTA) at 37° C. Lanes T1 and Im represent partial 3'-FITC- tRNA^{Phe} digestion with RNase T1 and imidazole, respectively. In lane C, 3'-FITC- tRNA^{Phe} was incubated without conjugates for 24 h. All Type 1 conjugates were shown to be catalytically inactive.

2.10.15 RNase H cleavage assay

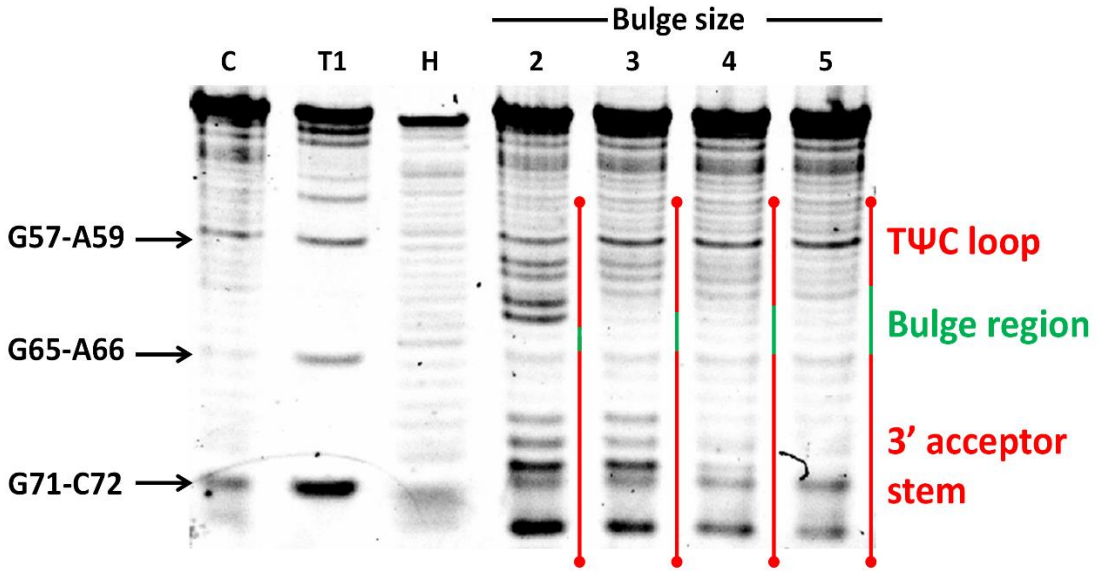

Figure 2.22. Ribonuclease H cleavage assay showing enhanced cleavage of 3'-FITC-tRNA^{Phe} when it is hybridised within the BC: 3'-FITC-tRNA^{Phe} heteroduplex (indicated by red lines). Absence of cleavage or reduced cleavage in bulge regions (green) is indicative of the presence of a single-stranded RNA bulge, which is not recognised and thus not cleaved by RNase H. 3'-FITC-tRNA^{Phe} (1 µM) was pre-incubated with BC2, BC3, BC4 or BC5 (40 µM) at 37°C for 30 minutes followed by incubation with RNase H (1U) for additional 15 minutes (lanes **2**, **3**, **4** and **5**, respectively). Lanes **T1** and **H**, partial RNA digestion with RNase T1 and hydrolysis ladder, respectively. Lane **C**, control lane containing tRNA^{Phe} in the absence of BCs. RNA cleavage

products were resolved in 12% polyacrylamide/8 M urea gel as described in the experimental section.

2.10.16 Distance distributions between guanidinium group of arginines and O2' or phosphorous atoms of the bulged nucleotides of RNA-conjugate duplex.

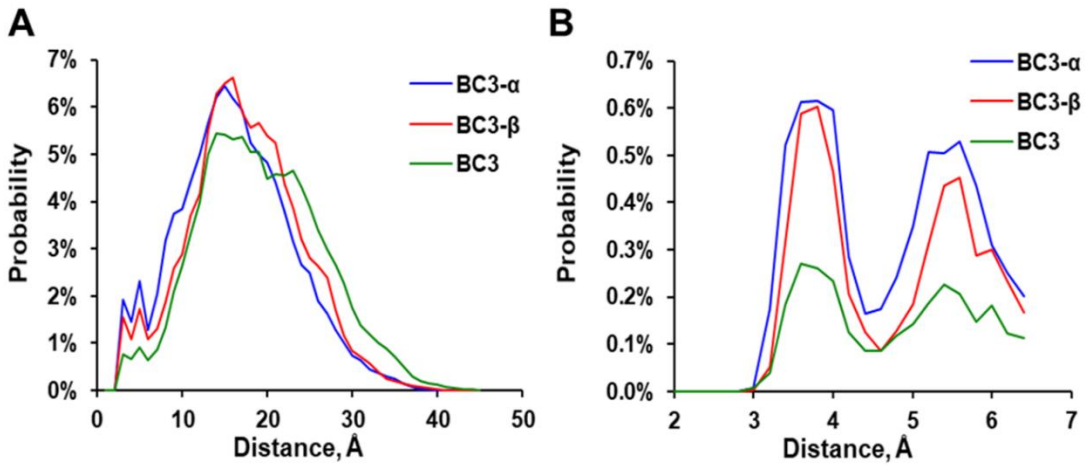

Figure 2.23. The long-range (**A**) and short-range (**B**) distance distributions between the atoms involved in RNA transesterification catalysis, measured for the hybrid complexes between RNA and BC3 (green), BC3-α (blue) and BC3-β (red). The values of all interatomic distances, including those between the two nitrogen atoms of the guanidinium groups from four arginines and O2' or phosporous atoms of the bulged nucleotide residues from the 3-nt bulge-loop regions, were averaged and normalised to the overall number of frames.

2.10.17 ZIP files (accessible via NAR website)

Clusters.zip: Rotating images of the structural clusters of:

(a) Type 1 conjugates (**BC3.mp4**)

(b) Type 2 conjugates, BC3-alfa anomer (**BC3-alfa.mp4**)

(c) Type 2 conjugates, BC3-beta anomer (**BC3-beta.mp4**)

In-Line Structures.zip:

(1) Rotating images of the representative *"in-line"* conformations of BC3-alfa and BC3-beta anomers:

(a) BC3- alfa_in-line_OVERALL.mp4

(b) BC3-alfa_in-line_ZOOMED.mp4

(c) BC3- beta_in-line_OVERALL.mp4

(d) BC3-beta_in-line_ZOOMED.mp4

BC3-alfa_in-line_OVERALL.mp4 and **BC3-alfa_in-line_OVERALL.mp4** show the whole structures of the calculated complexes obtained from MD simulations. **BC3-alfa_in-line_ZOOMED.mp4** and **BC3-beta_in-line_ZOOMED.mp4** show only the main players involved in the *"in-line attack"*, including two arginines of the catalytic

peptide and the key residues of the RNA cleavage site (i.e. cytidine residue including the aromatic ring, ribose and phosphate group).

(2) PDB files of the hybridised complexes between RNA and BC3-alfa and BC3-alfa anomers:

(e) BC3-alfa.PDB

(f) BC3-beta.PDB

Chapter 3

"*Bind, cleave and leave*": achieving multiple reaction turnover in catalytic cleavage of RNA substrates

"*Bind, cleave and leave*": achieving multiple reaction turnover in catalytic cleavage of RNA substrates

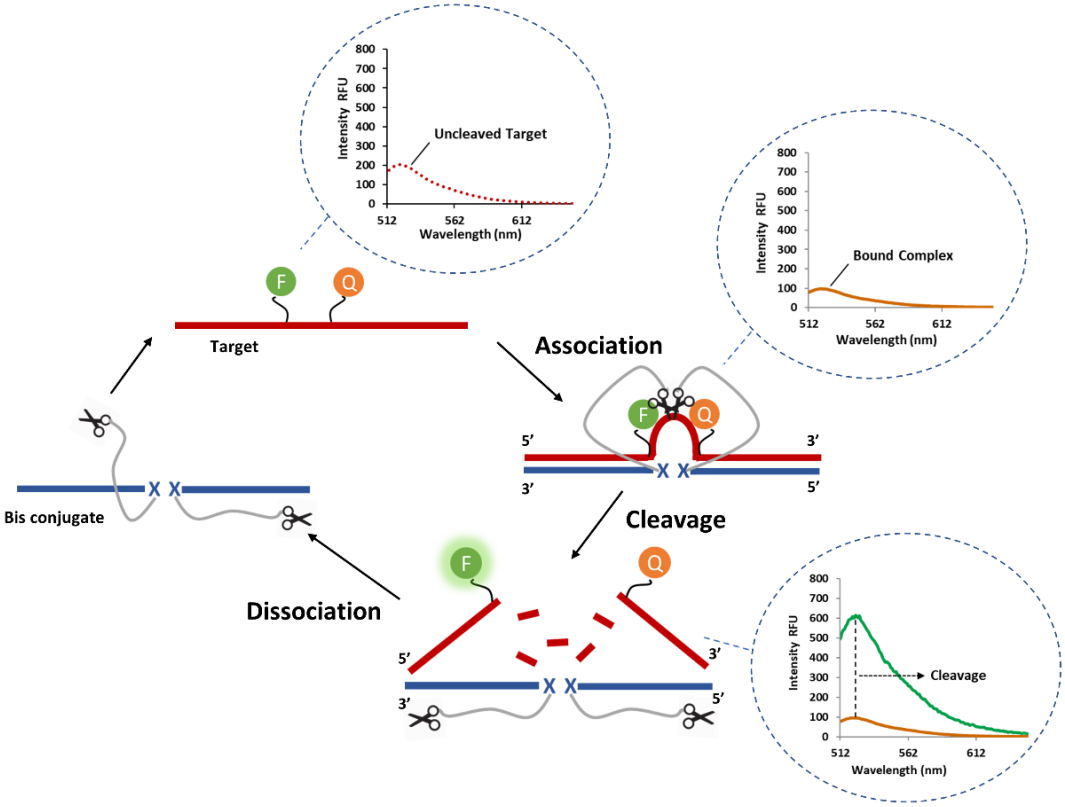

3.1 Declaration

This chapter consists of one paper awaiting submission to Nucleic Acids Research (NAR):

Bahareh Amirloo, Sameen Yousaf, Yaroslav Staroseletz, David J. Clarke, Tom Brown, Harmesh Aojula, Marina A. Zenkova, and Elena V. Bichenkova. **"***Bind, cleave and leave*": achieving multiple reaction turnover in catalytic cleavage of RNA substrates.

This paper is central to my research reported in this thesis, because the irreversible cleavage of many copies of RNA substrate by a single conjugate molecule through multiple catalytic turnover is the ultimate aim of my work. We report here how this challenging task can be achieved using our robust design platform (reported in **Chapter 2**) to produce new structural variants capable of destroying multiple RNA copies. To monitor the reaction catalytic turnover, we also developed a real-time fluorescence assay for rapid screening of RNA cleavage in multiple-turnover mode, which is presented here for the first time. This manuscript has been prepared in a format designed for journal submission, except for minor adjustments to incorporate it into this thesis.

As first author for this publication I carried out all the design, synthesis and characterisation of peptide and peptidyl-oligonucleotide conjugates. I and Sameen Yousaf developed and refined the fluorescence-based assay to monitor cleavage of the fluorescently labelled RNA and carried out fluorescent studies and data analysis. RNA binding and cleavage experiments with $tRNA^{Phe}$ using conventional electrophoresis were performed by Dr Yaroslav Staroseletz. Dr. Elena Bichenkova, Prof. Marina Zenkova and Prof. David Clarke conceived the scientific ideas. Prof. David Clarke conducted kinetic modeling analysis. I analysed the experimental data (with support and contribution from the other authors), prepared figures and drafted the manuscript with Sameen Yousaf's input. Dr. Elena Bichenkova, Prof. Marina Zenkova, Prof. David Clarke, Prof. Tom Brown and Dr. Harmesh Aojula supervised the relevant experimental work and were involved in project management, data analysis and manuscript editing at various stages.

"*Bind, cleave and leave*": achieving multiple reaction turnover in catalytic cleavage of RNA substrates

Bahareh Amirloo,[1] Sameen Yousaf,[1] Yaroslav Staroseletz,[2] David J. Clarke,[1] Tom Brown,[3] Harmesh Aojula,[1] Marina A. Zenkova,[2] and Elena V. Bichenkova[1, *]

[1] School of Health Sciences, Faculty of Biology, Medicine and Health, University of Manchester, Oxford Road, Manchester, M13 9PT, UK

[2] Institute of Chemical Biology and Fundamental Medicine SB RAS, 8 Laurentiev Avenue, 630090, Novosibirsk, RF

[3] Department of Chemistry, Chemistry Research Laboratory, University of Oxford, 12 Mansfield Road, Oxford, OX1 3TA, UK

3.2 Abstract

Sequence-specific destruction of pathogenic RNA through catalytic cleavage offers a major breakthrough in the treatment of human pathophysiology. To gain a desired therapeutic effect, the reaction catalytic turnover is critical to inactivate multiple RNA copies, which is difficult to achieve for sequence-specific RNA targeting. We overcame this challenge by engineering supramolecular assembly of biocatalysts incorporating several catalytic groups in the same molecular framework to (i) accelerate cleavage and (ii) promote multiple cuts in the target RNA thus facilitating the release of the catalyst for subsequent attacks. "*Single*", *"bis"* and *"triple"* bulge-loop inducing peptidyl-oligonucleotide conjugates comprising of one, two or three catalytic peptides linked to an RNA-recognising motif through internal abasic nucleotides were screened against fluorescently-labelled RNA model. Their potency correlated with the number of catalytic guanidinium groups. The representative conjugates showed the ability to cleave up to 10 copies of RNA present in excess, thus indicating multiple substrate turnover which can be further enhanced if the decline in active components due to substrate and conjugate self-complexation (indicated by our kinetic modelling simulations) is addressed. When tested against FITC-tRNA^{Phe}, *"bis"* and *"triple"* conjugates caused almost complete (100 %) demolition of target RNA in 24 hours through multiple sequence-specific cuts at different locations.

3.3 Introduction

RNA plays a pivotal role in controlling transformation from health to disease due to its involvement in many biological pathways, including transcriptional and translational regulation (1), epigenetic memory (2), RNA splicing (3) and retroviral replication (4). The involvement of many RNAs in the initiation and development of pathophysiology in humans (5) (cancer (6–8), inflammation (9), neurodegeneration (10, 11) or persistent intracellular infections (12)) sparks rapidly growing interest in sequence-specific targeting of disease-relevant RNAs (e.g. messenger RNA transcripts encoding pathogenic proteins, non-coding RNAs involved in cellular signalling pathways, or viral genomic RNAs).

Knockdown of gene expression via RNA silencing is widely used to study complex biological processes (13, 14) including disease origin, initiation and progression. More importantly, success here may facilitate the development of a new class of therapeutic interventions (15–17) to confront diseases "*upstream*" by targeting their genomic origin, thus leading to precise molecular destruction of pathogenic RNAs before they are translated into disease. The existing methods for RNA silencing, such as CRISPR, siRNAs and antisense oligonucleotides (ASO) (18–21), suffer from the inherent limitations, which may produce conflicting results, particularly as the level of biological complexity increases. Fundamentally, they all rely on the recruitment of intracellular enzyme complexes (Cas proteins for CRISPR, RISC complexes for siRNA and RNase H for ASOs) and other endogenous cofactors, whose levels fluctuate within and between cell types. The biological cascade triggered by siRNA is complex, which can initiate the activation of the innate immune response (19) and lead to high levels of off-target effects (18), detrimental both for therapeutic applications and functional screening. Saturation of cellular machinery and the subsequent interference with miRNA-mediated gene regulation raises concerns for clinical applications of siRNA in humans (22), although the first siRNA drug (Patisiran) has recently been approved by FDA for the treatment of polyneuropathy. CRISPR was mainly developed for DNA editing and is only recently reported for RNA editing (23). Moreover, very recently, alarming off-target effects have been observed (24). More developed and simpler ASO-mediated mRNA knockdown relies upon the rate-limiting availability of RNase H1 in the cytosol and nucleus, which varies considerably within and between different cell types (25), thus creating highly variable therapeutic responses (26, 27).

Recently discovered peptidyl-oligonucleotide conjugates (28–36) capable of cleaving functional or regulatory RNA sequences without the assistance of additional enzymes (to catalyse cleavage) and a guide RNA or DNA strand (for target recognition) offer a transformational solution to potent and fully autonomous posttranscriptional gene silencing. They can be produced through post-synthetic chemical conjugation of the RNA recognition motifs (antisense oligonucleotides) and the cleaving constructs (catalytic peptides) to provide an *"all in one"* attribute within the same molecular scaffold, so that the generated hybrid can recognise the target RNA, bind and destroy it without the necessity to rely on any "external" guidance and enzyme-mediated cleavage. The catalytic activity of such peptidyl-oligonucleotide conjugates is provided by a short amphiphilic peptide (31–33, 36), which contains alternating basic (arginine) and hydrophobic (leucine) amino acids. Arginine guanidinium groups, which are the key players in promoting catalysis (31, 32), appear to act as proton shuttles (37) through various tautomeric forms by facilitating the proton transfer between the attacking 2´-OH, non-bridging phosphate oxygen and departing 5´-O group. The merger of the recognising and catalytic functionalities into the same catalyst structure evades the complexities of existing gene-editing and RNA silencing approaches, which require Cas9 (for CRISPR), RISC (for siRNA), RNase H (for antisense), endogenous cofactors or exogenous agents (e.g. metal ions). The initial model structures (28–30, 34) have now progressed into biologically-active conjugates (31–33, 35) capable of inhibiting malignant growth in tumour models (33, 36), thus providing confidence that irreversible cleavage of biologically-significant or regulatory RNAs by such chemically-engineered conjugates may allow cellular pathways to be switched from *"diseased"* to "*normal"* to achieve desired therapeutic effect.

Hitherto, the developed peptidyl-oligonucleotide conjugates showed the ability to cleave RNA at two different extremes: (1) either sequence-specifically (31–33, 38) by site-directed cleavage of the regions adjacent to the RNA binding sites, but failing in catalytic turnover; or (2) non-specifically at non-complementary regions, which are located distantly from the major RNA binding region, but with a high level of catalytic turnover (29, 30, 34). Neither of these two extremes can satisfy the criteria essential for translation of these catalytic agents into successful therapeutics. Extreme (1) suffers from a relatively low potency and will therefore require high dosage administration, thus leading to possible side effects and high cost of treatment, whereas extreme (2) suffers from lack of selectivity towards the RNA target and could trigger off-target effects and systemic

toxicity in humans. Combining these two currently "conflicting" extremes in a single molecule is the challenge here. Indeed, precise sequence-specific recognition of the target, which is essential to avoid drug toxicity, apparently opposes the ability of the conjugate to leave RNA after each cleavage event and achieve the high level of catalytic turnover necessary for a potent drug. If however such challenge is addressed, this would open up a powerful opportunity to generate highly controllable, self-reliant RNA-specific chemical agents that combine absolute sequence-specificity with a high level of catalytic turnover and can operate fully autonomously from cellular machinery, which is often difficult to predict or control.

We paved our way to success here through our recent development of a series of bulge-loop inducing peptidyl-oligonucleotide conjugates that were able to hybridise to the target $tRNA^{Phe}$ in a sequence-specific manner and cut it at multiple positions (39). To achieve that, we designed the sequences of the conjugate recognition motifs in such a way that a short region (2nt – 5nt) in the middle of the target RNA sequence was not complementary, thus forcing the RNA to adopt a bulge-loop (B-L) structure upon hybridisation. By incorporating a single stretch of the catalytic peptide in the middle of the conjugate sequence we were able to control its location in such a way to juxtapose the induced RNA bulge-loop, which then became fully exposed for catalytic cleavage. As expected, the induced single-stranded B-L became highly susceptible to cleavage by an RNA cleaving peptide, when the size of the bulge-loop region exceeded 2nt residues. Interestingly, the flexibly anchored catalytic peptide was able to cleave the target $tRNA^{Phe}$ at multiple positions, including both closely located bulge-loops and distantly located regions, thus leading to almost complete (up to 90%) demolition of $tRNA^{Phe}$ in 48 hours.

By learning from the success and failure of these structurally diverse *"single"* bulge-loop inducing conjugates (39) and from their structural properties determined by molecular dynamics simulations, we aim here to improve potency and achieve reaction catalytic turnover in RNA cleavage through the incorporation of several catalytic peptides into the same conjugate scaffold (see **Figure 3.1** (**A**) for the concept). Since the transesterification of the RNA backbone is catalysed by the synchronised catalytic action of two guanidinium groups present in the same molecular scaffold through the formation of guanidine-guanidinium dyad (**Figure 3.1** (**B**)) (40), the incorporation of two or three peptides into the conjugate structure is expected to (i) increase the number of potential cleavage points in the RNA and (ii) enhance the probability of forming guanidine-guanidinium dyads, thus improving cleavage frequency and overall potency. We

hypothesise here that multiple cuts generated in the RNA strand will reduce the size of the cleaved products and facilitate collapse of the complex to achieve a catalytic *"bind, cleave and leave"* mode. To test this hypothesis, we shall apply our *in-house* developed real-time fluorescence assay using fluorescently labelled linear RNA target for rapid screening of cleavage of "*single*", *"bis"* and *"triple"* conjugates, both in a single-turnover and multiple-turnover modes, followed by comprehensive kinetics analysis. Finally, we shall test the catalytic performance of the newly developed *"bis"* and *"triple"* bulge-inducing conjugates against $tRNA^{Phe}$ and compare their activity with the "*single*" conjugate counterparts studied earlier (39).

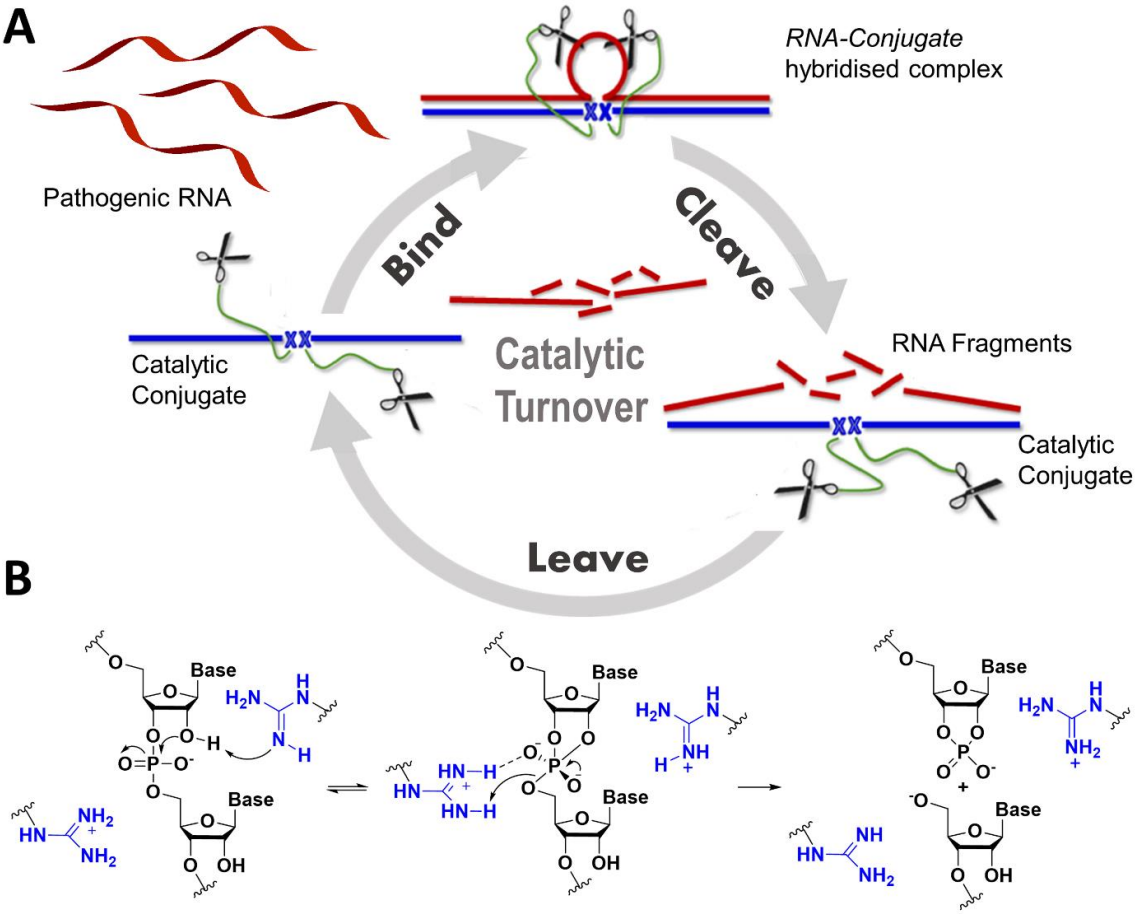

Figure 3.1. (**A**) Postulated cleavage cycle of "smart" catalytic conjugate cleaving multiple copies of the target RNA molecule. Multiple reaction turnover of RNA substrates requires a rapid release of the cleaved fragments after each cleavage event to liberate catalytic conjugates from the hybridised complexes and allow them to attack the next RNA target. (**B**) Hypothetical mechanism of phosphodiester bond cleavage catalysed by the arginine guanidinium groups of the amphiphilic peptide. The synchronised action of two guanidinium groups through formation of *guanidine-guanidinium* dyad facilitates the proton transfer between the attacking 2´-OH, non-bridging phosphate oxygen and departing 5´-O group (adapted from (40)). A neutral guanidine group (acting as a general base) deprotonate the 2'-OH group of RNA ribose leading to the formation of a di-anionic pentaoxyphosphorane intermediate, while the protonated (positively-charged) guanidinium moiety coordinates the negatively-charged phosphate group through an electrostatic interaction and acts as an electrophilic activator, thus facilitating the transesterification reaction.

3.4 Materials and Methods

3.4.1 Chemical, reagents, equipment and facilities

The peptide Ac-Leu-Arg-Leu-Arg-Gly-Leu-Arg-Leu-Arg-Gly (Ac-$[LRLRG]_2$-CO_2H) was purchased from Biomatik (Cambridge, Ontario, Canada). Modified oligonucleotide sequences containing two or more internal abasic nucleotides with aminohexyl linker attached at C1' position in α or β configuration were purchased from ATDBio Ltd (Southampton, UK). Alpha and beta aminohexyl amidate monomers were purchased from Link Technologies Ltd (Scotland, UK). Fluorescently labelled linear perfect-match target **F**-**Q**-RNA ($^{5'}$GTCCTGTGTTCGA**T$_F$CC_rA$_r$C$_r$A$_r$G$_r$**AA**T$_Q$**TCGCACCA^{3}) was purchased from ATDBio Ltd (Southampton, UK). The scrambled conjugate (5'-luc-h-9/1: $^{5'}$CAAGTCTCGTATGTGTCAGCGAAAGCTGAC$^{3'}$ (with the underlined font representing the hairpin)), which was used here as a control for sequence-specificity of RNA cleavage, was synthesised following the previously reported protocol (33). The unconjugated oligonucleotide for the scrambled conjugate was acquired from the Institute of Chemical Biology and Fundamental Medicine (Novosibirsk, Russian Federation).

All chemicals and solvents were purchased from Sigma-Aldrich (UK) unless otherwise stated. Water was purified in-house via a Milli-Q purification system (Millipore, USA). Reversed-phase HPLC purification of synthesised peptide and conjugates were carried out on PerkinElmer (Series 200, ACE 10 C4 250 × 21.2 mm, MA, US) and Agilent 1100 HPLC system (Agilent Technologies, Santa Clara, CA) equipped with a diode array detector and Rheodyne (3725i) manual injector on a semi-preparative Phenomenex Luna C-18 column (5 μm, 4.6 × 10 x 250 mm, 100 A, Phenomenex; CA, USA) respectively. NAP disposable columns prepacked with Sephadex G-25 DNA grade purchased from GE Healthcare Life Sciences were used to desalt peptidyl-oligonucleotide conjugates. Oligonucleotide concentrations were calculated using absorbance at 260 nm wavelength recorded via a UV-Vis spectrophotometer (Varian Cary 4000 dual beam; Australia) and extinction coefficients (see **Supplementary Table 3.2**).^{1}H NMR spectra were recorded using Bruker Avance II+ spectrometers operating at proton frequencies of 400 MHz using BBI ^{1}H/D-BB Z-GRD Z8202/0347 probe. Bruker software Topspin 4.0.3 was used for data processing. MALDI (matrix-assisted laser desorption ionisation) mass spectra were collected on a Bruker Dal-tonics Ultraflex TOF/TOF mass spectrometer (MA, USA) at the Manchester Interdisciplinary Biocentre, University of Manchester.

The analytical data presenting the full characterisation of the generated peptides and peptidyl-oligonucleotide conjugates are given in the Supplementary Information (see **Supplementary Figures 3.12 -3.20**).

3.4.2 Peptide synthesis, purification and characterisation

Ac-Leu-Arg-Leu-Arg-Leu-Arg-Gly (Ac-$[LR]_3G$) was synthesised manually using solid-phase peptide synthesis on Boc-Gly-PAM resin (211 mg, 0.148 mmol). Boc protective group was removed by the addition of 50% trifluoroacetic acid in dichloromethane (1:1, TFA: DCM) solution (2×15 mL for 2 and 5 minutes). The resin was subsequently washed with DCM (4×15 mL) and neutralised with 5% DIPEA in DCM. Before each coupling reaction, the resin washings were carried out with DCM (3×15 mL) and DMF (1×15 mL). The amino acid coupling reactions were achieved by pre-activating either Boc-Arg(Tos)-OH (193 mg, 0.45 mmol); or Boc-Leu-OH (104 mg, 0.45 mmol) in DMF (10 mL) with DIPEA (174 mg, 1.35 mmol) and HBTU (171 mg, 0.45 mmol). The coupling reaction proceeded for 45 minutes at room temperature under mechanical shaking. Following synthesis, N-terminus was acetylated through the addition of acetic anhydride (1.80 mmol) with DIPEA (1.80 mmol) in DMF (15 mL). The peptide was cleaved from the resin by shaking in an HF reactor equipped with a PTFE stirrer bar with p-cresol (0.75 g) and thiocresol (0.25 g) for 3 hours at room temperature. The crude peptide was precipitated in cold diethyl ether (2×30 mL) and separated through filtration. Once air-dried, the pellet was suspended in 10% acetic acid and 80% acetonitrile/0.1% TFA and freeze-dried.

The synthesised crude peptide was dissolved in 30% acetic acid and purified by reversed-phase (RP) HPLC (ACE 10 C4 250 × 21.2 mm, PerkinElmer Series 200, MA US) using 0.1% TFA in HPLC-grade water (eluent A) and 0.1% TFA in acetonitrile (eluent B) with a linear gradient of B (0-100 %) in 45 min at a flow rate of 8 ml/min. Following purification, the peptide was characterised using ^{1}H NMR spectroscopy (Bruker Avance II+ NMR spectrometer, operating at proton frequencies of 400 MHz) and MASS spectrometry (MALDI-ToF/ToF, spectra collected on Bruker Daltonics Ultraflex II mass spectrometer (MA, USA)). Analytical data for Acetyl-$[LRLRG]_2$-CO_2H peptide acquired from mass spectrometry and ^{1}H NMR has been previously reported in (39). MALDI-TOF and ^{1}H NMR spectra for Acetyl-$[LRLRG]_2$-CO_2H peptide can be seen in **Supplementary information** (see **Figure 3.12** and **Figure 3.13**).

Acetyl-[LR]$_3$G-CO$_2$H. MALDI-TOF-MS: *m/z* = 926 $[M+H]^+$, (MW = 925 calcd. for $[C_{40}H_{76}N_{16}O_9]$) (**Supplementary Figure 3.14**). ^{1}H-NMR (**Supplementary Figure 3.15**) (400MHz, D2O, 25°C, 0.35 mM TSP): δ 0.86-0.94 (m, 18H, Leu-H$^{\delta}$), 1.49-1.94 (m, 21H, 6 × Arg-H$^{\beta}$, 6 × Arg-H$^{\gamma}$, 6×Leu-H$^{\beta}$, 3 × Leu-H$^{\gamma}$), 2.02 (s, 3H, CH_3), 3.21 (m, 6H, Arg-H$^{\delta}$), 3.84-4.37 (m, 8H, 2 × Gly-H, 6 × Leu/Arg-H$^{\alpha}$).

3.4.3 Conjugate synthesis

Water-soluble lithium salt of oligonucleotide containing two or three abasic nucleotides was converted to cetyltrimethylammonium (CTAB) salt (50 nmol) soluble in DMSO through dropwise addition of 4% (w/v) cetyltrimethylammonium bromide solution following the previously described protocol (39). The conjugation reaction was conducted in accordance with the protocol described in Ref (39). The protocol was amended to accommodate higher excess of peptide over oligonucleotide where dried peptide dissolved in DMSO (100-fold excess, 5 μmol) was pre-activated using 4-Dimethylaminopyridine (DMAP) and N, N'-dicyclohexylcarbodiimide (DCC) (1.5-fold excess over peptide each, 7.5 μmol each). The resulting reaction mixture was incubated at 60°C for 24 hours. The conjugate along with unreacted starting oligonucleotide were precipitated in 4% $LiClO_4$ in acetone (1.8 mL) for 36 hours as described in Ref (39). Following the removal of excess reagent using size-exclusion chromatography, RP-HPLC was employed for final purification (see **Supporting Figure 3.16** for synthetic route). In instances where different amounts of the oligonucleotide were used, the concentration of the peptide, DMAP and DCC were re-scaled accordingly to maintain the consistent molar ratios.

3.4.4 Conjugate purification and characterisation

Crude conjugates were purified using RP-HPLC. Eluents used included 0.05 M $LiClO_4$ in water as eluent A and 0.05M $LiClO_4$ in acetonitrile as eluent B with 2.0 mL/min flow rate. The absorbance was monitored at 260 nm and the following gradient was applied: 0% B for 3 minutes, 0-100% B in 30 minutes. The identity and purity of conjugates were confirmed by RP-HPLC, ^{1}H NMR spectroscopy and mass spectrometry.

BC5-L-ββ. RP-HPLC fraction at 28 minutes was collected, combined and lyophilised to give a white powder (17 nmol, 34%) (**Supplementary Figure 3.17**). The excess salt was removed by size-exclusion chromatography using NAP disposable columns. MALDI-MS: *m/z* = 11189 $[M+Na]^+$ (MW = 11166 calcd. For $[C_{385}H_{563}N_{151}O_{187}P_{28}]$ (**Supplementary Figure 3.18**).^{1}H NMR (**Supplementary Figure 3.19** and **Figure 3.20**)

(D_2O with TSP (0.01 mM), 400 MHz): δ 0.79-0.86 (m, 48H, Leu- H^{δ}), 1.16-2.22 (m, 147H, 28×H2' and 28×H2'' sugar ring protons, 5×CH_3 of 5×dT, 16× Arg-H^{β}, 16×Arg-H^{γ}, 16×Leu-H^{β}, 8×Leu-H^{γ}, 12×CH_2 (two aminohexyl linker), 2×Acetyl-CH_3), 3.16 (m, 16H, 16×Arg-H^{δ}), 3.66-4.41 (m,108H, 84×H4'/H5'H5" sugar ring protons, 4×Gly- CH_2, 16×Leu/Arg-H^{α}), 4.99-6.27 (m, 33H, 28×H1' sugar ring protons, 5×H5 of dC), 7.23-8.47 (m, 34H, 34×Ar-H from dG(H8×8), dA(H8×8), dA(H2×8), dC(H6×5) and dT(H6×5)). H3' sugar ring protons (3.6-4.4 ppm) were not analysed due to suppression of residual water signal at 4.10 ppm.

BC5-L-αα. RP-HPLC fraction at 28 minutes was collected, combined and lyophilised to give a white powder (16 nmol, 32%) (**Supplementary Figure 3.17)**. The excess salt was removed by size-exclusion chromatography using NAP disposable columns. MALDI-MS: *m/z* = 11190 $[M+Na+H]^+$ (MW = 11166 calcd. For $[C_{385}H_{563}N_{151}O_{187}P_{28}]$) (**Supplementary Figure 3.18**).^{1}H NMR (**Supplementary Figure 3.19**) (D_2O with TSP (0.01 mM), 400 MHz): δ 0.78-0.85 (m, 48H, Leu- H^{δ}), 1.15-2.43 (m, 147H, 28×H2' and 28×H2'' sugar ring protons, 5×CH_3 of 5×dT, 16× Arg-H^{β}, 16×Arg-H^{γ}, 16×Leu-H^{β}, 8×Leu-H^{γ}, 12×CH_2 (two aminohexyl linker), 2×Acetyl-CH_3), 3.17 (m, 16H, 16×Arg-H^{δ}), 3.57-4.35 (m,108H, 84×H4'/H5'H5" sugar ring protons, 4×Gly- CH_2, 16 × Leu/Arg-H^{α}), 4.96-6.25 (m, 33H, 28×H1' sugar ring protons, 5×H5 of dC), 7.25-8.46 (m, 34H, 34×Ar-H from dG(H8×8), dA(H8×8), dA(H2×8), dC(H6×5) and dT(H6×5)). H3' sugar ring protons (3.6-4.4 ppm) were not analysed due to suppression of residual water signal at 4.12 ppm.

BC5-L-βα. RP-HPLC fraction at 28 minutes was collected, combined and lyophilised to give a white powder (19 nmol, 38%) **(Supplementary Figure 3.17)**. The excess salt was removed by size-exclusion chromatography using NAP disposable columns. MALDI-MS: *m/z* = 11189 $[M+Na]^+$ (MW = 11166 calcd. For $[C_{385}H_{563}N_{151}O_{187}P_{28}]$) (**Supplementary Figure 3.18)**. ^{1}H NMR (**Supplementary Figure 3.19**) (D_2O with TSP (0.01 mM), 400 MHz): δ 0.79-0.86 (m, 48H, Leu- H^{δ}), 1.13-2.38 (m, 147H, 28×H2' and 28×H2'' sugar ring protons, 5×CH_3 of 5×dT, 16× Arg-H^{β}, 16×Arg-H^{γ}, 16×Leu-H^{β}, 8×Leu-H^{γ}, 12×CH_2 (two aminohexyl linker), 2×Acetyl-CH_3), 3.17 (m, 16H, 16×Arg-H^{δ}), 3.51-4.45 (m,108H, 84×H4'/H5'H5" sugar ring protons, 4×Gly- CH_2, 16 ×Leu/Arg-H^{α}), 4.95-6.32 (m, 33H, 28×H1' sugar ring protons, 5×H5 of dC), 7.25-8.50 (m, 34H, 34×Ar-H from dG(H8×8), dA(H8×8), dA(H2×8), dC(H6×5) and dT(H6×5)). H3' sugar ring protons (3.6-4.4 ppm) were not analysed due to suppression of residual water signal at 4.10 ppm.

BC5-L-βββ. RP-HPLC fraction at 30 minutes was collected, combined and lyophilised to give a white powder (16 nmol, 32%) **(Supplementary Figure 3.17)**. The excess salt was removed by size-exclusion chromatography using NAP disposable columns. MALDI-MS: *m/z* = 11736 $[M+Na]^+$ (MW = 11713 calcd. For $[C_{409}H_{609}N_{156}O_{194}P_{29}]$) (**Supplementary Figure 3.18**).^{1}H NMR (**Supplementary Figure 3.19** and **Figure 3.20**) (D_2O with TSP (0.01 mM), 400 MHz): δ 0.78-0.88 (m, 54H, Leu- H^{δ}), 1.91-2.39 (m, 181H, 29×H2' and 29×H2'' sugar ring protons, 5×CH_3 of 5×dT, 18× Arg-H^{β}, 18×Arg-H^{γ}, 18×Leu-H^{β}, 9×Leu-H^{γ}, 18×CH_2 (three aminohexyl linker), 3×Acetyl-CH_3), 3.17 (m, 18H, 18×Arg-H^{δ}), 3.62-4.33 (m,111H, 87×H4'/H5'H5" sugar ring protons, 3×Gly- CH_2, 18× Leu/Arg-H^{α}), 5.03-6.35 (m, 34H, 29×H1' sugar ring protons, 5×H5 of dC), 7.25-8.47 (m, 34H, 34×Ar-H from dG(H8×8), dA(H8×8), dA(H2×8), dC(H6×5) and dT(H6×5)). H3' sugar ring protons (3.6-4.4 ppm) were not analysed due to suppression of residual water signal at 4.27 ppm.

3.4.5 Fluorescence-based ribonuclease activity assay

The reaction mixture (100 μL) containing labelled perfect-match linear target RNA (**F-Q**-RNA) (1μM) with internal Fluorescein **(F)** and Dabcyl quencher **(Q)** deoxythymidine residues and one of the POC conjugates (20 μM), was incubated at 37ºC for 96 hours in Tris-buffer (50 mM Tris−HCl pH 7.0, 0.2 mM KCl, and 1 mM EDTA). Aliquots (10 μL) were taken at regular time points (0, 24, 48, 72 and 96 hours) from the reaction mixture. Subsequently, the extent of cleavage was assessed by the increase in fluorescence at λ_{em} of 522 nm (following excitation at 496 nm) at 37 ºC in microwell plates using a Tecan Safire plate reader operated under Magellan Data Analysis Software (V.7). The combined effects of dilution (10-fold) and elevated temperature (80º C) was employed to facilitate the complete dissociation of the cleaved RNA fragments from the conjugate. As a control, the target was incubated in the presence and absence of unconjugated oligonucleotide and parallel measurements were conducted to rule out spontaneous cleavage. In addition, the target was incubated with a non-complementary scrambled conjugate (5'-luc-h-9/14) (33) to assess the possibility of non-sequence specific cleavage. The percentage of cleavage catalysed by each conjugate was measured against the complete (100%) cleavage of the same **F-Q**-RNA target achieved by RNase A (20 nM) in a parallel experiment.

3.4.6 Catalytic turnover

The reaction catalytic turnover was assessed using three selected conjugates (BC5-α, BC5-L-β or BC5-L-ββ) against fluorescently labelled **F-Q**-RNA target present at 2-fold,

5-fold, 10-fold, 20-fold and 30-fold molar excess over the corresponding conjugate. The reaction mixture (100 μL) containing 10 μM, 25 μM, 50 μM, 100 μM or 150 μM labelled linear **F**-**Q**-RNA target was incubated at 37°C with either 5-nt long bulge-loop inducing "*single*" conjugate (BC5-α or BC5-L-β) or one of the most active *"bis"* conjugates (BC5-L-ββ) at a concentration of 5 μM in the Tris buffer (50 mM Tris−HCl pH 7.0, 0.2 mM KCl, and 1 mM EDTA) for 96 hours. At different time points (0, 24, 48, 72 and 96 hours), aliquots (10 μL) were taken from the reaction mixture. To measure the true percentage of cleavage and minimise the presence of hybridised complex, the solution was diluted (10×) and subjected to high temperature (80° C for 3 min). The extent of cleavage was assessed in microwell plates by measuring fluorescence at λ_{em} of 522 nm (following excitation at 496 nm) at 37 ºC using Tecan Safire plate reader as described above. The extent of **F**-**Q**-RNA target cleavage by individual conjugates BC5-α, BC5-L-β or BC5-L-ββ was evaluated by measuring the increase in fluorescence intensity against that of the fully cleaved **F**-**Q**-RNA treated by RNase A (20 nM) in the parallel set of experiments. A conversion coefficient was estimated between fluorescence intensity and product concentration (or amount) to quantify the accumulation of the **F**-**Q**-RNA cleavage products upon treatment by the conjugates at different time points. The kinetic parameters K_m , V_{max} and K_{cat} were obtained from non-linear fit analysis of velocity (v_0) versus substrate [S_0] where [S_0] = [labelled linear target]. Detailed mathematical kinetic modelling is described in **Supplementary Information Section 3.8.14**.

3.4.7 Preparation of linearised plasmids and *in vitro* RNA transcripts

The detailed protocols for preparation of linearised plasmid p67YF0 and *in vitro* transcript of yeast $tRNA^{Phe}$ were reported earlier (31). Fluorescein labelling of RNA transcript (3'-end labelling with fluorescein isothiocyanate (FITC) and 5'-labeling of RNA fragments with [γ-^{32}P]ATP) was conducted in accordance to the previously described protocol (31, 41).

3.4.8 Hybridisation and cleavage of 3'-FITC $tRNA^{Phe}$ with *"bis"* and *"triple"* conjugates

The hybridisation assays and the subsequent data analysis were carried out in accordance with the previously reported protocol (31). In these experiments, 3'-FITC-$tRNA^{Phe}$ (1 μM) was incubated with one of the *"bis"* and *"triple"* conjugates (varying concentration from 1 to 20 μM).

Cleavage experiments were carried out according to the previously reported protocols (31). The reaction mixture contained 3'-FITC labelled $tRNA^{Phe}$ (1 µM, single turnover) and one of the *"bis"* and *"triple"* conjugates (either at 5 µM, 10 µM or 20 µM concentration, single turnover condition) in 50 mM Tris-HCl pH 7.0, 0.2 M KCl, 1 mM EDTA. Varying concentration of conjugate (1-20 µM) was used for concentration-dependent assay of ribonuclease activity.

3.5 Results and Discussion

3.5.1 Conjugate Design and Synthesis

Recently, we have engineered a new series of catalytically active peptidyl-oligonucleotide conjugates that were able to form and attack RNA bulge-loops upon sequence-specific hybridisation with TΨC loop and 3′-acceptor stem of $tRNA^{Phe}$, thereby leading to efficient cleavage of the exposed single-stranded regions (39). The potent catalytic transesterification of the RNA backbone was achieved by incorporating even a *single* chain of the amphiphilic peptide acetyl-$[LRLRG]_2$-CO_2H into the conjugate structure (to form *"single"* conjugates) through an internal abasic sugar residue via anomeric C1' carbon either in α- or in β-configuration. In contrast, peptide attachment via internal aminohexyl-modified adenosine led to a complete loss of catalytic activity. To understand the structural impact on catalytic success, we have varied (i) the length and the structure of the catalytic peptide, (ii) the size of the induced single-stranded RNA bulge-loop region, (iii) the length of the oligonucleotide recognition motif and (iv) the configuration of the peptide attachment in order to explore many different structural possibilities (39). This approach allowed us to quickly identify 10 out of 14 catalytically active *"single"* conjugates, with 3 conjugates showing ≥70% cleavage in 24 hours (BC3-α, BC5-α and BC5-L-β), and the 2 best structural candidates achieving overall 90% and 82% RNA cleavage (BC5-α and BC5-L-β, respectively). The success and failure of such *"single"* conjugates to cleave RNA was understood then through structural insights by molecular dynamics simulations. The flexible attachment of the catalytic peptide via an internal abasic nucleotide in either α- or β-configuration and induction of ≥ 3-nt bulge loop regions in the target sequence have been identified as the most important structural requisites to gain high catalytic efficacy (39). Building on our previous success in the development of such *"single"* bulge-loop inducing conjugates (39), we aim here to achieve irreversible cleavage of many copies of RNA substrate by every conjugate molecule through multiple catalytic turnover, which requires the rapid release of the

cleaved fragments to liberate the catalytic conjugates from the hybridised complexes and allow them to attack the next RNA target (see **Figure 3.1** and **Section 3.5.3**).

However, the high stability of DNA-RNA hybrids with long recognition motifs, essential to ensure high specificity, reduces the off-rate constant to non-catalytic levels, even after RNA cleavage. This challenge can be resolved by reducing the binding affinity of the cleaved RNA fragments in such a way that they rapidly leave the hybridised duplex after cleavage, thus enabling truly catalytic destruction of multiple copies of pathogenic RNAs. To promote catalytic turnover and potency, we shall (i) introduce the largest (5-nt) bulge-loop in the RNA upon hybridisation and (ii) incorporate several catalytic peptides into the same conjugate molecule for multiple attacks of the induced bulge-loop region (**Figure 3.2**). We hypothesise here that such design will (i) increase the number of accessible cleavage sites in the RNA, (ii) enhance the probability of forming guanidine-guanidinium dyads and (iii) improve cleavage frequency. Moreover, short products of RNA cleavage with decreased binding affinity will be readily displaced from the hybrids by intact RNA substrates via a strand invasion mechanism to enable reaction turnover and allow conjugates to *"bind, cleave and leave"* the next RNA molecule. Multiple cleaving moieties can be incorporated in the recognition motif via aminohexyl linker attached to the anomeric C1' carbon of an abasic sugar residue to form *"bis"* and *"triple"* conjugates, as illustrated in **Figure 3.2**.

Previously, a direct correlation between the size of induced RNA bulge-loop and catalytic activity of conjugate was seen, with 3- and 5-nt long bulge inducing conjugates exhibiting the highest degree of catalytic activity (39). Henceforth, the conjugate design, which forces RNA to form an elongated 5-nt long bulge-loop, was chosen as a cornerstone for *"bis"* and *"triple"* conjugates. The use of the longer oligonucleotide recognition motifs BC5-L-αα, BC5-L-ββ, BC5-L-αβ, BC5-L-βα or BC5-L-βββ, which are analogous to their counterparts (i.e. BC5-L-α and BC5-L-β) previously used for the construction of the *"single"* conjugates, allowed us to compensate for any significant loss of binding affinity due to incorporation of two or three abasic nucleotides in the sequence. An elongated catalytic peptide Acetyl-$[LRLRG]_2$-CO_2H was chosen for *"bis"* conjugation. The presence of an additional glycine residue in this peptide enhances the conformational flexibility of the molecule allowing it to explore more energetically favourable conformations (42–45). Both BC-α and BC-β single conjugates demonstrated sufficient cleavage activity against 3'-FITC-$tRNA^{Phe}$ with varying degree of effectiveness with α-conjugates exhibiting slightly superior total cleavage capabilities in comparison to β-

series (overall cleavage reaching 90% and 82% for the best structural variants of BC-α and BC-β respectively). Contrarily, the extent of cleavage within bulge-loop was higher in BC-β than in BC-α series (39). Consequently, both α- and β-configuration were used in various combinations to construct *"bis"* conjugates, thus generating a variety of stereospecific *"bis"* conjugates (BC5-L-ββ, BC5-L-αα, BC5-L-αβ and BC5-L-βα). This provided us with the opportunity to test every possible configurational arrangement to enhance the probability of finding the optimal orientations of the key players vital for achieving potent cleavage.

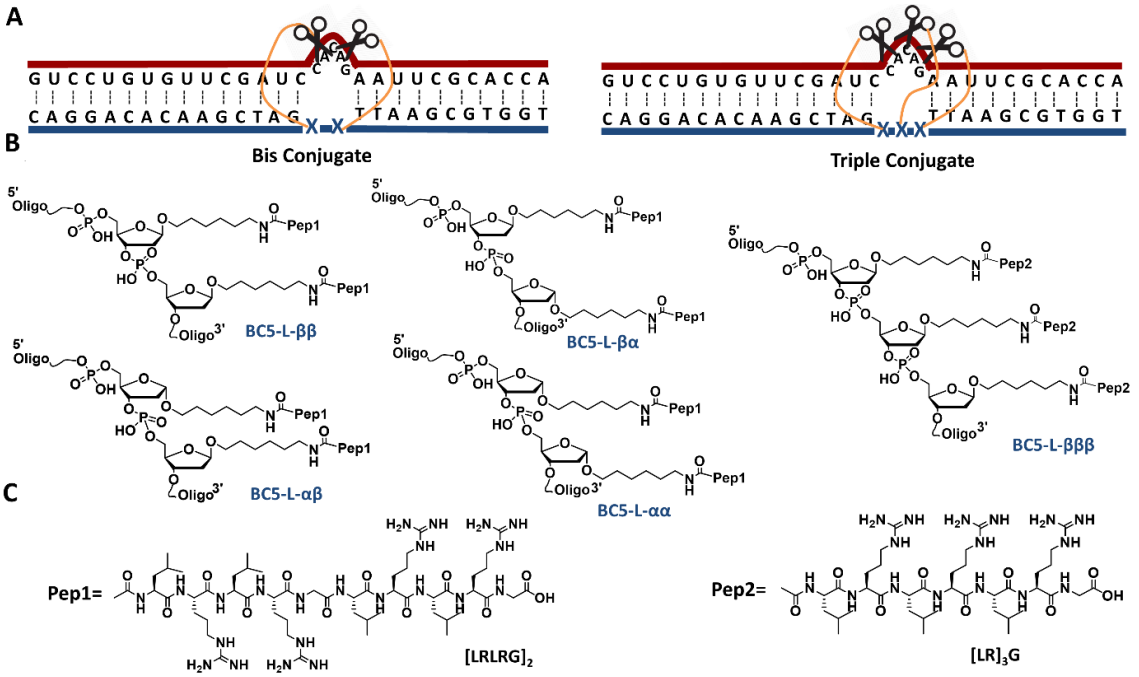

Figure 3.2. Schematic representation of the design concept for the construction of *"bis"* and *"triple"* conjugates. **(A)** The general illustration of bulge-loop inducing *"bis"* (left) and *"triple"* (right) conjugates (blue) bound to the target RNA region (red), corresponding to the 3'-acceptor stem and TΨC-arm of the $tRNA^{Phe}$, which is given here as a primary structure. The anomeric nucleotide representing the point of the peptide attachment is shown as **X**. The catalytic peptides are shown as scissors, and the aminohexyl linker between the peptide and oligonucleotide recognition motif is indicated as a flexible line in orange. **(B)** The chemical structures of *"bis"* (left) and *"triple"* (right) conjugates where the catalytic peptide Acetyl-$[LRLRG]_2$-CO_2H (Pep1) and Acetyl-$[LR]_3G$-CO_2H (Pep2) is conjugated to two or three internal abasic sugar residues via anomeric C1'carbon through aminohexyl linker attached in either ββ, βα, αβ, αα or βββ-configuration. **(C)** The chemical structure of peptide Acetyl-$[LRLRG]_2$-CO_2H (Pep1, left) and Acetyl-$[LR]_3G$-CO_2H (Pep2, right) used for *"bis"* and *"triple"* conjugation, respectively.

The superiority of cleavage within the bulge-loop region for β-conjugates seen previously (39), along with the preliminary cleavage results acquired from *"bis"* conjugates, influenced the *"triple"* conjugate design, where we chose to use β-configuration in the attachment of the peptide to the three abasic sugar moieties located in the middle of the antisense recognition motif (See **Figure 3.2**). A shorter heptapeptide (Acetyl-$[LR]_3G$-CO_2H) was chosen for *"triple"* conjugation to maintain the closest possible number of

arginine residues in the catalytic peptide as compared to that of *"bis"* conjugates (*cf.* 9 against 8 arginines, respectively). To bypass self-conjugation and cyclisation of the peptide during conjugation reaction, N-terminal amino acid was acetylated (33). The peptide sequence was synthesised using SPPS Boc chemistry. The detailed information on synthesis, purification and characterisation of Acetyl-$[LR]_3G$-CO_2H peptide is given in the **Materials and Methods** section.

A shift in HPLC retention time from 17 min (starting oligonucleotide) to 28 min (*"bis"* conjugate) and 30 min (*"triple"* conjugate), was seen, which was reproducible in all conjugation reactions (**Supplementary Figure 3.17**). The identity and purity of all *"bis"* and *"triple"* POCs were confirmed by ^{1}H NMR spectroscopy and MALDI-ToF/ToF spectrometry (see **Supplementary Figure 3.18, Figure 3.19 and Figure 3.20** and **Materials and Methods** section for full characterisation). ^{1}H NMR is convoluted by the sheer number of overlapping peaks in the peptide and oligonucleotide sugar ring region (0.5-4.7 ppm). The comparison between the NMR spectra of starting oligonucleotide and conjugates verified the successful conjugation. Characteristic peptide signals generated by Leu-H^δ and Arg-H^δ in resonance area of 3.2-4.8 ppm are visible in ^{1}H NMR spectra of conjugates (see **Supplementary Figure 3.19**). Comparison of ^{1}H NMR spectrum of the "*single*", *"bis"* and *"triple"* conjugates (see **Supplementary Figure 3.20)** further confirmed the stoichiometric ratio of attached peptide to the oligonucleotide. The presence of Arg- H^δ distinguishable peak at ~ 3.2 ppm in all three spectra signifies the presence of peptide. Careful integration of the oligonucleotide aromatic region (7.2-8.4 ppm), as well as H1' sugar ring protons (5.4-6.4 ppm), confirmed 2:1 and 3:1 stoichiometric ratio of peptide to oligonucleotides in *"bis"* and *"triple"* conjugates, respectively.

3.5.2 Fluorescence assay of hybridisation and ribonuclease activity

In order to rapidly screen conjugates on their ability to cleave RNA and test whether they can catalyse cleavage in multiple turnover mode, we have developed a real-time fluorescence assay. The most commonly used method to screen for cleavage activity is gel-electrophoresis of the isotopically labelled (e.g. [^{32}P]) RNAs and their degradation products to determine the exact positions of RNA cleavage (28-36), which raises some safety concerns and suffers from limitations such as unsafe isotope labelling, batch-wise analysis and hazardous radioactive waste (46). Other analytical separation approaches, such as capillary electrophoresis (CE) and high-performance liquid chromatography

(HPLC, either alone or in combination with mass spectrometry) are restricted by the variable abundance and the number of each RNA fragment in the reaction mixture to be evaluated simultaneously, which is not always possible. (47). Taking advantage of FRET principle, we developed a safe and quick fluorescent detection method to monitor cleavage in real-time. The overall design concept of the assay is shown schematically in **Figure 3.3** (**A-C**). This assay uses fluorescently labelled hybrid RNA/DNA sequence as a model target (**F-Q**-RNA, black), bearing fluorophore (**F**) and quencher (**Q**) at the positions flanking the bulge-loop region (shown here in blue). Such design allows us to monitor cleavage in bulge-loops only by eliminating any potential cleavage outside this region. This model target was designed to be the exact representation of 3'-acceptor stem and TΨC-loop of $tRNA^{Phe}$. The bulge-loop inducing conjugate is indicated in brown in **Figure 3.3** (**A**). Intact RNA is fully quenched and fluorescently silenced by the close proximity of **F** and **Q** (**Figure 3.3** (**A**), steps (i) and (ii)), thus allowing FRET and static quenching (**Figure 3.3**, (**C**); blue curve). The hybridisation of the conjugate to **F-Q**-RNA and subsequent cleavage of RNA stretch at the bulge-loop region triggers complex dissociation and separation of **F** and **Q** (**Figure 3.3** (**A**), steps (iii)), thus leading to gradual fluorescence increase (**Figure 3.3**, (**C**); green, orange, red and purple curves), which can be used for monitoring and quantification of cleavage over lengthy periods of catalysis needed therapeutically. RNA degradation is normalised here to complete (100%) cleavage of the same **F-Q**-RNA substrate by RNase A (**Figure 3.3 (C)**; black curve). Untreated **F-Q**-RNA and *RNA:Oligonucleotide* complexes (i.e. without catalytic peptides) are used as 'controls' to eliminate artefacts.

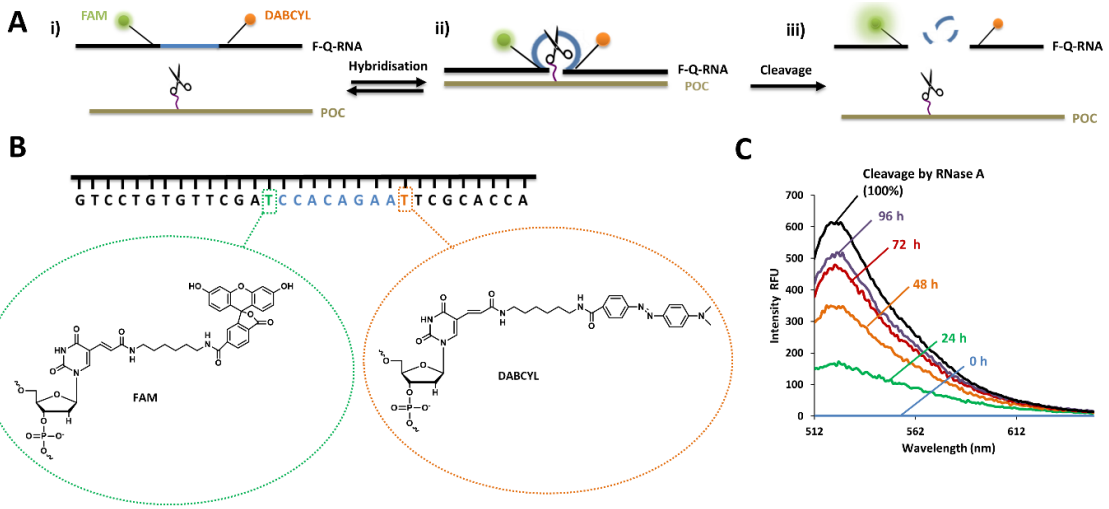

Figure 3.3. Schematic representation of FRET-based assay for detection of cleavage in RNA bulge-loops (**A**) using fluorescently labelled *RNA-DNA* hybrid sequence (**B**) through the development of fluorescence (**C**). **(A)** Design concept of the assay showing (i) the binding of the conjugate (brown) to the labelled **F-Q**-RNA target (black), leading to (ii) the formation of bulge-

loop (blue), which brings the two reporter groups (**F** and **Q**) to close proximity leading to the fluorescence quench. Cleavage of the target at the bulge-loop regions (iii) physically separates the fluorophore and the quencher, thus resulting in an increase of fluorescence intensity (**C**). **(B)** The linear model target is constructed here as *RNA-DNA* hybrid sequence, incorporating an internal Fluorescein **(F,** in green**)** and Dabcyl quencher **(Q,** in orange**)** covalently attached to the deoxythymidine residues, which are flanking the bulge-loop region and positioned 8-nt apart from one another. The sequence corresponding to the bulge-loop region (shown in blue) is made of ribonucleotides (to represent RNA stretch). **(C)** Progressive increase in fluorescence intensity over time (at 0, 24, 48, 72 and 96 h time points) as compared to that of the fully cleaved (100 %) **F**-**Q**-RNA target by RNase A (in black). Fluorescence was measured at λ_{em}= 522 nm following excitation at λ_{ex}= 494 nm.

Binding of POCs to the fluorescently labelled **F**-**Q**-RNA target (1 μM) resulted in a sharp decline in fluorescence intensity upon increase of the conjugate concentration from 0 to 30 μM (see **Supplementary Figure 3.21**). Presumably, hybridisation resulted in the formation of a bulge-loop structure in the target strand, which can enhance the quenching ability of dabcyl by positioning the fluorophore and quencher in close proximity of one another. Also, the closely located aromatic bases of the hybridised conjugate may contribute to the observed quenching. A negligible difference was witnessed between the binding affinity of the peptidyl-oligonucleotide conjugates and the related *unconjugated* oligonucleotides, with the conjugates exhibiting a slightly sharper drop in fluorescence intensity (see **Supplementary Figure 3.21**), presumably due to the additional quenching effect from the peptide moieties.

Using the above fluorescent detection assay (**Figure 3.3**), we tested the catalytic activity of a panel of selected representatives from each series of conjugates against **F**-**Q**-RNA target including (1) *"single"* bulge-loop inducing conjugates (BC2-α, BC3-α, BC4-α, BC5-α, BC2-β, BC3-β, BC4-β, BC5-β and BC5-L-β), previously studied in (39) to validate the assay, (2) selected *"bis"* conjugates from the new series (BC5-L-αα and BC5-L-ββ) and (3) *"triple"* conjugate (BC5-L-βββ) (see **Figure 3.4** (**A**-**D**)). Tris-buffer was selected for cleavage experiments since it does not interfere with RNA transesterification process (48–50). The presence of EDTA in the buffer minimises the probability of metal-ion induced RNA cleavage. To encourage dissociation of conjugate following cleavage and enhance reaction turnover, aliquots taken from the reaction vessel were first diluted (×10 fold) and then subjected to a high temperature (80°C for 3 minutes). A progressive increase in fluorescence intensity was observed resulting from the generation of cleaved fragments, indicating the extent of cleavage for *"single"*, *"bis"* and *"triple"* POCs over time (0-96 h) (data not shown). Cleavage of the linear target (**F**-**Q**-RNA) with RNase A was conducted under similar conditions to record the maximum cleavage of the target using a natural hydrolytic enzyme (see **Figure 3.4**).

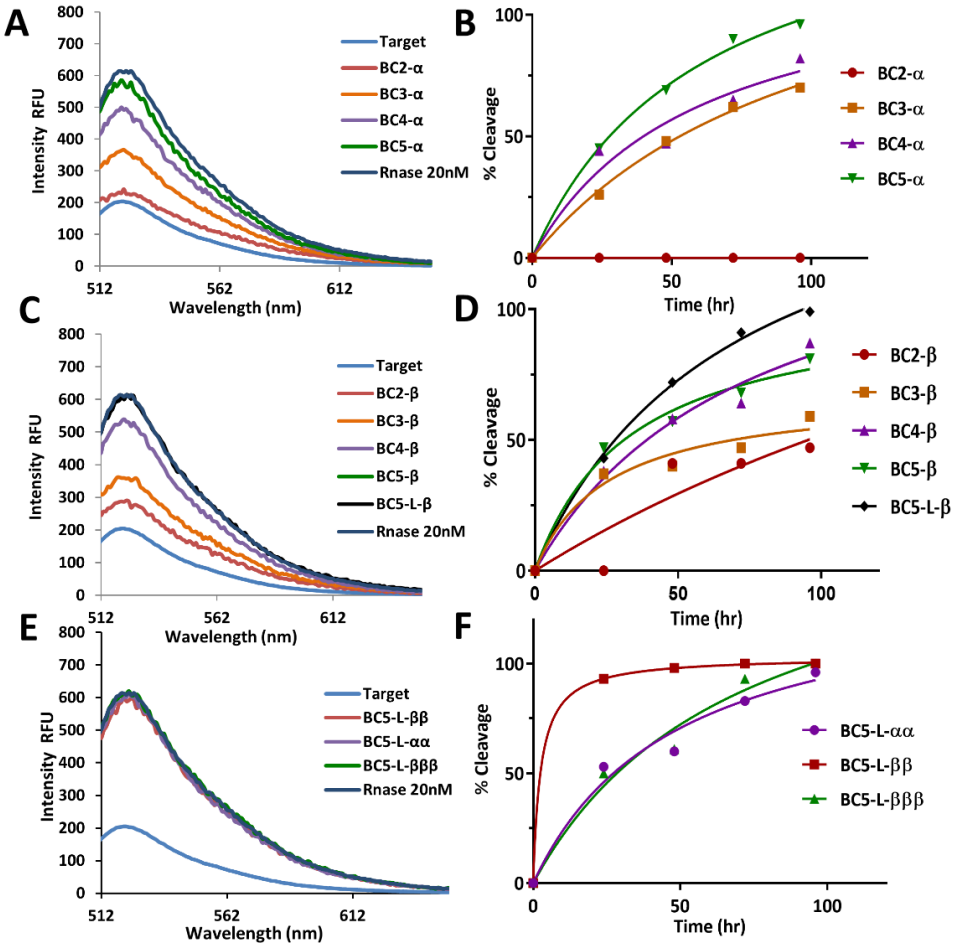

Figure 3.4. Cleavage of **F**-**Q**-RNA target with *"single"* (BCn-α and BCn-β), *"bis"* (BC5-L-αα and BC5-L-ββ) and *"triple"* (BC5-L-βββ) conjugates monitored through fluorescence detection over period of 96 hours in comparison to the complete (100%) cleavage of the same **F**-**Q**-RNA substrate by RNase A measured in a parallel experiment. (**A**, **C** and **E**) The end-point fluorescence detection of the cleavage. Linear target **F**-**Q**-RNA (1 μM) and each of the *"single"* α conjugates (20 μM) (**A**), "*single*" β conjugates (20 μM) (**C**) and *"bis"* and *"triple"* conjugates (20 μM) (**E**) were incubated at 37°C for 96 hours. (**B**, **D** and **F**) Kinetics of **F**-**Q**-RNA cleavage by "*single*" α conjugates (**B**), "*single*" β conjugates (**D**) and *"bis"* and *"triple"* conjugates (**F**). RNA degradation is normalised to complete (100%) cleavage of the same **F**-**Q**-RNA substrate treated by RNase A (20 nM). Fluorescence was measured at λ_{em}= 522 nm following excitation at λ_{ex}= 494 nm.

All designed "*single*" conjugates (expect BC2-α) catalysed cleavage within the bulge region. Previously, cleavage in the induced bulge-loop of $tRNA^{Phe}$ was reported with all "*single*" conjugates where the expansion of the bulge region led to numerous cuts in ^{61}C-^{62}A-^{63}C-^{64}A-^{65}G region (39). Herein, a variation in catalytic activity was seen between BCn-α and BCn-β conjugates with a progressive increase in cleavage activity in bigger bulge-loops where the extent of cleavage was increased from 47% for BC2-β to 59% for BC3-β, 86% for BC4-β, 83% for BC5-β and 99% for BC5-L-β (see **Figure 3.4** (**D**)). A higher extend of cleavage in the bulge-loop region was witnessed with linear **F**-**Q**-RNA target than the complex $tRNA^{Phe}$ (39). Amongst studied representatives of *"single"* conjugates, 5-nt bulge-loop inducing conjugates BC5-α (96%) and BC5-L-β (99%)

exhibited the highest level of cleavage for both α- and β-series configuration (see **Figure 3.4** (**B**) and (**D**)). The catalytic performance of BCn-β seemed slightly superior to BCn-α counterparts apart from BC3-α and BC5-α. Marginal dissimilarities were seen between the estimated percentage of cleavage of "*single*" conjugates calculated via the fluorescence-based assay and conventional gel electrophoresis (39). Overall, the data obtained against this model linear **F**-**Q**-RNA target is in correlation with the previous results obtained for the cleavage of the structurally complex biological RNA (i.e. $tRNA^{Phe}$) by these series of the conjugates, indicating the validity of the fluorescence assay (39).

Up to 100 % cleavage was observed with "*bis*" and "*triple*" conjugates, presumably indicating the cooperative effect of multiple peptide entities incorporated in the new series of the conjugates (see **Figure 3.4** (**F**)). Incorporation of two catalytic peptides in β configuration (BC5-L-ββ) resulted in a significant enhancement in cleavage activity where up to 100% cleavage was witnessed in 48 hours. Interestingly, incorporation of multiple β anomers provided a more favourable setting for cleavage and endowed accessibility to the bulged single-stranded cleavage site of the **F**-**Q**-RNA target as reflected in the higher cleavage efficiency witnessed in the assay. However, the extent of cleavage for BC5-L-αα and BC5-L-βββ was close to their "*single*" counterparts (*cf.* 97% vs 96 % for BC5-L-αα and BC5-α as well as 100% vs 99% for BC5-L-βββ and BC5-L-β respectively) (see **Figure 3.4** (**B**), (**D**) and (**F**)). This can be related to the fact that **F**-**Q**-RNA target design only permits cleavage within the bulge-loop region and the ability of the conjugates to attack structural elements outside the induced loop region is not monitored here. Previous studies have indicated the ability of conjugates to attack distantly located sites within the tertiary structure of the complex biological RNA (31, 32, 39). No spontaneous cleavage was seen when either a non-complementary (scrambled, 5'-luc-h-9/14) POC or an unconjugated oligonucleotide sequence were used against **F**-**Q**-RNA (see **Supplementary Figure 3.22**), thus verifying the lack of non-sequence specific cleavage and the inactive nature of unconjugated oligonucleotide.

3.5.3 Multiple turnover kinetic study

The irreversible cleavage of many copies of RNA substrate by a single conjugate molecule through multiple catalytic turnover was the ultimate aim of this study. An ideal artificial ribonuclease should exhibit reaction catalytic turnover, where upon cleavage of the target RNA the ribonuclease molecule dissociates from the cleaved fragments to

initiate the next catalytic event (see illustration of this concept in **Figure 3.1** (**A**)). Using a labelled linear target **F**-**Q**-RNA target and the developed fluorescence-based assay (**Figure 3.3**), the ability of the bulge-loop inducing *"bis"* conjugates to cleave multiple copies of RNA in excess of the target (up to 30-fold) over conjugate was evaluated by the example of the most active *"bis"* conjugate and compared with that of the two most active representatives of *"single"* conjugates identified earlier (see **Figure 3.4**). To draw a direct comparison between *"single"* and *"bis"* conjugates, 5-nt long bulge-loop inducing single conjugates with the shortest (BC5-α) and longest (BC5-L-β) antisense recognition motif exhibiting the highest catalytic efficacy (see **Figure 3.4** (**B**) and (**D**) and (39)) and one of the most catalytically active *"bis"* conjugates (BC5-L-ββ) were chosen and the catalytic activity was evaluated in multiple turnover mode. The conjugate at a concentration of 5 μM was incubated with 2-, 5-, 10-, 20- and 30-fold excess of the **F**-**Q**-RNA target at 37°C for 96 hours. To achieve that, several parallel reactions (100 μL each) were set up, with each reaction mixture containing 0.5 nmoles of the selected conjugate and 1, 2.5, 5, 10 or 15 nmoles of **F**-**Q**-RNA target. To follow the kinetics, 10 μl aliquots were taken from each reaction mixture at 0, 24, 48, 72 and 96-hour timepoints, and their fluorescent signal was analysed as described in "**Materials and Methods**" section.

Peptidyl-oligonucleotide conjugates (POCs) have been characterised hitherto as specific cleavage reagents, typically at concentrations in excess of their target, with reliance on analytical separation techniques (PAGE, CZE, HPLC) to detect cleavage by isolation of products. In contrast, biochemical catalysis by enzymes is typically characterised by 'one pot' biochemical assays, which do not require separation and operate under conditions of multiple turnover with their substrates in large excess. Our assay devised here allowed POCs to be considered as artificial enzymes, under multiple turnover conditions at increasing excesses of the fluorescent target substrate, when the kinetics of the sequence-selective catalysis of the cleavage reactions can be considered here for the first time (**Figure 3.5**).

Non-linear estimation of initial velocities was used throughout (51, 52). Progress curves approached linearity only for the 5-fold molar excess of substrate (**Figure 3.5** grey traces in (**A-C**)), where a consistently small non-linearity $\eta \sim 0$ held for the BC5 conjugates with α, β and double β attachment of catalytic peptide (**Figure 3.5** grey-filled circle in (**D-F**), respectively). However, at 2-fold molar excesses, small increases in velocity ($-\eta$) were evident for the single peptide conjugates, suggestive of activation during the reaction progress at low substrate concentration, not apparent for the dual peptide conjugate.

Otherwise, velocities decreased ($+\eta$) during reaction progress, suggestive of the decline of the substrate and/or increase in inhibition by the product. Strikingly, the most active conjugates suffered lower velocities at larger substrate excesses (20-30×), resulting in the atypical parabolic kinetic profiles (**Figure 3.5** (**G**) and (**I**)). However, the least active elongated single β conjugate (BC5-L-β) pretended a more hyperbolic profile reminiscent of Michaelis-Menten kinetics, but again with deviations at lower substrate excesses and the strongest decline in velocity of the conjugates at 30-fold substrate excess (**Figure 3.5** (**B**), (**E**) and (**H**)).

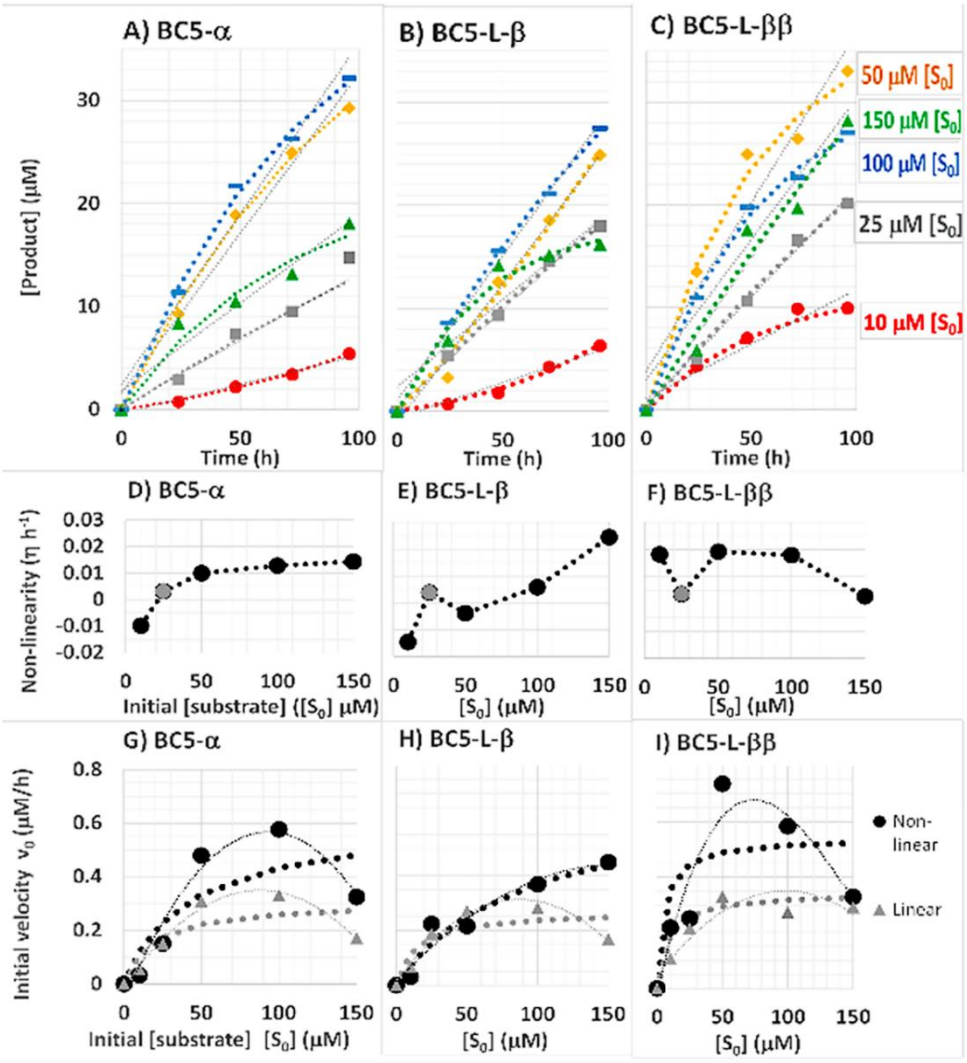

Figure 3.5. Atypical kinetics. Progress curves of cleaved product concentration [P] (top row: (**A-C**)) from increase in fluorescence scaled by full cleavage of each substrate concentration $[S]_0$ by RNase A. Non-linear curve fitting of $[P] = \frac{v_0}{\eta}(1 - e^{-\eta t})$ (51, 52) estimated non-linearities η (middle row: (**D-F**)) and initial velocities v_0 revealing atypical parabolic kinetics for both non-linear (black filled circles) and linear (grey-filled triangles) estimates of initial velocities v_0 rather than hyperbolic kinetics of Michaelis-Menten (dotted traces, bottom row: (**G-I**)).

When substrate depletion was considered, by subtraction of the observed increase in product, the decline in substrate appeared to be considerable during the progress of the

reactions, at least for substrate excesses greater than 2-fold (**Figure 3.6** (**A-C**)). This extent of substrate depletion would be expected to exert a greater effect on the decline in velocity during the course of the reactions, which was not apparent in the progress curves in their relative small curvatures (**Figure 3.5** (**A-C**)) and non-linearity (**Figure 3.5** (**D-F**)).

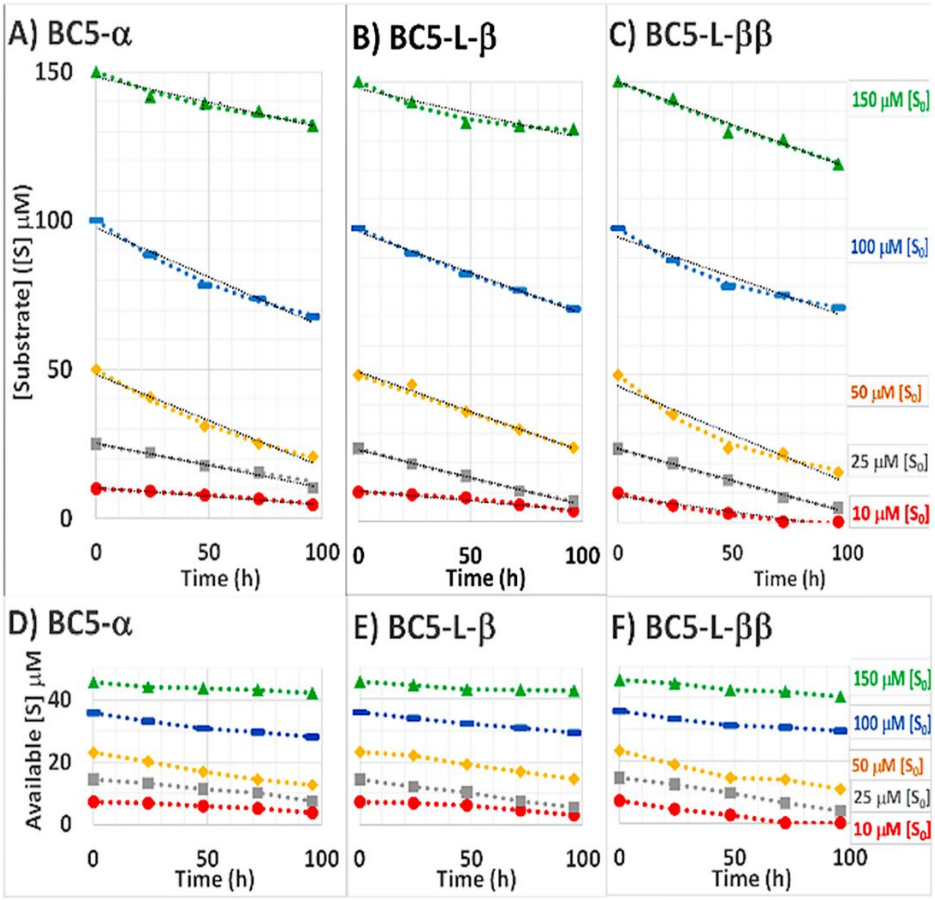

Figure 3.6. Substrate depletion & buffering**.** Progress curves of the expected depletion of substrate concentration [S] (top row: (**A-C**), by subtraction of [P] in **Figure 3.5**) and the progress curve of available [S] after consideration of substrate self-association (bottom row: (**D-F**)).

An explanation of this discrepancy is found in the likelihood of self-association of the target substrate into hairpin and duplex structures (**Supplementary Figure 3.23**). When dominant self-association is considered, both the un-complexed substrate available for reaction and its decline during reaction progress are much reduced, as complexed substrate can buffer the available substrate (**Figure 3.6** (**D-F**) and **Supplementary Figure 3.24**). Similar self-association of conjugate may also result in the observed POC activation and inactivation. A model combining the principal of such interactions was developed (**Supplementary Section 3.8.14,** and schematically summarised in **Figure 3.7**), as a first possible explanation of the atypical kinetics observed.

The target substrate expected to be complexed $[S]_c$ was calculated from its equilibrium dissociation K_s and the total substrate $[S]_t$, when the expected available substrate $[S]_a$ was obtained by difference. The complexed POC and its activation in competition with the initially-available substrate $[S]_a$ were calculated from its approximated dissociation K_c to provide the activated concentration of POC available $[C]_a$ dynamically during reaction progress. Initial approximated values were refined within the non-linear fitting of the model to observation data (**Supplementary Section 3.8.14**).

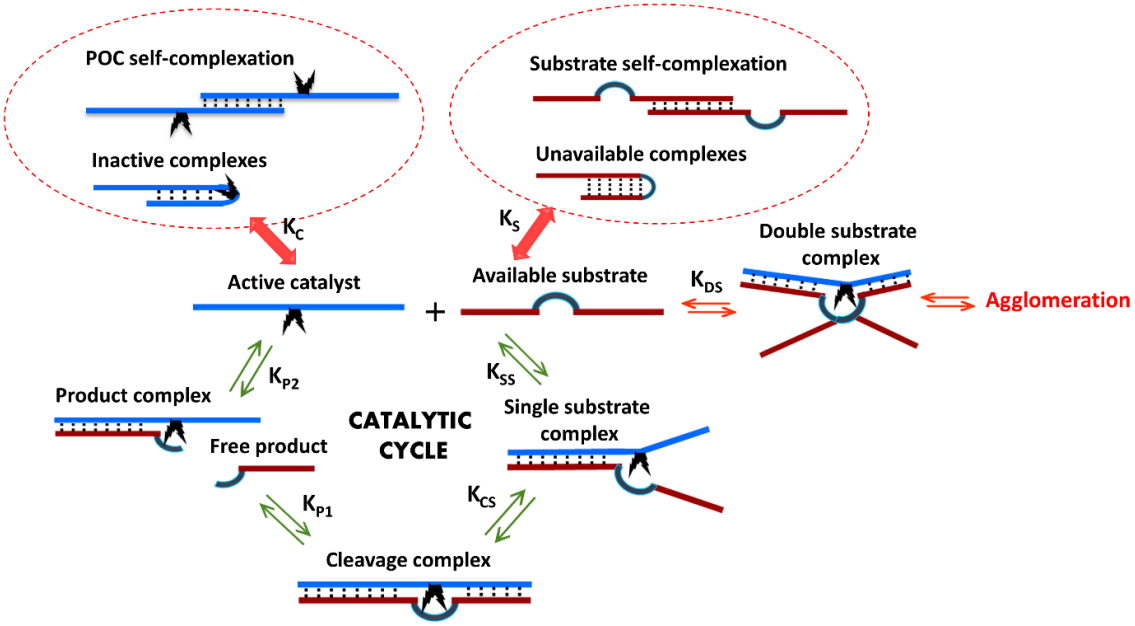

Figure 3.7. Model of dominant interactions of POC catalyst, its substrate and products. Additional to the catalytic cycle (green arrows), where active catalyst binds available substrate and forms cleavage products from a cleavable substrate complex, weaker self-associations are possible from sequence homologies within each component. Such side interactions sequester available substrate and inactivate the catalyst into complexes (red arrows), which do not then participate in the catalytic cycle. A dynamic numerical model of the equilibria, with equilibrium dissociation constants (K) characterises the interactions, under different conditions and during the catalytic reaction (**Supplementary Section 3.8.14**).

The expected weaker association of cleaved product and similar partial binding of substrate to the POC, in competition with the full binding of substrate (**Figure 3.7**) were calculated from their equilibrium dissociations K_{SS}, K_P and K_{CS} (respectively). Cleavable substrate will dominate the occupancy of the conjugate initially but, as substrate is cleaved, product occupancy will rise to <10% in this model. Products of cleaved substrate will have similar dissociation to partial binding of substrate in this model and will approximate the occupancy of product (**Supplementary Figure 3.25**).

At large excess of substrate, some of the POC fraction will be doubly occupied by a pair of partially-bound substrate molecules (K_{ds}), which will decline in competition with

cleaved product partially occupying the binding site. The rate of decline in double substrate occupancy will be greater at lower substrate concentrations than at higher, when double occupancy is retained for longer periods of reaction, and remained elevated at the higher substrate concentrations, where the conjugate was also prone to inactivation (**Supplementary Figure 3.25**). The two dangling ends of partially-bound substrate molecules and the two dangling positively-charged peptides are likely to promote agglomeration, which is likely to inactivate the POC. Inactivation will thereby increase with the greater extent and longer duration of double substrate occupancy at higher substrate concentrations (**Figure 3.7**). The lesser rate of decline of double substrate occupancy with increasing substrate concentrations (**Supplementary Figure 3.25**) was considered as the key determinant of inactivation in this first model.

Michaelis-Menten kinetics for initial velocities (v_0) and initial available substrate $[S]_{a0}$, including the active conjugate $[C]_a$ (in the $V_{max} = [C]_a \times k_{cat}$ term) was used to estimate k_{cat}, K_m and to refine approximated equilibrium dissociation characteristics (K_c, K_s, K_{ss}). Of the total POC, only a minor fraction (~10%) was available at small excesses of substrate. This model of activation by available substrate and inactivation in larger excess of substrate, allowed Michaelis-Menten kinetics to approach the observed velocities (**Figure 3.8** and **Supplementary Figure 3.26**).

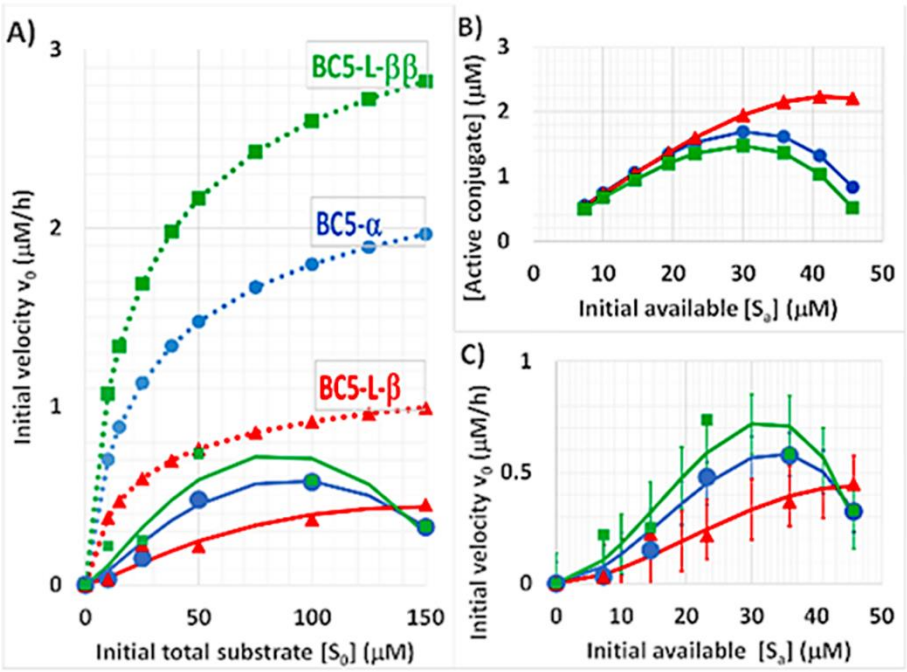

Figure 3.8. Active conjugate kinetics. **(A)** Michaelis-Menten parameters (K_m, k_{cat}) indicated expected kinetics at maximum activation of POCs (dotted traces) for the fit to observed velocities (continuous traces) for **(B)** the numerical model of dynamic change in active POC for the available substrate. **(C)** Initial velocities expected from the numerical model for available substrate

(continuous traces) after non-linear fitting to observed velocities (filled symbols for each POC) with error bars representing standard deviations at 95% confidence limits.

The conjugate with two catalytic peptides ($BC5-L-\beta\beta\ k_{cat}\ 0.8\ h^{-1}$) showed the greatest V_{max} (**Figure 3.8** (**A**) & **Supplementary Table 3.3**), but was approached by the conjugate with a single peptide from the α anomer ($BC5-\alpha\ k_{cat}\ 0.6\ h^{-1}$), whereas attaching the single peptide from the β anomer with an elongated recognition motif cut activity by half ($BC5-L-\alpha\ k_{cat}\ 0.29\ h^{-1}$). However, reflective of identical sequence complementarity, similar Michaelis-Menten constants were estimated in the range $K_m\ 20-24\ \mu M$. The dynamic changes in the activation of conjugates were similar, as was the profile of inactivation of single α and double β conjugates, whereas the single elongated β conjugate was least inactivated at higher substrate excess (**Figure 3.8** (**B**) and **Figure 3.26** for details).

Importantly, in all three cases, the extent of cleavage approached 100% or greater of the available substrate for total substrate excess up to 10-20 fold. The conjugates with a single catalytic peptide showed similar extents of cleavage, whereas the conjugate with double catalytic peptides had a greater extent of cleavage, consuming most of the self-complexed substrate, too. However, beyond 10-fold substrate excess, the extent of cleavage declined, presumably from conjugate inactivation (**Figure 3.9** (**A-C**)) with some product inhibition, as the molar ratio of product over conjugate exceeded 5 (**Figure 3.9** (**D-F**)) and the expected product-occupied POC increased towards 10% (**Supplementary Figure 3.25**).

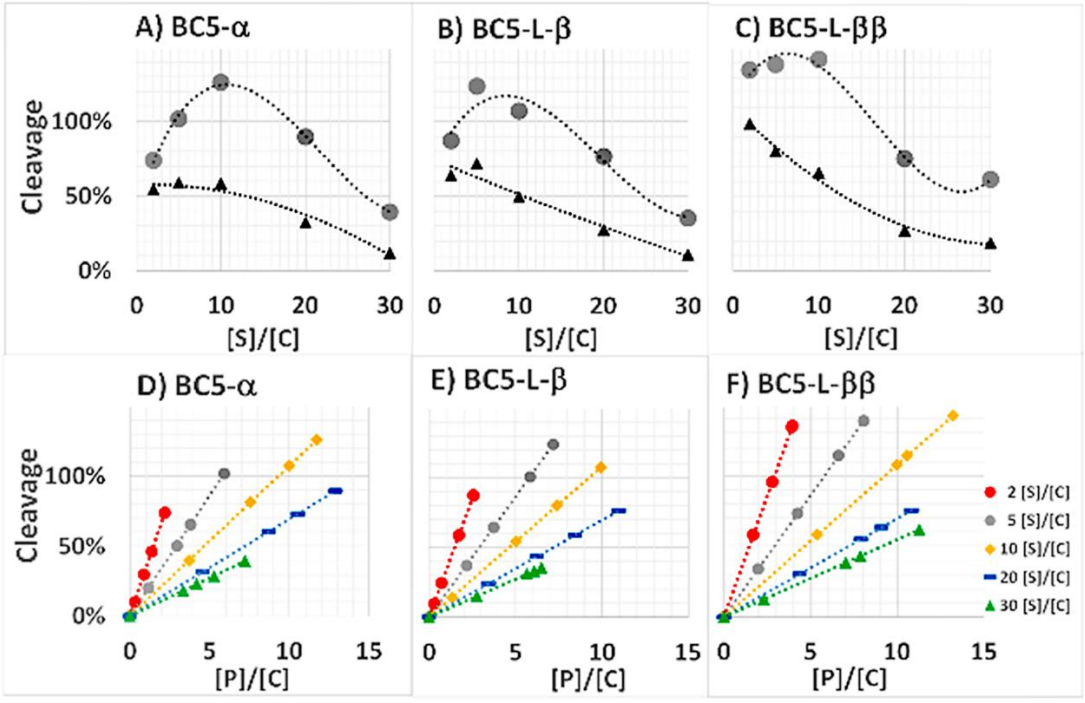

Figure 3.9. Extent of cleavage during multiple turnover. Extent of cleavage of available substrate (grey filled circles in (**A-C**) for respective conjugates) and total substrate (black filled triangles in

(**A-C**)) for different molar ratios of total substrate to conjugate. Extent of cleavage of available substrate against the molar ratio of product to conjugate (**D-F**) for different substrate excesses (red circles 2×, grey circles 5×, yellow diamonds 10×, blue dashes 20× and green triangles 30×).

Product inhibition presented as uncompetitive with K_i $18 - 21\ \mu M$ (**Supplementary Table 3.3**). Given the increase in product with lesser decline in available substrate during the progress of each reaction, the velocities expected from Michaelis-Menten kinetics with competitive and uncompetitive inhibition were also fitted to the estimated observed velocities as each reaction progressed (**Supplementary Figure 3.27**). Velocities expected from Michaelis-Menten kinetics with uncompetitive inhibition approached observed velocities for the upper substrate excesses (**Supplementary Figure 3.28**).

Full cleavage of target substrate at 10-20-fold molar excess offers considerable potency where a single catalyst molecule destroys at least 10 target molecules, even with a partially-active POC. Upon full activation, each POC may be capable of destroying over 30-50 target molecules. Such catalytic potency could allow a few active molecules to knock down the typical range of copy numbers of pathogenic RNA in each cell and to continue to do so for many days.

3.5.4 Hybridisation and cleavage against $tRNA^{Phe}$

The fluorescent assay indicated the ability of the conjugates to bind and cleave **F-Q**-RNA target. However, in order to investigate the ability of *"bis"* and *"triple"* conjugates to hybridise and cleave complex biological RNA (i.e. $tRNA^{Phe}$) and draw a direct comparison of RNA cleavage activity with "*single*" conjugates (39), RNA hybridisation and cleavage properties against $tRNA^{Phe}$ under physiological conditions were tested. First, the ability of "*bis*" and "*triple*" conjugates to hybridise with $tRNA^{Phe}$ was assessed via electrophoretic mobility shift assay (see **Supplementary Figure 3.29**). Compared to unbound 3'-FITC-$tRNA^{Phe}$, RNA:POC heteroduplex has reduced electrophoretic mobility distinguishable in gel-shift analysis. The association constants (Ka) were estimated based on the relative proportion of $tRNA^{Phe}$ bound to conjugate as a function of concentration. Full details of *"bis"* and *"triple"* conjugate nomenclature, composition and association constants are given in **Table 3.1**.

Table 3.1. "*bis*" and "*triple*" conjugate composition, nomenclature, and association constants (Ka).

Conjugate	Sequence (5'→3')	Peptide	Ka × 10^6 M^{-1}
BC5-L-ββ	TGGTGCGAATT-dR^{beta}dR^{beta}-GATCGAACACAGGAC	$[LRLRG]_2$	1.1±0.9
BC5-L-αα	TGGTGCGAATT-dR^{alpha}dR^{alpha}-GATCGAACACAGGAC	$[LRLRG]_2$	3.5±0.8
BC5-L-αβ	TGGTGCGAATT-dR^{alpha}dR^{beta}-GATCGAACACAGGAC	$[LRLRG]_2$	4.3±2.2
BC5-L-βα	TGGTGCGAATT-dR^{beta}dR^{alpha}-GATCGAACACAGGAC	$[LRLRG]_2$	6.2±2.3
BC5-L-βββ	TGGTGCGAATT-dR^{beta}dR^{beta}dR^{beta}-GATCGAACACAGGAC	$[LR]_3G$	0.5±0.1

Where $Ka = \frac{\alpha}{[BC]_0(1-\alpha)\left(1-\alpha\left(\frac{[\text{tRNA}]_0}{[BC]_0}\right)\right)}$, α= fraction bound, $[\text{tRNA}]_0$= total tRNA^{Phe} concentration and $[BC]_0$= total conjugate concentration

All conjugates were capable of binding to tRNA^{Phe} in concentration dependent manner (see **Supplementary Figure 3.29**). The incorporation of a longer recognition motif in *"bis"* conjugate design compensated for the instability stemmed from loop size and accommodated attachment of multiple cleaving constructs. All "*bis*" conjugates demonstrated saturation binding to tRNA^{Phe} where plateau was reached (100% binding) at a concentration above 5 μM (see **Supplementary Figure 3.29**). Incorporation of the peptide in α configuration (BC5-L-αα, BC5-L-αβ and BC5-L-βα) enhanced binding affinity in comparison to their "*single"* counterparts (BC5-L-α, Ka= (0.9±0.6)×10^6 M^{-1} and BC5-L-β, Ka= (0.5±0.2)×10^6 M^{-1}) (39). The difference witnessed in the association constant for BC5-L-αα, BC5-L-αβ and BC5-L-βα did not exceed statistical errors. Incorporation of the linker in β-configuration (BC5-L-ββ) reduced biding affinity towards the target molecule. *"triple"* conjugate demonstrated the lowest binding constant (ka= 0.5±0.1×10^6 M^{-1}). The addition of a shorter peptide sequence in triplicates did not counteract the negative effects of multiple peptide incorporation via anomeric nucleotide on hybridisation, suggesting that the predominant force for hybridisation is Watson and Crick base pairing and not the electrostatic interactions between multiple arginine residues and phosphodiester backbone.

Moreover, the cleavage activity of "*bis*" and "*triple*" conjugates under physiological conditions (pH 7.4 and temperature 37°C) against 3'-FITC-tRNA^{Phe} (1μM) over 4, 8, 24, 48 and 72 hours (see **Materials and Methods** for more information) was analysed by

12% PAGE electrophoresis under denaturing conditions and cleavage sites were identified through comparison with RNase T1 and imidazole $tRNA^{Phe}$ hydrolysis ladders (see **Figure 3.10** (**A-E**)). No spontaneous cleavage was seen in the absence of conjugate (lane C in **Figure 3.10** (**A-E**)).

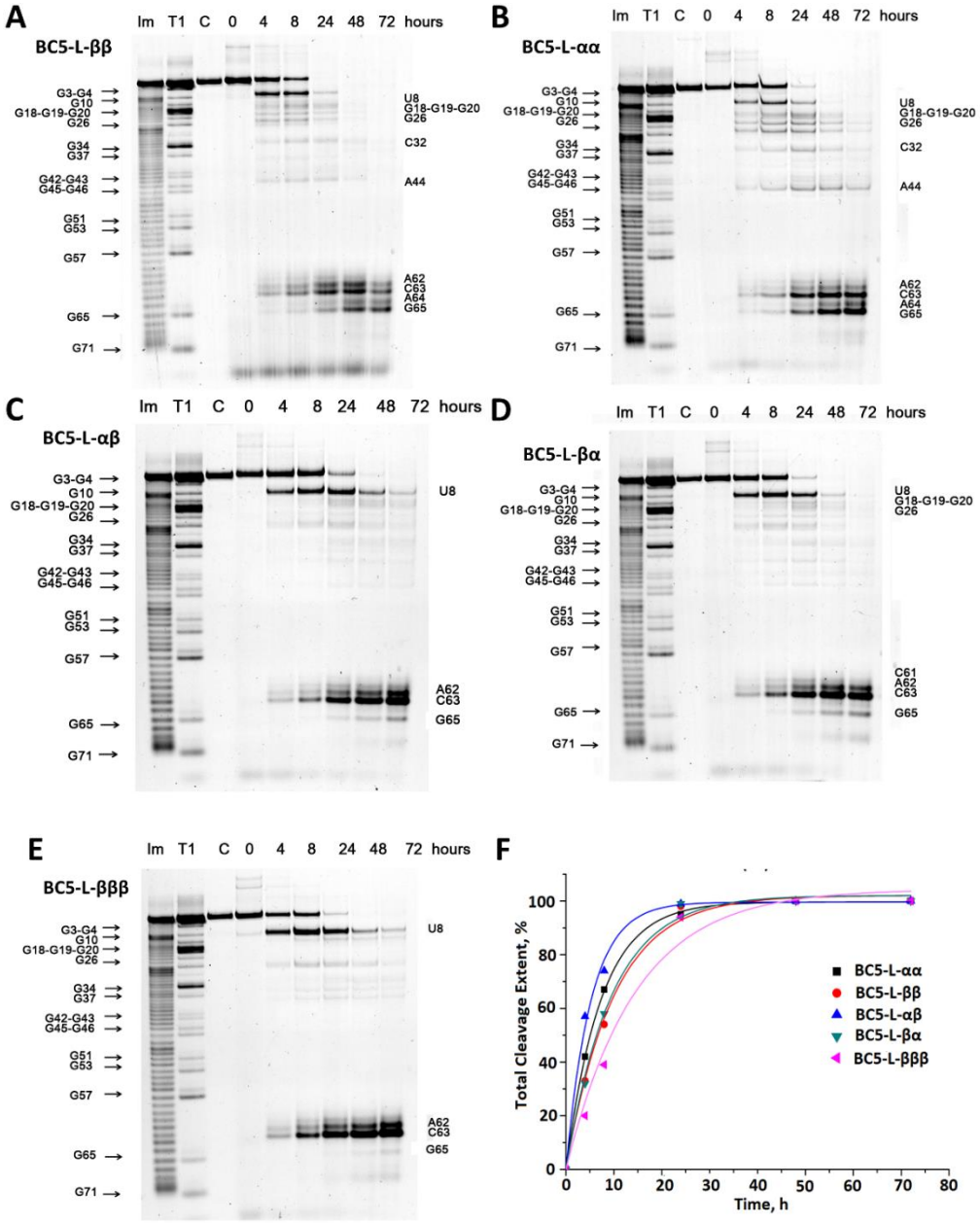

Figure 3.10. The extent of cleavage of 3'-FITC-$tRNA^{Phe}$ with *"bis"* and *"triple"* conjugates. **(A-E)** Representative images of 12% PAAM/8 M urea gel electrophoresis of cleavage products of 3'-FITC-$tRNA^{Phe}$ with BC5-L-ββ (**A**), BC5-L-αα (**B**), BC5-L-αβ (**C**), BC5-L-βα (**D**) and BC5-L-βββ (**E**) as a function of incubation time. Imidazole (lane Im) and RNase T1 (lane T1) digestion ladders have been used for identification of cleaved fragments. Lane C represents 3'- FITC-$tRNA^{Phe}$ incubated in the absence of conjugate for 72 hours. 3'- FITC-$tRNA^{Phe}$ at a concentration of 1 μM was incubated with different *"bis"* and *"triple"* conjugates at a concentration of 20 μM at 37°C for different time points. **(F)** Secondary plot of the data presented in (**A-E**) indicating the total extent of cleavage (%) vs the incubation time for all *"bis"* and *"triple"* conjugates.

A significant enhancement in cleavage activity was observed in *"bis"* and *"triple"* conjugates where all conjugates exhibited high ribonuclease activity with the overall cleavage reaching almost 100% in 24 hours (see **Figure 3.10** (**F**)). All designed *"bis"* and *"triple"* conjugates catalysed cleavage within the targeted bulge region (^{61}C-^{62}A-^{63}C-^{64}A-^{65}G). BC5-L-βα exhibited the highest extent of cleavage in loops followed closely by BC5-L-αβ and BC5-L-αα. Although conjugates were designed to bind to tRNA^{Phe} on 1:1 molecular ratio, 20-fold excess of conjugate over tRNA was used for cleavage experiments via gel-electrophoresis (20 μM conjugate against 1μM tRNA^{Phe}). The inherent potency of *"bis"* and *"triple"* conjugates is reflected in the fact that full cleavage efficacy (up to 100% cleavage of 3'-FITC-tRNA^{Phe}) was witnessed even at lower excess of conjugate over target (10:1 or 5:1 excess of conjugate over target) (see **Supplementary Figure 3.30**). At higher excess of conjugate over target (20:1), more pronounced cleavage was witnessed at the targeted region ^{61}C-^{62}A-^{63}C-^{64}A-^{65}G. Additionally, the *"triple"* conjugate exhibited marginally lower cleavage extent in comparison to *"bis"* conjugates. The reduction in cleavage activity can be attributed to the reduction of essential conformational freedom upon hybridisation. Minor alteration in the peptide composition, shorter peptide sequence and lack of central glycine residue reduce structural flexibility which might contribute to diminished cleavage capability. The negligible difference witnessed in quantifying cleavage activity between the two quantification methods can be attributed to the special orientation and conformation of the target: conjugate heteroduplex. Linear labelled **F**-**Q**-RNA and intact tRNA^{Phe} targets were used for cleavage assay and conventional gel electrophoresis, respectively.

"bis" and *"triple"* conjugates predominantly targeted A62-G65 region of tRNA^{Phe}. Minor products were generated by cleavage at C32-A44, G18-G20 and G22-G26 position (**Figure 3.10** (**A**-**E**)). In general, *"bis"* and *"triple"* conjugates showed a natural preference to pyrimidine-X phosphodiester bond cleavage with G-X cleavage specificity outside the bulge-loop target region. The major cleavage sites outside the bulge-loop region were in the 'reactive radius' of the peptide and are conformationally accessible to the cleaving moiety. Two distinctive cleavage patterns were witnessed amongst *"bis"* and *"triple"* conjugates in the loop region (see **Figure 3.11**). BC5-L-αα and BC5-L-ββ exhibited G-X and Pyr-X specificity, making two major cuts at C63 and G65 within the targeted region. A common cleavage trend within the target region was observed when diastereoisomer analogues were incorporated in antisense recognition motif (αβ or βα) as well as *"triple"* conjugate (**Figure 3.11**) with two major cuts at A62 and C63 positions.

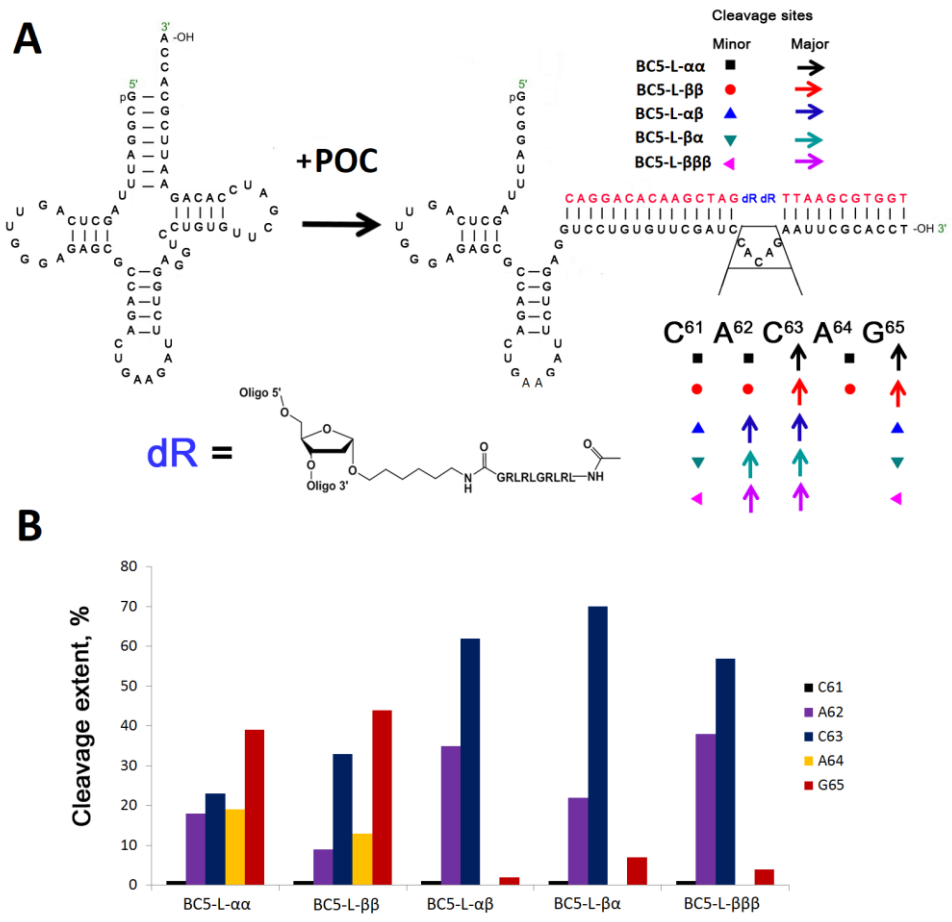

Figure 3.11. (**A**) Hybridisation of *"bis"* and *"triple"* conjugates (red) induces a 5-nt long bulge loop around the ^{61}C-A-C-A-G^{65} region of the tRNA^{Phe} (black), exposing the region and increasing its susceptibility to cleavage. Major cleavage sites are presented with arrows, whereas minor cleavage sites are indicated with dots. (**B**) Extent of cleavage (%) at the target bulge loop region (^{61}C-A-C-A-G^{65}) for different *"bis"* and *"triple"* conjugates indicating the percentage of cleavage at each nucleotide corresponding to major and minor cuts.

The cleavage of tRNA^{Phe} by *"bis"* and *"triple"* conjugates exhibited a linear pattern at lower excess concentration of conjugate over target (5:1 conjugate over target, **Supplementary Figure 3.30**). In contrast, cleavage for *"bis"* and *"triple"* conjugates exhibited the usual hyperbolic character with both 10 and 20 μM concentrations. A non-linear enhancement in cleavage activity with conjugate concentration was witnessed in previous studies where the self-assembly of conjugates and formation of multiplexes were suspected to be the key factor driving the catalysis (32, 33, 36, 53). Previously, circumstantial 2D NMR spectroscopy experiments demonstrated NOE cross-peaks indicating intra- and inter- nucleotide, peptide and peptide-nucleotide interactions further substantiating the formation of hairpin-like folded conformation of conjugates (54). At higher concentrations, cleavage hit the plateau swiftly, and a higher percentage of cleavage was observed. It is possible that the difference witnessed was due to the fact that RNA cleavage is only detectable beyond a certain concentration of catalytically active

conjugate. Furthermore, it is feasible that two or more conjugate molecules target the same tRNA sequence simultaneously, forming a productive complex with cleavage capability. Henceforth, incorporation of two or more cleaving moieties in a single molecule further encourages the formation of catalytically reactive confirmation.

As anticipated, the addition of multiple peptide entities resulted in a greater extent of cleavage in "*bis*" and "*triple*" conjugates. The incorporation of multiple peptide moieties amplified the cleavage within the target loop region where up to 100 % cleavage was achieved in comparison to 54% cleavage seen for the best "*single*" structural candidate (BC5-L-β) (39). The presence of di-guanidine functional groups encourages the hydrolysis of RNA backbone through the cooperative proton transfer between two guanidine groups (see **Figure 3.1** (**B**)) (55). Indeed, the presence of a neutral guanidine group is necessary for deprotonation of the 2'-OH group of RNA ribose to accelerate the formation of a di-anionic pentaoxyphosphorane intermediate, and the proximity of protonated guanidinium moiety is essential to facilitate the transesterification reaction. Therefore, the incorporation of multiple arginine-rich amphiphilic peptide residues increases the probability to form such guanidine-guanidinium dyads and facilitates the guanidinium-mediated RNA cleavage. The high catalytic efficiency and potency of "*bis*" and "*triple*" conjugates and their superiority to their "*single*" counterparts are evident from the extent and kinetic of cleavage.

3.6 Conclusion

In this study, the next generation *"bis"* and *"triple"* conjugates were synthesised to optimise the cleavage activity and accelerate phosphodiester transesterification. The catalytic activity of multiple artificial ribonucleases was assayed simultaneously in a single step using a fluorescent-based assay. The method presented herein provides a reliable, effective, simple, and accurate method to screen potential drug candidates which can revolutionise high-throughput drug discovery screening of artificial ribonucleases. The designed POCs promoted the hydrolytic cleavage of linear **F-Q**-RNA and full-length $tRNA^{Phe}$ molecules in a sequence-specific manner. The incorporation of multiple catalytic entities played an integral part in cleavage efficiency resulting in remarkably high cleavage activity (up to 100% cleavage of $tRNA^{Phe}$ in 24 hours). The results presented indicate the cleavage of target RNA molecule in single (excess of conjugate over target) and multiple (excess of target over conjugate) turnover mode stipulating the conjugates' ability to move from one target molecule to another following cleavage. The designed

POCs exhibited catalytic turnover without the need for exogenous enzymes. Hence, they hold the potential to selectively knock down multiple copies of RNA, a feature which can be further potentiated through recruitment of RNase H *in vivo*.

The kinetic analysis was convoluted by the formation of inter- and intramolecular assemblies stem from the interplay between the positively charged amphipathic peptide and negatively charged oligonucleotide components. Depletion of active conjugate and self-complexation of target molecules diminished the reaction rate, with target outcompeting the complexes to form a substrate: conjugate complex. The kinetic modelling simulation illuminated the true substrate turnover potential of these macromolecules indicating the obstructive effects of non-productive conformation. Destabilisation and destruction of non-productive conformations can unlock the full therapeutic potential of POC-mediated therapeutics, bringing us a step closer to achieving a stable, sequence-specific, efficient, and self-reliant catalyst.

3.7 References

1. Chang,T.C. and Mendell,J.T. (2007) microRNAs in vertebrate physiology and human disease. Annu. Rev. *Genomics Hum. Genet*., **8**, 215–239.

2. Holoch,D. and Moazed,D. (2015) RNA-mediated epigenetic regulation of gene expression. *Nat. Rev. Genet.*, **16**, 71–84.

3. Romero-Barrios,N., Legascue,M.F., Benhamed,M., Ariel,F. and Crespi,M. (2018) Splicing regulation by long noncoding RNAs. *Nucleic Acids Res.*, **46**, 2169–2184.

4. Zhang,X., Ma,X., Jing,S., Zhang,H. and Zhang,Y. (2018) Non-coding RNAs and retroviruses. *Retrovirology*, **15**, 20.

5. Esteller,M. (2011) Non-coding RNAs in human disease. *Nat. Rev. Genet*., **12**, 861–874.

6. Lin,S. and Gregory,R.I. (2015) MicroRNA biogenesis pathways in cancer. *Nat. Rev. Cancer*, **15**, 321–333.

7. Shi,C., Yang,Y., Xia,Y., Okugawa,Y., Yang,J., Liang,Y., Chen,H., Zhang,P., Wang,F., Han,H., et al. (2016) Novel evidence for an oncogenic role of microRNA-21 in colitis-associated colorectal cancer. *Gut*, **65**, 1470–1481.

8. Yeh,C.-H., Moles,R. and Nicot,C. (2016) Clinical significance of microRNAs in chronic and acute human leukemia. *Mol. Cancer*, **15**, 37.

9. Singh,R.P., Massachi,I., Manickavel,S., Singh,S., Rao,N.P., Hasan,S., Mc Curdy,D.K., Sharma,S., Wong,D., Hahn,B.H., et al. (2013) The role of miRNA in inflammation and autoimmunity. *Autoimmun. Rev.*, **12**, 1160–1165.

10. Lukiw,W.J. (2012) NF-κB-regulated, proinflammatory miRNAs in Alzheimer's disease. *Alzheimers. Res. Ther.*, **4**, 47.

11. Pogue,A.I. and Lukiw,W.J. (2018) Up-regulated Pro-inflammatory MicroRNAs (miRNAs) in Alzheimer's disease (AD) and Age-Related Macular Degeneration (AMD). *Cell. Mol. Neurobiol.*, **38**, 1021–1031.

12. Leon-Icaza,S.A., Zeng,M. and Rosas-Taraco,A.G. (2019) microRNAs in viral acute respiratory infections: immune regulation, biomarkers, therapy, and vaccines. *ExRNA*, **1**, 1.

13. Mocellin,S. and Provenzano,M. (2004) RNA interference: learning gene knock-down from cell physiology. *J. Transl. Med.*, **2**, 39.

14. Emilsson,V., Thorleifsson,G., Zhang,B., Leonardson,A.S., Zink,F., Zhu,J., Carlson,S., Helgason,A., Walters,G.B., Gunnarsdottir,S., et al. (2008) Genetics of gene expression and its effect on disease. *Nature*, **452**, 423–428.

15. Milhavet,O., Gary,D.S. and Mattson,M.P. (2003) RNA interference in biology and medicine. *Pharmacol. Rev.*, **55**, 629–648.

16. Jones,D. (2011) The long march of antisense. *Nat. Rev. Drug Discov*., **10**, 401–402.

17. Kole,R., Krainer,A.R. and Altman,S. (2012) RNA therapeutics: beyond RNA interference and antisense oligonucleotides. *Nat. Rev. Drug Discov*., **11**, 125–140.

18. Kanasty,R.L., Whitehead,K.A., Vegas,A.J. and Anderson,D.G. (2012) Action and reaction: the biological response to siRNA and its delivery vehicles. *Mol. Ther.*, **20**, 513–524.

19. Tiemann,K. and Rossi,J.J. (2009) RNAi-based therapeutics-current status, challenges and prospects. *EMBO Mol. Med.*, **1**, 142–151.

20. Xie,F.Y., Woodle,M.C. and Lu,P.Y. (2006) Harnessing in vivo siRNA delivery for drug discovery and therapeutic development. *Drug Discov. Today*, **11**, 67–73.

21. Sledz,C.A. and Williams,B.R.G. (2005) RNA interference in biology and disease. *Blood*, **106**, 787–794.

22. Lam,J.K.W., Chow,M.Y.T., Zhang,Y. and Leung,S.W.S. (2015) siRNA Versus miRNA as Therapeutics for Gene Silencing. *Mol. Ther. - Nucleic Acids*, **4**.

23. Cox,D.B.T., Gootenberg,J.S., Abudayyeh,O.O., Franklin,B., Kellner,M.J., Joung,J. and Zhang,F. (2017) RNA editing with CRISPR-Cas13. *Science.*, **358**, 1019 – 1027.

24. Zhang,X.-H., Tee,L.Y., Wang,X.-G., Huang,Q.-S. and Yang,S.-H. (2015) Off-target Effects in CRISPR/Cas9-mediated Genome Engineering. *Mol. Ther. - Nucleic Acids*, **4**, 264.

25. Vickers,T.A. and Crooke,S.T. (2015) The rates of the major steps in the molecular mechanism of RNase H1-dependent antisense oligonucleotide induced degradation of RNA. *Nucleic Acids Res.*, **43**, 8955–8963.

26. Hagedorn,P.H., Hansen,B.R., Koch,T. and Lindow,M. (2017) Managing the sequence-specificity of antisense oligonucleotides in drug discovery. *Nucleic Acids Res.*, **45**, 2262–2282.

27. ten Asbroek,A.L.M.A., van Groenigen,M., Nooij,M. and Baas,F. (2002) The involvement of human ribonucleases H1 and H2 in the variation of response of cells to antisense phosphorothioate oligonucleotides. *Eur. J. Biochem.*, **269**, 583–592.

28. Mironova,N.L., Pyshnyi,D. V, Ivanova,E.M., Zenkova,M.A., Gross,H.J. and Vlassov,V. V (2004) Covalently attached oligodeoxyribonucleotides induce RNase activity of a short peptide and modulate its base specificity. *Nucleic Acids Res.*, **32**, 1928–1936.

29. Mironova,N.L., Pyshnyi,D. V, Stadler,D. V, Prokudin,I. V, Boutorine,Y.I., Ivanova,E.M., Zenkova,M.A., Gross,H.J. and Vlassov,V. V (2006) G-specific RNA-cleaving conjugates of short peptides and oligodeoxyribonucleotides. *J. Biomol. Struct. Dyn.*, **23**, 591–602.

30. Mironova,N.L., Boutorine,Y.I., Pyshnyi,D. V, Ivanova,E.M., Zenkova,M.A. and Vlassov,V. V (2004) Ribonuclease Activity of the Peptides with Alternating Arginine and Leucine Residues Conjugated to Tetrathymidilate. *Nucleosides. Nucleotides Nucleic Acids*, **23**, 885–890.

31. Williams,A., Staroseletz,Y., Zenkova,M.A., Jeannin,L., Aojula,H. and Bichenkova,E. V. (2015) Peptidyl-Oligonucleotide Conjugates Demonstrate Efficient Cleavage of RNA in a Sequence-Specific Manner. *Bioconjug. Chem.*, **26**, 1129–1143.

32. Staroseletz,Y., Williams,A., Burusco,K.K., Alibay,I., Vlassov,V. V., Zenkova,M.A. and Bichenkova,E. V. (2017) 'Dual' peptidyl-oligonucleotide conjugates: Role of conformational flexibility in catalytic cleavage of RNA. *Biomaterials*, **112**, 44–61.

33. Patutina,O.A., Bichenkova,E. V, Miroshnichenko,S.K., Mironova,N.L., Trivoluzzi,L.T., Burusco,K.K., Bryce,R.A., Vlassov,V. V and Zenkova,M.A. (2017) miRNases: Novel peptide-oligonucleotide bioconjugates that silence miR-21 in lymphosarcoma cells. *Biomaterials*, **122**, 163–178.

34. Mironova,N.L., Pyshnyi,D. V, Shtadler,D. V, Fedorova,A.A., Vlassov,V. V and Zenkova,M.A. (2007) RNase T1 mimicking artificial ribonuclease. *Nucleic Acids Res.*, **35**, 2356–2367.

35. Patutina,O., Chiglintseva,D., Bichenkova,E., Gaponova,S., Mironova,N., Vlassov,V. and Zenkova,M. (2020) Dual miRNases for Triple Incision of miRNA Target: Design Concept and Catalytic Performance. *Molecules*, **25**, 2459.

36. Patutina,O.A., Miroshnichenko,S.K., Mironova,N.L., Sen'kova,A. V., Bichenkova,E. V., Clarke,D.J., Vlassov,V. V. and Zenkova,M.A. (2019) Catalytic Knockdown of miR-21 by Artificial Ribonuclease: Biological Performance in Tumor Model. *Front. Pharmacol.*, **10**, 1–13.

37. Mikkola,S., Lönnberg,T. and Lönnberg,H. (2018) Phosphodiester models for cleavage of nucleic acids. *Beilstein J. Org. Chem.*, **14**, 803–837.

38. Mironova,N.L., Pyshnyi,D. V, Ivanova,E.M., Zarytova,V.F., Zenkova,M.A., Gross,H.J. and Vlassov,V. V (2002) Sequence-specific RNA cleavage by oligonucleotide-peptide conjugates. *Russ. Chem. Bull.*, **51**, 1177–1186.

39. Staroseletz,Y., Amirloo,B., Williams,A., Lomzov,A., Burusco,K.K., Clarke,D.J., Brown,T., Zenkova,M.A. and Bichenkova,E. V. (2020) Strict conformational demands of RNA cleavage in bulge-loops created by peptidyl-oligonucleotide conjugates. *Nucleic Acids Res.* Accepted on 7 Sep 2020.

40. Salvio,R. and Casnati,A. (2017) Guanidinium Promoted Cleavage of Phosphoric Diesters: Kinetic Investigations and Calculations Provide Indications on the Operating Mechanism. *J. Org. Chem.*, **82**, 10461–10469.

41. Silberklang,M., Gillum,A.M. and RajBhandary,U.L. (1979) Use of in Vitro 32P Labeling in the Sequence Analysis of Nonradioactive tRNAs. *Methods Enzym.*, **59**, 58–109.

42. Yan,B.X. and Sun,Y.Q. (1997) Glycine residues provide flexibility for enzyme active sites. *J. Biol. Chem.*, **272**, 3190–3194.

43. Bartlett,G.J., Porter,C.T., Borkakoti,N. and Thornton,J.M. (2002) Analysis of catalytic residues in enzyme active sites. *J. Mol. Biol.*, **324**, 105–121.

44. Okoniewska,M., Tanaka,T. and Yada,R.Y. (2000) The pepsin residue glycine-76 contributes to active-site loop flexibility and participates in catalysis. *Biochem. J.*, **349**, 169–177.

45. Tiwari,M.K., Singh,R.K., Singh,R., Jeya,M., Zhao,H. and Lee,J.-K. (2012) Role of conserved glycine in zinc-dependent medium chain dehydrogenase/reductase superfamily. *J. Biol. Chem.*, **287**, 19429–19439.

46. Hoefer,F., Marquardt,K., Schmidts,T., Domann,E. and Runkel,F. (2017) HPLC based single-step kinetic assay to screen the activity of DNAzymes. *Anal. Methods*, **9**, 697–704.

47. Joyner,J.C., Keuper,K.D. and Cowan,J.A. (2013) Analysis of RNA cleavage by MALDI-TOF mass spectrometry. *Nucleic Acids Res.*, **41**, e2.

48. Kuznetsova,I.L., Zenkova,M.A. and Vlassov,V. V (2006) Cleavage of RNA bulge loops by artificial RNases. *Russ. Chem. Bull.*, **55**, 1284–1294.

49. Hall,J., Hüsken,D. and Häner,R. (1996) Towards artificial ribonucleases: the sequence-specific cleavage of RNA in a duplex. *Nucleic Acids Res.*, **24**, 3522–3526.

50. Jin,Y. and Cowan,J.A. (2006) Targeted Cleavage of HIV Rev Response Element RNA by Metallopeptide Complexes. *J. Am. Chem. Soc.*, **128**, 410–411.

51. Qi,X., Loiseau,F., Chan,W.L., Yan,Y., Wei,Z., Milroy,L.-G., Myers,R.M., Ley,S. V, Read,R.J., Carrell,R.W., et al. (2011) Allosteric modulation of hormone release from thyroxine and corticosteroid-binding globulins. *J. Biol. Chem.*, **286**, 16163–16173.

52. Bielec,K., Sozanski,K., Seynen,M., Dziekan,Z., ten Wolde,P.R. and Holyst,R. (2019) Kinetics and equilibrium constants of oligonucleotides at low concentrations. Hybridization and melting study. *Phys. Chem. Chem. Phys.*, **21**, 10798–10807.

53. Kovalev,N.A., Medvedeva,D.A., Zenkova,M.A. and Vlassov,V. V (2008) Cleavage of RNA by an amphiphilic compound lacking traditional catalytic groups. *Bioorg. Chem.*, **36**, 33–45.

54. Gebrezgiabher,M., Zalloum,W.A., Clarke,D.J., Miles,S.M., Fedorova,A.A., Zenkova,M.A. and Bichenkova,E. V (2020) RNA knockdown by synthetic peptidyl-oligonucleotide ribonucleases: behavior of recognition and cleavage elements under physiological conditions. *J. Biomol. Struct. Dyn.*, 1–20.

55. Salvio,R., Mandolini,L. and Savelli,C. (2013) Guanidine–Guanidinium Cooperation in Bifunctional Artificial Phosphodiesterases Based on Diphenylmethane Spacers; gem-Dialkyl Effect on Catalytic Efficiency. *J. Org. Chem.*, **78**, 7259–7263.

3.8 Supporting information

3.8.1 Sequences of the unconjugated oligonucleotides and peptides

Table 3.2. Sequences and millimolar extinction coefficients values for peptides, unconjugated oligonucleotide and labelled linear target used for this study.

Name	Sequence (5' to 3')	E_{260} ($mM^{-1}\cdot cm^{-1}$)[a]
Ac-[LR]$_3$G-CO$_2$H	Ac-Leu-Arg-Leu-Arg-Leu-Arg-Gly	n/a
Ac-[LRLRG]$_2$-CO$_2$H	Ac-Leu-Arg-Leu-Arg-Gly-Leu-Arg-Leu-Arg-Gly	n/a
BC5-L-ββ	TGGTGCGAATT- **dR^{beta} dR^{beta}** -GATCGAACACAGGAC [b]	269.1
BC5-L-αα	TGGTGCGAATT- **dR^{alpha} dR^{alpha}**-GATCGAACACAGGAC [b]	269.1
BC5-L-αβ	TGGTGCGAATT- **dR^{alpha} dR^{beta}** –GATCGAACACAGGAC [b]	269.1
BC5-L-βα	TGGTGCGAATT- **dR^{beta} dR^{alpha}** –GATCGAACACAGGAC [b]	269.1
BC5-L-βββ	TGGTGCGAATT- **dR^{beta} dR^{beta} dR^{beta}** – GATCGAACACAGGAC [b]	269.1
Labelled linear target	GTCCTGTGTTCGA**T$_F$C$_r$A$_r$C$_r$A$_r$G$_r$**AA**T$_Q$**TCGCACCA	337.5

a) **E_{260} denotes the millimolar extinction coefficient**

b) **dR denotes abasic nucleotide incorporated in oligonucleotide seqeucne**

3.8.2 MALDI-ToF mass spectra Acetyl-[LRLRG]$_2$-CO$_2$H

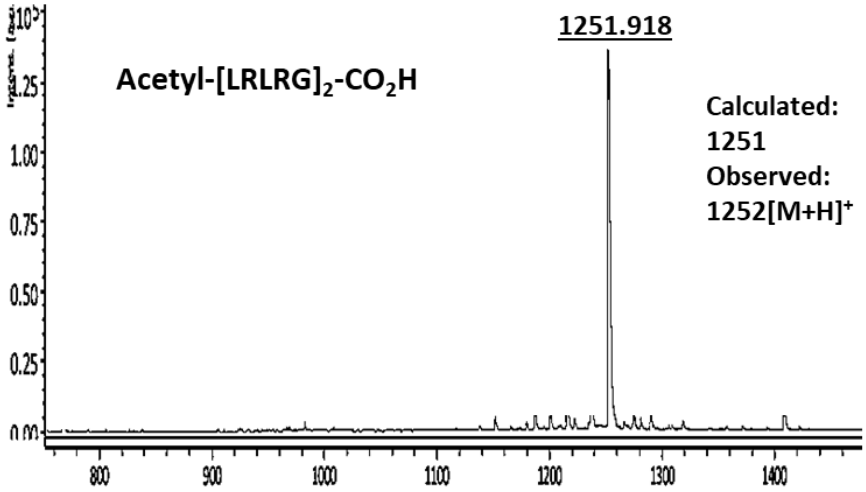

Figure 3.12. MALDI-TOF spectra of peptide Acetyl-[LRLRG]$_2$-CO$_2$H. Spectra were recorded using a Bruker Daltonics Ultraflex TOF/TOF mass spectrometer.

3.8.3 ^{1}H-NMR spectra of the Acetyl-[LRLRG]$_2$-CO$_2$H peptide

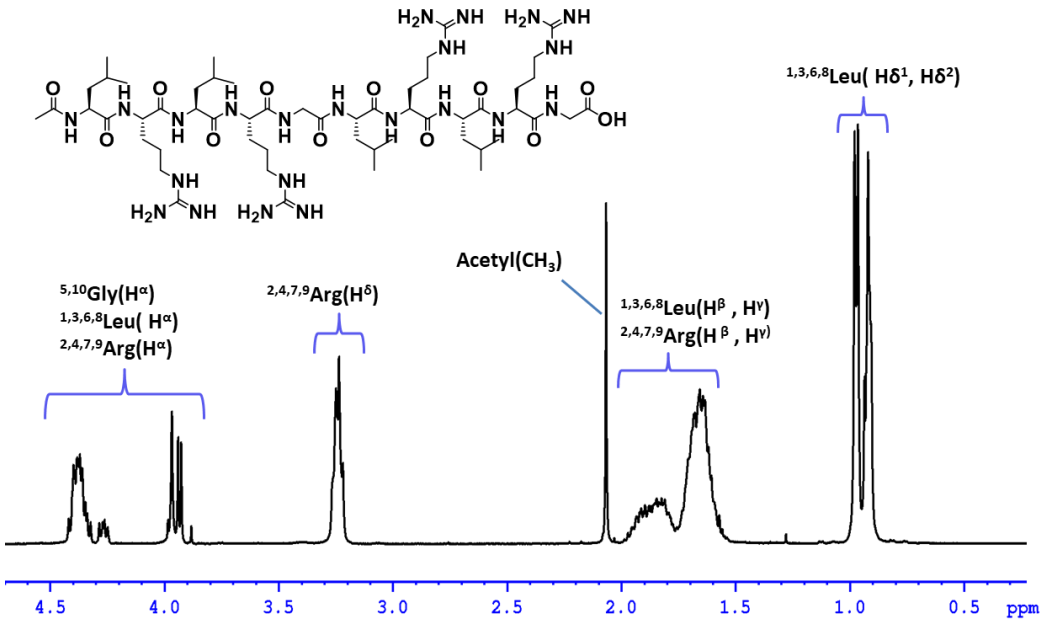

Figure 3.13. ^{1}H NMR spectrum for Acetyl-[LRLRG]$_2$-CO$_2$H peptide. The spectrum was recorded in D$_2$O at 25 °C using 400 MHz NMR spectrometer (Bruker Avance II+ 400).

3.8.4 MALDI-ToF mass spectra Acetyl-[LR]$_3$G-CO$_2$H

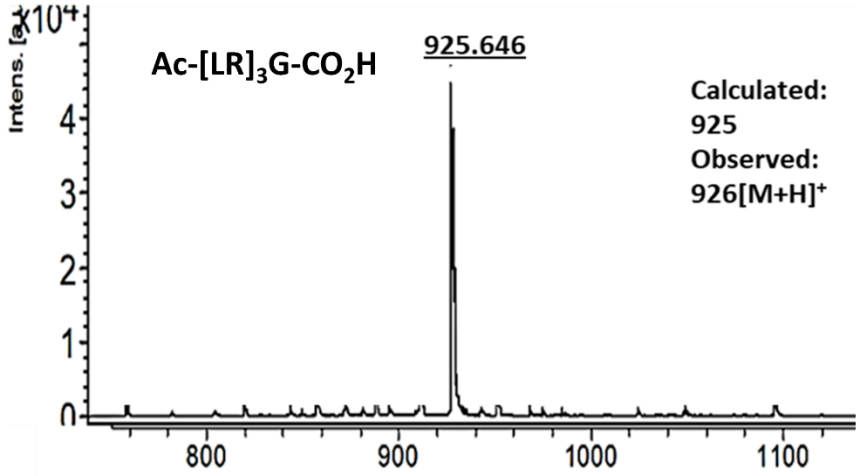

Figure 3.14. MALDI-TOF spectra of peptide Acetyl-[LR]$_3$G-CO$_2$H Spectra were recorded using a Bruker Daltonics Ultraflex TOF/TOF mass spectrometer.

3.8.5 ^{1}H-NMR spectra of the Acetyl-[LR]$_3$G-CO$_2$H peptide

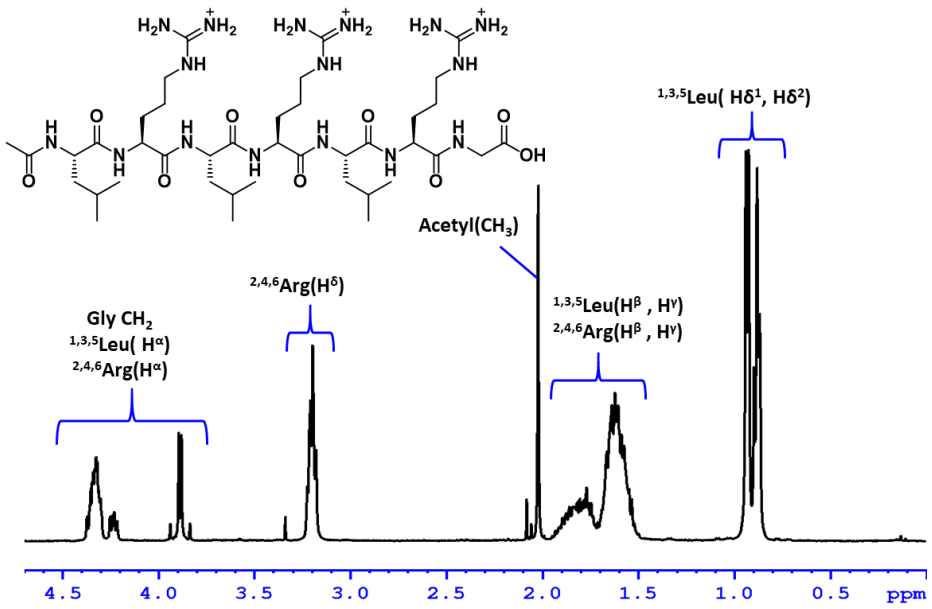

Figure 3.15. ^{1}H NMR spectrum for Acetyl-[LR]$_3$G-CO$_2$H peptide recorded in D$_2$O at 400 MHz.

3.8.6 General synthetic route of *"bis"* and *"triple"* conjugation

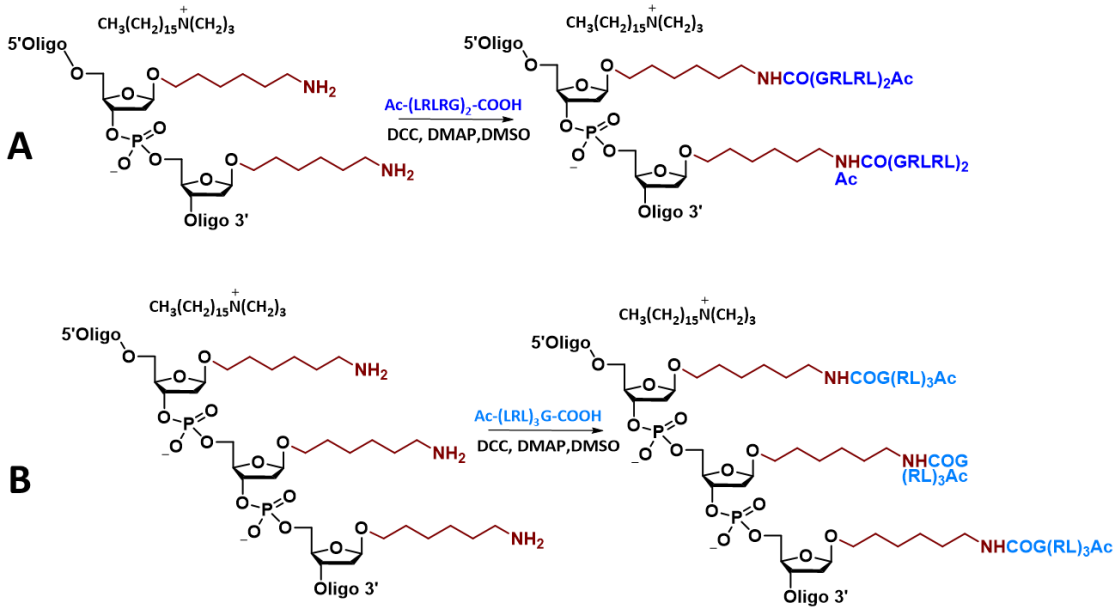

Figure 3.16. General synthetic route of conjugation. **A.** Synthetic route for the production of *"bis"* conjugates, demonstrated by the example of BC5-L-ββ conjugate synthesis, when β configuration was used for aminohexyl linker attachment at C1' position of abasic nucleotides. Similar synthetic route was used for the synthesis of BC5-L-αα, BC5-L-βα and BC5-L-αβ conjugates, when α configuration was also used for aminohexyl linker attachment at C1' position of abasic nucleotides. **B.** Synthetic route for the synthesis of *"triple"* conjugate BC5-L-βββ. Antisense oligonucleotide containing two or three internal abasic nucleotide either in α or β configuration was conjugated to catalytic peptide via aminohexyl linker. To avoid peptide self-conjugation and cyclisation during amide coupling reaction, the acetylated N-termini peptide was used.

3.8.7 Shift in RP-HPLC purification chromatogram for *"bis"* and *"triple"* conjugates

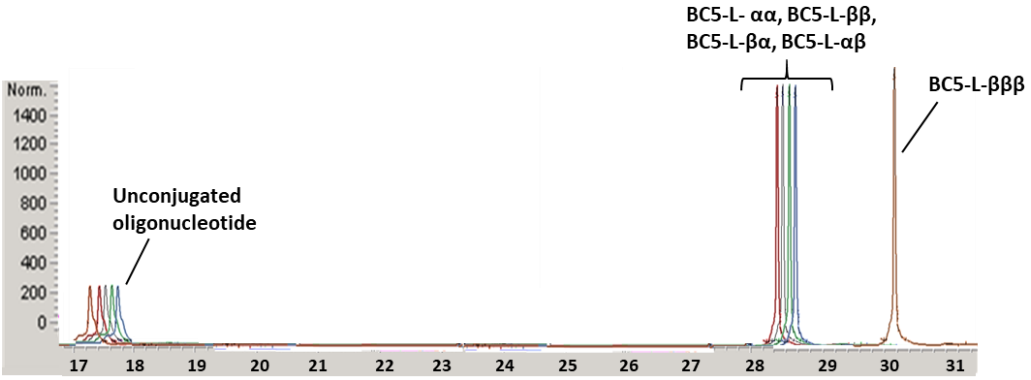

Figure 3.17. An overlay of the RP-HPLC purification chromatogram of BC5-L-αα (red), BC5-L-ββ (black), BC5-L-βα (green), BC5-L-αβ (blue) and BC5-L-βββ (orange), showing the shift in retention time from unconjugated oligonucleotide to "*bis"* and *"triple"* conjugates.

3.8.8 MALDI-ToF mass spectra of *"bis"* and *"triple"* peptidyl-oligonucleotide conjugates

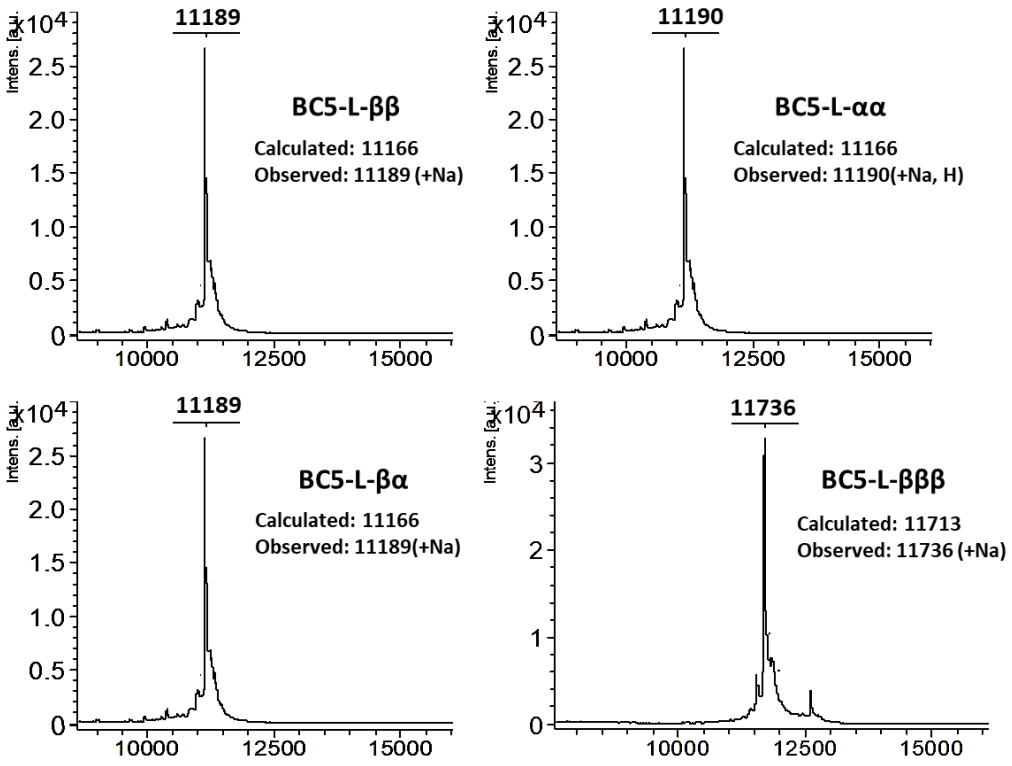

Figure 3.18. MALDI-TOF spectra of *"bis"* and *"triple"* peptidyl-oligonucleotide conjugates. Spectra were recorded using 0.7 M 3-Hydroxy picolinic acid matrix (97 mg/mL, with 0.07 M ammonium citrate, 16 mg/mL in 50:50 ACN:H_2O) on a Bruker Daltonics Ultraflex ToF/ToF mass spectrometer.

3.8.9 ^{1}H NMR spectra of the bulge-loop inducing *"bis"* and *"triple"* conjugates

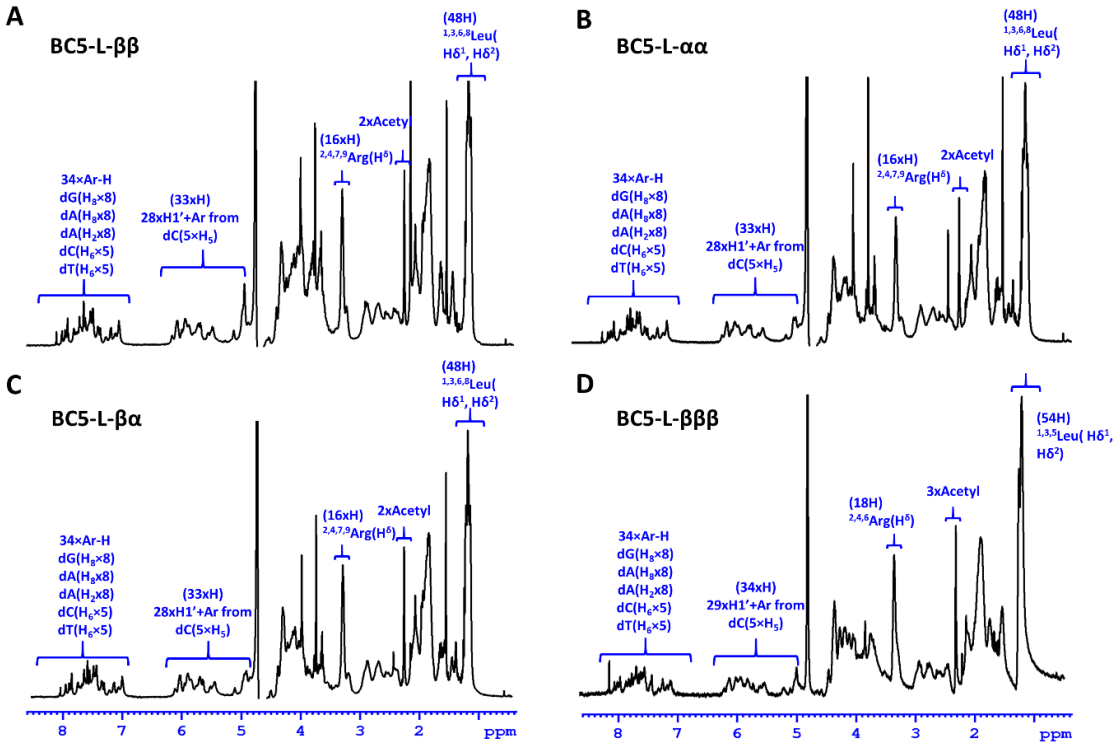

Figure 3.19. ^{1}H NMR spectra (400 MHz, Bruker Avance IIþ 400) of *"bis"* and *"triple"* conjugates indicating the prominent chemical shift of protons from oligonucleotides, peptide, aminohexyl linker and acetyl protecting group. In each spectrum, the breakdown of proton assignment for each region as well as integral intensity has been indicated. H3' region has not been assigned since water suppression prohibits full assignment.

3.8.10 ^{1}H NMR comparison of *"single"*, *"bis"* and *"triple"* conjugates

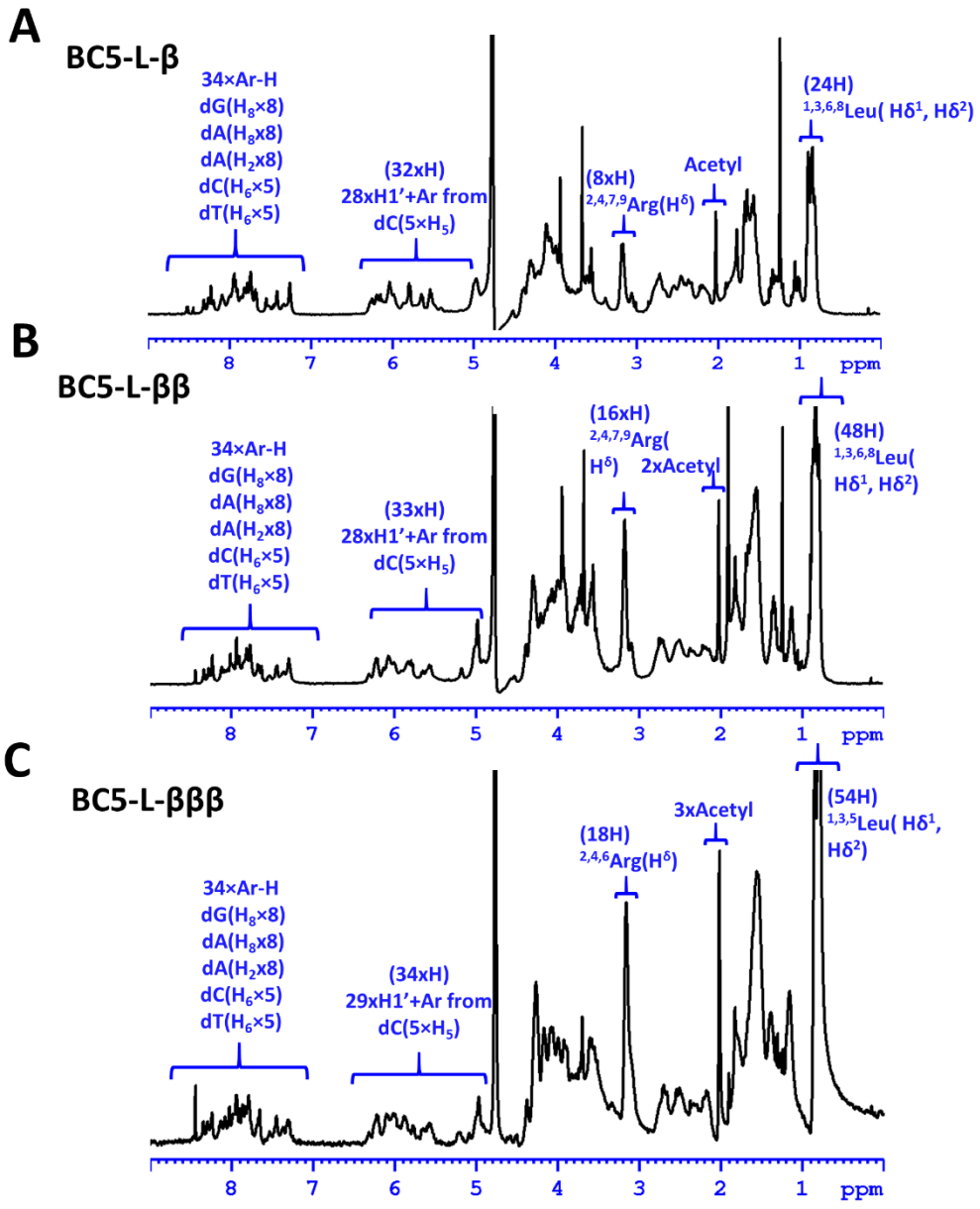

Figure 3.20. ^{1}H NMR spectra (400 MHz, Bruker Avance IIþ 400) of BC5-L-β *"single"* conjugate **(A)** BC5-L-ββ *"bis"* conjugate **(B)** and BC5-L- βββ *"triple"* conjugate **(C)**. The prominent chemical shifts corresponding to oligonucleotides, peptide, aminohexyl linker and acetyl protecting group can be clearly seen. Careful integration of the oligonucleotide aromatic region as well as H1' sugar ring protons confirmed 1:1, 2:1 and 3:1 stoichiometric ratio of peptide to oligonucleotide in *"single"*, *"bis"* and *"triple"* conjugates.

3.8.11 Representative qualitative image of hybridisation of conjugates to the labelled linear target

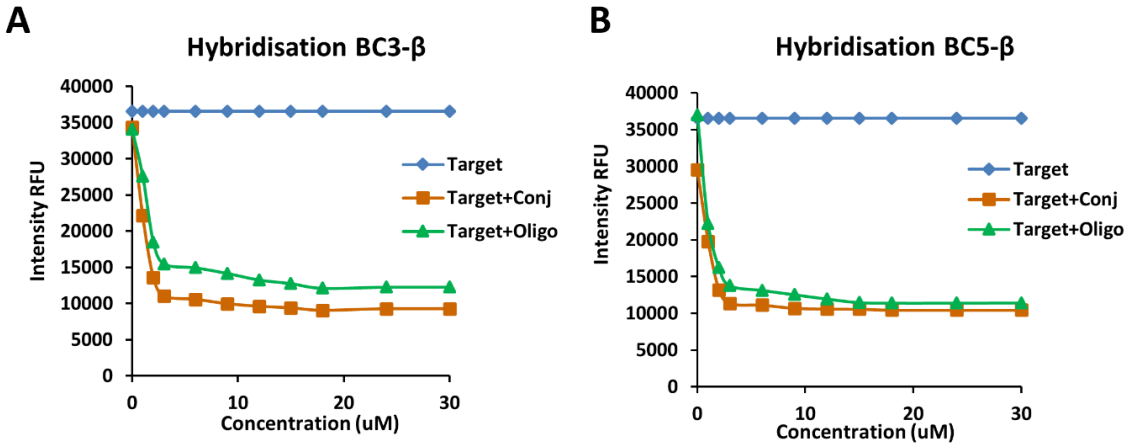

Figure 3.21. Representative titration experiments showing hybridisation of the selected *"single"* conjugates (BC3-β or BC5-β) to the fluorescently labelled **F**-**Q**-RNA target. (**A**) The labelled target **F**-**Q**-RNA (at 1μM concentration) was incubated either with BC3-β conjugate or with the corresponding unconjugated oligonucleotide at concentrations ranging from 0 to 30 μM (added in incremental steps) for 30 minutes followed by fluorescence detection. (**B**) The labelled **F**-**Q**-RNA was incubated with either BC5-β conjugate or with the corresponding unconjugated oligonucleotide at concentrations ranging from 0 to 30 μM (added in incremental steps) followed by fluorescence detection. The fluorescence readings were taking sequentially after addition of the subsequent aliquot of either conjugate or unmodified oligonucleotide. As a control, target sequence was incubated in a parallel reaction mixture in the absence of POC or the corresponding unconjugated oligonucleotide. Fluorescence was measured at λ_{em}= 522 nm following excitation at λ_{ex}= 494 nm. A distinctive decrease in fluorescence intensity signified hybridisation of the conjugate or the corresponding unconjugated oligonucleotide to the **F**-**Q**-RNA target.

3.8.12 Non-specific cleavage of labelled linear F-Q-RNA target

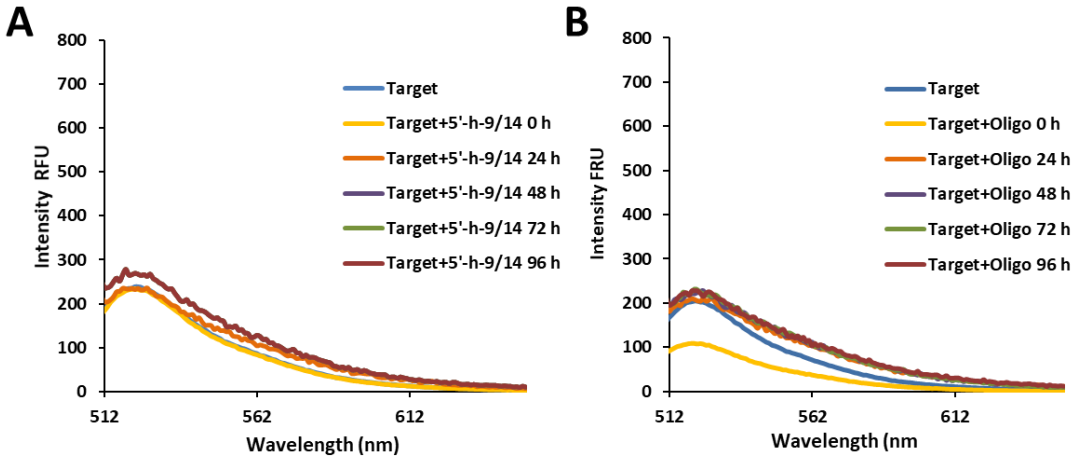

Figure 3.22. Control cleavage experiments of the fluorescently labelled linear **F**-**Q**-RNA target. (**A**) Assessment of cleavage sequence-specificity. Lack of cleavage was witnessed, when **F**-**Q**-RNA (1 μM) was incubated with a scrambled peptidyl-oligonucleotide 5'-h-9/14 (20 μM), lacking complementarity with the oligonucleotide sequence of **F**-**Q**-RNA. (**B**) Assessment of potential cleavage activity of an unconjugated oligonucleotide sequence. The incubation of **F**-**Q**-RNA (1 μM) with an unconjugated oligonucleotide sequence (20 μM) showed no spontaneous cleavage. (**B**). The reactions were incubated at 37°C, and aliquots were taken at certain time points (0,24,48,72 and 96 hours).

3.8.13 Representative examples of various possible hairpin and duplex secondary structures of POC catalysts and labelled linear target F-Q-RNA

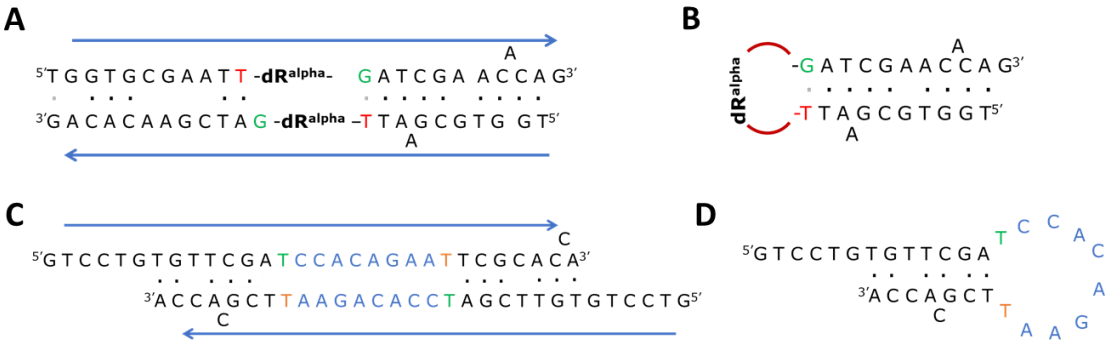

Figure 3.23. Representative image of inter- and intramolecular complexes of target and conjugate**. A.** Possible duplex structure formed between 2 antiparallel sequences of BC5-α. **B.** Internal hairpin structure of BC5-α. **C.** Intramolecular duplex structure formed between 2 antiparallel sequences of linear labelled target **F-Q**-RNA. **D.** Internal hairpin structure of linear labelled target **F-Q**-RNA.

3.8.14 Target and catalytic conjugate interaction model to explain atypical kinetic observations

The observed initial velocities of the POC-catalysed cleavage of excess target substrate showed behaviour that cannot be explained by Michaelis Menten kinetics, in three main regions:

(a) when substrate was in small excess (2 and 5-fold), initial velocities were lower than expected and even then increased with substantial depletion of substrate into product;
(b) with substrate in larger excesses (10 and 20-fold), initial velocities were higher than could be contiguous with the above velocities, and declined with substrate conversion to product;
(c) at higher substrate excesses (from 20 to 30-fold), initial velocities were much lower than could be contiguous with the above velocities and declined as substrate was converted to product.

Such behaviours did not lie on any hyperbolic velocity – substrate curve (even when substrate and product inhibitions had been considered - see later **Figure 3.27**). New kinetic principles might need to be elucidated with a novel catalyst. However, we first consider whether side interactions of the substrate, catalyst and product can explain these behaviours within an otherwise Michaelis Menten model, where the catalytic complexation of available substrate to POC is considered to be in competition with weaker self-associations, which both inactivate the POC catalyst and sequester substrate into complexes. Such an explanation first needs to consider the equilibrium dissociation constants (K) of each dominant interaction.

3.8.14.1 Model

The binding of free peptide-oligonucleotide conjugate catalyst (C) to free target substrate (S) and the formation of a cleavable substrate-catalyst complex (CS) may be considered, as a first approximation, in terms of a single-site competition, characterised by their respective self-association and dissociation equilibria, which are dynamic as catalysis progresses. Both the target substrate associates into a complex (S_c), unavailable for binding to the catalyst, and the catalyst associates into inactive complex (C_c), unable to attack the target substrate.

In order to determine whether such a model operating alongside Michaelis-Menten kinetics can simulate the observed velocities, we first considered the fractions (denoted

as [concentrations] in square brackets) involved in each self-interaction separately, in isolation from each other, and then in competition (1, 2).

Some of the total catalyst (C_t) is complexed (C_c), leaving available catalyst (C_a):

$[C]_t = [C]_a + [C]_c$ when $[C]_a = [C]_t - [C]_c$ with equilibrium dissociation $K_c = \frac{[C]_a^2}{[C]_C}$ (1)

Substituting into $K_c = \frac{([C]_t - [C]_c)^2}{[C]_c}$ & rearranging $[C]_C = \frac{K_c + 2[C]_t - \sqrt{[K_c + 2[C]_t]^2 - 4[C]_t^2}}{2}$ (2)

and, similarly, the total substrate (S_t) and available substrate (S_a):

$[S]_t = [S]_a + [S]_c$ when $[S]_a = [S]_t - [S]_c$ with equilibrium dissociation $K_s = \frac{[S]_a^2}{[S]_c}$ (3)

substituting into $K_s = \frac{([S]_t - [S]_c)^2}{[S]_c}$ & rearranging $[S]_C = \frac{K_s + 2[S]_t - \sqrt{[K_s + 2[S]_t]^2 - 4[S]_t^2}}{2}$ (4)

When the available conjugate associates with available substrate into the complex (CS):

$[C]_t = [C] + [CS] + [C]_c$ when from (1) available $[C]_a = [C]_t - [C]_c = [C] + [CS]$ (5)

$[S]_t = [S] + [CS] + [S]_c$ when from (2) available $[S]_a = [S]_t - [S]_c = [S] + [CS]$ (6)

whose equilibrium dissociation $K_{cs} = \frac{[C] \times [S]}{[CS]}$ (7)

Substituting into (7) from (5) $[C] = [C]_a - [CS]$ & from (6) $[S] = [S]_a - [CS]$

$K_{cs} = \frac{([C]_a - [CS]) \times ([S]_a - [CS])}{[CS]}$

provides estimate of the expected conjugate complex $[CS]$ at equilibrium with initial substrate, from the observed estimates of equilibrium dissociation K_{cs} and the available substrate $[S]_a$and conjugate $[C]_a$, when rearranged as:

$[CS] = \frac{([C]_a - [CS]) \times ([S]_a - [CS])}{[CS]} = \frac{K_{cs} + [C]_a + [S]_a - \sqrt{[K_{cs} + [C]_a + [S]_a]^2 - 4 \cdot [C]_a \cdot [S]_a}}{2}$ (8)

The target substrate and POC catalysts were purified into respective water solutions and lyophilised, where the removal of water into ice crystals before sublimation will

concentrate and promote their self-complexations. With diminished water, and thereby ionic and hydrogen bonding, hydrophobic bonding within complexes will dominate. When reconstituted back into water and low ionic strength reaction mixtures, the positively-charged peptide is likely to interact with the negatively-charged oligonucleotide (3).

Inactivated POC complexes are likely to be activated especially by binding of available substrate, initially to smaller exposed regions, which activation would increase with substrate concentration. Competitive activation of POC catalyst by the substrate available from self-complexation can consider the common POC available after their interaction at equilibrium (1, 2):

By substituting $[C] = [C]_a - [C]_c$ from (5) and rearranging (1) $K_c = \frac{[C]_a^2}{[C]_c}$ as $[C] = \frac{K_c \times [C]_c}{[C]_a - [C]_c}$

and by substituting $[S] = [S]_a - [CS]$ from (6) into (7): $K_{cs} = \frac{[C] \times [S]}{[CS]} = \frac{[C]([S]_a - [CS])}{[CS]}$

when common $[C] = \frac{K_{cs} \times [CS]}{[S]_a - [CS]} = \frac{K_c \times [C]_c}{[C]_a - [C]_c}$ and when rearranged

complexed $[C]_C = {}^{[C]_a}\Big/\left(\frac{K_c\ ([S]_a - [CS])}{K_{cs} \times [CS]} + 1\right)$ (9)

Similarly, product and substrate compete for POC available after their interactions:

by substituting $[S] = [S]_a - [CS]$ from (6) into (7): $K_{cs} = \frac{[C]([S]_a - [CS])}{[CS]}$

and for product $[P] = [P]_a - [C]_P$ substituting into $K_p = \frac{[C] \times [P]}{[C]_P} = \frac{[C]([P]_a - [C]_P)}{[C]_P}$

when common $[C] = \frac{K_{cs} \times [CS]}{[S]_a - [CS]} = \frac{K_p \times [C]_p}{[P]_a - [C]_p}$ and when rearranged

$[C]_p = {}^{[P]_a}\Big/\left(\frac{K_p\ ([S]_a - [CS])}{K_{cs} \times [CS]} + 1\right)$ (10)

3.8.14.2 Calculation of fractions expected from the model

The expected target substrate complexed $[S]_c$ was calculated from its input equilibrium dissociation K_s and the known total substrate concentration $[S]_t$ initially in isolation (eq. 4), when the available substrate $[S]_a$was obtained by difference (eq. 6). The complexed POC was also initially calculated in isolation from an approximated equilibrium

dissociation K_{cc} (eq. 2), when the activation of POC was calculated (eq. 9) from an initially approximated equilibrium dissociation K_c in competition with the initially-available substrate $[S]_a$ to provide the activated concentration of POC available $[C]_a$ for each reaction. Initial approximated values were refined within the non-linear fitting of the model below for the observed data sets of every reaction for each POC catalyst.

The full binding of substrate and weaker competitive partial binding of substrate to the POC (**Figure 3.7**) were calculated from their input equilibrium dissociations K_{CS} and K_{SS} (respectively), when partial binding of two substrate molecules (double substrate complex with K_{ds}) at higher substrate concentrations was also considered. As product formation was observed at each time point sampled, the corresponding depletion of substrate and the effect on the complexation of substrate were calculated to provide the dynamically-available substrate as the reaction progressed. The product bound to the available conjugate in competition with available substrate was also calculated for each time point from its dissociation K_P (eq. 10), as its observed equilibrium concentration dynamically changed as the reaction progressed.

Formation of the cleavable substrate complex $[CS]$ by full binding of the substrate to the different POC catalysts has dissociation K_{cs} characteristics reported here and earlier (4). Remaining dissociation characteristics were approximated initially as those expected from the dominant binding. The above calculations were completed alongside Michaelis-Menten kinetics for initial velocities (v_0) and initial available substrate $[S]_{a0}$ including the active conjugate $[C]_a$ (in the $V_{max} = [C]_a \times k_{cat}$ term):

$$v_0 = \frac{[C]_a \times k_{cat} \times [S]_{a0}}{K_m + [S]_{a0}} \qquad (11)$$

Non-linear numerical fitting (via 'Solver' add-in for Excel) was used to vary initial approximations of k_{cat} , K_m and to refine approximated equilibrium dissociation characteristics (K_c, K_s, K_{ss_s}) by iteratively calculating the resulting expected velocities, until minimised against the observed velocities (i.e. minimum sums of squares of differences between expected and observed velocities). All of the estimates of fractions of complexation expected were thereby calculated for each reaction time course, which are presented below on a log scale to discern also smaller-scale changes for three of the POC catalysts (**Figure 3.24**).

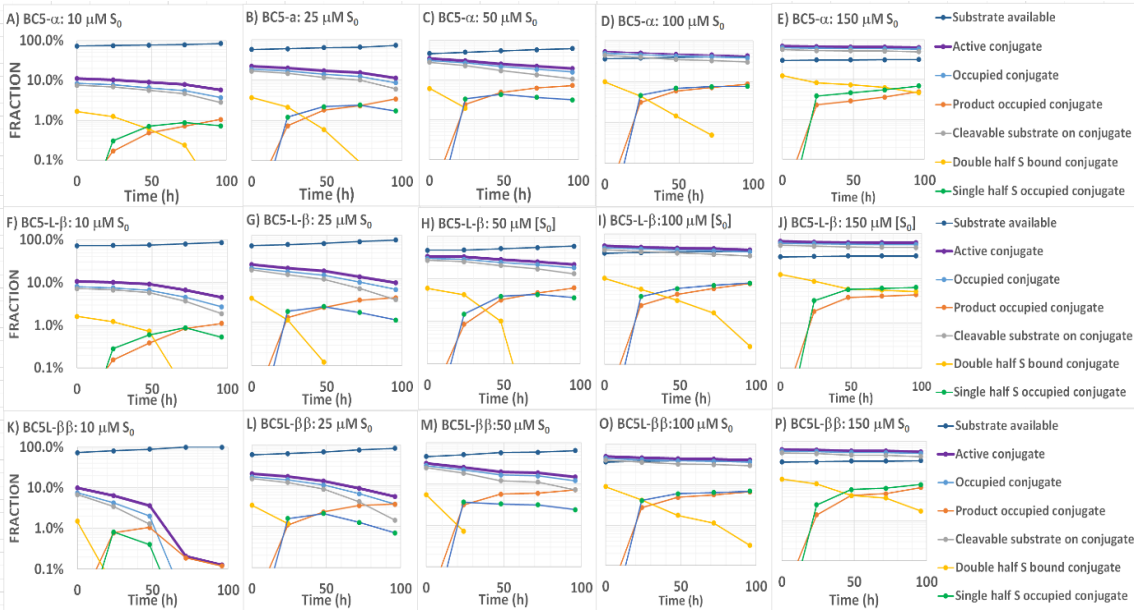

Figure 3.24. Fractional change in substrate, conjugate and product complexes during the progress of reactions of the POC catalysts BC5-α (top row), BC5-L-β (middle row) and BC5-L-ββ (bottom row) for excess initial (total) substrate concentrations (from left to right: $[S]_0$ 10, 25, 50, 100 & 150 μM).

Substrate available (dark blue trace, **Figure 3.24**). Despite consumption of substrate into product, in this model, the fraction of 'Substrate available' will not decline to the same extent and remains relatively steady. Such steady levels particularly at higher initial substrate concentrations were related by the replacement of 'Substrate available' from complexed substrate as total substrate was depleted. This buffering of 'Substrate available' manifests as slightly increasing fractional levels of 'Substrate available' at lower initial substrate concentrations.

Active conjugate (purple trace, **Figure 3.24**). Of the total POC (5 μM in all cases), only a minor fraction (~10%) was available at small excesses of substrate and fractional levels declined during the course of the reaction, as activating substrate declined with less buffering from complexed substrate. As the initial substrate concentration is increased, progressively greater proportions of the total POC will be activated in this part of the model. However, activated POC will become inactivated at still higher substrate concentrations (see below **Figure 3.25**, not shown in above **Figure 3.24**).

Substrate and product-occupied conjugate. Cleavable substrate dominated the occupancy of the conjugate (grey trace **Figure 3.24**). As substrate is cleaved, product occupancy will rise but, given ~10× greater equilibrium dissociation will be less than 10% occupancy (**Figure 3.25** (**A-C**) and orange-red trace, **Figure 3.24**). Products of cleaved substrate will have similar dissociation to partial binding of substrate in this model, and cleaved product

leaves part of the POC unoccupied for the partial binding of substrate (S) (**Figure 3.24**). 'Single half S occupancy' (green trace, **Figure 3.24**) will compete with and follow the occupancy of product. However, growing with large excesses of substrate, some of the POC will be doubly occupied by a pair of substrate molecules, each partially bound with the other respective unbound portions of the substrates dangling. However, such double substrate occupancy (**Figure 3.25** (**D-F**)) will decline in this model with occupancy of the POC by product (**Figure 3.24** (**A -C**), which is increased during catalysis and will leave only a partial binding site for substrate. The rate of decline in double substrate occupancy was greater at lower substrate concentrations than higher substrate concentrations, when double occupancy is retained for longer periods of reaction, and remained elevated at the higher substrate concentrations, where the conjugate was also prone to inactivation (**Figure 3.25** (**D-F**)).

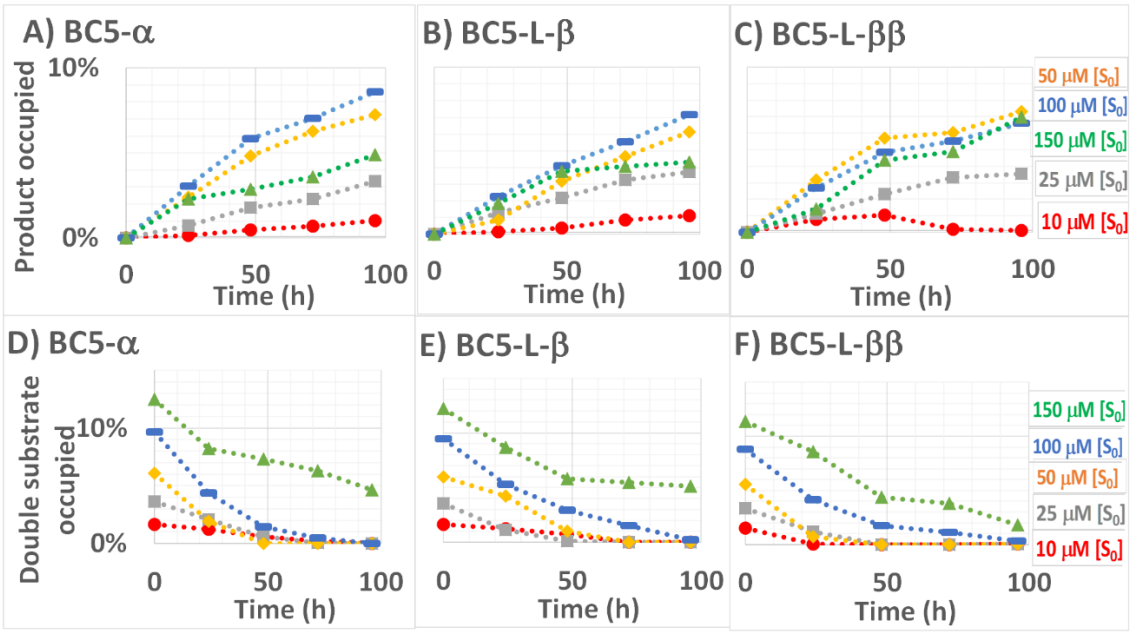

Figure 3.25. Fractional change in product (top row) and double substrate (bottom row) occupancy during the progress of reactions of the POC catalysts from left to right BC5-α, BC5-L-β and BC5-L-ββ for excess initial (total) substrate concentrations $[S]_0$ 10 μM (red-filled circles) , 25 μM (grey filled squares), 50 μM (yellow filled diamonds), 100 μM (blue dashes) & 150 μM (green-filled triangles).

The two dangling ends of the unbound substrate molecules and their two dangling positively-charged peptides are likely to promote agglomeration and inactivation of the POC, which will therefore increase with the greater extent and longer duration of double substrate occupancy at higher substrate concentrations (**Figure 3.7**). The lesser rate of decline of double substrate occupancy with increasing substrate concentrations was therefore used as the key determinant of inactivation in this model: where a power

function of the more parabolic nature of agglomeration was estimated as best fit to the rate of double substrate occupancy with available substrate concentration.

3.8.14.3 Activation and inactivation model

The above characterisation of activation and inactivation interactions was used as an explicit model to determine the active conjugate concentration and the inactivated concentration of conjugate, as they will vary according to this model with the dynamic changes in the available substrate concentration. The underlying equilibrium dissociation characteristics were refined to produce the best fit between the expected velocities calculated from this model and the velocities observed experimentally. The resultant sum of this activation and inactivation gave the active conjugate concentration. This explicit model was compared to an empirical model of hyperbolic activation (reciprocal of available substrate and product) and parabolic inactivation (square function of substrate), where the activation and inactivation variables were without such meaning and were simply those constructed to minimise the difference between observed and expected reaction velocities (**Figure 3.26** (**A-C**)).

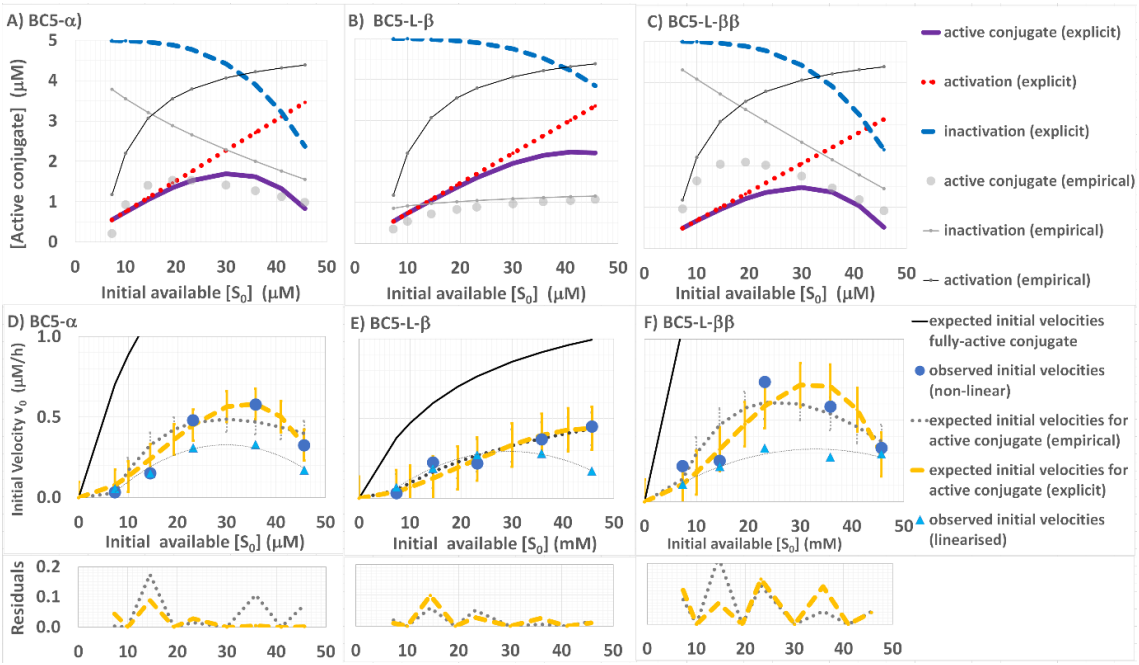

Figure 3.26. Comparison of explicit and empirical models of POC catalyst activation and inactivation to explain observed velocities within Michaelis-Menten kinetics. Top row compares the model of activation (red dotted trace, explicit & dark grey trace, empirical) and inactivation (blue-dashed trace, explicit & light grey trace, empirical), whose resultants gave the active conjugate concentrations (purple thick trace, explicit & light grey dots, empirical) for three POC catalysts from left to right: (**A)** BC5-α, (**B)** BC5-L-β and (**C)** BC5-L-ββ. Middle row compares the initial reaction velocities expected from the active conjugate (yellow dashed trace, explicit and black dot trace, empirical model) with the observed initial velocities estimated from non-linear fits (dark blue-filled dots) and linear fits (light blue-filled triangles) of the reaction progress

curves, from left to right: **(D)** BC5-α, **(E)** BC5-L-β and **(F)** BC5-L-ββ. Error bars are standard deviations from regression analysis of the observed and expected velocities for both the explicit (yellow) and empirical (black) fits. Bottom row compares the residuals of both fits for explicit (yellow dashed trace) and empirical (black dotted trace).

The explicit model defined by the refined equilibrium dissociation characteristics gave the closest fit to the observed initial reaction velocities from non-linear fitting (**Figure 3.26** (**D-F**) yellow dashed trace), with residuals raised for low substrate excesses (**Figure 3.26** bottom row), suggestive of another lesser factor here within the modelled complexity which had not been accounted for. Fitting empirically did not produce close fits for POC catalysts suffering greater inactivation (**Figure 3.26** (**D-F**) grey dotted trace).

3.8.14.4 Competitive and uncompetitive inhibition

Michaelis-Menten kinetics were considered with competitive K_{ic} and uncompetitive K_{iu} inhibitions (5):

$$v_0 = \frac{[C]_t \times k_{cat} \times [S]_0}{\left(1+{[P]_t}/{K_{ic}}\right)K_m + \left(1+{[P]_t}/{K_{iu}}\right)[S]_0} \qquad (12)$$

There was no possible fit to the observed velocities. Neither linear nor non-linear initial velocities were approached by any combination of inhibitions (**Figure 3.27**). The hyperbolic nature of Michaelis-Menten kinetics is unsuited to the peculiar bell-shaped or parabolic kinetics observed, where combination with conjugate activation and inactivation produced a much better fit (**Figure 3.26**).

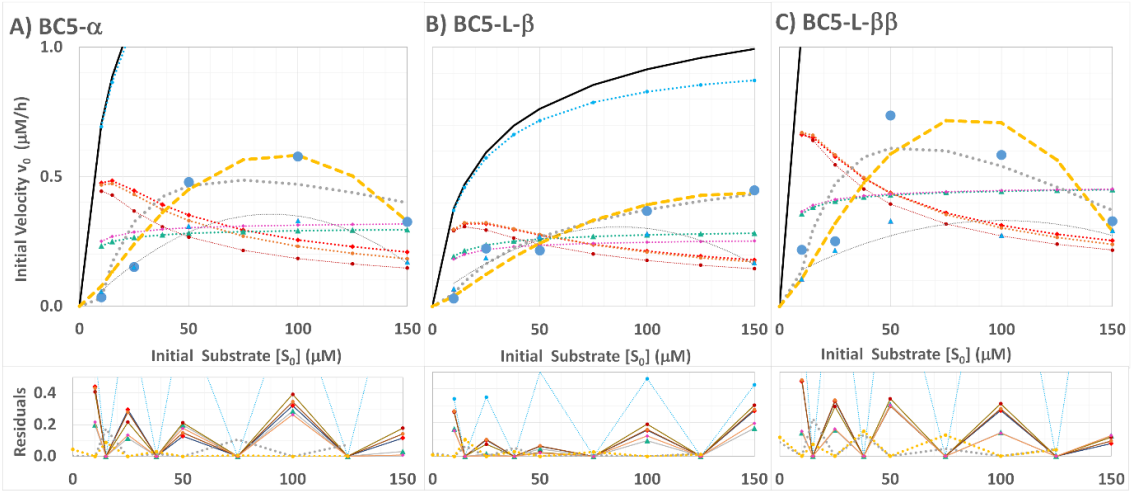

Figure 3.27. Comparison of Michaelis-Menten kinetics alone to the model of conjugate activation and inactivation for **(A)** BC5-α, **(B)** BC5-L-β and **(C)** BC5-L-ββ. Michaelis-Menten kinetics (black trace) combined with the conjugate activation and inactivation model (yellow dashed trace, explicit & grey dotted trace, empirical fits) are compared with fixed total conjugate (no activation & inactivation) as uncompetitive (red dotted trace) and competitive (green dotted trace) substrate inhibition; and with double half-substrate bound conjugate subtracted (light blue dotted trace) and additionally with uncompetitive (orange-red trace) or competitive substrate inhibition (pink

dashed trace). Observed initial velocities from non-linear progress curves (blue filled dots) were used for fitting rather than observed velocities from linearized progress curves (light blue filled triangles).

However, consideration of product inhibition proved more fruitful within the POC activation and inaction model. Product inhibition was considered by the increases in product concentrations during the progress of each of the catalytic reactions, where velocities were approximated from the initial velocity v_0 and non-linearity factor η by (5):

$$v = \frac{d[P]}{dt} = v_0 - \eta[P] \qquad (13)$$

The velocities estimated for the sampled points during reaction progress were then compared to expected velocities calculated from (5):

$$v_{exp} = \frac{[C]_a \times k_{cat} \times [S]_a}{\left(1+{[P]_t}/{K_{ic}}\right)K_m + \left(1+{[P]_t}/{K_{iu}}\right)[S]_a} \qquad (14)$$

where the active conjugate $[C]_a$ was used together with the changes in available substrate $[S]_a$ and product $[P]_t$ concentrations during the course of the reaction. Although the available substrate declined less during the course of the reaction than the total substrate, nevertheless, particularly at lower substrate concentrations, there was a greater decline in available substrate as product was produced and its inhibition could be discerned (**Figure 3.28**).

At low substrate concentrations, the reaction velocities increased during reaction progress for the POC catalysts with a single peptide (BC5-α, BC5-L-β), but velocities declined for the POC catalyst with two peptides (BC5-L-ββ). Although the velocities expected from Michaelis-Menten kinetics were in the same region, they did not show increases during reaction progress (**Figure 3.28** red and grey traces). However, at higher substrate concentrations, available substrate buffering maintained less change in available substrate (**Figure 3.24**). For the higher substrate concentrations, the velocities expected from the model of complex interactions around Michaelis-Menten kinetics with product inhibition approached those estimated from the reaction progress curves with relatively small residuals (**Figure 3.28**).

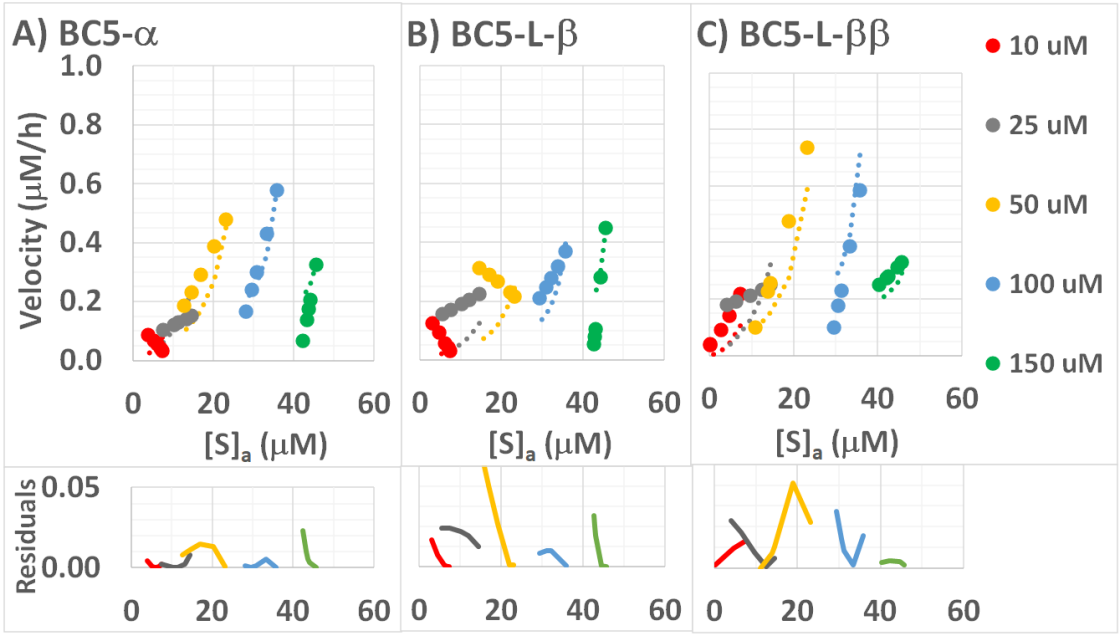

Figure 3.28. Uncompetitive product inhibition for POC catalysts **(A)** BC5-α, **(B)** BC5-L-β and **(C)** BC5-L-ββ. Velocities were estimated from the non-linear fit of reaction progress curves (filled dots) and compared to velocities expected (dotted traces) from the model of active catalyst and available substrate for the estimates of uncompetitive product inhibition.

Attempts were made to determine any competitive product inhibition using non-linear fitting by minimising residuals (sums of squares of difference between estimated and expected velocities), but competitive inhibition was consistently insignificant with large K_{ic} values (>>100,000). However, uncompetitive product inhibition had consistently significant values in the region of 18-21 μM, a little less than the $K_m$values 20-23 μM (**Table 3.3**). Similar values may be expected as the same oligonucleotide binding sequence is used in all cases, with changes in the way the catalytic peptide is attached.

Table 3.3. Kinetic characteristics input and output from the model. The equilibrium dissociation for the cleavable substrate complex K_{cs} was input from the reciprocal of the equilibrium association ($K_a \sim 0.5$) estimated experimentally. The binding of cleaved product and half substrate were assumed to be similar and input at the same value. All other kinetic characteristics were estimated by non-linear fitting.

			BC5-α	**BC5-L-β**	**BC5-L-ββ**
Michaelis-Menten	K_m	(μM)	23.81	20.65	20.69
Catalytic turnover	K_{cat}	(/h)	0.60	0.29	0.82
Maximum velocity	V_{max}	(μM/h)	2.99	1.44	4.10
Uncompetitive inhibition	K_{iu}	(μM)	20.73	20.98	18.71
Competitive inhibition	K_{ic}	(μM)	>100,000	>100,000	>100,000
Conjugate complex	K_{cc}	(μM)	22.10	21.91	21.49
Conjugate activation	K_c	(μM)	21.61	22.31	23.95
Substrate complex	K_{cs}	(μM)	2.00	2.00	2.00
Half substrate complex	K_{ss}	(μM)	20.00	20.00	20.00
Product complex	K_p	(μM)	20.00	20.00	20.00

The principal difference in kinetics arising from the structural differences in the POC catalysts was in V_{max} or the catalytic turnover k_{cat}. As may be expected, the POC with a pair of catalytic peptides had much higher reaction turnover (0.8 per hour), whereas, for single catalytic peptides, the α anomer produced the highest turnover (0.6 per hour), double that of the elongated β anomer (0.29 per hour).

3.8.15 Gel-shift analysis of hybridisation of *"bis"* and *"triple"* conjugates with 3'-FITC-tRNA^{Phe}

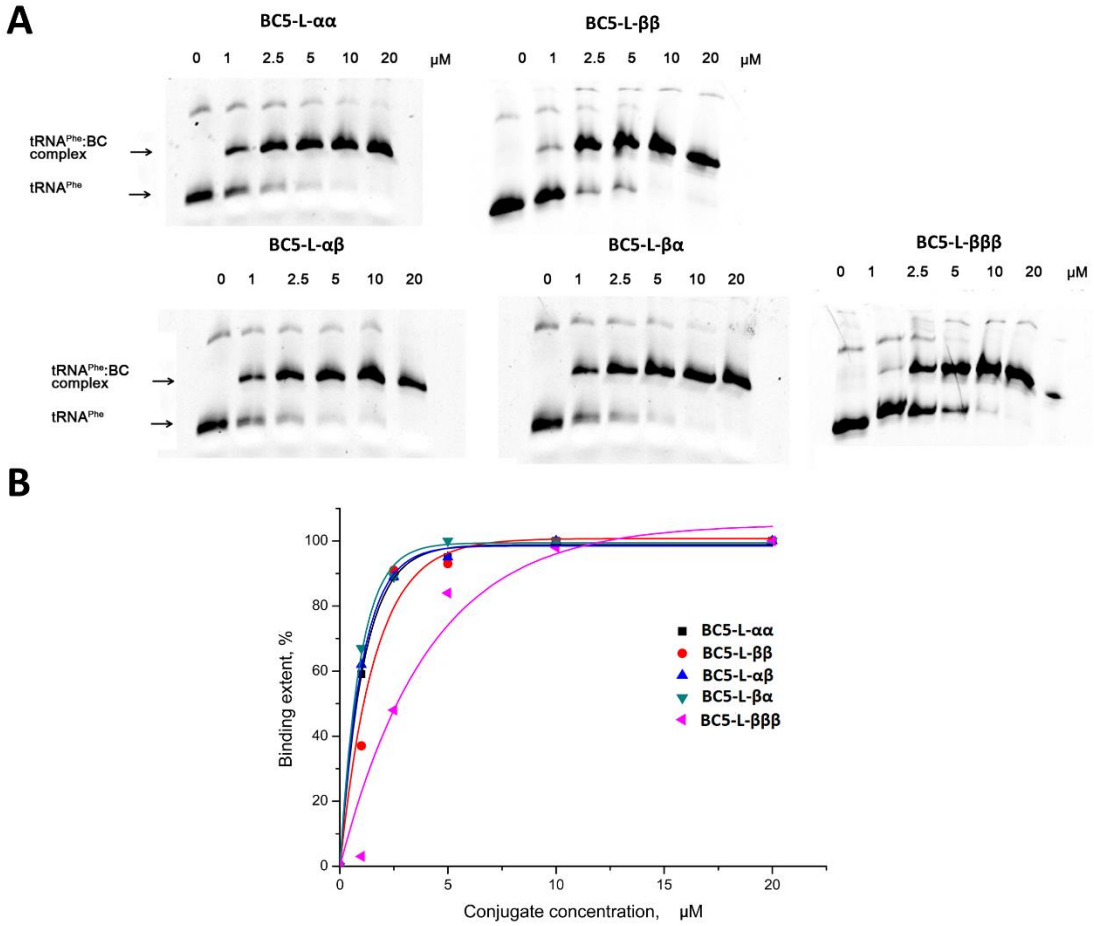

Figure 3.29. Gel-shift analysis of hybridisation of *"bis"* and *"triple"* bulge-loop inducing conjugates with 3'-FITC-tRNA^{Phe} (1 μM). (**A**) Representative images of PAGE indicating binding of conjugates to target tRNA^{Phe}. The type of conjugate and concentration (1-20 μM) are indicated at the top. (**B**) Secondary plot of data shown in (**A**).

3.8.16 Cleavage of 3'-FITC-tRNA^{Phe} at lower excess of *"bis"* and *"triple"* conjugates over target

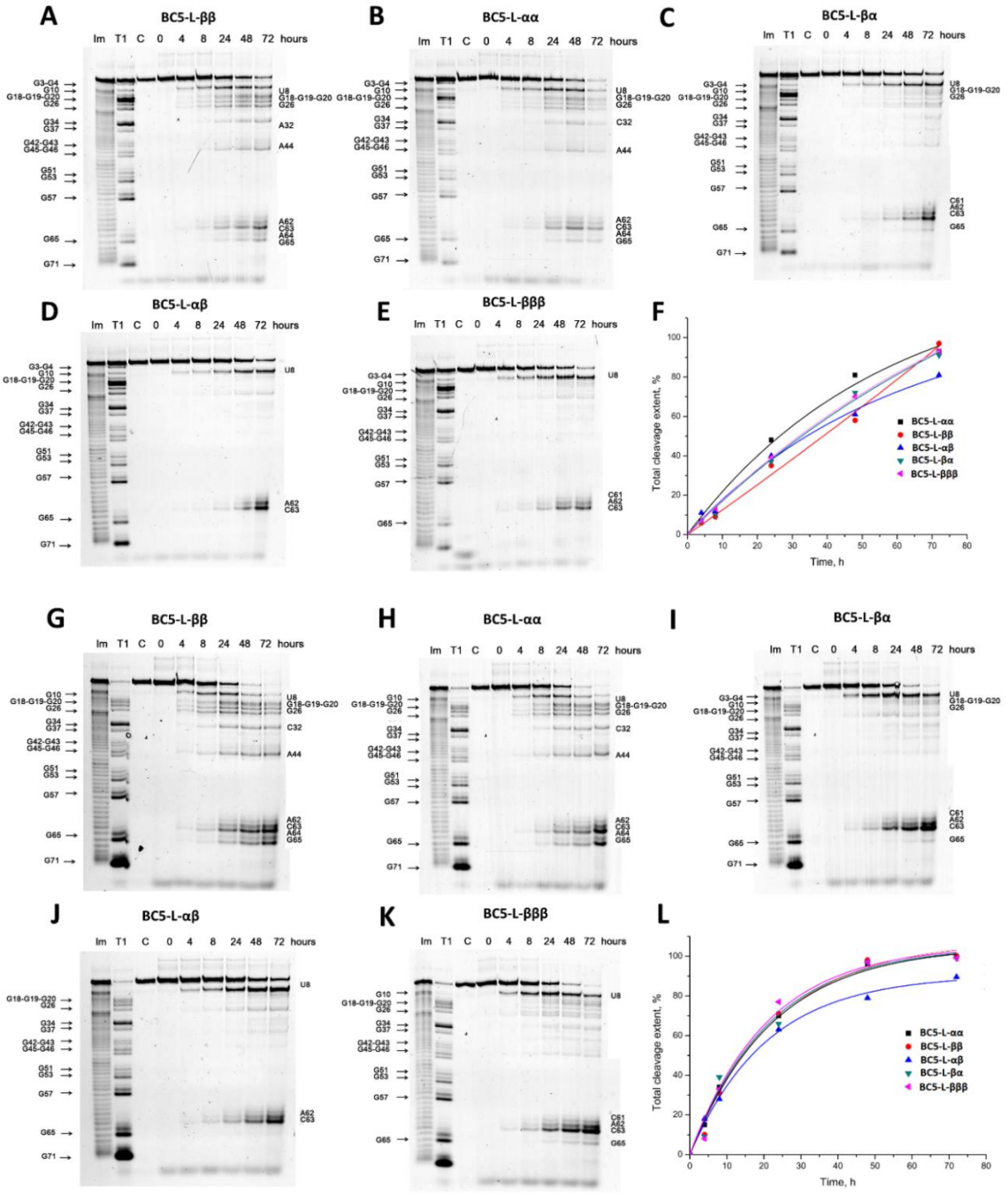

Figure 3.30. Cleavage of 3'-FITC-tRNA^{Phe} with *"bis"* and *"triple"* conjugates at lower excess of conjugate over target. **(A-E)** Representative images of 12% PAAM/8M urea gel after electrophoresis of 3'-FITC-tRNA^{Phe} (1 μM) cleavage products with *"bis"* and *"triple"* conjugates (5 μM) as a function of incubation time. **(G-K)** Representative images of 12% PAAM/8M urea gel after electrophoresis of 3'-FITC-tRNA^{Phe} (1 μM) cleavage products with *"bis"* and *"triple"* conjugates (10 μM) as a function of incubation time. Lanes T1 and Im represent partial 3'-FITC-tRNA^{Phe} digestion with RNase T1 and imidazole, respectively. In lane C, 3'-FITC- tRNA^{Phe} was incubated without conjugates for 72 h. Positions of RNA cleavage by RNase T1 and conjugates are shown on left and right respectively. **(F)** Secondary plot of the data indicating the total cleavage extent (%) plotted against the incubation time presented in **(A-E)** (at 5 μM conjugate concentration). **(L)** Secondary plot of the data indicating the total cleavage extent (%) plotted against the incubation time presented in **(G-K)** (at 10 μM conjugate concentration).

3.8.17 References for the Supporting Information

1. Bielec,K., Sozanski,K., Seynen,M., Dziekan,Z., ten Wolde,P.R. and Holyst,R. (2019) Kinetics and equilibrium constants of oligonucleotides at low concentrations. Hybridization and melting study. *Phys. Chem. Chem. Phys*., **21**, 10798–10807.

2. Qi,X., Loiseau,F., Chan,W.L., Yan,Y., Wei,Z., Milroy,L.-G., Myers,R.M., Ley,S. V, Read,R.J., Carrell,R.W., et al. (2011) Allosteric modulation of hormone release from thyroxine and corticosteroid-binding globulins. *J. Biol. Chem*., **286**, 16163–16173.

3. Gebrezgiabher,M., Zalloum,W.A., Clarke,D.J., Miles,S.M., Fedorova,A.A., Zenkova,M.A. and Bichenkova,E. V (2020) RNA knockdown by synthetic peptidyl-oligonucleotide ribonucleases: behavior of recognition and cleavage elements under physiological conditions. *J. Biomol. Struct. Dyn*., 1–20.

4. Staroseletz,Y., Amirloo,B., Williams,A., Lomzov,A., Burusco,K.K., Clarke,D.J., Brown,T., Zenkova,M.A. and Bichenkova,E. V. (2020) Strict conformational demands of RNA cleavage in bulge-loops created by peptidyl-oligonucleotide conjugates. *Nucleic Acids Res.* Accepted on 7 Sep 2020.

5. Cao,W. and De La Cruz,E.M. (2013) Quantitative full time course analysis of nonlinear enzyme cycling kinetics. *Sci. Rep*., **3**, 2658.

Chapter 4

Ultra-sensitive Detection of microRNA Biomarkers and their Disappearance upon Destructive Catalytic Treatment by Natural and Synthetic Ribonucleases

Ultra-sensitive Detection of microRNA Biomarkers and their Disappearance upon Destructive Catalytic Treatment by Natural and Synthetic Ribonucleases

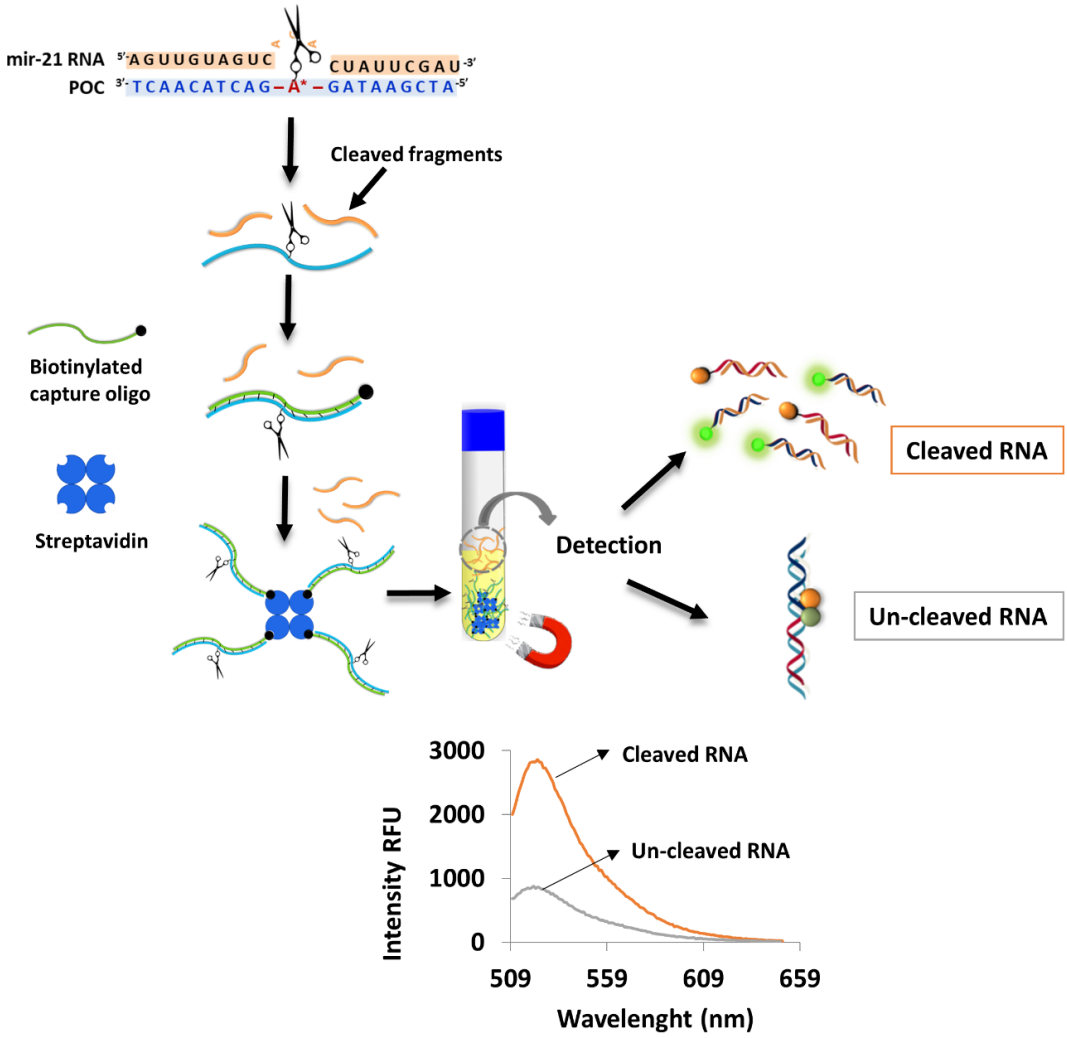

4.1 Declaration

This chapter consists of one paper awaiting submission to Biomaterials:

Sameen Yousaf, Bahareh Amirloo, Harmesh S. Aojula, David J. Clarke, Alberto Saiani, and Elena V. Bichenkova. Ultra-sensitive Detection of microRNA Biomarkers and their Disappearance upon Destructive Catalytic Treatment by Natural and Synthetic Ribonucleases.

Although the main aim of this paper is the development of new diagnostic approaches for detection of miRNA biomarkers, which is not my primary research focus, the use of the peptidyl-oligonucleotide conjugates developed in my research was crucial here to demonstrate the "prognostic" capability of this diagnostic device to monitor the disappearance of the target miRNA sequences upon cleavage. This manuscript has been prepared in a format designed for journal submission, except for minor adjustments to incorporate it into this thesis

Sameen Yousaf and Dr. Elena Bichenkova conceived the scientific ideas. As second author for this publication I carried out all the design, synthesis and characterisation of peptidyl-oligonucleotide conjugates used for cleavage of miR-21 and miR-17 (see **Appendix 1**). Sameen Yousaf designed the nano-biosensor components, synthesised and fully characterised the molecular probes and assembled the peptide hydrogel with the incorporated recognition motifs. Sameen Yousaf fully characterised the hydrogel materials by TEM and rheological analysis. I and Sameen Yousaf conducted the detection of natural and artificial ribonuclease-mediated miR-21 cleavage. Sameen Yousaf and I analysed the data, prepared figures and drafted the manuscript. Dr. Elena Bichenkova, Prof. David Clarke, Prof. Alberto Saiani and Dr. Harmesh Aojula supervised the relevant experimental work and were involved in project management, data analysis and manuscript editing at various stages.

Ultra-sensitive Detection of microRNA Biomarkers and their Disappearance upon Destructive Catalytic Treatment by Natural and Synthetic Ribonucleases

Sameen Yousaf,[1] Bahareh Amirloo[1], Harmesh S. Aojula[1], David J. Clarke[1], Alberto Saiani,[2] and Elena V. Bichenkova[1]

[1] School of Health Sciences, University of Manchester, Oxford Road, Manchester, M13 9PT, UK.

[2] Manchester Institute of Biotechnology, 131 Princess Street, Manchester, M1 7DN, UK.

4.2 Abstract

Short functional non-coding miRNAs are implicated in many types of cancer and act as active regulators in malignant growth, and thus can be used both as biomarkers for early-stage cancer detection and as potential biotargets for more selective and potent anticancer therapy. Distinctive profiles of miRNA expression in cancer mean that changes in specific expression patterns upon treatment could be used as prognostic markers to predict patient's response to treatment. However, the lack of standardised technologies for measuring miRNA levels *in situ* in clinical samples is a significant bottleneck in advancing miRNA biomarkers to the clinic. We report here a new "split-probe" self-assembling molecular probe system incorporated into a 3D peptide hydrogel nano-sensor platform for rapid, robust, and ultra-sensitive detection of miRNAs. We demonstrate its performance through detection of highly oncogenic miRNA-21 (miR-21) both *in vitro*, and in complex samples containing cancerous cell extract (MIA PaCa-2). The hydrogel nano-sensor was able to discriminate mismatches in miRNA targets down to a single nucleotide substitution, in the picomolar sensitivity (13 pM) range. The disappearance of miR-21 upon treatment by natural (RNase A and H) and synthetic (miR-21-miRNase) ribonucleases was tracked and quantified, thus providing a *proof-of-principle* for developing potential prognostic applications. Moreover, the new platform was able to measure the miRNA cleavage in multiple catalytic modes, including when the synthetic miRNases were able to cleave multiple miR-21 molecules, both alone and through the recruitment of RNase H. This versatile and quantitative approach can be easily adapted to follow unique miRNA expression profiles and rapid changes in their expression patterns for meeting future diagnostic and prognostic applications.

4.3 Introduction

MicroRNAs (miRNAs) are a new class of small, endogenous, non-protein-coding RNAs with more than 50% of genes located in cancer-associated regions in the human genome. The highly conserved small non-coding microRNAs (miRNAs) regulate gene expression by modulating translational efficacy of their target mRNAs in a tissue-specific manner, thus affecting cellular physiology (1). These short functional RNA molecules, which are typically 19-25 nucleotides long (2), regulate (mainly negatively) the gene expression in multiple biological processes, including cell proliferation, differentiation, cell regulation, metabolism and apoptosis (3). Based on their diverse role in different biological functions, it is now recognised that microRNAs expression is frequently dysregulated in case of various pathological conditions, including neurodegenerative diseases (4), autoimmune disorders (5) and carcinogenesis (6). The non-invasive nature of circulating miRNAs collection makes them ideal diagnostic and prognostic biomarkers for human diseases (7–9). Unique expression profiles of different miRNAs predispose to diverse types of cancer (10–13), thus implying that specific miRNAs expression patterns could be used as biomarkers for the early detection of tumorigenesis. Also, changes in miRNA expression after radiotherapy (14) and implication of miRNA in drug resistance (14) suggest that analysis of miRNA expression profiles could be used as prognostic markers (15) to predict patient response to therapy (16). Therefore, the choice of extracellular miRNAs as disease biomarkers offers multiple diagnostic and prognostic advantages.

Circulating miRNAs are readily accessible and stable targets, which in comparison to other RNA species can withstand extracellular environments for a long time (17). The majority of extracellular miRNAs are found circulating in different biological fluids including, serum, urine, sputum, plasma, cerebrospinal fluid, saliva, and peritoneal fluid (18). The increased stability of miRNAs is attributable to their close association with lipoproteins (LDL/HDL), Argonaute (AGO) protein complexes, and exosomes which protect them from degradation from RNases (16). Furthermore, the relatively small size of miRNA prevents the formation of intramolecular secondary structures, thus offering the ease of access, subsequent hybridisation, and detection by probes. Despite the substantial interest in miRNAs as clinical biomarkers, the use of miRNAs for diagnostic approaches is still in its infancy. The major disadvantages for miRNAs as potential biomarkers are largely due to the low expression levels, and interference from biological milieu affecting detection (19).

The lack of standardised technologies for measuring miRNA levels *in situ* in clinical samples is a significant bottleneck in advancing RNA biomarkers to the clinic. The present detection techniques involve *in vitro* amplification of nucleic acid target and are subject to several challenges. Though RT-qPCR is a highly sensitive technique, but it holds a number of analytical and procedural limitations: (i) it involves a number of additional steps, (ii) high cost and potential risk of contamination during each amplification step, and (iii) for shorter miRNAs, the specific primer designing is difficult. Northern blot offers low sensitivity and larger analyte concentration is needed alongside optimisation of cumbersome experimental procedures. Furthermore, the next-generation sequencing (NGS) is not considered ideal for quick and early diagnosis because of the high cost and longer time requirement (20). The majority of presently available 2D microarrays screening approaches with patterned monolithic surfaces typically suffer from issues of insufficient reproducibility, considerable variability in performance, low detection accuracy and poor sensitivity, which often lead to misdiagnosis (21). Furthermore, the absence of positive controls to establish the reference thresholds for normalised miRNA levels contributes to the major challenges in the advancement of miRNAs as clinical biomarkers.

Therefore, there is an urgent need for the development of novel technologies allowing easy *in situ* miRNA detection, preferably, as an early-stage diagnosis to improve health outcomes with the added benefit of more precise monitoring of treatment through tracking changes in miRNA expression profiles. However, the development of standardised diagnostic assays/sensing devices specific for detection and quantification of miRNAs and assessment of anti-miR based therapies have proven highly challenging because of their relatively small size, low abundance (or concentration), and high sequence homology to the closely related miRNAs species.

Previously, we developed a self-assembling 3D peptide hydrogel with covalently-attached molecular beacons (MB) as recognition elements immobilised on the surface of fibres (22). The designed system was not only able to '*fish out'* a complementary DNA sequence (16 nt long) embedded within the longer fragment (40 nt long), but was also able to identify the perfect-match target against mismatches with remarkable accuracy enabled by the triggered fluorescent signal. Although the system has achieved precise detection of a nucleic acid target with absolute sequence-specificity and high analytical sensitivity, which was crucial to demonstrate a *proof-of-concept* at the discovery stage, it has neither been tested against biologically relevant targets nor in the physiological

media/fluids. Therefore, there is a need to design a detection system that can signify the presence of nucleic acid biomarkers linked to human pathophysiology directly from biological samples, with minimum sample preparation. The complex, folded hairpin-like structure of the recognition motifs of the previously designed MB probes (22) is prone to formation of numerous alternative conformations, which may lead to a high background signal and/or reduce the *signal-to-noise* ratio. Also, this system may not be suitable for binding short (21-23 nt) miRNA sequences, which may not have sufficient hybridisation power to effectively invade the folded MB and sufficiently separate fluorophore and quencher. Here, we address these issues by the development of an alternative (i.e. "split-probe") system, which consists of two "split" RNA-recognising fragments complementary to the adjacent regions of the target RNA, one is labelled with a fluorophore (**F)** and the another with a quencher (**Q**) (see **Figure 4.1**). Such "split-probes" are immobilised here on the surface of 3D peptide hydrogel fibres to pull out the target sequence from the analyte solutions. Self-assembly of such "split-probes" through their sequence-specific hybridisation at the neighbouring regions of their biotarget brings **F** and **Q** together to silence fluorescence and indicates the presence of the target sequence.

To assess the performance of the "split-probe" hydrogel detector, we use here the highly oncogenic microRNA-21 (miR-21). Amongst many miRNAs identified as important inducers of oncogenesis, miR-21 acts as an extreme oncogene by repressing the expression of tumour suppressor genes. The miR-21 is the only known miRNA, which is up-regulated in almost all types of cancers, including hepatocellular carcinoma (23, 24), breast cancer (25–27), chronic myelogenous leukaemia (28), colorectal cancer (29), prostate cancer (30) and cervical cancer (31), thus making it a suitable diagnostic/prognostic biomarker, as well as a therapeutic target against human malignancy. We report here a *proof-of-concept* for fabricating a 3D "split-probe" hydrogel system capable of quantifying miR-21 biotarget and demonstrate its ability to perform in the complex environment of cancer cells (MIA PaCa-2). We also assessed the ability of this system to discriminate mismatches to avoid false positives, and to quantitatively monitor the disappearance of the target miR-21 upon its degradation by natural (RNase A and H) and synthetic (miR-21-miRNase) ribonucleases in order to evaluate its potential to follow the outputs of therapeutic treatments.

4.4 Materials and Methods

4.4.1 Peptides Synthesis

Lys-Lys-Phe-Glu-Trp-Glu-Phe-Glu-Lys-Lys (**p**$^{(+1)}$) and maleimide modified **p**$^{(+1)}$, Mal-Gly-Gly-Lys-Lys-Phe-Glu-Trp-Glu-Phe-Glu-Lys-Lys (Mal-Gly-Gly-**p**$^{(+1)}$) were synthesised using Fmoc solid-phase peptide synthesis chemistry (22). Peptides were purified by reversed-phase HPLC (ACE 10 Preparative C-8 250 × 21.2 mm, PerkinElmer Nelson 1022, MA US) using 0.1% TFA in distilled water (eluent A) and 0.1% TFA in acetonitrile (eluent B) with a gradient increasing linearly from 10 to 100% of eluent B in 55 min at a flow rate of 8mL/min. The characterisation was done by ^{1}H NMR recorded on Bruker Avance ll+ spectrometers operated at 400 MHz proton frequency using a BBI 1H/D-BB Z-GRD Z8202/0347 probe and MS-MALDI (Matrix-assisted laser desorption ionisation) spectrometry recorded on Bruker Daltonics Ultraflex TOF/TOF mass spectrometer (MA, USA), as described previously (22). Peptide Glu-Glu-Phe-Lys-Trp-Lys-Phe-Lys-Glu-Glu (**p1**$^{(-1)}$) was purchased from Biomatik (Cambridge, Ontario, Canada).

Oligonucleotides $^{5'}(CH_2)_6$-SS-TCAACATCAGT-**Q**$^{3'}$ (**pQ**, **Q** denotes dabcyl quencher) $^{5'}$**F**-CTGATAAGCTA$^{3'}$ (**pF**, **F** denotes fluorescein amidite (FAM), see **Figure 4.1** for representative structures), $^{5'}$UAGCUUAUCAGACUGAUGUUGA$^{3'}$ (perfect match, miR-21 RNA target), $^{5'}$UAGCU**A**AUCAGACUGAUGUUGA$^{3'}$ (mismatch 1), $^{5'}$UAGCU**A**AUCAGACUG**G**UGUUGA$^{3'}$ (mismatch 2), $^{5'}$U**U**GCUUAUCAGACUGAUGUUGA$^{3'}$ (mismatch 3) and $^{5'}$UAGCUUAUCAGACUGAUGUU**C**A$^{3'}$ (mismatch 4) were purchased from ATDbio Ltd (Southampton, United Kingdom). These oligonucleotides were desalted using G-25 DNA grade gel filtration columns (Sephadex^{TM} NAP-25, GE Healthcare, Life sciences Fisher Scientific UK Ltd) following the protocol described in the manual.

4.4.2 Conjugate Synthesis

Peptide-oligonucleotide conjugate (**pQ**-Mal-Gly-Gly-**p2**$^{(+1)}$) was synthesised using thiol-maleimide chemistry, as described previously (22) (see **Figure 4.9** for reaction route). Thiol-modified oligonucleotide ($^{5'}(CH_2)_6$-SS-TCAACATCAGT-**Q**$^{3'}$) was purchased from ATDbio Ltd. with a disulphide protected group (-S-S-) to prevent the spontaneous disulphide bond formation and conjugate (**pQ**-Mal-Gly-Gly-**p2**$^{(+1)}$) synthesis and purification was conducted according to the procedure described in (22). The successful

formation of the peptide-oligonucleotide conjugate (**pQ**-Mal-Gly-Gly-**p2$^{(+1)}$)** was confirmed by the change in HPLC retention time (see **Figure 4.10**) and by comparison of ^{1}H NMR spectrum of the reaction product with that of the starting materials (see **Figure 4.11**). In all cases, oligonucleotide concentrations were estimated using a UV-Vis spectrophotometer (Varian Cary 4000 dual beam: Australia) at 260 nm wavelength using extinction coefficients reported in **Table 4.2**.

Thiol-modified oligonucleotide ($^{5'}$(CH$_2$)$_6$-SS-TCAACATCAGT-Q$^{3'}$)

MALDI-MS; m/z = 4091.5 $[M-H]^{-1}$ MW = 4092.0 g mol^{-1} calcd. for $[C_{140}H_{189}N_{44}O_{73}P_{12}S_2]$ (**Figure 4.12** (**A**)).

^{1}H NMR (**Figure 4.11** (**A**)) (D_2O with TSP (0.1 μM), 400 MHz): 0.79-2.78 (m, 63H; 11H; 11×H2', 11H; 11×H2'' sugar ring protons 9H; T(3×CH_3) 24H; linker (12×CH_2) 6H; Dabcyl (2×CH_3) 2H; Dabcyl (1×CH_2)) 3.35-4.41 (m, 74H; 11H; 11×H4, 11H; 11×H5', 11H; 11×H5'', 6H; Dabcyl (3×CH_2) 2H; Dabcyl (1×CH_2) 4.87-6.37 (m, 16H; 11H, 11×H1' sugar ring protons, 3H; C(3×H5), 2H; Dabcyl (1×CH_2) 7.06-8.37 (m, 23H; 1H; G(1×H8) 8H; A(4×H2+4×H8) 3H; C(3×H6) 3H; T(3×H6) 8H; Dabcyl). Chemical shifts for 3H' sugar ring protons are not included due to spectral distortion caused by pre-saturation of the HOD NMR signal.

FAM-labelled oligonucleotide ($^{5'}$F-CTGATAAGCTA$^{3'}$)

MALDI-MS; m/z = 3878.1 $[M-H]^{-1}$ MW = 3879.6 g mol^{-1} calcd. for $[C_{135}H_{162}N_{43}O_{72}P_{11}]$ (**Figure 4.12** (**B**)).

^{1}H NMR (**Figure 4.13**) (D_2O with TSP (0.1 μM), 400 MHz): 1.05-2.72 (m, 51H; 11H; 11×H2', 11H; 11×H2'' sugar ring protons 9H; T(3×CH_3), 24H; linker (12×CH_2), 8H; FAM) 3.11-4.36 (m, 39H; 11H; 11×H4, 11H; 11×H5', 11H; 11×H5'', 6H; FAM) 5.44-6.52 (m, 13H; 11H, 11×H1' sugar ring protons, 2H; C(2×H5)) 6.90-8.09 (m, 24H; 2H; G(2×H8) 8H; A(4×H2+4×H8) 2H; C(2×H6) 3H; T(3×H6) 9H; FAM). Chemical shifts for 3H' sugar ring protons are not included due to spectral distortion caused by pre-saturation of the HOD NMR signal.

Peptide-oligonucleotide conjugate, pQ-Mal-Gly-Gly-p2$^{(+1)}$

MALDI-ToF: m/z = 5633.2 $[M+H]^{+1}$ MW = 5632.1 g mol^{-1} calcd. for $[C_{219}H_{208}N_{62}O_{95}P_{12}S]$(**Figure 4.14**).

^{1}H NMR (**Figure 4.11** (**B**)): (D_2O with TSP (0.1 μM), 400 MHz): 0.88-2.96 (m, 105H; 8H; 4×Lys-CH_2^{δ}, 8H; 4×Lys-CH_2^{β}, 8H; 4×Lys-CH_2^{ε}, 8H; 4×Lys-CH_2^{γ}, 6H; 3×Glu-CH_2^{γ}, 6H; 3×Glu-CH_2^{β}, 4H; 2×Phe-CH_2^{β}, 2H; Trp-CH_2^{β}, 4H; linker 2×CH_2, 11H; 11×H2', 11H; 11×H2'' sugar ring protons 9H; T(3×CH_3) 24H; linker (12×CH_2) 6H; Dabcyl (2×CH_3) 2H; Dabcyl (1×CH_2)) 2.97-4.45 (m, 55H; 4H; 4×Lys-CH^{α}, 3H; 3×Glu-CH^{α}, 4H; 2×Gly-CH_2^{α}, 1H; Trp-CH^{α}, 2H; 2×Phe-CH^{α}, 2H; maleimide N-CH_2, 11H; 11×H4, 11H; 11×H5', 11H; 11×H5'', 6H; Dabcyl (3×CH_2) 2H; Dabcyl (1×CH_2) 4.87-6.37 (m, 16H; 11H, 11×H1' sugar ring protons, 3H; C(3×H5), 2H; Dabcyl (1×CH_2) 6.89-8.34 (m, 38H; Trp-$CH^{\delta1}$,$CH^{\epsilon2}$,$CH^{\zeta1}$,$CH^{\zeta2}$,CH^{η} 4H; Phe-$CH^{\delta1}$, $CH^{\delta2}$ 4H; Phe-$CH^{\epsilon1}$, $CH^{\epsilon2}$ 1H; Phe-CH^{ζ}, 1H; G(1×H8) 8H; A(4×H2+4×H8) 3H; C(3×H6) 3H; T(3×H6) 8H; Dabcyl). Chemical shifts for 3H' sugar ring protons are not included due to spectral distortion caused by pre-saturation of the HOD NMR signal.

4.4.3 Hydrogel characterisation

For morphological and mechanical characterisation of hydrogel material, samples were prepared from 20 mM (27 mg ml^{-1}) **p1$^{(-1)}$** and **p2$^{(+1)}$** peptides functionalised with and without the peptide-oligonucleotide conjugate (**pQ**-Mal-Gly-Gly-**p2$^{(+1)}$**, 0.5μM, 0.003 %), at pH 7.2. Hydrogel samples were incubated at 20 °C for 24 h before negative staining for transmission electron microscopy (TEM). The samples were then diluted 500-fold in distilled water and deposited onto already glow-discharged carbon-coated grids (400 mesh Agar Scientific, Stansted, UK) for 1 min, followed by washing with distilled water three times for 10s and negative staining with 1% (w/v) uranyl acetate solution for 1 min. The prepared carbon grids were then blotted using Whatman filter paper and dried for 30 min. Hydrogel forming nanofibres were viewed on Tecnai Biotwin TEM (FEI, Oregon, USA) under an accelerating voltage of 100 KV, and imaged with a GATAN Orius CCD (Gatan, Oxford, UK). ImageJ analysis was performed to estimate the width and morphology of the fibres.

Mechanical characterisation of hydrogel was performed on a stress-controlled rheometer (Discovery HR-2, TA Instruments, Hertz, UK) using a 20 mm parallel plate. Hydrogel samples were prepared with and without the peptide fibres decorating detection probe, **pQ**-Mal-Gly-Gly-**p2$^{(+1)}$**, by mixing the equimolar concentrations (20 mM) of peptides **p1$^{(-1)}$** and **p2$^{(+1)}$**. The samples were incubated at 20 °C for 24 h before measurement, loaded (180 μl) onto the stage with the gap set at 500 μm between the upper plate and stage. Amplitude sweeps were undertaken at an oscillation frequency of 1 Hz between

0.02 and 40 % strain to determine the linear viscoelastic region (LVR). G' and G" moduli were estimated in frequency sweep experiments between the range of 0.01 to 15 Hz, at 0.2 % strain.

4.4.4 Hybridisation studies

In aqueous, all hybridisation experiments were conducted in 0.1 M Tris buffer (pH 7.2) containing 0.2 M KCl. Final peptides concentrations of 20 mM were used to prepare hydrogel samples. Peptides **p1$^{(-1)}$** and **p2$^{(+1)}$** were dissolved separately in the above hybridisation buffer at 10 mM concentration followed by mixing of the two peptide solutions and addition of peptide-oligonucleotide conjugate, **pQ**-Mal-Gly-Gly-**p2$^{(+1)}$**. The pH was then immediately adjusted to 7.2 with 1 M NaOH. Analyte sample was introduced on the top and hybridisation was assessed by a decrease in fluorescence at 522 nm (λ_{ex} 494 nm) at 24 ^{O}C (or 34 ^{O}C where stated) either in (a) 1 cm path-length quartz cuvettes, using a Shimadzu RF-5301 spectrofluorophotometer, operated with RF-5310PC software (Shimadzu Corporation, Kyoto, Japan), equipped with temperature-controlled cell holder and 150 W Xenon lamp; or (b) in microwell plates.

4.4.5 Cell extract preparation

Human pancreatic cancerous cell lines (MIA PaCa-2) were used to demonstrate the ability of the designed hydrogel nano-sensor to detect miR-21 biomarker in complex biological fluids. MIA PaCa-2 cell lines derived from tumour tissue of the pancreas of a 65 year old Caucasian male, were obtained from ATCC® CRL-1420™ (ECACC 85062806). Cells were cultured for 1 week in Dulbecco's Modified Eagle's media, 10 % FBS, 2mM L-glutamine in cell culture flasks (T-75), kept at 37°C in a humidified incubator with an atmosphere of 5% CO_2. Following cells cultivation, the growth media was decanted, and cells were washed 3 times with ice-cold 1X PBS (pH 7.0). Cells were scraped off from the plate surface into 150 µl of radioimmunoprecipitation assay (RIPA buffer) buffer (10 mM Tris (pH 7.4), 150 mM NaCl, 1 mM EDTA, 1 mM EGTA, 50 mM NaF, 1mM sodium orthovanadate, 1% Triton X-100 v/v, 0.5% Nonidet P-40 v/v, 2 mM leupeptin, 0.15 mM aprotinin, 1.46 mM pepstatin, and 1 mM phenylmethansulfonyl fluoride) and centrifuged at 13,000 g and 4 °C for 10 min. The supernatant was collected, and the miR-21 target was spiked in 1:1 of cell extract and 1X Tris buffer (0.1 M tris and 0.2 M KCl, pH 7.2) to achieve the final concentration of 0.5 µM under hybridisation conditions.

4.4.6 Limit of Detection (LoD)

The limit of detection (LoD) was estimated using a Tecan Safire plate reader equipped with Magellan Data Analysis Software (V.7) following an established protocol (32). The hybridisation of 'perfect-match' (PM) miR-21 target with "split-probes" (**pF**+**pQ**-Mal-Gly-Gly-**p2**$^{(+1)}$) bearing recognition motif was assessed over the concentration range of 50 pM to 50 nM. Hydrogel samples with detection probes (**pF**+**pQ**-Mal-Gly-Gly-**p2**$^{(+1)}$) doping levels ranging from 3.0×10^{-4} to 2.7×10^{-6} % were deposited in 200 µl aliquots into 96-well plates. Analyte samples (10 µl) containing PM miR-21 target were then introduced into the hydrogel samples in the same molar concentration as of recognition probes. Following incubation for over 24 h at 24 ^{O}C, decrease in fluorescence was recorded. For comparison, similar experiments were conducted in a solution containing 0.1 M Tris and 0.2 M KCl (pH 7.2). Measurements were repeated for 20 fresh-replicates containing equimolar concentrations of detection probes (**pF**+**pQ**-Mal-Gly-Gly-**p2**$^{(+1)}$) and target analyte introduced into the hydrogel, and 20 blank samples containing only "split-probes" (**pF**+**pQ**-Mal-Gly-Gly-**p2**$^{(+1)}$) with 10 µl hybridisation buffer added on top. The mean values for blank ($Mean_{blank,}$ n = 20) and standard deviation (SD_{blank} n = 20) of the 'blank' samples and low concentration (50 pM) samples (SD_{lcs} n = 20) were estimated using equations 1 and 2 (see **Results and Discussion**), to calculate the limit of blank (LoB) and limit of detection (LoD).

4.4.7 Detection of miR-21 cleavage by peptidyl-oligonucleotide conjugates

4.4.7.1 miR-21-miRNase conjugate synthesis

miR-21-miRNase and scrambled conjugates were synthesised using amide coupling chemistry following the protocol described in (33), and the final product was purified using RP-HPLC (semi-preparative Phenomenex Luna C-18 column), as described previously (33). The identity and purity of all conjugates were confirmed by MALDI-ToF/ToF spectrometry (Bruker Daltonics Ultraflex TOF/TOF mass spectrometer) (see **Figure 4.15**) and ^{1}H NMR spectroscopy (Bruker Avance ll+ spectrometers operated at 400 MHz proton frequency using a BBI 1H/D-BB Z-GRD Z8202/0347 probe) (see **Figure 4.16**). In all cases, oligonucleotide concentrations were estimated using a UV-Vis spectrophotometer (Varian Cary 4000 dual beam; Australia) at 260 nm wavelength using molar extinction coefficients. Shimadzu Biotech Axima Confidence mass spectrometer

using Time of Flight Matrix-Assisted Laser Desorption Ionisation (MALDI) was used to record miR-21-miRNase-mediated cleavage of RNA.

miR-21_3β1. MALDI-MS: *m/z* = 7333.1 $[M+K]^+$ adduct MW = 7294.6 g mol−1 calcd. For $[C_{250}H_{354}N_{95}O_{126}P_{19}]$ (**Figure 4.15**).

^{1}H NMR (**Figure 4.16**) (D_2O with TSP (0.01 mM), 400 MHz): δ 0.69-0.77 (m, 24H, Leu-H^{δ}), 0.99-2.77 (m, 98H, 20×H2' and 20×H2'' sugar ring protons, 5×CH_3 of 5×dT, 8×Arg-H^{β}, 8×Arg-H^{γ}, 8×Leu-H^{β}, 4×Leu-H^{γ}, 6×CH_2 (aminohexyl linker), Acetyl-CH_3), 3.1 (m, 8H, 8×Arg-H^{δ}), 3.30-4.38 (m, 72H, 60×H4'/H5'H5" sugar ring protons, 2×Gly-CH_2, 8 × Leu/Arg-H^{α}), 4.92-6.28 (m, 24H, 20×H1' sugar ring protons, 4×H5 of dC), 7.18-8.30 (m, 27H, 27×Ar-H from dG(H8×2), dA(H8×8), dA(H2×8), dC(H6×4) and dT(H6×5)). H3' sugar ring protons (4.3-5.2 ppm) were not analysed due to suppression of residual water signal at 4.76 ppm. Not all H4'/H5'H5" sugar ring protons were fully resolved and suppression of residual water prevented signal detection.

miR-21_3α1. MALDI-MS: *m/z* = 7333.1 $[M+K]^+$ adduct MW = 7294.6 g mol^{-1} calcd. for $[C_{250}H_{354}N_{95}O_{126}P_{19}]$ (**Figure 4.15**).

^{1}H NMR (**Figure 4.16**) (D_2O with TSP (0.01 mM), 400 MHz): δ 0.69-0.77 (m, 24H, Leu-H^{δ}), 1.10-2.78 (m, 98H, 20×H2' and 20×H2'' sugar ring protons, 5×CH_3 of 5×dT, 8×Arg-H^{β}, 8×Arg-H^{γ}, 8×Leu-H^{β}, 4×Leu-H^{γ}, 6×CH_2 (aminohexyl linker), Acetyl-CH_3), 3.1 (m, 8H, 8×Arg-H^{δ}), 3.36-4.37 (m,72H, 60×H4'/H5'H5" sugar ring protons, 2×Gly-CH_2, 8×Leu/Arg-H^{α}), 5.36-6.38 (m, 24H, 20×H1' sugar ring protons, 4×H5 of dC), 7.17-8.38 (m, 27H, 27×Ar-H from dG(H8×2), dA(H8×8), dA(H2×8), dC(H6×4) and dT(H6×5)). H3' sugar ring protons (4.3-5.2 ppm) were not analysed due to suppression of residual water signal at 4.76 ppm. Not all H4'/H5'H5" sugar ring protons were fully resolved and suppression of residual water prevented signal detection.

miR-21_3β2. MALDI-MS: *m/z* = 7358.3 $[M+Kl]^+$ adduct MW = 7319.6 g mol^{-1} calcd. for $[C_{250}H_{353}N_{98}O_{125}P_{19}]$ (**Figure 4.15**).

^{1}H NMR (**Figure 4.16**) (D_2O with TSP (0.01 mM), 400 MHz): δ 0.71-0.79 (m, 24H, Leu-H^{δ}), 1.14-2.90 (m, 95H, 20×H2' and 20×H2'' sugar ring protons, 4×CH_3 of 4×dT, 8×Arg-H^{β}, 8×Arg-H^{γ}, 8×Leu-H^{β}, 4×Leu-H^{γ}, 6×CH_2 (aminohexyl linker), Acetyl-CH_3), 3.09 (m, 8H, 8×Arg-H^{δ}), 3.29-4.39 (m,72H, 60×H4'/H5'H5" sugar ring protons, 2×Gly-CH_2, 8×Leu/Arg-H^{α}), 5.47-6.34 (m, 24H, 20×H1' sugar ring protons, 4×H5 of dC), 7.12-8.38 (m, 27H, 27×Ar-H from dG(H8×3), dA(H8×8), dA(H2×8), dC(H6×4) and dT(H6×4)).

H3’ sugar ring protons (4.3-5.2 ppm) were not analysed due to suppression of residual water signal at 4.76 ppm. Not all H4’/H5’H5” sugar ring protons were fully resolved and suppression of residual water prevented signal detection.

miR-21_3α2. MALDI-MS: m/z = 7358.2 $[M+K]^+$ adduct MW = 7319.6 g mol^{-1} calcd. for $[C_{250}H_{353}N_{98}O_{125}P_{19}]$ (**Figure 4.15**).

^{1}H NMR (**Figure 4.16**) (D_2O with TSP (0.01 mM), 400 MHz): δ 0.70-0.78 (m, 24H, Leu-H^{δ}), 0.95-2.95(m, 95H, 20×H2’ and 20×H2’’ sugar ring protons, 4×CH_3 of 4×dT, 8×Arg-H^{β}, 8×Arg-H^{γ}, 8×Leu-H^{β}, 4×Leu-H^{γ}, 6×CH_2 (aminohexyl linker), Acetyl-CH_3), 3.08 (m, 8H, 8×Arg-H^{δ}), 3.29-4.35 (m,72H, 60×H4’/H5’H5” sugar ring protons, 2×Gly-CH_2, 8×Leu/Arg-H^{α}), 5.32-6.33 (m, 24H, 20×H1’ sugar ring protons, 4×H5 of dC), 7.11-8.38 (m, 27H, 27×Ar-H from dG(H8×3), dA(H8×8), dA(H2×8), dC(H6×4) and dT(H6×4)). H3’ sugar ring protons (4.3-5.2 ppm) were not analysed due to suppression of residual water signal at 4.76 ppm. Not all H4’/H5’H5” sugar ring protons were fully resolved and suppression of residual water prevented signal detection.

Scarmbled conjugate (miR-17_3β). MALDI-MS: m/z = 7615.8 $[M+H]^+$ adduct MW = 7614.7 g mol^{-1} calcd. for $[C_{257}H_{366}N_{94}O_{137}P_{21}]$ (data not shown).

^{1}H NMR (data not shown) (D_2O with TSP (0.01 mM), 400 MHz): δ 0.72-0.80 (m, 24H, Leu- H^{δ}), 0.90-2.95(m, 100H, 21×H2’ and 21×H2’’ sugar ring protons, 5×CH3 of 5×dT, 8× Arg-H^{β}, 8×Arg-H^{γ}, 8×Leu-H^{β}, 4×Leu-H^{γ}, 6×CH_2 (aminohexyl linker), Acetyl-CH_3), 3.18 (m, 8H, 8×Arg-H^{δ}), 3.42-4.40 (m,75H, 63×H4’/H5’H5” sugar ring protons, 2×Gly-CH_2, 8×Leu/Arg-H^{α}), 5.50-6.35 (m, 28H, 21×H1’ sugar ring protons, 7×H5 of dC), 7.21-8.41 (m, 25H, 25×Ar-H from dG(H8×3), dA(H8×5), dA(H2×5), dC(H6×7) and dT(H6×5)). H3’ sugar ring protons (4.3-5.2 ppm) were not analysed due to suppression of residual water signal at 4.76 ppm. Not all H4’/H5’H5” sugar ring protons were fully resolved, and suppression of residual water prevented signal detection.

4.4.7.2 miR-21 cleavage studies

Cleavage of miR-21 RNA by peptidyl-oligonucleotide conjugates (POC) was conducted in Tris buffer (50 mM Tris−HCl containing 0.2 mM KCl, and 1 mM EDTA, pH 7.0). The reaction mixture (240 µl) was set up at 37 ^{o}C with miR-21 RNA target at 1 µM concentration and POC conjugate at 20 µM concentration to ensure 20-fold molar excess of conjugate over RNA. Aliquots (20 µl) were taken from the reaction mixture after regular time intervals (0, 24, 48, 72 and 96 h), with each aliquot containing 20 pmol miR-

21 and 400 pmol POC. Before incorporation into peptide hydrogel nano-sensor, the excess of the catalytic conjugate in the aliquot was removed by hybridisation with biotinylated capture oligonucleotide, followed by separation with streptavidin magnetic beads. To achieve that, 500 pmol (12.5 µl) of the single-stranded biotinylated oligonucleotide, complementary to the conjugate sequence was mixed with the reaction aliquot in Tris buffer (100mM Tris-base pH 7.2, 0.2 M KCl). To encourage the hybridisation between biotinylated capture oligonucleotide and POC, the mixture containing capture oligonucleotide, POC, uncleaved miR-21 target and cleaved fragments was subjected to heating and cooling cycles. The temperature profile used was as follows: heating to 85 ^{o}C for 5 min, followed by 2 cycles of heating to 85 ^{o}C for 5 min and cooling to 30 ^{o}C for 5 min and finally cooling to 30 ^{o}C for 5 min. The hybridised complex (POC-biotinylated capture oligonucleotide) was then separated by immobilisation on streptavidin-coated superparamagnetic beads (NanoLink® Streptavidin magnetic beads, TriLink, USA). The aliquot mixture was loaded onto the streptavidin beads (10 mg/ml), already suspended in 250 µl Tris buffer (100mM Tris-base containing 0.2 M KCl, pH 7.2) and incubated by shaking on a platform shaker at room temperature for 1 h. The beads containing immobilised complex were then separated by placing on magnetic particle concentrator (Dynal MPC®-S, UK) for 3 min and the supernatant was carefully removed and lyophilised. The lyophilisate was re-suspended into 15 µl of nuclease-free water (Fisher Scientific, UK) and incorporated into hydrogel pre-loaded with 0.5 µM "split-probes" (**pF** and **pQ**-Mal-Gly-Gly-**p2$^{(+1)}$**).

Similar experiments were carried out in free solution as well for comparison purpose. As a control, miR-21 RNA target was incubated in Tris buffer in the absence of POC conjugate. To rule out non-specific cleavage, miR-21 target was incubated with the scrambled POC (miR-17_3β, fully complementary to miR-17; CTACCTGCAC-dR^{beta}-AAGCACTTTG), which had no complementarity with the target miR-21 sequence. Unconjugated antisense oligonucleotide lacking the catalytic peptide -$[LRLRG]_2$ was also incubated with the miR-21 target, and parallel readings were recorded from 0-96 h alongside aliquots.

For catalytic turnover experiments, three reaction mixtures were set up (140 µl), each containing miR-21 at 25 µM and either (1) miR-21-miRNase (miR21-3α1; 5 µM), or (2) RNase H (100 U/ml) plus unconjugated oligonucleotide (5 µM), or (3) RNase H (100 U/ml) plus miR-21-miRNase (5 µM). The cleavage reactions were carried out in Tris-buffer (50 mM Tris−HCl containing 0.2 mM KCl, and 1 mM EDTA, 1 mM $MgCl_2$, 1

mM DTT, pH 7.0). Aliquots (10 µl) were taken after regular time intervals of 0, 24, 48, 72 and 96 h. Before loading into hydrogel sensor, the excess of the conjugate was removed by hybridisation with biotinylated capture oligonucleotide (2.5 µl, 100 pmol) in hybridisation buffer (in Tris buffer (100mM Tris-base pH 7.2, 0.2 M KCl). The complex was subjected to the heating and cooling cycle followed by separation through immobilisation on streptavidin-coated superparamagnetic beads, as described above. Measurements were recorded at λ_{em} 522 nm following excitation at λ_{ex} 494 nm, at 24 ^{O}C.

4.4.7.3 Anion-exchange chromatography of miR-21-miRNase-mediated cleavage of RNA

The reaction mixture (140 µl) was set up where miR-21 (25 µM) was incubated with miR-21_3α1 conjugate (5 µM) in Tris-buffer (50 mM Tris−HCl containing 0.2 mM KCl, and 1 mM EDTA, 1 mM $MgCl_2$, 1 mM DTT, pH 7.0). Aliquots (40 µl) containing 1 nmol of the target miR-21 were taken from the reaction mixture at 0 and 96 hours, and anion exchange chromatography was performed to assess the possibility of miR-21cleavage through the presence of cleaved fragments. Untreated miR-21 was used as a control to identify the retention time of the intact RNA sequence. PL-SAX 1000 Å column was used at a flow rate of 1.5 ml/min. Eluent used included 10 mM NaOAc in 30% acetonitrile (eluent A) and 1 mM $LiClO_4$+10 mM NaOAc in 30% acetonitrile (eluent B) in a gradient system increasing from 0 to 100% over 40 mins at 60°C.

4.4.7.4 MALDI-ToF MS analysis of miR-21-miRNase-mediated cleavage of RNA

For MS analysis, reaction mixture (140 µl) was set up as mentioned above. Aliquots (10 µl) were taken from the reaction mixture at 0 and 96 hours. Subsequently, the conjugate was removed by hybridisation with biotinylated capture oligonucleotide (2.5 µl, 100 pmol) in hybridisation buffer (in Tris buffer (100mM Tris-base pH 7.2, 0.2 M KCl). The complex was immobilised on streptavidin-coated superparamagnetic beads following heating and cooling cycle, as described above. C_{18} ZipTips (Merck, UK) were used for desalting and sample concentration using the previously reported protocol (34). Desalted reaction mixture aliquots in 5µl of 50/50 acetonitrile/water solution were mixed with 0.7 M 3-Hydroxy picolinic acid matrix (97 mg/mL, with 0.07 M ammonium citrate, 16 mg/mL in 50:50 ACN: H_2O) and the mass spectrometry was recorded in positive ion detection mode on Shimadzu Biotech Axima Confidence mass spectrometer using Time of Flight Matrix-Assisted Laser Desorption Ionisation (MALDI).

4.5 Results and Discussion

4.5.1 Design strategy, synthesis, and characterisation

We have designed a peptide hydrogel nano-biosensor through precise integration of recognition probes into the controlled self-assembly of peptide nanofibers, to achieve the sensitive and sequence-specific detection of miR-21 *in vitro*. Although the previous MB system was successful in achieving the precise detection of the model nucleic acid target with high sequence specificity and sensitivity (22), the stable hairpin structure of the MB recognition motif may represent a challenge for efficient hybridisation with short miR sequences (21-23 nt). Therefore, we used an alternative design for the molecular detector based on a "split-probe" concept, which divides the hybridisation domain of the recognition motif into two adjacent segments, i.e. fluorescent probe (**pF**) and quencher probe (**pQ**), each labelled with a reporter group, employing here fluorescein (as a fluorophore, **F**) and dabcyl (as a quencher, **Q**). In the absence of a complementary target, fluorophore (**F**) is completely fluorescent due to the spatial separation of FRET labelled probes. The hybridisation of 'perfect-match' complementary target (miR-21) is expected to considerably reduce the fluorescence from **F** by aligning the two "split-probes" adjacent to each other on a target strand leading to fluorescence quenching. To realise this design, the *fluorescein-dabcyl* FRET partners were covalently attached to the respective 5'-end and 3'-ends of **pF** and **pQ** oligonucleotides (see **Figure 4.1**). The 5'-end of quencher probe (**pQ**) was used to conjugate the first half of the recognition motif to the maleimide modification of **p2$^{(+1)}$** peptide decorating the hydrogel nanofibers. **pF** probe incorporating the second half of the RNA-recognising motif was then added externally, along with the analyte mixture containing miR-21 sequence, to allow the entire system to self-assemble on the surface of the peptide hydrogel, followed by fluorescence detection (**Figure 4.2**).

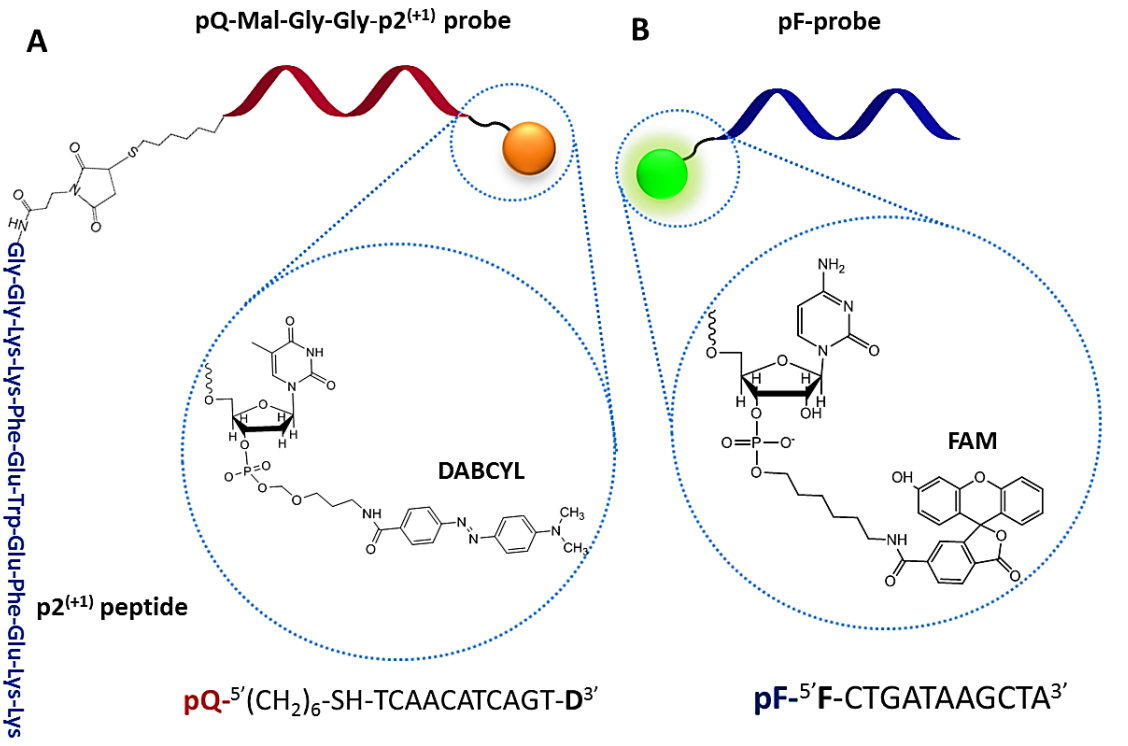

Figure 4.1. Attachment points and chemical modifications of "split-probes" (**pQ**-Mal-Gly-Gly-**p2**$^{(+1)}$ and **pF**). (**A**) The 5'-end of **pQ**-oligonucleotide was modified with a thiol group ($(CH_2)_6$-SS) for conjugation reaction and 3'-terminus was linked to the dabcyl quencher (**Q**). Peptide-oligonucleotide conjugate (pQ-Mal-Gly-Gly-**p2**$^{(+1)}$) was synthesised using thiol-maleimide chemistry, by linking the thiol-dT nucleotide to the N-terminus maleimide modification of ionic-complementary peptide (Mal-Gly-Gly-**p2**$^{(+1)}$). (**B**) The second component of the "split-probes" (**pF**) was modified with a fluorophore (**F**) group at the 5'-end to allow it to align next to the dabcyl quencher (**Q**) following hybridisation. Fluorophore and dabcyl are denoted as **F** and **Q**, and shown in green and orange spheres, respectively.

Peptide hydrogel was formed using equimolar concentrations (20 mM, 27 mg/L) of ionic-complementary peptides, **p1**$^{(-1)}$- Glu-Glu-Phe-Lys-Trp-Lys-Phe-Lys-Glu-Glu and **p2**$^{(+1)}$-Lys-Lys-Phe-Glu-Trp-Glu-Phe-Glu-Lys-Lys, at pH 7.2. The positively charged component, **p2**$^{(+1)}$ was selected for conjugation reaction with **pQ**-oligonucleotide due to its relatively higher critical gelation point in comparison to that of **p1**$^{(-1)}$ (22). Peptide-oligonucleotide conjugate, **pQ**-Mal-Gly-Gly-**p2**$^{(+1)}$ was synthesised using thiol-maleimide chemistry between thiol-modified **pQ**-oligonucleotide and N-terminally modified **p2**$^{(+1)}$ (see **Figure 4.9** and **Figure 4.1** (**A**) for synthetic route and design, respectively). The N-terminus of **p2**$^{(+1)}$ peptide was modified with a maleimide functional group to produce Mal-Gly-Gly-**p2**$^{(+1)}$ for conjugation with **pQ**-oligonucleotide. A two-glycine linker was introduced between the maleimide moiety and peptide sequence to avoid the agglomeration of biomolecules at the N-terminus following oligonucleotide conjugation and to provide conformational flexibility between recognition probe and hydrogel nanofibers. **p2**$^{(+1)}$ and Gly-Gly-**p2**$^{(+1)}$ were synthesised using Fmoc solid-phase

synthesis, Gly-Gly-**p2**$^{(+1)}$ was functionalised with N-maleoyl β-alanine at the N-terminus to form Mal-Gly-Gly-**p2**$^{(+1)}$. The successful syntheses of Mal-Gly-Gly-**p2**$^{(+1)}$ and **pQ**-Mal-Gly-Gly-**p2**$^{(+1)}$ conjugate was confirmed: (i) by the change in HPLC retention time from 26 min (thiol-oligonucleotide) to 27 min (conjugate) and from 31.5 min (**p2**$^{(+1)}$) to 33.5 min (Mal-Gly-Gly-**p2**$^{(+1)}$ see **Figure 4.10**), (ii) mass spectrometry (**Figure 4.14**), (iii) by the presence of ^{1}H NMR signal at 6.78 ppm for Mal-Gly-Gly-**p2**$^{(+1)}$ and by the disappearance of ^{1}H NMR signal from maleimide protons (CH=CH) at 6.78 ppm for conjugate and (iv) by comparing ^{1}H NMR spectra of reaction products with those of starting materials (see **Figure 4.11** (**A**) and **4.11** (**B**) and the experimental section for details).

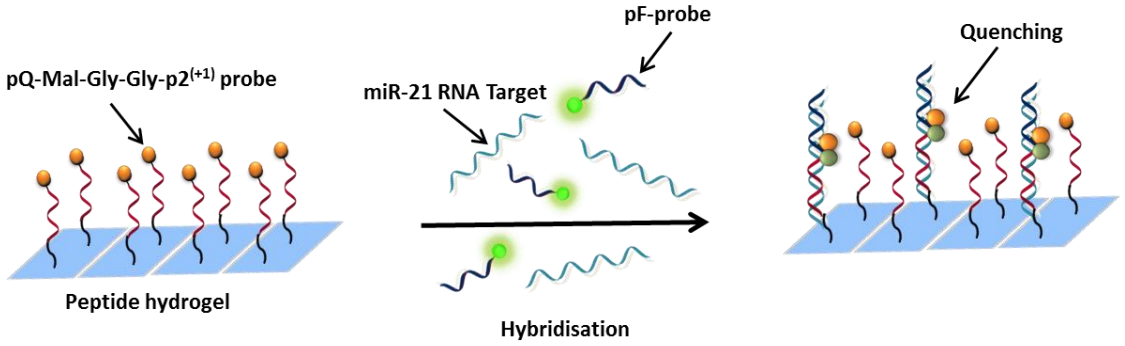

Figure 4.2. Schematic representation of the design of peptide hydrogel nano-biosensor incorporating the "split-probes" (**pQ**-Mal-Gly-Gly-**p2**$^{(+1)}$ and **pF**) bearing recognition motif for sequence-specific detection of miR-21. **Left**: The recognition probe **pQ**-Mal-Gly-Gly-**p2**$^{(+1)}$, labelled with dabcyl quencher (**Q**, in orange) is immobilised onto the surface of hydrogel nanofibers. **Middle**: The incorporation of the second probe, **pF** with a covalently attached fluorophore (**F**, in green) into the peptide hydrogel gives rise to the fluorescence, while not hybridised with the complementary target. **Right**: Hybridisation with the 'perfect-match' RNA target positions the **pQ**-Mal-Gly-Gly-**p2**$^{(+1)}$ and **pF** probes adjacent to each other on the target strand by Watson-Crick pairing, thus leading to quenching of fluorescence from **F** by **Q**.

4.5.2 Hydrogel characterisation

Transmission electron microscopy (TEM) of peptide hydrogel performed with and without the incorporation of the maximum amount of peptide-oligonucleotide conjugate **pQ**-Mal-Gly-Gly-**p2**$^{(+1)}$ showed that even at the highest doping level (0.003 % relative to the base peptides) used in this study, probe functionalisation of hydrogel did not affect the morphology of the fibres. The average diameter of peptide fibres in probe-functionalised and naked hydrogel was measured to be 5.12 nm (SD = 0.9, S.E = 0.07, n = 134) and 5.13 nm (SD = 0.9, S.E = 0.09, n = 110, see **Figure 4.3**) respectively. The morphological analysis also revealed some twisted helices and spirals along the fibre axes, which were presumed to be the result of specific ionic interactions between the complementary peptide chains.

For mechanical characterisation of peptide hydrogel, rheological measurements were conducted using an oscillatory shear rheometer. Storage (G') and loss moduli (G") were determined for both naked and decorated hydrogel in both amplitude and frequency-sweep modes. Amplitude sweep experiment showed that at 1% applied strain, both G' and G" were independent of the strain (see **Figure 4.3** (**C**)), which was later used for the frequency sweep experiments (**Figure 4.3** (**D**)). Incorporation of the peptide-oligonucleotide conjugate (**pQ**-Mal-Gly-Gly-**p2**$^{(+1)}$, 0.003 % relative to the base peptides) used in this study did not affect the mechanical properties of the hydrogel, suggesting that probe functionalisation of hydrogel did not interfere with the physical properties of peptide hydrogel. The hydrogel was prepared by mixing the equimolar concentrations (20 mM, 27 mg/L) of peptides (**p1**$^{(-1)}$ + **p2**$^{(+1)}$), incorporated with the highest doping level of recognition probe (**pQ**-Mal-Gly-Gly-**p2**$^{(+1)}$**,** 0.5 µM, 0.003 %), as described in the experimental section.

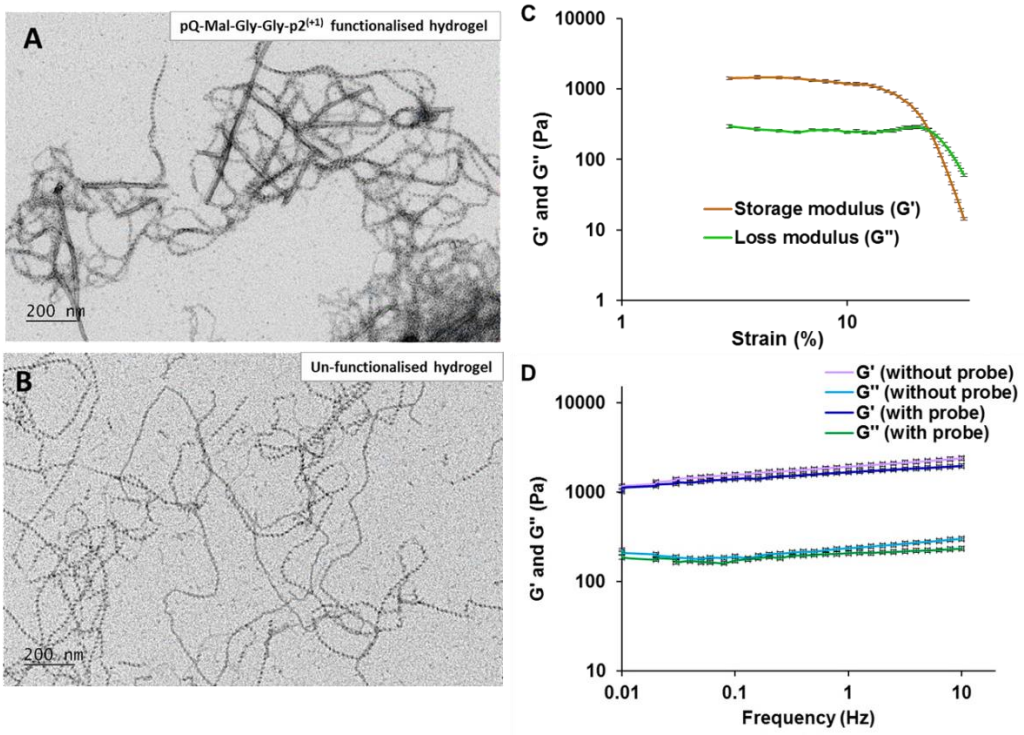

Figure 4.3. Morphological and mechanical characterisation of peptide hydrogel formed by **p1**$^{(-1)}$-Glu-Glu-Phe-Lys-Trp-Lys-Phe-Lys-Glu-Glu and **p2**$^{(+1)}$-Lys-Lys-Phe-Glu-Trp-Glu-Phe-Glu-Lys-Lys (1:1 molar ratio; 20 mM), using TEM and oscillatory rheometer, respectively. TEM images showing the peptide nanofibers used to construct the hydrogel nano-sensor in the presence (**A**) and absence (**B**) of detection probes **(pF** and **pQ**-Mal-Gly-Gly-**p2**$^{(+1)}$). Hydrogel samples (**A** and **B**) were diluted 500×fold to see the less dense network of peptide nanofibers. (**C**) Amplitude sweeps experiment conducted for mechanical characterisation of hydrogel (samples prepared by mixing equimolar concentrations of peptides, **p1**$^{(-1)}$ + **p2**$^{(+1)}$ at pH 7.2), showing the independencies of both storage (G') and loss (G") moduli at 1% strain. (**D**) Frequency sweeps of peptide hydrogel samples with and without the addition of highest concentration (0.5 µM, 0.01% relative to base peptides) of recognition probe used in this study, at 1% strain from 0.01 to 15 Hz. Average data of triplicate experiments are presented here.

4.5.3 Hybridisation studies

Hybridisation experiments were first conducted between the unmodified **pQ**-oligonucleotide ($^{5'}$T*CAACATCAGT-**Q**$^{3'}$, T* denotes $(CH_2)_6$-SS modified thymidine) or **pQ**-Mal-Gly-Gly-**p2**$^{(+1)}$ conjugate and 'perfect-match' (PM) miR-21 target ($^{5'}$UAGCUUAUCAGACUGAUGUUGA$^{3'}$) in solution (0.1 M Tris buffer containing 0.2 M KCl, pH 7.2). The two "split-probes", **pQ**;$^{5'}$T*CAACATCAGT-**Q**$^{3'}$ and **pF**;$^{5'}$**F**-CTGATAAGCTA$^{3'}$were designed to hybridise to the complete sequence of the miR-21 target. Before hybridisation with PM target, **pF**, **pQ** (unconjugated oligonucleotide sequences) or **pF**, **pQ**-Mal-Gly-Gly-**p2**$^{(+1)}$ (conjugate) were highly fluorescent due to the spatial separation of the two probes (**Figure 4.4**). Upon addition of 'perfect-match' RNA target, hybridisation between the complementary base pairs allowed the effective quenching of the fluorescence from fluorophore (**F**) by positioning the **pQ**-probe (quencher labelled fragment) into the proximity of fluorophore attached probe (**pF**). In Tris buffer solution, the fluorescence emission quenching of 87.1 % (7.6-fold) and 87.8 % (8.3-fold) was observed for the unconjugated oligonucleotide (**pQ**) and peptide-oligonucleotide conjugate (**pQ**-Mal-Gly-Gly-**p2**$^{(+1)}$, respectively see **Figure 4.17** (**A**)). However, hydrogel environment provided a higher level of quenching than that seen in solution (88.5 %, 8.8-fold for **pQ**-oligonucleotide and 92.3 %, 13.6-fold for **pQ**-Mal-Gly-Gly-**p2**$^{(+1)}$ conjugate, see **Figure 4.4** (**B**)), thus suggesting the favourable effect of using hydrogel medium for the sequence-specific detection of unlabelled nucleic acid sequences.

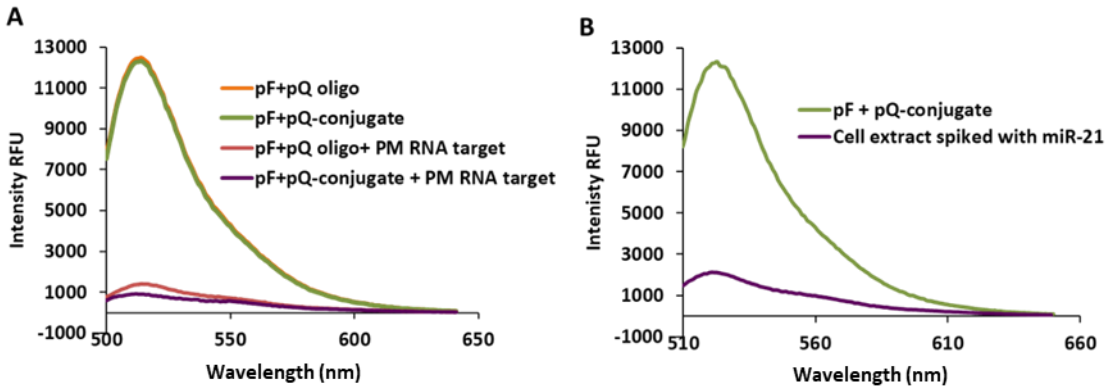

Figure 4.4. Quenching based detection of hybridisation of miR-21 target in hydrogel presented as (**A**) "clean" analyte solution and (**B**) MIA-PaCa 2 cell extract. The 'split-probes' (**pF**+**pQ** oligo, orange and **pF**+**pQ**-Mal-Gly-Gly-**p2**$^{(+1)}$ conjugate, green) were completely fluorescent in the absence of the complementary target due to the spatial separation of two probes. Addition of 'perfect-match' miR-21 target in either clear analyte form (**A**) or in cell extract (**B**) triggered the hybridisation events which led to the effective quenching of the fluorescence from **pF**+**pQ** oligonucleotide (red) and **pF**+**pQ**-Mal-Gly-Gly-**p2**$^{(+1)}$ conjugate (purple). All oligonucleotides components were at 0.5 µM concentration. miR-21 target was spiked in 1:1 of cell extract and tris

buffer to achieve the final concentration of 0.5 μM relative to the 'split-probes'. Hydrogel was prepared by mixing the equimolar concentrations (20 mM) of peptides (**p1**$^{(-1)}$ + **p2**$^{(+1)}$) at pH 7.2. Fluorescence was measured at λ_{em}= 522 nm following excitation at λ_{ex}= 494 nm.

The results suggest that in comparison to the solution, the hydrogel environment leads to better hybridisation events. The conformational constraints induced in the duplex formed following the hybridisation are likely to be more pronounced in the hydrogel. This could occur by several means. For instance, the hydrogel may restrict conformational freedom of the molecules in such a way as to allow more close positioning of the fluorophore (**F**) and quencher (**Q**) groups at a comparatively shorter distance following hybridisation. It is also plausible that hydrogel environment could increase the 'effective concentration' of negatively charged target nucleic acids around the recognition probes due to the presence of net positive-charge near the surface of the hydrogel nanofibers. Such electrostatic immobilisation of the 'recognition probe' to the surface of nanofibers could contribute towards the closer placement of reporter groups (**F** and **Q**), compared to that seen in solution, thereby resulting in more effective quenching of the fluorescence.

4.5.4 Detection of the target in complex biological samples

To demonstrate the potential of our nano-sensor device to detect the 'perfect match' target from complex biological fluids, cell extract was used from human pancreatic cancerous cell lines (MIA PaCa-2) containing the spiked level of the miR-21 target to achieve the final equimolar concentration of 0.5 μM under hybridisation conditions. 1:1 mixture of cell extract and 1X tris buffer (pH 7.2) with an elevated level of miR-21 RNA target was added to the sample pre-loaded with **pF**+**pQ**-Mal-Gly-Gly-**p2**$^{(+1)}$ probes either in solution (**Figure 4.17** (**B**)) or in hydrogel setup (**Figure 4.4** (**B**)) and tested under conditions identical to those described earlier. In comparison to the solution, the hydrogel medium demonstrated around 80% better detection of 'perfect match' target, comparable to the conditions when "clean" analyte sample was used without the interference of cellular components. This proved the superior capability of our nano-sensor system to detect the target sequence in complex biological samples in comparison to solution, presumably by shielding the detector probes from any cellular constituents, likely to interfere with the fluorescence emission. This filtering effect through the hydrogel surface may preferentially allow the oligonucleotide molecules into the peptide matrix for efficient hybridisation and detection.

4.5.5 Sequence specificity and mismatch discrimination

To determine the sequence specificity of our designed peptide hydrogel nano-biosensor, the ability of the system to distinguish between the 'perfect-match' target and related mismatches was investigated. The 'perfect-match' target was 'mutated' at one or two different positions, either in the centre or at the edge of the recognition motif to produce four 'mismatched sequences'. Mismatch 1 ($^{5'}$UAGCU**A**AUCAGACUGAUGUUGA$^{3'}$) had ***A*** (underlined) as a substitution for ***U*** at position 6, whereas, mismatch 2 sequence ($^{5'}$UAGCU**A**AUCAGACUG**G**UGUUGA$^{3'}$) had an additional replacement of ***G*** for ***A*** at position 16. Mismatch 3 ($^{5'}$U**U**GCUUAUCAGACUGAUGUUGA$^{3'}$) had a substitution of ***U*** for ***A*** at the 5'-end (position 2) of the miR-21 target and mismatch 4 ($^{5'}$UAGCUUAUCAGACUGAUGUU**C**A$^{3'}$) had a ***G*** replaced for ***C*** at the position 21 (3'-end edge) of the 'perfect-match' target (see **Table 4.2** for the sequences). Each mismatch sequence was incubated separately into the peptide hydrogel decorated with the "split-probes" (**pF** and **pQ**-Mal-Gly-Gly-**p2**$^{(+1)}$), as described earlier. For comparison, similar experiments were carried out in free solution (see Experimental section for details).

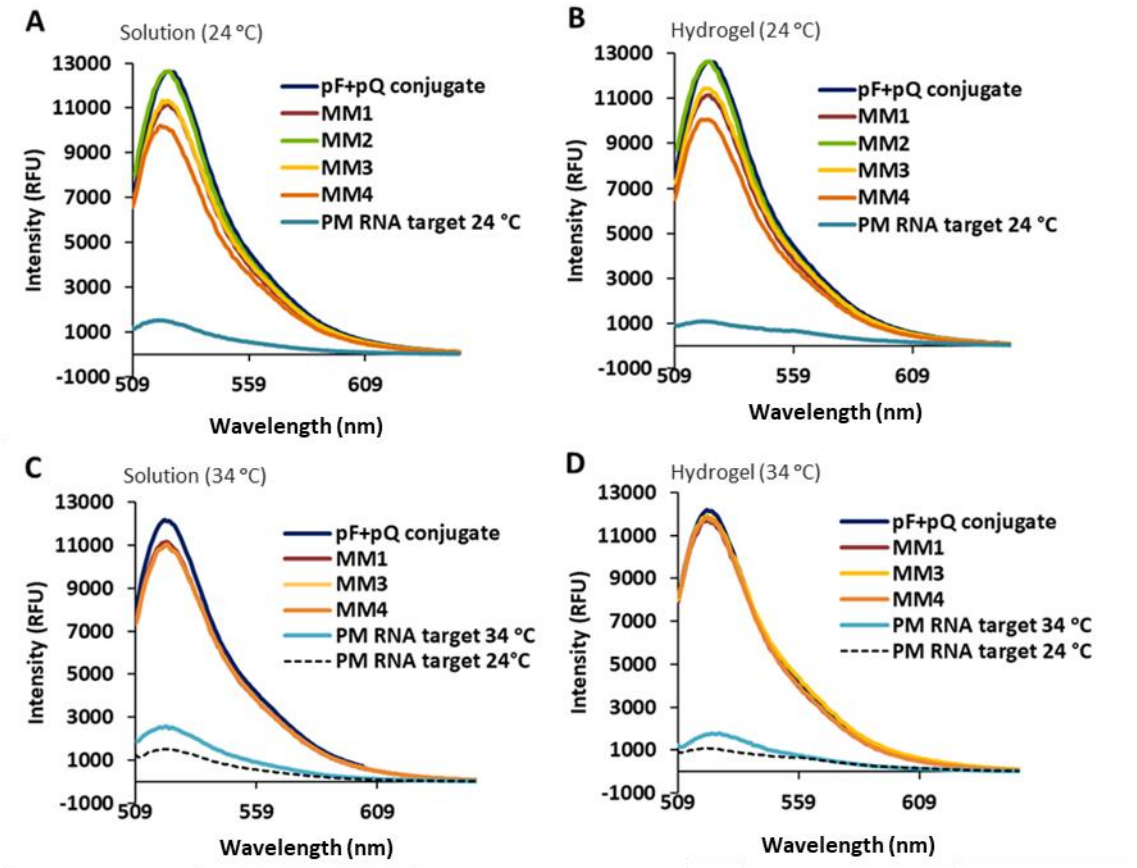

Figure 4.5. Comparison of the level of effective quenching following hybridisation between 'perfect-match' miR-21 target and mismatches (MM 1,2, 3 and 4) in solution (**A** and **C**) and peptide hydrogel (**B** and **D**) at 24 °C (**A** and **B**) and 34 °C (**C** and **D**). The 'split-probes' **pF**+**pQ**-Mal-Gly-Gly-**p2**$^{(+1)}$ (green) were completely fluorescent in isolation (i.e., in the absence of

complementary RNA target). The degree of effective quenching was dependent on the type of analyte sequence: 'perfect-match' RNA target (Light blue; at 24 °C and black; at 34 °C), mismatch 1 (red), mismatch 2 (green), mismatch 3 (yellow) and mismatch 4 (orange). Hydrogel was prepared by mixing the equimolar concentrations (20 mM) of peptides (**p1**$^{(-1)}$ + **p2**$^{(+1)}$) at pH 7.2. Fluorescence was measured at λ_{em}= 522 nm following excitation at λ_{ex}= 494 nm.

At 24 °C, almost no change in fluorescence was observed for mismatch 2 (data not shown) which had 2-point mutations at position 6 and 16, each located in the centre of hybridisation domain of one "split-probe", both in solution and hydrogel. A slight quenching was observed for mismatch-1 (11 %), mismatch-3 (8 %) and mismatch-4 (18 %) in both solution and hydrogel at 24 °C (see **Figure 4.5** (**A**) and **Figure 4.5** (**B**)), presumably caused by the weak hybridisation events between the detection probes and mismatched targets, when mutations were located at the ends of the binding domain. However, the probability of 'non-specific' hybridisation was eliminated under 'stringent conditions', which in this case were achieved by an increase in the hybridisation temperature from 24 °C to 34 °C (see **Figure 4.5**). Indeed, at 34 °C the fluorescence responses generated upon hybridisation with the mismatched targets were reduced to < 5% and < 15 % in hydrogel and solution, respectively (**Figure 4.5** (**C**) and **Figure 4.5** (**D**)), in comparison to the fluorescence response generated from the "split-probes" (**pF** and **pQ**-Mal-Gly-Gly-**p2**$^{(+1)}$) in isolation. "Split-probe" system eliminates the probability of false signal generation to a greater extent due to its higher responsiveness to the mismatches attributed to the short length sequences. Under optimised stringency conditions (i.e., 34 °C), the designed peptide hydrogel nano-biosensor was able to correctly distinguish between the 'perfect-match' target and mismatches down to 'single nucleotide substitution'.

4.5.6 Limit of Detection (LoD)

The lowest detection limit of the designed peptide-hydrogel nano-biosensor was calculated through a series of hybridisation studies replicated using "split-probes"; **pF** and **pQ**-Mal-Gly-Gly-**p2**$^{(+1)}$, incorporated into the peptide hydrogel over the concentration range of 50 nM to 50 pM (doping levels of 3.0×10^{-4} to 2.7×10^{-6} %). 'Perfect-match' miR-21 target was then introduced into the hydrogel sensor at the same concentration to achieve the equal molar ratio (1:1:1). The lowest concentration of miR-21 PM target that was reliably distinguishable at S/N = 3 (signal-to-noise) ratio was measured to be 50 pM (**Figure 4.18**). The limit of blank (LoB) and limit of detection (LoD) were calculated (see Experimental section for details) using the Equations (1) and (2):

$$LoB = Mean_{blank} + 1.645(SD_{blank}) \quad (1)$$

$$LoD = LoB + 1.645(SD_{lcs}) \quad (2)$$

To compare the performance of peptide hydrogel sensor, similar experiments were also carried out in free solution. The peptide hydrogel nano-sensor had a linear range of 50 nM to 50 pM, with a blank limit of 12.3 pM and a detection limit of 13.1 pM, which was 4-folds higher than the LoD calculated for **pQ**-Mal-Gly-Gly-**p2$^{(+1)}$** conjugate in solution (LoD = 51 pM). These experiments provided evidence that peptide hydrogel nano-sensor is capable of highly sensitive and sequence-specific nucleic acid detection and therefore can be applied to analyse biologically relevant samples without the need for prior labelling.

4.5.7 Design, synthesis and characterisation of catalytic POCs

We also evaluated the ability of the constructed peptide hydrogel nano-sensor to detect the disappearance of the miR-21 upon irreversible cleavage by natural (RNase A and H) and artificial ribonucleases, miR-21-miRNase. The success here not only allowed us to demonstrate the potential application of such detector for prognostic purposes but also the use of the detector to guide the future therapeutics and drug development. As discussed above, overexpressed miR-21 in serum, sputum, cerebrospinal fluid and urine can be used as a prognostic and diagnostic biomarker (7, 35). Numerous studies have also outlined the potential of miR-21 as a therapeutic target (36–38), which expands the prospects for drug discovery and therapy development applications. Metal-independent sequence-specific artificial ribonucleases targeting towards miRNAs (miRNase) have shown efficient and selective down-regulation of oncogenic miRNAs (39, 40). Therefore, natural and synthetic ribonucleases can be employed to monitor the down-regulation of miR-21 using peptide hydrogel nano-sensor.

Previously, *"single"* bulge-loop inducing peptidyl-oligonucleotide conjugates (POCs) complementary to TΨC-loop and 3'-accepter stem of $tRNA^{Phe}$ and capable of sequence-specific RNA cleavage were reported (33). These catalytically active bulge-loop inducing conjugates were synthesised by conjugation of the catalytic peptide Acetyl-$[LRLRG]_2$-CO_2H to an antisense recognising motif via a flexible aminohexyl linker attached to an internal abasic nucleotide in either α- or β-configuration. Both α- and β stereoisomers were catalytically active against RNA target with marginal catalytic superiority of α configuration over β (33). Furthermore, an induction of ≥3-nt RNA bulge-loop regions in

the target sequence resulted in high catalytic efficiency. The structural insights obtained from the previous study provided the foundations for miR-21-miRNases design. Building on the success of *"single"* bulge-loop inducing conjugates, the design was adjusted towards biologically relevant miR-21 through the incorporation of miR-21-complementary recognition motif for selective sequence-specific destruction of target RNA (see **Table 4.1** and **Figure 4.19** for nomenclature and composition of each miR-21-miRNase conjugates).

The successful conjugation was assessed through RP-HPLC as described in (33). The identity and purity of synthesised POCs were confirmed by mass spectrometry and ^{1}H NMR spectroscopy (see **Supporting information** for full characterisation, **Figure 4.15 and 4.16**). Indeed, careful integration of ^{1}H NMR signals for the characteristic peptide peaks corresponding to Gly-H$^{\alpha}$ and Leu/Arg-H$^{\alpha}$ protons in the spectral area of 3.29−4.74 ppm and oligonucleotides protons in the resonance region of 7.26−8.44 ppm (aromatic protons) and 5.4−6.4 ppm (H1' and Ar-H5 sugar ring protons) confirmed the precise 1:1 stoichiometric ratio of peptide to the oligonucleotide.

Table 4.1. Full antisense oligonucleotide sequences for miR-21-miRNase conjugates. The aminohexyl linker attached to anomeric nucleotide in alpha or beta configuration has been indicated by dR$^{alpha/}$ dR^{beta}.

Conjugate	Oligonucleotide (5'→3')	Bulge size	Peptide
miR-21_3β1	$^{5'}$TCAACATCAGT-**dR^{beta}**-ATAAGCTA$^{3'}$	3-nt long	$[LRLRG]_2$
miR-21_3α1	$^{5'}$TCAACATCAGT-**dR^{alpha}**-ATAAGCTA$^{3'}$	3-nt long	$[LRLRG]_2$
miR-21_3β2	$^{5'}$TCAACATCAG-**dR^{beta}**-GATAAGCTA$^{3'}$	3-nt long	$[LRLRG]_2$
miR-21_3α2	$^{5'}$TCAACATCAG-**dR^{alpha}**-GATAAGCTA$^{3'}$	3-nt long	$[LRLRG]_2$

4.5.8 Detection of POC-mediated miR-21 cleavage

The cleavage activities of POCs were assayed in Tris-EDTA buffer (see **Materials and Methods**; detailed description of the protocol given in (33)), under physiological conditions (37 ^{o}C and pH 7.0). Bulge-loop inducing peptidyl-oligonucleotide conjugates (POCs) were designed to cleave the miR-21 target at a central location, thus breaking the target into two halves. The process of POC-mediated cleavage over time (0-96 h) was analysed using peptide hydrogel nano-sensor at 24 ^{o}C, by an increase in fluorescence resulting from the generation of cleaved fragments. In case of the uncleaved miR-21 target ($^{5'}$UAGCUUAUCAGACUGAUGUUGA$^{3'}$), the two "split-probes" (**pF** and **pQ**-Mal-Gly-Gly-**p2$^{(+1)}$**) were aligned next to each other on a target strand, thereby quenching the fluorescence from **F** due to the proximity of **Q**. As the enzyme catalytic reaction

progresses over time, a gradual reduction in the intact target and simultaneous formation of the cleaved fragments hinders the alignment of the two "split-probes", hence increasing the fluorescence emission intensity proportional to the percentage of cleavage. Interestingly, the positioning of the abasic nucleotide with aminhexyl linker attached in 'α' configuration resulted in a higher percentage of cleavage than 'β' configuration. The estimated percent cleavage for 'α' miR-21-miRNases (miR-21_3α1 and miR-21_3α2) was approximately 70 % and 65 %, respectively (see **Figure 4.6** (**A**) and **4.6** (**C**)), whereas 'β' conjugates (miR-21_3β1 and miR-21_3β2) showed the respective cleavage percentage of 55 % and 52 % (see **Figure 4.6** (**B**) and **4.6** (**D**)), measured against the total RNase A cleavage of the miR-21 target (**Figure 4.7** (**A**)). Similar cleavage percentage was achieved in free solution (data not shown).

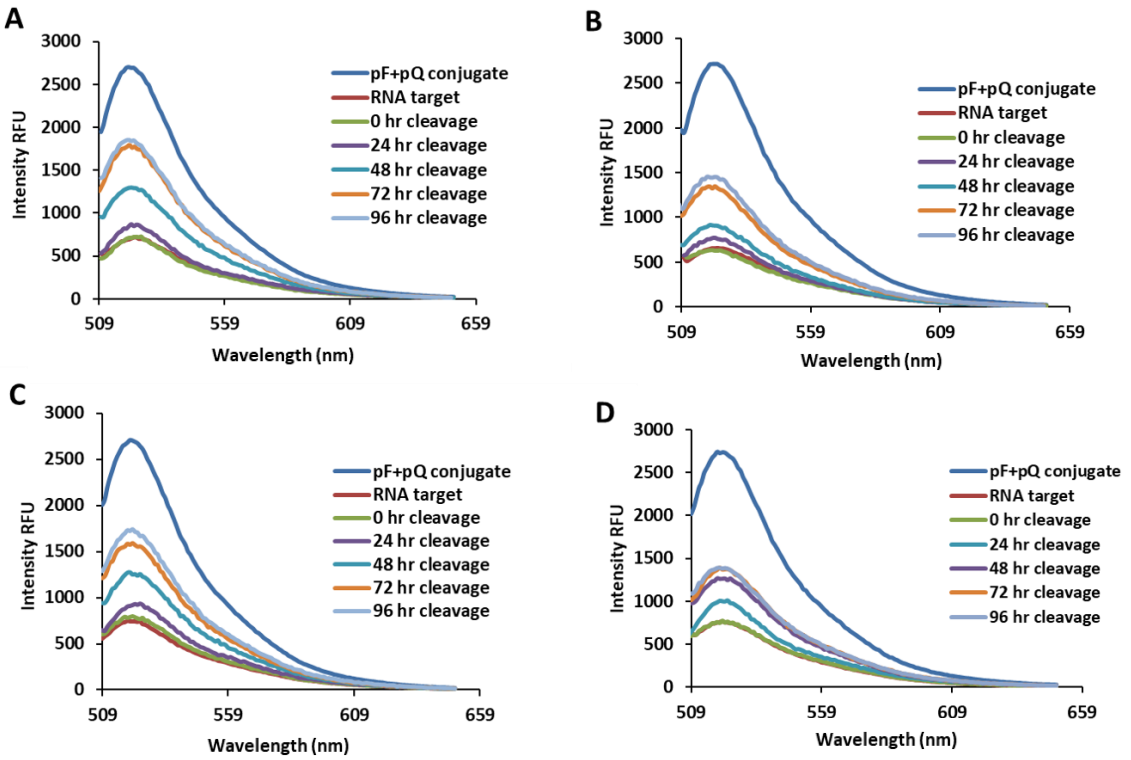

Figure 4.6. Fluorescence spectra illustrating the cleavage progress of miR-21 target mediated by catalytic POCs over the course of time (0-96 h). The extent of maximum cleavage was analysed for 'α' conjugates; miR-21_3α1 and miR-21_3α2 (**A** and **C**) and 'β' conjugates; miR-21_3β1 and miR-21_3β2 (**B** and **D**), in peptide hydrogel nano-sensor (pH 7.2) at 24 °C. The uncleaved miR-21 target formed a three-component hybridisation complex with the "split-probes" (**pF**+**pQ**-Mal-Gly-Gly-**p2**$^{(+1)}$, 200nM, 1:1:1), which resulted in quenching of fluorescence from **F** due to the close proximity of **Q**. The percent increase in fluorescence was strongly dependent on the catalytic potential of POC to cleave the miR-21 target and generate cleaved fragments. Peptide hydrogel was prepared by mixing the equimolar concentrations (20 mM) of peptides (**p1**$^{(-1)}$ + **p2**$^{(+1)}$) at pH 7.2. Fluorescence was measured at λ_{em}= 522 nm following excitation at λ_{ex}= 494 nm.

Careful analysis revealed that even minor alterations in the configuration (i.e., positioning of the bulge) could lead to a dramatic change in RNA cleavage profile. A shift in the

position of the loop towards the 5‘end of the target augmented the interaction between POC and target, resulting in more favourable setting for cleavage by providing accessibility to the bulged single-stranded cleavage site. The kinetics of POCs-mediated miR-21 cleavage was assessed by measuring the extent of total miR-21 cleavage against time of cleavage reaction. For all POCs, the cleavage pattern showed a gradual increase in activity with time, as indicated by time course increase in fluorescence from 0-72 h before reaching a plateau stage in 96 h (see **Figure 4.7** (**B**)). No cleavage activity was observed under the stated conditions with scrambled POC (miR-17_3β), which had non-complementarity to miR-21 sequence (see **Figure 4.20** (**A**)). Similarly, no spontaneous cleavage was seen when unconjugated miR-21-miRNase oligonucleotide sequence was incubated alone with miR-21 target in the absence of POCs (see **Figure 4.20** (**B**)), suggesting that POCs are catalytically active only when -$[LRLRG]_2$ peptide is chemically linked to the antisense oligonucleotide. This is in alignment with the results obtained from the previous studies (41).

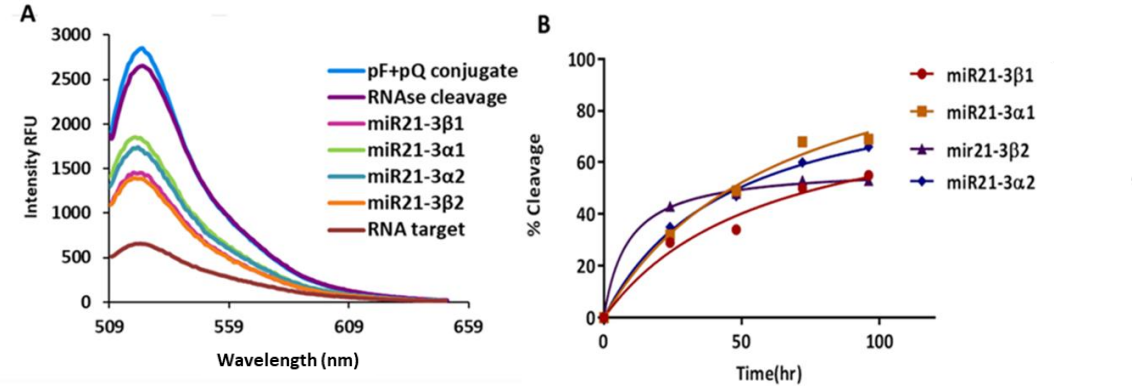

Figure 4.7. Cleavage analysis of ‘α’ and ‘β’ peptidyl-oligonucleotide conjugates. (**A**) Fluorescence spectra for the maximum cleavage of miR-21 (1 μM) achieved by POCs (20 μM) in 96 h compared against the total RNase A cleavage of the miR-21 target. (**B**) The secondary plot of the data shown in **Figure 4.6**, illustrating the time course cleavage of miR-21 target mediated by ‘α’ and ‘β’ POCs.

An artificial ribonuclease is expected to exhibit catalytic turnover activity resulting from the cleavage and release of cleaved target fragments followed by the attack of the next RNA molecule. The turnover ability of artificial ribonuclease to cleave multiple copies of miR-21 was evaluated using significantly higher concentration (up to 5-folds) of target molecules over miR-21-miRNase. Under these conditions, up to 50% cleavage of the miR-21 target was achieved in 96 h (**Figure 4.8**, black curve,). Indeed, the data presented here indicate the capability of miRNase to exert catalytic turnover. Additionally, anion-exchange chromatography and MALDI-TOF mass spectrometry techniques were used to corroborate cleavage and identify the prominent cleavage products (see **Figure 4.21** and

4.22). Aliquotes from point 0 and 96 hours were analysed through anion-exchange chromatography column to further confirm the POC-mediated cleavage activity. A quantitative (50%) reduction in the uncleaved target in the reaction mixture aliquot at 96 hours was evident, verifying the extent of cleavage obtained from the assay. In addition, a number of shorter fragments (few nt long) were visible as indicated from their lower retention time in comparison to the intact target (see **Figure 4.21** (**B**)).

Furthermore, Matrix-Assisted Laser Desorption/Ionization-Time Of Flight Mass Spectrometry (MALDI-TOF MS) was used to visualise the products of RNA cleavage. MALDI-TOF MS allowed identification of cleaved products of differing lengths in the complex reaction mixture. The presence of numerous peaks with unique mass differences indicated miR-21-miRNase-mediated cleavage of RNA, where three prominent primary fragments were identified ($^{5'}$UAGCUUAUCAG$^{3'}$, $^{5'}$ACUGAUGUUGA$^{3'}$ and $^{5'}$UAGCUUA$^{3'}$) (see **Figure 4.22**). Attachment of the peptide via C-terminus and the presence of a flexible linker resulted in G-X and A-U cleavage specificity where two linkages A_7U_8 and $G_{11}A_{12}$ are assumed to be the effective point of cleaveage.

In the cellular environment, it is anticipated that the duplex formed between the miR-21 and miRNase can easily be recognised by RNase H, thereby contributing to the catalytic activity. To demonstrate the synergistic effect of ribonucleases (RNase H and miRNase) on miR-21 cleavage (5-fold excess), first, the catalytic efficiency of RNase H alone was evaluated on the duplex formed between the miR-21 target and unconjugated miR-21-miRNase oligonucleotide lacking the catalytic peptide. A lower excess of the target over miRNase would have led to rapid degradation of the target by RNase H depriving the conjugate of the opportunity to exert catalytic activity. Additionally, high excess of overexpressed miR-21 is expected to be seen in malignant cells *in vivo* (42). The kinetics of miR-21 cleavage in a heteroduplex with oligonucleotide by RNase H reached a plateau in 8 h with a total extend of cleavage of 62% (**Figure 4.8**, green curve). However, a much greater extent of cleavage (up to 100%) was achieved through the synergistic effect of ribonucleases (RNase H + miRNase) in 24 h (**Figure 4.8**, red curve). The presence of RNase H and miRNase simultaneously in the reaction mixture led to a steep increase in the initial rate of cleavage where plateau was reached in almost 8 hours (around 85% cleavage). RNase H elevated the miRNase-mediated cleavage of miR-21 by a factor of 2. Previously, the synergetic effect from the joint action of miRNases and RNase H leading to selective knockdown of miR-21 in malignant cells was reported (40). The result reported here highlights the therapeutic potential of POCs capable of irreversible cleavage

of miR-21 in multiple turnover mode and recruiting intracellular RNase H. Clearly, this design shows high cleaving efficacy, far superior to the classical antisense approach. The synergistic actions with RNase H also boost POC potency, minimising the required therapeutic dose. The peptide hydrogel detector developed here was able to report and quantify the disappearance of the intact miRNA through de-assembly of the hybridised complex, triggered by the destructive cleavage of the biotarget.

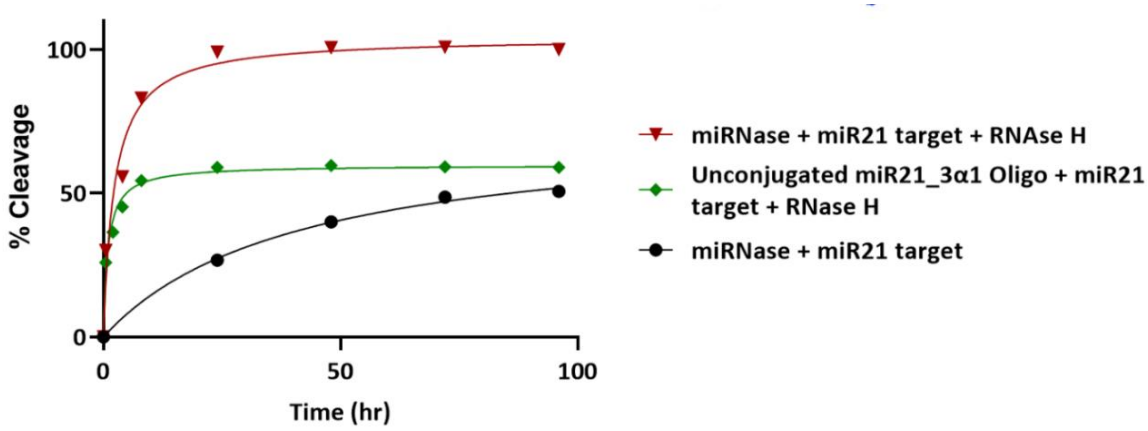

Figure 4.8. The catalytic activity of miRNase under different turnover conditions. A catalytic experiment set up with 5 folds higher concentration of miR-21 to miRNase (25 µM: 5 µM) to show the turnover rate of artificial ribonuclease. A synergistic reaction was set up with RNase H (100 U/ml) plus 5 µM of either unconjugated oligonucleotide or miR-21-miRNase (miR-21_3α1) (5:1).

4.6 Conclusion

We have demonstrated here the fabrication of a new peptide hydrogel nano-sensor for sequence-specific detection of oncogenic miR-21 and proven its ability to monitor the gradual disappearance of target miRNA upon treatment by ribonucleases. Our engineered oligonucleotide-peptide hydrogel system was able to distinguish the miR-21 target with high specificity and at low levels (13 pM) in its intact single-stranded form to meet the needs of early-stage diagnosis. The system could operate to analyse miR-21 from clean and complex biological samples such as cancerous MIA PaCa-2 extract. The platform proved to be more responsive to mismatches, because of the short length sequences, which minimise the probability of false signal generation. The quantification of miR-21 disappearance upon treatment by synthetic or natural (RNase A and H) ribonucleases, highlighted the prognostic potential of the designed nano-sensor. The system further confirmed the catalytic turnover and kinetic analysis of artificial ribonucleases which signifies its importance as a screening tool for drug development. The multifunctional conceptualisation of the designed nano-sensor, therefore, can facilitate monitoring of

serological miRNA profiling, screening of supramolecular ribonuclease activity against biological targets, and miRNA down-regulation in real-time.

4.7 References

1. Chang,T.C. and Mendell,J.T. (2007) microRNAs in vertebrate physiology and human disease. *Annu. Rev. Genomics Hum. Genet.*, **8**, 215–239.

2. Ma,X., Conklin,D.J., Li,F., Dai,Z., Hua,X., Li,Y., Xu-Monette,Z.Y., Young,K.H., Xiong,W., Wysoczynski,M., et al. (2015) The oncogenic microRNA miR-21 promotes regulated necrosis in mice. *Nat. Commun.*, **6**, 7151.

3. Lin,S. and Gregory,R.I. (2015) MicroRNA biogenesis pathways in cancer. *Nat. Rev. Cancer*, **15**, 321–333.

4. Thompson,A.G., Gray,E., Heman-Ackah,S.M., Mäger,I., Talbot,K., Andaloussi,S. El, Wood,M.J. and Turner,M.R. (2016) Extracellular vesicles in neurodegenerative disease - pathogenesis to biomarkers. *Nat. Rev. Neurol.*, **12**, 346–357.

5. Simpson,L.J. and Ansel,K.M. (2015) MicroRNA regulation of lymphocyte tolerance and autoimmunity. *J. Clin. Invest.*, **125**, 2242–2249.

6. Rupaimoole,R. and Slack,F.J. (2017) MicroRNA therapeutics: towards a new era for the management of cancer and other diseases. *Nat. Rev. Drug Discov.*, **16**, 203–222.

7. Peng,Q., Zhang,X., Min,M., Zou,L., Shen,P. and Zhu,Y. (2017) The clinical role of microRNA-21 as a promising biomarker in the diagnosis and prognosis of colorectal cancer: a systematic review and meta-analysis. *Oncotarget*, **8**, 44893–44909.

8. Matsumura,T., Sugimachi,K., Iinuma,H., Takahashi,Y., Kurashige,J., Sawada,G., Ueda,M., Uchi,R., Ueo,H., Takano,Y., et al. (2015) Exosomal microRNA in serum is a novel biomarker of recurrence in human colorectal cancer. *Br. J. Cancer*, **113**, 275–281.

9. Lai,N., Wu,D., Fang,X., Lin,Y., Chen,S., Li,Z. and Xu,S. (2015) Serum microRNA-210 as a potential noninvasive biomarker for the diagnosis and prognosis of glioma. *Br. J. Cancer*, **112**, 1241–1246.

10. Markou,A., Sourvinou,I., Vorkas,P.A., Yousef,G.M. and Lianidou,E. (2013) Clinical evaluation of microRNA expression profiling in non small cell lung cancer. *Lung Cancer*, **81**, 388–396.

11. Shen,J., Wang,A., Wang,Q., Gurvich,I., Siegel,A.B., Remotti,H. and Santella,R.M. (2013) Exploration of genome-wide circulating microRNA in hepatocellular carcinoma: MiR-483-5p as a potential biomarker. *Cancer Epidemiol. biomarkers Prev.*, **22**, 2364–2373.

12. Chan,M., Liaw,C.S., Ji,S.M., Tan,H.H., Wong,C.Y., Thike,A.A., Tan,P.H., Ho,G.H. and Lee,A.S.-G. (2013) Identification of circulating microRNA signatures for breast cancer detection. *Clin. cancer Res.*, **19**, 4477–4487.

13. Zhu,C., Ren,C., Han,J., Ding,Y., Du,J., Dai,N., Dai,J., Ma,H., Hu,Z., Shen,H., et al. (2014) A five-microRNA panel in plasma was identified as potential biomarker for early detection of gastric cancer. *Br. J. Cancer*, **110**, 2291–2299.

14. Ma,J., Dong,C. and Ji,C. (2010) MicroRNA and drug resistance. *Cancer Gene Ther.*, **17**, 523–531.

15. Crosbie,P.A.J., Shah,R., Summers,Y., Dive,C. and Blackhall,F. (2013) Prognostic and predictive biomarkers in early stage NSCLC: CTCs and serum/plasma markers. *Transl. lung cancer Res.*, **2**, 382–397.

16. Kreth,S., Hübner,M. and Hinske,L.C. (2018) MicroRNAs as Clinical Biomarkers and Therapeutic Tools in Perioperative Medicine. *Anesth. Analg.*, **126**.

17. Glinge,C., Clauss,S., Boddum,K., Jabbari,R., Jabbari,J., Risgaard,B., Tomsits,P., Hildebrand,B., Kääb,S., Wakili,R., et al. (2017) Stability of Circulating Blood-Based MicroRNAs - Pre-Analytic Methodological Considerations. *PLoS One*, **12**, e0167969.

18. da Silveira,J.C., Veeramachaneni,D.N.R., Winger,Q.A., Carnevale,E.M. and Bouma,G.J. (2012) Cell-secreted vesicles in equine ovarian follicular fluid contain miRNAs and proteins: a possible new form of cell communication within the ovarian follicle. *Biol. Reprod.*, **86**, 71.

19. Novak,J. and Souček,M. (2016) [microRNA and internal medicine: from pathophysiology to the new diagnostic and therapeutic procedures]. *Vnitr. Lek.*, **62**, 477–485.

20. Metcalf,G.A.D., Shibakawa,A., Patel,H., Sita-Lumsden,A., Zivi,A., Rama,N., Bevan,C.L. and Ladame,S. (2016) Amplification-Free Detection of Circulating microRNA Biomarkers from Body Fluids Based on Fluorogenic Oligonucleotide-Templated Reaction between Engineered Peptide Nucleic Acid Probes: Application to Prostate Cancer Diagnosis. *Anal. Chem.*, **88**, 8091–8098.

21. Gaharwar,A.K., Arpanaei,A., Andresen,T.L. and Dolatshahi-Pirouz,A. (2016) 3D Biomaterial Microarrays for Regenerative Medicine: Current State-of-the-Art, Emerging Directions and Future Trends. *Adv. Mater.*, **28**, 771–781.

22. Yousaf,S., King,P.J.S., Miller,A.F., Saiani,A., Clarke,D.J., Trivoluzzi,L.T., Aojula,H.S. and Bichenkova,E. V (2019) Sequence-Specific Detection of Unlabeled Nucleic Acid Biomarkers Using a "One-Pot" 3D Molecular Sensor. *Anal. Chem.*, **91**, 10016–10025.

23. Yang,N., Ekanem,N.R., Sakyi,C.A. and Ray,S.D. (2015) Hepatocellular carcinoma and microRNA: new perspectives on therapeutics and diagnostics. *Adv. Drug Deliv. Rev.*, **81**, 62–74.

24. Mizuguchi,Y., Takizawa,T., Yoshida,H. and Uchida,E. (2016) Dysregulated miRNA in progression of hepatocellular carcinoma: A systematic review. *Hepatol. Res.*, **46**, 391–406.

25. Gilam,A., Conde,J., Weissglas-Volkov,D., Oliva,N., Friedman,E., Artzi,N. and Shomron,N. (2016) Local microRNA delivery targets Palladin and prevents metastatic breast cancer. *Nat. Commun.*, **7**, 12868.

26. Bertoli,G., Cava,C. and Castiglioni,I. (2015) MicroRNAs: New Biomarkers for Diagnosis, Prognosis, Therapy Prediction and Therapeutic Tools for Breast Cancer. *Theranostics*, **5**, 1122–1143.

27. Hannafon,B.N., Trigoso,Y.D., Calloway,C.L., Zhao,Y.D., Lum,D.H., Welm,A.L., Zhao,Z.J., Blick,K.E., Dooley,W.C. and Ding,W.Q. (2016) Plasma exosome microRNAs are indicative of breast cancer. *Breast Cancer Res.*, **18**, 90.

28. Yeh,C.-H., Moles,R. and Nicot,C. (2016) Clinical significance of microRNAs in chronic and acute human leukemia. *Mol. Cancer*, **15**, 37.

29. Shi,C., Yang,Y., Xia,Y., Okugawa,Y., Yang,J., Liang,Y., Chen,H., Zhang,P., Wang,F., Han,H., et al. (2016) Novel evidence for an oncogenic role of microRNA-21 in colitis-associated colorectal cancer. *Gut*, **65**, 1470–1481.

30. Fabris,L., Ceder,Y., Chinnaiyan,A.M., Jenster,G.W., Sorensen,K.D., Tomlins,S., Visakorpi,T. and Calin,G.A. (2016) The Potential of MicroRNAs as Prostate Cancer Biomarkers. *Eur. Urol.*, **70**, 312–322.

31. Shishodia,G., Shukla,S., Srivastava,Y., Masaldan,S., Mehta,S., Bhambhani,S., Sharma,S., Mehrotra,R., Das,B.C. and Bharti,A.C. (2015) Alterations in microRNAs miR-21 and let-7a correlate with aberrant STAT3 signaling and downstream effects during cervical carcinogenesis. *Mol. Cancer*, **14**, 116.

32. Armbruster,D.A. and Pry,T. (2008) Limit of blank, limit of detection and limit of quantitation. Clin. *Biochem. Rev.*, **29 Suppl 1**, S49–S52.

33. Staroseletz,Y., Amirloo,B., Williams,A., Lomzov,A., Burusco,K.K., Clarke,D.J., Brown,T., Zenkova,M.A. and Bichenkova,E. V. (2020) Strict conformational demands of RNA cleavage in bulge-loops created by peptidyl-oligonucleotide conjugates. *Nucleic Acids Res.* Accepted on 7 Sep 2020.

34. Joyner,J.C., Keuper,K.D. and Cowan,J.A. (2013) Analysis of RNA cleavage by MALDI-TOF mass spectrometry. *Nucleic Acids Res.*, **41**, e2–e2.

35. Nalejska,E., Mączyńska,E. and Lewandowska,M.A. (2014) Prognostic and predictive biomarkers: tools in personalized oncology. *Mol. Diagn. Ther.*, **18**, 273–284.

36. Jazbutyte,V. and Thum,T. (2010) MicroRNA-21: from cancer to cardiovascular disease. *Curr. Drug Targets*, **11**, 926–935.

37. Markou,A., Zavridou,M. and Lianidou,E.S. (2016) miRNA-21 as a novel therapeutic target in lung cancer. *Lung Cancer (Auckland)*, **7**, 19–27.

38. Pan,X., Wang,Z.-X. and Wang,R. (2010) MicroRNA-21: a novel therapeutic target in human cancer. *Cancer Biol. Ther.*, **10**, 1224–1232.

39. Patutina,O.A., Bichenkova,E. V, Miroshnichenko,S.K., Mironova,N.L., Trivoluzzi,L.T., Burusco,K.K., Bryce,R.A., Vlassov,V. V and Zenkova,M.A. (2017) miRNases: Novel peptide-oligonucleotide bioconjugates that silence miR-21 in lymphosarcoma cells. *Biomaterials*, **122**, 163–178.

40. Patutina,O.A., Miroshnichenko,S.K., Mironova,N.L., Sen'kova,A. V, Bichenkova,E. V, Clarke,D.J., Vlassov,V. V and Zenkova,M.A. (2019) Catalytic Knockdown of miR-21 by Artificial Ribonuclease: Biological Performance in Tumor Model. *Front. Pharmacol.*, **10**, 879.

41. Williams,A., Staroseletz,Y., Zenkova,M.A., Jeannin,L., Aojula,H. and Bichenkova,E. V (2015) Peptidyl-oligonucleotide conjugates demonstrate efficient cleavage of RNA in a sequence-specific manner. *Bioconjug. Chem.*, **26**, 1129–1143.

42. Bhere,D., Arghiani,N., Lechtich,E.R., Yao,Y., Alsaab,S., Bei,F., Matin,M.M. and Shah,K. (2020) Simultaneous downregulation of miR-21 and upregulation of miR-7 has anti-tumor efficacy. *Sci. Rep.*, **10**, 1779.

4.8 Supporting information

4.8.1 Sequences of oligonucleotides, peptides and peptide-oligonucleotide conjugates

Table 4.2. Sequences, molecular weights (Mw), millimolar extinction coefficients and melting temperature (T_m) values for oligonucleotides, peptides and peptide-oligonucleotide conjugates used for this study.

Name	Sequence (5' to 3')	Mw (Da) [cal.] [b]	E_{260} ($mM^{-1} \cdot cm^{-1}$)[c]	Tm (°C) [d]
Dabcyl probe	$^{5'}(CH_2)_6$-SS-T*CAACATCAGT-**Q**$^{3'a}$	5634.1 (cal.) 5633.2 $[M-H]^{-1}$ (obs.)	120.6	18.4
FAM probe	$^{5'}$**F**-CTGATAAGCTA$^{3'}$	3879.6 (cal.) 3878.1 $[M-H]^{-1}$ (obs.)	133.3	18.4
miR-21 RNA target	$^{5'}$UAGCUUAUCAGACUGAUGUU GA$^{3'}$	7006.8 (cal.) 7005.9 $[M-H]^{-1}$ (obs.)	220.7	40.1
miR-21 mismatch 1	$^{5'}$UAGCUAAUCAGACUGAUGUU GA$^{3'}$	7045.5 (cal.) 7044.5 $[M-H]^{-1}$ (obs.)	226.7	41.8
miR-21 mismatch 2	$^{5'}$UAGCUAAUCAGACUGGUGUU GA$^{3'}$	7045.5 (cal.) 7044.5 $[M-H]^{-1}$ (obs.)	223.1	44.5
miR-21 mismatch 3	$^{5'}$UUGCUUAUCAGACUGAUGUU GA$^{3'}$	6982.8 (cal.) 6981.8 $[M-H]^{-1}$(obs.)	214.7	38.2
miR-21 mismatch 4	$^{5'}$UAGCUUAUCAGACUGAUGUU CA$^{3'}$	6965.5 (cal.) 6964.5 $[M-H]^{-1}$(obs.)	216.9	40.1
Base peptides	**p1$^{(-1)}$**-Glu-Glu-Phe-Lys-Trp-Lys-Phe-Lys-Glu-Glu	1398.6 (cal.) 1396.6 $[M-2H]^{-2}$(obs.)	n/a	n/a
	p2$^{(+1)}$-Lys-Lys-Phe-Glu-Trp-Glu-Phe-Glu-Lys-Lys	1397.7 (cal.) 1395.7 $[M-2H]^{-2}$(obs.)	n/a	n/a
Maleimide peptides	Mal-Gly-Gly-Lys-Lys-Phe-Glu-Trp-Glu-Phe-Glu-Lys-Lys	1305.7 (cal.) 1303.7 $[M-2H]^{-2}$(obs.)	n/a	n/a
Peptide-oligonucleotide conjugate	**pQ**-Mal-Gly-Gly-**p2$^{(+1)}$**, (Mal-Gly-Gly-Lys-Lys-Phe-Glu-Trp-Glu-Phe-Glu-Lys-Lys-$^{5'}$T*CAACATCAGT-**Q**^{3})[e]	5632.2 (cal.) 5633.1 $[M+H]^{+1}$(obs.)	n/a	n/a
miR-21-miRNases	**miR-21_3β1**, $^{5'}$TCAACATCAGT-dR^{beta}-ATAAGCTA$^{3'f}$	7294.6 (cal.) 7333.1 $[M+K]^{+}$ (obs.)	n/a	n/a
	miR-21_3α1, $^{5'}$TCAACATCAGT-dR^{alpha}-ATAAGCTA$^{3'f}$	7294.6 (cal.) 7333.1 $[M+K]^{+}$ (obs.)	n/a	n/a
	miR-21_3β2, $^{5'}$TCAACATCAG-dR^{beta}-GATAAGCTA$^{3'f}$	7319.6 (cal.) 7358.3 $[M+K]^{+}$(obs.)	n/a	n/a
	miR-21_3α2, $^{5'}$TCAACATCAG-dR^{alpha}-GATAAGCTA$^{3'f}$	7319.6 (cal.) 7358.2 $[M+K]^{+}$ (obs.)	n/a	n/a
Scrambled conjugate	**miR17-3β,** $^{5'}$CTACCTGCAC-dR^{beta}-AAGCACTTTG $^{3'f}$	7614 (cal.) 7615 $[M+H]^{+}$ (obs.)	n/a	n/a

a) **T* denotes $(CH_2)_6$-SS modified thymidine**

b) **denotes calculated mass**

c) **E_{260} denotes the millimolar extinction coefficient**

d) **T_m denotes the melting temperature**

e) **T* denotes $(CH_2)_6$-SS modified thymidine**

f) **dR denotes Ac--[LRLRG]$_2$ -COOH attached to abasic nucleotide**

4.8.2 Additional Figures and Data

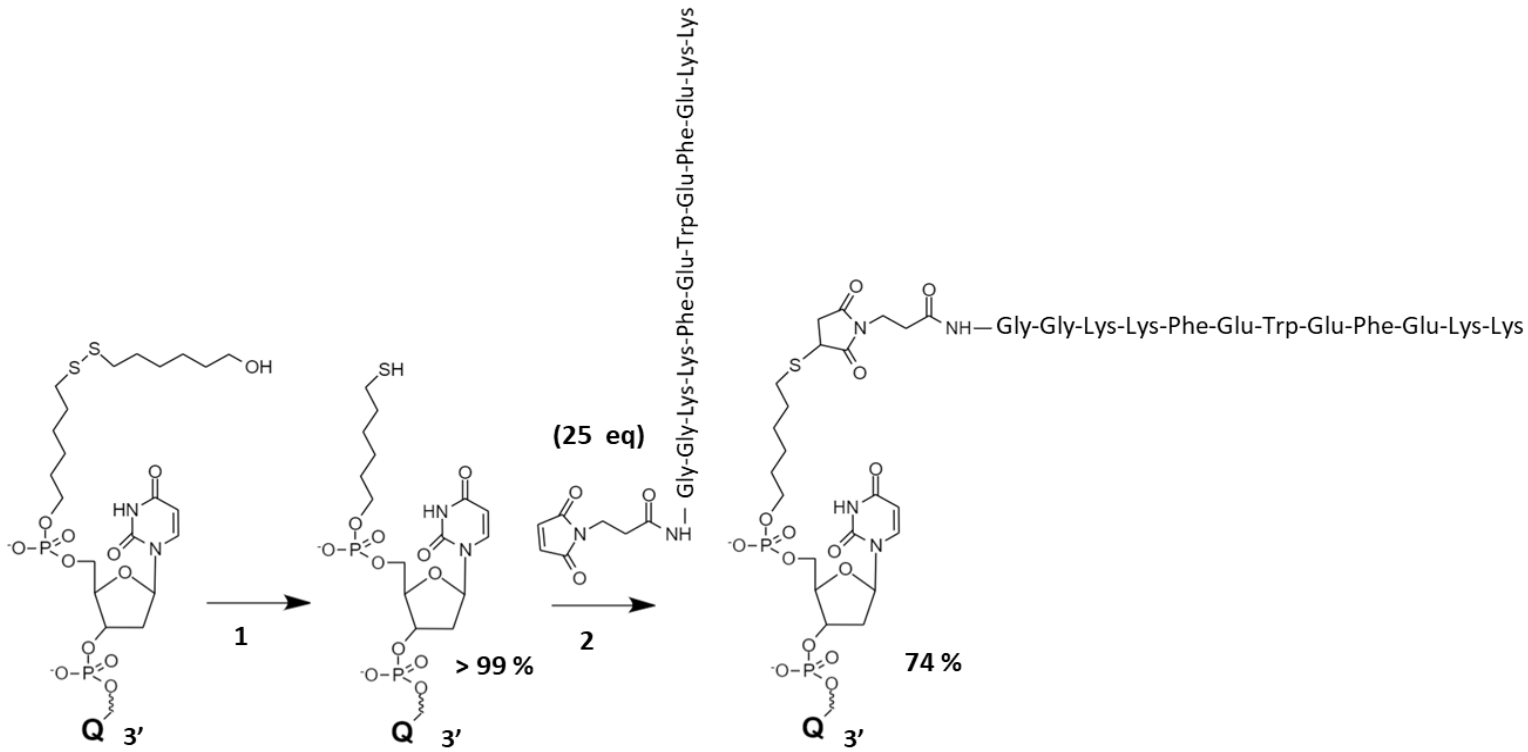

Figure 4.9. Schematic representation of the synthesis of the peptide-oligonucleotide conjugate, **pQ**-Mal-Gly-Gly-**p2**$^{(+1)}$**.** The peptide-oligonucleotide conjugate was synthesised by coupling reaction between the thiol-modified oligonucleotide and the N-maleoyl-β-alanine-modified peptide Mal-Mal-Gly-Gly-**p2**$^{(+1)}$ (conjugate yield, 74%). Purification was achieved using RP-HPLC (see Experimental section). (1) 10 eq TCEP, pH 3 for 2 h at RT to liberate the monomer, followed by 25 eq maleimide-labelled peptide (2), 4 h at RT in 30 % DMSO in PBS buffer, pH 7.2.

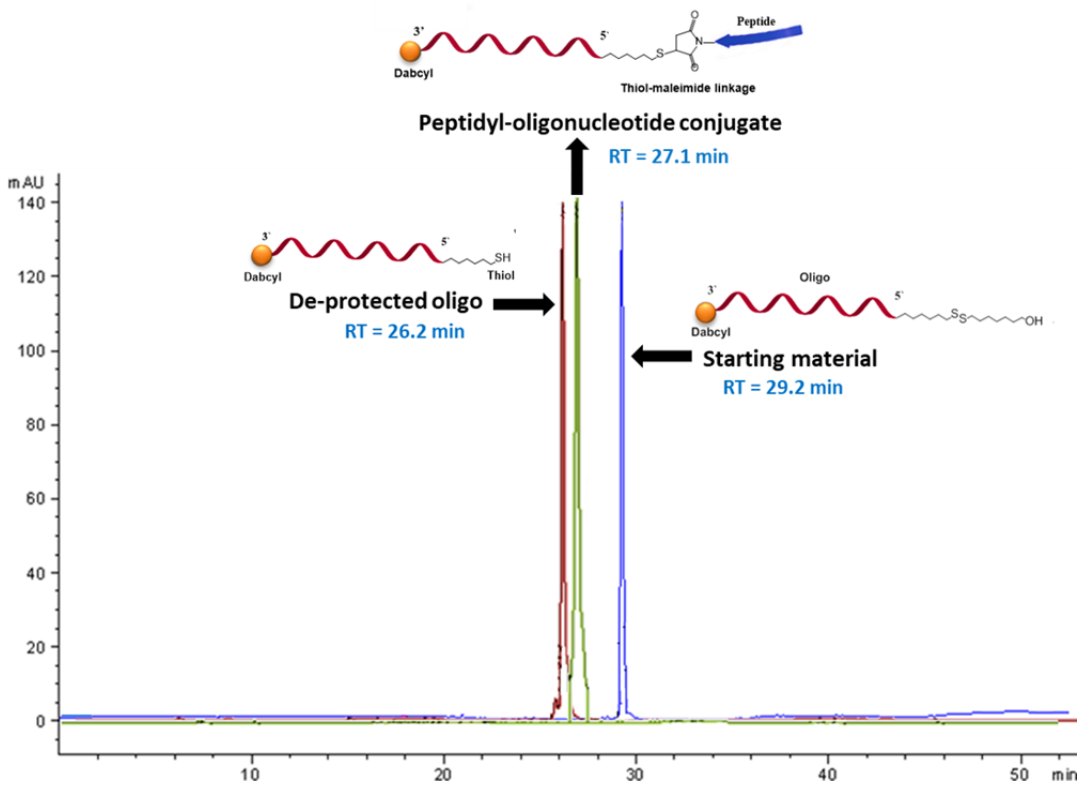

Figure 4.10. HPLC chromatograms of oligonucleotide materials. $^{5'}(CH_2)_6$-SS-T*CAACATCAGT-**Q**$^{3'}$ (blue), de-protected oligo $^{5'}(CH_2)_6$-SH-T*CAACATCAGT-**Q**$^{3'}$ (red) and peptide-oligonucleotide conjugate **pQ**-MAL-Gly-Gly-**p2**$^{(+1)}$ (green, 74 % yield). Eluents used included, water + 0.05 M $LiCLO_4$ (A) and acetonitrile + 0.05 M $LiCLO_4$ (B) with a gradient system increasing from 5 to 100 % over 40 mins at a flow rate of 2ml/min. RT refers to HPLC retention time.

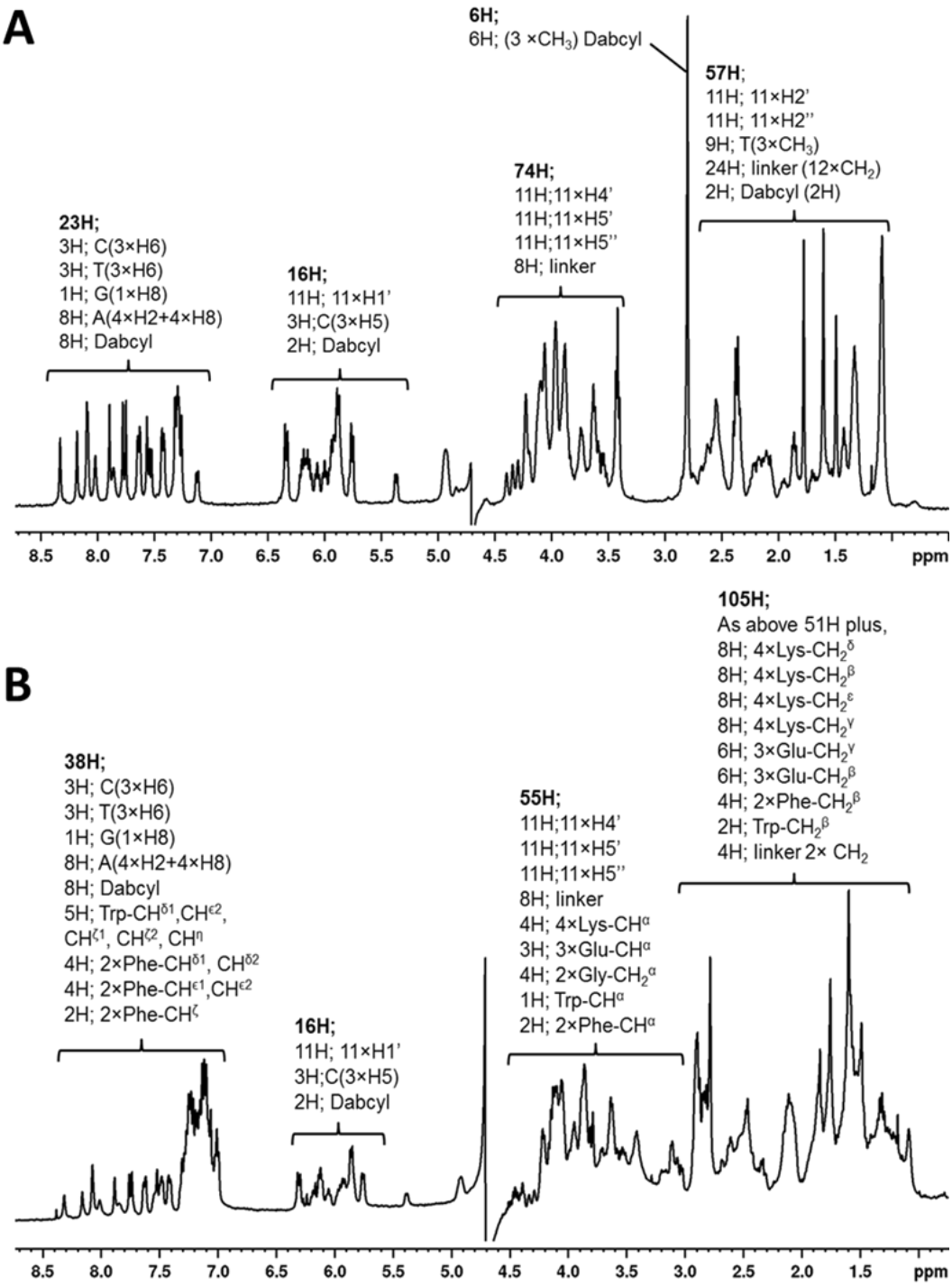

Figure 4.11. ^{1}H NMR spectra of oligonucleotide materials (**A**) thiol-modified **pQ**-oligonucleotide $^{5'}(CH_2)_6$-SS-T*CAACATCAGT-**Q**$^{3'}$, where Q is Dabcyl and T* is modified thymidine. (**B**) peptide-oligonucleotide conjugate, **pQ**-MAL-Gly-Gly-**p2**$^{(+1)}$, recorded in D_2O at 25°C using Bruker Avance II+ spectrometers operating at proton frequencies of 400 MHz.

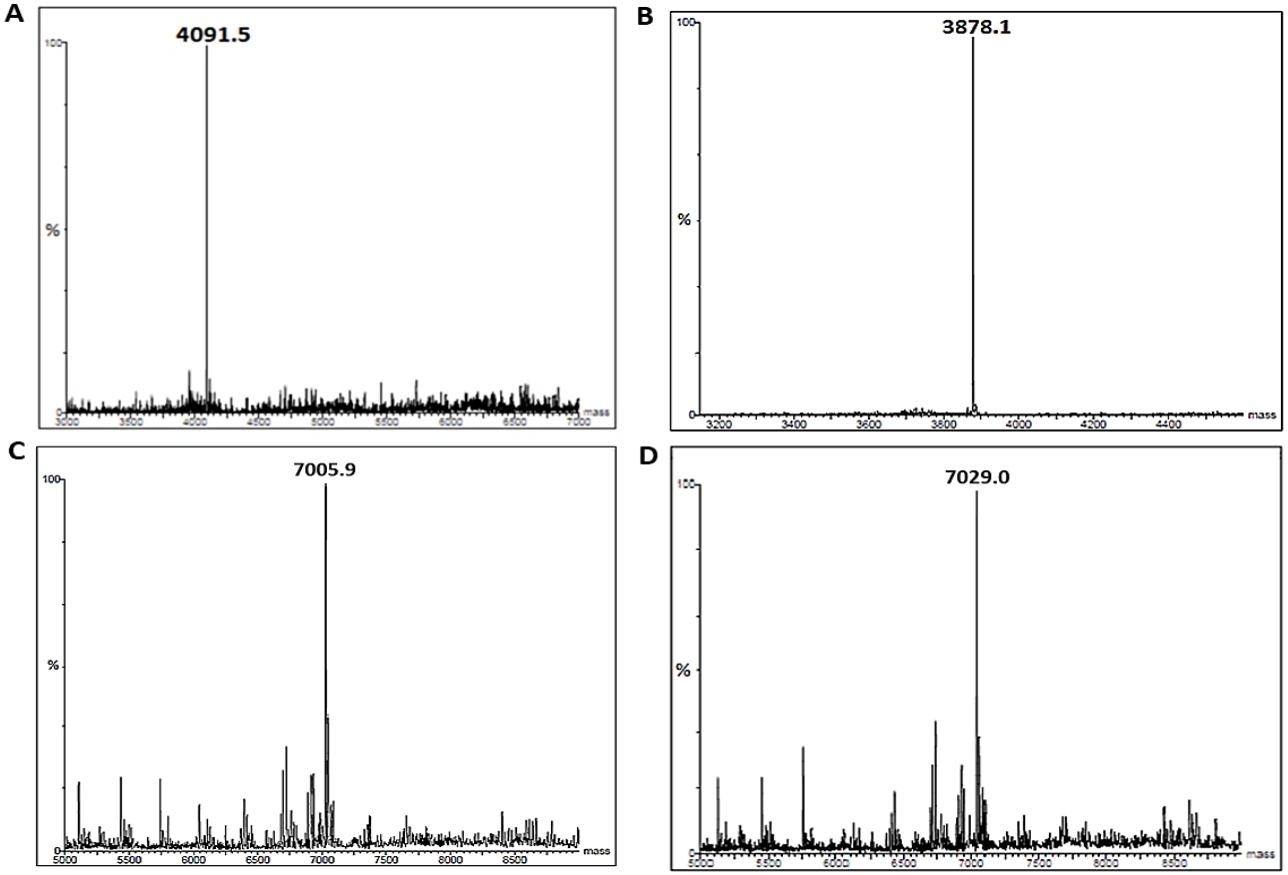
A
4091.5
100
%
0
3500
3900
4000
4500
5000
5500
6000
6500
7000
mass
B
3878.1
100
%
0
3200
3400
3600
3800
4000
4200
4400
mass
C
7005.9
100
%
0
5000
5500
6000
6500
7000
7500
8000
8500
mass
D
7029.0
100
%
0
6000
6500
6600
7000
7500
8000
8500
mass

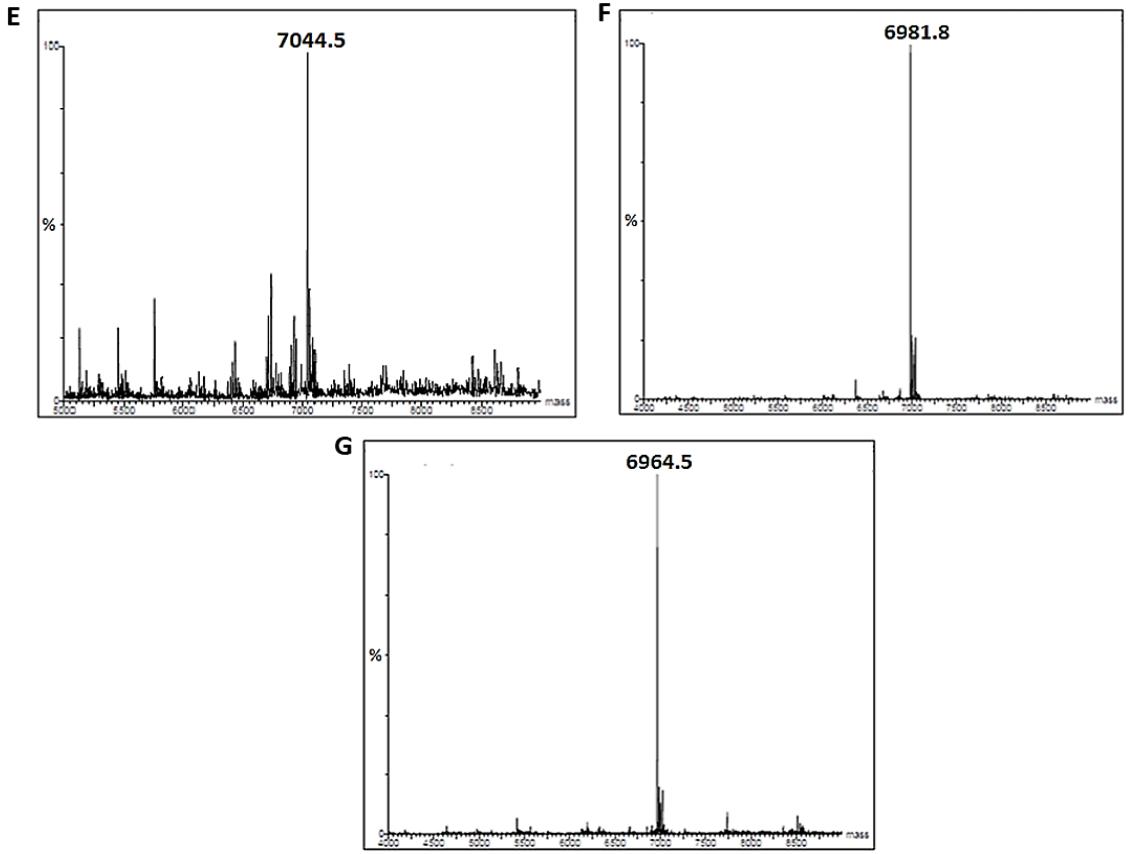

Figure 4.12. MALDI-ToF mass spectra of oligonucleotide materials. (**A**) **pQ**-probe, $^{5'}(CH_2)_6$-SS-T*CAACATCAGT-**Q**$^{3'}$ MALDI-MS; m/z = 4091.5 MW = 4092.0 g mol^{-1} calculated for [$C_{140}H_{189}N_{44}O_{73}P_{12}S_2$], (**B**) **pF**-probe $^{5'}$**F**-CTGATAAGCTA$^{3'}$ MALDI-MS; m/z = 3878.1 [M-H]$^{-1}$ MW = 3879.6 g mol^{-1} calculated for [$C_{135}H_{162}N_{43}O_{72}P_{11}$], (**C**) Perfect-match miR-21 target MALDI-MS; m/z =7005.9 [M-H]$^{-1}$ MW = 7006.8 g mol^{-1} calculated for [$C_{209}H_{259}N_{80}O_{154}P_{21}$], (**D**) Mismatch-1 MALDI-MS; m/z = 7029.0 [M-H]$^{-1}$ MW = 7030.0 g mol^{-1} calculated for [$C_{210}H_{261}N_{83}O_{152}P_{21}$], (**E**) Mismatch-2 MALDI-MS; m/z = 7044.5 [M-H]$^{-1}$ MW = 7045.2 g mol^{-1} calculated for [$C_{210}H_{260}N_{83}O_{153}P_{21}$], (**F**) Mismatch-3 MALDI-MS; m/z = 6981.8 [M-H]$^{-1}$ MW = 6982.8 g mol^{-1} calculated for [$C_{208}H_{257}N_{77}O_{156}P_{21}$] and (**G**) Mismatch-4 MALDI-MS; m/z = 6964.5 [M-H]$^{-1}$ MW = 6965.14 g mol^{-1} calculated for [$C_{208}H_{258}N_{78}O_{154}P_{21}$] (see **Table 4.2** for sequence).

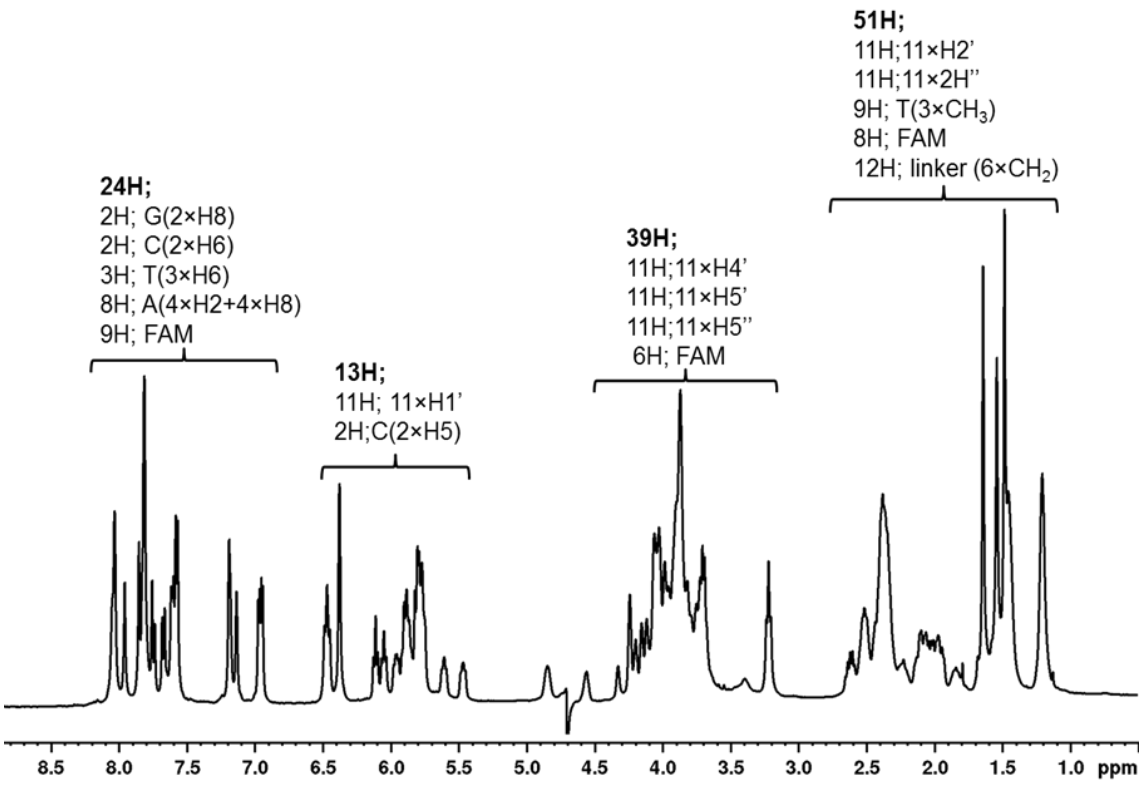

Figure 4.13. ^{1}H NMR spectra of fluorophore modified oligonucleotide, **pF** ($^{5'}$**F**-CTGATAAGCTA$^{3'}$), where **F** is fluorophore (FAM) recorded in D_2O at 25 $^{\circ}$C using Bruker Avance II+ spectrometers operating at proton frequencies of 400 MHz.

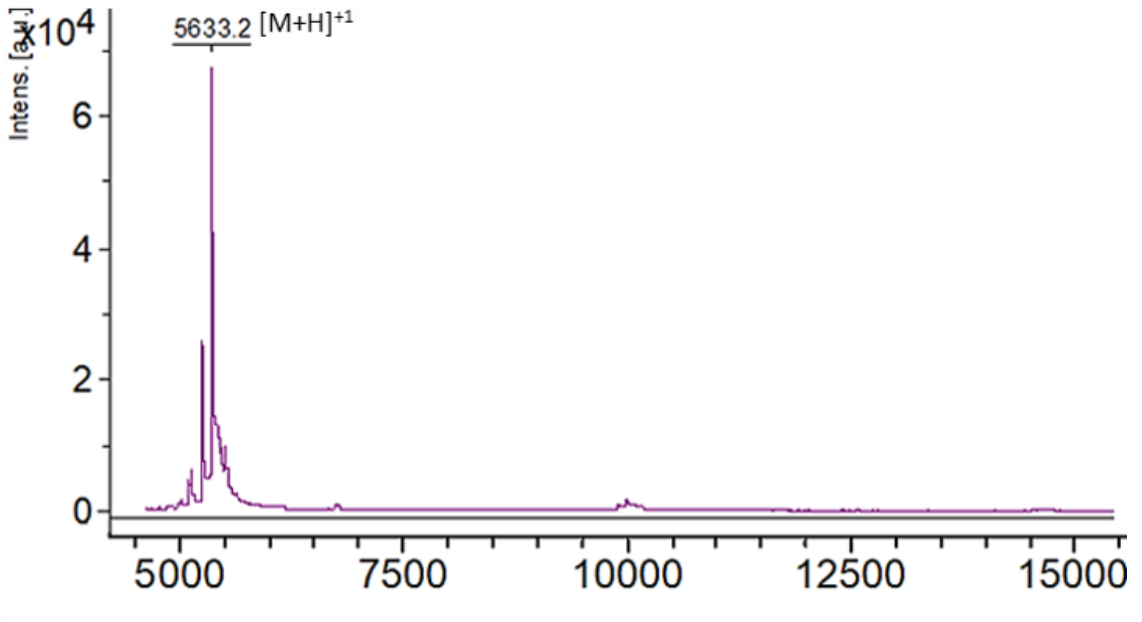

Figure 4.14. MALDI-ToF MS spectrum of peptide-oligonucleotide conjugate, **pQ**-Mal-Gly-Gly-**p2**$^{(+1)}$ MALDI-MS: m/z = 5633.2 $[M+H]^{+1}$ MW = 5632.1 g mol^{-1} calcd. for $[C_{219}H_{208}N_{62}O_{95}P_{12}S]$. Spectrum was recorded using 0.7 M 3-Hydroxy picolinic acid matrix (97 mg/mL, with 0.07 M ammonium citrate, 16 mg/mL in 50:50 ACN: H2O) on a Bruker Daltonics Ultraflex ToF/ToF mass spectrometer.

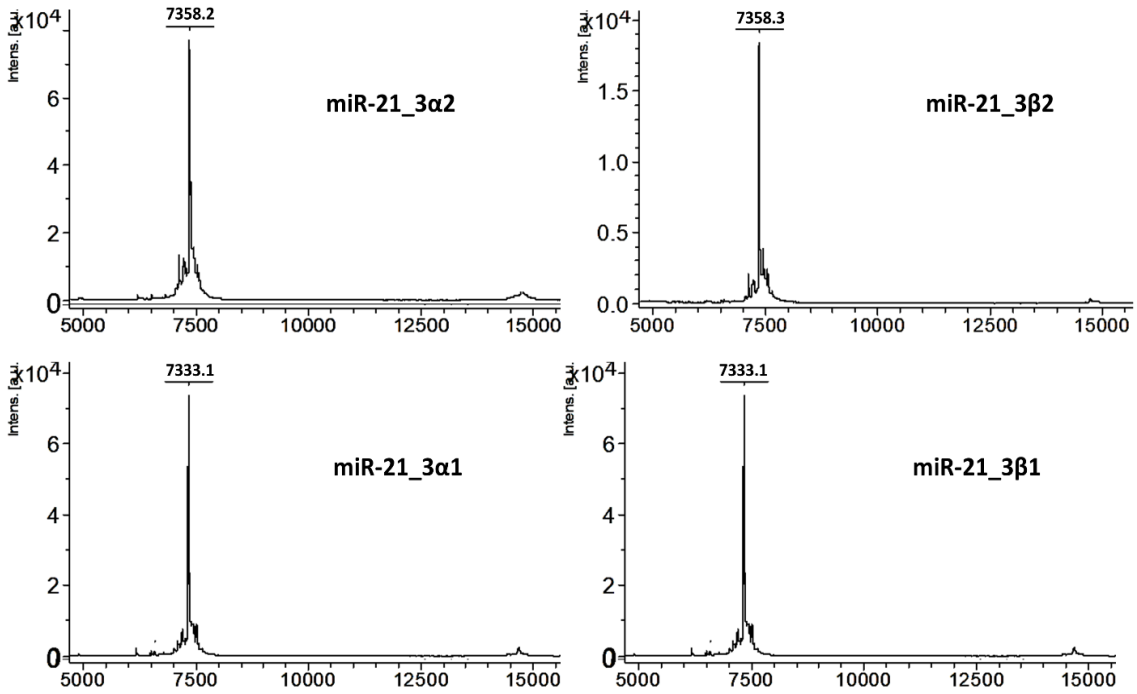

Figure 4.15. MALDI-ToF MS spectrum of peptide-oligonucleotide conjugates, miR-21_3α2: m/z = 7358.2 $[M+K]^+$ MW = 7319.6 g mol^{-1} calcd. for $[C_{250}H_{353}N_{98}O_{125}P_{19}]$. miR-21_3β2: m/z = 7358.3 $[M+K]^+$ MW = 7319.6 g mol^{-1} calcd. for $[C_{250}H_{353}N_{98}O_{125}P_{19}]$. miR-21_3α1: m/z = 7333.1 $[M+K]^+$ MW = 7294.6 g mol^{-1} calcd. for $[C_{250}H_{354}N_{95}O_{126}P_{19}]$. miR-21_3β1: m/z = 7333.1 $[M+K]^+$ MW = 7294.6 g mol^{-1} calcd. for $[C_{250}H_{354}N_{95}O_{126}P_{19}]$. Spectrum was recorded using 0.7 M 3-Hydroxy picolinic acid matrix (97 mg/mL, with 0.07 M ammonium citrate, 16 mg/mL in 50:50 ACN:H_2O) on a Bruker Daltonics Ultraflex ToF/ToF mass spectrometer.

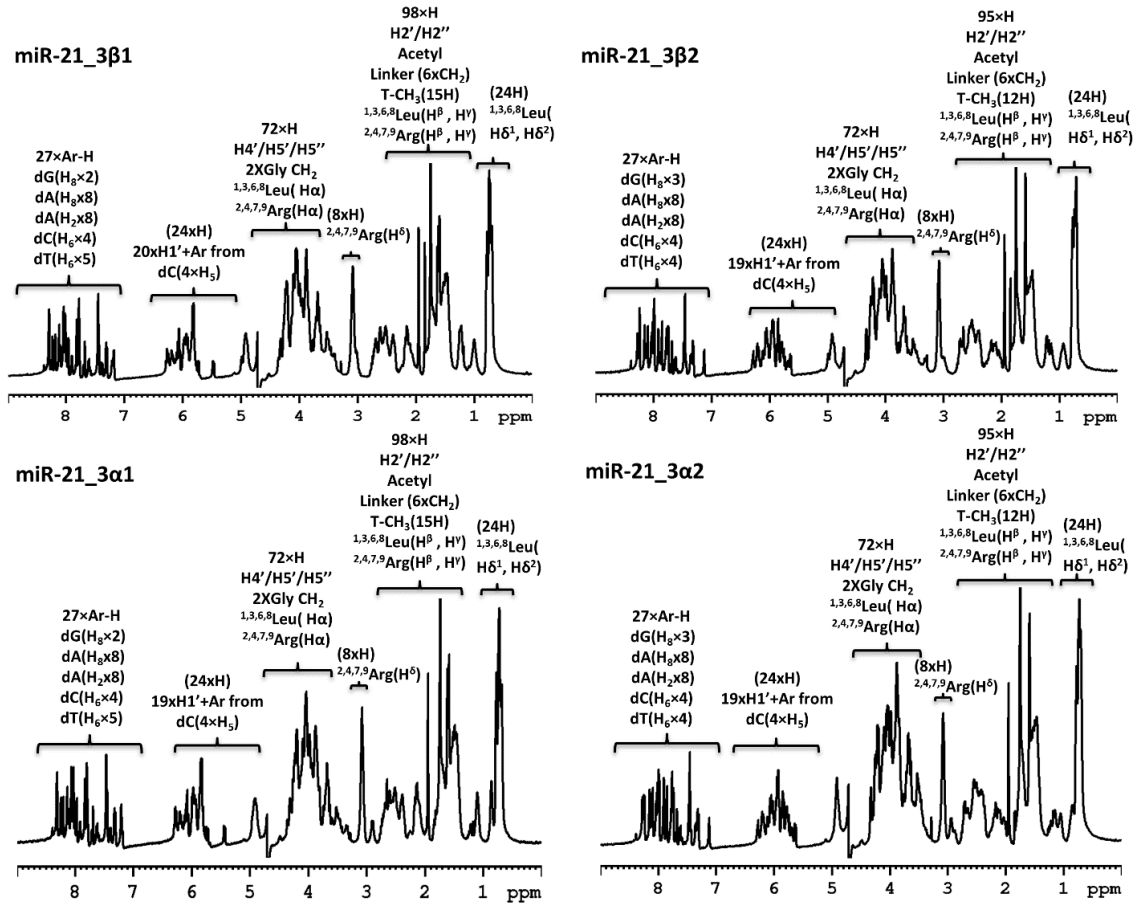

Figure 4.16. ^{1}H-NMR spectra of bulge peptidyl-oligonucleotide conjugates miR-21_3β1, miR-21_3β2, miR-21_3α1 and miR-21_3α2 showing the characteristic resonance areas of the oligonucleotide protons, peptide protons, aminohexyl linker and acetyl protecting group. Assignments of the key ^{1}H resonance regions are indicated above each spectrum. 1:1 stoichiometric ratio of peptide to oligonucleotide was confirmed through integration. The spectra were recorded in D_2O at 25 °C using 400 MHz NMR spectrometer (Bruker Avance II+ 400).

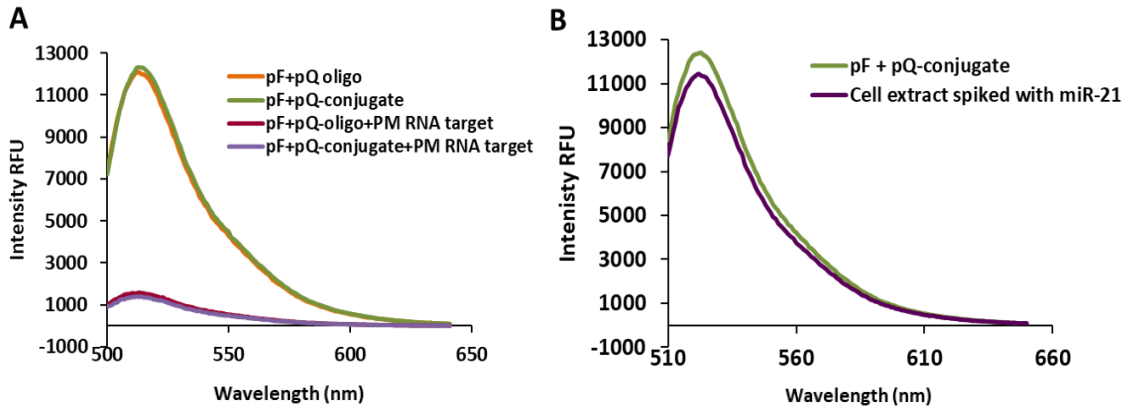

Figure 4.17. Detection of hybridisation of miR-21 target in solution (**A**) in "clean" analyte, and (**B**) from MIA-PaCa 2 cell extract. The "split-probes" (**pF**+**pQ** oligo, orange, and **pF**+**pQ**-Mal-Gly-Gly-**p2**$^{(+1)}$ conjugate, green) were completely fluorescent in the absence of the complementary target due to the spatial separation of two probes. Addition of 'perfect-match' miR-21 target in either clear analyte (**A**) or spiked with cell extract (**B**) triggered the hybridisation events which led to the effective quenching of the fluorescence from **pF**+**pQ** oligo (red) and **pF**+**pQ**-Mal-Gly-Gly-**p2**$^{(+1)}$ conjugate (purple). All oligonucleotides components were at 0.5 µM concentration. miR-21 target was spiked in 1:1 of cell extract and tris buffer to achieve the final concentration of 0.5 µM relative to the split probes. Fluorescence was measured at λ_{em}= 567 nm following excitation at λ_{ex}= 450 nm.

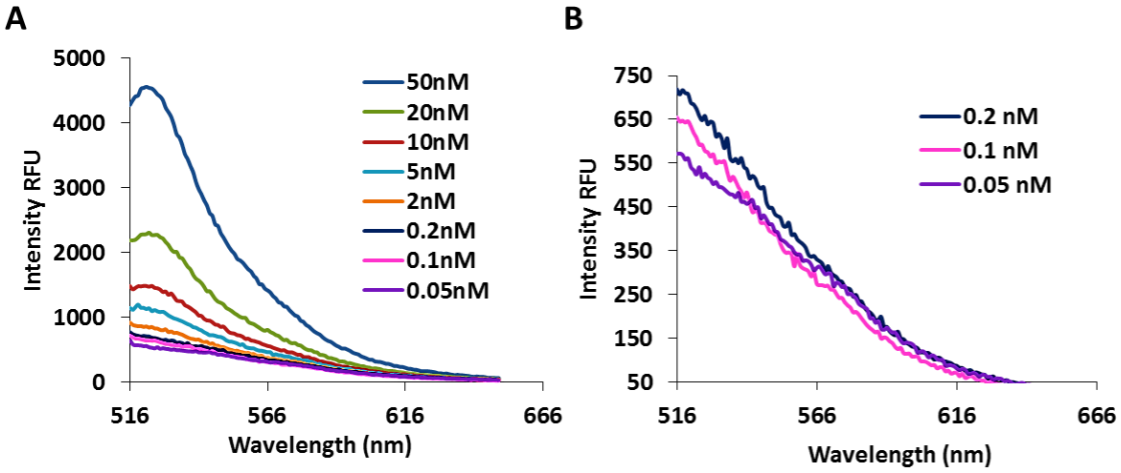

Figure 4.18. Limit of detection of peptide hydrogel nano-biosensor estimated at 24 °C using Tecan Safire plate reader. (**A**) Fluorescence quenching of fluorophore (**F**) by quencher (**Q**) at the concentration range of 50 nM to 0.05nM of "split-probes" and miR-21 PM target (doping level, 3.0×10^{-4} to 2.7×10^{-6} %). (**B**) The level of fluorescence quenching at 0.2 nM to 0.05 nM concentrations. The LoD was estimated to be 13 pM, using equations 1 and 2. Hydrogel was prepared by mixing the equimolar concentrations (20 mM) of peptides (**p1**$^{(-1)}$ + **p2**$^{(+1)}$) at pH 7.2. Fluorescence was measured at λ_{em}= 522 nm following excitation at λ_{ex}= 494 nm.

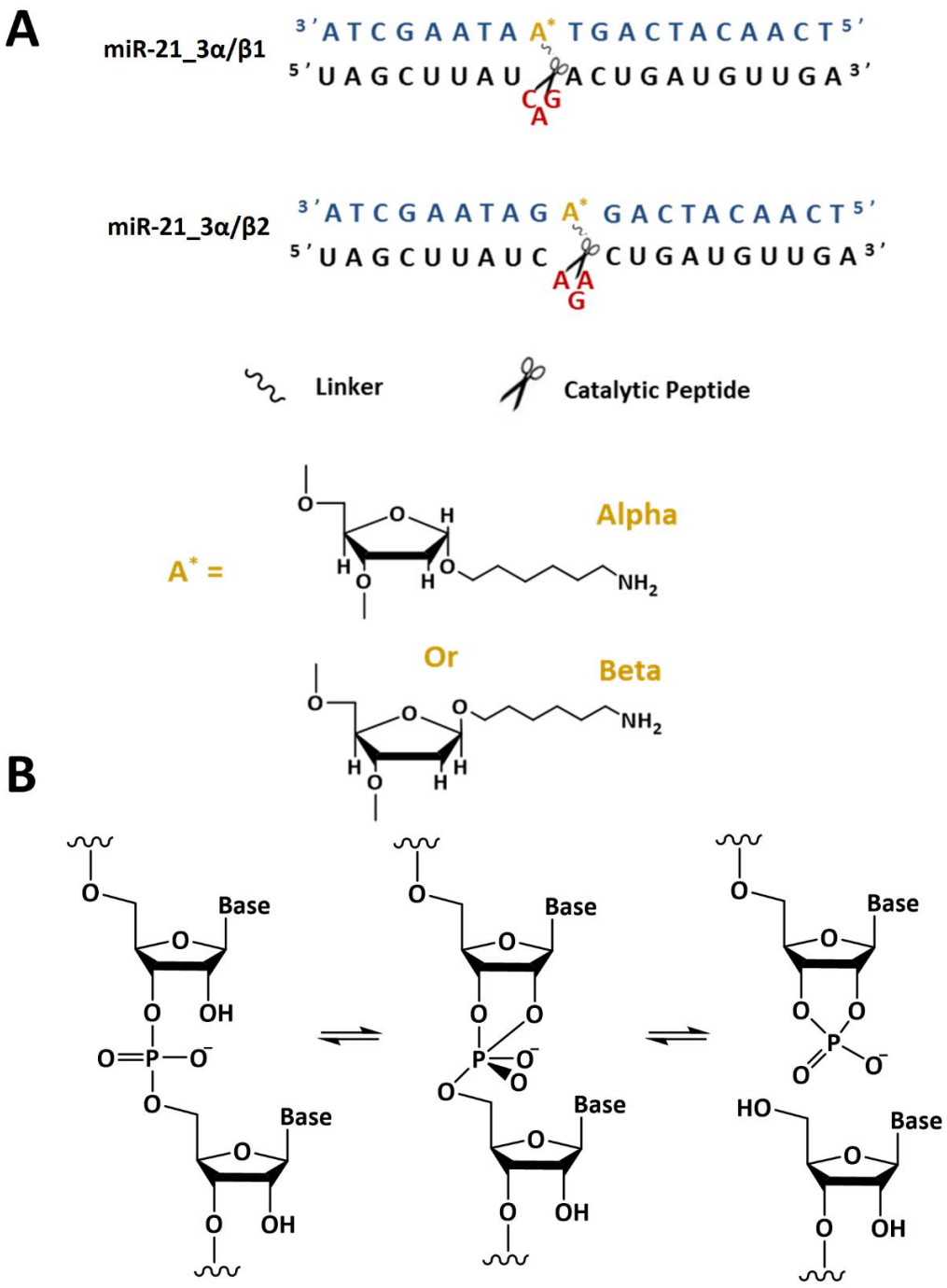

Figure 4.19. (**A**) Schematic representation of the design concept for α and β anomer bulge-loop inducing conjugates. (**B**) Mechanism of RNA transesterification mediated by the catalytic peptide.

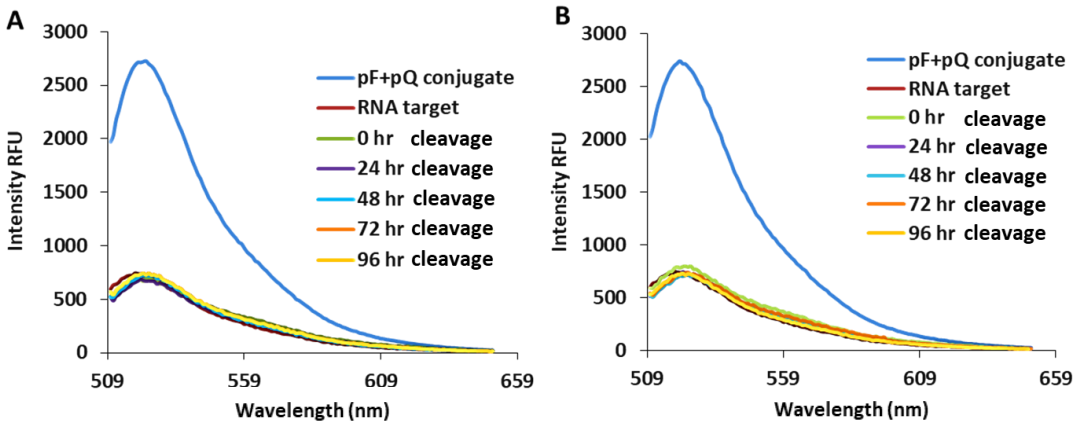

Figure 4.20. Fluorescence spectra for the control experiments conducted at 37 °C in Tris-EDTA buffer (see Experimental section for details). No cleavage activity was seen when the miR-21 target was incubated with, (**A**) scrambled POC, which had no complementarity to the miR-21 target and (**B**) when unconjugated antisense oligonucleotide was incubated with the miR-21 target in the absence of -[LRLRG]$_2$ peptide. Analysis of cleavage was recorded at λ_{em}= 522 nm following excitation at λ_{ex}= 494 nm, in peptide hydrogel at 24 °C. Hydrogel was prepared by mixing the equimolar concentrations (20 mM) of peptides (**p1**$^{(-1)}$ + **p2**$^{(+1)}$) at pH 7.2.

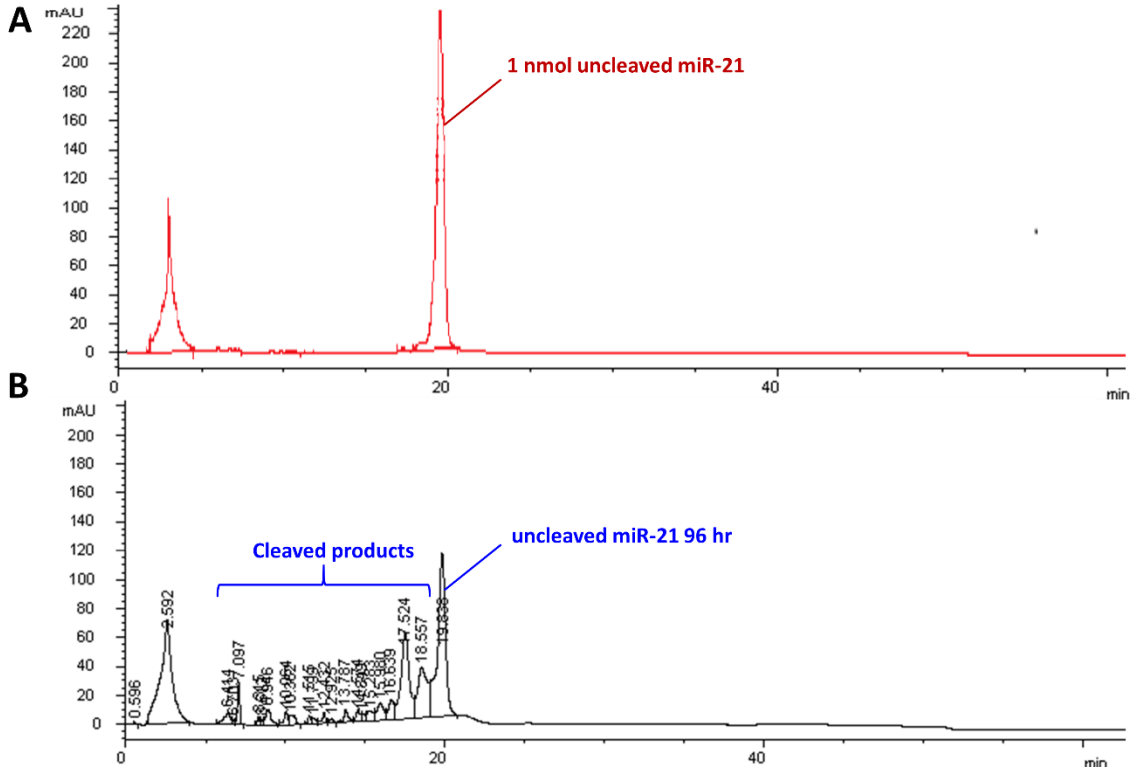

Figure 4.21. Anion-exchange chromatography of (**A**) uncleaved miR-21 target and (**B**) miR-21 target + miR-21_3α1 conjugate at 96 hours. (**A**) The red spectrum represents 1 nmol of the uncleaved miR-21 target (≈ 0.22 o.u.). The target peak had a retention time of 19.8 min. (**B**) The black spectrum represents the reaction mixture containing 1 nmol miR-21 target incubated with miR-21_3α1 conjugate (target to conjugate ratio, 5:1) for 96 hours. Cleaved fragments are visible in the spectra. Moreover, the amount of uncleaved target present in the reaction medium has been reduced by 50%. Eluents used included 10 mM NaOAc in 30% acetonitrile (eluent A) and 1 mM $LiClO_4$+10 mM NaOAc in 30% acetonitrile (eluent B) with a gradient system increasing from 0 to 100% over 40 mins at a flow rate of 1.5 ml/min at 60°C.

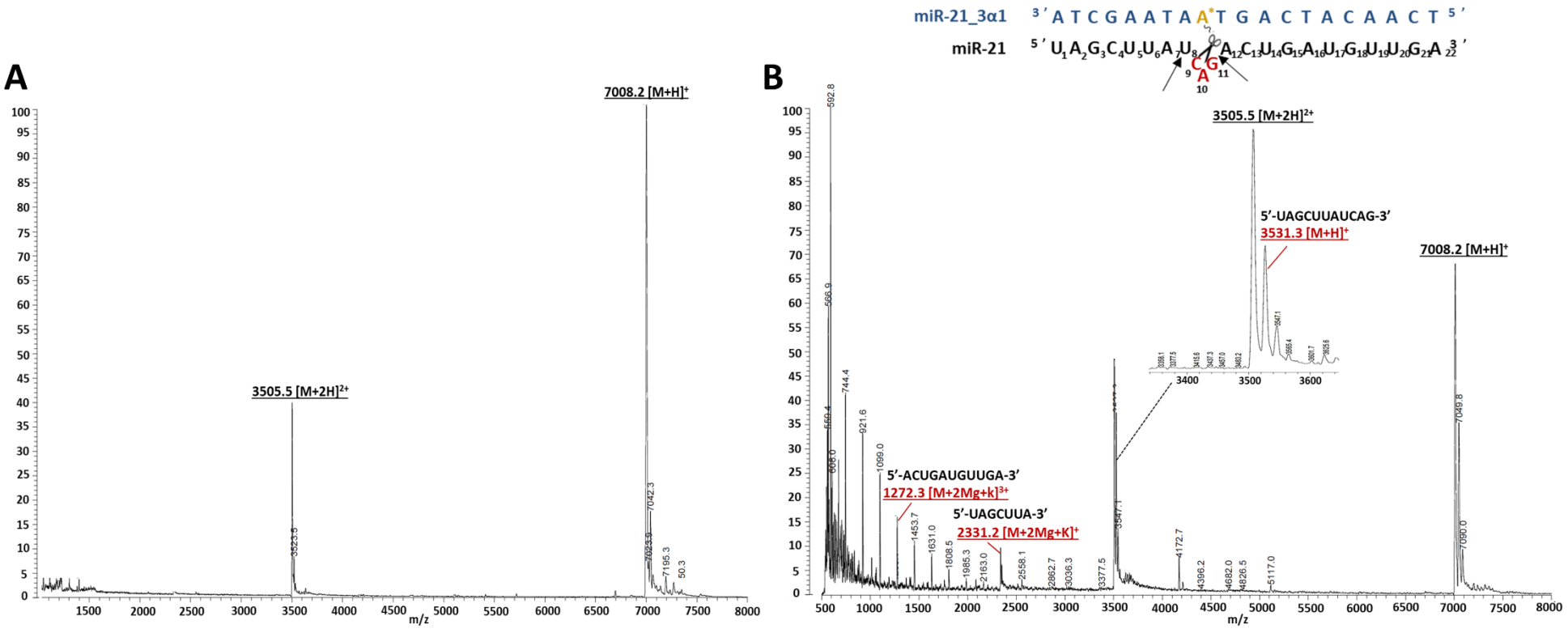

Figure 4.22. MALDI-TOF mass spectra for reaction mixture miR-21 (25 µM, MW: 7006.8 Da); (**A**) in the absence of conjugate, and (**B**) with miR-21_3α1 conjugate (5 µM, MW: 7294.6 Da) in Tris-buffer (50 mM Tris−HCl containing 0.2 mM KCl, and 1 mM EDTA, 1 mM $MgCl_2$, 1 mM DTT, pH 7.0). The conjugate was removed by hybridisation with biotinylated capture oligonucleotide prior to mass spectrometry. (**A**) MS spectrum for the reaction mixture without conjugate, and (**B**) Spectrum following 96 hours reaction between catalytic conjugate (miR-21_3α1) and miR-21 target. The sequence of the cleaved fragments, as well as their corresponding observed mass are annotated in the figure. The proposed positions of miR-21 (black) cleavage induced by miR-21_3α1 conjugate (blue) has been indicated by arrows. All MALDI-TOF MS analysis was performed on Shimadzu Biotech Axima Confidence, Time of Flight Matrix-Assisted Laser Desorption Ionisation (MALDI) mass spectrometer using 0.7 M 3-Hydroxy picolinic acid matrix (97 mg/mL, with 0.07 M ammonium citrate, 16 mg/mL in 50:50 ACN: H_2O) in positive mode.

Peptide charge calculation

Peptide charge was calculated from pH 1 to 14 using the following expression, derived from the Henderson-Hasselbalch equation (1) (see **Figure 4.23**)

$$Q_{\substack{EEFKWKFKEE+\\KKFEWEFEKK=}} \left(\frac{+2}{1+10^{(pH-9.72)}}\right) + \left(\frac{+7}{1+10^{(pH-10.53)}}\right) + \left(\frac{-7}{1+10^{-(pH-4.07)}}\right) + \left(\frac{-2}{1+10^{-(pH-2.18)}}\right)$$

(3)

(N-terminal) (Lysine) (Glutamic acid) (C-terminal)

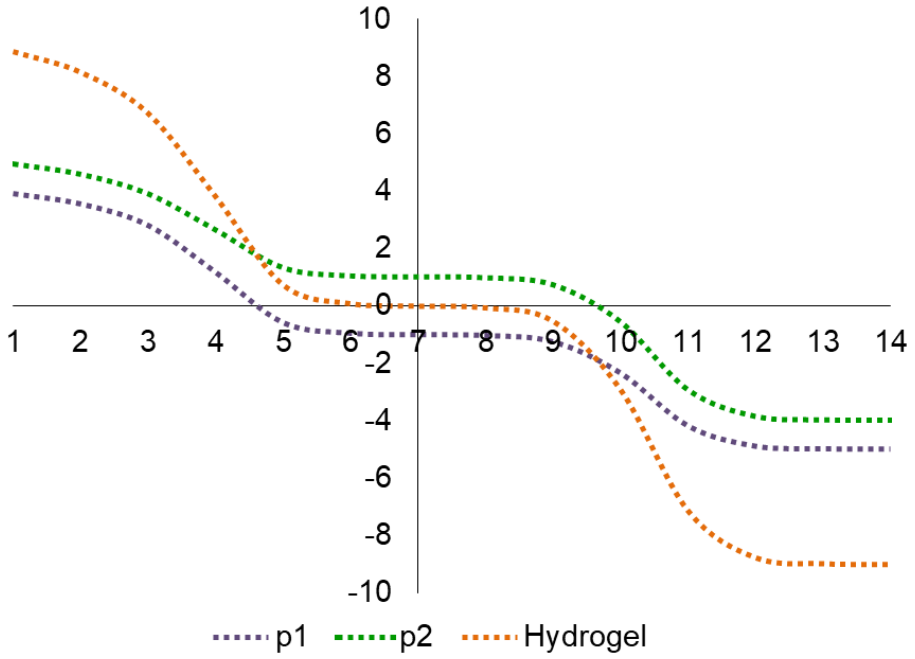

Figure 4.23. The net charge of peptides **p1**$^{(+)}$, **p2**$^{(-)}$ and hydrogel with respect to pH. Peptide **p1**$^{(-)}$ carries a net charge of -1, peptide **p2**$^{(+)}$ carries a net charge of +1 and hence hydrogel carries a neutral charge under molecular sensor working conditions (pH 7.2). Peptide charge was calculated as described above (see equation 3).

4.8.3 References for the Supporting Information

1. Armbruster,D.A. and Pry,T. (2008) Limit of blank, limit of detection and limit of quantitation. *Clin. Biochem. Rev.*, **29 Suppl 1**, S49–S52.

Chapter 5

2'OMe Modification of Anti-miRNA-21 Oligonucleotide–Peptide Conjugate Improves Its Hybridisation Properties and Catalytic Activity

2'OMe Modification of Anti-miRNA-21 Oligonucleotide–Peptide Conjugate Improves Its Hybridisation Properties and Catalytic Activity

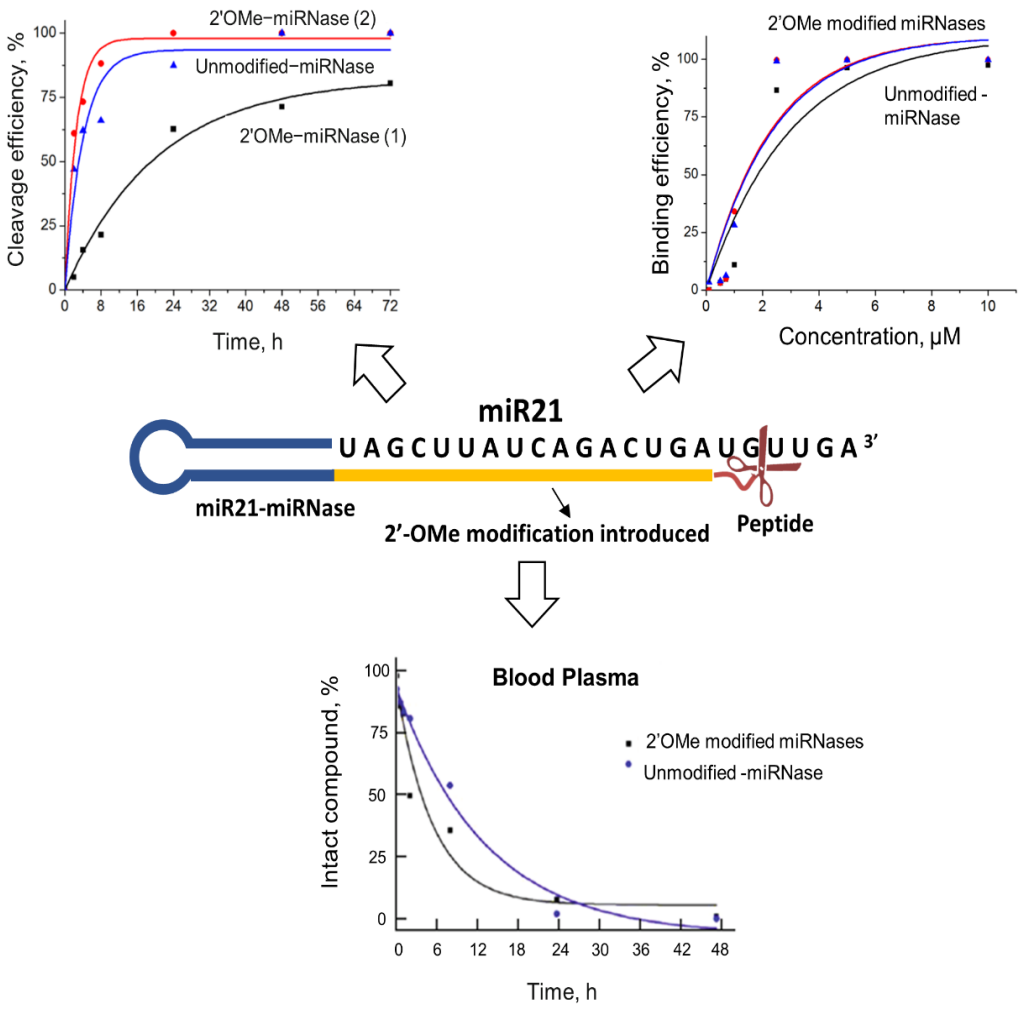

5.1 Declaration

This chapter consists of one published article:

Svetlana K. Miroshnichenko, Bahareh Amirloo, Elena V. Bichenkova, Valentin V. Vlassov, Marina A. Zenkova and Olga A. Patutina. (2019) 2'OMe Modification of Anti-miRNA-21 Oligonucleotide–Peptide Conjugate Improves Its Hybridisation Properties and Catalytic Activity. *Russ J Bioorg Chem.* **45,** 803–812. https://doi.org/10.1134/S1068162019060281

Although the hairpin peptidyl-oligonucleotide conjugates, reported in this paper, fall slightly outside of my primary research focus, the stability of this class of peptidyl-oligonucleotide conjugates against cellular nucleases in serum is essential for future *in vivo* application. I contributed to this research by replacement of the previously "naked" oligonucleotide recognition motifs with *nuclease-resistant,* chemically-modified 2'-O-methyl analogues. This article has been reproduced in an unchanged format except for minor adjustments to incorporate it into this thesis. Supporting information has been added to provide a detailed characterisation of the synthesised conjugates in line with the thesis.

As second author for this publication I carried out all the design, synthesis and characterisation of peptide and peptidyl-oligonucleotide conjugates. Svetlana Miroshnichenko, Prof. Valentin Vlassov, Prof. Marina Zenkova and Dr. Olga Patutina conceived the scientific ideas. Svetlana Miroshnichenko and Dr. Olga Patutina were involved in design, execution and analysis of hybridisation, stability, ribonuclease activity, cell proliferation and migration studies. Svetlana Miroshnichenko and Dr. Olga Patutina drafted the manuscript with input from all authors. Prof. Marina Zenkova and Dr. Olga Patutina and Dr. Elena Bichenkova supervised the relevant experimental work and were involved in project management, data analysis and manuscript editing at various stages.

2'OMe Modification of Anti-miRNA-21 Oligonucleotide–Peptide Conjugate Improves Its Hybridisation Properties and Catalytic Activity

Svetlana K. Miroshnichenko, [1] Bahareh Amirloo, [2] Elena V. Bichenkova,[2] Valentin V. Vlassov, [1] Marina A. Zenkova, [1] and Olga A. Patutina [*, 1]

[1] Institute of Chemical Biology and Fundamental Medicine SB RAS, 8 Laurentiev Avenue, 630090, Novosibirsk, Russia.

[2] School of Health Sciences, Faculty of Biology, Medicine and Health, University of Manchester, Oxford Road, Manchester, M13 9PT, UK.

.

5.2 Abstract

Nowadays, application of miRNases—artificial ribonucleases aimed at degradation of noncoding RNAs, in particular, miRNAs—represents one of the novel experimental approaches to inhibit tumorigenesis. miRNases integrate in their structure an addressing oligonucleotide, which provides specific binding with miRNA target, and a catalytic group, which promotes cleavage of the RNA substrate. The introduction of chemical modifications to the oligonucleotide domain of miRNases in the region that is complementary to miRNA may significantly increase the hybridisation properties and nuclease resistance of this type of compound. However, the influence of such structural changes to the ribonuclease activity of miRNases remains unclear. In this work, to investigate the effect of 2'OMe modifications on the activity of miRNases, we synthesised two types of anti-miRNA-21 conjugates of the peptide $[(ArgLeu)_2Gly]_2$ and hairpin oligonucleotides in which 14-mer binding region to the miRNA target was fully or partially modified. It is shown that the introduction of 2'OMe modifications promotes a considerable increase in the affinity of miRNases to miRNA-21 but does not significantly change their nuclease resistance. Full modification of conjugates in the region that is complementary to miRNA negatively affects their ribonuclease activity, whereas partial introduction of 2'OMe nucleotides considerably enhances the cleavage activity of miRNases, which leads to a substantial decrease in the proliferation rate and migration potential of tumour cells which are determined by the miRNA-21 expression.

5.3 Introduction

Currently, one of the most actively developing experimental approaches in the fight against cancer is the application of oligonucleotide constructs that inhibit the activity of oncogenic miRNAs, short single-stranded regulatory RNA molecules that promote carcinogenesis. To increase the resistance to nucleases and enhance the affinity for the miRNA target, the majority of miRNA-targeted oligonucleotides developed to date contain chemical modifications. The latter, in most cases, are incompatible with the activity of intracellular RNase H, which is recruited in the classical antisense technology, and the inhibitory effect of oligonucleotides is limited by the number of molecules that bind to the target miRNA (1). In some cases, the use of such oligonucleotides is advantageous. However, in the case of malignant growth suppression, the use of a technology that provides multiple-turnover target inactivation seems more effective.

A new efficient approach for inactivation of harmful miRNA in cells, which is based on miRNA degradation, is the creation of miRNA-targeted artificial ribonucleases (miRNases). Such compounds include an oligonucleotide component, which provides specific recognition of the target miRNA, and a catalytic group covalently bound to it, which promotes cleavage of the target (2). Today, some advances in designing miRNases have already been achieved. In particular, the conjugates of oligonucleotides with diethylenetriamine (DETA) or peptide HGG and Cu^{2+}, as well as with tris(2-aminobenzimidazole), aimed at cleaving miRNA-1323 and miRNA-20a, were created (3, 4). However, such constructs are capable of efficient degradation of only artificial miRNA substrates.

Previously, we have developed miRNases which were artificial ribonucleases targeted at oncogenic miRNA-21 and miRNA-17 which exhibited effective catalytic activity leading to selective knockdown of highly oncogenic miRNAs (2, 5). The most productive variants of miRNases are conjugates of hairpin deoxyribooligonucleotides, which contain a region complementary to oncogenic miRNAs, with peptides based on alternating arginine and leucine residues. miRNases were shown to be highly specific inhibitors of oncogenic miRNA-21 and miRNA-17, capable of quantitatively cleaving the miRNA-substrate in a catalytic manner and exhibiting high biological activity in tumour cells (2, 5). The designed miRNases had a relatively high affinity for respective miRNA target and were resistant to intracellular nucleases due to the hairpin structure of the oligonucleotide at the 3'-end and the presence of the peptide at the 5'-end (2). To further improve the hybridisation properties and nuclease resistance of the constructed miRNases, it seemed

appropriate and promising to introduce chemical modifications into their structure. However, such reconstruction of artificial ribonucleases may greatly change their structure and unpredictably affect their ribonuclease activity, because the catalytically active conformation of the peptide is formed with the involvement of the oligonucleotide component (6).

In this study, based on the design of the miRNase targeted at miRNA-21, exhibiting the highest inhibitory potential (2), we synthesised conjugates of the peptide $[(ArgLeu)_2Gly]_2$ and a hairpin oligonucleotide whose 14-mer region, complementary to the target miRNA, was altered as a result of 2'OMe modifications. We obtained two types of 2'OMe conjugates with fully or partially modified oligonucleotide component. The hybridisation and catalytic properties of these conjugates were studied, and their antiproliferative and antimigration activities in human epidermoid carcinoma KB-8-5 cells were analysed.

5.4 Results and Discussion

5.4.1 Design of Oligonucleotide–Peptide Conjugates Containing 2'OMe Modification and Analysis of Their Hybridisation Properties

Earlier (2), we developed and comprehensively investigated various structural variants of miRNA-21-miRNases. It was found that one of the most effective compounds exhibiting the greatest ribonuclease and biological activities is the conjugate consisting of the peptide $[(ArgLeu)_2Gly]_2$ bound through the aminohexyl linker to the 5'-end of a hairpin deoxyribonucleotide containing a 14-mer fragment complementary to the target miRNA (2). This design of miRNase increased its affinity for the target RNA due to stacking interactions with the adjacent double-stranded region (2, 7), limited the binding of the conjugate only to the mature miRNA form, and increased the resistance of the oligonucleotide component of miRNase to nucleases. The high ribonuclease activity of the developed miRNA-21-miRNase promoted a significant decrease in the level of oncogenic miRNA in tumour cells and triggered a wide range of biological effects leading to inhibition of tumour cell growth *in vitro* and *in vivo* (8).

In this study, in order to increase the resistance to nucleases and the affinity for the target miRNA, on the basis of the structure of the previously obtained miRNase we developed and studied the conjugates containing 2'OMe-modified nucleotides in the region complementary to the target miRNA. Two types of 2'OMe–ribonucleases were created: 2'OMe–miRNase (1), containing a fully modified binding region to miRNA-21, and 2'OMe–miRNase (2), whose 5'-end region contained three deoxyribonucleotides located

in close proximity to the binding site for the catalytic peptide (**Figure 5.1** (**a**)). The hybridisation and catalytic properties and stability of the constructed 2'OMe–miRNases were compared to the unmodified DNA analogue of the same sequence (PO–miRNase).

The hybridisation properties of the conjugates in the concentration range 0.1–10 μM were studied at 37°C at a miRNA-21 concentration of 1 μM under nearly physiological conditions. It was found that the introduction of 2'OMe modifications improves the hybridisation properties of conjugates as compared to their DNA analogue (**Figure 5.1** (**b**) and (**c**)), promoting a three-fold increase in the binding efficiency of the target miRNA and 2'OMe-conjugates at equimolar concentrations. In addition, quantitative binding of 2'OMe– miRNases (1) and (2) was detected at a concentration of 2.5 μM, whereas for the PO–miRNase 96% binding to the target RNA was observed only at concentrations greater than 5 μM (**Figure 5.1** (**b**) and (**c**)). Thus, the introduction of 2'OMe modifications to the binding region of the conjugate to miRNA increases their affinity for the target RNA. According to the previously obtained data (9), this is associated with the increase in the melting temperature of the miRNA:conjugate duplex by 1–1.5°C per each 2'OMe modification.

5.4.2 Resistance of Oligonucleotide–Peptide Conjugates in Medium Containing 50% Fetal Calf Serum (FCS) and in Mouse Blood Plasma

The introduction of modifications into oligonucleotide constructs may increase their resistance to intracelllar nucleases (10). In this study, we investigated the resistance of 2'OMe–miRNases in comparison with the original PO–miRNase and respective oligonucleotides (ONs) in a medium containing 50% fetal calf serum (FCS) and in mouse blood plasma (i.e., under the conditions that most closely simulate the aggressive physiological environment).

It was found that the resistance of all tested oligonucleotides and miRNases in the medium containing 50% FCS did not differ significantly from their nuclease resistance in mouse blood plasma (**Figure 5.2**). The assessment of the $\tau_{1/2}$ value (the period during which 50% of agent is degraded) showed that the resistance of 2'OMe–miRNase and respective 2'OMe-ON coincided both in 50% FCS and in blood plasma and was 4.14 ± 1.81 and 4.36 ± 1.44 h in 50% FCS and 4.87 ± 1.64 and 6 ± 1.39 h in blood plasma, respectively (**Figure 5.2**). In addition, it was established that the introduction of 2'OMe modifications does not increase the stability of the compounds. No significant differences in the

nuclease resistance of 2'OMe– and PO–miRNases in the medium containing 50% FCS and in the blood plasma were found: $\tau_{1/2}$ values were 4.14 ± 1.81 and 6 ± 0.35 h in 50% FCS and 4.87 ± 1.64 and 6.76 ± 1.42 h, respectively (**Figure 5.2**).

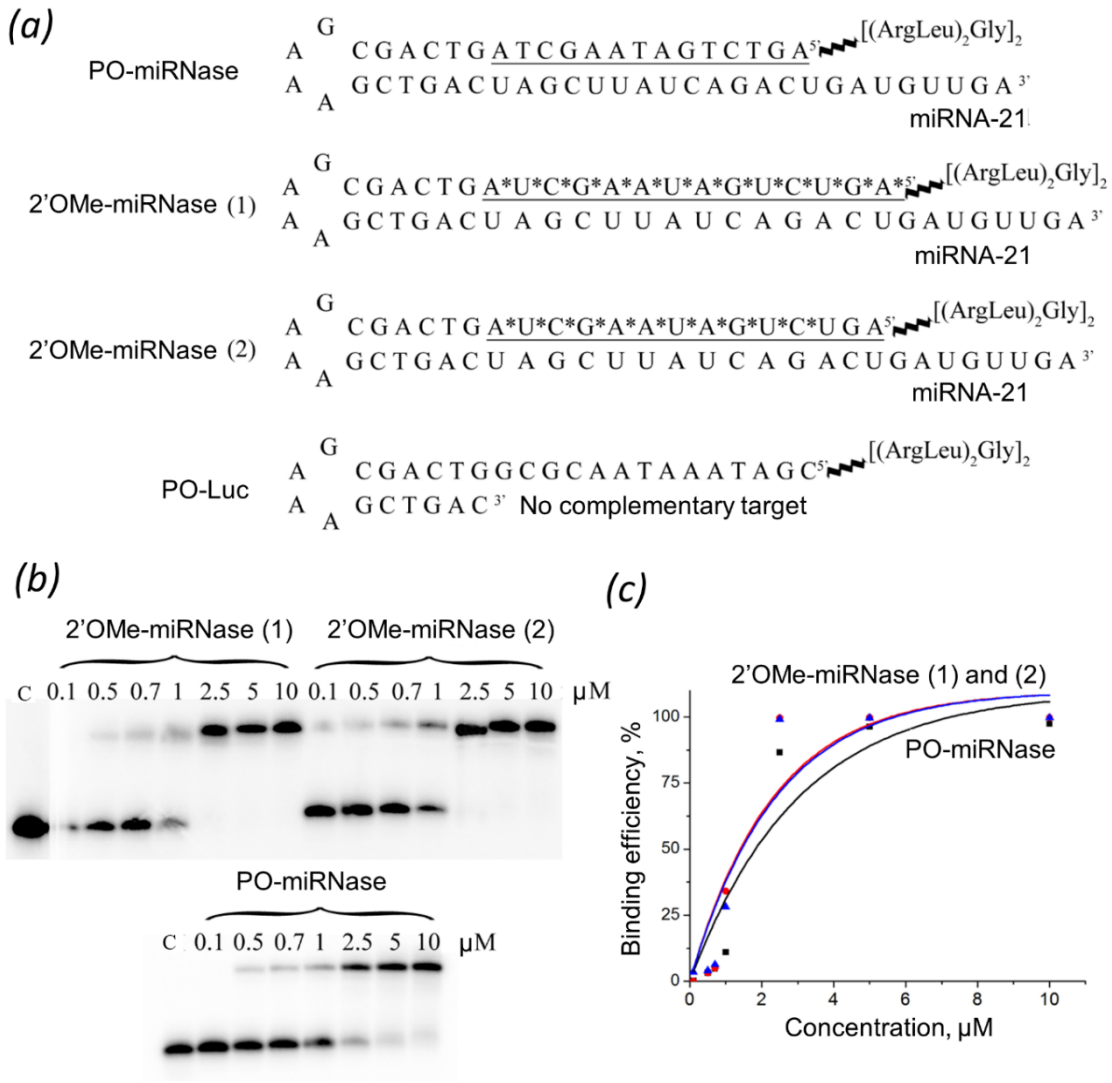

Figure 5.1. Structure and hybridisation properties of anti-21-miRNA oligonucleotide–peptide conjugates. **(a)** Structure of the complexes of the conjugates based on deoxyribo (PO-) or 2'OMe (2'OMe-) oligonucleotides and the peptide $[(ArgLeu)_2Gly]_2$ with miRNA-21. **(b)** Autoradiograph of native 15% polyacrylamide gel. **(c)** Concentration dependence of the conjugate binding to miRNA-21. [^{32}P] miRNA-21 (1 μM) was incubated with the conjugates at a concentration of 0.1–10 μM at 37°C for 1 h. In C, miRNA-21 was incubated in the absence of conjugates. After the completion of the reaction, samples were loaded onto the gel subjected to electrophoresis at an interval of 1 min.

Thus, the introduction of 2'OMe modifications into the oligonucleotide–peptide conjugates increased their resistance neither in the medium with 50% FCS nor in mouse blood plasma. Most likely, the developed conjugate structure is sufficiently stable under physiological conditions per se, and the introduction of 2'OMe modifications does not give an additional gain in their nuclease resistance. The absence of differences in the stability of 2'OMe– and PO–miRNases may also be a consequence of the extremely

aggressive conditions (50% FCS and mouse blood serum), in which both the concentration of nucleases and the degradation rate of the compounds are very high. It can be assumed that the differences in the stability of the compounds may be detected under significantly milder conditions (e.g., in the presence of 10% FCS).

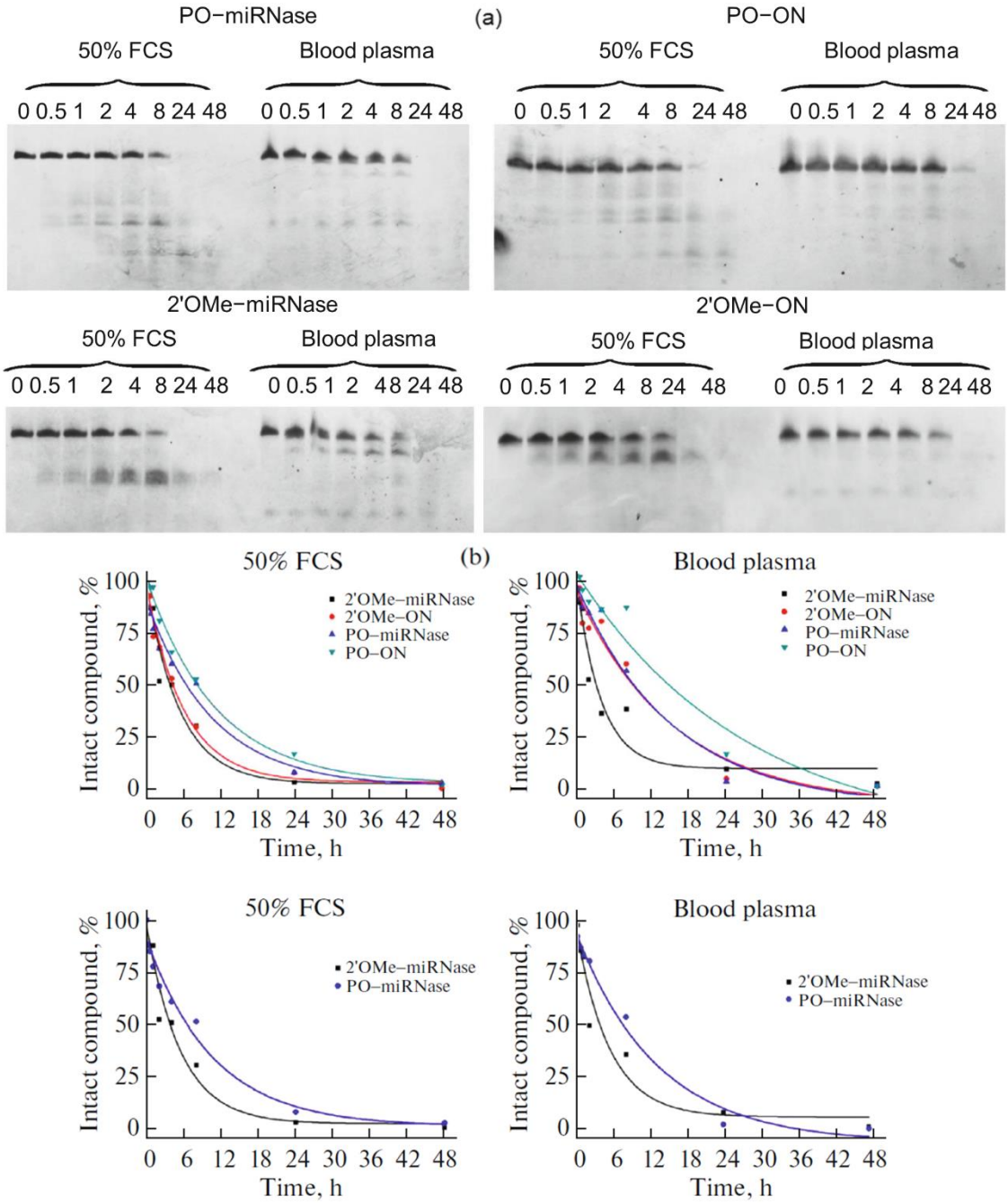

Figure 5.2. Stability of PO- and 2'OMe-oligonucleotides and oligonucleotide–peptide conjugates in 50% fetal bovine serum and in mouse blood plasma. (**a**) Photographs of denaturing 12% polyacrylamide gels. (**b**) Dependence of the kinetics of degradation of oligonucleotides and oligonucleotide–peptide conjugates in 50% FCS and in mouse blood plasma. Oligonucleotides and oligonucleotide–peptide conjugates were incubated in 50% FCS or in mouse blood plasma at 37°C for 0–48 h.

It should be noted that the introduction of 2'OMe modifications promotes changes in the degradation patterns of the compounds in 50% FCS and in blood plasma. As can be seen in **Figure 5.2** (**a**), the cleavage sites of PO and 2'OMe analogues differ depending on the conditions. The data obtained can be explained by the differences in the composition of plasma and FCS nucleases and by different levels of their activity. In addition, the sensitivity of PO and 2'OMe analogues to endo-and exonucleases present in these media may differ.

5.4.3 Ribonuclease Activity of 2'OMe Oligonucleotide–Peptide Conjugates

It is known that the introduction of chemical modifications into the structure of oligonucleotide constructs as well as oligonucleotide–peptide conjugates may affect their activity. In view of this, the search for a modification pattern that ensures the preservation or enhancement of the catalytic activity of the compounds remains the main task in the development of oligonucleotide-based catalytic constructs. The effect of 2'OMe modifications on the activity of the developed miRNases was evaluated under conditions of single-turnover (20-fold excess of miRNase relative to miRNA) and multiple-turnover (two-fold excess of miRNA relative to miRNase) reactions (**Figure 5.3**).

A complete replacement of the deoxyribonucleotide backbone in the addressing oligonucleotide region with a 2'OMe oligonucleotide fragment causes a significant decrease in the ribonuclease activity of the conjugate. For example, it was shown that, under the conditions of a 20-fold excess of the conjugate relative to the target miRNA, the fully modified 2'OMe–miRNase (1) cleaved miRNA-21 by 5 and 22% for 2 and 8 h, respectively, and the total degradation efficiency did not exceed 81% even after 72 h of incubation (**Figure 5.3** (**a**)). For comparison, PO–miRNase cleaved the miRNA substrate by 47 and 66% for 2 and 8 h, respectively, and quantitative cleavage of miRNA-21 was observed after 48 h of incubation (**Figure 5.3** (**a**)). Partial modification of the addressing oligonucleotide region in the structure of 2'OMe–miRNase (2), conversely, enhanced the target miRNA cleavage. This conjugate cleaved miRNA-21 by 60 and 89% for 2 and 8 h of incubation, respectively, and a complete cleavage of the target miRNA was observed after 24 h of incubation. Under these conditions, all the studied ribonucleases cleaved miRNA-21 only at the G–X bonds (where X = A, U, C) (**Figures 5.3** (**a**) and (**b**)).

Under conditions of a two-fold excess of miRNA-21 relative to the conjugate, a complete modification of the addressing oligonucleotide region significantly reduced the activity

of miRNase. For example, in the case of 2'OMe–miRNase (1), the total cleavage of miRNA-21 did not exceed 42% even after 72 h of incubation (**Figure 5.3**). In contrast, 2'OMe–miRNase (2) cleaved miRNA more effectively; 63% of miRNA-21 was cleaved after 8 h of incubation (**Figure 5.3** (**c**)). For comparison, PO–miRNase for the same time cleaved only 46.5% of the substrate miRNA; after 24 h of incubation the rate of cleavage by 2'OMe–miRNase (2) and PO–miRNase became comparable, and after 72 h of incubation the cleavage efficiency reached a plateau at 77 and 79%, respectively (**Figure 5.3**). It was found that, under the conditions of a two-fold excess of miRNA-21, the chemically modified miRNases cleaved miRNA-21 not only at G–X but also at C–A/U–A bonds (**Figure 5.3** (**c**) and (**d**)).

Thus, the introduction of the 2'OMe modification does not prevent the functioning of the conjugates under conditions of both excess and shortage of the conjugates relative to the target miRNA. However, it was found that the complete 2'-O-methylation of the oligonucleotide component of the conjugates in the region complementary to miRNA caused a two-fold decrease in the efficiency of miRNA-21 cleavage as compared to the PO- and partially modified miRNase, which was most likely due to a change in the conformation of the catalytic peptide and/or the pattern of its interaction with the adjacent oligonucleotide.

5.4.4 Biological Activity of Conjugates in Human Epidermoid Carcinoma KB-8-5 Cells

The high efficiency of miRNA-21 degradation by the modified conjugates *in vitro* served as a basis for the study of their biological activity in tumour cell culture. The antiproliferative and antimigration effects of 2'OMe-conjugates were studied using human epidermoid carcinoma KB-8-5 cells, for which a high level of miRNA-21 expression had been previously shown. The PO–Luc conjugate, containing a 14-mer luciferase gene fragment and having no complementary targets in the mammalian genome, was used as a control conjugate (**Figure 5.1** (**a**)).

The antiproliferative effect of 2'OMe–miRNases was studied in real time using the xCELLigence cell analysis system. Cells were transfected with the conjugates PO–Luc, PO–miRNase, 2'OMe–miRNase (1), 2'OMe–miRNase (2), and 2'OMe–ON at a concentration of 0.5 μM using Lipofectamine™ 3000. We showed that 2'OMe–ON had no statistically significant effect on cell proliferation (**Figure 5.4**). The deceleration of KV-8-5 cell growth after incubation with the control conjugate PO–Luc did not exceed

10%. The transfection of cells with the conjugates 2'OMe–miRNase (1), 2'OMe–miRNase (2), and PO–miRNase resulted in a significant inhibition of cell proliferation. We found that 72 h after transfection, the tumour cell growth inhibition was 58, 48, and 75%, respectively, compared to the control cells (**Figure 5.4**). A more pronounced anti-proliferative effect, which was observed for the PO– miRNase, was probably due to the fact that, unlike the 2'OMe–miRNase, the PO–miRNase is able to recruit intracellular RNase H, as a result of which the synergistic effect of PO–miRNase and RNase H is observed in the cell (5, 8).

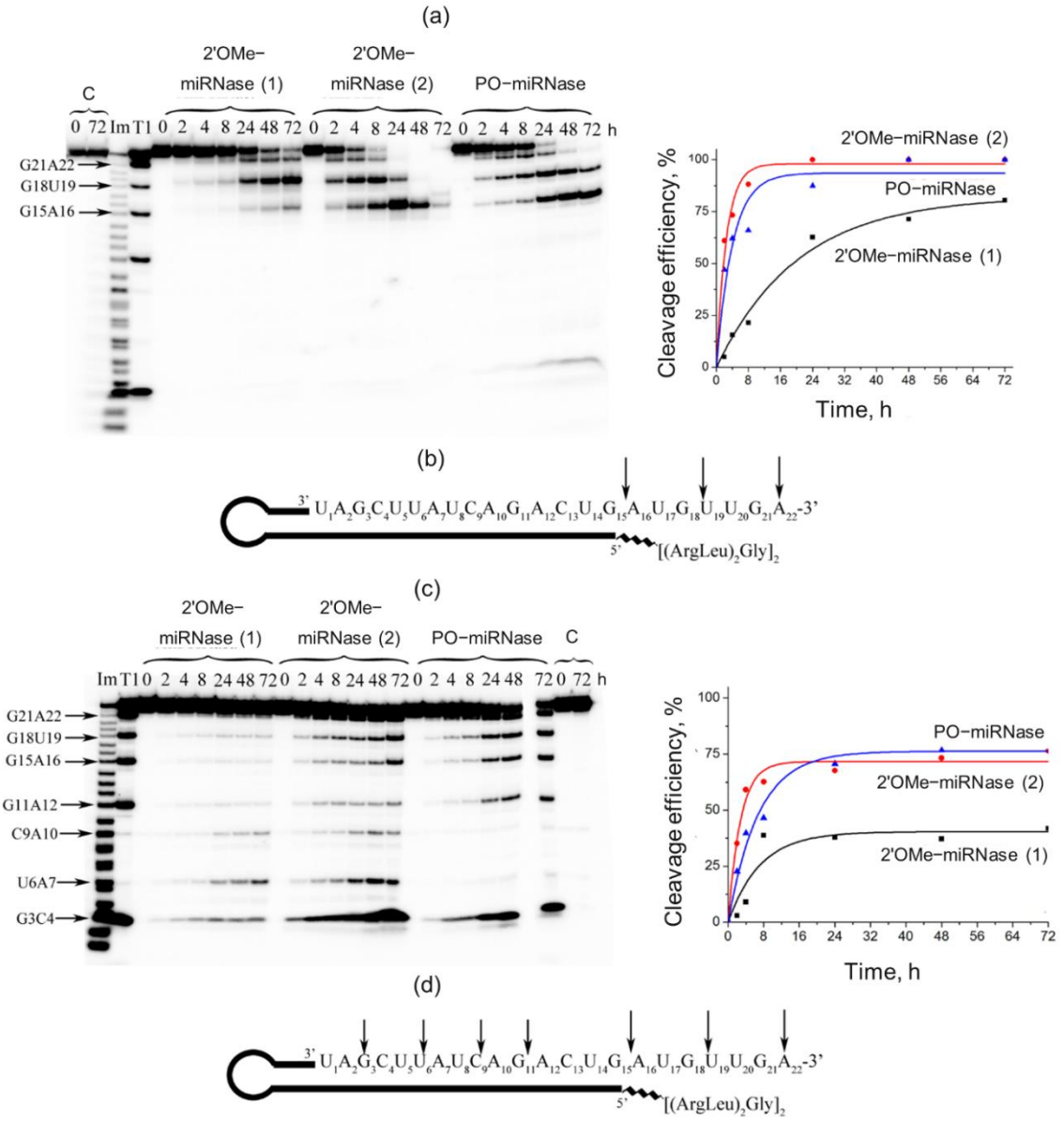

Figure 5.3. Kinetics of miRNA-21 cleavage by PO- and 2'OMe-oligonucleotide–peptide conjugates. (**a, c**) Autoradiographs of denaturing 18% polyacrylamide gels and kinetic dependences of miRNA-21 cleavage at a 20-fold excess of the conjugates (**a**) and at a two-fold excess of miRNA-21 (**c**). [^{32}P]miRNA-21 (1 μM) was incubated with the conjugates (20 μM) (**a**) or [^{32}P]-miRNA-21 (10 μM) was incubated with the conjugates (5 μM) (**c**) at 37°C for 0–72 h. (**b,**

d) Sites of miRNA-21 cleavage by 2'OMe-conjugates at a 20-fold excess of the conjugates (**b**) or a two-fold excess of miRNA-21 (**d**).

The effect of conjugates on the migratory activity of KB-8-5 cells was studied by the scratch assay. Analysis was performed for the 2'OMe–miRNase (2), which showed the highest ribonuclease activity *in vitro*. Cells were transfected with PO–Luc, PO–miRNase, 2'OMe–miRNase (2) conjugates as well as PO–ON and 2'OMe–ON oligonucleotides at a concentration of 0.5 μM using Lipofectamine™ 3000. It can be seen in **Figure 5.5** that, for the intact KB-8-5 cells and Lipofect-amine™ 3000-treated cells, the degree of scratch closure with KB-8-5 cells after 72 h of incubation was 90.2 and 83.4%, respectively (**Figure 5.5**). The control compounds PO–ON, 2'OMe–ON, and PO–Luc did not significantly inhibit the cell migration activity, and the percentage of scratch closure after the treatment with these compounds was 81.2, 73.1, and 82%, respectively (**Figure 5.5**). 2'OMe–miRNase (2) had the greatest antimigration effect on tumour cells: after 72 h of incubation, the percentage of scratch closure with KB-8-5 cells was only 45% (**Figure 5.5**). During the same time, the degree of scratch closure with the cells treated with PO–miRNase was 62%.

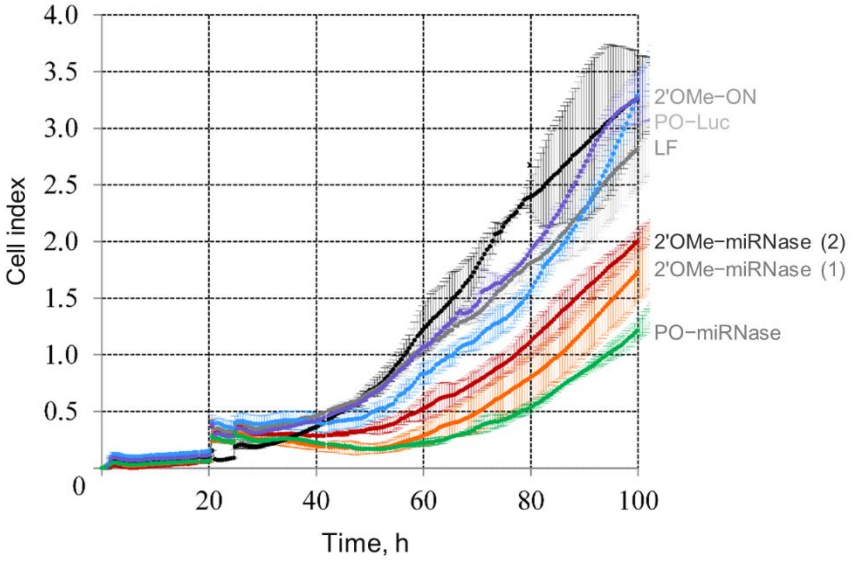

Figure 5.4. Proliferation of KB-8-5 cells after transfection with conjugates PO–Luc, PO–miRNase, 2'OMe–miRNase (1), 2'OMe– miRNase (2), and oligonucleotide 2'OMe–ON recorded in real time

According to our data, the introduction of 2'OMe modifications into the structure of miRNA-targeted oligonucleotide–peptide conjugates significantly increases their affinity for the target miRNA. However, the complete modification of the addressing component of miRNases in the binding region to the miRNA target did not enhance the nuclease resistance of the compound and even adversely affected the ribonuclease activity of the

conjugate, causing a two-fold decrease in the rate of cleavage of the substrate miRNA by miRNase. This reduction in the efficacy of nucleic acid-based compounds as a result of the introduction of chemical modifications into their structure was also observed earlier. In particular, it is known that the introduction of even two 2'OMe modifications into siRNA duplexes causes a many-fold decrease in their efficiency, and the complete modification causes a total loss of activity (11, 12).

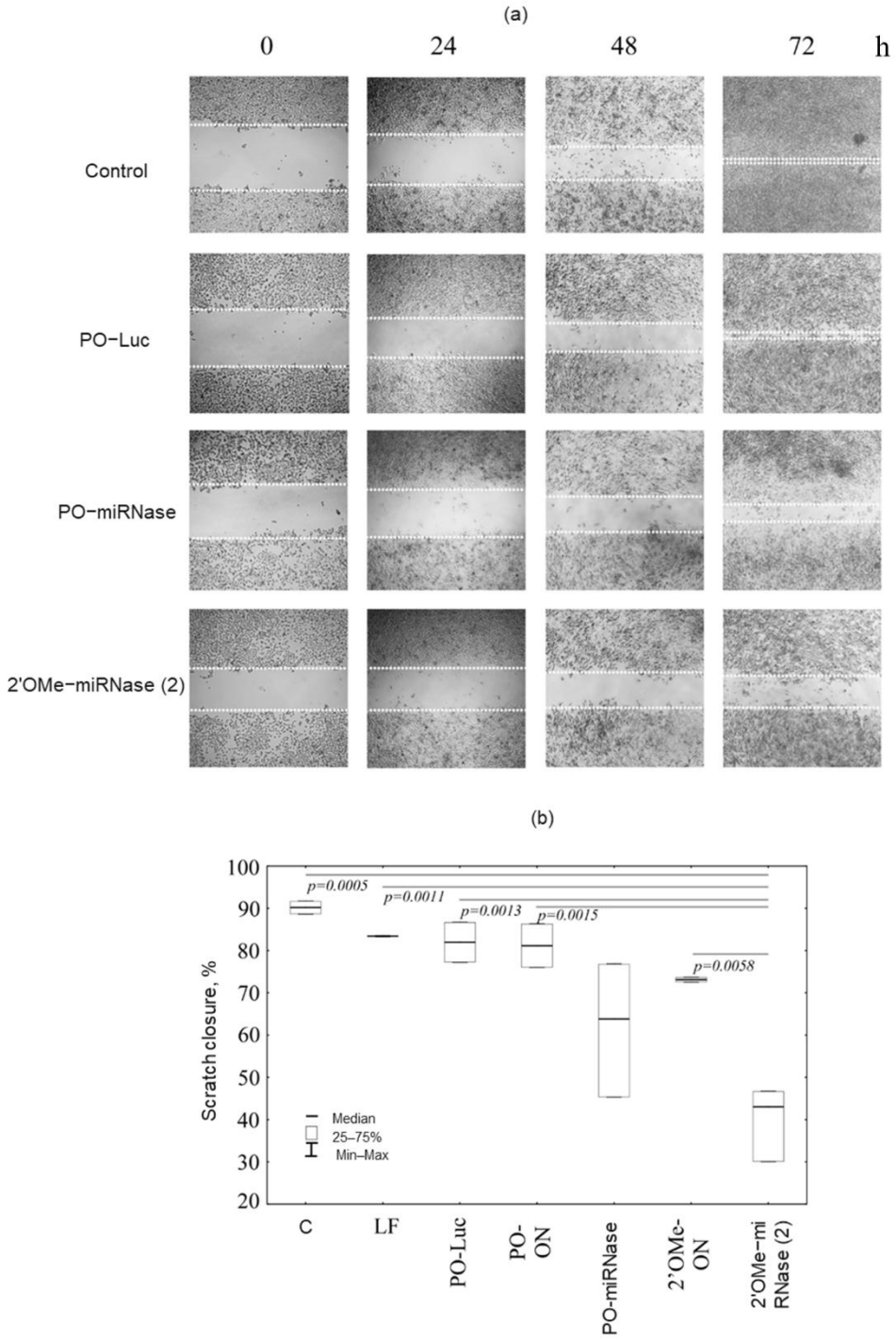

Figure 5.5. Migration activity of human epidermoid carcinoma KB-8-5 cells after transfection with PO- and 2'OMe-oligonucleotides and oligonucleotide–peptide conjugates. (**a**) Photograph of

the KB-8-5 cell monolayer after scratching (magnification, 4×). Control: intact KB-8-5 cells. PO–Luc, PO–miRNase, and 2'OMe–miRNase (2) cells were transfected with the corresponding conjugates at a concentration of 0.5 μM, complexed with Lipofectamine™ 3000 24 h before scratching. The dotted line shows the boundaries of the scratch. (**b**) Degree of scratch closure after 72 h of incubation.

In turn, partial modification of the oligonucleotide component of miRNases in the region complementary to miRNA significantly increases the degradation efficiency of the target miRNA under the conditions of both excess and shortage of the conjugate relative to miRNA as well as increases the antimigration activity of miRNase in tumour cells as compared to the PO analogue.

The revealed advantages of 2'OMe–miRNases may disappear *in vivo*. It is known that RNA and 2'OMe–miRNase duplexes will not be recognised by RNase H (1), which, according to our data, can multiply and enhance the target miRNA cleavage and increase the antitumor effect of miRNase due to synergistic action with them (5, 8). It follows from this data that, in order to preserve and increase the ribonuclease activity, nuclease resistance, and affinity for the target of the constructed miRNases, the chemical modifications introduced into their structure must possess RNase H-activating ability which was described, in particular, for phosphorothioate, *N*-mesylphosphoramide, or boranophosphate analogues (13, 14). Modifications of the addressing miRNase component in the region complementary to the target miRNA should be introduced at the nuclease-sensitive sites in the sequence, excluding the region adjacent to the peptide attachment site.

5.5 Materials and Methods

5.5.1 Synthesis and Characterisation of Oligonucleotides and Oligonucleotide–Peptide Conjugates

miRNA-21 5'-UAGCUUAUCAGACUGAUG-UUGA-3', containing an OH group at the 5'-end of the molecule, was synthesised by the solid-phase phosphite-amide technique (15) in an ASM-800 automatic synthesiser (Biosset, Russia) and purified by gel electrophoresis under denaturing conditions.

Oligodeoxyribonucleotides and 2'OMe-ribonucleotides with the aminohexyl linker attached at the 5'-end phosphate were synthesised in the Laboratory of Medical Chemistry (Institute of Chemical Biology and Fundamental Medicine, Siberian Branch, Russian Academy of Sciences) using the standard phosphite-amide method and isolated by reverse-phase HPLC.

The synthesis and characterisation of the peptide–oligonucleotide conjugates based on PO, 2'OMe- oligonucleotides, PO-Luc and peptide were performed according to the protocol described in (2, 16) (see **Supplementary Information Figure 5.6**) Crude conjugates were purified using RP-HPLC. Eluents used included 0.05 M $LiClO_4$ in water as eluent A and 0.05M $LiClO_4$ in acetonitrile as eluent B with 2.0 mL/min flow rate. The absorbance was monitored at 260 nm and the following gradient was applied: 0% B for 3 minutes, 0-100% B in 30 minutes, isocratic 100% B for 8 minutes and 100-0% B for 1 minute. HPLC fraction at 24 min was collected, combined and lyophilised (**Supplementary Figure 5.7**). The conjugates were characterised using ^{1}H NMR spectroscopy (**Supplementary Figure 5.8**) and mass spectrometry (**Supplementary Figure 5.9**). The ^{32}P-label at the 5'-end of miRNA-21 was incorporated using γ-[^{32}P]ATP and T4 polynucleotide kinase (Thermo Scientific, United States) according to the protocol described in (6, 17).

2'OMe-miRNase (1). MALDI-MS: *m/z* = 11089 $[M+Na+K]^+$ (MW = 11027 calcd. For $[C_{363}H_{499}N_{143}O_{202}P_{30}]$) (**Supplementary Figure 5.9**). ^{1}H NMR (**Supplementary Figure 5.8**) (D_2O with TSP (0.01 mM), 400 MHz): δ 0.69-0.80 (m, 24H, Leu- H^{δ}), 1.20-2.84 (m, 151H, 30×H2' and 30×H2'' sugar ring protons, 2×CH_3 of 2×dT, 14×CH_3 (2'-OMe) 8× Arg-H^{β}, 8×Arg-H^{γ}, 8×Leu-H^{β}, 4×Leu-H^{γ}, 6×CH_2 (aminohexyl linker), Acetyl-CH_3), 3.14 (m, 8H, 8×Arg-H^{δ}), 3.46-4.28 (m,102H, 90×H4'/H5'H5" sugar ring protons, 2×Gly-CH_2, 8 × Leu/Arg-H^{α}), 5.65-6.30 (m, 36H, 30×H1' sugar ring protons, 6×H5 of dC), 7.20-8.45 (m, 44H, 44×Ar-H from dG(H8×8), dA(H8×10), dA(H2×10), dC(H6×6), dT(H6×2), dU(H5×4) and dU(H6×4)). H3' sugar ring protons (3.6-4.3 ppm) were not analysed due to suppression of residual water signal at 4.12 ppm.

2'OMe-miRNase (2). MALDI-MS: *m/z* = 11013 $[M+Na+K]^+$ (MW = 10951 calcd. For $[C_{361}H_{495}N_{143}O_{199}P_{30}]$) (**Supplementary Figure 5.9**). ^{1}H NMR (**Supplementary Figure 5.8**) (D_2O with TSP (0.01 mM), 400 MHz): δ 0.68-0.78 (m, 24H, Leu- H^{δ}), 1.0-2.80 (m, 145H, 30×H2' and 30×H2'' sugar ring protons, 3×CH_3 of 3×dT, 11×CH_3 (2'-OMe) 8× Arg-H^{β}, 8×Arg-H^{γ}, 8×Leu-H^{β}, 4×Leu-H^{γ}, 6×CH_2 (aminohexyl linker), Acetyl-CH_3), 3.11 (m, 8H, 8×Arg-H^{δ}), 3.41-4.23 (m,102H, 90×H4'/H5'H5" sugar ring protons, 2×Gly-CH_2, 8 × Leu/Arg-H^{α}), 5.61-6.26 (m, 36H, 30×H1' sugar ring protons, 6×H5 of dC), 7.16-8.40 (m, 43H, 43×Ar-H from dG(H8×8), dA(H8×10), dA(H2×10), dC(H6×6), dT(H6×3), dU(H5×3) and dU(H6×3)). H3' sugar ring protons (3.5-4.3 ppm) were not analysed due to suppression of residual water signal at 4.10 ppm.

5.5.2 Hybridisation of Oligonucleotide–Peptide Conjugates with miRNA-21

The reaction mixture (4 μL) containing 50 mM Tris-HCl (pH 7.0), 0.2 mM KCl, 1 mM EDTA, 400 ppm (according to Cherenkov) γ-[^{32}P]-miRNA-21, 1 μM miRNA-21, and the conjugate in the concentration range from 10^{-7} to 10^{-5} M were incubated at 37°C for 1 h. The reaction was stopped by adding a solution containing 20% ficoll, 0.025% bromophenol blue, and 0.025% Xylene cyanol. The reaction mixture was loaded onto a 12% native polyacrylamide gel equilibrated at 4°C. The gels were analysed using the Molecular Imager FX system (Bio-Rad, United States). The binding efficiency was determined as the ratio of the radioactivity of the complex to the total radioactivity located in the lane.

5.5.3 Stability of Oligonucleotides and Oligonucleotide–Peptide Conjugates in 50% Fetal Bovine Serum and in Mouse Blood Plasma

To evaluate the nuclease resistance of the oligonucleotides and oligonucleotide–peptide conjugates, we obtained fresh blood plasma of C57/Black mice immediately before the experiment. Immediately after bleeding, blood samples were incubated at 37°C for 30 min with subsequent cooling at –20°C overnight. Then, the samples were centrifuged at 4000 rpm at 4°C for 20 min. The obtained blood plasma was immediately used to study the nuclease resistance of oligonucleotides and oligonucleotide–peptide conjugates. Oligonucleotides and oligonucleotide–peptide conjugates at a concentration of 0.1 μg/μL were incubated in mouse blood plasma or in Dulbecco's Modified Eagle Medium (DMEM; Sigma, United States) containing 50% FCS at 37°C for 48 h. Aliquots (10 μL) were taken after 0, 0.5, 1, 2, 4, 8, 24, and 48 h of incubation; the reaction was stopped by adding 10 μL of 8 M urea, and the reaction mixture was immediately frozen in liquid nitrogen. The integrity of oligonucleotides and oligonucleotide–peptide conjugates in the obtained samples was assessed by denaturing PAGE in 12% polyacrylamide gel. Gels were stained with the Stains-All dye (MP Biomedicals, United States) and photographed using a gel documentation system (Vilber Lourmat, France).

5.5.4 Ribonuclease Activity of Oligonucleotide–Peptide Conjugates

Study of ribonuclease activity of the conjugates was performed at a 20-fold excess or a 2-fold shortage of conjugate relative to the target miRNA. For this purpose, the reaction mixture (18 μL) containing 50 mM Tris-HCl (pH 7.0), 0.2 mM KCl, 1 mM EDTA, 1800

ppm (according to Cherenkov) γ-[^{32}P]-miRNA-21, 1 μM miRNA-21, and conjugates at a concentration of 2×10^{-5} M, or miRNA-21 at a concentration of 10^{-5} M and conjugates at a concentration of 5×10^{-6} M were incubated at 37°C for 72 h. Aliquots (2 μL) were taken after 0, 2, 4, 8, 24, 48, and 72 h of incubation. The reaction was stopped by precipitating RNA in 2% $LiClO_4$ in acetone. Samples were centrifuged at 13000 rpm at 4°C for 20 min, the supernatant was discarded, and the pellet was dissolved in 8 M urea containing 0.025% Bromophenol blue and 0.025% Xylene cyanol. The miRNA-21 cleavage products were analysed by PAGE in 18% polyacrylamide gel under denaturing conditions. The miRNA-21 cleavage sites were determined using ladders, partial cleavage products of miRNA-21 with RNase T1 or in 2 M imidazole buffer (pH 7.0) (18, 19). To obtain quantitative data, the gels were dried and analysed using the Molecular Imager FX system (Bio-Rad, United States). The total efficiency of miRNA cleavage was determined using the Quantity One software.

5.5.5 Analysis of Cell Proliferation Rate in Real Time

Cell proliferation was recorded in real time using the xCELLigence system (ACEABiosciences, United States) in a 5% CO_2 atmosphere at 37°C. For this purpose, KB-8-5 cells were seeded in 16-well E-Plate plates at a density of 5×10^3 cells per well. The next day, the cells were transfected with the conjugates and oligonucleotide at a concentration of 0.5 μM, complexed with Lipofectamine™ 3000 (Invitrogen, United States). Then, 4 h after transfection, the medium in the wells was replaced with DMEM containing 10% FCS and 1% solution of antibiotics and antimycotic. Experiments on cell proliferation were carried out for 144 h, the cell index was recorded every 30 min throughout the experiment.

5.5.6 Analysis of Migration Activity (Scratch Assay)

Cell migration activity was recorded in a 5% CO_2 atmosphere at 37°C. KB-8-5 cells were seeded in 6-well plates at a density of 5×10^5 cells per well. The next day, cells were transfected with the conjugates and oligonucleotide at a concentration of 0.5 μM, complexed with Lipofectamine™ 3000. Then, 4 h after transfection, the medium in the wells was replaced with DMEM containing 10% FCS and 1% solution of antibiotics and antimycotic. Thereafter, 24 h after transfection, the KB-8-5 cell monolayer was scratched. Then, the cells were washed with sterile saline (0.9% NaCl) and incubated under the same conditions for 72 h. After 0, 24, 48 and 72 h of incubation, the cells were photographed using a Zeiss Primo Vert microscope (Zeiss, Germany) at a 4× magnification. The images

of cells were processed using the ImageJ software. The degree of scratch closure was evaluated by the formula $\upsilon = (1 - x) \times 100\%$, where x is the ratio of the scratch width after 24, 48, and 72 h of incubation to the scratch width at 0 h.

5.6 References

1. Zamaratski,E., Pradeepkumar,P.I. and Chattopadhyaya,J. (2001) A critical survey of the structure-function of the antisense oligo/RNA heteroduplex as substrate for RNase H. *J. Biochem. Biophys. Methods*, **48**, 189–208.

2. Patutina,O.A., Bichenkova,E. V, Miroshnichenko,S.K., Mironova,N.L., Trivoluzzi,L.T., Burusco,K.K., Bryce,R.A., Vlassov,V. V and Zenkova,M.A. (2017) miRNases: Novel peptide-oligonucleotide bioconjugates that silence miR-21 in lymphosarcoma cells. *Biomaterials*, **122**, 163–178.

3. Gaglione,M., Milano,G., Chambery,A., Moggio,L., Romanelli,A. and Messere,A. (2011) PNA-based artificial nucleases as antisense and anti-miRNA oligonucleotide agents. *Mol. Biosyst.*, **7**, 2490–2499.

4. Danneberg,F., Ghidini,A., Dogandzhiyski,P., Kalden,E., Strömberg,R. and Göbel,M.W. (2015) Sequence-specific RNA cleavage by PNA conjugates of the metal-free artificial ribonuclease tris(2-aminobenzimidazole). *Beilstein J. Org. Chem.*, **11**, 493–498.

5. Patutina,O.A., Bazhenov,M.A., Miroshnichenko,S.K., Mironova,N.L., Pyshnyi,D. V, Vlassov,V. V and Zenkova,M.A. (2018) Peptide-oligonucleotide conjugates exhibiting pyrimidine-X cleavage specificity efficiently silence miRNA target acting synergistically with RNase H. *Sci. Rep.*, **8**, 14990.

6. Mironova,N.L., Pyshnyi,D. V, Shtadler,D. V, Fedorova,A.A., Vlassov,V. V and Zenkova,M.A. (2007) RNase T1 mimicking artificial ribonuclease. *Nucleic Acids Res.*, **35**, 2356–2367.

7. Sunami,T., Kondo,J., Hirao,I., Watanabe,K., Miura,K. and Takénaka,A. (2004) Structure of d(GCGAAAGC) (hexagonal form): a base-intercalated duplex as a stable structure. *Acta Crystallogr. Sect. D*, **60**, 90–96.

8. Patutina,O.A., Miroshnichenko,S.K., Mironova,N.L., Sen'kova,A. V, Bichenkova,E. V, Clarke,D.J., Vlassov,V. V and Zenkova,M.A. (2019) Catalytic Knockdown of miR-21 by Artificial Ribonuclease: Biological Performance in Tumor Model. *Front. Pharmacol.*, **10**, 879.

9. Malek-Adamian,E., Patrascu,M.B., Jana,S.K., Martínez-Montero,S., Moitessier,N. and Damha,M.J. (2018) Adjusting the Structure of 2′-Modified Nucleosides and Oligonucleotides via C4′-α-F or C4′-α-OMe Substitution: Synthesis and Conformational Analysis. *J. Org. Chem.*, **83**, 9839–9849.

10. Lennox,K.A. and Behlke,M.A. (2010) A Direct Comparison of Anti-microRNA Oligonucleotide Potency. *Pharm. Res.*, **27**, 1788–1799.

11. Choung,S., Kim,Y.J., Kim,S., Park,H.-O. and Choi,Y.-C. (2006) Chemical modification of siRNAs to improve serum stability without loss of efficacy. *Biochem. Biophys. Res. Commun.*, **342**, 919–927.

12. Petrova Kruglova,N.S., Meschaninova,M.I., Venyaminova,A.G., Zenkova,M.A., Vlassov,V. V and Chernolovskaya,E.L. (2010) 2'-O-methyl-modified anti-MDR1 fork-siRNA duplexes exhibiting high nuclease resistance and prolonged silencing activity. *Oligonucleotides*, **20**, 297–308.

13. Miroshnichenko,S.K., Patutina,O.A., Burakova,E.A., Chelobanov,B.P., Fokina,A.A., Vlassov,V. V, Altman,S., Zenkova,M.A. and Stetsenko,D.A. (2019) Mesyl phosphoramidate antisense oligonucleotides as an alternative to phosphorothioates with improved biochemical and biological properties. *Proc. Natl. Acad. Sci.*, **116**, 1229–1234.

14. Rait,V.K. and Shaw,B.R. (1999) Boranophosphates Support the RNase H Cleavage of Polyribonucleotides. *Antisense Nucleic Acid Drug Dev.*, **9**, 53–60.

15. Damha,M.J. and Ogilvie,K.K. (1993) Oligoribonucleotide synthesis. The silyl-phosphoramidite method. *Methods Mol. Biol.*, **20**, 81–114.

16. Williams,A., Staroseletz,Y., Zenkova,M.A., Jeannin,L., Aojula,H. and Bichenkova,E. V. (2015) Peptidyl-Oligonucleotide Conjugates Demonstrate Efficient Cleavage of RNA in a Sequence-Specific Manner. *Bioconjug. Chem.*, **26**, 1129–1143.

17. Silberklang,M., Gillum,A.M. and RajBhandary,U.L. (1979) Use of in Vitro ^{32}P Labeling in the Sequence Analysis of Nonradioactive tRNAs. *Methods Enzym.*, **59**, 58–109.

18. Donis-Keller,H., Maxam,A.M. and Gilbert,W. (1977) Mapping adenines, guanines, and pyrimidines in RNA. *Nucleic Acids Res.*, **4**, 2527–2538.

19. Vlasov,A. V, Vlasov,V. V and Giege,R. (1996) Imidazole catalyzed hydrolysis of RNA as a reaction for probing the structure of RNA and RNA oligonucleotide complexes. *In Doklady Akademii Nauk.Vol*. **349**, 411–413.

5.7 Supplementary information

5.7.1 Additional Figures and Data

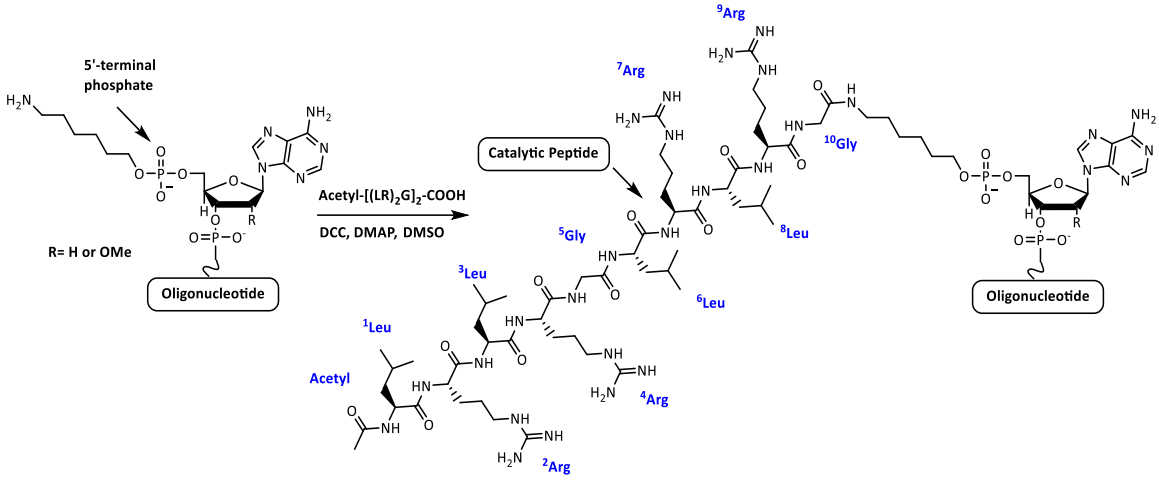

Figure 5.6. Synthetic route for preparation of modified oligonucleotide conjugates (2'OMe-miRNase (1) and (2)). To avoid peptide self-conjugation and cyclisation during amide coupling reaction, acetylated N-termini peptides were used

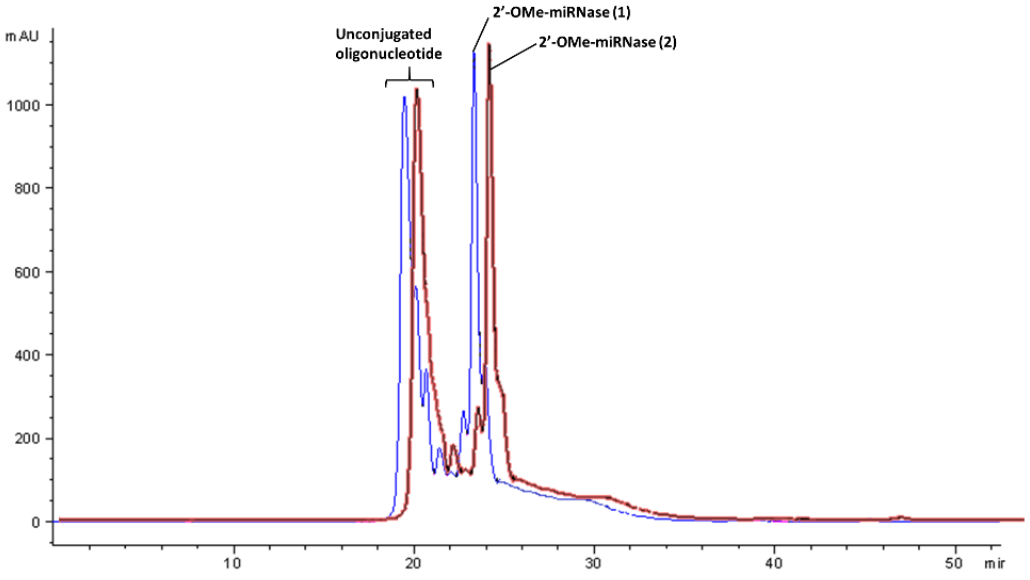

Figure 5.7. An overlay of HPLC chromatograms of modified oligonucleotide conjugates (2'OMe-miRNase (1) and (2)) showing a shift in retention time from unconjugated oligonucleotide (RT 20 min) to conjugates (RT 24 min).

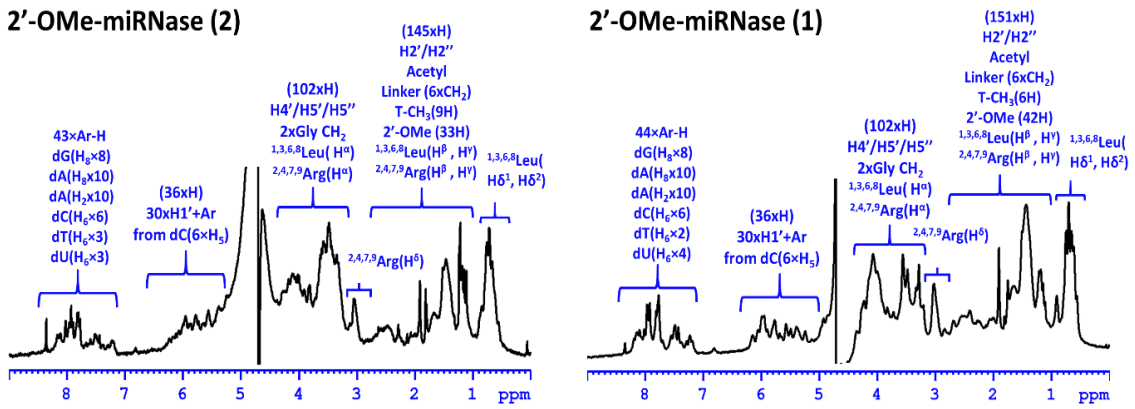

Figure 5.8. ^{1}H-NMR spectra of modified oligonucleotide-peptide 2'OMe-miRNase (1) and 2'OMe-miRNase (2) conjugates showing the characteristic resonance areas of the oligonucleotide protons, peptide protons, aminohexyl linker and acetyl protecting group. Assignments of the key ^{1}H resonance regions are indicated above each spectrum. 1:1 stoichiometric ratio of peptide to oligonucleotide was confirmed through integration. The spectra were recorded in D_2O at 25 °C using 400 MHz NMR spectrometer (Bruker Avance II+ 400).

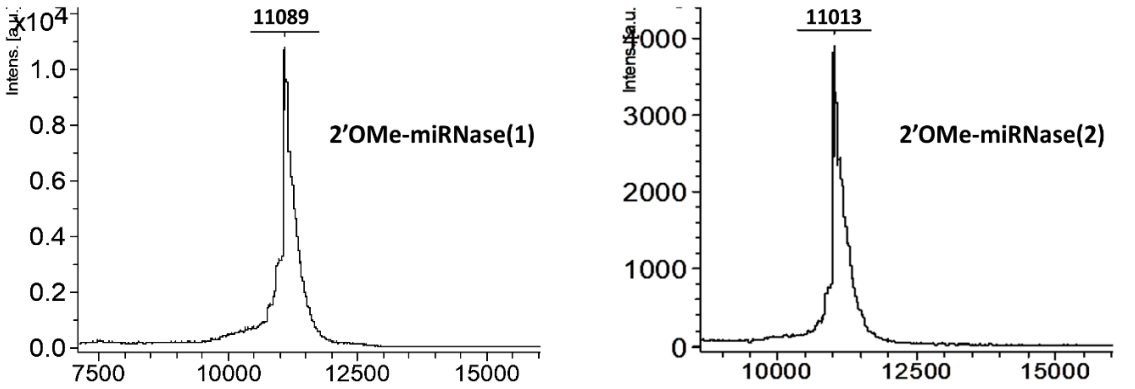

Figure 5.9. MALDI-ToF MS spectrum of modified oligonucleotide–peptide conjugates, 2'OMe-miRNase (1) MALDI-MS: m/z = 11089 $[M+Na+K]^+$ (MW = 11027 calcd. For $[C_{363}H_{499}N_{143}O_{202}P_{30}]$) and 2'OMe-miRNase (2) MALDI-MS: m/z = 11013 $[M+Na+K]^+$ (MW = 10951 calcd. For $[C_{361}H_{495}N_{143}O_{199}P_{30}]$). Spectrum was recorded using 0.7 M 3-Hydroxy picolinic acid matrix (97 mg/mL, with 0.07 M ammonium citrate, 16 mg/mL in 50:50 ACN:H_2O) on a Bruker Daltonics Ultraflex ToF/ToF mass spectrometer.

Chapter 6

Conclusion and Future Work

The aim of the research presented here has been to increase potency, selectivity and catalytic turnover capabilities of peptidyl-oligonucleotide conjugates in order to facilitate the design of a truly catalytic bioconjugate, which could open the translational pathway to the development of successful therapeutics. Several different design approaches have been attempted here and assessed through hybridisation, ribonuclease activity, catalytic turnover and kinetic studies against various RNA targets. Collectively, the results presented herein allude to the following conclusions (the summary is presented in chronological order and future studies have been outlined):

6.1. Strict conformational demands of RNA cleavage in bulge-loops created by peptidyl-oligonucleotide conjugates (Chapter 2)

In this chapter a library of metal-free *"single"* bulge-loop inducing peptidyl-oligonucleotide conjugates targeting TΨC loop and 3' acceptor stem of $tRNA^{Phe}$ were designed and synthesised. Through variation in the structure of the catalytic peptide, orientation of linker, point and/or configuration of peptide attachment and the size of induced loop in the target RNA, we aimed to cover as many as possible structural variations to investigate the impact of these structural parameters on the catalytic activity of the conjugates. These conjugates can be classified into two general types: Type 1 where amphiphilic peptide acetyl-$[LR]_4$-COOH was conjugated to an antisense recognition motif via a centrally modified adenosine residue, and Type 2 where the peptide acetyl-$[LRLRG]_2$-COOH was incorporated into an elongated recognition motif via an internal sugar residue with the linker attached at either α- or β- configuration. The following conclusions can be drawn from the work presented in this chapter:

1. All Type 1 and Type 2 conjugates were capable of biding to the target $tRNA^{Phe}$ in a concentration dependent manner. A progressive decline in association constants was seen with an increase in loop size in Type 1 conjugates. Association constant remained invariable in Type 2 conjugates, indicating the counteracting effects of recognition motif elongation, which can mask destabilisation effects of larger loop-sizes.

2. None of the Type 1 conjugates were catalytically active. Contrarily, all Type 2 conjugates demonstrated catalytic activity with BC-α being somewhat catalytically superior to BC-β.

3. Induction of ≥3-nt long RNA bulge loop in the target sequence resulted in high catalytic efficacy.

4. 10 out of 14 catalytically active conjugates were identified, with 3 conjugates showing ≥70% cleavage in 24 hours (BC3-α, BC5-α and BC5L-β), and 2 best structural candidates achieving overall 90% and 82% RNA cleavage (BC5-α and BC5L-β, respectively). Enzymatic probing studies of the inactive Type 1 conjugates confirmed the formation of the bulge-loops in the structure of $tRNA^{Phe}$ upon hybridisation with POCs, thus ruling out the absence of the bulge-loop as the reason behind their catalytic failure.

5. Molecular modelling simulations indicated a correlation between the probability of adopting *"in-line"* geometry and the length of induced bulge loop, with a clear preference for larger loop sizes. The cluster analysis revealed the inherent vulnerability of single-stranded RNA regions for cleavage. Furthermore, the lack of central glycine in peptide sequence and the attachment of peptide via modified adenosine residue hindered the ability of peptide to reach the bulge region and distanced the guanidinium groups from the key constructs in cleavage (O2' and phosphorus atoms).

Future work: The results presented in this chapter demonstrated the structural requisites of a catalytically active conjugate and illuminated the coordinated network of atomic interactions between POCs and target molecule. The precision and efficiency with which our conjugates can recognise and destroy their target molecules provides a solid ground for the development of catalytic bioconjugate. However, catalytic turnover capabilities of conjugates were not tested here. In order for this class of bioconjugates to be clinically beneficial, serum stability needs to be enhanced. Stabilisation of the antisense sequence by chemical modifications and the development of an optimal delivery modality would encourage cellular uptake, increase biostability and prolong half-life, thereby augmenting POC-mediated *in vivo* gene silencing.

6.2 "*Bind, cleave and leave*": achieving multiple reaction turnover in catalytic cleavage of RNA substrates (Chapter 3)

The key structural components highlighted in **Chapter 2** formed the cornerstone for the next generation bulge-loop forming conjugates to enhance their potency and achieve reaction catalytic turnover. In this chapter, the bulge-loop inducing design was further optimised by increasing the number of cleaving constructs (catalytic peptides) incorporated in each conjugate molecule. The design consisted of two or three amphiphilic peptide residues, each attached via a flexible aminohexyl linker to an

anomeric C1' carbon in *"bis"* and *"triple"* conjugate series, respectively. The elongated peptide with central glycine residue was chosen for *"bis"* conjugation, whereas a shorter hepta peptide acetyl-$[LR]_3G$-COOH was chosen for *"triple"* conjugation. Incorporation of the linker in either α- or β- configuration led to the design of a variety of stereospecific *"bis"* conjugates. The POCs were designed in such a way to induce 5-nt long bulges. The destabilising effects of the bulge was counteracted by using an elongated recognition motif. The following conclusion can be drawn here:

1. All designed conjugates demonstrated the ability to hybridise with either $tRNA^{Phe}$ molecules or fluorescently labelled linear **F-Q**-RNA target.

2. The addition of multiple peptide entities amplified the ribonuclease activity of the conjugates, where up to 100% $tRNA^{Phe}$ cleavage was witnessed within 24 hours with the best structural candidate (BC5-L-αβ).

3. The increased potency of conjugates is reflected in the fact that even in the lower excess of conjugate over target (with 5:1 molar ratio for the conjugate against the target) full catalytic efficacy (up to 100 % cleavage) was also achieved with BC5-L-ββ conjugate.

4. Comparison of the ribonuclease activity of the representative *"single"* conjugates (BC5-α and BC5-L-β) and *"bis"* conjugate (BC5-L-ββ) in multiple turnover mode demonstrated again the superiority of *"bis"* conjugates and their potential to act as a true catalyst. A decline in velocity was witnessed at increased substrate concentration over conjugate.

5. All representative *"single"* (BC5-α and BC5-L-β) and *"bis"* (BC5-L-ββ) conjugates exhibited catalytic turnover in excess of target over conjugate (2-, 5-, 10-, 20- and 30-fold excess of **F-Q**-RNA target over selected conjugates), where a single conjugate molecule destroyed at least 10 copies of RNA target.

6. Similar Michaelis-Menten constants (K_m 20-24 μM) were estimated for all selected conjugates (BC5-α, BC5-L-β and BC5-L-ββ). However, the conjugate with a pair of catalytic peptides (BC5-L-ββ) showed the greatest reaction turnover (K_{cat} 0.8 h^{-1}) followed by the *"single"* α conjugate (BC5-α) (K_{cat} 0.6 h^{-1}). A diminished reaction turnover (by half) was witnessed in the elongated *"single"* β conjugate (BC5-L-β) (K_{cat} 0.29 h^{-1}).

7. Multiple turnover and kinetic studies indicated the presence of non-productive inter- and intramolecular complexes which can deaccelerate cleavage and dissociation. Self-association of the target substrate into hairpin and duplex structures resulted in the depletion of available substrate and conjugate inactivation which diminished the turnover number. Upon full activation, each conjugate can potentially destroy over 30-50 target molecules.

Future work: Although the designed POCs demonstrated considerable potency where a single catalyst molecule destroyed at least 10 target molecules, the obstructive effects of non-productive conformation prevented the conjugates from reaching their full potential. Future work should focus on the destabilisation and destruction of these non-productive conformations and increasing the potency of POCs. Kinetic modelling demonstrated that full activation of each POC can increase their potency by a factor of 3-5, allowing substoichiometric concentration of POCs in cellular environment.

6.3 Ultra-sensitive Detection of microRNA Biomarkers and their Disappearance upon Destructive Catalytic Treatment by Natural and Synthetic Ribonucleases (Chapter 4)

In this chapter, the bulge-loop conjugate design was directed towards biologically relevant targets (miR-21) [or miR-17, results presented in **Appendix 1**]. POCs were designed in such a way to induce 3-nt long bulges in the target miRNA sequence. Similar to Type 2 conjugates reported in **Chapter 2**, Acetyl-$[LRLRG]_2$-COOH peptide was conjugated to the antisense recognition motif via an internal abasic nucleotide with aminohexyl linker attached at C1' position. A self-assembling peptide hydrogel-based device was used for detection of POC-mediated miR-21 cleavage. The results acquired are summarised below:

1. All miR21-miRNases (miR-21_3β1, miR-21_3α1, miR-21_3β2 and miR-21_3α2) exhibited ribonuclease activity, as reflected in the increase in fluorescence intensity as a result of the de-assembly of the hybridised complex, with α conjugates exhibiting a higher extent of cleavage than β. A shift in bulge-loop position towards the 3'end of the target reduced ribonuclease activity.
2. No spontaneous cleavage was witnessed when miR-21 was incubated with unconjugated miR-21-miRNase oligonucleotide sequence in the absence of POC.

3. Conjugates exerted catalytic activity in multiple turnover mode (5-fold excess of target over conjugate) where each conjugate molecule destroyed about 2-3 copies of target.

4. miR-21-miRNases worked synergistically with RNase H where RNase H elevated the miRNase-mediated cleavage of miR-21 by a factor of 2.

Future work: The results presented here shows the promise of bulge-design to produce sequence-specific biologically relevant catalysts. However, ribonuclease activity was not tested in a cellular environment. It is therefore vital to test the inherent stability of conjugates in serum and investigate the biological performance. The effects of miR-21-miRNases on tumour cell proliferation and malignant behaviour should be tested in the future.

6.4 2'OMe Modification of Anti-miRNA-21 Oligonucleotide–Peptide Conjugate Improves Its Hybridisation Properties and Catalytic Activity (Chapter 5)

To test the effects of chemical modifications on serum stability, hybridisation and catalytic properties, 2'OMe modifications were introduced in the recognition motif of a miRNase with established catalytic activity. The catalytic moiety (acetyl-$[LRLRG]_2$-COOH peptide) was incorporated into a hairpin oligonucleotide in which recognition motif was either fully or partially modified. The summary of results obtained can be seen below:

1. Introduction of 2'OMe modification increased binding affinity of both fully and partially modified conjugates to target RNA.

2. No discernible increase in serum stability was witnessed in fully or partially modified conjugates. Indeed, half-life values remained constant regardless of modifications.

3. Full modification of the complementary region dramatically decreased catalytic activity whereas partial modification resulted in an increase in cleavage efficacy.

4. All conjugates exhibited strong antiproliferative effects with partially modified conjugate displaying the greatest antimigration effects on tumour cells.

Future work: Despite the encouraging cleavage, hybridisation and biological activity results, incorporation of 2'OMe modification did not lead to nuclease resistance. Moreover, 2'OMe modified duplexes are unable to recruit intracellular RNase H. Therefore, any advantage pertaining to this type of modification is forfeited *in vivo*.

Future work should focus on introducing RNase H-activating chemical modifications into the recognition motif of POCs at a distant position from the catalytic peptide.

Appendix 1: miR-17-miRNase

Table A.1. Sequences of the unconjugated oligonucleotides and peptides used for conjugate reactions along with their millimolar extinction coefficients.

Name	Sequence (5' to 3')	E_{260} ($mM^{-1}\cdot cm^{-1}$)[a]
Acetyl-[LRLRG]$_2$-CO_2H	Ac-Leu-Arg-Leu-Arg-Gly-Leu-Arg-Leu-Arg-Gly	n/a
miR-17_3α	CTACCTGCAC-**dR**^{alpha}-AAGCACTTTG [b]	186.1
miR-17_3β	CTACCTGCAC-**dR**^{beta}-AAGCACTTTG [b]	186.1

a) **E_{260} denotes the millimolar extinction coefficient**

b) **dR denotes abasic nucleotide incorporated in oligonucleotide seqeucne**

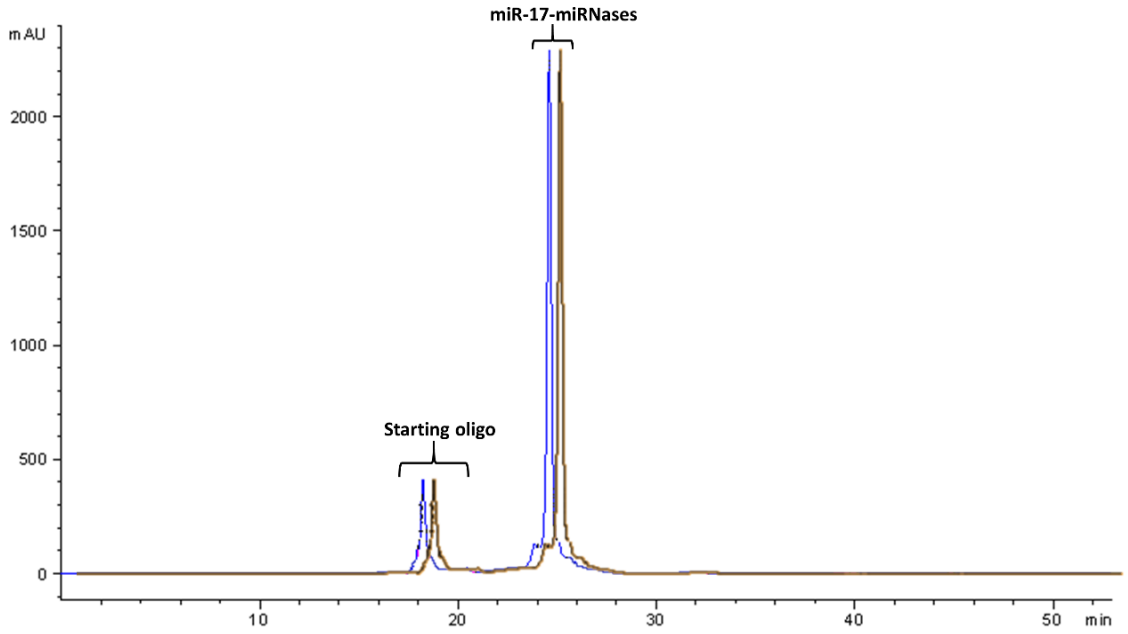

Figure A.1. An overlay of the RP-HPLC purification chromatogram of miR-17_3α (blue), miR-17_3β (orange) showing the shift in retention from unconjugated oligonucleotide to conjugate.

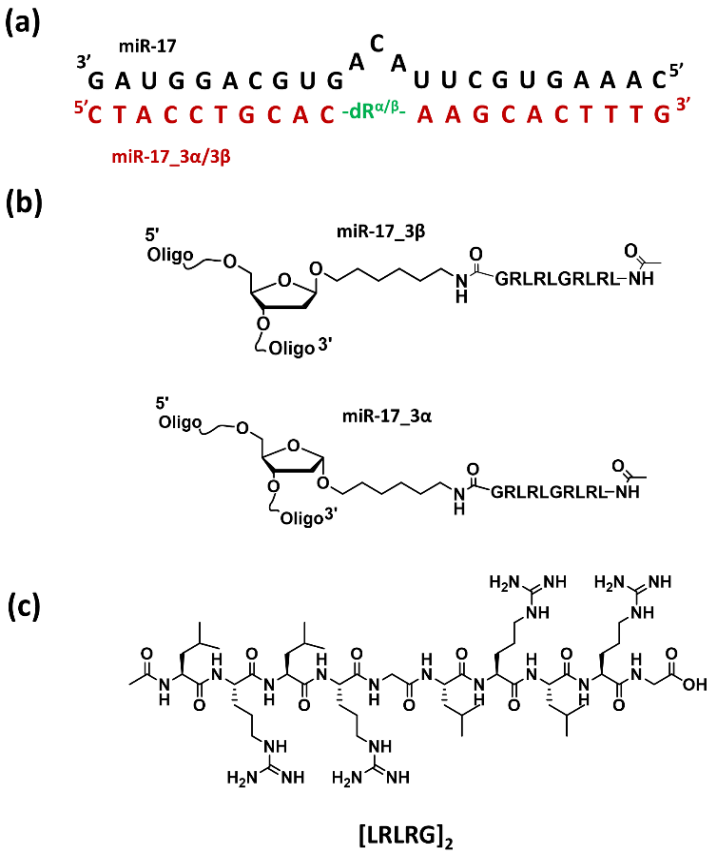

Figure A.2. General structure of miR-17-miRNases bulge-loop inducing peptidyl-oligonucleotide conjugates. **A.** Sequence of antisense recognition motif of the miR-17-miRNases and schematic representation of a general complex of miR-17 (in black) and miRNase (in red). Chemical structure of the abasic nucleotide with aminohexyl linker attached at C1' position is indicated with **dR$^{\alpha/\beta}$**. **B.** Chemical structure of bulge-loop inducing single miR-17-miRNases. The peptide acetyl-[LRLRG]$_2$-CO_2H was covalently attached via an aminohexyl linker to an abasic nucleotide in either α- or β-configuration. To avoid peptide self-conjugation and cyclisation during amide coupling reaction, the acetylated N-termini peptide was used. **C.** Chemical structure and nomenclature of Acetyl-[LRLRG]$_2$-CO_2H peptide used in synthesis.

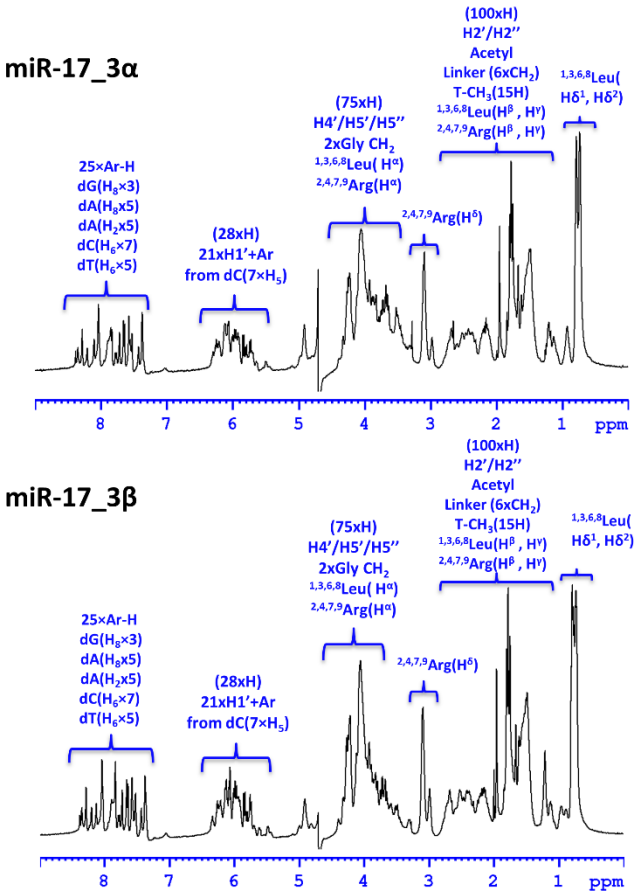

Figure A.3. ^{1}H NMR spectra (400 MHz, Bruker Avance IIþ 400) of single miR-17-miRNases conjugates indicating prominent chemical shift of protons from oligonucleotides, peptide, aminohexyl linker and acetyl protecting group. In each spectrum, the breakdown of proton assignment for each region as well as integral intensity has been indicated. H3' region has not been assigned since water suppression prohibits full assignment.

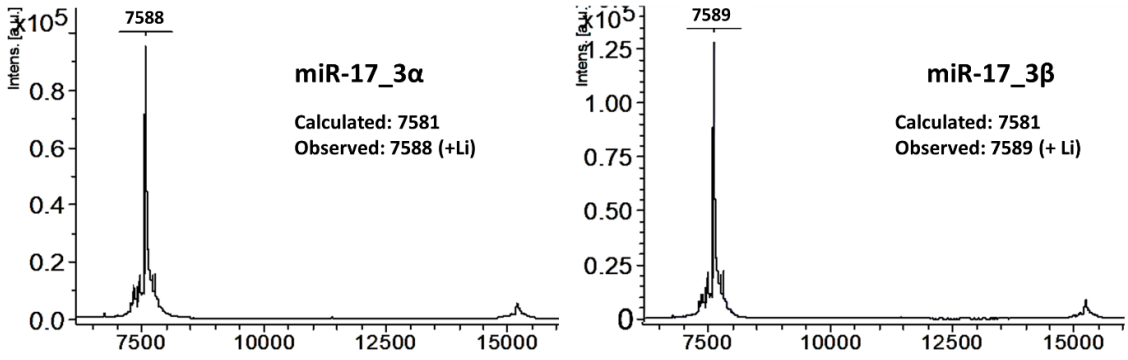

Figure A.4. MALDI-TOF spectra of bulge-loop inducing single miR-17-miRNases. Spectrum was recorded using 0.7 M 3-Hydroxy picolinic acid matrix (97 mg/mL, with 0.07 M ammonium citrate, 16 mg/mL in 50:50 ACN: H2O) on a Bruker Daltonics Ultraflex ToF/ToF mass spectrometer.

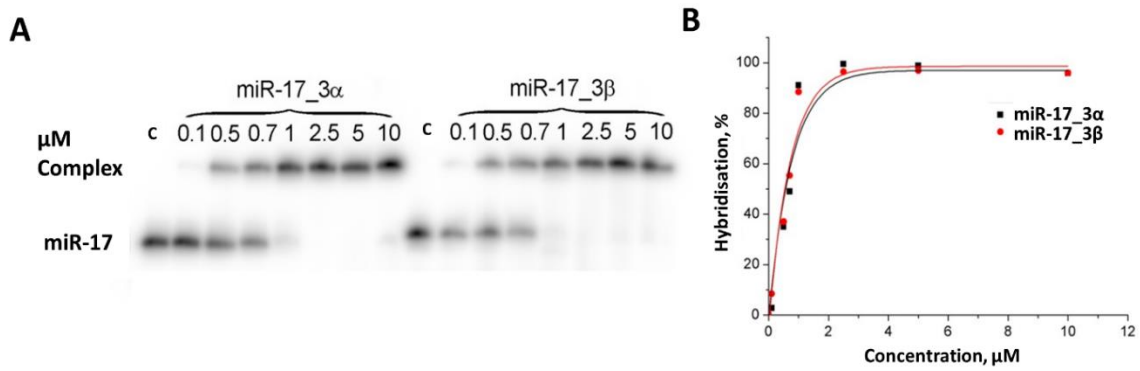

Figure A.5. Hybridisation of bulge-loop inducing single miR-17-miRNases. **A.** Representative images of the 12% PAAG showing binding of single miR-17-miRNases to the target. miR-17_3α and miR-17_3β (0.1 – 10 μM) was incubated with target miR-17 (1 μM) in Tris buffer (20 mM Tris-HCl (pH 7.8), 40mM KCl, 8 mM $MgCl_2$, 1 mM DTT) at 37°C For 45 min. Lane C was incubated without conjugates. **B.** Hybridisation efficiency of conjugates with miR-17 depending on concentration.

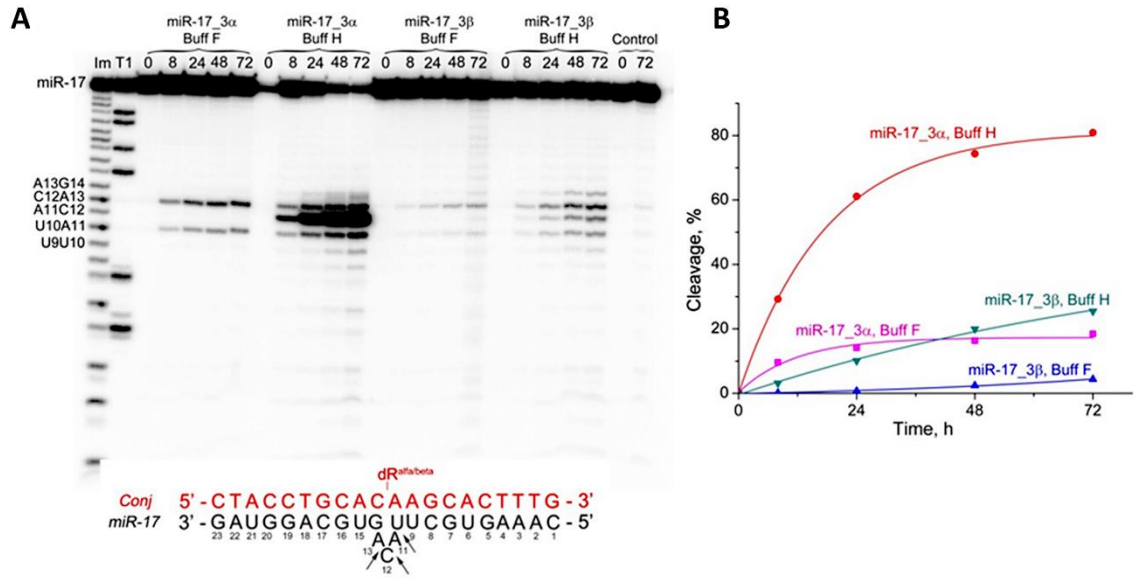

Figure A.6. Ribonuclease activity of bulge conjugates miR-17_3α and miR-17_3β targeted to miR-17. **A.** Representative images of 12% PAAM/8 M urea gel after electrophoresis of cleavage products with miR-17_3α and miR-17_3β. miR-17 (1 μM) and miR-17_3α or miR-17_3β (20 μM) were incubated at 37°C for 72 h in two cleavage buffers. Buff F: 50 mM Tris-HCl (pH 7.0), 200 mM KCl, 0.1 mM EDTA; Buff H: 20 mM Tris-HCl (pH 7.8), 40mM KCl, 8 mM $MgCl_2$, 1 mM DTT. **B.** Secondary plot of data indicating total cleavage extent (%) plotted against incubation time.